Fault Tolerant Flight Control
A Physical Model Approach

Thomas Lombaerts

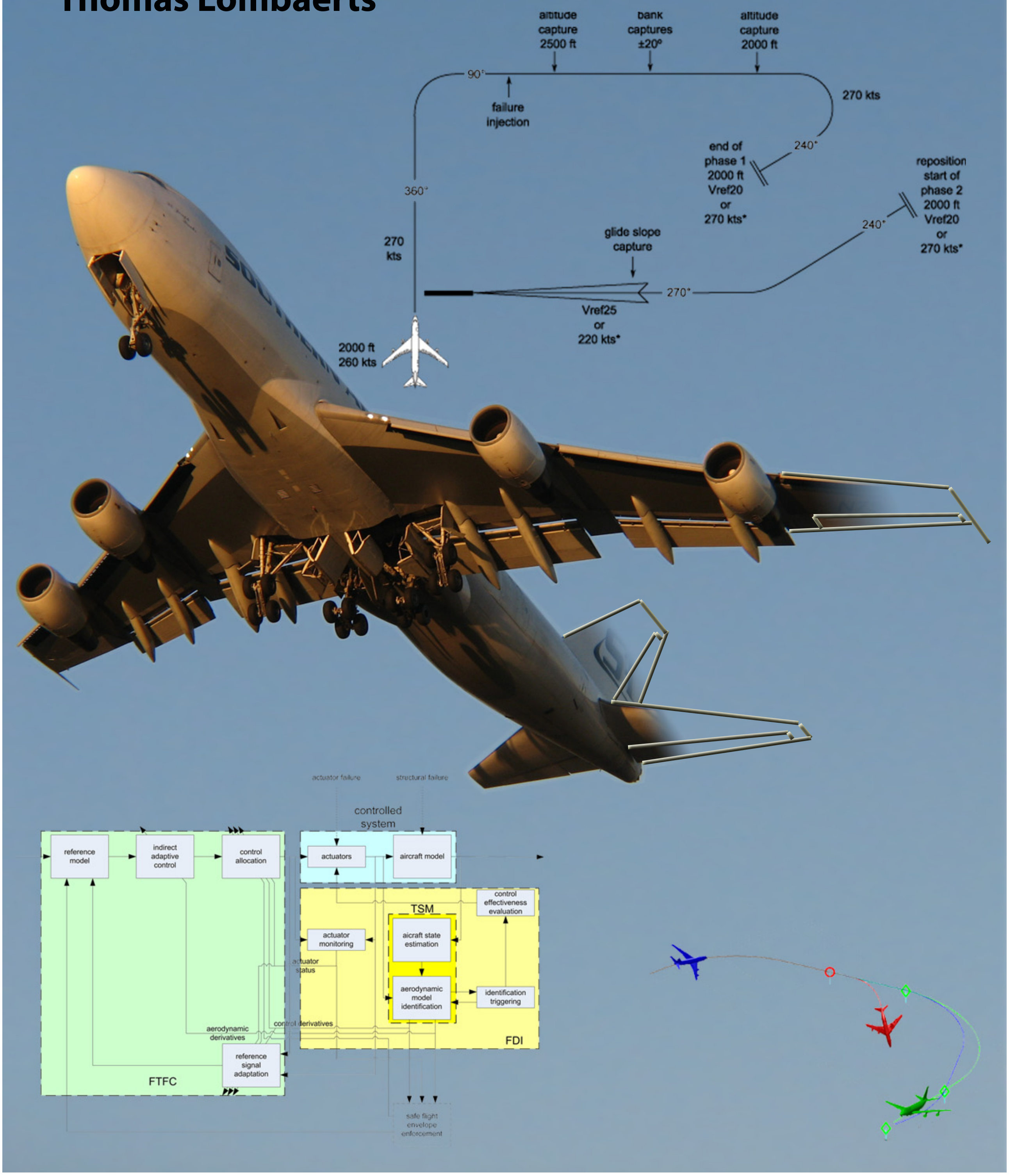

PhD. Thesis

Fault Tolerant Flight Control

A Physical Model Approach

T.J.J. Lombaerts

Fault Tolerant Flight Control

A Physical Model Approach

T.J.J. Lombaerts

ISBN 978-90-815443-1-3

Published and distributed by T.J.J. Lombaerts.

Printed by Wöhrmann Print Service, Zutphen, The Netherlands.

Cover design by T.J.J. Lombaerts
Cover picture by T.J.J. Lombaerts

Fault Tolerant Flight Control

A Physical Model Approach

PROEFSCHRIFT

Ter verkrijging van de graad van doctor
aan de Technische Universiteit Delft,
op gezag van de Rector Magnificus Prof. ir. K.Ch.A.M. Luyben,
voorzitter van het College voor Promoties,
in het openbaar te verdedigen
op dinsdag 25 mei 2010 om 15.00 uur

door

Thomas Jan Jozef LOMBAERTS

Ingenieur Luchtvaart en Ruimtevaart
geboren te Brussel (Etterbeek), België.

Dit proefschrift is goedgekeurd door de promotor:
Prof. dr. ir. J.A. Mulder

Copromotor:
Dr. Q.P. Chu

Samenstelling promotiecommissie:

Rector Magnificus,	voorzitter
Prof. dr. ir. J.A. Mulder,	Technische Universiteit Delft, promotor
Dr. Q.P. Chu,	Technische Universiteit Delft, copromotor
Prof. dr. ir. C. Edwards,	University of Leicester
Prof. Dr.-Ing. F. Holzapfel,	Technische Universität München
Dr. ir. G.H.N. Looye,	Deutsches Zentrum für Luft und Raumfahrt (DLR)
Prof. dr. ir. J.M. Maciejowski,	Cambridge University
Prof. dr. ir. M. Verhaegen,	Technische Universiteit Delft
Prof. dr. ir. M. Mulder,	Technische Universiteit Delft, reservelid

This dissertation has been completed in partial fulfillment of the requirements for the graduate study of the Dutch Institute of Systems and Control (DISC).

The research work presented in this thesis was financially supported by the Dutch Technology Foundation STW under project number 06515.

Part of the work presented in this thesis has contributed to action group FM-AG(16) on Fault Tolerant Flight Control in the European GARTEUR framework. The work presented in chapter 8 has been performed in cooperation with the German Aerospace Center DLR during a four month research visit in Oberpfaffenhofen.

”When once you have tasted flight,
you will forever walk the earth with your eyes turned skyward,
for there you have been,
and there you will always long to return.”
Leonardo da Vinci

To my parents, my brother Bart and Patricia

Summary

Fault Tolerant Flight Control, a Physical Model Approach

Thomas Lombaerts

Safety is of paramount importance in all transportation systems, but especially in civil aviation. Therefore, in civil aviation, all developments focus on the improvement of safety levels and reducing the risks that critical failures occur. When one analyses recent aircraft accident statistics, there are two major categories of accidents which can be attributed to a single primary cause. The largest category is ”collision with ground” (controlled flight into terrain, CFIT) where a fully functional aircraft hits terrain due to the loss of situational awareness by the pilot, which counts for as much as 26% of the accidents. This percentage is decreasing over the years thanks to the continuously evolving amount and manner of cockpit display information. The second major category is ”loss of control in flight”, which can be attributed to mistakes made by the pilot or a technical malfunctioning. This category counts for 17% of all aircraft accident cases and is not decreasing.

Analysing a major part of the accidents in the latter category has led to a common conclusion: from a flight dynamics point of view, with the technology and computing power available on this moment, it might have been possible to recover the aircraft in many accident situations in this category, on the condition that non-conventional control strategies would have been available. These non-conventional control strategies involve the so-called concept of active fault tolerant flight control (FTFC), where the control system is capable to detect the change in the aircraft behaviour and to adapt itself so that it can handle the perturbed aircraft dynamics. Earlier research projects in FTFC involve the Self-Repairing Flight Control System (SRFCS) program, the MD-11 Propulsion Controlled Aircraft (PCA), the Self-Designing Controller for the F-16 VISTA, Reconfigurable Systems for Tailless

Fighter Aircraft, the X-36 RESTORE program, the NASA Intelligent Flight Control System (IFCS) F-15 program and Damage Tolerant Flight Control Systems for Unmanned Aircraft by Athena/Honeywell. There are many alternative control approaches to achieve FTFC. In all these control approaches, there remain some problems and limitations, varying from the limitation to a restricted number of failure cases to the limitation of the type and extent of damage which can be compensated for due to fixed model structures for identification. Another frequently encountered issue are convergence problems. Besides, black box structures like for neural networks reduce the transparency of the approach. Moreover, for many approaches it is not clear what will happen when the reference model behaviour is not achievable in post-failure conditions.

The approach as elaborated in this thesis uses a physical modular approach, where focus is placed on the use of mathematical representations based on flight dynamics. All quantities and variables which appear in the model have a physical meaning and thus are interpretable in this approach, and one avoids so-called black and grey box models where the content has no clear physical meaning. Besides the fact that this is a more transparent approach, allowing the designers and engineers to interpret data in each step, it is assumed that these physical models will facilitate certification for eventual future real life applications, since monitoring of data is more meaningful.

Globally, the overall architecture of this modular approach consists of three major assemblies, namely the controlled system, the Fault Detection and Identification (FDI) assembly and the Fault Tolerant Flight Control (FTFC) assembly. The controlled system comprises the aircraft model and the actuator hardware. Possible failures in this controlled system are structural failures and actuator hardware failures in the latter. Sensor failures have not been considered in this research, since it has been assumed that effects of these failures can be minor thanks to sensor redundancy and sensor loss detection. However, the latter component is part of recommended future research.

The Fault Detection and Identification (FDI) architecture consists of several components. The core of this assembly is the two step method (TSM) module. This module consists of a separate aircraft state estimation step followed by an aerodynamic model identification step, where the latter is a joint structure selection and parameter estimation (SSPE) procedure. The state estimation step is a nonlinear problem solved by an Iterated Extended Kalman Filter. The preferred SSPE algorithm is Adaptive Recursive Orthogonal Least Squares. In case a structural failure occurs (in the aircraft structure or in one of the control surfaces), re-identification is triggered when the average square innovation exceeds a predefined threshold. For successful identification of the control derivatives of every individual control surface, control effectiveness evaluation is needed after failure. This can be done by inserting multivariate orthogonal input signals in the actuators. Although this must be done carefully such that the damaged aircraft cannot be destabilized, it is necessary in order to obtain sufficient control surface efficiency information for the control allocation module, to be discussed later. A valid approach might be to introduce these evaluation signals only when strictly needed, i.e. when successful reconfiguration is not possible due to a lack of this control efficiency information. The two step method is ideally suited to deal with structural failures, but for the detection of actuator failures a separate actuator monitoring algorithm is needed, such as an Actuator Health Monitoring System (AHMS).

Four other functions can be grouped to form the Fault Tolerant Flight Control (FTFC) assembly. The core for this group are indirect adaptive control and control allocation. Indirect adaptive control can be achieved by adaptive nonlinear dynamic inversion (ANDI). The advantage of ANDI is that it removes the need for gain scheduling over different operating conditions and it effectively decouples input-output relationships. Moreover, the NDI control algorithm automatically involves some form of control allocation, due to the structure of the control law. This structuring allows a clear separation how different failure types are dealt with. Structural failures independent of the control surfaces are detected by the TSM and this damage information is supplied to the ANDI algorithm by means of the aerodynamic derivatives. On the other hand control surface related failures, aerodynamics or actuator related, are identified by the TSM or the actuator monitoring algorithm respectively. This information is sent to the adaptive control allocation block. The preferred control allocation approach is found to be the control distributor concept (CDC), combined with the weighted pseudo inverse (WPI). This method assumes the presence of a large amount of similar control surfaces. This assumption holds for the type of aircraft considered in this research project, such as the Boeing 747. This approach fits in the modular setup of the global procedure, where the CDC principle takes into account aerodynamic changes and the WPI provides the adaptivity with reference to actuator failures. Furthermore, a reference model defines the reference signal that the closed loop configuration has to track. However, this reference model needs to be adaptive such that its signals are limited based upon the achievable performance of the damaged closed loop configuration. This reference signal adaptation can be achieved by Pseudo Control Hedging. This modulation is based upon the difference between the demanded input signal and the achieved input signal by the actuators. This reference signal adaptation is primarily driven by saturation effects. Besides, this hedging operation takes into account the updated model information via actuator status, aerodynamic derivatives and control derivatives. In this way, one makes sure that no unreachable reference signals are given to the closed loop configuration. This PCH operation can be considered as a first degree of safe flight envelope enforcement, based upon input saturation effects and updated model information. Experiments have shown that especially the throttle channel is prone to saturation effects.

During this research, it has been found that safe flight envelope enforcement is a crucial aspect in this control setup, and it is part of recommended future research. This protection algorithm, based upon the achievable performance which can be estimated based upon actuator status, aerodynamic derivatives and control derivatives, should contribute on two levels. On one hand, it has to assist the PCH algorithm by limiting the reference model output appropriately. Moreover, the output of the control allocation block, and thus the input to the actuators, should be limited based upon this reachable flight envelope information.

The main limitation of the indirect adaptive control approach as chosen here is that it relies on the certainty equivalence principle. This means that the controller parameters are computed from the estimates of the plant parameters as if they were the true ones. However, it has been shown that this assumption is not absolutely necessary when applied to ANDI. More precisely, it has been found that that the combination of ANDI and a linear controller in the outer loop is asymptotically insensitive for misfits in the estimates of the aerodynamic derivatives, especially thanks to the presence of integral action in the linear controller. On the other hand, this robustness does not hold for identification errors in the control derivative values. However, these estimates are well identifiable due to the control surface excitations which are steered directly.

This aforementioned modular control approach has been applied successfully on a high fidelity simulation model of a Boeing 747-100/200 aircraft, including several failure scenarios. One of the failure scenarios has been validated with real accident data, obtained from a digital flight data recorder. In this research, an automatic as well as a manually operated fault tolerant flight controller have been developed and implemented on this simulation model. The automatic controller satisfied most performance requirements and succeeded to keep the aircraft under control. The manual controller has been evaluated extensively in the SIMONA Research Simulator, and it has been found that the fault tolerant controller was successful in recovering the ability to control the damaged aircraft scenarios investigated in this research project. Simulation results have shown that the handling qualities of the fault tolerant controller devaluate less for most failures, indicating improved task performance. Moreover, it has been found that the average increase in workload after failure is considerably reduced for the fault tolerant controller, compared to the classical controller. The data shows more consistency amongst the pilots in most cases for the FTFC configuration. These observations apply for physical as well as compensatory (mental) workload. These extensive evaluations have led to the technology increasing in its Technology Readiness Level scale (TRL) level from 3/4 to 5/6.

During this research project, some comparative studies have been performed for the SSPE algorithm and for the ANDI setup, together with an optimization procedure for the outer loop linear controller gains in the ANDI setup. With respect to the SSPE procedure, two algorithms have been compared, namely Modified Stepwise Regression (MSWR) and Adaptive Recursive Orthogonal Least Squares (AROLS). Comparing both structure selection and parameter estimation procedures gives a clear advantage to the AROLS algorithm. First of all because of its recursive and computationally efficient nature which makes it suitable for real-time on-line applications. Compared with the modified stepwise regression procedure, it only needs a forward sweep, instead of combined addition and elimination criteria which apply for the latter. Moreover, no major modifications are required to AROLS for damaged aircraft applications, as opposed to MSWR which needs priority scheduling among the candidate regressors.

In the ANDI setup, a baseline control structure has been defined, consisting of a double NDI loop, and an improved control structure was developed, consisting of a triple NDI loop. Comparing simulation results from both versions shows clear improvements for the latter. The fact that the improved version has an additional inversion loop and relies on less assumptions, makes that it has more control authority and results in a larger flight envelope where it is capable to keep the aircraft under control compared with the baseline controller.

A multi-objective optimization procedure has been performed for parameter synthesis of the linear controller gains. This allowed to improve the controller gains based upon predefined optimization criteria while taking into account inequality constraints. Comparing this optimized result with the initial performance shows subtle improvements, especially in the speed disturbance rejections. Thanks to the good initial choice of control gain values according to the principle of time scale separation, no major improvement can be made in the field of gain tuning. However, Multiobjective Parameter Synthesis is still capable to enforce small improvements in the tuning so that optimal performance can be achieved with respect to the defined criteria.

An important and big next step in the development process of Fault Tolerant Flight Control is the application of this physical modular approach in a flying testbed, preferably a dedicated unmanned aircraft. This is an important recommendation for future research.

Contents

Chapter 1

Introduction

1.1 Towards more Resilient Flight Control

Within the aviation community, especially for commercial transport aircraft design, all developments focus on ensuring and improving the required safety levels and reducing the risks that critical failures occur. Recent airliner accident and incident statistics (published in 2008), [10], show that about 16% of the accidents between 1993 and 2007 can be attributed to Loss of Control In-flight (LOC-I), caused by a piloting mistake (e.g. due to spatial disorientation), technical malfunctions or unusual upsets due to external disturbances. Loss of flight control is a subcategory of Loss of Control In-flight (LOC-I), where a technical malfunction is the initial event which causes control loss. LOC-I remains the second largest accident category after Controlled Flight Into Terrain (CFIT) which accounts for 23% of air accidents. However, a short term study for the year 2008 shows that loss of control comes at the top in the list of catastrophic accidents, according to the UK Civil Aviation Authority (UK-CAA). Data examined by the international aviation community shows that, in contrast to CFIT, the share of LOC-I occurrences is not significantly decreasing. Resilient flight control, or fault tolerant flight control (FTFC), allows improved survivability and recovery from adverse flight conditions for occurrences induced by faults, damage and associated upsets. This can be achieved by 'intelligent' utilisation of the control authority of the remaining control effectors in all axes consisting of the control surfaces and engines or a combination of both. In this technique, control strategies are applied to restore stability and manoeuvrability of the vehicle for continued safe operation and a survivable recovery. The aim of this research is to explore new developments in fault tolerant control design and to implement these in practical and real-time operational aerospace applications. This addresses the need to improve the resilience and safety of future aircraft and aiding the pilot to recover from adverse conditions induced by (multiple) system failures and damage that would otherwise be potentially catastrophic. Up until now, faults or damage on board aircraft have been accommodated by hardware design using duplex, triplex or even quadruplex redundancy of critical components. However, the approach of the research presented in this thesis is to focus on new control law design methods to accommodate (unanticipated) faults and/or damage that dramatically change the configuration of the aircraft. These methods take into account a unique combination of robustness, reconfiguration and (real-time) adaptation of the control laws.

1.1.1 History of Flight Control Systems, source: [249]

Shortly after the German aviation pioneer Otto Lilienthal (1848-1896) left the ground for the first time in his self-made glider from the Windmuhlenberg (windmill hill) of Derwitz (Germany) in the summer of 1891, the problem of flight in a heavier-than-air vehicle created a new challenge: namely that of controlled flight. The Wright Brothers stated in 1912 that no one else grasped the basics of human flight as clearly and thoroughly as Lilienthal did. Based on his basic understanding of the principles of the curved wing, enabling it to produce more lift, Otto Lilienthal realized during his numerous experimental flights that leaving the ground was easier than staying in the air. For controlling his flights, he invented the first means of lateral stabilization using a vertical rudder. Just before crashing to his death in 1896, he characterized the complexity and importance of aircraft flight control by stating:

Figure 1.1: Otto Lilienthal (1848-1896) glider showing vertical tail for lateral stabilisation (1894), source: Otto Lilienthal Museum

> To design one is nothing, to build one is easy, to fly one is everything.

Following the first successful motorised flight of the Wright Brothers in 1903, the first artificially controlled flight was demonstrated in 1914 by Lawrence Sperry (1892-1923), the third son of the gyrocompass co-inventor Elmer Ambrose Sperry, by flying his Curtiss-C-2 airplane hands-free in front of a speechless crowd. The autopilot, or as it was nicknamed Metal Mike, consisted of three gyroscopes and a magnetic compass both linked to the pneumatically operated flight control surfaces. The autopilot enabled stabilized flight by holding the pitch, roll and yaw attitudes constant while maintaining the compass course. During the next decades, Sperry and other engineers further improved the concept of automatic stabilized flight for aircraft stabilization to improve weapon targeting accuracy. By the

Figure 1.2: Commercial and military aircraft that include modern fly-by-wire technologies (Airbus A380, Dassault Falcon 7X, Eurofighter Typhoon, Joint Strike Fighter, Boeing 777), sources: Creative Commons Attribution License, Kevin Koske, Naddsy, Keta

1950s, analog flight control computers allowed artificial modification of the aircrafts handling qualities on top of the basic stabilization functions of the autopilot. The Canadian Avro CF-105 Arrow interceptor, which flew in 1958, and the inherently unstable Lockheed Martin F-16 fighter, which entered service in the late 1970s, were the first aircraft utilizing an analog flight control computer demonstrating impressive manoeuvering capabilities. On the civil front, the Aerospatiale-BAC Concorde supersonic transport (SST) made its first flight in 1969 equipped with a commercial version of an analog flight control system. In 1972, NASA performed flight experiments with a modified F-8C Crusader to investigate the potential of software controlled flight, instead of analog circuits, by means of digital fly-by-wire flight control (DFBW) technology. Allowing better and safer airplane manoeuvering and control while providing substantial cost reductions, DFBW technology as a full-time critical digital control system, was made commercial in 1987 with the first flight of the Airbus A320. Although, in 1982, the Airbus A310 and then the A300-600 flew with digital FBW technology on the spoilers, the A320 was the first commercial use of digital FBW on the primary control surfaces.

During the evolution of aircraft flight control systems, several versions have been developed, dependent upon the moment in history and on the type of aircraft where they have been applied. In the following, three categories of aircraft flight control systems are described in more detail:

- mechanical systems
- mechanical-hydraulic systems
- fly-by-wire systems

Mechanical [176, 212]

The most elementary design of a flight control system is a mechanical one, consisting of cables, pulleys, capstans, levers and other mechanical devices. This kind of flight control system was used in early aircraft and is still used in current light aircraft, like the Cessna Skyhawk. Figure 1.3 illustrates a mechanical type of control system.

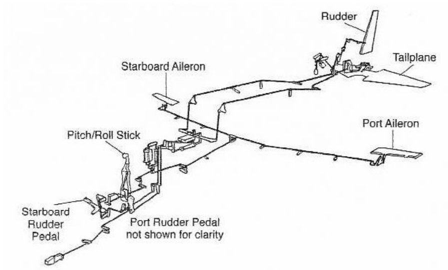

(a) roll, pitch and yaw channel of an early military jet, ©BAE Systems, Reproduced with permission

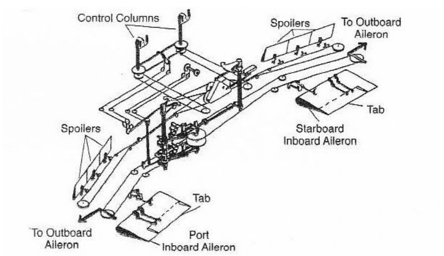

(b) roll channel of a transport aircraft

Figure 1.3: Illustrations of mechanical flight control systems, source: ref. [228]

In larger aircraft, the control loads due to the aerodynamic forces acting on the control surfaces are too excessive for simple mechanical control. Therefore, two mechanical solutions have been developed. One option is to attempt to extract the maximum possible mechanical advantage through the levers and pulleys, however the maximum reduction in forces is limited by the inherent strength of the mechanical components in this system. One example of this type of application can be found in the Fokker 50. The alternative is to rely on so-called control tabs or servo tabs that provide aerodynamic assistance to reduce complexity. These are small surfaces hinged at the end of the control surfaces which reduce the required control force exerted by the pilot by exploiting the aerodynamic forces which act on the tabs themselves. The pilot controls are directly linked to these control tabs, and the aerodynamic force generated by the tab then in turn moves the main control surface itself. The Boeing 707 used the concept of control tabs in its flight control system.

Hydro-mechanical [176, 212]

Due to the ever increasing size and flight envelopes of aircraft, mechanical flight control systems are not sufficient. Due to the increasing speed of the aircraft, it becomes more difficult to move the control surfaces as a result of high aerodynamic forces. This led to the application of hydraulic power. A hydro-mechanical control system consists of two parts:

- a mechanical circuit, essentially the same as the mechanical flight control system

- a hydraulic circuit

Compared to the mechanical flight control system, the hydraulic part takes over the interface between the conventional mechanical circuit and the control surfaces. More precisely, the hydraulic system generates the forces for the actuators which move the aerodynamic surfaces, but it still receives its signals from the mechanical circuit which is steered by the pilot. The Boeing 727 and 737, Trident, Caravelle and the Airbus A300, used such a flight control system, including a mechanical backup, despite the fact that a total loss of the flight control system is extremely improbable. The Boeing 747 was the first aircraft in the Boeing series to have a fully powered actuation system, because the control forces required for any flight condition would have been too large to be generated by the pilot.

The benefits of the hydro-mechanical flight control system compared to the purely mechanical one are the reduction in drag and the increase of control surface effectiveness due to the omission of the servo tabs. Moreover, the higher mechanical stiffness of the hydraulics leads to better flutter characteristics of the control surfaces. The main drawbacks of the hydro-mechanical control systems are its structural complexity and weight.

Fly-By-Wire Flight Control [176, 188, 212]

In more recent civil airliners, military transport aircraft and especially military jets, the mechanical linkage between control column and control surface has been omitted and replaced by electrical wirings (hence the name fly-by-wire). All these wirings are connected to each other by means of the flight control computer (FCC). Figure 1.4 shows the situation for the General Dynamics F-16 Fighting Falcon aircraft. The computer sends electronic signals to all actuators, in this specific case flaperons and slats.

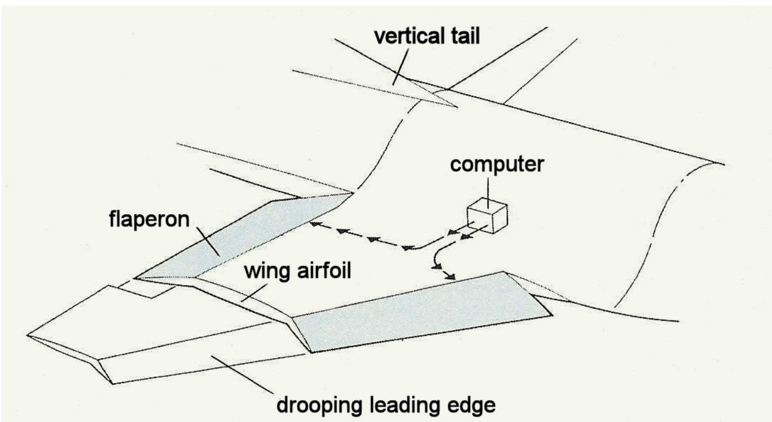

Figure 1.4: Illustration of the Fly-By-Wire principle on the F-16, source: ref. [108]

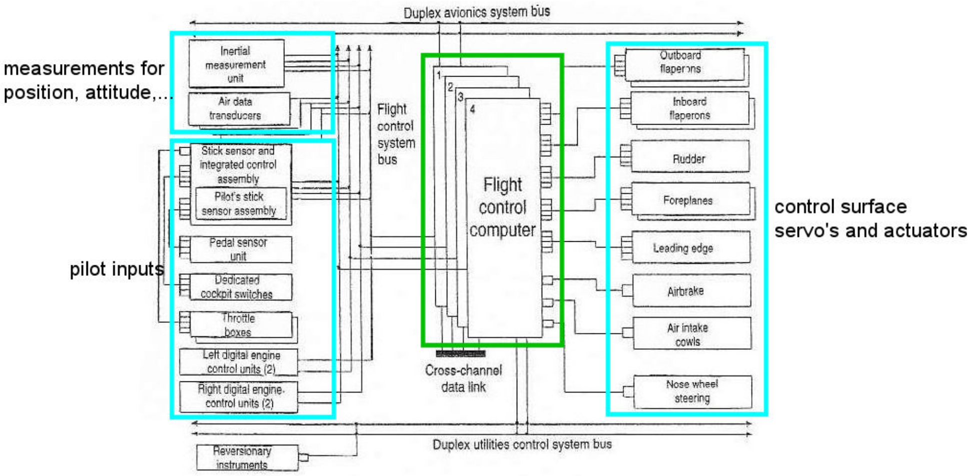

Figure 1.5: Flight Control System architecture of the Eurofighter Typhoon, ©BAE Systems, Reproduced with permission

Figure 1.5 shows the hierarchy of the wiring network for the Eurofighter Typhoon. The FCC bridges the gap between measurement signals (from the inertial measurement unit and the air data transducers) and pilot inputs (such as the pilot's stick, pedal and throttle displacements) on one hand, and control surface actuators (such as flaperons, rudder and canards) on the other. Based upon the pilot control inputs and the available measured signals, the computer calculates independently the required surface deflections and gives the appropriate commands to the servos. Note the quadruplex implemented FCC. This is the fail safety principle and the approach adopts a vote by majority principle. The same procedure is applied for the most essential components.

The advent of Fly-By-Wire Flight Control With the invention of the computer it became possible to control an aircraft electronically. The major initial advantages of the fly-by-wire FCS is that there is no longer a complex and heavy mechanical linkage needed between the pilot and the hydraulic system. But it is also possible to control the aircraft more accurately, flight safety is enhanced, a safe flight envelope can be defined with so-called flight control law protection, and finally this setup offers greater flexibility for evolution and for implementations of improvements in the system. During the subsequent evolution of the fly-by-wire concept, additional advantages arose, such as increased flexibility in setting the flight control characteristics of an aircraft. Another important benefit of Fly-By-Wire Flight Controls is that they define identical handling characteristics for all members of an aircraft family, from the smallest twinjet to the long-range widebody jetliners. This commonality does not only apply for the normal flight envelope, but also under extreme emergency conditions. With such a computer-based flight control system, other major advantages are that its design and maintenance are much simpler, while significantly reducing aircraft weight. Both commercial and military aircraft are now being developed with fly-by-wire flight control systems. For military aircraft, the benefits include increased agility and reduced supersonic trim drag (in conjunction with reduced static stability) and carefree handling. For commercial aircraft, the benefits include lower weight (attributed to flight controls), lower maintenance costs as well as passenger comfort and carefree handling. In both categories, the provision of flight envelope protection is another important benefit of fly-by-wire flight control systems.

How Fly-By-Wire Control works In contrast to mechanical and hydro-mechanical control systems, in a fly-by-wire system the pilot's commands are fed into computers, which in turn route electrical signals along wires to the actuators driving the control surfaces. Sometimes there is a mechanical backup to keep the aircraft under manual control when control of the aircraft becomes impossible with the nominal flight control system (electricity loss, the loss of all flight control computers, etc.). The computers controlling the fly-by-wire system provide multiple backup or redundancy. In the Airbus A340 for example, there are five computers in all, and a single one can fly the plane. All five computers work together. If one fails, another automatically takes over. Moreover, each of the five fly-by-wire computers is composed of two independent units which are constantly monitoring each other. Furthermore, these computers are made by different manufacturers, using different software and components. They are also programmed by independent teams, using different computer languages. This means that it is virtually impossible for the same problem to affect all computers simultaneously. It should be noted that the number of computers and units etc. differs for other aircraft in the Airbus family and also the Boeing philosophy is significantly different. The Airbus fly-by-wire system operates according to three control laws: normal, alternate and direct.

- The normal law applies when all systems are working correctly, or during a single failure of a computer or peripheral. It requires a high level of integrity and redundancy of the computers, the peripherals (i.e. sensors, actuators and servo-loop), and the hydraulics. When operating in normal mode, a forward or backward movement of the sidestick corresponds to a vertical load factor command by the pilot. The computers translate this demand into a pitch change, immediately moving the aircraft's nose up or down to the desired attitude. Once the sidestick is released, the aircraft will maintain this flight path until the next pilot input. Lateral control is similar to pitch control except that the pilot sets a roll rate command. Operation under normal laws provides flight envelope protection against excessive load factors, overspeed, stall, extreme pitch attitude and extreme bank angle.

- The alternate law applies when at least two failures occur. Within the normal flight envelope, the handling characteristics under alternate control laws are the same as under normal laws, if the integrity and redundancy are not enough to achieve the normal law with its protections. Out of the normal flight envelope, the pilot must take proper preventive action to avoid loss of control or high speed excursions, just as he/she would on a non-protected aircraft, but this holds only for manoeuvres corresponding to the protection that is lost.

- The direct law applies when more than two failures occur, if the alternate law can not be safely achieved. In the unlikely event of a multiple system failure, direct control laws provide the same handling characteristics as a good-handling conventional aircraft, almost totally independently of configuration and centre of gravity. The side-stick and control surfaces move in a direct relationship to each other. Pitch trim is no longer automatic and must be manually controlled using the trim wheel.

Flight Envelope Protection All aircraft have physical limits they must not exceed. For example, if the airspeed is too low the aircraft may stall, if the speed is too high or a manoeuvre too violent, excessive loads can be generated, with the risk of damaging the structure. These limits define the flight envelope, not to be exceeded during normal operation. The fly-by-wire concept offers inherent flight envelope protection, which is an additional guarantee against crossing these limits. Thanks to this built-in protection, pilots can count on their aircraft providing maximum performance and safety under any circumstances. The flight envelope protection function also protects against wind shear. These are strong, sudden downdrafts that may occur during storms or even in clear weather, and have caused many accidents. With a flight envelope protection system, the pilot can utilize maximum climb performance, escaping wind shear and other conditions in relative safety. It also increases the aircraft's agility. For example, the pilot can act much more quickly when he has to carry out a sudden avoidance manoeuvre, while keeping the aircraft under perfect control. Flight envelope protection does not limit the pilot's options, but rather allows him to use the aircraft's maximum safe performance capacity. At the same time, the system minimizes the risk of losing control of the aircraft or subjecting it to loads it was not designed to handle.

1.1.2 Fault Tolerant Control in Fly-by-Wire Systems, [249]

In aviation, all developments focus on the improvement of safety levels and reducing the risks that critical failures occur, on all possible system levels. Although most civil transport fly-by-wire aircraft are fitted with a backup system, the basic FBW system integrity is considered as critical. In Boeing and Airbus aircraft, where a total loss of the FCS is already very improbable, and beyond the certification requirements, see [86, 90], there is a mechanical or electrical back-up system. To further improve the levels of integrity, new aircraft configurations have a degree of redundancy in terms of controls, sensors and computing. Control effector redundancy means that there are more than the minimum required control effectors, or motivators, to control the pitch axis on one hand, and the combined roll/yaw axis on the other, although the full set of controls is required to satisfy the normal performance requirements. The combination of these features provides the opportunity to reconfigure the control system in the event of failures with the aim of increasing the survivability of the aircraft. As a result, the digital fly-by-wire flight control system is a safety driven design built to very stringent dependability requirements. These requirements ensure that the system will not generate erroneous or faulty signals compromising flight safety and that the system remains available even in faulty conditions. The certification requirements state that all potentially catastrophic failure scenarios should have a probability rate of less than 10^{-9} per flight hour and no single failure should be catastrophic. Potentially catastrophic failures include control surface runaways (elevator, rudder and horizontal stabiliser), loss of control in pitch, oscillatory failures at frequencies which are critical to the aircraft's structure and insufficient lateral control during engine failures. Failure detection and reconfiguration is performed via self-tests, signal comparison and hardware and software redundancy. Self-tests are performed by the hardware equipment to prevent any undetected failures (latent failures) and to ensure that the probability of a failure remains low.

Airbus philosophy, sources: [104, 169]

In Airbus aircraft, comparison of signals from both control and monitoring channels enables detection of failures in the case that one of the signals differs from the other above a certain threshold. The detection threshold should be sufficiently robust against sensor inaccuracies and system tolerances to prevent false alarms but tight enough to detect unwanted failures. Hardware reconfiguration in the Airbus family is performed at system level whereby for each function one computer operates in active mode, and the remaining computers are in standby mode. When the active computer fails, one of the standby computers changes to active mode and immediately takes over the function. This holds for example for servo-loops in the case of a duplex architecture. Flight control law reconfiguration is performed in the case when sensor information, processed by the control laws, becomes unavailable or no longer trustworthy (for example, one source failed, followed by a disagreement between the two remaining sources). This control law reconfiguration is also performed in the case of flight control surface or hydraulic circuit loss. In this situation, the flight control computer switches to alternate control laws providing less protection depending on the remaining sensory information and equipment. A FBW system architecture showing its redundancy components and reconfiguration scheme (Airbus A340 [49, 169, 104]) is illustrated in fig. 1.7. Moreover, the flight control computer (FCC) architecture is a so-called COM/MON architecture where the fail-safe computers consist of a control and monitoring channel, ensuring the permanent monitoring of all the FCS components. The control channel executes the relevant function (e.g. a pilot command to a surface) while the monitoring channel guards against any faults in the control channel and ensures permanent monitoring of all the components in the flight control system (sensors, actuators, other computers, etc. ...). The monitoring (MON) channel is designed to detect failure cases and to trigger reconfiguration by pointing out the failure detection to the command (COM) channel and to the other computers. Fault mitigation is achieved by means of redundancy and software and hardware dissimilarities. In the case of the Airbus A340, the redundancy components include five FBW computers and three power sources for surface actuation. Dissimilarity is achieved through the use of two completely different types of computers and two independently developed software packages designed by different teams. It should be noted that these numbers vary for other aircraft as well as for other manufacturers. Reconfiguration, for instance in pitch, consists of switching from the Primary computer (P1) to the second Primary computer (P2). In this situation, elevator actuation switches from the green system for both elevators to the blue system for the left elevator and the yellow system for the right elevator. Following a possible failure of P2, reconfiguration can be performed up to the second Secondary computer (S2).

Figure 1.6: Hainan Airlines A340-642 B-6510, ©Thomas Lombaerts

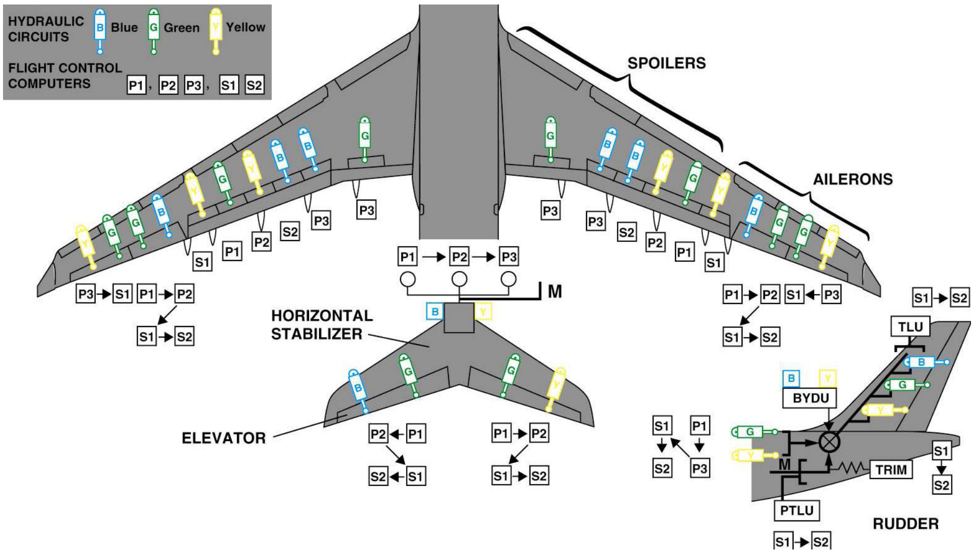

Figure 1.7: Modern fly-by-wire system architecture including redundancy components and reconfiguration scheme (A340), source: [169]

Boeing philosophy, sources: [113, 293]

A completely different fault tolerance approach has been adopted by Boeing in the Boeing 777 for example. The heart of its FBW concept is the use of triple redundancy for all hardware resources, varying from the computing system through electric and hydraulic power to the communication path. The 777 FBW design philosophy for safety considers the following constraints:

1. Common mode/common area faults: by designing the systems to both component and functional separation requirements.

2. Separation of FBW (line replaceable unit LRU) components: isolation and separation of redundant flight control elements to the greatest extent possible in order to minimize the possibility of loss of function.

3. FBW functional separation: allocation of electrical power to the primary flight computer (PFC) and the actuator control electronics (ACE) LRUs to provide maximum physical and electrical separation between the flight control electrical buses. The ACE functional actuator control is distributed to maximize controllability in all axes after loss of function of any ACE or supporting subsystem. The hydraulic systems are also aligned with the actuator functions to provide maximum controllability after the loss of hydraulics in one or two systems.

4. Dissimilarity: various combinations of dissimilar hardware, different component man-

ufacturers, dissimilar control/monitor functions, different hardware and software design teams, and different compilers are considered at the level of PFCs, ACEs, inertial data, the Autopilot Flight Director Computer (AFDC) and ARINC bus.

5. The FBW effect on the structure: FBW component failures can result in oscillatory or hardover control surface motion. Structural requirements are analysed and apportioned to all FBW components. (This constraint is a safety consideration in the Airbus philosophy too.)

The system is designed to provide uninterrupted control following any two failures. Although the flight control function is necessary for safe flight and landing of the aircraft, the system includes a direct backup mode that allows the pilot to electrically position flight control surfaces without using the flight control computers. The flight control computers are configured as a Triple Modular Redundancy (TMR) system. Because of concerns about generic hardware or software failures, each of the three computers is itself a TMR unit. These TMR computers use three internal channels that use different processor hardware from different manufacturers. Within each TMR computer, the choice of which output is to be the output of the computer is determined using the so-called principle of median value select.

Figure 1.8: KLM Boeing 777-206/ER PH-BQD, ©Tommy Desmet, via airliners.net

Each PFC lane operates in two roles: a command role or monitor role. Only one lane in each channel is allowed to be in the command role. The command lane will send the proposed surface commands, its own, together with those received from two other PFC channels, to its ARINC 629 bus. The hardware device residing in the PFC lane will perform a median select of these three inputs of each variable. The output of the median select hardware is sent in the same wordstring as the 'selected' surface commands. The PFC lanes in the monitor role perform a 'selected output' monitoring of their command lane. The PFC command lane, meanwhile, performs 'selected output' monitoring of the other two PFC channels. The median value select provides fault blocking against PFC faults until the completion of the fault detection and identification and reconfiguration via PFC cross-lane monitoring.

Should any of the three dissimilar processors produce an output different from the other two, it will not be selected. The three dissimilar processors are kept tightly synchronized and receive bit identical input data from the system data buses. The three channels of computers at the next level of TMR are also kept in synchronization and exchange data

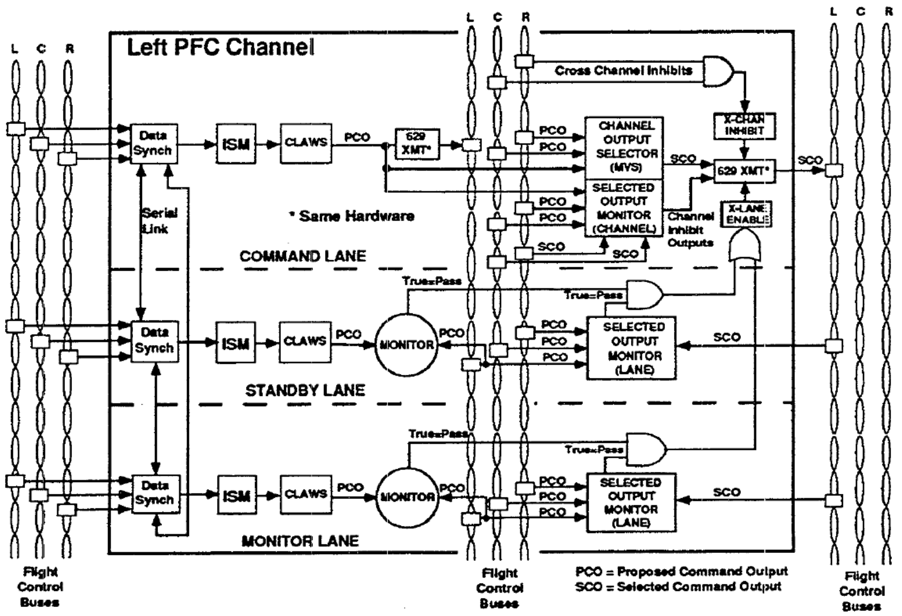

Figure 1.9: Boeing 777 PFC Lane Redundancy Management (Output Signal Monitoring), source: [293]

to keep state data consistent between the channels. The 777 actuators rely on the vote by majority principle.

Short case study of other fault tolerant systems, source: [113]

Many fault-tolerant control systems have been produced and used successfully for other aerospace applications. The following is a brief survey of a few of these other systems with a discussion of the requirements they satisfy and the design approach that was used. The systems described were selected based on the availability of information and the personal experience of the author of ref. [113]. These are believed to be representative of the many excellent systems in use. Tables 1.1 and 1.2 form a summary of the systems surveyed and capture the primary attributes of these systems.

Table 1.1: Survey of typical in-service fault-tolerant systems, part 1, source: ref. [113]

Application	Vehicle & System Type	Impact of Loss of Function	Impact of Malfunction	Fault-Tolerant System Description
Military Aircraft	F-16 FBW flight control, analog	loss of aircraft control	loss of aircraft control	4-channel analog computer NMR identical hardware, approx. agreement MVS computer selection, MVS on computer inputs, voting hydraulic actuators, analog integrator states held consistent
Military Aircraft	F-16 FBW flight control, digital	loss of aircraft control	loss of aircraft control	4-channel digital computer NMQ identical hardware and software, simple analog backup control, voted computer selection, voted computer inputs, voting hydraulic actuators, digital state data exchanged and kept consistent
Commercial Aircraft	B-757, Pratt & Whitney PW2037 jet engine control	shutdown engine, land using one engine	mechanical overspeed protection, shutdown engine	Dual standby system
Manned Space	Space Shuttle	loss of vehicle and crew	loss of vehicle and crew	4-channel NMR, identical hardware and software, 5th channel backup using same hardware but dissimilar software, identical inputs by data bus monitoring, computer outputs compared for crew annunciation only, computer selection by external voters (hydraulic voting actuators, pyro fire electronic discrete voting), exchange and vote of some state data
Commercial aircraft	B-777, AIMS	limp home on backup instruments	potentially hazardous faulty display data	Two separate units, one for pilot and one for copilot displays, each unit uses 3 sets of selfchecking dual processors, Arinc-659 Safebus to distribute identical inputs, select output from a healthy pair, exchange state data, identical hardware and software in all processing pairs

Table 1.2: Survey of typical in-service fault-tolerant systems, part 2, source: ref. [113]

Application	Vehicle & System Type	Impact of Loss of Function	Impact of Malfunction	Fault-Tolerant System Description
Unmanned space	Inertial upper stage, flight controller	destruction of vehicle by range safety	destruction of vehicle by range safety	Dual self-checking pair processing, no dissimilar hardware or software, both pairs must send same critical actuation signals
Manned space Experimental	X-33 Reusable Launch Vehicle	destruction of vehicle by range safety	destruction of vehicle by range safety	TMR 3 identical COTS hardware and software channels, RMS provides same inputs by exchange and MVS, voting of outputs and some state data, dual actuation, transient fault recovery
Manned space Experimental	X-38 Crew Return Vehicle	loss of vehicle	loss of vehicle	NMR 4 identical hardware and software channels, identical inputs by exchange and voting, voting of outputs transient fault and state data recovery, any 2 FCCs can control single fault tolerant actuation.

F-16 Analog Fly-by-Wire Flight Control [21] Early production F-16A/B aircraft used an analog electronic FBW flight control system. From Block 25 F-16C/D onward, a digital system has been used. The F-16 is an inherent unstable aircraft that requires continuous stability augmentation. In case of problems with the flight control system, the F-16 aircraft can fail catastrophically. The system was designed to deal with two failures. The analog FBW used a quad-redundant N-fold Modular Redundancy (NMR) computer architecture with approximate consensus Middle Value Selection (MVS) electronics to determine which computers' signals are transmitted to the flight control actuators. The hydraulic actuators include voting to reject possible faulty outputs from any computer MVS or its servo amplifier. Both the computer MVS electronics and the hydraulic actuators make use of fault down logic to disengage a known, faulty signal. The analog computers use MVS on the sensor inputs to provide the same inputs to the redundant computers. Analog control integrators, the only state data involved, are held in agreement between the redundant channels by means of cross-connecting signals. The design uses neither design diversity (identical hardware) nor software.

Figure 1.10: Belgian Air Component F-16AM FA-126, ©Dirk Voortmans, via Airliners.net

F-16 Digital Fly-by-Wire Flight Control [24] Experience with a triplex digital system on the AFTI/F-16 gave General Dynamics the confidence to abandon the proven analog FBW system of the earlier Fighting Falcon and adopt the quadruplex digital FBW system for the Block 25 and beyond F-16C/D. This choice resulted in capability and integration advantages with other aircraft systems, such as displays via 1553 buses. The quad-redundant analog NMR computers used in earlier production F-16A/Bs were replaced by quad-redundant digital computers. These digital computers also include simple analog backups in each computer to protect against generic hardware or software design error failures. Digital data exchange is used between computers for various reasons, namely to mechanize computer output voting, to ensure identical inputs, to keep the computers synchronized, and to maintain consistent state data.

Figure 1.11: AFTI/F-16, source: NASA Multimedia Gallery

Pratt and Whitney PW2037 Electronic Engine Control [163] The PW2037 was the first production commercial jet engine to use a Full-Authority Digital Electronic Control (FADEC) system with no mechanical backup control. It was introduced on the Boeing 757 civil airliner and remains representative of state of the art commercial engine controls. Because all commercial transport aircraft have at least two engines, loss of thrust from one engine is not catastrophic. An engine control malfunction leading to a potentially catastrophic engine overspeed is mitigated by mechanical overspeed protection. Because of this, electronic engine controls are capable of meeting FAA safety requirements using a dual standby system. In the worst case scenario, an engine control failure not detected by BIT (Built-In-Test) will trip the overspeed protection, resulting in the shutdown and loss of thrust from one engine only. Also this set-up does not rely on hardware design diversity. The risk of a common design error affecting both channels of one engine or all engines on the aircraft is addressed through exhaustive testing.

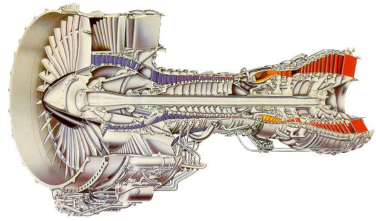

Figure 1.12: Pratt & Whitney PW2037, source: Pratt & Whitney

Boeing 777 Airplane Information Management Systems (AIMS) [82] The B-777 AIMS system is used to command all cockpit displays and to interact with the crew via keyboards to provide flight management functions. Total loss of cockpit displays, a system loss of function, is potentially hazardous, particularly in adverse weather, but is not by itself a catastrophic event. A malfunction resulting in erroneous display information to the crew is possibly a greater hazard, which is mitigated somewhat by requiring that pilot and copilot displays are driven by different sources, allowing the crew to detect faulty display data by proper cross-checking. In addition to requiring fault tolerance for safety, airline operators of transport aircraft desire systems that can be operated safely with known failures until repairs can be made without interruption to revenue-generating aircraft service. For this purpose, the so-called Minimum Equipment List (MEL) has been defined, which is specific for every aircraft and type of operation, and approved by the appropriate authority. The AIMS is required to fail operationally only after two failures and must provide very robust protection against malfunctions that would produce erroneous crew displays. AIMS uses a triple, self-checking pair architecture. The complete system actually consists of two separate triple self-checking units in separate cabinets, separately driving the pilot's and copilot's displays. This allows the flight crew to manually compare displays. The AIMS uses the same hardware and software in both systems and in all self-checking pairs, so they do not provide dissimilarity for protection against a generic software error. A unique type of backplane bus, the Arinc-659 'Safebus', is used to mechanize switchover between the redundant self-checking pairs and to provide a robust method for transferring state data between the processor pairs. Switchover to backup occurs when the backup processor pair detects that the primary processor pair has failed to transmit its data on the Safebus.

US Space Shuttle FBW Flight Control [127] Together with the McDonnell Douglas F/A-18 Hornet, the Space Shuttle was one of the first digital FBW flight control systems and remains a representative example of today's systems. The Space Shuttle is a very demanding control problem throughout an extensive flight envelope, requiring a single system that provides uninterrupted control of a space launch vehicle, control of an orbiting spacecraft, and both space and atmospheric flight control during the return to Earth. The shuttle uses a four-channel NMR approach, with a fifth computer used as a backup system. The fifth computer uses no hardware design diversity compared to the other four, but is programmed with dissimilar software. The fifth channel can be engaged manually by the crew in case the primary system fails, but this has never been necessary during the 100+ Shuttle flights to date. The Shuttle operates the four primary computers as a redundant set, providing them with identical input data by monitoring the same data buses and holding the computers in close synchronization. The computers are programmed with the same software and should produce the same outputs. No attempt is made by the computers to select the correct output, but instead, these redundant outputs are transmitted to external voting devices. On one hand, these external voters include voting hydraulic actuators for control surfaces and thrust vector control. On the other hand, there are electronic discrete command voters that control pyrotechnic ignition of the Shuttles engines and to separate the solid rockets and the external tank. The redundant computers do exchange and compare outputs in order to alert the crew if a computer is producing a different output from the others. The crew may then choose to remove power from a faulty computer to configure the system to operate following additional failures. In fact, this is a manual fault down.

Figure 1.13: Space Shuttle, source: NASA Multimedia Gallery

Boeing Inertial Upper Stage (IUS) Guidance and Control System [48] The IUS is an example of a typical high-value unmanned space launch vehicle guidance and control system. This IUS has been used to launch the spacecraft Ulysses, Galileo and Magellan in the right orbit for interplanetary missions after they have been brought to space in the cargo bay of the Space Shuttle. Space launch vehicles must provide a high level of reliability to be economical and must not malfunction in a manner that endangers human safety or property. In the event of a malfunction, ground crews can monitor the vehicle and command destruction thanks to the incorporation of a vehicle self-destruct system and range safety systems. The control system for the IUS uses four processors configured as a dual self-checking pair. The switchover from the primary processor pair to the backup pair will occur if there is disagreement between the processor pairs. A form of electronic voting is used for critical pyrotechnic signals, requiring both processor pairs produce the same command to these actuators.

Figure 1.14: Boeing Inertial Upper Stage (IUS), source: Boeing Multimedia Gallery

X-33 Reusable Launch Vehicle Control System [40] The X-33 program was a technology demonstrator for the next generation of single stage to orbit reusable launch vehicles. This prototype was unmanned. Thus, a control system failure would have primarily economic consequences. A TMR (Triple Modular Redundancy) fault-tolerant computer with dual standby actuation was selected to guarantee a high probability of successfully completing a series of sub-orbital test flights. The system used commercial-off-the-shelf (COTS) computers with custom Redundancy Management System (RMS) hardware and software to form the TMR fault-tolerant computer. It was planned to expand from TMR to quad NMR and to increase the level of actuation redundancy for the manned, operational system, for which even higher safety requirements would be imposed, however budget cuts and technical troubles have led to the cancellation

Figure 1.15: X-33 Reusable Launch Vehicle, source: NASA Multimedia Gallery

of these plans. The TMR computers used MVS to vote outputs, maintain identical inputs, and to maintain consistent state data. Voting was selectively applied to some, but not to all data, to minimize the data exchange and voting required. The TMR computers were designed in order to fault down to a self-checking pair after one persistent failure. The system was designed to recover the use of a computer that had experienced a transient fault. The COTS computers and the software that runs on them are identical: no dissimilarity was used to protect from generic design errors.

X-38 Prototype Crew Return Vehicle (CRV) Control System [22] The X-38 program was an unmanned technology demonstrator for a reentry vehicle that would be used for emergency return from the International Space Station. However, budget cuts have led to the cancellation of this development program after a few unmanned demonstrator test flights. The demonstration system was required to operate following any two Flight Control Computer (FCC) failures and following any one non-computer failure. A four channel NMR FCC with dual standby actuation was selected to meet these requirements. Sensors and actuators were connected to the FCCs such that any two operating FCCs can control the vehicle. The FCCs were COTS computers and were interconnected by special network element hardware and fault tolerant systems serviced software to form a Fault Tolerant Parallel Processor (FTPP). The FTPP was designed to provide resilience to Byzantine failures. A Byzantine fault is an arbitrary fault that occurs during the execution of an algorithm by a distributed system. It encompasses those faults that are commonly referred to as ”crash failures” and ”send and omission failures”. When a Byzantine failure has occurred, the system may respond in any unpredictable way, unless it is designed to have Byzantine fault tolerance. These arbitrary failures may be loosely divided into three categories, namely a failure to take another step in the algorithm (crash failure), a failure to correctly execute a step of the algorithm, and arbitrary execution of a step other than the one indicated by the algorithm. The FTPP was also designed to discriminate between transient and permanent faults, allowing recovery of an FCC that had a transient fault. The COTS computers and the software that ran on them were identical, no dissimilarity was used to protect from generic design errors.

Figure 1.16: X-38 Prototype Crew Return Vehicle, source: NASA Multimedia Gallery

A final note on fault tolerance properties incorporated in current fly by wire flight control systems

Based upon this information, it is clear that up to now, faults or damage on board an aircraft like computer failures, power/hydraulic failures, engine failures, linkage breaks and sensor failures, have been accommodated by hardware design. Critical components (flight control computers, actuators and sensors) have been implemented duplex, triplex or even quadruplex redundantly. Additionally, one can choose distributed systems and alternate controls or sensors. As a consequence, today's research efforts are gradually shifting from correcting additive failures (sensors and actuators) towards dealing with parametric failures (major structural and engine failures). The approach discussed in this thesis is to focus on control law design such that more severe kinds of faults and/or damage, like aerodynamic changes (damage), control surface damage and actuator failures can be tackled. This can be done by means of robustness, reconfiguration and adaptation of the control laws. This method of control law design is motivated by a survey of recent LOC-I accident cases in which the control and performance capabilities of the aircraft were compromised due to the failure of one or more critical systems and structural damage.

1.2 Rationale of Damage Tolerant Control - Aircraft Accident Survey

Recent flight control research activities are currently exploring the potential benefits of fault tolerant flight control (FTFC) techniques, in particular the mitigation of (severe) damage to the aircraft and its systems using reconfiguration methods. The reason for this is the observation that a considerable number of aircraft accidents over the last thirty years could possibly have been prevented in one way or another if considered from an aeronautical-technical point of view. A reconfigurable flight control system might have prevented the loss of two Boeing 737s due to rudder actuator hard overs and of a Boeing 767 due to inadvertent asymmetric thrust reverser deployment. The 1989 Sioux City DC-10 incident is an example of the crew performing their own reconfiguration using asymmetric thrust from the two remaining engines to maintain limited control in the presence of total hydraulic system failure. The crash of a Boeing 747 freighter in 1992 near Amsterdam, the Netherlands, following the separation of the two right-wing engines was potentially survivable given adequate knowledge about the remaining aerodynamic capabilities of the damaged aircraft. New forms of threat within the aviation community have recently come into play from deliberate hostile attacks on both commercial and military aircraft. A surface-to-air missile (SAM) attack has recently been demonstrated to be survivable by the crew of an Airbus A300B4 freighter performing a successful emergency landing at Baghdad International Airport after suffering from complete hydraulic system failures and severe structural wing damage. Apart from system failures and hostile actions against commercial and military aircraft, recent incident cases also show the destructive impact of hazardous atmospheric weather conditions on the structural integrity of the aircraft. In some cases, clear air turbulence (CAT) has resulted in aircraft incurring substantial structural damage and loss of engines.

An increasing number of measures are currently being taken by the international aviation community to prevent LOC-I accidents due to failures, damage and upsets for which the pilot was not able to recover successfully despite available performance and control capabilities. This not only includes improvements in procedures training and human factors, but also finding measures to better mitigate system failures and increase aircraft survivability in the case of an accident or degraded flight conditions. Six recent airliner LOC-I accidents will be described in detail which demonstrate that better situational awareness or guidance would have recovered the impaired aircraft and improved survivability if unconventional control strategies were used. In some of the cases described, the crew was able to adapt to the unknown degraded flying qualities by applying control strategies (e.g. using the engines effectors to achieve stability and control augmentation) that are not part of any standard airline training curriculum. A selection of the accident cases as described in this chapter formed the basis for the reconstruction of realistic and validated aircraft accident scenarios as part of the simulation benchmark. This was partly based on available flight data of the accident cases, simulation models and results from earlier studies. Although the accident survey in this chapter shows that the aircraft propulsion system can be used as the only effective means of controlling and landing a damaged aircraft when the complete flight control system is lost, this control strategy has not been investigated (despite having evaluated some control options using differential thrust for stabilisation). This is mainly due to the additional design requirements on engine performance (e.g. response time) and health monitoring to allow them to be used as an integrated part of the flight control system. This subject is currently the topic of other proposed research initiatives in the area of damage tolerant flight control [7]. The majority of documentation of the aircraft accident cases, described in this section, is based on reference [134]. Selected graphics and diagrams used in this thesis have been reproduced from the original artwork created by Matthew Tesch for the "Air Disaster" series of books published by the-then Aerospace Publications (Canberra) and appear here by kind permission of the artist and the publisher. To distinguish these from other graphic material used in this document, the shorter acknowledgement (MT/AA) appears at the end of each caption.

1.2.1 American Airlines Flight AA191, source: [134]

On May 25 1979, the American Airlines widebody DC-10-10, registered N110AA, was preparing at Chicago O'Hare International Airport for departure with 271 people aboard on the transcontinental flight AA191 to Los Angeles, California. At the start on the runway, the DC-10's acceleration and takeoff roll seemed perfectly normal at a flap setting of 10 degrees and left rudder with right aileron use as compensation for the right crosswind. But at 6000 feet down the runway, just before rotating into the takeoff attitude, pieces of the port (No 1) engine pylon fell away from the aircraft, and white vapour began to stream from the mounting. A moment later, during the rotation itself, the entire No 1 engine and pylon tore themselves loose from the aircraft, flew up over the top of the wing, and smashed back onto the runway behind the still accelerating DC-10 as it lifted into the air. The aircraft's port wing had dropped slightly as the DC-10 lifted off, but this was quickly picked up by application of aileron and rudder and the DC-10 continued to climb out with its wings level while accelerating to a maximum speed of 172 knots. The nose up attitude of about 14 °, as well as the aircraft's heading, appeared stable with the right aileron and right rudder being used to maintain equilibrium and it seemed that, despite the loss of its port engine, the DC-10 was

Figure 1.17: AA DC-10-10 N110AA, ©Werner Fischdick

responding well to control. But 10 seconds later, when the DC-10 had climbed to about 300 feet, the speed decreased to 159 knots and it began to roll to the left at an increasing rate, despite the crew's application of right aileron. The roll quickly steepened alarmingly, even though increasing amounts of opposite rudder and aileron were being applied, and it began yawing to the left as well. Simultaneously, the nose lowered and the aircraft began to loose height, despite increasing the up elevator. At the same time, the bank increased still further. Finally, the DC-10's wings were past the vertical in a 112 degree left roll and a 21 degree nosedown attitude, with full opposite aileron and rudder, and almost full up elevator being applied. At this point the wingtip struck the ground, pivoting the DC-10 into the ground, nose first, with enormous impact. The aircraft exploded in an enormous flash of flames and a cloud of black smoke. The DC-10 had been airborne for only 31 seconds, and none of the occupants survived. The trajectory of this ill-fated flight is illustrated in fig. 1.18.

During the subsequent investigation by the National Transportation Safety Board NTSB, two key questions dominated the investigators'minds: What had caused the engine pylon to break away so unexpectedly from the aircraft's wing under perfectly normal operating conditions? And why had this led to such a complete loss of control? In theory, the DC-10

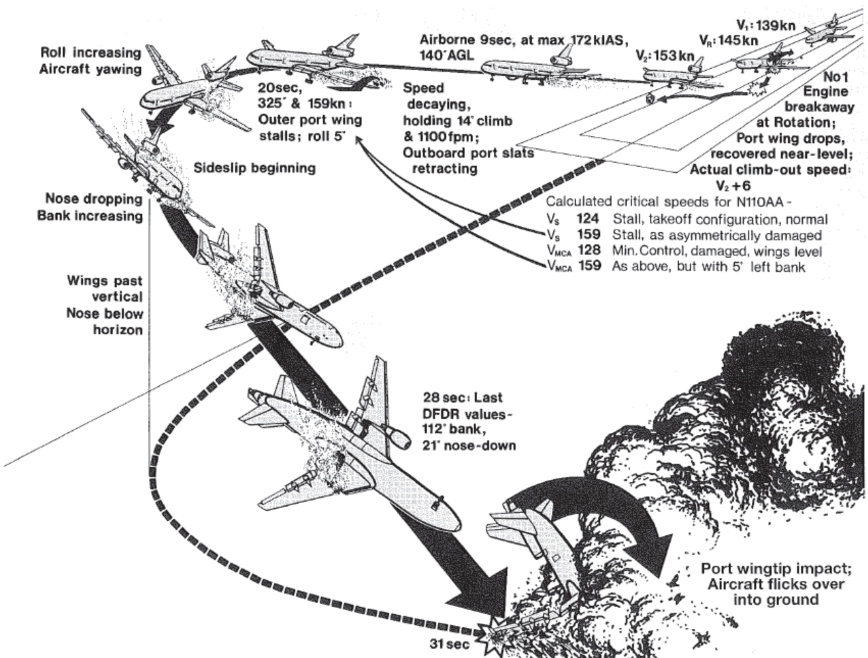

Figure 1.18: Main developments in the DC-10's disastrous takeoff, from engine separation to impact, (MT/AA)

should certainly have been aerodynamically capable of climbing away successfully after the physical loss of the engine, and returning for a safe landing. The overall investigation therefore concentrated primarily on two major areas:

1. Identifying the structural failure which led to the engine-pylon separation and determining its cause;

2. Determining the effects of the structural failure on the aircraft's performance and systems, and identifying what led to the loss of control.

The following observations in these areas were made during the analysis:

1. The analysis of the pylon structural failure revealed that fractures in the upper flange of the pylon rear bulkhead at the joint between the pylon and wing resulted in this structural failure. Moreover, a subsequent fleetwide grounding and inspection of all US registered DC-10's revealed that in total six other American Airlines and Continental aircraft had similar fractures. All six had been subjected to the same maintenance procedures, involving removal and reinstallation of the engines and pylons. Both airlines had individually devised a procedure which they believed to be more efficient than that one recommended by the manufacturer, involving the removal of the engine and pylon as a single unit instead of removing the engines from the pylons before the pylons are removed from the wing. Altogether the evidence was compelling that the cracks in the rear bulkhead upper flanges were being introduced as a result of these irregular maintenance practices, which were unauthorized by the manufacturer as well as the FAA.

2. During the wreckage analysis, it was found that a three metre section of the port wing's leading edge, just forward of the join between the No 1 engine pylon and the wing, was torn away with the pylon, severing the hydraulic system's lines for the port wing's outboard slats. Thirty five of the 36 leading edge slat tracks were subsequently examined, disclosing that, at impact, the port wing's outboard slats were retracted, while its inboard slats, together with the starboard wing's inboard and outboard slats, were in an extended position, as illustrated in fig. 1.19. This retraction of the port wing's outboard slats was caused by the combination of a lack of hydraulic pressure and the air loads. This retraction was critical since it had a profound effect on the aerodynamic performance and controllability of the aircraft. The lift on the port wing was reduced and its stalling speed increased to 159 knots. Since the aircraft's speed reduced to 159 knots during the 14° pitch attitude climb[1], the port wing stalled and the roll to the left was initiated. With the loss of engine No 1, all other accessories driven by this engine were lost, namely the pressure pumps of hydraulic system No 1

[1] In accordance with the airline's prescribed engine failure procedures.

and the No 1 AC generator[2]. The separation also severed electrical wiring, resulting in the loss of power to the captain's instrument panel, the slat disagreement warning system, stall warning system and its stick-shaker function. This implied that there was little or no warning to the pilot of the onset of the stall on the outboard section of the port wing. The loss of control of the DC-10 was thus the result of a combination of three events: the retraction of the port wing's outboard leading edge slats, the loss of the slat disagreement warning system, and the loss of the stall warning system. All were consequences of the separation of the engine and pylon assembly. Each on its own would not have resulted in the crew losing control. But together, during a highly critical phase of flight, they posed a problem that gave the crew insufficient time to recognize and correct.

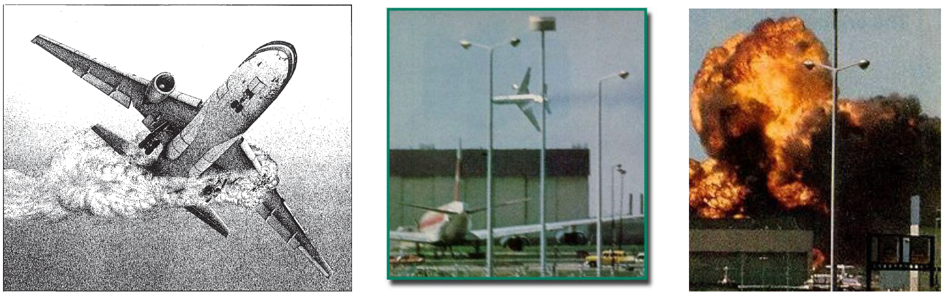

(a) Artist impression of the damaged aircraft during its 31 second flight, note the retracted outboard slats on the port wing, (MT/AA)

(b) Picture of the damaged aircraft just before impact, source: [1]

(c) Picture of the damaged aircraft just after impact, source: airdisasters.com

Figure 1.19: Drawings and pictures of heavy damage to AA DC-10-10 N110AA

The National Transportation Safety Board finally determined the cause of the accident to be the asymmetric stall and ensuing roll of the aircraft because of the retraction of the port wing outboard leading edge slats, and the loss of stall warning and slat disagreement indicator systems resulting from the separation of the No 1 engine and pylon assembly, at a critical point during takeoff. The separation resulted from damage inflicted by improper maintenance procedures which led to the failure of the pylon structure.
Contributing to the cause were:

- The vulnerability of pylon attachment points to maintenance damage and of the leading edge slat system to the damage which produced asymmetry;

[2]These accessories would have remained operational when an engine ceased to operate, but these were severed in this situation because of the physical separation of the engine from the aircraft and the damage to the hydraulic power and other lines.

- Deficiencies in the FAA's surveillance and reporting systems in failing to detect improper maintenance procedures;
- Deficiencies in communication between the aircraft operators, the manufacturer and the FAA in failing to disseminate details of previous maintenance damage;
- The inadequacy of prescribed engine failure crew procedures to cope with unique emergencies.

Post accident analysis has indicated that the pilot had about 15 seconds to react to the failure before control was completely lost. If corrective action had been taken, the plane could have been saved [132]. Obviously, under such emergency conditions, an automatic fault-tolerant control system could have been extremely useful to assist the pilots, and on-line generated diagnostic information could have been useful to recover the plane. However, it should be noted that once the pilot let the speed decrease to V2, the angle of attack of the affected left wing exceeded its stall limit thus causing a non recoverable loss of control. It is important to realize that the main contribution fault tolerant control could most probably provide in this situation, was to improve the reaction time of the pilot to recover and stabilize the aircraft and to prevent the speed to decay by taking into account the minimum speed limit. Once the stall limit was exceeded, fault tolerant control could not recover from this fatal condition anymore as there would not be enough control authority by the remaining effectors to recover from the loss of control. From an operational standpoint, a too low airspeed combined with a very low altitude leads to a lack of sufficient energy to escape from this catastrophic situation.

1.2.2 Japan Airlines Flight JL123, source: [134]

On August 12 1985, the Japan Airlines short range Boeing 747SR with registration JA8119 departed as domestic flight JL123 from Tokyo Haneda towards Osaka. Despite the usual meticulous maintenance, an ill-accomplished fuselage repair more than seven years before was in effect a time bomb which unfortunately went off during this flight. The repair was necessary because of a tail strike at a landing performed by the aircraft at Osaka in 1978. The damage required repair to the aft fuselage and even the rear pressure bulkhead, which sustained heavy damage from the impact on the fuselage hull. Unfortunately, the repair work on the bulkhead involved rivet numbers and placement which was

Figure 1.20: JAL B747SR JA8119, ©Werner Fischdick Collection

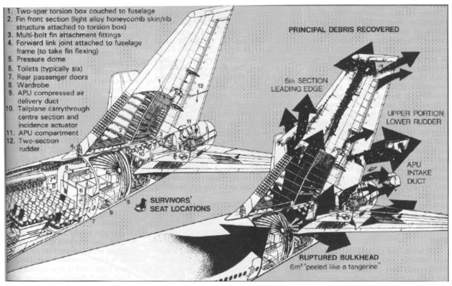

(a) Illustration of explosive decompression, (MT/AA, with acknowledgement to Flight International/John Marsden & Time magazine/Joe Lertola)

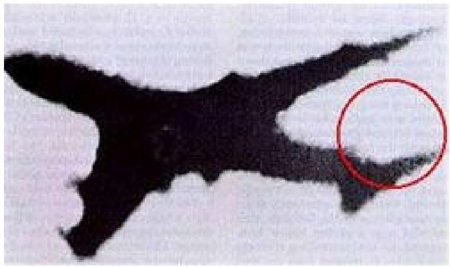

(b) Picture of crippled tailless aircraft

Figure 1.21: Illustrations of heavy damage to JAL Boeing 747 JA8119, (MT/AA)

not optimized for long term fatigue, as explained in [134]. The repaired pressure dome held for seven years. Unfortunately, on flight JL123 the repaired dome joint broke and resulted in an explosive decompression, as illustrated by figure 1.21(a). The volume of air escaping violently from the passenger cabin through the ruptured bulkhead, the failure of which in itself did not destroy the aircraft, had the same impact on the tailcone and tail surfaces as an explosion. Almost the complete vertical fin was blown off, together with components of all four independent hydraulic systems powering the primary flight controls. This meant that all hydraulics were lost and the crew was left with no means to control the aircraft except for the engines. An amateur photographer took a picture of the crippled tailless aircraft, as seen in figure 1.21(b).

The loss of the vertical tail rendered the heavy aircraft de facto laterally unstable and led to a hopeless situation for the crew. The loss of hydraulics halted the functioning of all stability augmentation equipment, resulting in the appearance of phugoid as well as Dutch roll behaviour[3]. The only way for the crew to stabilize the aircraft, was to apply differential thrust by handling the four throttle levers separately. In this way the experienced crew succeeded in stabilizing the aircraft for half an hour, and almost managed to bring the aircraft back to Haneda's airport. Unfortunately, they did not make it to the airport and crashed on Mount Osutaka. According to [134], it is widely accepted that the aircraft crashed because of crew fatigue and experts believe they would never have succeeded in performing a successful landing even if they had managed to bring the crippled aircraft back to the airport. A sketch of the aircraft trajectory can be found in figure 1.22.

[3] After this accident, the manufacturer included some safety measures in the hydraulic circuit to prevent the total loss of all hydraulics in future in similar scenarios. This led to the choice to include the vertical tail loss in the RECOVER accident scenarios list without considering the total loss of hydraulics, see appendix A.

From the flown trajectory shown in fig. 1.22, the aircraft was still controllable to some degree through differential thrust from its engines: the only problem is that this was not an efficient way to do so by the crew. With the available controls, they did not have the necessary capabilities to bring the aircraft and the passengers back to safety.

Figure 1.22: Fatal trajectory of flight JL123, (MT/AA)

1.2.3 United Airlines Flight UA232, source: [134]

On July 19 1989, United Airlines flight UA232 going from Denver to Chicago was operated by one of the company's McDonnell Douglass DC-10-10's. The aircraft involved had the registration N1819U. A little more than an hour after departure from Denver, when the DC-10 was flying above the state of Iowa, North of the town Alta, it attempted to make a heading change from 15° to 95° at an airway intersection point. Close to the end of that turn, at 80°, the fan disk of engine number two, which is placed on the aircraft's tail, fractured due to a disk forging flaw. The debris of this explosive engine failure punctured the horizontal stabilizer as well as the tailcone. Also the tubes of all three independent hydraulic systems powering the flight controls were damaged, which resulted in the loss of all hydraulics, just like the situation with the JAL jumbo jet four years before. This event is illustrated by some pictures. Figure 1.24(a) is a picture of the aircraft, where the small blue arrows indicate the punctured areas on the right elevator. Note the large hole in the elevator leading edge, and the missing tailcone. Note that the major damage is clearly situated in the plane of the no 2 fan disk. Finally, fig. 1.24(b) shows a picture of the stabilizer on the re-assembled wreckage after the crash. This is a top view, the structure on the top left is the tail engine housing. It is clear where the no 2 fan disk is located in that housing, since the skin is completely missing there. With regard to the stabilizer, it is clear that the inner part was damaged to a significantly larger extent than the outer one.

Figure 1.23: UA DC-10-10 N1819U, ©Werner Fischdick

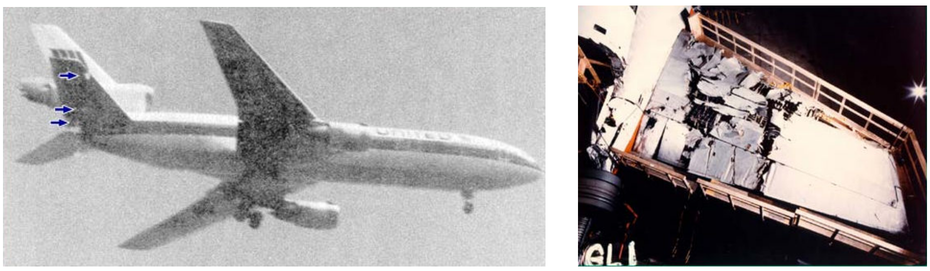

(a) Bad quality picture of the aircraft with blue arrows indicating the damage locations on elevator and tailcone, source: NTSB

(b) Picture of re-assembled stabilizer wreckage after crash, source: [1]

Figure 1.24: Illustrations of heavy damage to UA DC-10-10 N1819U

Since the aircraft was swinging through a gradual right turn at the airway intersection at the moment the tail-mounted engine disintegrated, its 'frozen' control surfaces left it with the tendency to continue the turn. Figure 1.25 shows a map of the aircraft's radar-plotted track. The post failure ground track shows the right hand turn tendency. In their fight to retain control with engine power alone, the DC-10 crew had small but crucial advantages over the hapless Japanese Boeing 747 crew in a similar predicament four years before, as described above. The undamaged fin gave the aircraft some measure of directional stability, moreover a 'dead-heading' check pilot joined the United crew on the flight deck. The check pilot's remarkable skills in handling the power levers undoubtedly allowed the operating crew to concentrate more closely on their crucial individual tasks. Thanks to the joint efforts of the highly experienced crew, they managed to divert the aircraft to the airport closest in the vicinity, namely the Sioux Gateway Airport. As can be seen in fig. 1.25, they succeeded only once to make a left turn, but this was sufficient to line the crippled DC-10 up with one of the airport's runways. Unfortunately, since the flaps were stuck at their 'in'-position, the crew was forced to make their approach at high speed. Moreover, the sluggish aircraft responses to the throttle setting changes made it particularly difficult to make changes in the aircraft final approach path and speed close to the runway. This resulted in the final seconds of flight being in a nearly unsurvivable situation. Any throttle change induced some weakly damped phugoid oscillations, which is undesirable at this altitude. Moreover it was impossible to set the throttles to idle at finals. All this resulted in the situation whereby the aircraft made extremely hard and rough contact with the ground, rolling and tumbling upside down as it broke up. Despite this dramatic end, and although 111 people died in the valiant landing attempt, the superb airmanship of the crew to nurse the aircraft back to the closest airport led to the survival of 185 passengers, including all the four crew on the flight deck. The survival of a considerable number of the passengers depended entirely on the magnificent skills of the crew. Without these highly experienced pilots, this situation would have been definitely unsurvivable.

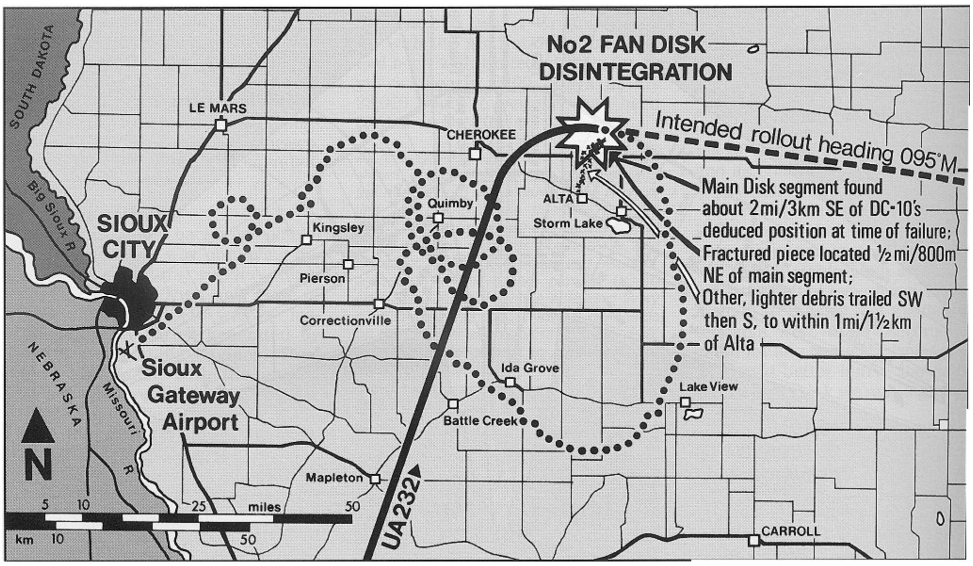

Figure 1.25: Map of the aircraft trajectory, (MT/AA)

1.2.4 El Al Cargo Flight LY1862, source: [249]

On October 4 1992, a Boeing 747-200F freighter aircraft operated by Israel's national airline EL AL (registration: 4X-AXG) departed from Amsterdam airport on cargo flight 1862 towards Tel Aviv. Unfortunately, while the aircraft was climbing over the most southern part of the Ijsselmeer, the pylon of engine no 3 broke off due to metal fatigue. Without the usual heavy aircraft inertia, the engine raced in front of the aircraft, but due to the moment of the rotating parts it started tumbling and impacted on engine no 4. This resulted in the loss of both right wing engines, including serious damage to the wing leading edge resulting in the loss of lift force and a significant drag increase. Due to this extensive damage, the aircraft was rendered considerably asymmetric. Moreover, this damage resulted in a partial loss of the hydraulics, more precisely hydraulic systems 3 and 4 were lost. As illustrated in fig. 1.27, a significant number of control surfaces were paralysed after the engine separation. The outboard (low speed) ailerons, outboard flaps, spoilers no 1, 4, 5, 6, 7, 8, 9, 12 as well as the inner left and outer right elevator were lost

Figure 1.26: EL AL B747-200F 4X-AXG, ©Werner Fischdick

El Al Flight 1862 Failure Mode Configuration
Aircraft Systems
Hydraulic systems 3 and 4 off
Engine 1 and 2 thrust asymmetry
Lower rudder lag
Mass Properties
Engine no. 3 and 4 weight loss, 4,014 kg each
Pylon no. 3 and 4 weight loss, ± 1,000 kg each
Lateral center of gravity displacement
Total weight loss: 10,0028 kg
Aerodynamics
Lift loss due to wing damage (ΔL_{wing})
Rolling moment due to wing damage (ΔL_{wing})
Drag due to wing damage (ΔD_{wing})
Yawing moment due to wing damage (ΔN_{wing})
Pitching moment due to wing damage (ΔM_{wing})
Right inboard aileron and spoiler 10 and 11 aerodynamic efficiency loss

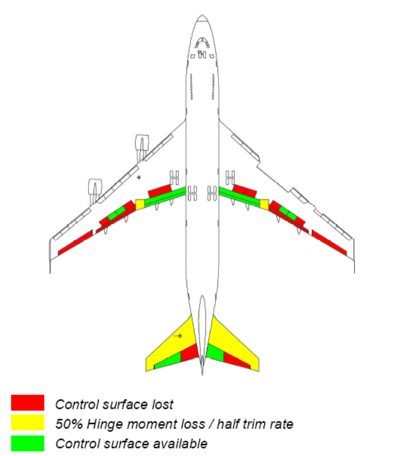

Figure 1.27: Illustration of aircraft damage, source: [249]

completely, while the inner (high speed) ailerons suffered a 50% hinge moment loss and the functionality of the horizontal stabilizer was reduced to half trim rate.

After experiencing the limping behaviour of the crippled aircraft, the crew decided to return to the airport. In an attempt to make an emergency landing, the aircraft flew several right-hand circuits in order to lose altitude and to line up with runway 27. During the second line-up, the aircraft entered an unrecoverable roll-dive. As a result, the aircraft crashed, 13 km east of the airport, into an eleven-floor apartment building in the Bijlmermeer, a suburb of Amsterdam. The trajectory of the aircraft is shown in figure 1.28. Since the crew was not aware of the actual scale of the damage, they decided to return to the airport as quickly as possible. However, this resulted in the fact that they attempted to make an emergency landing with the heavy take off weight of 317 tons. This would have required such a high approach speed of 133.8m/s, that no safe landing would have been possible. Jettisoning fuel in order to reduce the aircraft weight to a more acceptable 263 tons would have resulted in a lower minimum speed of 108m/s that possibly would have led to a more survivable emergency landing, even with the flaps stuck at position 1.

The official analysis from this investigation concluded that given the performance and controllability of the aircraft after the separation of the engines, a successful landing was highly improbable. In 1997, the division of Control and Simulation in the Faculty of Aerospace Engineering at the Delft University of Technology (DUT), in collaboration with the Netherlands National Aerospace Laboratory NR, performed an independent analysis of the accident. In contrast to the analysis performed by the Netherlands Accident Investigation Bureau, the DFDR flight parameters were reconstructed using modelling, simulation

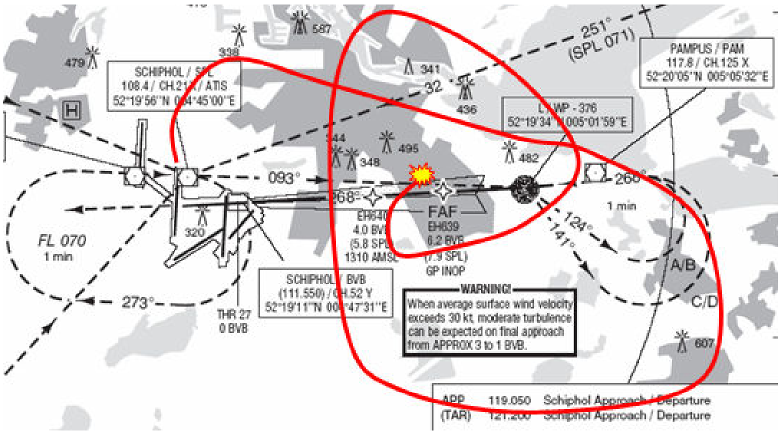

Figure 1.28: Trajectory of EL AL flight 1862

and visualisation techniques in which the DFDR pilot control inputs were applied to detailed flight control and aerodynamic models of the accident aircraft. The purpose of the analysis was to acquire an estimate of the actual flying capabilities of the aircraft and to study alternative control strategies for a successful recovery. The application of this technique resulted in a simulation model of the impaired aircraft that could reasonably predict the performance, controllability effects and control surface deflections observed on the DFDR. Analysis of the reconstructed model (later used for the simulation benchmark described later), indicated that from a technical point of view the damaged aircraft was recoverable if unconventional control strategies were used. Further results of this investigation, including detailed qualitative results of the analysis, can be found in [247, 248]. Comparing this aircraft accident analysis with the previous two, shows that differential thrust is not the only way of recovering a crippled aircraft. It is possible that a limited number of control surfaces are still operative, and these should be taken into account when attempting to apply a form of unconventional control in order to bring the aircraft back to safety.

1.2.5 USAir Flight 427 and United Airlines Flight 585, Sources: [4, 5, 13]

On March 3, 1991, a United Airlines (UAL) Boeing 737-200, registration number N999UA, operating as flight 585, was on a scheduled passenger flight from Denver, Colorado, to Colorado Springs, Colorado. Visual meteorological conditions (VMC) prevailed at the time, and the flight was on an instrument flight rules (IFR) flight plan. Numerous witnesses reported that shortly after completing its turn onto the final approach course to runway 35 at Colorado Springs Municipal Airport (COS), at about 0944 Mountain Standard Time,

Figure 1.29: United Airlines B737-200 N999UA, ©Werner Fischdick

the airplane rolled steadily to the right and pitched nose down until it reached a nearly vertical attitude. In the last 8 seconds, the pilot requested 15 degrees of flaps, which was confirmed by the first officer and it has been noted in the recorded cockpit sounds of the CVR that both engines were accelerating just prior to impact. This selection of 15-degrees flaps, in combination with increased thrust, is consistent with the initiation of a go-around. Despite this crew effort, the altitude continued decreasing rapidly, the indicated airspeed increased to over 200 knots, and the normal acceleration increased to over 4 G, before hitting the ground in an area known as Widefield Park, less than four miles from the runway threshold. Figure 1.30 shows a plot of United flight 585s ground track based on FDR and radar data. The airplane was destroyed completely by the impact forces and post-crash fire, and the 2 flight crew-members, 3 flight attendants and 20 passengers aboard were fatally injured.

The subsequent investigation by the NTSB lasted one year and 9 months. Despite extensive damage to the flight data recorder (FDR), all the data was extractable. The FDR

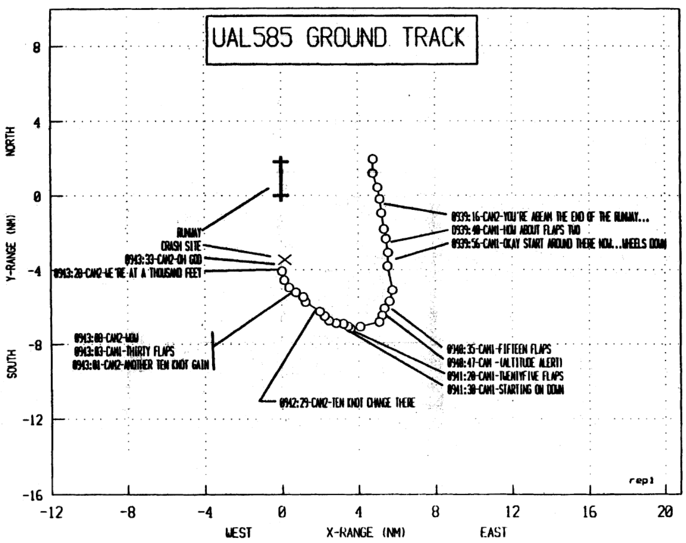

Figure 1.30: Trajectory of United Airlines Flight 585, source: [5].

only recorded five parameters[4]. The flightpath, pitch and roll angles were determined by calculations using the heading and normal acceleration (G-loads) data. The direct availability of roll attitude data would have provided direct information about sideslip angles when the roll angle and heading data were compared, thus permitting a more accurate analysis to determine the nature of the airplane's final manoeuvre. Had rudder, aileron and spoiler deflection data been available, investigators would have been able to compare the airplane's theoretical performance with other data that described the airplane's flight profile to determine with a high level of confidence the effect of external (atmospheric) forces. The direct evidence provided by the parameters would also have permitted an analysis of the flight control system and engine function. Consequently, the data proved insufficient to establish why the plane suddenly went into the fatal dive. The NTSB did not rule out the possibilities of a malfunction of the rudder PCU servo (possibly causing a rudder reverse) and the effect that powerful rotor winds coming off the Rocky Mountains might have had, but there simply was not enough evidence to judge the expected cause. In the first NTSB report (issued on December 8, 1992) no "probable cause" could be given. Instead, it said "The National Transportation Safety Board, after an exhaustive investigation effort, could not identify conclusive evidence to explain the loss of United Airlines flight 585."

Sadly enough, three years later, a highly similar accident occurred... On September 8, 1994, at about 1903 local time, USAir flight 427, a Boeing 737-3B7 (737-300), N513AU, crashed while manoeuvring to land at Pittsburgh International Airport, Pittsburgh, Pennsylvania. Flight 427 was operating as a scheduled domestic passenger flight from Chicago-O'Hare International Airport, Chicago, Illinois, to Pittsburgh. The flight departed at about 1810, with 2 pilots, 3 flight attendants, and 127 passengers on board. FDR data indicated that the accident airplane was rolling out of a left bank to its assigned heading of 100°, after which it began to yaw and roll; the airplane's heading moved left past 100° at an increasing rate. Thereafter, the airplane's heading moved left at a rate of at least 5° per second. The airplane's heading continued to move left at least at this rate until the stickshaker activated[5]. The airplane's left roll angle was also increasing rapidly during this time: the airplane's left roll angle was about 28° and 5 seconds later the airplane's left roll angle exceeded 70°. All this

Figure 1.31: USAir B737-300 N513AU, ©Werner Fischdick Collection

[4]Since 1994, FDRs are required to have more parameters, including those to provide roll and pitch attitude data, as well as thrust data.

[5]This system warns the pilot when the aircraft is critically close to stalling.

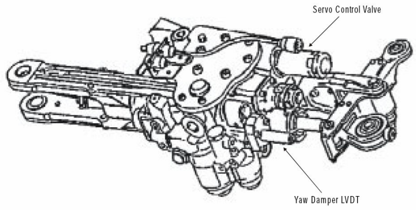

(a) Main rudder power control unit (PCU)

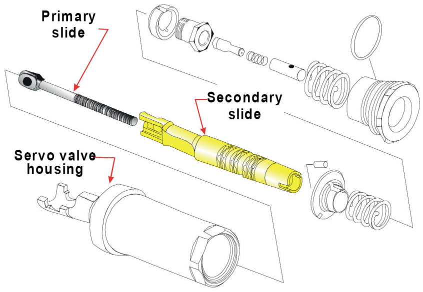

(b) PCU servo valve

Figure 1.32: Drawings of the rudder PCU and faulty servo valve, source: [5].

happened in less than 15 seconds. The airplane kept rolling to the left and finally entered an uncontrolled descent and impacted terrain near Aliquippa, Pennsylvania, about 6 miles northwest of the destination airport. All 132 people on board were killed, and the airplane was destroyed by impact forces and fire. The Safety Board therefore considered various scenarios that could have resulted in such an abrupt heading change, including asymmetric engine thrust reverser deployment, asymmetrical spoiler/aileron activation, transient electronic signals causing uncommanded flight control movements, yaw damper malfunctions, and a rudder cable break or pull. At the end, the Safety Board ruled out each of these scenarios as a possible factor or cause of the left yaw/roll and heading change for various reasons.

After this second similar accident to the USAir Flight 427, the NTSB reopened the investigation of Flight 585, discussed earlier[6], and came up with the following identical conclusion for both accidents: "The National Transportation Safety Board determines that the probable cause of the United Airlines flight 585 and USAir flight 427 accidents was a loss of control of the airplane resulting from the movement of the rudder surface to its blowdown limit. The rudder surface most likely deflected in a direction opposite to that commanded by the pilots as a result of a jam of the main rudder power control unit servo valve secondary slide to the servo valve housing offset from its neutral position and overtravel of the primary slide", see fig.1.32.

Comparing this aircraft accident analysis with the previous ones, shows that not only a (partial) loss of hydraulics can lead to disastrous situations. Here, all hydraulics were still operational, but the rudder actuator suffered from a malfunction, leading to an extreme deflection up to its blowdown limits. Since all other control effectors, surfaces and engines, were still operative, their control authority could have been exploited by a form of uncon-

[6]and even another related accident with the same type of aircraft, namely Eastwind flight 517

ventional control in order to bring the aircraft back to safety. In this scenario of a rudder hardover, the ailerons and differential thrust on both engines would be the steering channels par excellence to compensate for the failure.

Finally, flight tests conducted in a Boeing 737-300 aircraft, following the accident, demonstrated that an airspeed of 190 KIAS was close to the crossover speed for the weight and configuration of USAir Flight 427. At this speed, it was found that the ailerons and spoilers were sometimes unable to stop the roll induced by a (faulty) full rudder deflection. Moreover, the investigation by NTSB showed that if a B-737-300 aircraft cruising at an airspeed of 190 knots with flaps 1 encountered a rudder hardover, recovery was impossible if altitude was maintained by the pilot. In these conditions, aircraft recovery was only possible if the pilot descended to gain airspeed, which decreases the effectiveness of the rudder and increases aileron/spoiler authority enough to compensate for the rolling moment. However, the natural reaction of the pilot would be to maintain altitude while analysing a control problem as was the case for this accident. Simulations have shown that a roll/yaw upset is almost likely to be unrecoverable due to the surprise reaction of the pilot and the aircraft being below the crossover speed and/or close to the ground. However, a rudder hardover of a Northwest Airlines Boeing 747-400 aircraft (Flight 85) in 2002 showed that the remaining control capabilities of the aircraft, including the engines, could be used to recover the aircraft and reduce speed to conduct a successful landing. Also for these scenarios, fault tolerant control could assist to recover correctly and timely from a fault induced upset and stabilise the aircraft for an emergency landing.

1.2.6 DHL Cargo Flight above Baghdad, sources: [170, 172]

On November 22 2003, the DHL Airbus A300B4-203F freighter, registered OO-DLL, took off from Baghdad, bound for Bahrain. While in initial climb, at about 8000 ft, the aircraft was hit by a surface-to-air missile. The missile entered the aircraft's left wing from below at approximately half span. By perforating the wing skin, the projectile entered the outer wing fuel tank 1A. After it ignited, it destroyed the tank so comprehensively that the fuel just drained out. This tank was full of fuel and luckily contained no fuel-air vapour, otherwise the wing would have been blown off the aircraft. However, it still proceeded to burn away at the rear spar. The fuel tank ribs in the area directly in front of the outboard flap burnt almost

Figure 1.33: DHL A300-B4 OO-DLL, ©Werner Fischdick Collection

50% through, but the front spar remained intact. Besides destroying tank 1A, the missile also pierced the inboard left wing tank 1, so it too was losing fuel. Since this inboard tank feeds directly the left engine, this leads to a very time critical situation. Once the left inboard tank lost all its fuel content, the left wing engine would have stopped working. The crew knew they had to land quickly because the wing was trailing a 50m flame, see fig.1.34(a). They also knew that if a part of the wingtip separated they would lose all control of the aircraft. Despite the fact that the leading edge of the wing was complete along almost its entire length, unknown to the crew, the fire was gradually destroying the outer wing, creeping forward from the trailing edge. At some stage before they landed, the rear wing spar separated and the remaining structure was held together by the forward spar only, see fig.1.34(b). The impact hole where the surface to air missile (SAM) entered the wing box is visible in fig.1.34(c).

(a) Picture of the flying aircraft with the left wing on fire, the flames eating slowly their way through the wing structure

(b) Picture of damaged trailing edge wing structure

(c) Picture of missile hole in lower skin of wing structure

Figure 1.34: Pictures of heavy damage to DHL A300B4-203F OO-DLL

Within a few seconds after impact, the aircraft lost all pressure in the three separate hydraulic systems. Consequently, the primary flight control surfaces (ailerons, rudder, elevators) and the spoilers were no longer powered and went limp as their actuators drained, trailing in the slipstream. The aircraft was rendered uncontrollable by conventional means and adopted a rapid phugoid motion. The horizontal stabilizer setting was frozen at the trim position for 215 KIAS, while flaps and slats were unavailable. Fortunately, it was a short flight with a light load, the total weight being only 220 klb, well below maximum landing weight. This was a significant and essential advantage compared with the EL AL scenario described earlier, since the aircraft was in an acceptable configuration in order to perform immediately a relatively safe landing with acceptable approach speed. Because of the expanding left wing damage, the only way to control the aircraft, namely by applying differential thrust, had also a time critical issue which ruled out any option of fuel jettison before switching over to the landing. If they had taken too long to return to the airport, the no 1 engine could have fallen dry of fuel due to the leaking no 1 fuel tank, or the structural integrity of the left wing could have been compromised because of the expanding fire, slowly 'eating' its way through the structure. Both would lead to unsurvivable additional damage. As the aircraft climbed towards a maximum altitude of about 12,000 feet, within 10 minutes, the crew essentially managed to apply an 'adaptive control strategy' regaining control and understanding the basic principles of the flying characteristics induced by the phugoid motion. In addition to controlling pitch and roll of the aircraft by the engine throttles only, the additional drag and lift loss due to the damaged left wing needed to be compensated for. A welcome help was the fact that deploying the gear during the descent increased the damping of the phugoid. After a first unsuccessful attempt to land the aircraft using the engines only, the crew made a go-around and finally made a successful landing at Baghdad International Airport, see fig.1.35. This was a tremendous achievement, and the crew made the most of the little chance they were given. It was a remarkable premiere.

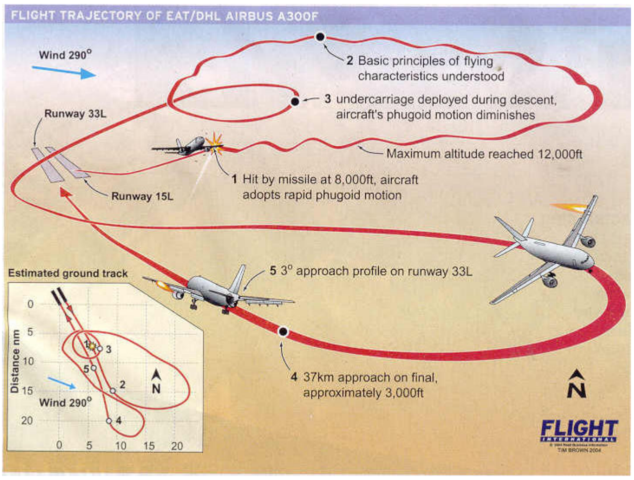

Figure 1.35: DHL A300 flight trajectory, acknowledgement to Flight International

This failure resulted in additional challenges with respect to the previous situations. This time, there was not only a sudden failure, but it was also developing and expanding. This lead to additional challenges for the identification routine, as it has to be continuously monitoring, even after failure detection. Also some kind of indication of time critical issues to the crew could be interesting to contribute to their situational awareness. Finally, it should be noted that this accident is an extreme situation which only serves as one of the accidents motivating the need for a fault tolerant flight control system. It is not our goal to discuss this failure specifically.

1.2.7 Final note in accident analysis

Only a few aircraft accidents have been analysed in detail above. Three of the above examples concern the total loss of the hydraulic circuits, leaving thrust control as the only way to steer the crippled aircraft. It should be noted that these accidents just serve as a general introduction and motivation for FTFC. Thrust control only was not a specific point of research, since it has been explored already in depth (see section 1.3.2). Moreover, there are many other examples of loss of control in flight. For example, there was an unintentional asymmetric thrust reverser deployment in flight on a Lauda Air Boeing 767 above Thailand, which left the crew a 'recovery window' of only 4 to 6 seconds. This failure was very improbable to survive with the current autopilot systems, but the presence of an automatic adaptive control strategy would have compensated for this. Also the crash of an Air Florida Boeing 737 due to ice accretion would probably have been avoidable with this strategy, as well as the American Airlines DC-10 accident at Chicago O'Hare International Airport, described earlier. Moreover, there have been several other engine separation incidents on Boeing 747's and DC-8's, similar to the EL AL situation. There is even the documented story of a McDonnell Douglas F-15 performing an emergency landing with only one wing due to a mid-air collision with another aircraft. After some attempts, the pilot succeeded in regaining control over the aircraft, and nursed the crippled vehicle back to the airport. Key aspects were the fact that the aircraft kept flying and even landed at high speed and that the F-15 fuselage is quite wide, containing two engines, so that it has some lifting body behaviour. After landing, the pilot acknowledged that he was not aware of missing his entire right wing, and if he had been, he would certainly have ejected...

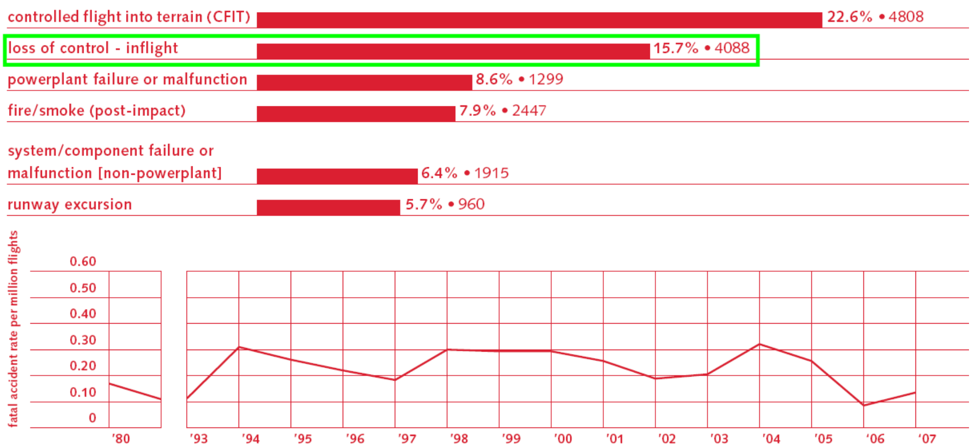

Figure 1.36: Accident statistics, source: [10]

A recent worldwide civil aviation accident survey for the period 1993 to 2007, conducted by the Civil Aviation Authority of the Netherlands (CAA-NL) and based on data from the National Aerospace Laboratory NLR [10], indicates two major categories of accidents which can be attributed to a common initial event, namely 'controlled flight into terrain' where an aircraft, despite being fully controllable and under control, hits terrain due to the loss of situational awareness of the crew, counts for as much as 23% of all the accidents. This percentage is decreasing over the years thanks to the enormous international attention given to CFIT with respect to crew resource management training and development and implementation of new systems in the cockpit. The second major category is 'loss of control in flight', which can be attributed to mistakes made by the pilot or a technical malfunctioning. This category counts for 16% of all aircraft accidents and is not decreasing. Figure 1.36 shows a table from this survey. According to the research team for this project, a reconfiguring flight control system would make the success of the United Airlines and DHL examples less dependent on the extreme skills of the pilots. Moreover, the other examples explained above, and a significant part of this 16% of aircraft accidents due to loss of control in flight could be prevented if some form of reconfiguring control was implemented in the aircraft. It is important to acknowledge that these accidents could not have been prevented at the time when they occurred, since computer capabilities at that time were not at the level they are now. From this perspective, it can be stated that research on fault tolerant flight control is in the interest of the civil as well as military aviation industry.

1.3 Earlier accomplishments in this field, [249]

Motivated by several aircraft accidents at the end of the 1970s, including the crash of American Airlines Flight 191 DC-10 at Chicago in 1979, research on reconfigurable fault tolerant flight control (RFTFC) was initiated to accommodate in-flight failures and to improve the safety and reliability of onboard avionics and flight control system equipment. Reconfigurable control aims to utilise all remaining control effectors on the aircraft (control surfaces and engines) after an unanticipated mechanical or structural failure, to recover the performance of the original system by automatic redesign of the flight control system in order to resemble the unfailed aircraft design. The first objective of reconfiguration is to guarantee system stability while the original performance is reconstructed as much a possible. Due to limitations of the control allocation scheme caused by, for instance, actuator position and rate limits, the system performance of the unfailed aircraft may not be fully achieved. In this case, the failed aircraft would be flown in a degraded mode but with sufficiently acceptable handling qualities for a successful recovery. Reconfigurable flight control systems have been successfully flight tested [97, 71, 6] and evaluated in manned simulations [97], but up to date, no RFTFC has been certified or applied in both commercial and military aircraft.
Passive design approaches are robust control techniques that can handle model uncertain-

ties, flight condition changes and several types of faults and failures without on-line fault information within the robust boundary region. Unanticipated failures that occur outside the stability region of the robust controller may result in catastrophic system instability or performance degradation. For the mitigation of mechanical or structural failures that occur outside the stability region of the robust controller, the use of active reconfigurable control becomes necessary. Fault detection and isolation (FDI) modules are necessary to deliver on-line fault information for control reconfiguration. Active fault accommodation may then be performed based on off-line predetermined (a-priori) fault scenarios, control law switching, or by means of on-line and real-time control law restructuring (architecture changes) or reconfiguration (parameter recalculation).

1.3.1 Self-Repairing Flight Control System (SRFCS) program

The earliest flight tests of reconfigurable flight control systems were performed during the Self-Repairing Flight Control System (SRFCS) program [71], sponsored by the US Air Force Wright Research and Development Center in 1984. Using a categorised predetermined set of failure modes, the states of the system were estimated, based on the known list of failures, to determine the failed component. Residual errors were generated by comparison with a nominal model to isolate failures and estimate the control derivatives of the failed damaged surface for use in a control allocation scheme. The probability of the pre-defined failure cases was estimated and used to determine the weighted average for the control inputs. The limitation of this method is that modelling errors can be interpreted as a failure while the only failures that can be identified 'correctly' are those that fall into the predetermined fault list. The SRFCS was successfully flight tested by NASA in 1989 and 1990 on a F-15 aircraft at the Dryden Flight Research Center [71]. Real-time control reconfiguration was demonstrated for fault cases that included loss of control surfaces due to battle damage.

1.3.2 MD-11 Propulsion Controlled Aircraft (PCA)

Following the Sioux City incident in 1989, the SRFCS project was followed by a program at the NASA Dryden Flight Research Center on Propulsion Controlled Aircraft (PCA). The system aims to provide a safe landing capability using only augmented engine thrust for flight control. Throughout the 1990s, the system has been successfully tested on several aircraft, including both commercial (Figure 1.37) and military, but the acceptance of PCA technology in the commercial and military field has still not been achieved.

Initially, classical methods were used to design the longitudinal controllers with reasonable first cut results. Later in the flight-test phase, nonlinear time domain methods were employed for rapid control gain adjustments. The nonlinear simulators were also used to adjust the initial gains determined from linear design. The control law used flightpath angle

Figure 1.37: A McDonnell Douglas MD-11 lands at Dryden Flight Research Center equipped with a computer-assisted engine control landing system developed by a NASA-Industry team. NASA Dryden Flight Research Center Photo Collection, photo by J. Ross

commands to control the glideslope for up-and-away as well as for approach and landing. This control setup is illustrated in fig. 1.38. Ref. [55] provides more background on the PCA concept.

1.3.3 Self-Designing Controller for the F-16 VISTA, source: [47]

The objective of the Self-Designing Controller (SDC) Program was to develop and flight test a reconfigurable flight control algorithm for a conventional aircraft. The SDC employed an indirect adaptive controller strategy. The two major pieces of the algorithm included real-time parameter identification and on-line control optimization using a Receding Horizon Optimal Controller. The SDC continuously identified stability and control derivatives by using a Modified Sequential Least Squares approach which penalized changes in the derivatives and used a priori relationships between parameters to significantly improve the estimates, such that an up to date mathematical model of the aircraft dynamics could be generated. The SDC was flown on the USAF VISTA F-16 in-flight simulation aircraft, see fig. 1.39, in the spring and summer of 1996. The flight test program consisted of five flights totaling 6 flight hours. These flight tests focused on close tracking of flying-qualities models and continuous control law adaptation, including reconfiguration for single and multiple unforeseen effector impairments. The controller was tested at two flight conditions, 250 KCAS at 15,000 feet and a landing condition. The following failures were simulated at the up and away condition: rudder, right flaperon, simultaneous rudder and left flaperon, and left horizontal tail. Level I and Level II flying qualities were demonstrated throughout the flight test. The SDC Program culminated in the landing in crosswind conditions of the

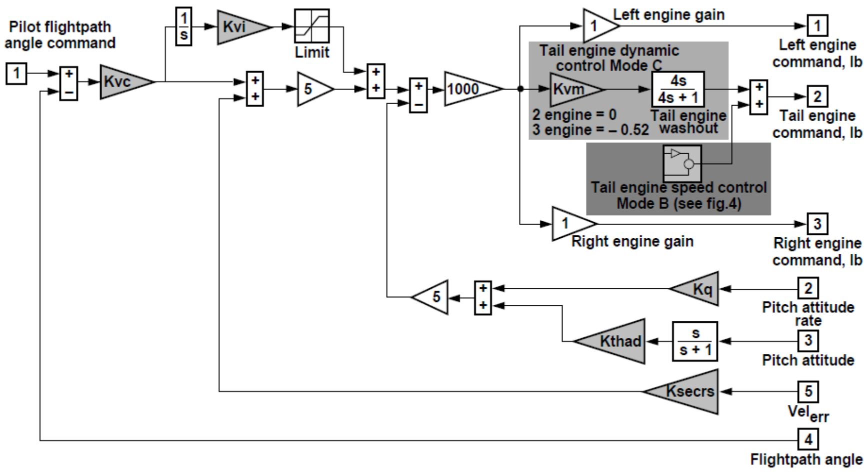

Figure 1.38: Longitudinal MD-11 PCA block diagram two- and three-engine control, source: [55]

VISTA F-16 with a missing left horizontal tail surface (as a simulated failure) under full adaptive control. This was a major milestone and the first flight test of continuous in-flight system identification and on-line control law design to land with major damage.

The linear quadratic optimal controller as employed in this research was based on solving algebraic Riccati equations (ARE) on-line, where optimization was performed over a short prespecified receding time horizon. This limited the computational load of solving the ARE. More information about this control approach can be found in ref. [285].

Figure 1.39: The sole NF-16D is still used in the MATV/VISTA programs. Note the tail-mounted spin chute. Photo by NASA.

1.3.4 Reconfigurable Systems for Tailless Fighter Aircraft, the X-36 RESTORE program, source: [47, 51]

The Reconfigurable Control for Tailless Fighter Aircraft (RESTORE) Program developed and refined the adaptive control methodology further. The objective of the RESTORE Program was to develop reconfigurable control law design methods and algorithms and to apply them to a tailless fighter configuration. The products of the RESTORE Program are a set of algorithms that include system identification to account for damage and modeling errors, control laws that meet handling qualities and tracking requirements, constrained optimization to account for actuator saturation, load limits, etc., and control allocation over a suite of effectors to minimize surface activity, drag, and radar signature. In this research project, the Air Force Research Laboratory (AFRL), Wright-Patterson Air Force Base, Ohio, contracted with Boeing to fly an X-36 scale model of a tailless fighter aircraft, fig. 1.40, with on-board AFRL's Reconfigurable Control for Tailless Fighter Aircraft (RESTORE) software as a demonstration of the adaptability of the neural network algorithm to compensate for in-flight damage or malfunction of effectors, such as flaps, ailerons and rudders. Two RESTORE research flights were flown in December 1998, proving the viability of the software approach. The X-36 aircraft flown at the Dryden Flight Research Center was a 28-percent scale representation of a theoretical advanced fighter aircraft. The Boeing Phantom Works (formerly McDonnell Douglas) in St. Louis, Missouri, built two of the vehicles in a cooperative agreement with the Ames Research Center, Moffett Field, California.

Figure 1.40: X-36 tailless fighter agility research aircraft in flight. NASA Dryden Flight Research Center Photo Collection, photo by C. Thomas

The reconfigurable control law architecture developed for this research is shown in figure 1.41. It is based on a dynamic inversion control law in an explicit model following framework. The reconfigurable control law was created by converting the X-36 implicit model following dynamic inversion control laws to an explicit model following architecture and adding the adaptive neural network. The on-line neural network adaptively regulates the inversion error between the plant model assumed by the dynamic inversion control law and the true vehicle dynamics. These inversion errors may be due to modeling uncertainties or induced by failures/damage. The neural network detects that an inversion error is present by monitoring the tracking error between the desired response model and the true aircraft. Errors will cause the network to augment the desired dynamics input signal to the inverting controller with a signal that attempts to cancel the inversion error. The neural network has the ability to stabilize the vehicle following failures/damage without requiring system identification estimates of the stability and control derivatives. This reduces the criticality of system identification in the overall reconfigurable control law. More information about the reconfigurable control setup in the RESTORE programme can be found in ref. [51].

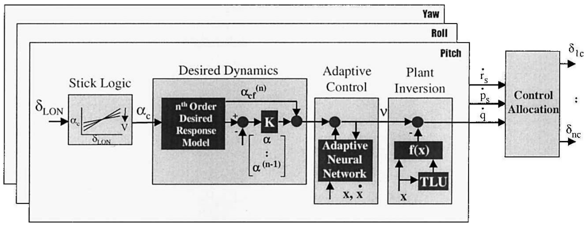

Figure 1.41: RESTORE Reconfigurable flight control system architecture as tested on the X-36, source: [51]

1.3.5 NASA Intelligent Flight Control System (IFCS) F-15 program

In 1992, the Intelligent Flight Control (IFC) research program was established to explore the possibilities of utilising adaptive flight control technology to accommodate unanticipated failures through self-learning neural networks. Within the 1999-2004 Intelligent Flight Control System (IFCS) F-15 program [6, 288], sponsored by NASA Dryden, pre-trained and on-line learning neural networks were flight tested on the NASA IFCS F-15 testbed (Figure 1.42). The pre-trained neural networks provide estimates of the stability and control characteristics for model inversion. The on-line learning neural networks provide on-line compensation of errors in the estimates and from the model inversion. In addition, the adaptive neural networks compensate for changes in the aircraft dynamics due to failures or damage. Piloted simulation studies have been performed at NASA Ames of Integrated Neural Flight and Propulsion Control Systems (INFPCS) in which neural flight control architectures are combined with PCA technology. The evaluation successfully demonstrated the benefits of intelligent adaptive control [160]. Subsequent evaluations are planned to further validate the IFC technologies in a C-17 testbed [160]. Adaptive neural network based technology was further investigated in the Reconfigurable Control for Tailless Aircraft (RESTORE) program in which reconfigurable control design methods were applied to a tailless aircraft [50, 57]. Within the Active Management of Aircraft System Failures (AMASF)

Figure 1.42: NASA Drydens highly modified F-15B, tail number 837, performing Intelligent Flight Control System (IFCS) project flights. NASA Dryden Flight Research Center Photo Collection, photo by C. Thomas

project, as part of NASA's Aviation Safety Program, several issues in the area of FTFC technology were addressed. These include detection and identification of failures and icing, pilot cueing strategies to cope with failures and icing, and control reconfiguration strategies to prevent extreme flight conditions following a failure of the aircraft. In this context, a piloted simulation was conducted early in 2005 of a Control Upset Prevention and Recovery System (CUPRSys). Despite a few limitations, CUPRSys provided promising fault detection, isolation and reconfiguration capabilities.

Fig. 1.43 shows the Generation 2 IFCS architecture. This second generation uses a direct adaptive control algorithm and has model inverse control with feedback error regulation and neural network augmentation providing the online adaptation. The research controller was in fact a hybrid controller using dynamic inversion-type control in the longitudinal and lateral axes, and with a classical controller used in the directional axis. The latter was reportedly needed in order to obtain reasonable flying qualities in the presence of a simulated failure. Ref. [288] provides more background on the IFCS concept.

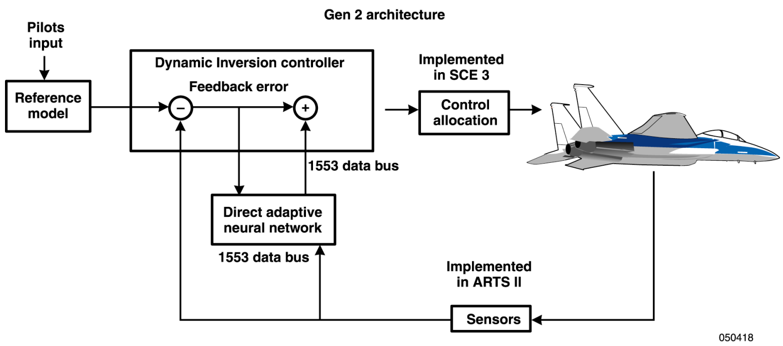

Figure 1.43: Gen 2 Intelligent Flight Control System architecture, source: [288]

1.3.6 Damage Tolerant Flight Control Systems for Unmanned Aircraft

Recently, Rockwell Collins Control Technologies, formerly Athena technologies, developed damage tolerant flight control systems for unmanned aircraft. The Damage Tolerant Control part of the control setup is situated in the high level architecture of the control system, see fig. 1.44. Key technologies include emergency mission management system (EMMS), automatic supervisory adaptive control (ASAC), all-attitude controllers and model reference adaptive control (MRAC) in the inner loop. The EMMS takes into account possible flight envelope restrictions and updates the flight plan accordingly after failure, while ASAC uses the entire aircraft as an actuator by directly controlling the vehicle attitude with respect to the wing vector, see fig. 1.45(a). This allows to return to trimmed and controlled flight. MRAC finally recovers baseline performance. This is achieved by comparing the observed aircraft performance to the desired performance and appropriately adapting the autopilot gains. When an actuator fails or is damaged, then MRAC increases the loop gain until the observed plant performance matches that of the original model, see fig. 1.45(b).

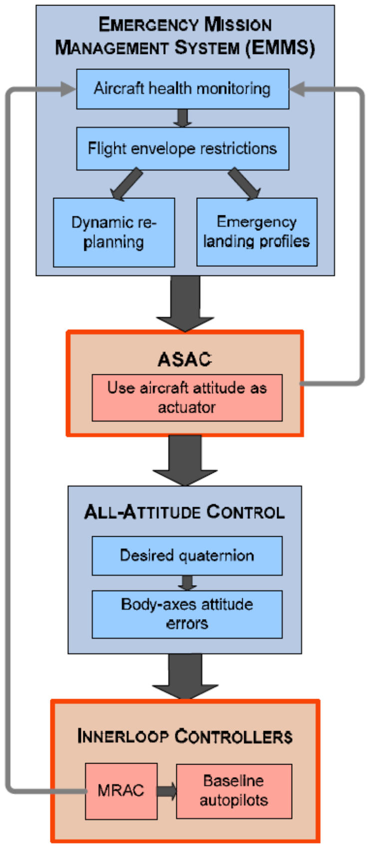

Figure 1.44: Damage tolerant control setup, source: [99]

This technology is being validated on a subscale F/A-18 UAV testing platform at Philips Army Airfield in Aberdeen, Maryland (USA), see fig. 1.46(a). Two demonstration phases have taken place. In the first phase, in April 2007, the right aileron was intentionally released, see fig. 1.46(b). The adaptive control system automatically evaluates the situation and recovers for the failure, after which the system performs an autoland manoeuvre. The second phase with two flight tests followed in April 2008, involving more substantial damage. In the first flight 41% of the right wing was ejected, this increased to even 60% during the second flight, see fig. 1.46(c). The Automatic Supervisory Adaptive Control (ASAC) technology reacted to the new vehicle configuration and automatically regained baseline performance. Again, the system performed an autoland manoeuvre using INS/GPS measurements only. More information can be found in ref. [99].

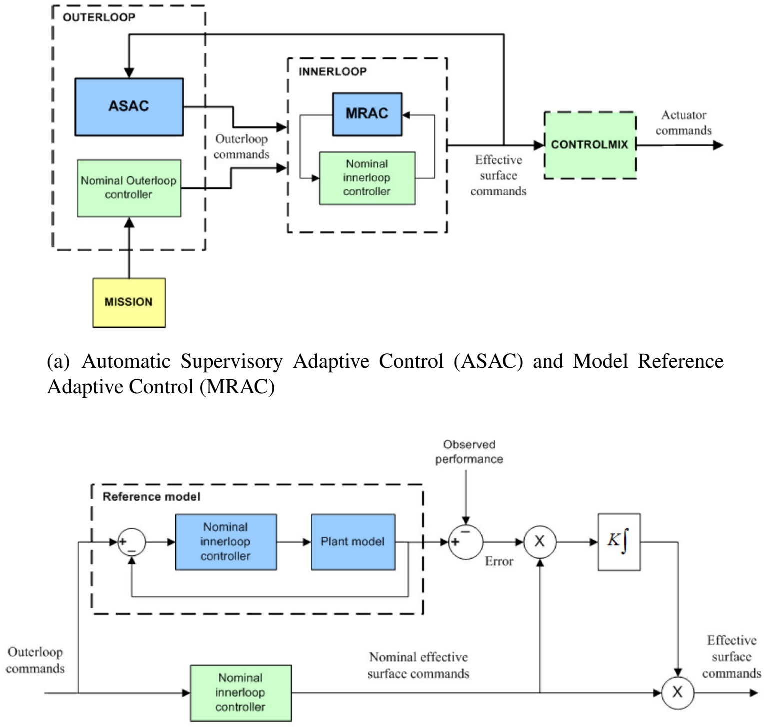

(a) Automatic Supervisory Adaptive Control (ASAC) and Model Reference Adaptive Control (MRAC)

(b) Model Reference Adaptive Control (MRAC)

Figure 1.45: Control architecture of Damage Tolerant Flight Control System, source: [99]

1.4 The choice of reconfiguring control

The accident survey and statistics presented in section 1.2 substantiate the need for reconfiguring or fault tolerant flight control. There are several possible control approaches available to achieve reconfiguring control. A few of them are given in section 1.3, such as the multiple model approach (SRFCS and PCA are examples of this approach[7]), optimal control (like SDC), neural networks (such as RESTORE and IFCS) and model reference adaptive control (as implemented in DTC), the latter three being adaptive control approaches. A more extensive discussion of alternative approaches for reconfiguring control can be found in chapter 2. The approach chosen in this research is the adaptive control approach, because of its flexibility to change (adapt) itself so that its behaviour will conform to new

[7]PCA is a rather specific multiple model approach example for only one failure type, namely a total hydraulic failure.

(a) subscale F/A-18 UAV (b) loss of right aileron (c) loss of 60% of the right wing

Figure 1.46: Failure handling demonstrations of Damage Tolerant Flight Control System, source: [99]

or changed circumstances, [126]. Adaptive control has been mentioned as early as 1950. One notable application is the Honeywell First-Generation Adaptive Autopilot, which has been applied to, among others, the X-15, see fig. 1.47, [42]. This was was called the MH-90 Three-Axis Adaptive System, which comprised an automatic gain changer. This system automatically compensated for the airplane's behaviour in various flight regimes throughout the vast flight envelope of the X-15, simultaneously integrating the aerodynamic control surfaces and the reaction controls. Moreover, it was also designed to prevent unacceptable ringing at the limit-cycle frequency during transients. At that time, this was considered as the way future high-speed aircraft and spacecraft would be controlled, but this type of control system was very demanding for the technologies of the 1960s. Unfortunately, in 1967 a tragic accident in the X-15 flight campaign ended prematurely the early development of adaptive control. An electrical disturbance early in the flight degraded the overall effectiveness of the aircraft's control system and increased the pilot workload. Subsequently, the aircraft entered a spin. During reentry, the MH-96 began a limit-cycle oscillation just as the airplane came out of the spin, preventing the gain changer from reducing pitch as dynamic pressure increased. This caused the airplane to break up during reentry. More information about the X-15 flight campaign and this accident can be found in [131]. This disaster, combined with the lack of stability proofs and the lack of understanding of the properties of the proposed adaptive control schemes caused the interest in adaptive control to diminish, [126]. Nowadays, adaptive control theory as well as technology is in a much more advanced stage than at that time.

Figure 1.47: X-15 #2 just after launch, NASA Dryden Flight Research Center Photo Collection

It should be noted that an adaptive controller is a dynamic system which requires on-line parameter estimation. In adaptive control, there are multiple classifications, such as integrated or direct versus modular or indirect, or physical versus black box approaches. All of them have their specific advantages and drawbacks. The advantage of the integrated approach is that it is possible to prove stability of the control setup. On the other hand, the modular approach allows to split up the control problem over an identification and a model based control step. This helps to reduce the overall controller complexity, although no formal proof of stability can be given. After all, the performance of the controller depends primarily on the convergence of the estimated model parameters to their true unknown values, according to the *certainty equivalence principle*, which will be further explained in chapter 2. There are several model based control techniques which can be used in the indirect adaptive control setup. In this research, the modularity of this adaptive control setup has been exploited to choose for a physical control technique, namely adaptive nonlinear dynamic inversion in combination with on-line recursive aerodynamic model identification. In this way, it is possible to use physical meaningful quantities for the internal signals in the algorithm, avoiding black boxes such as in neural networks. A more elaborate discussion about the different reconfiguring control techniques, their specific advantages and drawbacks, and the motivation for the selection of the control approach for this research can be found in chapter 2.

1.5 Problem statement with research challenges

In the chosen control approaches as described in the previous work in section 1.3, there remain some problems and limitations. The multiple model control approach is limited to a restricted number of failure cases which have been taken into account a priori when setting up the multiple model database. Optimal control makes use of an identified model, but sequential least squares is not able to alter the model structure and is therefore limited with respect to the type and extent of damage which can be compensated for. Neural networks on the other hand suffer frequently from convergence problems. Besides the fact that there is no guaranteed convergence, a black box structure is relied upon which reduces the transparency of the approach. The control setup of damage tolerant control is modular, but the concept of aerodynamic angle control is preferable above attitude control as used in this setup, because of its relationship with the navigational quantities. Moreover, it is not clear what will happen when the reference model behaviour is not achievable in post-failure conditions.

Summarizing, the approach as elaborated in this thesis uses a physical modular approach, where focus is placed on the use of mathematical representations based on flight dynamics. All quantities and variables which appear in the model have a physical meaning and thus are interpretable in this approach, and one avoids so-called black and grey box models where the content has no clear physical meaning. Besides the fact that this is a more transparent approach, allowing the designers and engineers to interpret data in each step, it is assumed that these physical models will facilitate certification for eventual future real life applications, since monitoring of data is more meaningful. Moreover, changing model structures can be taken into account in the joint structure selection and model identification step and pseudo control hedging ensures that the reference model signal is downscaled in the case that this signal cannot be reached post-failure.

Following the choice of the reconfiguring control technique, namely a physical modular approach, the following challenges can be defined which can be considered as the stimuli for the objectives of the project:

- **Damaged aircraft model identification.** Aircraft failures or damage, limited or considerable, have an influence on the aerodynamics, which needs to be identified on-line in a recursive manner. Significant structural damage to the aircraft will have detrimental effects on aerodynamic model structure. Asymmetric damage will contribute to the complexity of the problem. Moreover, this serious damage can also have an impact on the mass, center of gravity and inertia of the aircraft.

- **Damaged aircraft control.** On the control side, there are internal as well as external challenges. Internally, the control law must be adapted for the damage or failures, which is the most obvious need, although not exhaustive. Externally, reference signals will need adaptation too in some circumstances to take into account the maximum achievable values of the steering signals. This is important in order to prevent control saturation and subsequently loss of control.

- The demonstration of the capability and viability of **integrated fault detection, identification and reconfiguration (FDIR)** to a realistic nonlinear design problem. This has only been done by a few studies so far [226, 299]. In particular, most of the fault detection and isolation methodologies are developed independently as diagnostic or monitoring tools and not as an integral part of a reconfigurable fault tolerant control system. On the other hand, most of the current reconfigurable control systems are developed under the assumption of perfect information from the FDI system.

- **The application of this reconfiguring control setup on the RECOVER high fidelity benchmark simulation model.** This reconfiguring control technique needs to be evaluated analytically as well as experimentally on the **Simona Research Simulator**. This contributes to an increase in level on the technology readiness scale of this control technique.

1.6 Research approach

The research approach can be deduced from the research challenges described in the previous section, and are enumerated in an analogous structure.

- **Damaged aircraft model identification.** Aerodynamic model identification including failures can be achieved in the time domain by making use of the two step method. Aerodynamic model structure changes due to significant structural damage to the aircraft can be taken into account by joint structure selection and parameter estimation techniques (SSPE). Two SSPE techniques have been investigated in detail. Furthermore, the effects of aircraft mass property changes on aerodynamic forces and moments have been analysed briefly.

- **Damaged aircraft control.** Internally, adaptive nonlinear dynamic inversion (ANDI) can be employed for control law adaptation. Two ANDI setups have been investigated in detail, one with two and one with three inversion loops. Externally, reference signals adaptation for prevention of control saturation can be achieved by Pseudo Control Hedging (PCH).

- The demonstration of the capability and viability of **integrated fault detection, identification and reconfiguration (FDIR)** to a realistic nonlinear design problem. In the applications of this research, special attention has been given to this topic.

- **The application of this reconfiguring control setup on the RECOVER high fidelity benchmark simulation model.** This reconfiguring control technique has been evaluated on a desktop simulation environment including performance assessment criteria, which is called RECOVER, as well as on the **Simona Research Simulator** in order to assess handling qualities and to evaluate pilot workload.

Several realistic failure modes have been considered in this research project. The most important scenarios are the engine separation (inspired by the El Al accident, see 1.2.4) and the rudder hardover (inspired by the US Airways and United Airlines accidents, see 1.2.5) cases. However, it should be noted that the scenario 'total loss of hydraulics', leading to the need of 'thrust control only' has not been considered explicitly in this research. An important motivation for this is the fact that this case has been considered intensively in the PCA project of NASA, discussed in 1.3.2, and the performance limitations of engines as control effectors, as described earlier.

1.7 Outline of the thesis

This thesis consists of ten chapters which can be grouped in three major parts. Throughout the thesis, it is also possible to divide most of the chapters between identification and control related content, as illustrated in fig. 1.48.

The first part is the background and the motivation of the chosen approach. This part consists of the introduction in chapter 1 and the state of the art literature surveys in fault tolerant control and aerodynamic model identification, discussed in chapters 2 and 3 respectively. The subsequent major part are the scientific developments in identification as

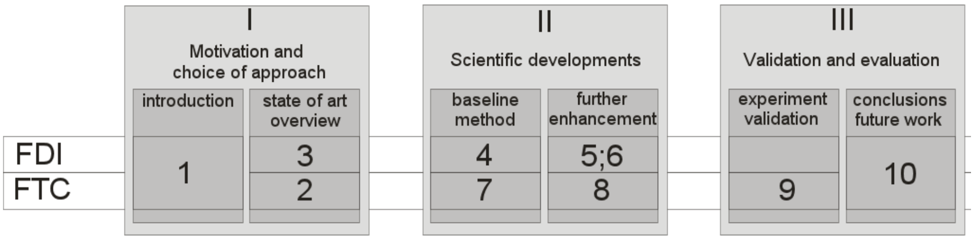

Figure 1.48: Structure of the thesis, chapters divided over three parts and identification (FDI) versus control (FTC) related content

well as control, where each category can be divided over baseline methods and further enhancements. Chapter 4 discusses the baseline identification method of damaged aircraft in real time, based on physical models. This chapter elaborates the theoretical framework and considers some practical applications. A further enhancement of this method can be found in chapter 5, where aerodynamic changes due to extensive structural damage are taken into account. Chapter 6 analyses briefly the effects of mass property changes on aerodynamic forces and moments. On the control side, chapter 7 discusses the baseline flight controller synthesis process, providing theoretical background and flight control law design, where manual as well as autopilot control have been investigated. This chapter includes also desktop simulations to demonstrate the autopilot fault tolerant controller capabilities. Chapter 8 treats some improvements of this baseline flight controller, including Multi-Objective Parameter Synthesis for gain tuning of the control structure, pseudo control hedging for reference signal adaptation, and control allocation. At the end of this chapter, the performances of the baseline controller versus the improved one are compared. The third and final part is about validation and evaluation. Chapter 9 describes the piloted simulator evaluation of the manual reconfiguring controller in the SIMONA Research Simulator, which resulted in a handling quality as well as a pilot work analysis. Finally, chapter 10 provides the conclusions and recommendations, as well as a short discussion about new developments and the way ahead for future research.

Chapter 2

Control literature survey and motivation of the research

This chapter elaborates the literature survey of reconfiguring control. In this chapter, the most important control approaches are enumerated and briefly described, after which a motivation is given how the control method for this research has been selected. Since this preferred control method is a model-based control routine, aerodynamic model identification is another important aspect which is elaborated in the subsequent chapter.

There exists a wealth of control techniques in the literature, which can be placed under the collective noun reconfiguring control, all of them are more or less suitable for applications in Fault Tolerant Flight control. In order to provide some structure in this collection, a classification has been set up as illustrated in Fig. 2.1. This figure is partially inspired by ref. [20, 138, 226] and extended by means of information found in ref. [126, 234], as well as personal information of the author. It is emphasized that this is one possible and by no means unique classification of Fault Tolerant Control techniques, according to the viewpoint of the author, based upon current knowledge and background. However, deviating classifications exist, as well as specific exceptions that do not fit exactly in this structure. This is discussed further in section 2.11.

Figure 2.1 illustrates the classification structure as well as the different control approaches. First these classifications of the different methods will be elaborated, after which the approaches are discussed in detail.

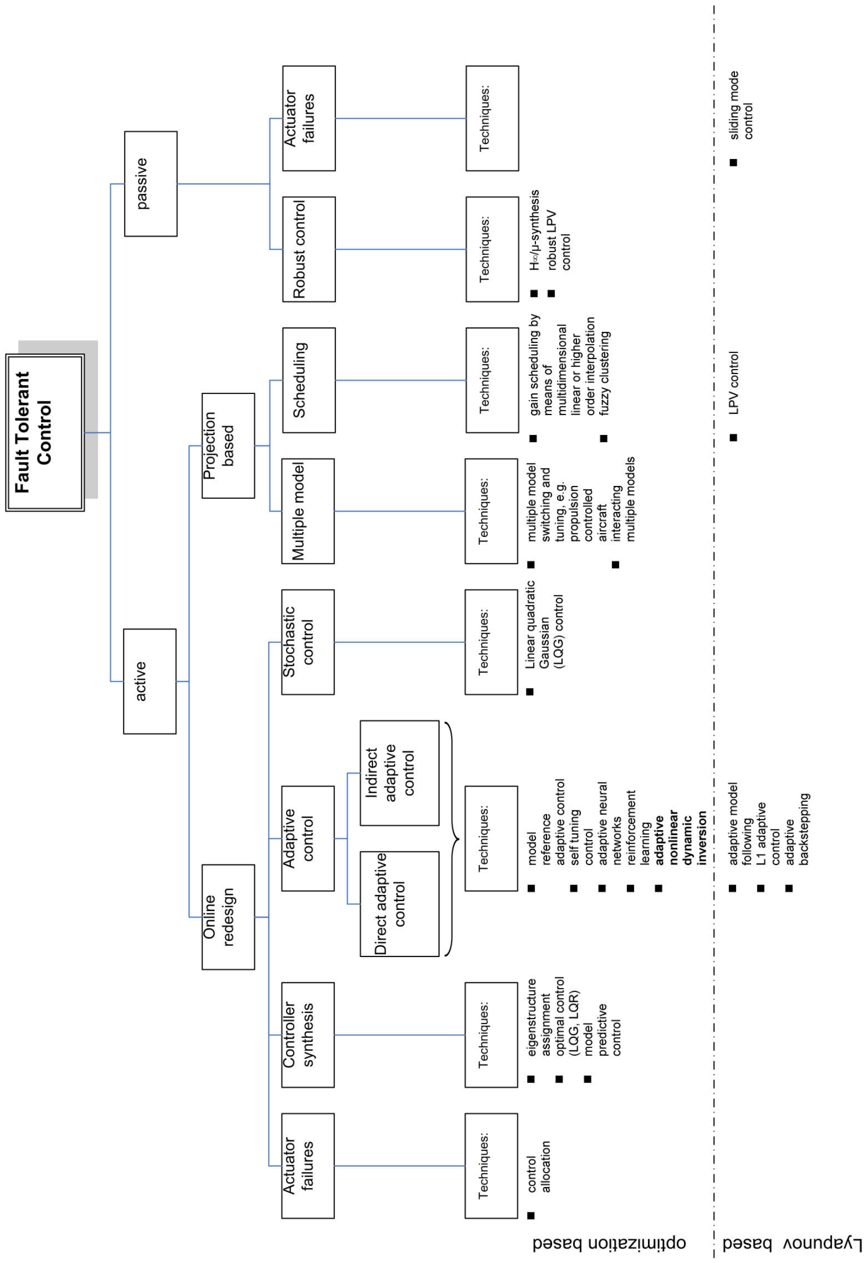

Figure 2.1: Classification of approaches to Fault Tolerant Control

2.1 Passive versus active methods

Passive control methods involve some robustness for certain types of failures that can be modelled as uncertainty regions around a nominal model. Satisfactory stability and performance are guaranteed for any failure of which the model remains inside the stability radius of the robust controller. However, there are some considerable drawbacks. Larger stability radii than needed lead to unnecessary conservativeness, the existence of a satisfying controller is not guaranteed, neither that unanticipated or multiple failures, resulting in models outside the stability radius, can be handled. Moreover, representing failures in an uncertainty description works only for certain structural failures. Many common failure types, such as actuator and sensor faults, cannot be adequately modelled as an uncertainty. All these limitations motivate the need for a controller with a larger flexibility to deal with failures.

Active fault tolerant control is considerably different from passive control methods because it is significantly more flexible by explicitly taking into account fault information instead of assuming a static nominal model like in the passive approach. This means that this active approach needs some external information, supplied by either a fault detection and isolation (FDI) module, sometimes also called a fault detection and diagnosis (FDD) module, some type of (state) observer, or an identification algorithm which supplies an identified mathematical model to the control module.

2.2 Projection based vs on-line redesign methods

Depending on the way the post-fault controller is formed, active FTC methods are divided into projection-based methods and on-line redesign methods. The projection based methods rely on the controller selection from a set of off-line predesigned controllers. Usually each controller from the set is designed for a particular fault situation and is switched on by the reconfiguration mechanism (RM) whenever the corresponding fault pattern has been diagnosed by the FDD scheme. In this way only a restricted, finite class of faults can be treated. Comparing the achievable post-fault system performances, the on-line redesign method is superior to the passive method and the off-line projection-based method. However, it is computationally the most expensive method as it often boils down to on-line optimization.

2.3 Lyapunov vs optimization based methods

Next to the above mentioned structuring of fault tolerant control methods, there is an alternative classification, namely Lyapunov versus optimization based control methods. Control methods can be designed using Lyapunov's theorem, as a result it can be proven that these controllers have globally asymptotically stabilizing properties, such as Sliding Model Control, Backstepping and $\mathcal{L}_1$ adaptive control. On the other hand, control methods can be based upon an optimization procedure, which enforces maximal performance. Examples of these controllers are $\mathcal{H}_\infty$ and μ-synthesis, Control Allocation, Multiple Model Switching and Tuning, Optimal Control and Model Predictive Control among others.

2.4 Robust control, sources: [31, 279]

Robust control is a specific control domain which focuses on uncertainties and disturbances in the controller design. The uncertainties concern primarily plant model uncertainties, which can be attributed to unmodelled or unknown plant dynamics as well as production tolerances. Uncertainties can be represented in many ways, namely like additive and input or output multiplicative uncertainties, depending on what they need to represent, namely system, actuator and sensor dynamics respectively. For each of these three classes, a regular as well as an inverse structure exist. Figure 2.2 illustrates block diagram representations for the different uncertainty types.

On the other hand, there are also three major kinds of disturbances. These are input disturbances, such as actuator perturbations, output disturbances, like wind gusts or atmospheric turbulence in case of an aircraft, and finally measurement disturbances, e.g. sensor noise or biases which can perturb the feedback signal. Figure 2.3 shows the location of the disturbance signals in a typical feedback control structure.

Over the years, robust control techniques have been developed which are robust against, i.e. insensitive with respect to these kinds of uncertainties and disturbances. This insensitivity implies that they are static, meaning that not any internal change is needed to deal with these above mentioned uncertainties and disturbances.

$\mathcal{H}_\infty$ and μ-synthesis

In $\mathcal{H}_\infty$ methods, the controller $\mathbf{K}$ is explicitly designed for worst case uncertainty values, hence its index ∞ which refers to the peak norm $\|\mathbf{\Delta}\|_\infty$. Weighting transfer functions $\mathbf{W}_i$ are used to normalize the uncertainty $\mathbf{\Delta}$. As a matter of fact, they quantify the size of the allowable uncertainty $\boldsymbol{\Delta}$, which is structured as follows:

$$\boldsymbol{\Delta} = \begin{bmatrix} p_1\mathbf{I} & & & & & & & & 0 \\ & \ddots & & & & & & & \\ & & p_{n_r}\mathbf{I} & & & & & & \\ & & & \delta_1\mathbf{I} & & & & & \\ & & & & \ddots & & & & \\ & & & & & \delta_{n_c}\mathbf{I} & & & \\ & & & & & & \boldsymbol{\Delta}_1 & & \\ & & & & & & & \ddots & \\ 0 & & & & & & & & \boldsymbol{\Delta}_{n_f} \end{bmatrix} \in \mathbb{C}^{p\times q} \tag{2.1}$$

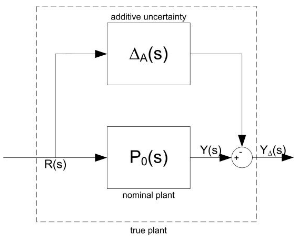

(a) additive uncertainty

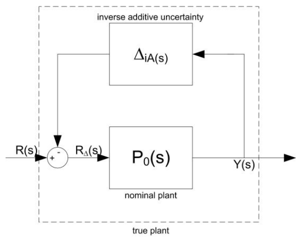

(b) inverse additive uncertainty

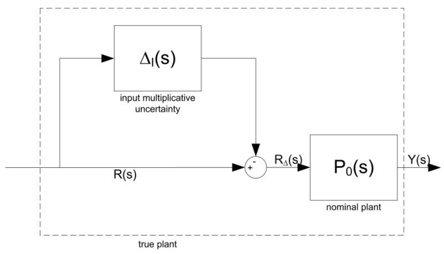

(c) input multiplicative uncertainty

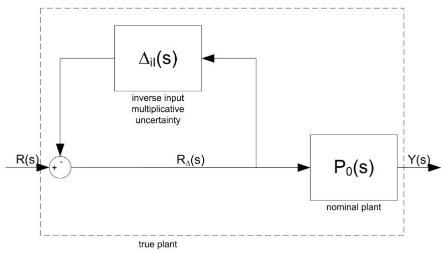

(d) inverse input multiplicative uncertainty

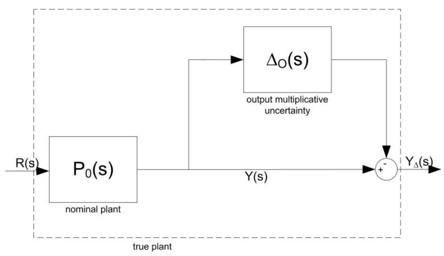

(e) output multiplicative uncertainty

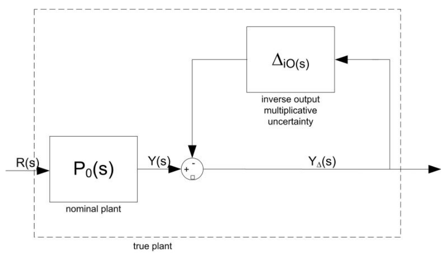

(f) inverse output multiplicative uncertainty

Figure 2.2: Different model representations for uncertainties

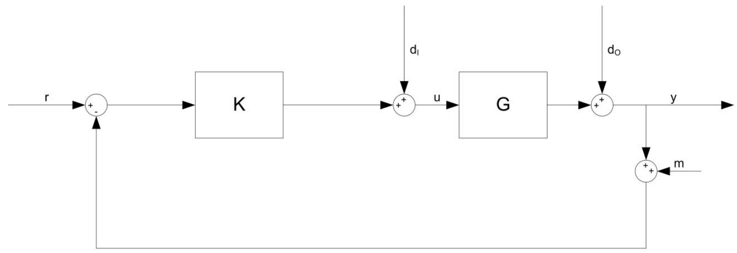

Figure 2.3: Different disturbance types in a typical feedback control structure: input disturbance d_i, output disturbance d_o and measurement disturbance m

where p_i denotes real uncertainties, δ_j stands for structured complex uncertainties and finally unstructured complex uncertainties are represented by $\mathbf{\Delta}_k$.

In the $\mathcal{H}_\infty$ domain, there are three major design methodologies, namely mixed sensitivity, loop shaping and μ optimal controller design. Each of them is briefly discussed.

In the mixed sensitivity approach, design specifications are defined as robust stability (RS), nominal performance (NP) and robust performance (RP). Each of them is based on the singular value σ or the structured singular value μ of the sensitivity function S, the sensitivity function at the controller KS or the complementary sensitivity function T. Freedom for iterative tuning is given by the selection of weighting functions which are modelled as low and high pass filters.

The problem formulation is as follows. Consider the general feedback configuration shown in Figure 2.4. The various signals in the figure are: $\mathbf{u}$ the control variables, $\mathbf{v}$ the signals which the controller has access to, $\mathbf{w}$ the exogenous signals such as disturbances, pilot commands, measurement noise, etc, and $\mathbf{z}$ the controlled variables, typically error signals and control signals which are to be minimised in some sense to meet the control objectives. Now by partitioning the plant $\mathbf{P}$ compatibly with $\mathbf{K}$, the closed loop transfer

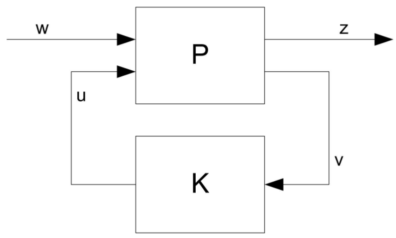

Figure 2.4: A general configuration for $\mathcal{H}_\infty$ controller design.

matrix from $\mathbf{w}$ to $\mathbf{z}$ is given by a lower LFT:

$$\begin{aligned} \mathbf{z} &= \{\mathbf{P}_{11} + \mathbf{P}_{12}\mathbf{K}(\mathbf{I} - \mathbf{P}_{22}\mathbf{K})^{-1}\mathbf{P}_{21}\}\ \mathbf{w} \qquad (2.2) \\ &= F_l(\mathbf{P}, \mathbf{K})\ \mathbf{w} \qquad (2.3) \end{aligned}$$

The standard $\mathcal{H}_\infty$ optimal control problem is then the minimisation of the $\mathcal{H}_\infty$ -norm of $F_l(\mathbf{P}, \mathbf{K})$ over all stabilising controllers, i.e.

$$\inf_{\mathbf{K}} \parallel F_l(\mathbf{P}, \mathbf{K})(j\omega) \parallel_\infty = \inf_{\mathbf{K}} \max_{\omega} \overline{\sigma}(F_l(\mathbf{P}, \mathbf{K})(j\omega)) = \inf_{\mathbf{K}} \max_{\mathbf{w} \neq \mathbf{0}} \frac{\parallel \mathbf{z}(j\omega) \parallel_2}{\parallel \mathbf{w}(j\omega) \parallel_2} \qquad (2.4)$$

In practice, it is usually not necessary to compute the optimal $\mathcal{H}_\infty$ controller, and it is computationally (and theoretically) simpler to design a sub-optimal controller via the following iterative procedure. Let $\gamma_{\min}$ be the minimum value of $\parallel F_l(\mathbf{P}, \mathbf{K})(j\omega) \parallel_\infty$ over all stabilising controllers $\mathbf{K}$. Then the $\mathcal{H}_\infty$ sub-optimal control problem is: given a $\gamma > \gamma_{\min}$, find all stabilising controllers $\mathbf{K}$ such that

$$\parallel F_l(\mathbf{P}, \mathbf{K})(j\omega) \parallel_\infty < \gamma$$

This problem can be solved efficiently using standard MATLAB software which uses the algorithm of Doyle et al, [80]. By iteratively reducing the value of γ an optimal solution is approached.

Loop shaping is similar as the mixed sensitivity approach, except for the use of the open loop transfer function $L = GK$ instead of the sensitivity functions S, KS and T in the design specifications.

The final variant is μ optimal controller design. This design is specifically focused on robust performance. This can be achieved by means of a so-called DK-iteration, which consists of two major iterative steps. In the K-step, an $\mathcal{H}_\infty$ controller is synthesized for the scaled problem $\min_K \|DM(K)D^{-1}\|_\infty$ with fixed $D(s)$. The D-step on the other hand is intended to find $D(j\omega)$ to minimize $\overline{\sigma}\left(DMD^{-1}(j\omega)\right)$ at each frequency with fixed M.

Figure 2.5: IRIS-T air-to-air missile, source: Saab

μ-synthesis control has been applied in the InfraRed Imagining System-Tail (IRIS-T) air-to-air missile, [29]. Control laws are scheduled over the dynamic pressure. It is a next generation short-range missile with thrust-vectored control, being developed by Greece, Italy, Norway and Sweden. First successful flight test was in May 2000.

Robust Linear Parameter Varying control (RLPV)

An alternative approach to fault-tolerant control is the implementation of robust linear parameter varying (RLPV) control, [34]. This has been applied on an aircraft control problem in which the tailplane is assumed to suffer from degraded control effectiveness. This is modelled by a scaling of the input to the tailplane actuator. A robust LPV controller achieves the desired performance objective for the degradation levels without loss of robustness to system uncertainties. First of all, Linear Matrix Inequalities (LMI's) are set up for controller synthesis and stability analysis. Subsequently, A D/K-like iteration, similar to μ-synthesis, is performed to synthesize a robust LPV controller, without ruining the essential convexity of the LMI's. Because of the generalized synthesis framework used to design the controller, it is possible to integrate other scheduling objectives, such as speed or dynamic pressure scheduling. However, since the LPV controller synthesis relies on quadratic stability analysis it is not possible to take into account any varying system structure, which occurs a.o. for the specific situation of complete failure of the tailplane actuator. Therefore, the freedom of using the throttle channel more effectively cannot be exploited in this control setup.

To overcome this, an alternative approach has been presented in [268], called eigenstructure assignment (EA). This technique belongs to the category of controller synthesis and will be discussed in section 2.8.

2.5 Control focused on actuator failures

There are two control approaches specifically focused to deal with actuator failures. One relies on some form of FDI/FDD or identification, where the other approach is completely independent of this. The former is the concept of control allocation (CA), the latter is the domain of sliding mode control (SMC).

Control Allocation (CA), sources: [138]

The general purpose of control allocation is the mapping of a set of six desired forces and moments towards a (usually large) set of actuators, steering the control effectors (control surface deflections and engines in the case of an aircraft). In active fault tolerant control, control allocation has the purpose to separate controller parts dealing with actuator failure types. Actuator failures can be dealt with by the control allocation algorithm only, where the controller itself does not need to be compensated for actuator failures. This principle is illustrated in fig. 2.6.

By assuming the structure as shown in fig. 2.6, the controller output defines a set of commanded forces and moments. These forces and moments are not influenced by possible actuator failures. The control allocation block, on the other hand, translates these desired forces and moments into appropriate commanded actuator positions which serve as input signals to the system, or aircraft in this case. By providing an estimate of the control effi-

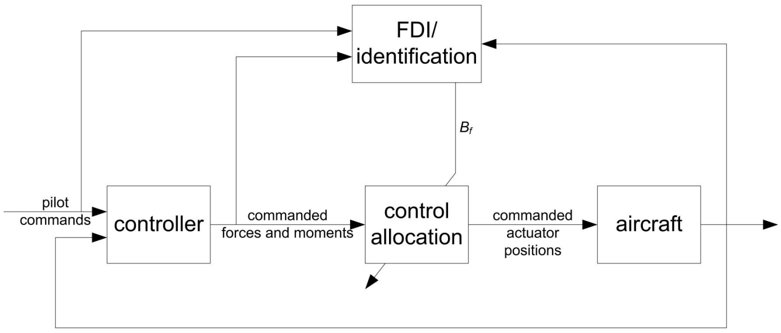

Figure 2.6: Control allocation for fault tolerant control

ciencies ($\mathbf{B}_f$ matrix) from either an FDI or a system identification algorithm, an adaptive control algorithm can use this information about actuator failures and reconfigure for them. On the other hand, structural failures cannot be compensated for by this type of controller. From the perspective of control allocation, the goal is thus to produce the desired forces and moments $\mathbf{u}_d$ by selecting the appropriate inputs to the system $\mathbf{u}$. Whether these force and moment values are reachable depends on the difference between the size of $\mathbf{u}_d \in \mathbb{R}^m$, where m is the number of command channels (forces and moments) and the column rank of $\mathbf{B}_f \in \mathbb{R}^{m \times k}$, where k is the number of control effectors.

There are three distinguishable cases:

$m < k$**:** This is the overactuated case, which can degenerate to the exactly actuated case or eventually the underactuated case in the presence of failures. The moments can be selected exactly and the remaining degrees of freedom can be used (for example) to drive the actuators towards a desired position $\mathbf{u}_p$ by minimizing [289, 51, 56]:

$$\begin{array}{l}\frac{1}{2}\|\mathbf{u}-\mathbf{u}_p\|_{\mathbf{W}_p} = \frac{1}{2}(\mathbf{u}-\mathbf{u}_p)^T\mathbf{W}_p(\mathbf{u}-\mathbf{u}_p) \text{ where } \mathbf{W}_p = \mathbf{W}_p^T > 0 \\ \text{subject to } \mathbf{B}\mathbf{u} = \mathbf{u}_d\end{array}$$

where $\mathbf{W}_p$ is a weighting matrix prioritizing critical actuators and penalizing possible faulty actuators.

$m = k$**:** This is the exactly actuated case. There is only one solution which places the moments exactly:

$$\mathbf{u} = \mathbf{B}^{-1}\mathbf{u}_d$$

$m > k$**:** This is the underactuated case. There are not enough degrees of freedom in the number of control inputs to achieve $\mathbf{u}_d$ and so a compromise must be made by (for example) minimizing the weighted norm:

$$\frac{1}{2}\|\mathbf{Bu} - \mathbf{u}_d\|_{\mathbf{W}_d}$$

Control allocation received a lot of attention in relation to over-actuated systems (see [88] for a survey) and for reconfigurable systems as it allows actuator failures to be handled internally without the need to modify the controller itself, as illustrated in fig. 2.6. However, there are two major limitations to this approach to reconfiguration. First, there is no guarantee for stability, even with a stabilizing control law, when $m > k$, as the input seen by the system may not be equal to that intended by the controller. Second, the dynamics and limitations of the actuators after a failure are not taken into account in the control law. This means that the controller will still be attempting to achieve the original system performance even though the actuators are not capable of achieving it. Therefore, the control allocation problem can mathematically be defined in terms of solving a system of linear equations subject to constraints for, mostly, redundant actuator control variable commands. There is one equation for each controlled axis (force and moment). The constraints arise from actuation rate and position limits, and they can change after a failure. An axis priority weighting can be introduced when the equations cannot be solved exactly because of the constraints, [88].

With the development of more advanced aircraft with highly redundant actuator systems to counter the increasing safety risk and to improve performance, in the last 5-10 years a lot of research has been done concerning the control allocation problem of redundant actuator systems, [37, 84, 88]. Different algorithms have been developed based on quadratic programming or linear programming.

Figure 2.7: The X-35B prototype in hovering configuration

During the X-35 program a cascaded pseudo inverse method has been applied for the control allocation problem, see [41]. Based on the pseudo inverse solution, four cases can be considered for the calculation of the gain matrix $\mathbf{P}$ (n the number of commanded axis, m the number of effectors):

Case 1: The over-determined solution (more effectors than commanded axis, $n < m$) Minimize $J(\Delta\boldsymbol{\delta}) = \Delta\boldsymbol{\delta}^T\mathbf{W}_p^{-1}\Delta\boldsymbol{\delta}$ subject to $[\mathbf{CB}]\,\Delta\boldsymbol{\delta} = \frac{\mathbf{dcv}_{\text{des}}}{dt} - \frac{\mathbf{dcv}_{\text{nom}}}{dt} = \Delta\mathbf{d}$

$$\mathbf{P} = \mathbf{W}_p[\mathbf{CB}]^T\,\left[[\mathbf{CB}]\,\mathbf{W}_p\,[\mathbf{CB}]^T\right]^{-1}$$

where the matrix $\mathbf{W}_p$ is used to weight the effectors to prioritize their usage.

Case 2: The exactly determined solution (equal number of effectors and commanded axis, $n = m$)

$$\mathbf{P} = [\mathbf{CB}]^{-1}$$

The algorithm contains protection against inverting singular matrices, [41].

Case 3: The under-determined solution (less effectors than commanded axis, $n > m$)

Minimize $J(\Delta\boldsymbol{\delta}) = (\Delta\mathbf{d} - [\mathbf{CB}]\Delta\boldsymbol{\delta})^T\ \mathbf{W}_d\ (\Delta\mathbf{d} - [\mathbf{CB}]\Delta\boldsymbol{\delta})$

$$\mathbf{P} = \left([\mathbf{CB}]^T\,\mathbf{W}_d\,[\mathbf{CB}]\right)^{-1}[\mathbf{CB}]^T\mathbf{W}_d$$

Case 4: Singular matrix handling.

This case provides protection in the event that the inverted matrix does not have full rank due to low control effectiveness in the remaining active effectors or having very similar control effectiveness between two or more remaining active effectors. For this case, the columns of $[\mathbf{CB}]$ are summed up to combine the remaining active effectors into a single pseudo-effector, and the solution method of case 3 is used for solving the effector positions.

Once the gain matrix, $\mathbf{P}$, is computed, the algorithm computes $\Delta\boldsymbol{\delta}$ and checks the position, rate, gain limits. If none of the limits are exceeded, the algorithm stops and the gain matrix is unmodified. If any limit is exceeded, scale factors are computed to insure the limits associated with each effector are satisfied. A detailed description of the control allocation algorithm is given in [41]. It should be noted that the accuracy of the control allocation highly depends on the available on-board model for the calculation of the control effectiveness matrix.

Besides this cascaded pseudo inverse method, there exists a wealth of other control allocation methods, which can be classified in four major categories, namely optimization based control allocation, direct control allocation, dynamic control allocation and nonlinear control allocation. Optimization based control allocation comprises many different methods, [118]. First of all, there are the pseudo inverse based methods, as introduced previously in the X-35B example, such as regular pseudo inverses, cascaded generalized inverses and daisy chain control allocation. Another branch are the active set methods, like simplex and sequential least squares methods. The other optimization based control allocation approaches are fixed point methods and quadratic programming methods, such as the ellipse constraint method. Two popular direct control allocation techniques are the attainable moments method and linear programming.

Sliding Mode Control (SMC), source: [20]

Sliding mode control is a nonlinear control method that can be described as high-frequency switching control. Sliding mode schemes are an established method for controlling uncertain systems. In this approach closed loop performance is achieved through the selection of a surface in the state-space that represents desired performance requirements, such that if the system is forced to evolve on the surface, the resulting reduced order motion satisfies the performance requirements. Traditionally in order to force the system states to reach the surface in finite time and subsequently remain there, discontinuous control (across the surface) is applied. Thus, the controller can be split into two phases: reaching and sliding. During the reaching mode a stabilizing control law is needed, where global asymptotic stability is achieved by using Lyapunov's Theorem. The motion whilst constrained to the surface is described as a sliding mode. More recent work seeks to achieve the same effect using continuous control strategies (so-called higher order sliding mode schemes). The key property of sliding mode control schemes is that during the sliding motion the closed-loop system is completely invariant to uncertainty in the channels of the input – so-called matched uncertainty. This extreme robustness property has motivated a good deal of research activity into the design and analysis of such systems.

Recent work in the USA by Hess and co-workers, [119], and also NASA funded work by Shtessel, [242, 243], has considered the use of sliding mode ideas for fault tolerant control. The insensitivity and robustness properties of sliding modes to certain types of disturbance and uncertainty make it attractive for applications in the area of flight control and fault tolerant control. The work by Hess argues that sliding mode control has the potential to become an alternative to reconfigurable control and has the ability to maintain performance without requiring fault detection and isolation (FDI). This represents a so-called 'passive' approach to FTC. Shtessel adopts a slightly different approach and uses sliding mode ideas with online reconfiguration of the sliding surface boundary layer to control an aircraft system in the presence of actuator faults. More recent work at Leicester University by Alwi and Edwards, [20], has investigated the use of sliding mode fault tolerant control for total actuator failures. In particular, actuator and sensor fault tolerant control schemes have been developed for the same high fidelity full nonlinear Boeing 747 simulation model as used in the research presented this thesis. The work considers sliding mode control allocation schemes for fault tolerant control based on integral action and a model reference framework. Unlike many control allocation schemes in the literature, actuator effectiveness levels have been used to redistribute the control signals to the remaining healthy actuators when faults/failures occur. A stability analysis and design procedure have been developed from a theoretical perspective for this scheme. A fixed control allocation structure is also analysed in the situation when information on actuator effectiveness level is not available. The proposed scheme shows that faults and even certain total actuator failures can be handled directly without reconfiguring the controller actively. An adaptive gain for the nonlinear component of the sliding mode controller for handling faults has also been designed. Valuable results have been obtained from real time hardware implementations of the controllers on the 6-DOF SIMONA flight simulator at Delft University of Technology as part of the GARTEUR FM-

AG(16) programme. The schemes have been evaluated by experienced pilots and the results have shown good performance in both nominal and failure scenarios. A reconstruction of the Bijlmermeer ELAL 1862 scenario on SIMONA using one of the controllers shows that a safe flight and landing is possible.

2.6 Multiple model approach, source: [138]

The multiple model method, introduced in the early 1990's, is an active approach to FTC that belongs to the class of projection based methods rather than to the on-line redesign methods. It is based on a finite set of linear models that describe the system in different operating conditions, in the case of FTC in the presence of different faults in the system. A (static) controller is designed off-line for each local model. An on-line procedure determines the global control action through switching between (MMST) or weighted combining of (IMM) the different local control actions that can be taken. Both approaches require a Failure Modes and Effects Analysis (FMEA), in which all expected failure scenarios are enumerated.

This multiple model method is a very attractive tool for piecewise linear modelling and control of global nonlinear systems. However, these approaches are restricted to a finite number of a priori anticipated faults (and possibly all possible combinations), by considering a specific model corresponding to every fault in the FMEA. And even if a convex combination of the local models in the model set is formed, such as in the IMM approach, then the control action is in general not the optimal one for this model, possibly leading to instability of the closed loop system. This instability risk has been avoided by an approach proposed in [151], using a bank of predictive controllers that forms the global control action in an optimal way.

Multiple Model Selection and Tuning (MMST), source: [218]

In this technique, illustrated in fig. 2.8, the dynamics of each fault scenario are described by a different dedicated model M_i, set up in parallel, which is paired with its respective controller K_i. Reconfiguration of the control system takes place by choosing the model/controller pair that is most applicable and that needs to be switched to at every time step.

In this setup, the reconfiguration mechanism (RM) which is responsible for the switching between the different controllers is a crucial part. At each time step, the model which is closest to the current system is determined by computing a performance index $J_i(t)$, which is a function of the errors $\epsilon_i(t)$ between the estimated outputs of model M_i and the measurements at time t.

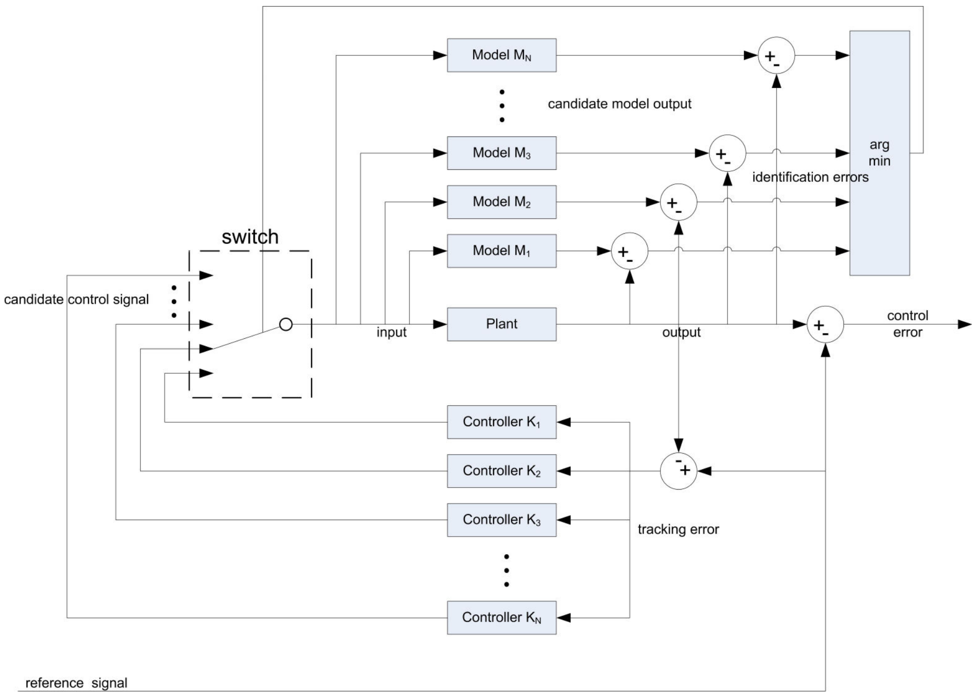

Figure 2.8: MMST control strategy

A commonly used index is [218]:

$$J_i(t) = \alpha\epsilon_i^2(t) + \beta \int_0^t e^{-\lambda(t-\tau)}\epsilon_i^2(\tau)d\tau$$
$$\alpha \geq 0, \beta > 0, \lambda > 0$$

where α and β are chosen to give a desired combination of instantaneous and long-term accuracy measures. The forgetting factor λ ensures the boundedness of $J_i(t)$ for bounded ϵ_i. The model/controller, M_i/K_i with the smallest index is switched to and a waiting period of $T_{\min} > 0$ is allowed to pass in order to prevent arbitrarily fast switching. Most MMST algorithms include a 'tuning' part which occurs during the period while a controller K_i is active, during which time the parameters of the corresponding model, and only the corresponding model M_i, are being updated using an appropriate identification technique (e.g. [25]).

Recent interest in this control method has been stimulated by the fact that [218] has stated that the MMST system is stable if the set of models M_i is dense enough in the parameter space and the sampling rate is fast enough, depending on the particular system concerned.

For systems with a limited number of well described failure modes, multiple model switching and tuning is advantageous because of its speed and stability. However, aerospace systems are in general very complex, involving a large number of possible failure modes which are not all equally well definable, especially concerning structural failures, making this method less beneficial for fault tolerant flight control.

Propulsion Controlled Aircraft (PCA) The Propulsion Controlled Aircraft case (PCA), introduced in section 1.3.2, is a very specific example of MMST, in which only one, but a very drastic, failure mode has been considered, namely total loss of hydraulics. This research has been motivated initially by the Sioux city accident, see section 1.2.3, but the accidents described in sections 1.2.2 and 1.2.6 provide additional proof of the relevance of this specific research. Following a recommendation from the National Transportation Safety Board of America, the PCA problem was taken up by the NASA Dryden Flight Research Center [55] in order to provide a backup in case of total hydraulics failure. In 1995, a demonstration was made during which an MD-11 and an F-15 recovered from a complete hydraulic failure and landed successfully under propulsion-only control. PCA is a useful and important idea and solves a very practical problem. However, it is not sufficient to solve the general reconfigurable control problem.

Interacting Multiple Models (IMM), source: [286, 298]

The method of interacting multiple models (IMM) attempts to deal with the key limitation of MMST, namely that every fault scenario must be modelled, by considering fault models

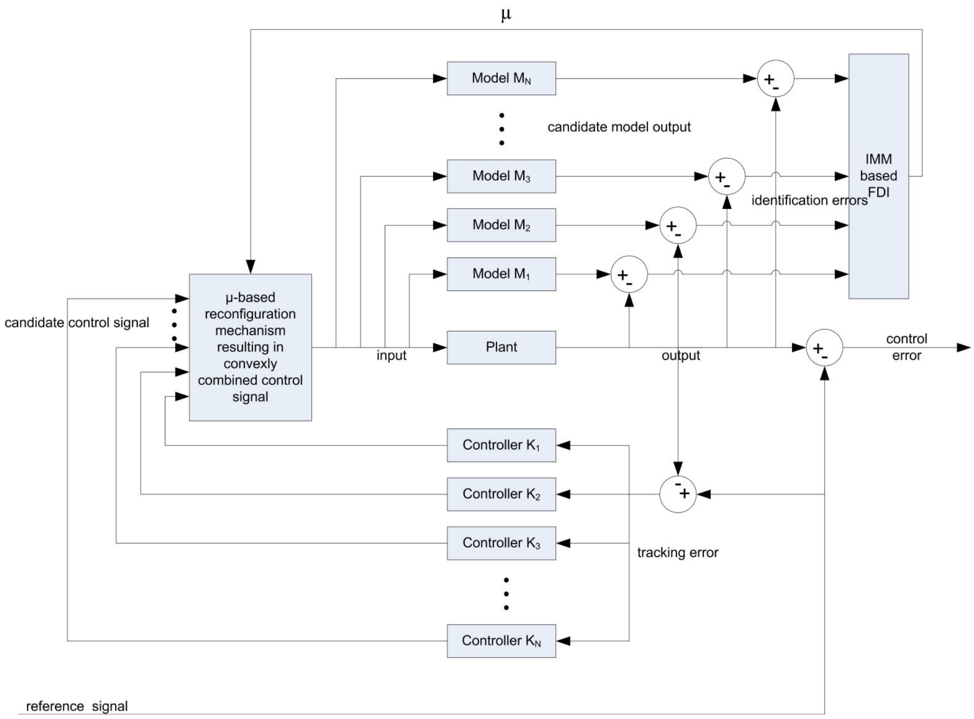

Figure 2.9: IMM control strategy

which are convex combinations of models M_i in a predefined model set $\mathcal{M}$. The set-up of the IMM approach is illustrated in fig. 2.9.

Consequently, the failed model can be defined as follows:

$$M_f = \sum_{i=1}^{N} \mu_i M_i = \mu^T \begin{bmatrix} M_1 \\ \vdots \\ M_N \end{bmatrix}, \quad M_i \in \mathcal{M},\ \mu_i > 0 \in \mathbb{R}, \sum_{i=1}^{N} \mu_i = 1, \tag{2.5}$$

where the variables μ_i are identified online in the fault detection and modelling step.

However, despite IMM being attractive because of its inherent ability to handle multiple combined failure scenarios, it still assumes that every possible failure can be modelled as a convex combination of models in a pre-determined model set, which is generally not true, especially for structural failures. Moreover, the need to identify values for the variables μ_i requires some additional time and as a result the IMM approach is somewhat slower than the MMST approach.

2.7 Scheduling, sources: [126, 234]

One of the earliest and most intuitive approaches to adaptive control is gain scheduling. It was introduced in particular in the context of flight control systems in the 1950's and 1960's. The idea is to find auxiliary process variables, which are different from the plant outputs used for feedback, that correlate well with the changes in process dynamics. It is then possible to compensate for plant parameter variations by changing the parameters of the regulator as functions of the auxiliary variables. This principle is illustrated in fig. 2.10. However, there are many types of functions that can describe how the regulator parameters depend on these auxiliary variables. The most important ones are described below.

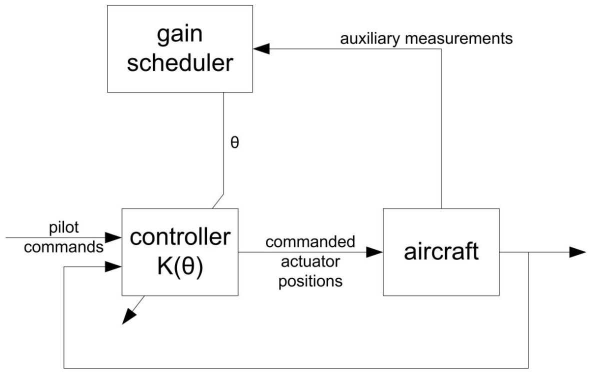

Figure 2.10: Gain scheduling

Multidimensional linear or higher order interpolation

The most straightforward gain scheduling setup consists of a look-up table and a multidimensional linear or higher order interpolation logic. In the case of aircraft, the auxiliary measurements are Mach number M and the dynamic pressure $\overline{q} = \frac{1}{2}\rho V^2$. The advantage of this setup lies in its speed, which depends only on the responses of the auxiliary measurements. The disadvantage is that it relies on an off-line precomputed database, which makes that it is restricted to the range of values for the auxiliary measurements as defined in the database and it lacks true flexibility for unpredictable changes, which makes it less suitable for fault tolerant control.

Figure 2.11: Boeing CH-47 Chinook of RNLAF, ©Ramon Berk, via Airliners.net

Further, the extent of design required for its implementation can be enormous, as can be illustrated by the flight control system implemented on a Boeing Vertol CH-47 Chinook helicopter. The flight envelope of the helicopter is divided into ninety flight conditions corresponding to thirty discretized horizontal flight velocities and three vertical velocities. Ninety controllers were designed, one corresponding to each flight condition, and a linear interpolation between these controllers (two-dimensional linear in the horizontal as well as vertical flight velocities) was programmed onto a flight computer. Airspeed sensors provided the auxiliary measurements to the control scheme of the helicopter in flight, and the effectiveness of the design was corroborated by simulation. The space shuttle is another example of an aerospace vehicle that uses gain scheduling during the entry phase [114]. The scheduling is based on dynamic pressure and Mach number and interpolates over 182 flight conditions representing the vast flight envelope of the shuttle during re-entry with respect to altitude and speed range.

Linear Parameter Varying control (LPV)

Classical interpolation is not the only way to achieve scheduling. Linear parameter varying (LPV) control design is closely related to it. Several shortcomings of classical gain scheduling motivated the LPV approach. First of all, the former lacks proofs of performance and stability, while obtaining and designing multiple controllers for a large flight envelope becomes easily very tedious, as illustrated by the Boeing Vertol CH-47 Chinook example.

By means of LPV methods, one obtains smooth semi-linear models, whose state-space descriptions are known functions of time-varying descriptive parameters such as altitude and/or airspeed. Hence, the actual nonlinear plant is mimicked through a parametrically changing model instead of choosing a combination of predefined linear models. The LPV model structure is represented as a linear system with $\mathbf{A}$, $\mathbf{B}$, $\mathbf{C}$ and $\mathbf{D}$ matrices, but each matrix can change based on the chosen descriptive parameter p, e.g. altitude and/or airspeed:

$$\dot{\mathbf{x}}(t) = \mathbf{A}(p)\,\mathbf{x}(t) + \mathbf{B}(p)\,\mathbf{u}(t) \tag{2.6}$$

$$\mathbf{y}(t) = \mathbf{C}(p)\,\mathbf{x}(t) + \mathbf{D}(p)\,\mathbf{u}(t) \tag{2.7}$$

If p is a constant, then the LPV system becomes an LTI (linear time invariant) system [96]. Methods for obtaining LPV models are discussed in [28]. The first method is based on linear fractional transformations and relies on the small gain theorem for bounds on performance and robustness. The other methods make use of either a single (SQLF) or parameter-dependent (PDQLF) quadratic Lyapunov function to bound the achievable level of performance. LPV models can be constructed from Jacobian linearizations at fixed power codes for control design. The results are polynomially fitted state space matrices which are continuous throughout the operating conditions [28, 189].

After the LPV modelling phase, the controller design follows. Instead of the classical approach above where predesigned controller gains are interpolated, Lyapunov methods have been used here to design LPV controllers, [28, 292] which depend on parametric changes in the system. In the field of fault tolerant control, LPV ideas have been used for dealing with actuator faults/failures [96]. LPV observers have also been considered for FDI purposes to generate residual signals for the fault detection of actuator and sensor faults [193].

Some general papers on LPV are [28, 292]. In the field of FTC, papers such as [96, 193] represent some of the research work in this area, more precisely they consider an LPV approach for dealing with faults/failures in the Boeing 747 model. The most recent LPV papers in the field of FTC are [232, 239, 240].

Fuzzy clustering

In the literature, even a third way is mentioned to achieve scheduling. In [236] a fuzzy logic approach is suggested, where fuzzy sets are represented by membership functions. For each failure hypothesis one model and control mode are used. Through the use of fuzzy measures that indicate the failure state, interpolation between the predefined failure modes and control modes is achieved. Each fuzzy controller corresponds to a particular failure type. In contrast to the multiple model control approach, smooth transitions and a gradual interpolation between the failure modes is achieved by using fuzzy logic rules. Moreover, in contrast to classical gain-scheduling approaches, control modes with different structure can still be defined. It has been shown that the method shows satisfactory performance in case of realistically modeled severe actuator failures. Smooth transition between the control modes is automatically achieved in case of a gradual degradation of control system components.

2.8 Controller synthesis

Three controller synthesis methods are briefly described, namely eigenstructure assignment, optimal control and model predictive control. The two latter methods involve the optimization of a certain cost function which serves as optimality criterion.

Eigenstructure Assignment (EA)

The output $\mathbf{y}(t)$ of a linear system depends on its eigenvalues λ_i, eigenvectors $\mathbf{v}_i$, initial condition $\mathbf{x}(0)$ and the input to the system $\mathbf{u}(t)$. Applying eigenstructure assignment [74] enables the selection of both eigenvalues λ_i and eigenvectors $\mathbf{v}_i$ and therefore provides the tools to shape the transient response $\mathbf{y}(t)$ of the system by adjusting the magnitude of each eigenmode that appears in each of the outputs. In Direct Eigenstructure Assignment (DEA), [23], the idea is to place first the eigenvalues using state feedback and then use any remaining degrees of freedom to align the eigenvectors as accurately as possible. However, there are several limitations to this approach when applied for reconfiguration purposes. First, only linear systems have been considered and actuator limitations have not been taken into account. Second, a perfect fault model is assumed and the effects of possible uncertainties have not been extensively studied. Finally, the effect of the eigenvectors in the failed system not being exactly equal to those in the nominal system is not well understood. The result of these significant limitations is that only a few researchers have proposed this approach.

Ref. [268] focusses on the stability analysis of a nonlinearly scheduled fault tolerant control system with varying structure. An aircraft problem is considered in which the tailplane suffers from degraded control effectivity, including the possibility of complete failure of the tailplane actuator, leaving the engines as only input to the system. Based upon Eigenstructure Assignment , three controllers are designed for three specific values of the control effectivity parameter. A scheme is set up which enables nonlinear interpolation between the three controllers based on the actual value of the effectivity parameter. One of the three controllers is designed for the case that the tailplane becomes completely inoperative. In this case the controller can only use the engines using a complete different control strategy for tracking. This controller synthesis procedure gives the designer the freedom to change the structure of the controller, which is necessary in case of complete failure of control surfaces. This set up provides fault tolerance of the controller for the specified failure. Other references about reconfigurable eigenstructure assignment can be found in [296, 297, 298]. Classical control combined with eigenstructure assignment has been applied in the Lockheed-Martin F-22 Raptor, [29].

Figure 2.12: A Lockheed-Martin F-22A Raptor of the US Air Force, ©Jonathan Derden, via Airliners.net

Optimal Control (OC)

Optimal control is related to finding a control law for a given system such that a certain optimality criterion is achieved. This criterion is a cost function which depends on state and control variables. An optimal controller description is a set of differential equations describing the paths of the control variables that minimize the cost functional. This can be derived using Pontryagin's maximum principle (a necessary condition), or by solving the Hamilton-Jacobi-Bellman equation (a sufficient condition).

A more abstract framework goes as follows. Given a dynamical system with time-varying input $\mathbf{u}(t)$, time-varying output $\mathbf{y}(t)$ and time-varying state $\mathbf{x}(t)$, define a cost function to be minimized. The cost function is the sum of the path costs, which usually take the form of an integral over time, and the terminal costs, which is a function only of the terminal (final) state, $\mathbf{x}(T)$. Thus, this cost function typically takes the form:

$$J = \phi\left(\mathbf{x}\left(T\right)\right) + \int_0^T L\left(\mathbf{x}(t), \mathbf{u}(t), t\right) dt \tag{2.8}$$

where T is the terminal time of the system. It is common, but not required, to have the initial (i.e., starting) time of the system be 0 as shown. The minimization of a function of this nature is related to the minimization of action in Lagrangian mechanics, in which case $L(\mathbf{x}(t), \mathbf{u}(t), t)$ is called the Lagrangian.

Linear Quadratic Control Considering LTI models as we are used to:

$$\begin{aligned} \dot{\mathbf{x}} &= \mathbf{A}\mathbf{x} + \mathbf{B}\mathbf{u} && (2.9) \\ \mathbf{y} &= \mathbf{C}\mathbf{x} && (2.10) \end{aligned}$$

One common cost function used together with this system description is:

$$J = \int_0^{\infty} \left(\mathbf{x}^T(t)\, \mathbf{Q}\mathbf{x}(t) + \mathbf{u}^T(t)\, \mathbf{R}\mathbf{u}(t) \right) dt \tag{2.11}$$

where the matrices $\mathbf{Q}$ and $\mathbf{R}$ are positive-semidefinite and positive-definite, respectively. Note that this cost function is thought in terms of penalizing the control energy (measured as a quadratic form) and the time it takes the system to reach zero-state.

The optimal control problem defined with the previous function is usually called the state regulator problem and its solution the linear quadratic regulator (LQR) which is no more than a feedback matrix gain of the form

$$\mathbf{u} = -\mathbf{K}\mathbf{x} \tag{2.12}$$

where $\mathbf{K}$ is a properly dimensioned matrix and solution $\mathbf{K} = \mathbf{R}^{-1}\mathbf{B}^T\mathbf{S}$ of the continuous time algebraic Riccati equation:

$$\mathbf{A}^T\mathbf{S} + \mathbf{S}\mathbf{A} - \mathbf{S}\mathbf{B}\mathbf{R}^{-1}\mathbf{B}^T\mathbf{S} + \mathbf{Q} = 0 \tag{2.13}$$

This problem was elegantly solved by Rudolf Kalman (1960).
For LQR control, the following requirements must be satisfied:

- the pair $(\mathbf{A}, \mathbf{B})$ is stabilizable
- $\mathbf{R} > 0$ and $\mathbf{Q} \geq 0$
- $(\mathbf{Q}, \mathbf{A})$ has no observable mode on the imaginary axis

In [133], an optimal control law is designed for Fault Tolerant Control Systems with Markovian Parameters. The matrix maximum principle is used to minimize an equivalent deterministic cost function. Three scenarios are considered. In these scenarios, optimal control laws are developed to reduce the risk of losing system stability. A computational algorithm is constructed to calculate the optimal control law.

LQR control has been applied in the Rockwell and MBB X-31 extreme manoeuvrability research aircraft for post-stall flight analysis, and integrated LQR/LQG control approach has been applied in the Boeing B-767, the Boeing X-32 JSF contender, Boeing X-45 J-UCAS, Boeing JDAM MMT and ACTIVE F-15, [29].

(a) Rockwell MBB X-31 in flight at high angle of attack, NASA Dryden Flight Research Center Photo Collection

(b) Boeing X-45A J-UCAS in flight, NASA Dryden Flight Research Center Photo Collection, photo by J. Ross

Figure 2.13: LQR control aircraft applications

Model Predictive Control (MPC), source: [265, 266]

A conventional MPC scheme works as follows (see also Figure 2.14). A model (usually a linear time-invariant discrete-time description of relevant process dynamics) is used to predict the outcome $\mathbf{y}(k)$ (the controlled variables) of the process based on an input sequence $\mathbf{u}(k)$ (the sequence of control inputs or manipulated variables) supplied to the process and on past measurements of the process. The goal is to achieve that $\mathbf{y}(k)$ follows a given reference trajectory $\mathbf{r}(k)$ (often a constant set-point) closely with reasonable control costs (related to e.g. energy consumption and pollution). A cost criterion reflects the reference tracking error and the control effort. The prediction horizon p is the number of time steps at which the reference trajectory is compared with the controlled variables $\mathbf{y}(k)$. The optimal input sequence over a given horizon can now be computed by solving an optimization problem (i.e. minimize the cost criterion over the allowed input sequences – and the corresponding $\mathbf{y}(k)$ predicted on the basis of the model – given the information of the past behaviour of the process). After computation of the optimal control sequence only the first control sample will be implemented, subsequently the horizon is shifted one sample and the optimization is restarted with new information of the measurements. This strategy makes adaptation to unexpected situations possible at a sample by sample basis. Consequently, the optimization problem has to be solved at every (discrete) time step. A key advantage

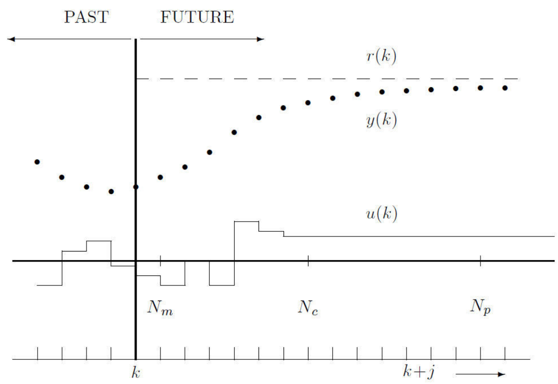

Figure 2.14: The moving horizon in predictive control, source: [266]

of MPC is that one can immediately accommodate for constraints on the input and outputs of the process. This changes the optimization problem only by incorporating the additional limitations. However, this renders the optimization much more complex and will require more computation time. To reduce the computational complexity the input is often taken to be constant outside a given control horizon m. This leads to a reduction of the number of optimization variables, and thus to a decrease of the computational burden. In addition it results in a smoother controller signal (because of the emphasis on the average behaviour rather than on aggressive noise reduction), and has a stabilizing effect (since the output signal is forced to its steady-state value).

As discussed in [185], the fault tolerance can be incorporated in an MPC architecture in a relatively easy way by:

a. redefining the constraints to represent certain faults (usually actuator faults),

b. changing the internal model to represent structural failures,

c. changing the control objectives to reflect limitations due to the faulty mode of operation.

Consequently, there is practically no additional optimization that needs to be executed online as a consequence of a fault being diagnosed, so that this method can be viewed as having an inherent self-reconfiguration property. However, with respect to item b., it needs to be said that changing the internal model can only be done when some identification algorithm or observer is supplying updated model information including faults/failures to the model predictive controller. Examples of the application of MPC to FTC are numerous [148, 151, 152, 186, 227, 271]. Currently, the author is involved in research being performed at Delft University of Technology, Delft Center of Systems and Control (DCSC), where adaptive feedback linearization in the inner loop is integrated with model predictive control in the outer loop. This research makes explicit use of on-line aerodynamic model identification, by means of the identification method elaborated in this thesis. Intermediate results of this research can be found in [141, 142, 143].

Subspace Predictive Control (SPC) Like most active FTC methods, MPC-based FTC requires availability of fault information to accommodate faults. This information can be supplied by an identification algorithm, as already discussed in the last section. A possible integrated solution is subspace predictive control (SPC). This algorithm consists of a predictor that is derived using subspace identification theory [278], making it a data-driven control method. This subspace predictor is subsequently integrated into a predictive control objective function. The basic SPC algorithm was introduced by [92] and has since been used by various researchers [147, 283, 291]. If the subspace predictor is updated on-line with new input-output data as soon as these become available, then SPC has the ability to adapt to changing system conditions, which can also include unanticipated faults. Besides having this ability, another important advantage of the SPC algorithm is that the issue of robustness with respect to model uncertainty is implicitly addressed because of the adaptation of the predictor. In [110, 111] the SPC algorithm is used for FTC of the RECOVER benchmark model used in this thesis.

2.9 Adaptive control

Adaptive control methods are a subcategory of on-line redesigning active fault tolerant control methods, which have the inherent ability to adapt to changes in the system parameters. This type of adaptive controller is formed by combining an on-line parameter estimator, providing unknown parameter estimates at each time instant, with a control law which is motivated from the known parameter case. This category is very extensive on its own, and can be subdivided into direct and indirect adaptive control. Two important types of adaptive control are Model Reference Adaptive Control (MRAC) and Self Tuning Control (STC). Both can be designed using the direct as well as the indirect approaches. This section describes briefly a selection of adaptive control methods which have been used in recent research for fault tolerant flight control, but this list of methods is far from complete.

2.9.1 Direct versus indirect adaptive control

The way how the earlier mentioned parameter estimator, which provides unknown parameter estimates at each time instant, is combined with the control law results in two different approaches. In the first approach, referred to as indirect adaptive control, the plant parameters are estimated on-line and used to calculate the controller parameters in a separate subsequent step. This approach has also been referred to as modular adaptive control, because this setup assumes two separate modules: a plant parameter estimation step and a control parameter calculation step. An alternative name is explicit adaptive control, since the design is based on an explicit plant model. In the second approach, referred to as direct adaptive control, the plant model is parameterized in terms of the controller parameters that are estimated directly without intermediate calculations involving plant parameter estimates. This approach has also been referred to as integrated adaptive control, since the aforementioned separate modules in the modular setup have been replaced by one integrated step, which estimates the controller parameters immediately without intermediate steps. Another frequently used name for this approach is implicit adaptive control, because the design considers the plant model only implicitly, without actually estimating the plant parameters. Figure 2.15 illustrates the difference between direct and indirect adaptive control.

As a final remark, it is important to be aware of the fact that the indirect adaptive control setup in fig. 2.15(b) relies on the convergence of the estimated parameters $\hat{\boldsymbol{\theta}}$ to their true unknown values $\boldsymbol{\theta}$. This means that the controller parameters are computed from the estimates of the plant parameters as if they were the true ones. This is called the certainty equivalence principle. On the other hand, in general, a convenient (for the purpose of estimation) parameterization of the plant model in terms of the desired controller parameters is not possible for non-minimum phase (NMP) plant models, according to ref. [126].

2.9.2 Model Reference Adaptive Control (MRAC) versus Self Tuning Control (STC)

There are two main approaches for constructing adaptive controllers, independent from the direct/indirect classification. One is the so-called model-reference adaptive control method, and the other is the so-called self-tuning method.

Generally, a model-reference adaptive control system (MRAC) can be schematically

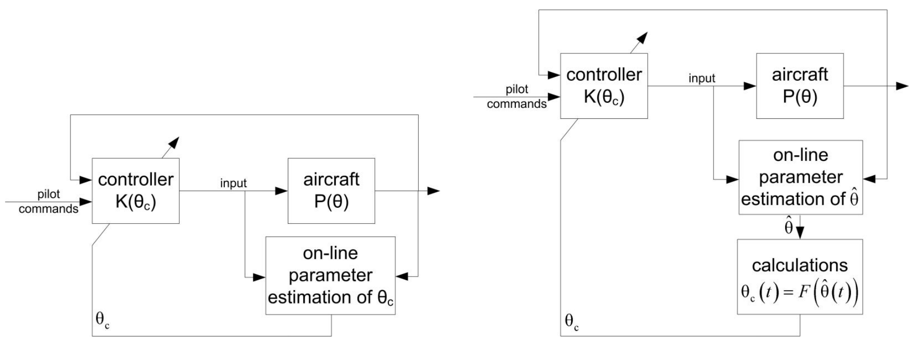

(a) direct adaptive control (b) indirect adaptive control

Figure 2.15: Direct versus indirect adaptive control

represented by figure 2.16(a). It is composed of three parts besides the to-be-controlled aircraft containing unknown parameters: a reference model for compactly specifying the desired output of the control system, a feedback control law containing adjustable parameters, and an adaptation mechanism for updating the adjustable parameters. Each of them will be described briefly. The reference model is used to specify the ideal response of the adaptively controlled system to the external reference command. It provides the ideal plant response which the adaptation mechanism should search for in adjusting the controller parameters. This reference model needs to reflect the performance specifications and its output should be achievable for the adaptive control system. The controller is usually parameterized by a number of adjustable parameters. Perfect tracking capacity of the controller is required in order to achieve tracking convergence. For perfectly known aircraft parameters, the controller makes the output identical to the reference output. For unknown plant parameters, perfect tracking is asymptotically achieved through controller parameter adjustment by the adaptation mechanism. This adaptation law searches for parameters such that the response of the plant under adaptive control becomes the same as that of the reference model. The adaptation objective is to eliminate the tracking error.

On the other hand, a controller obtained by coupling it with an on-line (recursive) parameter estimator is called a self-tuning controller (STC). Figure 2.16(b) illustrates the schematic structure of such an adaptive controller. A self-tuning controller is a controller which performs simultaneous identification of the unknown plant, in this case the aircraft. This type of controller operates as follows. At each time instant, the estimator estimates the plant parameters $\hat{\boldsymbol{\theta}}$, which are computed based on aircraft in- and output. These parameters are sent to the control law design computer, which computes the corresponding controller parameters and sends them to the controller, which computes a control input based on the controller parameters and the measured signals. Also in this approach, one relies on the certainty equivalence principle.

An example of application of STC for fault tolerant flight control can be found in [14], where a self-tuning controller has been developed by combining the controller with a recur-

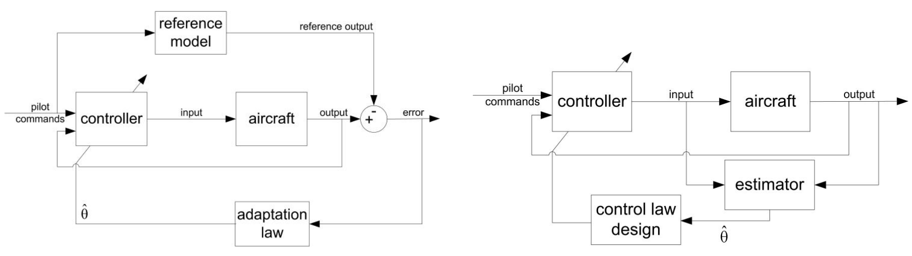

(a) model-reference adaptive control (MRAC) (b) self-tuning control (STC)

Figure 2.16: Model-reference adaptive control versus self-tuning control

sive least squares parameter estimation method with an adaptive forgetting factor which is calculated through the multiple model (XAFMM, or extended adaptive forgetting through multiple model) approach, consisting of a bank of Kalman Filters. In addition, a switching algorithm is used to overcome the identifiability problem whenever the aircraft experiences non-persistently exciting input signals.

The control law design algorithm uses the pole placement method. The STC method has been applied to the design of a longitudinal autopilot mode and has been evaluated in several linear and nonlinear computer simulations as well as flight tests using the DHC-2 BEAVER laboratory aircraft of Delft University of Technology in the 1990's.

Figure 2.17: Delft University DHC2 Beaver PH-VTH, photo by Jack Wolbrink

A whole world of adaptive control methods exists. In the following paragraphs, a selection of methods will be briefly discussed, namely adaptive model following, adaptive neurocontrol, which can be augmented with σ and e-modifications, reinforcement learning, $\mathcal{L}_1$ adaptive control, adaptive backstepping and finally adaptive nonlinear dynamic inversion.

Adaptive Model Following (AMF)

The model following method is one possible approach to adaptive FTC. Basically, the method considers a reference model of the form

$$\begin{aligned} \mathbf{x}_{k+1}^M &= \mathbf{A}_M \mathbf{x}_k^M + \mathbf{B}_M \mathbf{r}_k, \\ \mathbf{y}_k^M &= \mathbf{x}_k^M, \end{aligned}$$

where $\mathbf{r}_k$ is a reference trajectory signal. The goal is to compute matrices $\mathbf{K}_r$ and $\mathbf{K}_x$ such that the feedback interconnection of the open-loop system

$$\begin{cases} \mathbf{x}_{k+1} = \mathbf{A}\mathbf{x}_k + \mathbf{B}\mathbf{u} \\ \mathbf{y}_k = \mathbf{C}\mathbf{x}_k, \end{cases}$$

and the state-feedback control action

$$\mathbf{u}_k = \mathbf{K}_r \mathbf{r}_k + \mathbf{K}_x \mathbf{x}_k$$

matches the reference model. To this end the reference model and closed-loop system are written in the form

$$\begin{aligned}\mathbf{y}_{k+1}^{M} &= \mathbf{A}_M\mathbf{x}_k^M + \mathbf{B}_M\mathbf{r}_k,\\ \mathbf{y}_{k+1} &= (\mathbf{CA} + \mathbf{CBK}_x)\mathbf{x}_k + \mathbf{CBK}_r\mathbf{r}_k,\end{aligned}$$

so that *perfect model following* (PMF) can be achieved by selecting

$$\text{PMF:} \begin{cases} \mathbf{K}_x = (\mathbf{CB})^{-1}(\mathbf{A}_M - \mathbf{CA}), \\ \mathbf{K}_r = (\mathbf{CB})^{-1}\mathbf{B}_M, \end{cases} \tag{2.14}$$

provided that the system is square (i.e. $\dim(\mathbf{y}) = \dim(\mathbf{u})$), and that the inverse of the matrix $\mathbf{CB}$ exists. When the exact system matrices $(\mathbf{A}, \mathbf{B})$ in (2.14) are unknown, they can be substituted by some estimated values $(\hat{\mathbf{A}}, \hat{\mathbf{B}})$, resulting in *the indirect (explicit) method* [39]. The indirect method provides no guarantees for closed-loop stability, and in addition, the matrix $(\mathbf{C}\hat{\mathbf{B}})$ may not be invertible. In order to avoid the need for estimating the plant parameters, the *direct (implicit) method* of model following can be used, which directly estimates the controller gain matrices $\mathbf{K}_r$ and $\mathbf{K}_x$ by means of an adaptive scheme. Two approaches to direct model following exist, the output error method and the input error method. Examples of the application of the model following approach can be found in [39, 107, 153, 205, 262].

In [253], adaptive model following has been applied on the RECOVER benchmark model as used in this thesis.

Adaptive Neurocontrol (ANC)

Adaptive neurocontrol combines the concepts from artificial neural networks and adaptive control, [161]. Artificial neural networks (ANN) are mathematical networks that mimic the working principle of neural connections in the human brain. The main components of the adaptive neuro-controllers are an identification network and a controller network, and both can be based on ANN's. Both these networks are trained using the back-propagation of an error learning paradigm. There are several benefits in using neural networks in adaptive nonlinear control. These include:

- A neuro-controller learns to control a system based on the input-output couplings that exist. Also, neural networks have been shown to extract input-output mapping even out of noise-corrupted data. This implies that a decentralized controller can be implemented using neuro-controllers with direct output feedback.

- The necessity for a learning-type controller for fault tolerant flight control applications arises due to the conditions of uncertainty in the environment of operation and due to the possibility of component or structural failures.

Artificial Neural Networks have been used for identification as well as for control purposes. Ref. [78] has used neural networks for aerodynamic model identification for the purpose of reconfiguring control. However, this section will focus on an aircraft control application, [46]. As already introduced in section 1.3.5, a direct adaptive neural-network based flight control system was developed for the NASA NF-15B airplane in the Intelligent Flight Control System (IFCS) research project. Figure 2.18 shows the intelligent flight control system control architecture.

In this project, the goal of the neural network system is to accommodate large errors that are not anticipated in the nominal control law design. A well-designed adaptive flight control system, in this case the combination of a linear controller and a dynamic inversion block, is to some extent robust and maintains stability and controllability for a fairly large range of uncertainty or changes in airplane behaviour, besides its adaptivity ensures it is able to readjust the controller to re-achieve desired stability and controllability or regain robustness about new operating points. In the case of a failure (structural or actuator failure), larger-than-expected errors will develop, which cannot be compensated by the aforementioned components of the controller. The reason why the dynamic inversion block cannot deal with this kind of failures is the fact that the state and control inversion matrices are static. They are not updated by means of an on-line identification algorithm. The adaptive neural networks compensate for this and operate in conjunction with the measured response error of the control system. Weights (gains) on the neural network parameters are dynamically adjusted until the error is reduced. These weights act as parallel augmenting adjustments to the proportional, integral and forward-loop gains. These weights can also provide a control bias, a new feedback to the system, or new crossfeed paths between the control axes. When optimal weights are achieved, the feedback error is minimized and the system

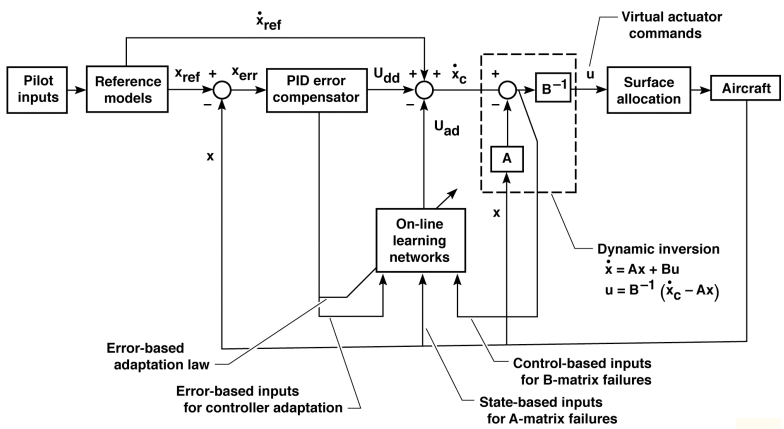

Figure 2.18: The intelligent flight control system control architecture, source: [46]

achieves better reference model-following performance and better handling qualities. Ref. [46] provides more details about the exact setup of the simplified sigma-pi neural network for the IFCS research project.

Ref. [135] is another aerospace application where neural networks augment a feedback linearization control setup, applied on the X-33. Other aerospace applications of adaptive neurocontrol can be found in ref. [219, 221].

σ-, e- and $Q-$modification to neuroadaptive controllers To improve robustness and the speed of adaptation of neuroadaptive controllers, several controller architectures have been proposed in the literature. These include the $\sigma-$ and $e-$modification architectures used to keep the system parameter estimates from growing without bound in the face of system uncertainty and system failures, [217]. More recently, a $Q-$modification has been suggested as a superior alternative for the two former architectures, [280].

Among the many robustifying modifications which have been suggested for the adaptive control purpose of an unknown plant in the presence of disturbances (failures), few have gained wide acceptance. Besides the use of dead-zones in the adaptive law to assure boundedness of all the signals in the adaptive loop, another widely accepted modification, generally referred to as $\sigma-$modification, introduces an additional term of the form $-\sigma\boldsymbol{\theta}$ in the adaptive law for adjusting the parameter vector $\boldsymbol{\theta}$, [125]. While this has the advantage that it assures boundedness of solutions without additional information regarding the system, it suffers from drawbacks which are essentially caused by the bias due to the additional term in the adaptive law. In [217], an alternative adaptive law is proposed in which the aforementioned constant σ is replaced by a term proportional to $|\mathbf{e}|$ where $\mathbf{e}$ is the output error. This modification, referred to as $e-$modification, is shown to improve the performance of the system in all respects while retaining the advantage of assuring robustness in the presence of bounded disturbances, without requiring additional information regarding the plant or the disturbance (failure). One of the major advantages of the $e-$modification scheme over that of the $\sigma-$modification, arises from the fact that in the ideal case the former results in exponential stability of the origin of the error equations if the reference input is persistently exciting with a large amplitude.

More recently, in [280], a new modification term has been suggested, referred to as $Q-$modification. The proposed framework involves a new controller architecture containing additional terms ($Q-$modification terms) in the update law that are constructed using a moving window of the integrated system uncertainty. The $Q-$modification terms can be used to identify the ideal neural network weights which can be used in the adaptive law, and these terms effectively suppress system uncertainty as well as system failures.

Recent fault tolerant flight control applications of these modification terms can be found in [220, 294].

Reinforcement Learning (RL)

Reinforcement learning labels the collection of methods and procedures where interaction with the environment is used to gather information which is then used to reach certain goals related to this interaction. Reinforcement learning methods try to capture a primitive part of human or animal learning into mathematical algorithms and are mostly used to create self-learning or adapting controllers for real or simulated systems. The ability to adapt itself to the environment makes reinforcement learning controllers especially useful in the field of reconfigurable flight control. The difference between reinforcement learning and supervised learning is that for supervised learning the correct control output is given to the controller and learning is based on the error between the correct output and the controller output, while in reinforcement learning the feedback is a more abstract reward signal and learning is based on maximizing this reward over time. Rather than learning from the required control actions, which are not always available, a reinforcement learning controller is taught what the favourable states of the plant are and the controller must learn for itself what kind of control actions are required to reach these favourable states.

However, due to the severe computational load and its related restrictions to on-line applications, reinforcement learning has not been applied frequently for fault tolerant flight control. Recent FTFC applications of reinforcement learning can be found in [85, 270], where reinforcement learning is applied off-line in most cases.

$\mathcal{L}_1$ adaptive control

Recent papers [59, 60] introduced the $\mathcal{L}_1$ adaptive control architecture, which has guaranteed transient and steady-state performance bounds for system's input and output signals in the presence of fast adaptation.

Consider the scalar system given by:

$$\dot{x}(t) = ax(t) + bu(t), \quad x(0) = x_0 \tag{2.15}$$

where $x \in \mathbb{R}$ is the state, $u \in \mathbb{R}$ is the control signal, a is unknown, $b \in \mathbb{R}$ is known, $a = a_m - b\theta$, $a_m < 0$, the unknown parameter θ belongs to a given closed interval $[\theta_l, \theta_u], \theta_l < \theta_u$. The control objective is to design an adaptive controller $u(t)$ to ensure that system state $x(t)$ follows a given bounded reference signal $r(t)$ with quantifiable bounds both in transient and steady state.

Rewrite system (2.15) as:

$$\dot{x}(t) = a_m x(t) - b\theta x(t) + bu(t), \quad x(0) = x_0 \tag{2.16}$$

For this linearly parameterized system, consider the following state predictor:

$$\dot{\hat{x}}(t) = a_m \hat{x}(t) - b\hat{\theta}(t)\hat{x}(t) + bu(t), \quad \hat{x}(0) = x_0 \tag{2.17}$$

along with the adaptive law for $\hat{\theta}(t)$:

$$\dot{\hat{\theta}}(t) = -\gamma \text{Proj}(\hat{\theta}(t), b\tilde{x}(t)x(t)) \tag{2.18}$$

where $\gamma > 0$ is the adaptation gain. This projection type adaptive law ensures that $\hat{\theta}(t) \in [\theta_l, \theta_u]$ for all $t \geq 0$. Let

$$u(s) = C(s)(\overline{r}(s) + k_g r(s)), \quad k_g = \frac{a_m}{b} \tag{2.19}$$

where $\overline{r}(t) = \hat{\theta}x(t)$, while $C(s)$ is an asymptotically stable and strictly proper transfer function with steady state gain $C(0) = 1$ and zero initialization. The $\mathcal{L}_1$ adaptive control consists of (2.17), (2.18) and (2.19), with $C(s)$ satisfying

$$\lambda \triangleq \|\overline{G}(s)\|_{\mathcal{L}_1}\theta_{\max} < 1, \quad \overline{G}(s) = \frac{b(1 - C(s))}{s - a_m}, \quad \theta_{\max} = \max\{|\theta_l|, |\theta_u|\} \tag{2.20}$$

The stability proof of this control approach is Lyapunov based.

In [173], it has been shown that this control approach, with some adjustments, works satisfactorily in the presence of input saturation, including proof of stability and computation of performance bounds.

$\mathcal{L}_1$ adaptive control attracts a lot of interest for fault tolerant flight control. Recent results are presented in [79, 106, 154].

Adaptive backstepping

Backstepping is a systematic, Lyapunov-based method for nonlinear control design, which can be applied to a broad class of systems. The name backstepping refers to the recursive nature of the design procedure. The design procedure starts at the scalar equation which is separated by the largest number of integrations from the control input and steps back toward the control input. Each step an intermediate or virtual control law is calculated and in the last step the real control law is found. An important feature of backstepping is the flexibility of the method. For instance, stabilizing nonlinearities of the system can be retained in the design. This is in contrast with feedback linearization designs, where all nonlinearities are canceled. The advantages of not canceling the useful nonlinearities is that it requires less accurate system models, while at the same time it possibly requires also less control effort. Main issue for backstepping is to define a so-called control Lyapunov function (clf), which is smooth and positive definite. If such a clf exists, a control law can be found which makes the closed-loop system globally asymptotically stable (GAS). However, the problem is how to find a clf of the corresponding control law. The backstepping procedure allows to find a clf and a control law simultaneously. By providing model identification information to this control approach, one obtains adaptive backstepping. More theoretical background information can be found in chapter 2 of [162] and chapter 3 of [118].

Applications of adaptive backstepping for flight control can be found in [91] and for fault tolerant flight control can be found in [254, 255].

Adaptive Nonlinear Dynamic Inversion (ANDI)

A major attraction of dynamic inversion is its ability to naturally handle changes of operating condition, which removes the need for gain scheduling, e.g. for classical control methods. This is especially advantageous for control of space re-entry vehicles, due to their extreme and wide operating conditions which vary from supersonic speed during re-entry and subsonic regions during the terminal glide approach phase to the runway. Another advantage is its natural property of decoupling the control axes, i.e. no coupling effects remain between steering channels and the different degrees of freedom. NDI control has been implemented in the Lockheed F-35 Lightning II, [29, 282].

Nonlinear dynamic inversion considers original nonlinear systems of the affine form:

$$\dot{\mathbf{x}} = \mathbf{a}(\mathbf{x}) + \mathbf{b}(\mathbf{x})\,\mathbf{u} \tag{2.21}$$

and provides a solution for the physical control input $\mathbf{u}$ by introducing an outerloop virtual control input $\boldsymbol{\nu}$:

$$\mathbf{u} = \mathbf{b}^{-1}(\mathbf{x})\,[\boldsymbol{\nu} - \mathbf{a}(\mathbf{x})] \tag{2.22}$$

which results in a closed-loop system with a decoupled linear input-output relation:

$$\dot{\mathbf{x}} = \boldsymbol{\nu} \tag{2.23}$$

Figure 2.19 shows the control architecture related to Nonlinear Dynamic Inversion.

A linear outer loop control law is sufficient to enforce exponentially stable tracking dynamics, where the control gains can be determined by the required closed loop characteristics.

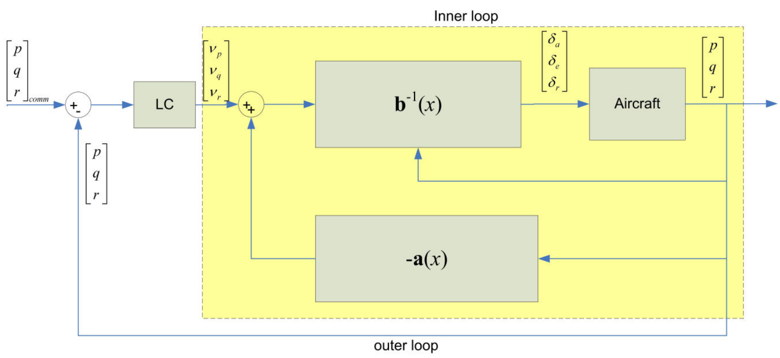

Figure 2.19: Setup of the Nonlinear Dynamic Inversion control architecture

Dynamic inversion is a popular control method for flight control and aircraft guidance, [15, 27, 58, 72, 146, 231, 229, 273] as well as reconfiguring control, [97, 98, 223, 225].

The main assumption in NDI is that the plant dynamics are assumed to be perfectly known and therefore can be cancelled exactly. However, in practice this assumption is not realistic, not only with respect to system uncertainties but especially to unanticipated failures for the purpose of fault tolerant flight control. In order to deal with this issue, one can make use of robust control methods such as $\mathcal{H}_\infty$ and μ-synthesis as outer loop control to minimize or suppress undesired behaviour due to plant uncertainties which cause imperfect plant dynamic cancellation. Other control methods such as neural networks also have been proposed in the literature, in order to augment the control signal as a compensation for the non-inverted dynamics, as explained previously. However, another solution to the weakness of classical NDI, namely its sensitivity to modelling errors, is the use of a real time identification algorithm, which supplies updated model information to the dynamic inversion controller. These augmented structures are called adaptive nonlinear dynamic inversion (ANDI). The latter procedure is the method of choice for this research which led to the results presented in this thesis. This choice will be motivated at the end of this survey of fault tolerant control methods.

2.10 Stochastic control, source: [234]

All control methods considered until now are based on heuristic arguments. It would be appealing to obtain such structures from a unified theoretical framework. This can be done, in principle, by stochastic control. A stochastic model describes the system and a criterion is formulated to minimize the expected value of a cost function based on states and controls. It is usually very difficult to solve stochastic optimal control problems (except for linear quadratic Gaussian problems). When they are solvable, the optimal control setup structure looks like in figure 2.20: an hyperstate identifier (estimator) followed by a nonlinear feedback regulator.

The estimator generates the conditional probability distribution of the state from the measurements, called hyperstate in an infinite dimensional vector space. The hyperstate steers the self tuning controller.

From some limited experience with stochastic control, some interesting observations can be made. Next to the driving signals providing the desired reference signals, the controller introduces probing signals in order to improve identification and subsequently control activities. This comes at the cost of some additional control activity. In fact, the optimal regulator generates a well-balanced control activity between learning and controlling, also referred to as dual control. This principle applies for other fault tolerant control techniques too, in order to optimize identification results.

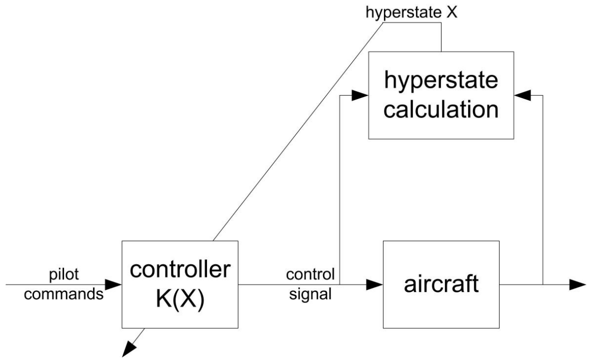

Figure 2.20: Generic stochastic controller

The stochastic control approach is not very recent, and only one application for fault tolerant control has been found in [256].

2.11 Final remark with respect to fault tolerant control classification

It is once again emphasized that this fault tolerant flight control survey has been made rather extensively, but it can never be complete with reference to all the methods ever used for FTFC research. Moreover, the classification as illustrated in fig. 2.1 is not unique and corresponds with the personal point of view of the author. Other classifications are possible and a lot of exceptions exist to this structure. A few of them are given here. LPV control is arguably placed in the scheduling approach, but it can be classified as well under the label adaptive control. Moreover, the integrated approach of feedback linearization and model predictive control described in [141, 142, 143] belongs partially to adaptive control and partially to the controller synthesis approach. The work described in [14] is a combination of Self Tuning Control and the Multiple Model approach. In [220], a combination of MRAC control and optimal control is presented. Ref. [171] shows a hybrid approach combining neural networks and dynamic model inversion for helicopter flight control. The enumerations of control methods in fig. 2.1 is not exhaustive either, as an example ref. [45] presents a direct and an indirect adaptive control technique, where both do not clearly fit in any of the subcategories elaborated here. Related work can be found in ref. [43, 44]. Finally, [168] presents a combined / composite model reference adaptive control approach in which direct and indirect adaptive control have been integrated. This control setup is sometimes also referred to as hybrid control. Despite numerous exceptions, the classification presented in this survey creates some structure in the rich collection of all kinds of FTFC methods.

2.12 Chosen method and motivation

Because of its inherent flexibility to adapt to changes in the system parameters, adaptive control has been preferred in this research project. More precisely, the combination of adaptive nonlinear dynamic inversion, augmented with control allocation, and a real-time aerodynamic model identification routine has been chosen here as the control approach to be followed, where focus is placed on the use of mathematical representations based on flight dynamics. The drawback of ANDI is that, since it is not based upon Lyapunov's Theorem like adaptive backstepping or sliding mode control, no formal stability proof can be given. However, relying on the certainty equivalence principle, the stability proof is implicitly removed in this setup. Moreover, all quantities and variables which appear in the model have a physical meaning and thus are interpretable in this approach, and one avoids so-called black and grey box models where the content has no clear physical meaning. Besides the fact that this is a more transparent approach, allowing the designers and engineers to interpret data in each step, it is assumed that these physical models will facilitate certification for eventual future real life applications, since monitoring of data is more meaningful.

Chapter 3

Aerodynamic Model Identification

Since a model based control method has been chosen for the purpose of fault tolerant flight control, namely adaptive nonlinear dynamic inversion, one needs also a real-time aircraft model identification routine. A brief literature survey is given in this chapter about different methods for model identification, but also about other aspects which are closely related, like excitation issues, required sensors, etc. Main sources of information for this literature study are ref. [65, 159]. A historical overview of the evolution of flight vehicle system identification is given in ref. [112].

3.1 Mathematical modeling

Before the actual aircraft system identification procedure can start, one needs to select the appropriate type of mathematical model. This model describes the dynamic motion of an aircraft, such as the nonlinear differential equations. However, there are many alternatives with varying suitability, dependent on the chosen purpose and identification methods. The most popular types of models are state space models, differential equations and transfer functions. Principal categorizations of these models is possible such as linear versus non-linear, representing local versus global validity of models, time invariant versus time varying, depending if the system properties are constant or varying, continuous versus discrete time, which depend on the choice for analog or digital equipment, and finally deterministic versus stochastic, which is determined by the choice to consider Gaussian processes or not. All these above models are finite dimensional and are grouped under the label parametric models. On the other hand, there exist non-parametric models, which are in fact infinite dimensional, like impulse or step responses, frequency responses, correlation functions, spectral densities, etc.

3.2 Aircraft system identification

The actual system identification phase follows after the mathematical model type has been chosen. The general system identification approach steps for an aircraft are respectively: model postulation, experiment design, data compatibility analysis, model structure determination, parameter and state estimation, collinearity diagnostics and finally model validation. A graphical overview of these steps and their mutual links is given in figure 3.1. Each step will be concisely elaborated below. The most important steps are model structure determination and parameter-state estimation, as can be seen in figure 3.1, and these will be extensively elaborated thereafter. A crucial issue in this matter is the identifiability of the system. Questions related to system identifiability are about information content and data richness so that different models are distinguishable, model formulation leading to unique parameter values, and physical realism of estimated parameter values and their (small) error bounds. Identifiability is mentioned in a rigorous way in ref. [174].

3.2.1 Model postulation

The postulation of a model is based on a priori knowledge. As an example, aerodynamic forces and moments can be expressed in linear expansions, or polynomials, or alternatively polynomial spline functions, or otherwise. These types of models are sufficient for modeling steady state aerodynamics. However, in the presence of unsteady aerodynamic effects, one needs indicial functions, see e.g. ref. [214], or additional state equations in order to take these effects correctly into account.

A collection of equations of motion allows to define a mathematical model of an aircraft:

- **Rigid body equations of motion:** These are based on Newton's second law of motion in translational and rotational form. They represent the nonlinear relationship between the applied forces **F** and moments **M** on one hand, and the kinematics on the other:

$$\mathbf{F} = m\dot{\mathbf{V}} + \boldsymbol{\omega} \times m\mathbf{V} \tag{3.1}$$

$$\mathbf{M} = \mathbf{I}\dot{\boldsymbol{\omega}} + \boldsymbol{\omega} \times \mathbf{I}\boldsymbol{\omega} \tag{3.2}$$

  The applied forces **F** and moments **M** arise from aerodynamics, gravity and propulsion contributions.

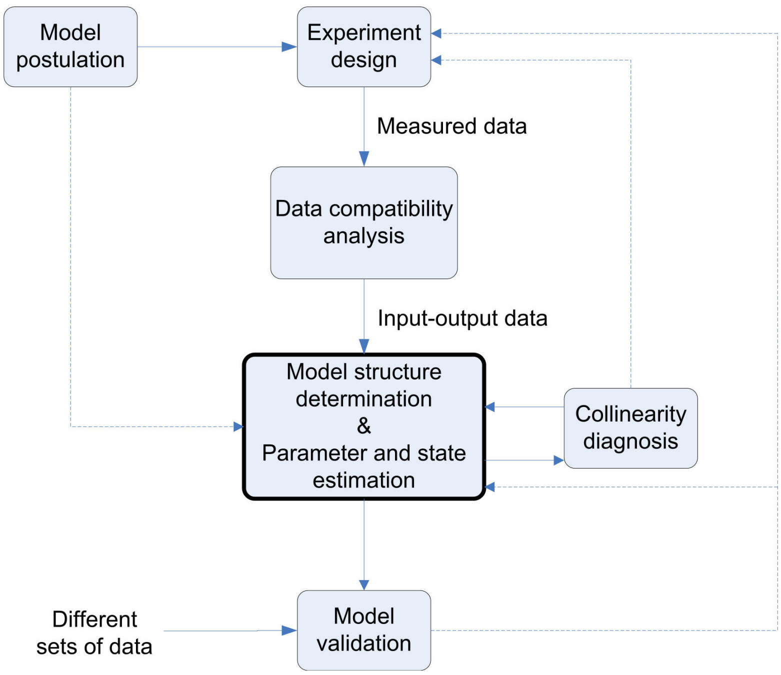

Figure 3.1: Block diagram with overview of aircraft system identification, source: [159]

- **Rotational kinematic equations:** This is essentially a transformation between frames of reference, where the first order time derivatives of the Euler angles $\dot{\phi}, \dot{\theta}, \dot{\psi}$, defined in the Earth fixed reference frame, are written in terms of angular velocity components p, q, r, defined in the body fixed reference frame. For a definition of the different frames of reference, see ref. [212].
- **Navigation equations:** Basically another reference frame transformation, where the body axes related velocity vector components u_b, v_b, w_b are described with reference to the earth axes u_n, v_n, w_n.
- **Wind axis force equations:** These make the connection from the body axes related velocity vector components u_b, v_b, w_b towards the sensor measurements of airspeed V, angle of attack α and sideslip angle β, including sensor disturbances, such as bias and noise.

Finally, if the wind axis force equations are not included, then the output equations have to be added to the equations of motion, which include the sensor disturbance contributions. These above mentioned equations are all well known. The aerodynamic model equations, on the other hand, cannot be defined as clearly as the others in a general set-up. Reason for this is the fact that the mathematical structure depends on the situation and assumptions. Here is the focus of system identification.

For the aerodynamic model equations, one can choose between a quasi-steady flow with time-invariant parameters, and an unsteady flow with unsteady aerodynamics. In the former category, one can choose between linear models, consisting of first order linear Taylor expansions, and nonlinear models. In such a linear quasi-steady model, contributions from aircraft states to the dimensionless forces and moments are expressed in terms of the so-called aerodynamic derivatives: [1]

$$C_X = C_{X_0} + C_{X_\alpha}\alpha + C_{X_{\alpha^2}}\alpha^2 + C_{X_q}\frac{q\bar{c}}{V} + C_{X_{\delta_e}}\delta_e + C_{X_{T_c}}T_c \tag{3.3}$$

$$C_Z = C_{Z_0} + C_{Z_\alpha}\alpha + C_{Z_q}\frac{q\bar{c}}{V} + C_{Z_{\delta_e}}\delta_e + C_{Z_{T_c}}T_c \tag{3.4}$$

$$C_m = C_{m_0} + C_{m_\alpha}\alpha + C_{m_q}\frac{q\bar{c}}{V} + C_{m_{\delta_e}}\delta_e + C_{m_{T_c}}T_c \tag{3.5}$$

$$C_Y = C_{Y_0} + C_{Y_\beta}\beta + C_{Y_p}\frac{pb}{2V} + C_{Y_r}\frac{rb}{2V} + C_{Y_{\delta_a}}\delta_a + C_{Y_{\delta_r}}\delta_r \tag{3.6}$$

$$C_l = C_{l_0} + C_{l_\beta}\beta + C_{l_p}\frac{pb}{2V} + C_{l_r}\frac{rb}{2V} + C_{l_{\delta_a}}\delta_a + C_{l_{\delta_r}}\delta_r \tag{3.7}$$

$$C_n = C_{n_0} + C_{n_\beta}\beta + C_{n_p}\frac{pb}{2V} + C_{n_r}\frac{rb}{2V} + C_{n_{\delta_a}}\delta_a + C_{n_{\delta_r}}\delta_r \tag{3.8}$$

More nonlinear terms can be added to these expansions. This is necessary for large amplitudes, flight profiles with high angle of attack, and rapid excursions. These nonlinearities

[1] A discussion about the need of $\dot{\alpha}$ in this model is given in section 4.2.

can in one way be represented by multivariate polynomials. These consist of non-truncated Taylor expansions including higher order and coupling terms. An alternative to include nonlinear effects is to treat the aerodynamic and control derivatives as functions of important explanatory variables (such as the angle of attack α and Mach number M). In the previous example, the nonlinear model would be then:

$$C_m = C_{m_0}(M) + C_{m_\alpha}(\alpha, M)\,\alpha + C_{m_q}(\alpha, M)\,\frac{q\bar{c}}{V} + C_{m_{\delta_e}}(\alpha, M)\,\delta_e + C_{m_{T_c}}(\alpha, M)\,T_c \tag{3.9}$$

Each of the aerodynamic and control derivative functions in this representation can be approximated by either polynomials or polynomial splines in the explanatory variables. The latter are piecewise polynomials of a given degree, connected to each other by knots. These are better suited to approximate local behaviour. Both representations of nonlinear models rely on flight envelope partitions, which are treated as subproblems. For situations with unsteady aerodynamics, indicial functions or internal state variables can be used, as stated earlier. In all representations, the parameters, like the dimensionless coefficients in eq. (3.3) till (3.8), are the unknowns to be estimated, based upon the available measured data.

3.2.2 Experiment design

The experiment design is an essential part of the aircraft system identification process. It involves important considerations, such as the data acquisition system characteristics (sampling rate, sensor range and resolution,...), flight instrumentation system characteristics (what are the physical quantities to be measured, and how are these measurements contaminated), the configuration of the aircraft, the flight conditions where the experiment has to be performed, and the manoeuvres which are required for the identification task. Main issue is the development of optimized inputs for aircraft parameter estimation, in order to obtain the parameters in an efficient way with high accuracy. There are several approaches to design the excitation input. Heuristic input design approaches generally implement some form of wideband input, with frequency content selected to include or be concentrated near the expected modal frequencies of the aircraft. Optimal imput design for parameter estimation manoeuvres involves optimizing a scalar measure of signal-to-noise ratios for the modeling problem, or an input efficiency metric. Some important practical problems in this matter are the risk for data collinearities which, when present, have a detrimental effect on the identification results, possible input distortion due to active feedback control (as a consequence, a doublet input at the pilot controls will not result in a perfect doublet motion of the corresponding control surface), and the difficulties to estimate the bare airframe model parameters from measurement data collected with closed loop feedback controls.

In ref. [208], an extensive study has been performed in the field of experiment design, where dynamic flight test manoeuvres have been designed to optimize identification results, a thorough comparison is provided of five input signals, and a.o. orthogonal functions have been used in the optimization of multidimensional input excitation signals for dynamic flight test manoeuvres. The findings of this research have been validated in flight tests. Ref. [197, 198] investigate the usefulness of Prescribed Simultaneous Independent Surface Excitations (PreSISE) to provide data for rapidly obtaining estimates of the stability and control derivatives.

3.2.3 Data compatibility analysis

This analysis is about the verification of data accuracy of the measured aircraft responses, which can be contaminated by the presence of systematic errors. Accurate measured data are required for successful modeling, in order to obtain reliable parameter estimates. Data compatibility analysis includes comparing measured and reconstructed responses, aircraft state estimation and the estimation of systematic instrumentation errors, such as sensor biases and scale factors.

There are basically three types of corrections for aircraft instrumentation errors: ground calibration, provided by the equipment manufacturer or by lab testing (rate table or wind-tunnel), sensor alignment and position corrections, and systematic instrumentation error corrections. Sensor dynamics are usually neglected due to their high frequency range.

Aircraft kinematic equations, specified in section 3.2.1, are used for two purposes. The first purpose is flight path reconstruction, where the aircraft states are reconstructed using all contaminated measurements. The other purpose is a data compatibility check for systematic instrumentation errors. Generally, the sensor measurement $\mathbf{z}(i)$ is built up by the following terms:

$$\mathbf{z}(i) = (1+b)\mathbf{y}(i) + \boldsymbol{\lambda} + \boldsymbol{\nu}(i) \quad i = 1, 2, \ldots, N \tag{3.10}$$

where $(1 + b)$ is a constant scale factor error parameter, $\mathbf{y}(i)$ is the true output, $\boldsymbol{\lambda}$ is a constant bias error parameter and $\boldsymbol{\nu}(i)$ is random measurement noise. There exist 2 groups of methods for estimating the instrumentation errors b and $\boldsymbol{\lambda}$. The first group is the so-called simultaneous estimation of aircraft states and instrumentation error parameters, which can be done by filtering and/or smoothing methods. The other group is the separate estimation of aircraft states and instrumentation error parameters. The stochastic approach is maximum likelihood estimation, as opposed to the deterministic output error methods.

3.2.4 Model structure determination

This part concerns the selection of the specific model form or structure and is closely related to the parameter and state estimation step, discussed in the next section. A very important criterion in this respect is the principle of parsimony, which searches for a trade-off between good data fitting and prediction capabilities.

Principle of parsimony: if there are two mathematical models to represent the same system with equal accuracy, then the model with the fewest parameters is preferable.

Interesting techniques to determine the model structure are stepwise regression, [81, 157], which consists of the steps candidate term postulation – selection – validation, and multivariate orthogonal modeling functions, [159, 199, 200, 201]. The idea is to generate multivariate orthogonal modeling functions from measured data, ranking those orthogonal functions by fit error reduction capability, and using the predicted square error metric (PSE) for model structure determination. The retained functions can then be decomposed in ordinary polynomial terms. The PSE metric was originally developed by Barron[30]. As already introduced earlier, these extended structures allow to take into account nonlinear aerodynamic effects, such as stall and large amplitudes, which are crucial aspects in the field of damaged aircraft model identification, however it is important to realize that the two methods mentioned here can only be applied off-line.

3.2.5 Parameter and state estimation

There are two main methods to perform parameter and state estimation, namely the equation error and the output error based methods. A popular category of equation error methods are the least squares methods. Output error methods, on the other hand, involve iterative nonlinear optimization and this requires more complex algorithms such as the maximum likelihood (ML) method. ML is also suitable for equation error types of estimation problems. Parameter and state estimation can also be done in the frequency domain via Fourier transforms, [159, 203]. (Extended) Kalman Filters are the methods of choice to deal with stochastic models (including e.g. turbulence). Section 3.3 will elaborate more extensively on the subject of parameter and state estimation.

3.2.6 Collinearity diagnostics

Collinearities are defined as correlation levels between different model terms, and have usually low values. However, linearly related terms have high correlation levels and result in misleading or even erroneous data inferences. Collinearities diagnostics involve two steps, namely the detection of their presence and subsequently the assessment of the extent of their adverse effects. After these diagnostics, decisions can be taken on corrective actions.

Data collinearities are a data problem, which there are three possible sources for: the experiment design (the conducted experiment must not lead to proportional regressors or low signal to noise ratios), data constraints (control with proportional feedback) and model specifications (near zero or constant regressors). There are three major methods for detection and assessment of data collinearities. A total diagnosis should combine all of them.

- *Examination of regressor correlation matrix and its inverse:* The variance inflaction factors $VIF_j = \text{diag}(\mathbf{X}^{*T}\mathbf{X}^{*})^{-1}$ provides an indication for data collinearities, but only pairwise.

- *Eigensystem analysis and singular value decomposition:* the condition number $\kappa = \frac{\overline{\sigma}}{\underline{\sigma}} = \sqrt{\frac{\lambda_{\max}}{\lambda_{\min}}}$ provides a severity assessment of particular dependencies. The singular values σ are preferred for the calculation of the condition number because of their greater numerical stability in the computing algorithms.

- *Parameter variance decomposition:* the variance proportion $\pi_{k,j}$, [33], allows to determine the regressors involved and to analyse the extent of dependency.

The adverse effects of data collinearities are that they lead to unrealistic large parameter estimate values $\hat{\boldsymbol{\theta}}$ and large corresponding variances because of insufficient data since they render the estimation problem underdetermined. A satisfactory solution is the mixed estimator, [264]. This is a Bayesian estimation method for data augmented with prior information about the parameters and a formulation of prior constraints. An example of prior information from flight mechanics enhancing the performance of identification algorithms for adaptive and reconfigurable control is given in ref. [62]. Another example of prior information about the constraints is given in ref. [179], where relationships are given between the stability derivatives of a delta wing UAV. These relationships were used to decrease the number of independent uncertainties for designing a robust controller, but they could serve here as well as prior parameter information.

3.2.7 Model validation

The validation of the identified model is to demonstrate that the model values are reasonable and accurate. This can be done through comparisons with available information from other experiments, like windtunnel tests. Nevertheless these comparisons have limitations which must be taken into consideration. Also, prediction capabilities of the identified model should be tested on data sets which are different from the set used for the parameter estimation process.

3.3 Parameter and State estimation

Parameter and state estimation is one of the key aspects of aerodynamic model identification. This subject of research will be elaborated in depth. First, a summary of estimator characteristics and properties is given, after which state estimation and parameter estimation are described in more detail. The former focuses on different versions of Kalman Filters and Smoothers, where the latter presents different versions of least squares algorithms and the maximum likelihood approach. Thereafter, joint as well as separate state and parameter estimation procedures are introduced. Subsequently, some information is given about a selection of alternative approaches for system identification. As last but one, a brief discussion of identification in the frequency domain is introduced. Finally, a motivation is

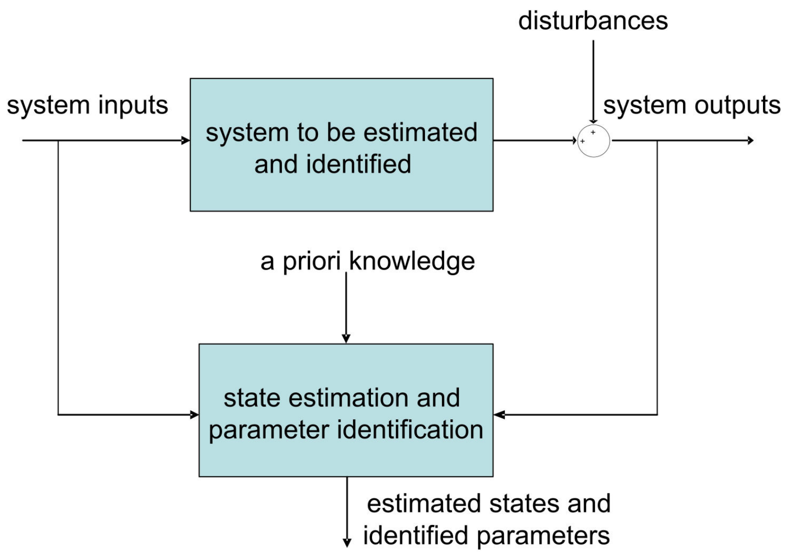

Figure 3.2: General overview of the setup of system identification, source: [65]

included of the chosen identification method in this research. Excellent references in the field of estimation theory are [53, 216, 230].

As shown in figure 3.2, the goal is to estimate state variables and to identify parameter values from measured system inputs and outputs, where the latter signals are usually contaminated by disturbances. Moreover, the estimation and identification procedure makes use of a priori knowledge about the physical system.

A linear time varying system model, which is considered affine with respect to states, inputs and noise, has the form:

$$\dot{\mathbf{x}}(t) = \mathbf{F}(\boldsymbol{\theta}, t)\mathbf{x}(t) + \mathbf{B}(\boldsymbol{\theta}, t)\mathbf{u}(t) + \mathbf{G}(\boldsymbol{\theta}, t)\mathbf{w}(t), \qquad \mathbf{x}(t_0) = \mathbf{x}_0 \tag{3.11}$$

$$\mathbf{z}(t) = \mathbf{H}(\boldsymbol{\theta}, t)\mathbf{x}(t) + \mathbf{D}(\boldsymbol{\theta}, t)\mathbf{u}(t) + \mathbf{v}(t) \qquad t = t_i, \quad i = 1, 2, \ldots \tag{3.12}$$

where $\mathbf{x}$ is the state vector with dimension n and $\boldsymbol{\theta}$ is the parameter vector with dimension k, $\mathbf{x}_0$ is the initial condition of the state, $\mathbf{u}(t)$ is the control input of dimension l, $\mathbf{w}(t)$ is the system noise, also called process noise, with dimension m, $\mathbf{z}(t)$ is the measurements vector of dimension p, $\mathbf{v}(t)$ is the measurement noise with dimension p. Furthermore, $\mathbf{F}(\boldsymbol{\theta}, t)$ is the system matrix with dimensions $n \times n$, $\mathbf{B}(\boldsymbol{\theta}, t)$ is the input matrix with dimensions $n \times l$, $\mathbf{G}(\boldsymbol{\theta}, t)$ is the system noise input matrix of dimensions $n \times p$, $\mathbf{H}(\boldsymbol{\theta}, t)$ is the observation matrix with dimensions $m \times n$ and finally $\mathbf{D}(\boldsymbol{\theta}, t)$ is the feedforward matrix of dimensions $m \times l$.

Additionally, $\mathbf{w}(t)$ is a continuous time white noise process, $\mathbf{v}(t_i)$ is a discrete time white noise sequence, and $\mathbf{w}(t)$ and $\mathbf{v}(t_i)$ are mutually uncorrelated at all $t = t_i$, $i = 1, 2, \ldots$; hence:

$$E\{\mathbf{w}(t)\} = 0; \quad E\left\{\mathbf{w}(t)\mathbf{w}^T(\tau)\right\} = \mathbf{Q}\delta(t-\tau) \tag{3.13}$$

$$E\{\mathbf{v}(t_i)\} = 0; \quad E\left\{\mathbf{v}(t_i)\mathbf{v}^T(t_j)\right\} = \mathbf{R}\delta_{ij} \tag{3.14}$$

$$E\left\{\mathbf{w}(t)\mathbf{v}^T(t_i)\right\} = 0, \quad \text{for} \quad t = t_i, \quad i = 1,\ 2, \ldots \tag{3.15}$$

State estimation is searching for the best estimate of $\mathbf{x}$ while $\boldsymbol{\theta}$ is known. Parameter estimation is searching for the best estimate of $\boldsymbol{\theta}$ while $\mathbf{x}$ is known. Therefore, state estimation is an inverse problem of parameter estimation. If both state and parameter vectors are to be estimated, the problem is defined as a joint state and parameter estimation problem. Estimation methods can be classified according to the noise presence assumptions. If only process noise is considered, i.e. $\mathbf{w}(t) \neq 0$ and $\mathbf{v}(t) = 0$, equation error methods can be used. On the other hand, output error methods consider only output noise, i.e. $\mathbf{w}(t) = 0$ and $\mathbf{v}(t) \neq 0$. Finally, filter error methods can deal with process as well as output noise, i.e. $\mathbf{w}(t) \neq 0$ and $\mathbf{v}(t) \neq 0$.

3.3.1 Estimator characteristics and properties

Knowledge about the parameters of interest can be expressed in terms of the probability density function $p(\boldsymbol{\theta}; T)$ or $p(\boldsymbol{\theta}; k)$, which depends on the observation interval length T or the number of processed signal samples k. This possibly multi-dimensional function is the most complete type of knowledge one can obtain through application of statistical techniques, but it is quite complicated and impractical to work with. For that reason, in most cases the interest is reduced from the complete probability density function to its most significant characteristics, as defined in the statistical literature, e.g. [89]:

- expected value $E[\boldsymbol{\theta}]$
- bias $\boldsymbol{\lambda}(\boldsymbol{\theta})$
- covariance Cov($\boldsymbol{\theta}$)= $E\left[(\boldsymbol{\theta} - E[\boldsymbol{\theta}])(\boldsymbol{\theta} - E[\boldsymbol{\theta}])^T\right]$

In statistical literature, e.g. [89, 174, 216], some desirable properties are defined for the estimates $\hat{\boldsymbol{\theta}}$ of the parameters $\boldsymbol{\theta}$:

1. The estimator $\hat{\boldsymbol{\theta}}$ is unbiased:

$$E\left[\hat{\boldsymbol{\theta}}\right] = E\left[\boldsymbol{\theta}\right] + E\left[\lambda\left(\boldsymbol{\theta}\right)\right] = E\left[\boldsymbol{\theta}\right]$$

   An estimator is called biased when $\boldsymbol{\lambda}(\boldsymbol{\theta}) \neq 0$

2. The estimator $\hat{\boldsymbol{\theta}}$ is consistent, which means that $\hat{\boldsymbol{\theta}}$ converges in probability to the true value $\boldsymbol{\theta}$ for increasing N:

$$\lim_{N\to\infty} P[|\boldsymbol{\theta} - \hat{\boldsymbol{\theta}}| > \epsilon] = 0$$

with ϵ arbitrary small.

3. The estimator $\hat{\boldsymbol{\theta}}$ is efficient if

$$\mathrm{Cov}(\hat{\boldsymbol{\theta}}) = E\left[\left(\hat{\boldsymbol{\theta}} - \boldsymbol{\theta}\right)\left(\hat{\boldsymbol{\theta}} - \boldsymbol{\theta}\right)^T\right] \leq E\left[\left(\hat{\boldsymbol{\theta}}_k - \boldsymbol{\theta}\right)\left(\hat{\boldsymbol{\theta}}_k - \boldsymbol{\theta}\right)^T\right] = \mathrm{Cov}(\hat{\boldsymbol{\theta}}_k)$$

for all unbiased estimators $\hat{\boldsymbol{\theta}}_k$

A selection of other estimator properties are the following: The mean square error (MSE) is defined as:

$$\text{MSE} = E\left[\left(\hat{\boldsymbol{\theta}} - \boldsymbol{\theta}\right)^T\left(\hat{\boldsymbol{\theta}} - \boldsymbol{\theta}\right)\right] \tag{3.16}$$

The Fisher information matrix $\mathbf{M}$ is defined as:

$$\mathbf{M} \equiv E\left[\left(\frac{\partial \ln \mathbb{L}}{\partial \boldsymbol{\theta}}\right)\left(\frac{\partial \ln \mathbb{L}}{\partial \boldsymbol{\theta}}\right)^T\right] = -E\left(\frac{\partial^2 \ln \mathbb{L}}{\partial \boldsymbol{\theta} \partial \boldsymbol{\theta}^T}\right) \tag{3.17}$$

where $\mathbb{L}$ is the likelihood function, which is equal to the probability density function of $\mathbf{z}$ given $\boldsymbol{\theta}$:

$$\mathbb{L}\left(\mathbf{z}; \boldsymbol{\theta}\right) \equiv p\left(\mathbf{z}|\boldsymbol{\theta}\right) \tag{3.18}$$

Given the above information, an unbiased estimator is called efficient if the covariance matrix equals the inverse of the Fisher information matrix:

$$\mathrm{Cov}(\hat{\boldsymbol{\theta}}) = E\left[\left(\hat{\boldsymbol{\theta}} - \boldsymbol{\theta}\right)\left(\hat{\boldsymbol{\theta}} - \boldsymbol{\theta}\right)^T\right] = \mathbf{M}^{-1} \tag{3.19}$$

The matrix $\mathbf{M}^{-1}$ is known as the Cramer-Rao lower bound, and the expression

$$\mathrm{Cov}(\hat{\boldsymbol{\theta}}) \geq \mathbf{M}^{-1} \tag{3.20}$$

is the Cramer-Rao inequality for an unbiased estimator $\hat{\boldsymbol{\theta}}$, see [159]. This inequality indicates that any unbiased estimator can have a covariance matrix no smaller than $\mathbf{M}^{-1}$. If the Cramer-Rao inequality becomes an equality as $N \to \infty$, then the estimator is called asymptotically efficient.

3.3.2 State estimation

State estimation can be applied on deterministic as well as stochastic systems. Here focus is placed on a Bayesian approach for the stochastic systems, by making use of probabilistic formulations describing the states and measured variables.

3.3.2.1 Optimal state estimation for linear systems

Optimal state estimation can be divided into filtering, prediction and smoothing. Filtering is estimating the state based on past and present measurements of input and output. Prediction is estimating the state based only on past measurements. Smoothing, finally, is estimating the state based on past, present and future measurements of in- and output.

In case a basic linear, possibly time varying, discrete time dynamic system description is available, optimal state estimation is possible by means of regular Kalman Filters and Smoothers.

Optimal filtering: Kalman Filter

When the state must be estimated based on past and present measurements of input and output, a Kalman filter can be used, see ref.[149, 150]. In ref. [65], the Kalman Filter equations are derived as a weighted least squares estimate which minimises a quadratic value function J.

The linear Kalman Filter consists of five steps, where the first two steps are the prediction steps of state and covariance matrix. In the third step, the Kalman gain is calculated, which depends on the covariance matrix and thus on the uncertainty of the estimation. This Kalman gain is used in the two consecutive update steps, where more state uncertainty in the prediction step provides more "correcting power" in the update steps via this gain. Knowledge of the system model description is crucial, together with information of noise statistics since the system matrices are needed in these steps. A fully observable system is required in order to guarantee convergent Kalman filtering.

This is the most basic working principle of all Kalman Filter variants, due to the assumption of linearity. For significant non-linearities, an extension needs to be incorporated, as will be seen in a later stage.

Optimal state prediction

Optimal state prediction is based on the filtered result presented above with past and present measurements and predicts (propagates) the states using only the model under the form of differential or difference equations. Because of the initial condition problem, the present state serving as initial state for the prediction must be estimated with a required accuracy. Moreover, in the case where linear time varying (LTV) models are considered, the system model information needs to be available for all future time samples and the future deterministic input $\mathbf{u}(k)$ needs also to be known for the state propagation.

Only the first two predictive steps in the Kalman Filter (for state and covariance) are used for state prediction. Since the input noise covariance matrices are positive semi-definite, the covariance matrices will grow over time even for stable systems.

Optimal smoothing

Following the solution for the filtering problem discussed earlier, estimation can also be performed backwards to improve estimates of state $\mathbf{x}$ and measurements $\mathbf{w}$ by using the output measurements $\mathbf{z}$.

In ref. [65], the Kalman smoother equations are again derived as a least squares estimate which minimises a quadratic value function J with constraints. As a result, one obtains optimal smoothing for multistage processes, also called Kalman smoother.

3.3.2.2 State estimation for nonlinear systems: Extended Kalman Filter

The Kalman filtering algorithm has been designed to estimate the state vector for linear systems. In practice however, the system and measurement equations turn out to be nonlinear most of the time, especially in aerospace applications. If the model turns out to be nonlinear, the Extended Kalman Filter (EKF), which is a form of the Kalman Filter "extended" to nonlinear dynamical systems, can be applied to estimate the state vector.

The general nonlinear state space model is:

$$\dot{\mathbf{x}}(t) = \mathbf{f}\left[\mathbf{x}(t), \mathbf{u}(t), t\right] + \mathbf{G}\left[\mathbf{x}(t), t\right]\mathbf{w}(t)\ ; \qquad \mathbf{x}(0) = \mathbf{x}_0 \tag{3.21}$$

$$\mathbf{z}_n(t) = \mathbf{h}\left[\mathbf{x}(t), \mathbf{u}(t), t\right] \tag{3.22}$$

$$\mathbf{z}(t_k) = \mathbf{z}_n(t_k) + \mathbf{v}(t_k)\ ; \qquad k = 1,\, 2,\, ... \tag{3.23}$$

The nonlinear vector functions $\mathbf{f}$ and $\mathbf{h}$ may depend both implicitly and explicitly on the time t and it will be assumed that both $\mathbf{f}$ and $\mathbf{h}$ are continuous and continuously differentiable with respect to all elements of $\mathbf{x}(t)$ and $\mathbf{u}(t)$. The noise properties are the same as given for the linear case in eq. (3.13) to (3.15).

The five standard steps for an Extended Kalman Filter are as follows:

1. one step ahead prediction (time propagation):

$$\hat{\mathbf{x}}(k+1\,|k) = \hat{\mathbf{x}}(k\,|k) + \int_{k}^{k+1} \mathbf{f}\left(\mathbf{x}(t), \mathbf{u}_m(t), \boldsymbol{\theta}, t\right) dt \tag{3.24}$$

2. prediction of covariance matrix of the state prediction error vector:

$$\mathbf{P}\left(k+1|\,k\right) = \mathbf{\Phi}\left(k,\tau\right)\mathbf{P}\left(k\,|k\right)\mathbf{\Phi}^{T}\left(k,\tau\right) + \mathbf{Q}_d\left(k\right) \tag{3.25}$$

where $\mathbf{\Phi}$ is calculated by a linearization and discretization procedure as follows :

$$\mathbf{F}(k) = \left.\frac{\partial \mathbf{f}\left(\mathbf{x}(t), \mathbf{u}_m(t), \boldsymbol{\theta}, t\right)}{\partial \mathbf{x}(t)}\right|_{\mathbf{x}=\hat{\mathbf{x}}_{k|k}} \tag{3.26}$$

$$\mathbf{\Phi}(k, \tau) = e^{\mathbf{F}(k)\Delta t} = \sum_{n}^{\infty} \frac{\mathbf{F}_k^n \left(\Delta t\right)^n}{n!} \tag{3.27}$$

and $\mathbf{Q}_d$ as follows, according to ref. [65]:

$$\mathbf{Q}_d\left(k+1|k\right) = E\left\{\mathbf{w}_d(k)\mathbf{w}_d^T(k)\right\} \tag{3.28}$$

$$= \int_{t_k}^{t_{k+1}} \mathbf{\Phi}\left(t_{k+1}, \tau\right) \mathbf{G}_k \mathbf{Q}_k \mathbf{G}_k^T \mathbf{\Phi}^T \left(t_{k+1}, \tau\right) d\tau \tag{3.29}$$

$$\approx \sum_{m}^{\infty}\sum_{n}^{\infty} \frac{\mathbf{F}_k^m}{m!} \mathbf{G}_k \mathbf{Q}_k \mathbf{G}_k^T \frac{\left(\mathbf{F}_k^n\right)^T}{n!} \frac{\left(\Delta t\right)^{n+m+1}}{(n+m+1)!} \tag{3.30}$$

A commonly used approximation for $\mathbf{Q}_d$ is the following:

$$\mathbf{Q}_d\left(k\right) = \mathbf{\Gamma}(k)\mathbf{Q}\left(k\right)\mathbf{\Gamma}^T(k) \tag{3.31}$$

where $\mathbf{\Gamma}$ is calculated as follows:

$$\mathbf{\Gamma}(k) = \left(\int_{k-1}^{k} \mathbf{\Phi}(k)\Delta t\right) \mathbf{G}(k) \tag{3.32}$$

3. Kalman gain:

$$\mathbf{K}\left(k+1\right) = \mathbf{P}\left(k+1\left|k\right.\right)\mathbf{H}^T\left(k+1\right)\left[\mathbf{H}\left(k+1\right)\mathbf{P}\left(k+1\left|k\right.\right)\mathbf{H}^T\left(k+1\right) + \mathbf{R}\left(k+1\right)\right]^{-1} \tag{3.33}$$

where $\mathbf{H}$ is calculated as follows by linearization only:

$$\mathbf{H}(k) = \left.\frac{\partial \mathbf{h}\left(\mathbf{x}(t), \mathbf{u}_m(t), \boldsymbol{\theta}, t\right)}{\partial \mathbf{x}(t)}\right|_{\mathbf{x}=\hat{\mathbf{x}}_{k|k}} \tag{3.34}$$

4. measurement update step:

$$\hat{\mathbf{x}}\left(k+1\left|k+1\right.\right) = \hat{\mathbf{x}}\left(k+1\left|k\right.\right) + \mathbf{K}\left(k+1\right)\left[\mathbf{z}\left(k+1\right) - \mathbf{H}\left(k+1\right)\hat{\mathbf{x}}\left(k+1\left|k\right.\right)\right] \tag{3.35}$$

5. update covariance matrix of state estimation error vector:

$$\begin{aligned}\mathbf{P}(k+1|\,k+1) &= [\mathbf{I}-\mathbf{K}(k+1)\,\mathbf{H}(k+1)]\,\mathbf{P}(k+1\,|k)\times \\ &\quad \times[\mathbf{I}-\mathbf{K}(k+1)\,\mathbf{H}(k+1)]^{T}+ \\ &\quad +\mathbf{K}(k+1)\,\mathbf{R}(k+1)\,\mathbf{K}^{T}(k+1)\end{aligned} \tag{3.36}$$

where the first two steps are the prediction steps of state and covariance matrix. In the third step, the Kalman gain is calculated, which depends on the covariance matrix and thus on the uncertainty of the estimation. This Kalman gain is used in the two consecutive update steps, where it can be seen that the more state uncertainty provides the more "correcting power" in the update steps via this gain.

Fig. 3.3 illustrates the working principle of the Extended Kalman Filter, where the known kinematics model **f** is used for the one time step ahead prediction, and the correction has been performed by means of the Kalman gain **K** and observation model **H**. This working principle is highly similar to the basic Kalman Filter presented earlier, but with some modification due to the assumption of minor non-linearity, indeed all models are still close to linearity. For significant non-linearities, iteration procedures or other routines need to be incorporated, as will be seen later in chapter 4 and appendix C.

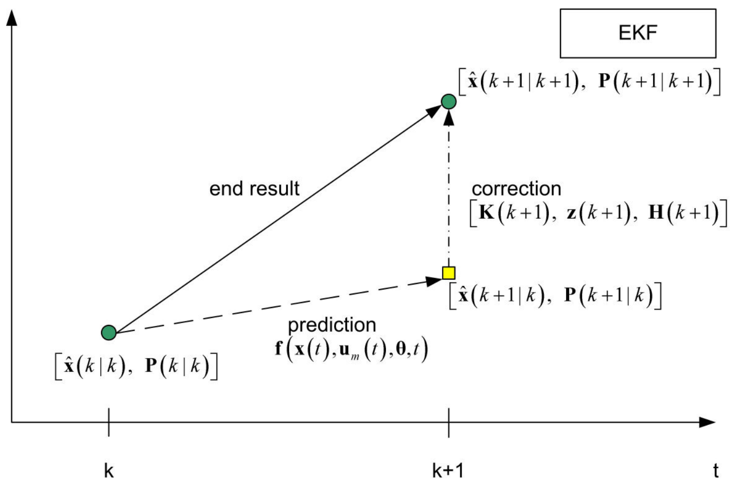

Figure 3.3: Working principle of the Extended Kalman Filter

3.3.2.3 Computational aspects of the Kalman Filter

The computational aspects of Kalman Filter and Extended Kalman filter are illustrated in fig. 3.4. The loop as shown in the figure illustrates all computational steps to be performed for every time sample in the data sets. From a computational point of view, the Kalman Filter is very efficient, and the computational load comes primarily from the size of the model considered (number of states, observations and inputs).

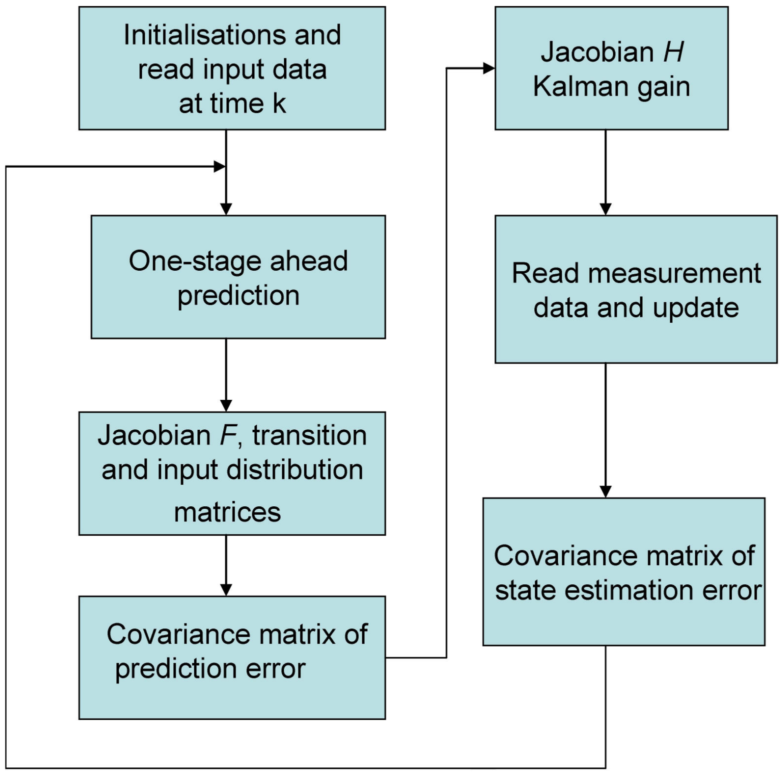

Figure 3.4: Computational aspects of Kalman Filter and Extended Kalman Filter, source: [65]

There have been numerous books and papers published on optimal filtering, optimal smoothing, and specifically on the Kalman Filter. Excellent references are [100, 103, 130, 195, 233].

3.3.3 Parameter estimation

Parameter estimation is the process of finding values of unknown system parameters $\boldsymbol{\theta}$, given noisy time-varying measurements $\mathbf{z}(t)$. The linear measurement equation can be described as:

$$\mathbf{z}(t) = \mathbf{H}\boldsymbol{\theta} + \boldsymbol{\nu} \tag{3.37}$$

Its nonlinear counterpart is:

$$\mathbf{z}(t) = \mathbf{h}(\boldsymbol{\theta}) + \boldsymbol{\nu} \tag{3.38}$$

where $\mathbf{H}$ and $\mathbf{h}(\boldsymbol{\theta})$ are the known observation matrix and observation function respectively, $\boldsymbol{\nu}$ is the unknown measurement error vector, and models for uncertainty in $\boldsymbol{\theta}$ and $\boldsymbol{\nu}$ can be specified by probability density functions $p(\boldsymbol{\theta})$ and $p(\boldsymbol{\nu})$, respectively.

Three mathematical models for the uncertainties in the parameters and the measurements will be considered. They are designated according to ref. [159, 238] as the Bayesian model, the Fisher model, and the least-squares model, formed as follows:

- *Bayesian model:*
  1. $\boldsymbol{\theta}$ is a vector of random variables with probability density $p(\boldsymbol{\theta})$
  2. $\boldsymbol{\nu}$ is a random vector with probability density $p(\boldsymbol{\nu})$
- *Fisher model:*
  1. $\boldsymbol{\theta}$ is a vector of unknown constant parameters
  2. $\boldsymbol{\nu}$ is a random vector with probability density $p(\boldsymbol{\nu})$
- *Least squares model:*
  1. $\boldsymbol{\theta}$ is a vector of unknown constant parameters
  2. $\boldsymbol{\nu}$ is a random vector of measurement noise

Estimators have been developed for each type of model. The two former models will be briefly introduced, but most emphasis is placed on the latter type of model, since the least squares model is the most important for aerospace applications.

3.3.3.1 Estimator for Bayesian models

In the Bayesian type of models, the unknown parameters, which are assumed to be random variables, are estimated using Bayes's rule, which assumes the existence (and knowledge) of an a priori probability density for parameters as well as measurements. From this information, Bayes's rule provides the a posteriori probability density for the parameters. Despite the generality of the Bayes estimator, the method has not found wide application in aircraft parameter estimation. Main reason for this is the difficulty to make any explicit statement about a priori probability densities for parameters and measurements.

In equation form, the parameter estimator for a Bayesian model can be expressed as follows:

$$\hat{\boldsymbol{\theta}} = \max_{\boldsymbol{\theta}} p(\boldsymbol{\theta}|\mathbf{z}) \quad \text{with:} \quad p(\boldsymbol{\theta}|\mathbf{z}) = \frac{p(\mathbf{z}|\boldsymbol{\theta})p(\boldsymbol{\theta})}{p(\mathbf{z})} \tag{3.39}$$

3.3.3.2 Estimator for Fisher models

In the Fisher model, the estimator is based on maximization of a likelihood function, which is equal to the conditional probability density of the measurements, given the parameters:

$$\hat{\boldsymbol{\theta}} = \max_{\boldsymbol{\theta}} \mathbb{L}(\mathbf{z};\boldsymbol{\theta}) = \max_{\boldsymbol{\theta}} p(\mathbf{z}|\boldsymbol{\theta}) \tag{3.40}$$

Maximum Likelihood

In parameter estimation one usually uses some objective criterion to measure the relative merits of one set of parameter estimates compared with another. In general, the criterion function can be a highly nonlinear function of the parameters and thus its minimization requires off-line optimisation techniques of an iterative nature. Criterion functions can be chosen arbitrarily. However, use of the earlier mentioned likelihood criterion function is particularly useful, as this criterion function gives also information about the noise statistics[36]. The corresponding optimization algorithm is known as the iterative Maximum Likelihood method.

As explained in ref. [65], the maximum likelihood estimate of the unknown parameters $\boldsymbol{\Theta}$ is obtained by maximising the conditional probability density function $p\left\{\hat{\mathrm{E}}_N, \boldsymbol{\Theta}\right\}$, i.e.

$$\hat{\boldsymbol{\Theta}}_{ML} = \max_{\boldsymbol{\Theta}} p\left\{\hat{\mathrm{E}}_N, \boldsymbol{\Theta}\right\} \tag{3.41}$$

where:

$$\hat{\mathrm{E}}_N = \left[\hat{\boldsymbol{\varepsilon}}_{1,0}(\boldsymbol{\Theta}), \hat{\boldsymbol{\varepsilon}}_{2,1}(\boldsymbol{\Theta}), \cdots, \hat{\boldsymbol{\varepsilon}}_{k,k-1}(\boldsymbol{\Theta}), \cdots, \hat{\boldsymbol{\varepsilon}}_{N,N-1}(\boldsymbol{\Theta})\right] \tag{3.42}$$

in which $\hat{\boldsymbol{\varepsilon}}_{k,k-1}$ is the prediction error vector or innovation vector obtained from an extended Kalman filter:

$$\hat{\boldsymbol{\varepsilon}}_{k,k-1}(\boldsymbol{\Theta}) = \mathbf{z}_{m,k} - \hat{\mathbf{z}}_{k,k-1}(\boldsymbol{\Theta}) \;; \hat{\mathbf{z}}_{k,k-1}(\boldsymbol{\Theta}) = \mathbf{h}\left(\hat{\mathbf{x}}_{k,k-1}, \ \mathbf{u}_{m,k}, \ \boldsymbol{\Theta}\right) \tag{3.43}$$

By a successive application of Bayes rules and a Gaussian distribution assumption of the probability density function, the likelihood function can be written in an exponential form, and it is convenient to use the negative logarithm of the likelihood function as the objective criterion, which eliminates constant terms and results in a minimization problem.

The Newton-Raphson iteration method is an often applied algorithm for numerical minimization. This method uses the values of the first- and the second order gradients of the objective criterion with respect to parameters $\boldsymbol{\Theta}$. A difficulty with the Newton-Raphson method is that the required Hessian Matrix $\frac{\partial^2 V_N(\boldsymbol{\Theta})}{\partial\boldsymbol{\Theta}\partial\boldsymbol{\Theta}^T}$ may not be positive definite and thus may not point in a downhill direction. A sensible remedy is to apply the so-called Gauss-Newton iteration method in which the Hessian matrix is replaced by its expectation. This latter matrix is known as the Fisher information matrix and can be shown to be non-negative definite.

The iteration starts with initial estimates of all unknown parameters and computes parameter updates using the total number of sample observations $(k = 1, 2, ..., N)$ until the minimum of the objective criterion is reached.

Aerospace applications of the maximum likelihood identification method for can be found in ref. [64, 66, 129, 156].

Recursive Maximum Likelihood

The discussed iterative Maximum Likelihood method in the above section is an off-line approach that processes the observation data after the total length of data samples is recorded. Numerical minimisation of the objective criterion typically requires several iterative passes through the complete data record. For on-line applications, however, the processing must be recursive, which implies that only new data is used to improve the parameter estimate. The consequence is that recursive parameter estimates will be different from off-line estimates even for equal data lengths.

The Recursive Maximum Likelihood method (RML) is derived in ref. [65]. The combination of the RML algorithm and the prediction error estimator, i.e. the EKF, constitutes the complete algorithm for the RML joint state and parameter estimator. This estimator can, in fact, be seen as an adaptive filter, as the noise covariance matrices can also be estimated with this estimator.

An adaptive filter based on RML still needs the model structure of the system, i.e. system state and observation equations. In many practical applications, the structure of the system model may not be precisely known. Estimators discussed so far may not be convergent due to mismatches of models to be used in the algorithm and real systems. Alternative approaches have been considered. In recent years, fuzzy logic and neural networks have been applied to these adaptive state and parameter estimation problems. These alternative techniques are briefly discussed in section 3.3.6.

Applications of the recursive maximum likelihood identification method can be found in ref. [36, 67, 68].

3.3.3.3 Estimator for Least Square models and their variants

In the least-squares model, the estimator is obtained by application of the least squares (LS) principle. The most simple least square variant is the linear one. One assumes that the dependent variable signal is a linear combination of independent variable signals. It is assumed that the dependent variable is perturbed, but the independent variable measurements are considered as accurate. In linear least squares, one wants to find the optimal constant parameter estimate $\hat{\boldsymbol{\theta}}$ in order to minimize the fit error $\boldsymbol{\epsilon}(t) = \mathbf{z}(t) - \boldsymbol{\Phi}(t)\boldsymbol{\theta}$. By defining the convex cost function $J(t)$ as the sum of the square fit errors over time, $J(t) = \boldsymbol{\epsilon}^T(t)\boldsymbol{\epsilon}(t) = (\mathbf{z}(t) - \boldsymbol{\Phi}(t)\boldsymbol{\theta}(t))^T(\mathbf{z}(t) - \boldsymbol{\Phi}(t)\boldsymbol{\theta}(t))$, one can calculate the optimal estimator by searching for the zero of the derivative $\frac{\partial J(t)}{\partial \boldsymbol{\theta}}$, this leads to the commonly known least squares expression:

$$\hat{\boldsymbol{\theta}} = (\boldsymbol{\Phi}^T(t)\boldsymbol{\Phi}(t))^{-1}\boldsymbol{\Phi}^T(t)\mathbf{z}(t) \tag{3.44}$$

Besides this basic linear version, there are many variants. The most important ones are given here.

Nonlinear (Weighted) Least Squares

Alternatively, a nonlinear least squares method can be applied to parameter estimation. The nonlinear observation equation has the form:

$$\mathbf{y}(k) = \mathbf{f}(k, \mathbf{p}) + \mathbf{e}(k) \tag{3.45}$$

where $\mathbf{f}(k, \mathbf{p})$ is a computable function vector, $\mathbf{p}$ is the parameter vector to be estimated, and $\mathbf{e}(k)$ is the measurement error vector on the k-th measurement. The least squares fitting for m measurements becomes the minimisation of the value function:

$$V(\mathbf{p}) = \frac{1}{2}\sum_{k=1}^{m}\left[\mathbf{y}(k) - \mathbf{f}(k, \mathbf{p})\right]^T \mathbf{R}^{-1}(k)\left[\mathbf{y}(k) - \mathbf{f}(k, \mathbf{p})\right] \tag{3.46}$$

by adjusting the vector $\mathbf{p}$, given a starting value, and where $\mathbf{R}$ is the corresponding residuals (fit errors) covariance matrix.For nonlinear unweighted least squares it is sufficient to substitute $\mathbf{R} = \mathbf{I}$ in the cost function. If a sufficiently good first estimate is available, local linearisation of the nonlinear function $\mathbf{f}$ should be valid and the function V will be convex, and linear least squares fitting will yield a solution. Ref. [65] derives a solution by considering the first order Taylor expansion of the nonlinear equation and differentiating towards the parameter vector. Since this algorithm needs measurements over a period of time, the method refers therefore to a batch method which gives the solution of unknown constant parameters.

Ref. [284] shows the application of sequential least squares for self-designing flight control.

Total Least Squares

The main disadvantage of the least squares methods presented earlier lies in the assumption of perfect observations of the independent variables, without noise. If this assumption is violated, then the estimates become biased. The bias depends on the amount of noise in the independent variables. A solution to this problem is to use a generalization of the least squares algorithm, called the Total Least Squares (TLS) algorithm. The TLS algorithm assumes errors in both the dependent variables and the independent variables, [269]. Figure 3.5 illustrates the difference in assumptions.

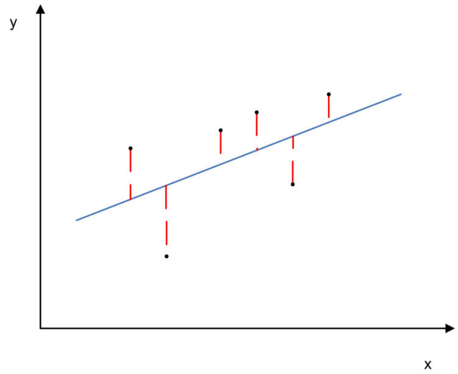

(a) ordinary least squares

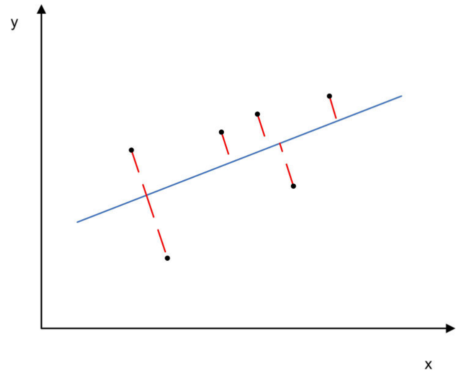

(b) total least squares

Figure 3.5: Illustration of difference in assumptions between ordinary least squares and total least squares

The goal is thus to minimize the Frobenius norm:

$$\|(\mathbf{E},\mathbf{f})\|_F \quad \text{subject to:} \quad (\mathbf{A}+\mathbf{E})\mathbf{x} = \mathbf{b}+\mathbf{f} \tag{3.47}$$

This parameter estimate can be found by solving:

$$\left[\begin{array}{c|c} \hat{\mathbf{A}} & \hat{\mathbf{b}} \end{array}\right] \begin{bmatrix} \mathbf{x}_{TLS} \\ -1 \end{bmatrix} = \mathbf{0} \quad ; \quad \hat{\mathbf{A}} = \mathbf{A}+\mathbf{E} \quad \hat{\mathbf{b}} = \mathbf{b}+\mathbf{f} \tag{3.48}$$

This can be solved via the singular value decomposition of the augmented matrix $\left[\begin{array}{c|c} \hat{\mathbf{A}} & \hat{\mathbf{b}} \end{array}\right]$:

$$\begin{bmatrix} \mathbf{x}_{TLS} \\ -1 \end{bmatrix} = \frac{-1}{v_{n+1,n+1}} \mathbf{v}_{n+1} \tag{3.49}$$

where: $\mathbf{v}_{n+1}$ is the $(n+1)^{\text{th}}$ column vector of $\mathbf{V}$ and $v_{n+1,n+1}$ is the $(n+1)^{\text{th}}$ scalar in vector $\mathbf{v}_{n+1}$, with $n = \text{rank}(\hat{\mathbf{A}})$ and where $\mathbf{V}$ comes from the singular value decomposition: $\left[\begin{array}{c|c} \hat{\mathbf{A}} & \hat{\mathbf{b}} \end{array}\right] = \mathbf{U\Sigma V}^T$ with $\mathbf{\Sigma} = \text{diag}\{\sigma_1, \ldots, \sigma_n, \sigma_{n+1}\}$ and $\mathbf{U}$ and $\mathbf{V}$ orthonormal. In this derivation, the knowledge of the rank is exploited to find the desired solution $\hat{\boldsymbol{\theta}}$ as part of the vector $\begin{bmatrix} \hat{\boldsymbol{\theta}}^T & -1 \end{bmatrix}^T$ which is part of the kernel of $\mathbf{U\Sigma V}^T$ and must be perpendicular to the first n column vectors of $\mathbf{V}$. As $\mathbf{V}$ is orthonormal, the desired vector equals the last column vector of $\mathbf{V}$, normalized by the diagonal element.

Ref. [166] shows the application of total least squares for the estimation of aerodynamic model parameters from flight data.

Sequential Total Least Squares

Although the TLS can be written in a recursive form, the computational load prevents practical real-time applications. In ref. [252], a procedure is proposed for the sequential computation of total least squares parameter estimates which is computationally more efficient than the strictly recursive method.

At this point, a sequential algorithm for computing the TLS estimates can be formulated on the basis of propagation of the matrix $\mathbf{P} = ([\mathbf{A}, \mathbf{b}]^T [\mathbf{A}, \mathbf{b}])^{-1}$, similar to the role of the matrix $\mathbf{P}$ in recursive ordinary least squares. Because the power method computes the parameter estimate from the propagated matrix directly, the estimate itself is not used in the recursion. Hence, the complete TLS propagation consists only of

$$\mathbf{P}_m = \mathbf{P}_{m-1} - \frac{\mathbf{p}^T \mathbf{p}}{1 + \mathbf{p}[\mathbf{a}_m,\ \mathbf{b}_m]^T} \tag{3.50}$$

with $\mathbf{p} = [\mathbf{a}_m,\ \mathbf{b}_m]\mathbf{P}_{m-1}$. If the actual estimate is required, it can be computed by updating the eigenvector estimate $\mathbf{v}$ in the iteration

$$\mathbf{v}_{k+1} = \mathbf{P}(\mathbf{v}_k, v_{k,n+1}) \tag{3.51}$$

In Eq. (3.51) $v_{k,n+1}$ denotes the $(n+1)^{th}$ element of the vector $\mathbf{v}_k$. By dividing the vector by its last element, an explosion of the iterated vector and potential numerical problems are avoided. Because eigenvectors can arbitrarily be scaled, this does not influence the iteration itself. Instead, because the last element of the vector is repeatedly scaled to 1, $v_{k+1,n+1}$ converges to the largest eigenvalue of $\mathbf{P}$ and can be used as a convergence requirement for the iteration: the dominant eigenvector is found when the difference between $v_{k,n+1}$ and $v_{k+1,n+1}$ drops below a preset convergence requirement. By choosing $\mathbf{v}_0 = [0,\ \ldots,\ 0,\ 1]^T$, it is guaranteed that the vector has a component along the desired eigenvector. Because the converged vector can be used as starting point for a later iteration when $\mathbf{P}$ has been updated, $\mathbf{v}$ needs to be initialized only once. Finally, the actual parameter estimate is obtained from the eigenvector estimate:

$$\mathbf{x}_{TLS} = -\mathbf{v}_{1:n}/v_{n+1} \tag{3.52}$$

Recursive (Weighted) Least Squares

For on-line applications, the (weighted) least squares approach needs to be rewritten in a recursive form. This can be done by separating the data from the last time step from older data. The crux is to rewrite the updated parameter covariance matrix, assuming that the weighting $\mathbf{R}_{N+1}$ is a diagonal matrix:

$$\mathbf{P}_{N+1} = \left(\begin{bmatrix} \mathbf{X}_N \\ \mathbf{x}_{n+1}^T \end{bmatrix}^T \mathbf{R}_{N+1} \begin{bmatrix} \mathbf{X}_N \\ \mathbf{x}_{n+1}^T \end{bmatrix} \right)^{-1} \tag{3.53}$$

$$= \left(\lambda \mathbf{X}_N^T \mathbf{R}_N \mathbf{X}_N + \mathbf{x}_{n+1} r_{n+1} \mathbf{x}_{n+1}^T \right)^{-1} \tag{3.54}$$

By means of the matrix inversion lemma, this can be rewritten as the parameter estimate update equation:

$$\mathbf{P}_{N+1} = \frac{1}{\lambda} \left(\mathbf{I} - \mathbf{P}_N \left(\frac{\mathbf{x}_{n+1} \mathbf{x}_{n+1}^T}{\lambda + \mathbf{x}_{n+1}^T \mathbf{P}_N \mathbf{x}_{n+1}} \right) \right) \mathbf{P}_N \tag{3.55}$$

where λ is the forgetting factor. The equation for the parameter is then derived, see [103]:

$$\hat{\boldsymbol{\theta}}_{N+1} = \hat{\boldsymbol{\theta}}_N + \mathbf{K}_{N+1} \left(\mathbf{y}_{n+1} - \mathbf{x}_{n+1}^T \hat{\boldsymbol{\theta}}_N \right) \tag{3.56}$$

Where the update weighting matrix $\mathbf{K}_{N+1}$ is defined as follows:

$$\mathbf{K}_{N+1} = \frac{\mathbf{P}_N \mathbf{x}_{n+1}}{\lambda + \mathbf{x}_{n+1}^T \mathbf{P}_N \mathbf{x}_{n+1}} \tag{3.57}$$

As can be seen in this representation, the recursive least squares (RLS) algorithm can be put in a prediction error correction formulation. Calculation of a matrix inverse is avoided by reducing it to a scalar division by using the matrix inversion lemma.

3.3.4 Joint state and parameter estimation: one step method

In joint state and parameter estimation, states as well as parameters are estimated simultaneously in one procedure. Hence the name, one step method (Ref. [213]). There are many one step identification routines, such as maximum likelihood identification (MLI), which attempts to solve the joint estimation problem by searching for the global optimum of a likelihood function composed of output errors (Ref. [187]) or prediction errors, as discussed in section 3.3.3.2, but not all of them are applicable on line. One of the few procedures which can be implemented in real time is the so-called filtering method developed at the German Aerospace Research Center DLR, see ref. [128]. This is a joint state and parameter estimation algorithm, but computationally demanding. In general, a drawback of joint state and parameter estimation methods is that aerodynamic model errors affect state estimates and one is often faced with cumbersome convergence problems.

3.3.5 Separate state and parameter estimation: two step method

In the two-step method, the state trajectory is estimated in the first step while the aerodynamic parameters are estimated in the second step. The first step is also a joint state and parameter estimation problem, since several unknown parameters appear in the models of the flight test instrumentation system. However, the number of unknown parameters in the flight test instrumentation system is much less than the number of aerodynamic parameters, and therefore, this estimation problem is relatively easy to solve. There is also an important factor to guarantee the estimation accuracy in the first step due to applications of only kinematic models of aircraft. The complex yet uncertain aerodynamic model is not included in the first step. Once the flight path trajectory has been estimated, the aerodynamic model becomes *linear-in-the-parameters* (Refs. [207, 209, 211, 213]). Simple regression methods can be applied to estimate these parameters. This is considered to be a great advantage of the two-step method which can be implemented recursively and therefore is suitable for real-time applications.

Convergence problems may often be encountered when applying the one-step Maximum Likelihood method if a large number of unknown parameters is involved (ref. [3]). The two-step method does not suffer from such problems and is therefore very suitable for routine analysis of large amounts of flight test data.

This section presents an analytical comparison of the two-step method and the one-step Maximum Likelihood method. It is shown that in contrast to Maximum Likelihood estimates, the estimates as generated by the two-step method are neither (asymptotically) unbiased nor efficient when linear regression methods are applied to the second step of the two-step method. This holds true, however, except for a limit case in which measurement noise becomes negligible as compared to aerodynamic process noise. This limit case is argued to be representative for state of the art flight test instrumentation systems.

Ref. [165] showed that the two step method is a practical feasible approach to achieve real time identification of aerodynamic models. This research included the validation of the method in a flight test program with the Fairchild Metro II experimental aircraft of the Dutch Aerospace Laboratory NLR. These experiments have demonstrated that estimation of the aircraft state, as well as the identification of longitudinal and lateral aerodynamic model parameters can be performed on-board in real time (Refs. [164, 165, 167]). In the same flight test program, attention was focused on different measurement and analysis methods to identify propeller thrust in dynamic flight test manoeuvres (Ref. [206]). More recently, the two step method has been applied off-line on flight test data obtained from the Cessna Citation II CE-550 laboratory aircraft jointly owned by Delft University of Technology and the Dutch Aerospace Laboratory NLR, [222], and on flight test data obtained from the Eclipse 500 very light jet, [281].

(a) NLR Fairchild Metro II, PH-NLZ, ©Terence Li, via airliners.net

(b) DUT/NLR Cessna Citation II CE-550 laboratory aircraft, PH-LAB, photo by P.M.T. Zaal

(c) Eclipse 500 very light jet, ©John R. Beckman, via airliners.net

Figure 3.6: Aircraft which provided flight data for the two step method

3.3.5.1 Decomposition of aircraft state and parameter estimation, source: ref. [66]

The proof that warrants the decomposition of the identification problem in a separate aircraft state and aerodynamic parameter estimation procedure is given in ref. [66]. Because of its major importance in this setup, it is repeated here.

Consider the equation of motion of an aircraft flying over a flat, non-rotating earth, through an atmosphere that is moving uniformly with the earth.

The rates of change of the velocity components in F_n are related to the specific force components A_x, A_y, and A_z in the aircraft body-fixed reference frame F_b as follows:

$$\begin{aligned} \dot{u}_n &= A_x \cos\theta \cos\psi + A_y (\sin\phi \sin\theta \cos\psi - \cos\phi \sin\psi) + \\ &\quad + A_z (\cos\phi \sin\theta \cos\psi + \sin\phi \sin\psi) \\ \dot{v}_n &= A_x \cos\theta \sin\psi + A_y (\sin\phi \sin\theta \sin\psi + \cos\phi \cos\psi) + \\ &\quad + A_z (\cos\phi \sin\theta \sin\psi - \sin\phi \cos\psi) \\ \dot{w}_n &= -A_x \sin\theta + A_y \sin\phi \cos\theta + A_z \cos\phi \cos\theta + g \end{aligned} \tag{3.58}$$

in which g denotes acceleration due to gravity. A convenient expression for the magnitude of gravity is:

$$g = 9.80665 \left(\frac{R_e}{R_e + h} \right)^2 \tag{3.59}$$

where the average radius of the earth $R_e = 6367434m$. The relation between the time derivatives of the Euler angles ϕ, θ, ψ and the rotational rates p, q, r in the body-fixed reference frame is:

$$
\begin{aligned}
\dot{\phi} &= p + q\sin\phi\tan\theta + r\cos\phi\tan\theta \\
\dot{\theta} &= q\cos\phi - r\sin\phi \\
\dot{\psi} &= q\frac{\sin\phi}{\cos\theta} + r\frac{\cos\phi}{\cos\theta}
\end{aligned} \tag{3.60}
$$

In Eq. (3.58) A_x , A_y and A_z denote the aerodynamic specific force components directly sensed by ideal accelerometers. From these the aerodynamic forces $X = m\,A_x$, $Y = m\,A_y$ and $Z = m\,A_z$, and the dimensionless aerodynamic force coefficients $C_X = \frac{X}{\frac{1}{2}\rho V^2 S}$, $C_Y = \frac{Y}{\frac{1}{2}\rho V^2 S}$ and $C_Z = \frac{Z}{\frac{1}{2}\rho V^2 S}$ are derived, where ρ, V and S are the air density, true airspeed and wing area. The aircraft rotational motion can be described by Euler's dynamic equation. Assuming that the aircraft inertia matrix is given by $\mathbf{I}$, Euler's equation has the following form:

$$\dot{\boldsymbol{\omega}} = \mathbf{I}^{-1}\left(\mathbf{M} - \boldsymbol{\omega} \times \mathbf{I}\boldsymbol{\omega}\right) \tag{3.61}$$

where $\boldsymbol{\omega} = \begin{bmatrix} p & q & r \end{bmatrix}^T$ denotes the rotational rate vector and $\boldsymbol{M} = \begin{bmatrix} L & M & N \end{bmatrix}^T$ is the total moment vector about the center of gravity of the aircraft. The dimensionless moment coefficients about each axis follow from $C_l = \frac{L}{\frac{1}{2}\rho V^2 S b}$, $C_m = \frac{M}{\frac{1}{2}\rho V^2 S \bar{c}}$ and $C_n = \frac{N}{\frac{1}{2}\rho V^2 S b}$ with the wing span b and aerodynamic mean chord $\bar{c}$.

The observations of the system are provided by a flight instrumentation system including inertial sensors, airdata sensors and satellite radio navigation devices. The observation model is given after laboratory calibrations (Ref. [209]) as

1. inertial sensors

$$
\begin{bmatrix} A_{x_m} \\ A_{y_m} \\ A_{z_m} \end{bmatrix} = \begin{bmatrix} A_x \\ A_y \\ A_z \end{bmatrix} + \begin{bmatrix} \lambda_x \\ \lambda_y \\ \lambda_z \end{bmatrix}; \qquad \begin{bmatrix} p_m \\ q_m \\ r_m \end{bmatrix} = \begin{bmatrix} p \\ q \\ r \end{bmatrix} + \begin{bmatrix} \lambda_p \\ \lambda_q \\ \lambda_r \end{bmatrix} \tag{3.62}
$$

2. airdata sensors

$$V = \sqrt{(U_N - W_N)^2 + (U_E - W_E)^2 + (U_D - W_D)^2} \tag{3.63}$$

$$\alpha = \arctan\frac{(U_N - W_N)\left(c_\phi s_\theta c_\psi + s_\phi s_\psi\right) + (U_E - W_E)\left(c_\phi s_\theta s_\psi - s_\phi c_\psi\right) + (U_D - W_D)\,c_\phi c_\theta}{(U_E - W_E)\,c_\theta c_\psi + (U_E - W_E)\,c_\theta s_\psi - (U_E - W_E)\,s_\theta} \tag{3.64}$$

$$\beta = \arctan\frac{(U_N - W_N)\left(s_\phi s_\theta c_\psi - c_\phi s_\psi\right) + (U_E - W_E)\left(s_\phi s_\theta s_\psi + c_\phi c_\psi\right) + (U_D - W_D)\,s_\phi c_\theta}{(U_E - W_E)\,c_\theta c_\psi + (U_E - W_E)\,c_\theta s_\psi - (U_E - W_E)\,s_\theta} \tag{3.65}$$

where $c_\theta = \cos\theta$, $s_\phi = \sin\phi$ etc.

3. position and velocity sensors

$$x_m = x;\ y_m = y;\ z_m = z;\ u_{n_m} = u_n;\ v_{n_m} = v_n;\ w_{n_m} = w_n \tag{3.66}$$

4. attitude angle sensors:

$$\phi_m = \phi;\ \theta_m = \theta;\ \psi_m = \psi \tag{3.67}$$

where λ and W are the known sensor biases and wind velocity components.

Combining all these equations in a general form, the aircraft model is given as

$$\begin{aligned} \dot{\mathbf{x}}(\mathbf{t}) &= \mathbf{f}[\mathbf{x}(t), \mathbf{u}(t), \boldsymbol{\xi}] \\ \mathbf{y}(t) &= \mathbf{h}[\mathbf{x}(t), \mathbf{u}(t), \boldsymbol{\xi}] \\ \mathbf{y}_m(k) &= \mathbf{y}(k) + \mathbf{v}(k) \end{aligned} \tag{3.68}$$

The dimensionless force and moment coefficients can be expressed in terms of aerodynamic, engine thrust and control surface deflection angle variables. This is called the aerodynamic model.

Applying the *output-error method* (Ref. [3]), the unknown parameters $\boldsymbol{\xi}$ are estimated by minimizing the negative logarithm of the likelihood function composed of the *output errors*:

$$\ell(\boldsymbol{\xi}) = \frac{1}{2} \sum_{k=1}^{N} \boldsymbol{\mu}(k, \boldsymbol{\xi})^T \mathbf{V}_v^{-1}(\boldsymbol{\xi}) \boldsymbol{\mu}(k, \boldsymbol{\xi}) + \frac{N}{2} \ln \det \mathbf{V}_v(\boldsymbol{\xi}) \tag{3.69}$$

where $\boldsymbol{\mu}(k, \boldsymbol{\xi})$ is the computed system output error vector and $\mathbf{V}_v(\boldsymbol{\xi})$ is the covariance matrix of the output errors.

Since the state and the parameter estimation problems are solved simultaneously, the method may be termed the One-Step Method (OSM) (Ref. [209]).

The aircraft model to be used for the following discussion is a reorganization of the same model as used in the one-step method in the sense that the accelerometers and the rate gyros serve as system inputs.

With this organization of the model, the unknown parameter vector $\boldsymbol{\xi}$ can be separated into two sets $\boldsymbol{\xi} = \begin{bmatrix} \boldsymbol{\xi}_1^T & \boldsymbol{\xi}_2^T \end{bmatrix}^T$ in which $\boldsymbol{\xi}_1$ consists only of unknown parameters from the flight test instrumentation system. These parameters are biases and scale factors in the models of the inertial and air data transducers. The $\boldsymbol{\xi}_2$ are the aerodynamic parameters. The aircraft model can then be written in the following form:

$$
\begin{aligned}
\dot{\mathbf{x}}(\mathbf{t}) &= \mathbf{f}[\mathbf{x}(t), \mathbf{u}_{m_1}(t), \boldsymbol{\xi}_1] + \mathbf{G}[\mathbf{x}(t)]\mathbf{w}(t) \\
\mathbf{y}_1(t) &= \mathbf{h}[\mathbf{x}(t), \mathbf{u}_{m_1}(t), \boldsymbol{\xi}_1, \mathbf{w}(t)] \\
\mathbf{y}_{m_1}(k) &= \mathbf{y}_1(k) + \mathbf{v}_1(k) \\
\mathbf{y}_2(t) &= \mathbf{h}[\mathbf{x}(t), \mathbf{u}_{m_1}(t), \mathbf{u}_{m_2}(t), \boldsymbol{\xi}_2, \mathbf{w}(t)] \\
\mathbf{y}_{m_2}(k) &= \mathbf{y}_2(k) + \mathbf{v}_2(k)
\end{aligned}
\tag{3.70}
$$

It should be noticed that in order to meet this model, certain conditions have to be satisfied. These are:

1. The mass and inertial characteristics have to be known.
2. The measured or calculated angular acceleration must be available.

It can be seen that the aerodynamic model only appears in the second observation equation. The first observation equation only consists of air data measurements. It can also be recognized that the system inputs consist of $\mathbf{u}_{m_1}$ and $\mathbf{u}_{m_2}$. The $\mathbf{u}_{m_1}$ denote the measured quantities of specific forces and the rotation rates and $\mathbf{u}_{m_2}$ represents the elevator deflection and the thrust force. The process noise vector $\mathbf{w}(t)$ then consists of the measurement noise of the accelerometers and rate gyros.

Although the system state equations are decomposed from aerodynamic models, $\mathbf{y}_2$ will be compatible if and only if the state variables $\mathbf{x}$, parameters $\boldsymbol{\xi}_1$ and measured quantities $\mathbf{u}_{m_1}$ and $\mathbf{u}_{m_2}$ are the true values. Therefore the system model is not totally decomposed. In this situation, joint state and parameter estimation is the only viable solution.

Using the Maximum Likelihood method all the parameters $\boldsymbol{\xi}$ may be estimated by minimizing the negative logarithm of the likelihood function composed of the *prediction errors*:

$$
\begin{aligned}
\ell(\boldsymbol{\xi}) = \tfrac{1}{2}\sum_{k=1}^{N} &\boldsymbol{\mu}(k|k-1,\boldsymbol{\xi})^T \mathbf{V}_{\boldsymbol{\mu}}^{-1}(k|k-1,\boldsymbol{\xi})\boldsymbol{\mu}(k|k-1,\boldsymbol{\xi}) \\
&+\tfrac{1}{2}\sum_{k=1}^{N} \ln\det \mathbf{V}_{\boldsymbol{\mu}}(k|k-1,\boldsymbol{\xi})
\end{aligned}
\tag{3.71}
$$

where $\boldsymbol{\mu}(k|k-1,\boldsymbol{\xi})$ is the predicted output error vector:

$$
\begin{aligned}
\boldsymbol{\mu}(k|k-1,\boldsymbol{\xi}) &= \begin{bmatrix} \boldsymbol{\mu}_1(k|k-1,\boldsymbol{\xi}) \\ \boldsymbol{\mu}_2(k|k-1,\boldsymbol{\xi}) \end{bmatrix} \\
&= \begin{bmatrix} \mathbf{y}_{m_1}(k) - \mathbf{h}_1[\hat{\mathbf{x}}(k|k-1,\boldsymbol{\xi}), \mathbf{u}_{m_1}(k), \boldsymbol{\xi}_1] \\ \mathbf{y}_{m_2}(k) - \mathbf{h}_2[\hat{\mathbf{x}}(k|k-1,\boldsymbol{\xi}), \mathbf{u}_{m_1}(k), \mathbf{u}_{m_2}(k), \boldsymbol{\xi}] \end{bmatrix}
\end{aligned}
\tag{3.72}
$$

As the prediction error vector and its covariance matrix in Eq. (3.71) are calculated from an extended or iterated-extended Kalman filter with two sets of observation equations, it may be seen that it is a joint state and parameter estimation problem. In order to decompose the estimation problem, following assumptions have to be made:

Assumption 1: The measured aerodynamic specific force and rotation rate are very accurate. This is equivalent to the case that process noise in Eq. (3.71) is negligible.

(a) High performance accelerometers as part of TU Delft flight test instrumentation system, source: Honeywell

(b) High performance fiber optical rate sensors as part of TU Delft flight test instrumentation system, source: Fizoptika

(c) Inertial sensor calibration facility at TU Delft, source: Acutronic

Figure 3.7: Inertial measurement unit equipment used at Delft University of Technology

Note that modern inertial sensors are nearly noise free; therefore this assumption has indeed a practical meaning, and the system state equations in Eq (3.71) reduces to a deterministic type while the prediction errors are simplified to output errors. Furthermore, the observation noise in practice is assumed to be uncorrelated and the likelihood function for this case becomes:

$$\begin{aligned}
\ell(\boldsymbol{\xi}) &= \frac{1}{2}\sum_{k=1}^{N}\boldsymbol{\mu}^T(k,\boldsymbol{\xi})\mathbf{V}_v^{-1}(\boldsymbol{\xi})\boldsymbol{\mu}(k,\boldsymbol{\xi}) + \frac{N}{2}\ln\det\mathbf{V}_v(\boldsymbol{\xi}) \\
&= \frac{1}{2}\sum_{k=1}^{N}\boldsymbol{\mu}_1^T(k,\boldsymbol{\xi}_1)\mathbf{V}_{v_1}^{-1}(\boldsymbol{\xi}_1)\boldsymbol{\mu}_1(k,\boldsymbol{\xi}_1) + \frac{N}{2}\ln\det\mathbf{V}_{v_1}(\boldsymbol{\xi}_1) \\
&\quad + \frac{1}{2}\sum_{k=1}^{N}\boldsymbol{\mu}_2^T(k,\boldsymbol{\xi})\mathbf{V}_{v_2}^{-1}(\boldsymbol{\xi}_2)\boldsymbol{\mu}_2(k,\boldsymbol{\xi}) + \frac{N}{2}\ln\det\mathbf{V}_{v_2}(\boldsymbol{\xi}_2) = \ell_1(\boldsymbol{\xi}_1) + \ell_2(\boldsymbol{\xi})
\end{aligned} \tag{3.73}$$

in which $\boldsymbol{\mu}_1$, $\boldsymbol{\mu}_2$, $\mathbf{V}_{v_1}$, and $\mathbf{V}_{v_2}$ are the calculated output errors and corresponding covariance matrices with

$$\mathbf{V}_v(\boldsymbol{\xi}) = \begin{bmatrix} \mathbf{V}_{v_1}(\boldsymbol{\xi}_1) & 0 \\ 0 & \mathbf{V}_{v_2}(\boldsymbol{\xi}_2) \end{bmatrix}$$

It may be seen from Eq. (3.73) that the likelihood function is now decomposed into two terms with respect to two observation models. All cross coupling terms in Eq. (3.71) are neglected (Ref. [66]).

The necessary condition for a minimum of Eq. (3.73) is:

$$\frac{\partial \ell(\boldsymbol{\xi})}{\partial \boldsymbol{\xi}} = \begin{bmatrix} \frac{\partial \ell_1(\boldsymbol{\xi}_1)}{\partial \boldsymbol{\xi}_1} \\ 0 \end{bmatrix} + \begin{bmatrix} \frac{\partial \ell_2(\boldsymbol{\xi})}{\partial \boldsymbol{\xi}_1} \\ \frac{\partial \ell_2(\boldsymbol{\xi})}{\partial \boldsymbol{\xi}_2} \end{bmatrix} = 0 \tag{3.74}$$

The equivalent forms of Eq. (3.74) are:

$$\begin{aligned} \frac{\partial \ell_1(\boldsymbol{\xi}_1)}{\partial \boldsymbol{\xi}_{1_i}} + \frac{\partial \ell_2(\boldsymbol{\xi})}{\partial \boldsymbol{\xi}_{1_i}} = &\sum_{k=1}^{N} \frac{\partial \boldsymbol{\mu}_1^T(k,\boldsymbol{\xi}_1)}{\partial \boldsymbol{\xi}_{1_i}} \mathbf{V}_{v_1}^{-1}(\boldsymbol{\xi}_1)\boldsymbol{\mu}_1(k,\boldsymbol{\xi}_1) \\ &-\frac{1}{2}\sum_{k=1}^{N} \boldsymbol{\mu}_1^T(k,\boldsymbol{\xi})\,\mathbf{V}_{v_1}^{-1}(\boldsymbol{\xi}_1)\,\frac{\partial \mathbf{V}_{v_1}(\boldsymbol{\xi}_1)}{\partial \boldsymbol{\xi}_{1_i}}\mathbf{V}_{v_1}^{-1}(\boldsymbol{\xi}_1)\boldsymbol{\mu}_1(k,\boldsymbol{\xi}_1) \\ &+\sum_{k=1}^{N} \frac{\partial \boldsymbol{\mu}_2^T(k,\boldsymbol{\xi})}{\partial \boldsymbol{\xi}_{1_i}} \mathbf{V}_{v_2}^{-1}(\boldsymbol{\xi}_2)\boldsymbol{\mu}_2(k,\boldsymbol{\xi}) \\ &+\frac{N}{2}\mathrm{Tr}\left(\mathbf{V}_{v_1}^{-1}(\boldsymbol{\xi}_1)\frac{\partial \mathbf{V}_{v_1}(\boldsymbol{\xi}_1)}{\partial \boldsymbol{\xi}_{1_i}}\right) = 0; \quad (i = 1,\ 2, \ldots, L_1) \end{aligned} \tag{3.75}$$

and:

$$\begin{aligned} \frac{\partial \ell_2(\boldsymbol{\xi})}{\partial \boldsymbol{\xi}_{2_i}} = &\sum_{k=1}^{N} \frac{\partial \boldsymbol{\mu}_2^T(k,\boldsymbol{\xi})}{\partial \boldsymbol{\xi}_{2_i}} \mathbf{V}_{v_2}^{-1}(\boldsymbol{\xi}_2)\boldsymbol{\mu}_2(k,\boldsymbol{\xi}) \\ &-\frac{1}{2}\sum_{k=1}^{N} \boldsymbol{\mu}_2^T(k,\boldsymbol{\xi})\,\mathbf{V}_{v_2}^{-1}(\boldsymbol{\xi}_2)\,\frac{\partial \mathbf{V}_{v_2}(\boldsymbol{\xi}_2)}{\partial \boldsymbol{\xi}_{2_i}}\,\mathbf{V}_{v_2}^{-1}(\boldsymbol{\xi}_2)\boldsymbol{\mu}_2(k,\boldsymbol{\xi}) \\ &+\frac{N}{2}\mathrm{Tr}\left(\mathbf{V}_{v_2}^{-1}(\boldsymbol{\xi}_2)\,\frac{\partial \mathbf{V}_{v_2}(\boldsymbol{\xi}_2)}{\partial \boldsymbol{\xi}_{2_i}}\right) = 0; \quad (i = 1,\ 2, \ldots, L_2) \end{aligned} \tag{3.76}$$

in which L_1 and L_2 are the sizes of the parameter sets $\boldsymbol{\xi}_1$ and $\boldsymbol{\xi}_2$ respectively.

Eq. (3.75) shows that the gradient of the second term of the likelihood function with respect to the first set of parameters $\boldsymbol{\xi}_1$ should also be evaluated to satisfy the minimization condition because the second output error vector is also the function of the first set of parameters $\boldsymbol{\xi}_1$. This leads to the following assumption which has to be made:

Assumption 2: With only the first set of observation equations $\mathbf{y}_1(t)$ the identifiability of parameter $\boldsymbol{\xi}_1$ is guaranteed and the state variables $\mathbf{x}(k)$, parameters $\boldsymbol{\xi}_1$ can be estimated by minimizing the first term of the likelihood function.

In order to satisfy this assumption, the flight instrumentation system should make information available about ground velocity, air velocity, altitude, and aircraft attitude[2]. This is in practice achievable with modern flight instrumentation systems. With this assumption, the contribution from the second observation equation can be neglected with respect to the estimation accuracy. It is equivalent to the case that the second output error vector only takes the estimated states and parameters as perfect measurements, therefore, $\boldsymbol{\mu}_2(k,\boldsymbol{\xi})$ is no longer a function of $\boldsymbol{\xi}_1$, i.e.:

$$\boldsymbol{\mu}_2(k,\boldsymbol{\xi}) = \boldsymbol{\mu}_2(k,\boldsymbol{\xi}_2) \tag{3.77}$$

The gradient of the second likelihood function with respect to the first set of parameters is

[2]Aircraft attitude measurements are necessary when biases of the rate gyros need to be estimated, such as for fiber optical gyros, in contrast to ring laser gyros.

then:

$$\frac{\partial \ell_2(\boldsymbol{\xi})}{\partial \boldsymbol{\xi}_1} = \sum_{k=1}^{N} \frac{\partial \boldsymbol{\mu}_2^T(k, \boldsymbol{\xi}_2)}{\partial \boldsymbol{\xi}_1} \mathbf{V}_{v_2}^{-1}(\boldsymbol{\xi}_2) \boldsymbol{\mu}_2(k, \boldsymbol{\xi}_2) = 0 \tag{3.78}$$

The necessary conditions in Eqs. (3.75),(3.76) become:

$$\begin{aligned} \tfrac{\partial \ell_1(\boldsymbol{\xi}_1)}{\partial \boldsymbol{\xi}_{1_i}} = & \sum_{k=1}^{N} \tfrac{\partial \boldsymbol{\mu}_1^T(k,\boldsymbol{\xi}_1)}{\partial \boldsymbol{\xi}_{1_i}} \mathbf{V}_{v_1}^{-1}(\boldsymbol{\xi}_1) \boldsymbol{\mu}_1(k, \boldsymbol{\xi}_1) \\ & -\tfrac{1}{2} \sum_{k=1}^{N} \boldsymbol{\mu}_1^T(k, \boldsymbol{\xi})\, \mathbf{V}_{v_1}^{-1}(\boldsymbol{\xi}_1)\, \tfrac{\partial \mathbf{V}_{v_1}(\boldsymbol{\xi}_1)}{\partial \boldsymbol{\xi}_{1_i}} \mathbf{V}_{v_1}^{-1}(\boldsymbol{\xi}_1) \boldsymbol{\mu}_1(k, \boldsymbol{\xi}_1) \\ & + \tfrac{N}{2} \mathrm{Tr} \left(\mathbf{V}_{v_1}^{-1}(\boldsymbol{\xi}_1)\, \tfrac{\partial \mathbf{V}_{v_1}(\boldsymbol{\xi}_1)}{\partial \boldsymbol{\xi}_{1_i}} \right) = 0; \quad (i = 1,\ 2, \ldots, L_1) \end{aligned} \tag{3.79}$$

and:

$$\begin{aligned} \tfrac{\partial \ell_2(\boldsymbol{\xi})}{\partial \boldsymbol{\xi}_{2_i}} = & \sum_{k=1}^{N} \tfrac{\partial \boldsymbol{\mu}_2^T(k,\boldsymbol{\xi}_2)}{\partial \boldsymbol{\xi}_{2_i}} \mathbf{V}_{v_2}^{-1}(\boldsymbol{\xi}_2) \boldsymbol{\mu}_2(k, \boldsymbol{\xi}_2) \\ & -\tfrac{1}{2} \sum_{k=1}^{N} \boldsymbol{\mu}_2^T(k, \boldsymbol{\xi}_2)\, \mathbf{V}_{v_2}^{-1}(\boldsymbol{\xi}_2)\, \tfrac{\partial \mathbf{V}_{v_2}(\boldsymbol{\xi}_2)}{\partial \boldsymbol{\xi}_{2_i}}\, \mathbf{V}_{v_2}^{-1}(\boldsymbol{\xi}_2) \boldsymbol{\mu}_2(k, \boldsymbol{\xi}_2) \\ & + \tfrac{N}{2} \mathrm{Tr} \left(\mathbf{V}_{v_2}^{-1}(\boldsymbol{\xi}_2)\, \tfrac{\partial \mathbf{V}_{v_2}(\boldsymbol{\xi}_2)}{\partial \boldsymbol{\xi}_{2_i}} \right) = 0; \quad (i = 1,\ 2, \ldots, L_2) \end{aligned} \tag{3.80}$$

Now the original joint state and parameter estimation problem Eq. (3.71) is solved in two consecutive steps. In the first step the state trajectory is estimated simultaneously with some unknown parameters from the flight test instrumentation system Eq. (3.79) named *Flight Path Reconstruction* (Refs. [67, 68, 69, 139]) for off-line identification and *Aircraft State Estimation* for on-line identification purposes, while the aerodynamic parameters are estimated in the second step Eq. (3.80). The method is then called the *two-step method* (Refs. [209, 213]).

From above discussions it is shown that in the limiting case, the two-step method may be expected to produce the same results as the joint state and parameter estimation algorithm i.e. one-step Maximum Likelihood method. This limit case requires an accurate flight test instrumentation system to make the flight path reconstruction perfect, i.e.:

$$\hat{\mathbf{x}}_{\text{FPR}}(k|k-1) = \mathbf{x}(k); \qquad \hat{\boldsymbol{\xi}}_{1_{\text{FPR}}} = \boldsymbol{\xi}_1 \tag{3.81}$$

where the subscript FPR means Flight Path Reconstruction.

In practice, the measurements of the inertial, air data and other navigation sensors are accurate but certainly not perfect, and the result of the flight path reconstruction depends on the accuracies of these measurements. The aerodynamic parameter estimation takes the result from the flight path reconstruction as state and parameter measurements whether it is perfectly estimated or not, i.e.:

$$\mathbf{x}_m(k) = \hat{\mathbf{x}}_{\text{FPR}}(k|k-1); \qquad \boldsymbol{\xi}_{1_m} = \hat{\boldsymbol{\xi}}_{1_{\text{FPR}}} \tag{3.82}$$

The second set of the observation equations, which is in fact the aerodynamic model, is now written as:

$$\mathbf{y}_2(k) = \mathbf{h}_2[\mathbf{x}_m(k), \mathbf{u}_{m_1}(k), \mathbf{u}_{m_2}(k), \boldsymbol{\xi}_{1_m}, \boldsymbol{\xi}_2] \tag{3.83}$$

It should be noticed that Eq. (3.83) is usually not compatible due to the errors in $\mathbf{x}_m$,$\mathbf{u}_{m_1}$, $\mathbf{u}_{m_2}$, and $\boldsymbol{\xi}_{1_m}$, i.e.:

$$\mathbf{y}_2(k) \neq \mathbf{h}_2[\mathbf{x}_m(k), \mathbf{u}_{m_1}(k), \mathbf{u}_{m_2}(k), \boldsymbol{\xi}_{1_m}, \boldsymbol{\xi}_2] \tag{3.84}$$

Once the flight path reconstruction is performed, the second set of observation equations becomes *Linear-in-the-parameters*. This means that the aerodynamic models are linear functions of aerodynamic parameters when all the measurements, which are needed to identify the aerodynamic parameters are available from direct measurements and the result of the flight path reconstruction. Therefore Eq (3.71), and the nonlinear observation model Eq. (3.83), can be written in the form:

$$\mathbf{y}_{m_2}(k) = \mathbf{H}_m[\mathbf{x}_m(k), \mathbf{u}_{m_1}(k), \mathbf{u}_{m_2}(k), \boldsymbol{\xi}_{1_m}]\boldsymbol{\xi}_2 + \mathbf{v}_2(k) \tag{3.85}$$

where $\mathbf{H}_m[\mathbf{x}_m(k), \mathbf{u}_{m_1}(k), \mathbf{u}_{m_2}(k), \boldsymbol{\xi}_{1_m}]$ is a matrix of the variables $\mathbf{x}_m$,$\mathbf{u}_{m_1}$, $\mathbf{u}_{m_2}$ and $\boldsymbol{\xi}_{1_m}$. Since these variables are all available, this matrix may be called a data matrix. The model becomes now a set of linear regression equations and the estimation problem for this type of model is easier to solve than nonlinear models. This is considered to be a great advantage of the two-step method.

Eq. (3.85) can further be written in terms of the total number of samples:

$$\mathbf{Y}_m = \boldsymbol{\Xi}_m \boldsymbol{\xi}_2 + \boldsymbol{\zeta} \tag{3.86}$$

in which:

$$\begin{aligned} \mathbf{Y}_m &= [y_{m_2}^T(1),\ \ y_{m_2}^T(2), \ldots, y_{m_2}^T(k), \ldots, y_{m_2}^T(N)]^T \\ \boldsymbol{\zeta} &= [v_2^T(1),\ \ v_2^T(2), \ldots, v_2^T(k), \ldots, v_2^T(N)]^T \\ \boldsymbol{\Xi}_m &= [\mathbf{H}_m^T(1),\ \ \mathbf{H}_m^T(1), \ldots, \mathbf{H}_m^T(k), \ldots, \mathbf{H}_m^T(N)]^T \end{aligned} \tag{3.87}$$

The likelihood function to model Eq. (3.85) becomes now:

$$\ell_2(\boldsymbol{\xi}_2) = \frac{1}{2}(\mathbf{Y}_m - \boldsymbol{\Xi}_m\boldsymbol{\xi}_2)^T \boldsymbol{\Sigma}_\zeta^{-1}(\mathbf{Y}_m - \boldsymbol{\Xi}_m\boldsymbol{\xi}_2) + \frac{1}{2}\ln\det\boldsymbol{\Sigma}_\zeta \tag{3.88}$$

where:

$$\boldsymbol{\Sigma}_\zeta = E\{\boldsymbol{\zeta}\boldsymbol{\zeta}^T\} \tag{3.89}$$

The maximum Likelihood estimates of $\boldsymbol{\xi}_2$ is then:

$$\hat{\boldsymbol{\xi}}_{2_{ML}} = (\boldsymbol{\Xi}_m^T \boldsymbol{\Sigma}_\zeta^{-1} \boldsymbol{\Xi}_m)^{-1} \, \boldsymbol{\Xi}_m^T \boldsymbol{\Sigma}_\zeta^{-1} \mathbf{Y}_m \tag{3.90}$$

It is shown from the aerodynamic model Eq. (3.71) that the aerodynamic parameters are all independent from each other. Therefore, the multi-output parameter estimation problem of Eq. (3.88) can be simplified as number of single-output parameter estimations. For each parameter estimation problem the Maximum Likelihood parameter estimation is reduced to a Least Squares estimation problem (Ref. [66]):

$$\hat{\boldsymbol{\xi}}^{(i)}_{2_{ML}} = (\boldsymbol{\Xi}_m^{(i)T} \boldsymbol{\Xi}_m^{(i)})^{-1} \, \boldsymbol{\Xi}_m^{(i)T} \mathbf{Y}_m^{(i)} = \hat{\boldsymbol{\xi}}^{(i)}_{2_{LS}} \tag{3.91}$$

In Eq. (3.91) index *i* denotes the i^{th} aerodynamic model. In the present case $i = 1, 2, 3$, see Eq. (3.71). This approach is polynomial based.

3.3.6 Alternative approaches for system identification

As already mentioned earlier, some alternative approaches recently emerged for aerodynamic model identification. Main motivation for this research is to find aerodynamic models which are locally as well as globally valid over the entire flight envelope, without crisp transitions. A few approaches are briefly explained here.

Neural-networks

As shown in ref. [78], neural networks can be an alternative method for aerodynamic model identification, replacing the least squares approach mentioned above in the second step. The main advantage of using neural networks is that the internal structure of the aerodynamic model does not have to be defined. Keeping the input span of the neural networks general will ensure that all possible dependencies between input and output can be learned, resulting in an accurate aerodynamic model. A drawback of neural networks is that they suffer from the recency-effect. Neural networks tend to forget knowledge which has been learned in the past if that knowledge is no longer in the recent input-output (IO) pairs presented to the network. To prevent the recency effect the aerodynamic model is defined by a nine dimensional hyperbox structure. Each hyper- box contains neural networks which learn a small local IO-mapping of the aerodynamic model. Experimental results show that an accuracy of $> 99\%$ in the approximation of the aerodynamic model can be obtained throughout the flight envelope with off-line learning using the Levenberg-Marquardt algorithm. The aircraft under consideration is the F-16 and wind tunnel test data have been used for the off-line training. Other neural network based identification research can be found in ref. [102].

Fuzzy Aerodynamic Modeling and Identification

In ref. [274], an alternative framework has been explored for the development and identification of globally valid aerodynamic models using a multiple model network approach and new fuzzy estimation methods. The framework should be as transparent as possible, to allow analysis of the physical aerodynamic behaviour of the aircraft. The aerodynamic models should be able to use the information from a priori aerodynamic models and update it using new information from, for instance, flight data. This local model updating task is far from trivial. This is achieved by combining conventional flight test estimatiom methods with fuzzy modeling and identification methods. The result is a multiple local model network approach, where each model is representative of the local aerodynamic behaviour of the aircraft. By using a so-called Takagi-Sugeno fuzzy model structure, it is possible to combine multiple local models such that the transitions between the local models is continuous and smooth. Manual, automatic and hybrid partitioning algorithms have been investigated that partition the flight envelope into hyperboxes in which the local models are defined. The proposed framework has also been applied on the F-16 aerodynamic and simulation model.

Multivariate splines

The current consensus in aerodynamic model identification is to assume a polynomial model structure for a force or moment coefficient, after which parameter estimation techniques are employed to estimate the parameters of the polynomials such that they, in some way, optimally fit a set of wind tunnel or flight test data. It is well known that polynomials have a limited approximation power that is proportional with their degree. The limited approximation power of polynomials requires the design of flight test manoeuvres specifically designed to reduce the effects of dimensional couplings and high order nonlinearities such that the resulting datasets can be adequately modeled with polynomials. From the perspective of aerodynamic model identification it would be more desirable to execute long duration, high amplitude manoeuvres designed to cover as much of the flight envelope as possible. Polynomial models, however, are inadequate for fitting the datasets resulting from such manoeuvres. Many authors have therefore suggested the use of polynomial spline functions for fitting the flight data [52, 159]. Spline functions are piecewise defined polynomials with a predefined continuity order between the pieces. The approximation power of spline functions not only is proportional with the degree of the polynomial but also with the number and density of the polynomial pieces. In the past, multivariate tensor product splines have been used to model aircraft aerodynamics [52]. It is well known, however, that the multivariate tensor product spline is incapable of fitting scattered data, making it inadequate for the fitting of flight test data, which is inherently scattered. Recently, a new method for nonlinear system identification based on multivariate simplex splines was introduced [75]. This multivariate spline type has the unique advantage over other spline types that it is capable of fitting scattered data on non-rectangular domains. The linear regression framework for multivariate simplex splines as introduced in [75] allows the use of standard parameter estimation techniques such as Least Squares (LS) or Maximum Likelihood (ML) for estimating the parameters of the simplex spline polynomials. The new identification method was used to identify the global aerodynamic model of the F-16 fighter aircraft based on the original NASA wind tunnel tables [76] and on a set of simulated flight test data [77]. Results from these identification experiments showed that the new identification method based on multivariate simplex splines was capable of producing highly accurate results, with a global error RMS smaller than 1%.

3.3.7 Identification in the frequency domain

All research work discussed so far focuses on identification in the time domain. However, aerodynamic model identification can also be performed in the frequency domain. Therefore, a transformation of the measured data is needed from the time domain to the frequency domain. This can be done by the fast Fourier transform (FFT) for computational efficiency. Frequency domain based identification methods have advantages as well as disadvantages compared to the time domain, as discussed in ref. [159]. References for more information over frequency domain methods can be found in ref. [155, 156, 158, 215]. Real time frequency based methods are discussed in ref. [202, 203, 204, 250, 251]. Ref. [263] focuses on system identification using a frequency-response method, achieving improvements with the chirp z-transform and a numerical optimization procedure that combines the results of individual spectral window calculations.

3.4 Chosen method and motivation

The identification method considered in this study is the two step method. In this context, one is looking for real-time physical parameter estimates in nonlinear models. Therefore, the two step method has shown to be the most appropriate and direct method. One of the major advantages of the two step method is the decomposition of a global non-linear one step identification method in two separate steps, as substantiated earlier, where the nonlinear part is isolated in the aircraft state estimation step. The use of a state estimator in the first step makes it fairly straightforward to merge redundant but contaminated data, resulting in even higher accuracies. Consequently, the aerodynamic model parameter identification procedure in the second step can be simplified to a procedure which is linear in the parameters.

Chapter 4

Real time damaged aircraft model identification based on physical models

This chapter elaborates the initial part of the aerodynamic model identification related component of this research project. In this chapter, the baseline version of the identification method has been considered, including crucial modifications needed to apply this method for model identification of damaged aircraft. In subsequent chapters, research has been performed in order to investigate the damage induced effects on aerodynamic and mass property changes, which are significant when severe structural failures occur.

The identification method considered in this study is the so-called two step method, which has been continuously under development at Delft University of Technology over the last 20 years, see ref. [65, 208]. The last major milestones in this development process can be found in ref. [165, 210]. As already explained earlier in section 3.4, there are many identification algorithms available in the literature, but not all of them are applicable on line. In this context, one is looking for real-time physical parameter estimates in nonlinear models. Therefore, the two step method has shown to be the most appropriate and direct. The advantage of the two step method over other identification methods is that it is easier to implement on-line and in the time domain. Key concept of the two step method, is that the identification procedure has been split into two consecutive steps, as substantiated in section 3.3.5.1. One of the major advantages of the two step method, is the decomposition of a global non-linear one step identification method in two separate steps, where the non-linear part is isolated in the aircraft state estimation step. Consequently, the aerodynamic model parameter identification procedure in the second step can be simplified to a procedure which is linear in the parameters. The aim is to update a local a priori aerodynamic model (obtained by means of windtunnel tests and CFD calculations) by means of on-line flight data. As a result of the two step method, only locally valid models are obtained. As a consequence the complete flight envelope must be covered by multiple local models with crisp transitions at the boundaries between them. By applying the principle of fuzzy clustering, described in section 3.3.6, it is possible to create a non-linear aerodynamic model, with varying model parameters, which is globally valid over the entire flight envelope while the crisp transitions have been smoothened. In ref. [274], research has already been performed in this field for an F-16 model. The first step in the two step method is called the Aircraft State Estimation phase, where the second one is the Aerodynamic Model Identification step. In the Aircraft State Estimation procedure, an Iterated Extended Kalman Filter is used to determine the aircraft states, the measurement equipment properties (sensor biases) and the wind components, by making use of the nonlinear kinematic and observation models, based upon redundant but contaminated information from all sensors (air data, inertial, magnetic and GPS measurements). By means of this state information, combined with the input signals of the pilot and the aforementioned measurements, it is possible to construct the combined aerodynamic and thrust forces and moments acting on the aircraft. Using a recursive least squares operation, the aerodynamic derivatives can be deduced. Validation tests by means of batch process identification, least squares innovation analysis and reconstruction of velocity and angular rate components using these aerodynamic derivatives have shown that this method is very accurate. Finally, figure 4.1 gives a high-level logical structure overview of the two step method algorithm, pointing out the inputs and outputs of each macro-step.

In the classical two step methodology presented above, some bottlenecks can be identified for application to a damaged aircraft. There are three important limitations, as enumerated below:

1. When the combined aerodynamic and thrust forces and moments acting on the aircraft are constructed, one assumes that mass, location of center of gravity and inertia are perfectly known. Besides, the aircraft is considered symmetric. For conventional aircraft and situations, these are realistic assumptions (varying mass properties can be derived by means of preflight weight and balance calculations and in-flight fuel flow measurements). However, some attention is needed here for structurally damaged aircraft.

2. The model structure is considered fixed when the aerodynamic derivatives are deduced by means of the recursive least squares procedure. However, for failure situations, it is highly probable that the conventional model structure must be extended with additional non-linear terms and their accompanying derivatives.

3. Especially in the case of fault tolerant flight control, it is important that the contri-

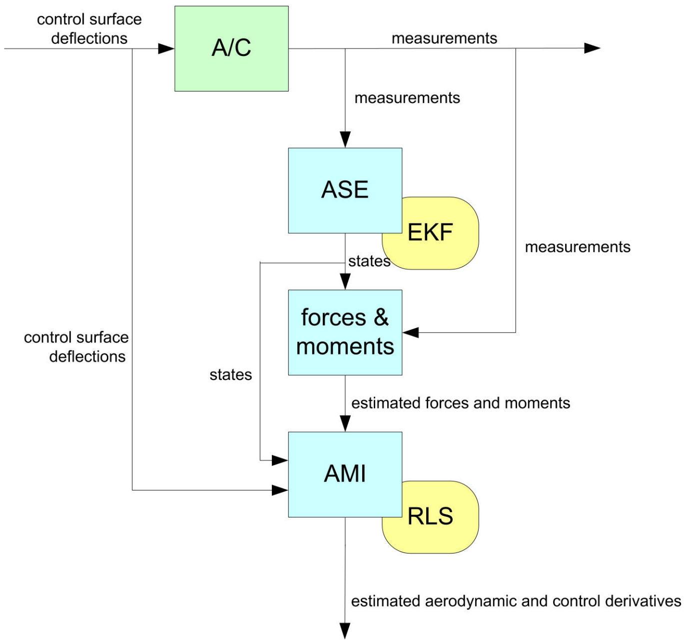

Figure 4.1: Overview of the two step method: measurements serve for ASE step, which estimates the aircraft states. These states, combined with the measurements, allow to calculate the forces and moments. The latter are used, together with the estimated states and control surface deflections, for the AMI step, which produces the estimated aerodynamic and control derivatives.

butions of all different control channels (surfaces and engines) are analysed independently, this augments the degrees of freedom available for the control allocation procedure.

Chapter 5 will focus on the second item, namely the expansion of the model structure with relevant terms such that the perturbed aircraft dynamics can be represented accurately. This model structure expansion can be performed in many ways. The two methods considered here are the so-called modified stepwise regression procedure and adaptive recursive orthogonal least squares. The first item of the enumeration above will be briefly discussed in chapter 6, by analysing the influence of mass property changes on aerodynamic forces and moments.

This approach can deal with component failures as well as structural failures. An overview of fault scenarios for which this method is valid can be found in table 4.1, building on a similar table with failure scenarios from [124, 138]. These failure characteristics are set up generally and are by no means specific to a particular aircraft. The different types of failures can be grouped into three categories: sensor, actuator, and structural failures. For each failure, the physical consequences are described and the model parameters which are possibly affected are enumerated. It should be noted that this method is not explicitly valid for the structural loss of engine(s) and severe structural damage. However, experiments have shown that the method is implicitly valid for these scenarios. Research results presented in chapters 5 and 6 focus on the extension of the explicit validity of this method for these failure scenarios, as stated earlier.

In this chapter, focus is placed on the two consecutive steps of this method: Aircraft State Estimation (ASE) and Aerodynamic Model Identification (AMI) in sections 4.1 and 4.2. Also two important validation tests of this method are illustrated in section 4.3. Section 4.4 discusses briefly the real time computer based aerodynamic model identification tool which has been developed. Thereafter, as an application, some preliminary identification results are shown for damaged aircraft models, see section 4.5. Part of the information obtained in this step can be presented to the pilot, in order to augment his situational awareness of the health status of the aircraft. This is discussed in section 4.6. Finally, the required triggering routine for reconfiguration will be introduced in section 4.7.

4.1 Aircraft State Estimation

Estimating the aircraft states can be based upon redundant but contaminated information from all sensors. Standard available sensor information on civil airliners is classified in three categories. First there are the air data sensors, providing true airspeed V_{TAS}, angle of attack α, angle of sideslip β. A second class are the data from the inertial navigation system (INS, consisting of inertial and magnetic equipment) giving measurement values for the specific forces A_x, A_y, A_z, the rotational rates p, q, r and aircraft attitude angles ϕ,

Table 4.1: Overview of fault scenarios and effects in vehicle and aerodynamic model, ✓ indicates explicit validity of the method, (✓) points out implicit validity.

sensor	actuator	structural	failure	effect	affected parameters	method validity
✓			sensor loss	minor with sensor redundancy and sensor loss detection (usually the case)	parameters related to sensor output	(✓)
✓			sensor miscalibration	inertial sensor miscalibrated (accelerometer or gyro)	$\lambda_{\mathrm{acc}_{\mathrm{X/Y/Z}}}$ or $\lambda_{\mathrm{rg}_{\mathrm{p/q/r}}}$	✓
	✓		partial hydraulics loss	maximum rate/deflection decrease on several control surfaces	$C_{(Y/l/n)_{\delta_a}}$, $C_{(X/Z/m)_{\delta_e}}$, $C_{(Y/l/n)_{\delta_r}}$	✓
	✓		full hydraulics loss	one or more control surfaces become stuck at last position or start floating	$C_{(Y/l/n)_{\delta_a}}$, $C_{(X/Z/m)_{\delta_e}}$, $C_{(Y/l/n)_{\delta_r}}$ and/or $C_{(X/Y/Z/l/m/n)_0}$	✓
	✓		*control* loss on one or more actuators	one or more control surfaces become stuck at last position	$C_{(Y/l/n)_{\delta_a}}$, $C_{(X/Z/m)_{\delta_e}}$, $C_{(Y/l/n)_{\delta_r}}$ and/or $C_{(X/Y/Z/l/m/n)_0}$	✓
	✓	✓	*structural* loss of (part of) control surface	effectiveness of control surfaces is reduced minor change in aerodynamics	$C_{(Y/l/n)_{\delta_a}}$, $C_{(X/Z/m)_{\delta_e}}$, $C_{(Y/l/n)_{\delta_r}}$ and/or $C_{(X/Z/m)_{0/\alpha/q}}$ and/or $C_{(Y/l/n)_{0/\beta/p/r}}$	✓
	✓		engine(s) out	thrust becomes asymmetric, increased drag due to nonzero sideslip β	$C_{(X/Y/Z/l/m/n)_{T_{(l/r)}}}$ and/or $C_{(X/Z/m)_{0/\alpha/q}}$ and/or $C_{(Y/l/n)_{0/\beta/p/r}}$	✓
	✓	✓	*structural* loss of engine(s)	large change in possible operating region; significant change in aerodynamics, mass and moments of inertia	all aerodynamic parameters, aerodynamic model structure, m_{aircraft}, $(x/y/z)_{\text{cg}}$ and $\mathbf{I}$	(✓)
	✓	✓	severe structural damage	large change in possible operating region; significant change in aerodynamics, mass and moments of inertia	all aerodynamic parameters, aerodynamic model structure, m_{aircraft}, $(x/y/z)_{\text{cg}}$ and $\mathbf{I}$	(✓)

θ, ψ. The third and last category is a combination of INS and GPS measurements leading to data for three dimensional position x, y, z and inertial velocity components u_n, v_n, w_n. Another set of velocity information, namely true airspeed V_{TAS}, angle of attack α, angle of sideslip β allows to derive the wind components. Table 4.2 gives information about the instrumentation errors which generally occur for each kind of measuring equipment mentioned above. By making use of the kinematic and observation model of the aircraft, it is possible to estimate a part of the instrumentation errors, which will be discussed in more detail below.

Table 4.2: Instrumentation error information for measuring equipment

sensor	variables	bias error	noise error
translational accelerometer	A_x, A_y, A_z	✓	✓
rate gyro	p, q, r	✓	✓
integrating gyro	ϕ, θ, ψ		✓
INS/GPS	x, y, z		✓
INS/GPS	u_n, v_n, w_n		✓
pitot tube, static port, TAT probe	V_{TAS}		✓
airflow angle vane	α, β		✓

Note from table 4.2 that the computation of the true airspeed requires measurement of total pressure (pitot tube), static pressure (static port), total air temperature (TAT probe) and finally air density information (via altitude information) to convert the calibrated airspeed towards the true airspeed. Moreover, measurements of angle of attack α and sideslip angle β by airflow angle vanes are perturbed by upwash, sidewash and fuselage effects. In flight test practice, the observation model uses total air pressure p_t, static pressure p_s, total air temperature T_t [165], vane angle of attack α_v and vane sideslip angle β_v [208] rather than V_{TAS}, α and β. Biases and gain errors are estimated in this step. However, the research presented in this thesis considers flight path reconstruction with a loosely coupled flight instrumentation system using processed observations, as opposed to the tightly coupled counterpart with raw measurement data.

4.1.1 Nonlinear aircraft kinematics model

The general state space model set of nonlinear system equations describing the kinematics of the aircraft is given as follows:

$$\dot{\mathbf{x}}(t) = \mathbf{f}[\mathbf{x}(t), \mathbf{u}_m(t), \boldsymbol{\theta}, t] + \mathbf{G}[\mathbf{x}(t)]\mathbf{w}(t), \quad \mathbf{x}(t_0) = \mathbf{x}_0 \tag{4.1}$$

$$\mathbf{z}_m(t) = \mathbf{h}[\mathbf{x}(t), \mathbf{u}_m(t), \boldsymbol{\theta}, t] + \mathbf{v}(t), \quad t = t_i, \quad i = 1,\ 2, \ldots \tag{4.2}$$

where equation (4.1) is known as the kinematic state equation with input noise vector $\mathbf{w}$ and expression (4.2) is called the observation equation with output noise vector $\mathbf{v}$. The nonlinear vector functions $\mathbf{f}$ and $\mathbf{h}$ may depend both implicitly (via $\mathbf{x}$ and $\mathbf{u}_m$) and explicitly on t and it will be assumed that both $\mathbf{f}$ and $\mathbf{h}$ are continuous and continuously differentiable with respect to all elements of $\mathbf{x}$ and $\mathbf{u}_m$. The system equation variables are defined as follows:

$$\begin{aligned}
\mathbf{x} &= [x, y, z, u_b, v_b, w_b, \phi, \theta, \psi]^T && (4.3)\\
\mathbf{u}_m &= \mathbf{u} + \boldsymbol{\lambda} + \mathbf{w} = [A_x, A_y, A_z, p, q, r]^T + [\lambda_x, \lambda_y, \lambda_z, \lambda_p, \lambda_q, \lambda_r]^T + \mathbf{w} && (4.4)\\
\boldsymbol{\theta} &= \boldsymbol{\lambda} = [\lambda_x, \lambda_y, \lambda_z, \lambda_p, \lambda_q, \lambda_r]^T && (4.5)\\
\mathbf{z}_m &= [x_{\text{INS}}, y_{\text{INS}}, z_{\text{INS}}, u_{\text{INS}}, v_{\text{INS}}, w_{\text{INS}}, \\
&\quad \phi_{\text{INS}}, \theta_{\text{INS}}, \psi_{\text{INS}}, V_{\text{TAS}}, \alpha_{\text{ADS}}, \beta_{\text{ADS}}]^T && (4.6)
\end{aligned}$$

where the aircraft state vector $\mathbf{x}$ in eq. (4.3) contains inertial position, body airspeed velocity components and aircraft attitude angles. The measured input vector $\mathbf{u}_m$ in eq. (4.4) consists of specific forces and angular rates, perturbed with sensor biases and input noise, where the sensor biases are collected in vector $\boldsymbol{\theta}$ in eq. (4.5), which contributes for the augmended state vector as $\mathbf{x}_{\text{aug}} = [\mathbf{x}, \boldsymbol{\theta}]$. Finally, there is the measured output vector $\mathbf{z}_m$ in eq. (4.5), consisting of GPS-aided INS measurement data of position, velocity components (navigational frame of reference) and attitude angles as well as air data system (ADS) measurements for true airspeed, angle of attack and angle of sideslip. Also the measured output vector is perturbed with output noise.

Additionally, the input noise vector $\mathbf{w}(t)$ is a continuous time white noise process and the output noise vector $\mathbf{v}(t_i)$ is a discrete time white noise sequence. Both are mutually uncorrelated as well as between the different input and output channels individually. Moreover, based upon the known on-board measurement equipment characteristics, standard deviations are specified by the equipment manufacturers. Therefore, the error model can be described as follows:

$$\begin{aligned}
\mathbf{v}(t_i) &= [v_x, v_y, v_z, v_u, v_v, v_w, v_\phi, v_\theta, v_\psi, v_V, v_\alpha, v_\beta]^T && (4.7)\\
\mathbf{w}(t) &= [w_x, w_y, w_z, w_p, w_q, w_r]^T && (4.8)\\
E\left\{\mathbf{w}(t)\mathbf{w}^T(\tau)\right\} &= \mathbf{Q}\delta(t-\tau); \quad \mathbf{Q} = \text{diag}(\sigma^2_{w_x}, \sigma^2_{w_y}, \sigma^2_{w_z}, \sigma^2_{w_p}, \sigma^2_{w_q}, \sigma^2_{w_r}) && (4.9)\\
E\left\{\mathbf{v}(t_i)\mathbf{v}^T(t_j)\right\} &= \mathbf{R}\delta_{ij}; \quad \mathbf{R} = \text{diag}(\sigma^2_{v_x}, \sigma^2_{v_y}, \sigma^2_{v_z}, \sigma^2_{v_u}, \sigma^2_{v_v}, \sigma^2_{v_w}, \\
&\qquad \sigma^2_{v_\phi}, \sigma^2_{v_\theta}, \sigma^2_{v_\psi}, \sigma^2_{v_V}, \sigma^2_{v_\alpha}, \sigma^2_{v_\beta}) && (4.10)\\
E\left\{\mathbf{w}(t)\mathbf{v}^T(t_i)\right\} &= 0, \quad \text{for} \quad \mathrm{t = t_i}, \quad \mathrm{i = 1,\ 2, \ldots} && (4.11)
\end{aligned}$$

The kinematic equations can be written as follows, where the aircraft is considered as a rigid body above a flat non-rotating earth:

$$\begin{aligned}
\dot{x}_{\mathrm{GS}} &= [u_{\mathrm{AS}}\cos\theta + (v_{\mathrm{AS}}\sin\phi + w_{\mathrm{AS}}\cos\phi)\sin\theta]\cos\psi + \\
&\quad - (v_{\mathrm{AS}}\cos\phi - w_{\mathrm{AS}}\sin\phi)\sin\psi + u_{\text{wind}} && (4.12)\\
\dot{y}_{\mathrm{GS}} &= [u_{\mathrm{AS}}\cos\theta + (v_{\mathrm{AS}}\sin\phi + w_{\mathrm{AS}}\cos\phi)\sin\theta]\sin\psi + \\
&\quad + (v_{\mathrm{AS}}\cos\phi - w_{\mathrm{AS}}\sin\phi)\cos\psi + v_{\text{wind}} && (4.13)\\
\dot{z}_{\mathrm{GS}} &= -u_{\mathrm{AS}}\sin\theta + (v_{\mathrm{AS}}\sin\phi + w_{\mathrm{AS}}\cos\phi)\cos\theta + w_{\text{wind}} && (4.14)\\
\dot{u}_{\mathrm{AS}} &= A_x - g\sin\theta + rv_{\mathrm{AS}} - qw_{\mathrm{AS}} && (4.15)\\
\dot{v}_{\mathrm{AS}} &= A_y + g\cos\theta\sin\phi + pw_{\mathrm{AS}} - ru_{\mathrm{AS}} && (4.16)\\
\dot{w}_{\mathrm{AS}} &= A_z + g\cos\theta\cos\phi + qu_{\mathrm{AS}} - pv_{\mathrm{AS}} && (4.17)\\
\dot{\phi} &= p + q\sin\phi\tan\theta + r\cos\phi\tan\theta && (4.18)\\
\dot{\theta} &= q\cos\phi - r\sin\phi && (4.19)\\
\dot{\psi} &= q\frac{\sin\phi}{\cos\theta} + r\frac{\cos\phi}{\cos\theta} && (4.20)
\end{aligned}$$

In this system of kinematic equations, the subscript AS indicates airspeed components, where GS stands for ground speed. Equations (4.15) till (4.17) represent the true airspeed components in the body fixed reference frame. Expressions (4.18) till (4.20) are the kinematic relations for a sequential rotation along the $Z-$, $Y-$ and $X-$axis respectively and constitute as the conversions of the angular rates from body fixed reference frame towards the earth fixed reference frame (Euler angles). The first three equations, (4.12) till (4.14) serve as the conversions of the linear velocity components from body fixed reference frame towards earth fixed reference frame. Moreover, by adding the atmospheric wind components, which can be considered as constants since they are expressed in the earth fixed reference frame, the transition is made from airspeed towards ground speed. In vectorform, these equations can be written as follows:

$$\begin{aligned}
\mathbf{V}_{\mathrm{GS}} &= \mathbf{\Omega}_{\mathrm{tot}}\mathbf{V}_{\mathrm{AS}} + \mathbf{V}_{\mathrm{wind}} \quad \text{with :}\\
\mathbf{\Omega}_{\mathrm{tot}} &= \mathbf{\Omega}_{\phi}\mathbf{\Omega}_{\theta}\mathbf{\Omega}_{\psi} = \begin{bmatrix} 1 & 0 & 0 \\ 0 & \cos\phi & \sin\phi \\ 0 & -\sin\phi & \cos\phi \end{bmatrix} \begin{bmatrix} \cos\theta & 0 & -\sin\theta \\ 0 & 1 & 0 \\ \sin\theta & 0 & \cos\theta \end{bmatrix} \begin{bmatrix} \cos\psi & \sin\psi & 0 \\ -\sin\psi & \cos\psi & 0 \\ 0 & 0 & 1 \end{bmatrix}
\end{aligned}$$

Equations (4.15) to (4.18) can be written in vector form as:

$$\dot{\mathbf{V}}_{\mathrm{AS}} = \mathbf{a} - \boldsymbol{\omega}_b \times \mathbf{V}_{\mathrm{AS}} = \mathbf{A} - \mathbf{\Omega}_{\phi}\mathbf{\Omega}_{\theta}\begin{bmatrix} 0 \\ 0 \\ g \end{bmatrix} - \boldsymbol{\omega}_b \times \mathbf{V}_{\mathrm{AS}}$$

where $\mathbf{a}$ are the kinematic accelerations, $\mathbf{A}$ are the specific forces, and g is the gravitational constant. Finally $\boldsymbol{\omega}_b$ are the body fixed rotational rates: $\boldsymbol{\omega}_b = [p \;\; q \;\; r]^T$. The last three equations are the Euler equations and can be derived from the following inverse vector form:

$$\boldsymbol{\omega}_b = \boldsymbol{\Omega}_\phi \boldsymbol{\Omega}_\theta \begin{bmatrix} 0 \\ 0 \\ \dot{\psi} \end{bmatrix} + \boldsymbol{\Omega}_\phi \begin{bmatrix} 0 \\ \dot{\theta} \\ 0 \end{bmatrix} + \begin{bmatrix} \dot{\phi} \\ 0 \\ 0 \end{bmatrix}$$

The specific forces and angular rates, which are available in the input vector, can be found in expressions (4.15) till (4.20). However, since they are supplied as measurements, they are not exact, but contaminated with bias and noise. Consequently, they must be corrected in order to rewrite the system of state equations in the form of expression (4.1) and the following equalities can be substituded in expressions (4.15) till (4.20):

$$A_x = A_{x_m} - \lambda_x - w_x \quad (4.21)$$
$$A_y = A_{y_m} - \lambda_y - w_y \quad (4.22)$$
$$A_z = A_{z_m} - \lambda_z - w_z \quad (4.23)$$

$$p = p_m - \lambda_p - w_p \quad (4.24)$$
$$q = q_m - \lambda_q - w_q \quad (4.25)$$
$$r = r_m - \lambda_r - w_r \quad (4.26)$$

Moreover, the system of state equations can be extended with the following array of equations:

$$\dot{\lambda}_x = 0 \quad (4.27)$$
$$\dot{\lambda}_y = 0 \quad (4.28)$$
$$\dot{\lambda}_z = 0 \quad (4.29)$$
$$\dot{\lambda}_p = 0 \quad (4.30)$$
$$\dot{\lambda}_q = 0 \quad (4.31)$$
$$\dot{\lambda}_r = 0 \quad (4.32)$$
$$\dot{u}_{\text{wind}} = 0 \quad (4.33)$$
$$\dot{v}_{\text{wind}} = 0 \quad (4.34)$$
$$\dot{w}_{\text{wind}} = 0 \quad (4.35)$$

Equations (4.27) till (4.35) exploit the knowledge that biases as well as wind components are constant.

This rewritten set of state equations can be split up over the nonlinear continuous function $\mathbf{f}$ and the noise contribution function $\mathbf{G}$, which is linear in $\mathbf{w}(t)$. First the nonlinear continuous $\mathbf{f}[\mathbf{x}(t), \mathbf{u}_m(t), \boldsymbol{\theta}]$ is given:

$$\mathbf{f}[\mathbf{x}(t), \mathbf{u}_m(t), \boldsymbol{\theta}] =$$
$$\begin{bmatrix} [u_{\text{AS}} \cos\theta + (v_{\text{AS}} \sin\phi + w_{\text{AS}} \cos\phi) \sin\theta] \cos\psi - (v_{\text{AS}} \cos\phi - w_{\text{AS}} \sin\phi) \sin\psi + u_{\text{wind}} \\ [u_{\text{AS}} \cos\theta + (v_{\text{AS}} \sin\phi + w_{\text{AS}} \cos\phi) \sin\theta] \sin\psi + (v_{\text{AS}} \cos\phi - w_{\text{AS}} \sin\phi) \cos\psi + v_{\text{wind}} \\ -u_{\text{AS}} \sin\theta + (v_{\text{AS}} \sin\phi + w_{\text{AS}} \cos\phi) \cos\theta + w_{\text{wind}} \\ (A_{x_m} - \lambda_x) - g \sin\theta + (r_m - \lambda_r) v_{\text{AS}} - (q_m - \lambda_q) w_{\text{AS}} \\ (A_{y_m} - \lambda_y) + g \cos\theta \sin\phi + (p_m - \lambda_p) w_{\text{AS}} - (r_m - \lambda_r) u_{\text{AS}} \\ (A_{z_m} - \lambda_z) + g \cos\theta \cos\phi + (q_m - \lambda_q) u_{\text{AS}} - (p_m - \lambda_p) v_{\text{AS}} \\ (p_m - \lambda_p) + (q_m - \lambda_q) \sin\phi \tan\theta + (r_m - \lambda_r) \cos\phi \tan\theta \\ (q_m - \lambda_q) \cos\phi - (r_m - \lambda_r) \sin\phi \\ (q_m - \lambda_q) \frac{\sin\phi}{\cos\theta} + (r_m - \lambda_r) \frac{\cos\phi}{\cos\theta} \\ \mathbf{0}_{6\times1} \end{bmatrix}$$

After which the linear $\mathbf{G}[\mathbf{x}(t)]$ is defined as:

$$\mathbf{G}[\mathbf{x}(t)] = \begin{bmatrix} & & & \mathbf{0}_{3\times6} & & \\ -1 & 0 & 0 & 0 & w_{\text{AS}} & -v_{\text{AS}} \\ 0 & -1 & 0 & -w_{\text{AS}} & 0 & u_{\text{AS}} \\ 0 & 0 & -1 & v_{\text{AS}} & -u_{\text{AS}} & 0 \\ 0 & 0 & 0 & -1 & -\sin\phi\tan\theta & -\cos\phi\tan\theta \\ 0 & 0 & 0 & 0 & -\cos\phi & \sin\phi \\ 0 & 0 & 0 & 0 & -\frac{\sin\phi}{\cos\theta} & -\frac{\cos\phi}{\cos\theta} \\ & & & \mathbf{0}_{9\times6} & & \end{bmatrix} \tag{4.36}$$

After discussing the kinematic equations in detail, the nonlinear continuous observation equations can be considered, including the output noise contribution $\mathbf{v}(t)$ from (4.7):

$$x_{\text{INS}} = x_{\text{GS}} + v_x \tag{4.37}$$
$$y_{\text{INS}} = y_{\text{GS}} + v_y \tag{4.38}$$
$$z_{\text{INS}} = z_{\text{GS}} + v_z \tag{4.39}$$
$$\begin{aligned} u_{\text{INS}} = & [u_{\text{AS}} \cos\theta + (v_{\text{AS}} \sin\phi + w_{\text{AS}} \cos\phi) \sin\theta] \cos\psi + \\ & - (v_{\text{AS}} \cos\phi - w_{\text{AS}} \sin\phi) \sin\psi + u_{\text{wind}} + v_u \end{aligned} \tag{4.40}$$
$$\begin{aligned} v_{\text{INS}} = & [u_{\text{AS}} \cos\theta + (v_{\text{AS}} \sin\phi + w_{\text{AS}} \cos\phi) \sin\theta] \sin\psi + \\ & + (v_{\text{AS}} \cos\phi - w_{\text{AS}} \sin\phi) \cos\psi + v_{\text{wind}} + v_v \end{aligned} \tag{4.41}$$
$$w_{\text{INS}} = - u_{\text{AS}} \sin\theta + (v_{\text{AS}} \sin\phi + w_{\text{AS}} \cos\phi) \cos\theta + w_{\text{wind}} + v_w \tag{4.42}$$

$$\begin{aligned}
\phi_{\text{INS}} &= \phi + v_{\phi} &(4.43)\\
\theta_{\text{INS}} &= \theta + v_{\theta} &(4.44)\\
\psi_{\text{INS}} &= \psi + v_{\psi} &(4.45)\\
V_{\text{TAS}} &= \sqrt{u_{\text{AS}}^2 + v_{\text{AS}}^2 + w_{\text{AS}}^2} + v_V &(4.46)\\
\alpha_{\text{ADS}} &= \text{atan}\left(\frac{w_{\text{AS}}}{u_{\text{AS}}}\right) + v_{\alpha} &(4.47)\\
\beta_{\text{ADS}} &= \text{atan}\left(\frac{v_{\text{AS}}}{\sqrt{u_{\text{AS}}^2 + w_{\text{AS}}^2}}\right) + v_{\beta} &(4.48)
\end{aligned}$$

Consequently the nonlinear continuous $\mathbf{h}[\mathbf{x}(t), \mathbf{u}_m(t), \boldsymbol{\theta}]$ in (4.2) looks as the system of equations (4.37) to (4.48) grouped in matrix form, but without the noise contributions.

4.1.2 State estimator

As already mentioned in the introduction and apparent from the structure above in this section, a nonlinear state estimator can be used in order to estimate the aircraft states, inertial sensor biases and wind velocity components. An Extended Kalman Filter (EKF), described in section 3.3.2.2, is proposed in this application, since the equations given above are nonlinear. However, due to the significant nonlinearities in the observation equations $\mathbf{h}[\mathbf{x}(t), \mathbf{u}_m(t), \boldsymbol{\theta}]$, the Iterated Extended Kalman Filter (IEKF) has been selected. The five steps of the Iterated Extended Kalman Filter are:

1. one step ahead prediction (time propagation):

$$\boldsymbol{\eta}_1 = \hat{\mathbf{x}}\left(k+1\left|k\right.\right) = \hat{\mathbf{x}}\left(k\left|k\right.\right) + \int\limits_{k}^{k+1} \mathbf{f}\left(\mathbf{x}(t), \mathbf{u}_m(t), \boldsymbol{\theta}, t\right) dt \tag{4.49}$$

2. prediction of covariance matrix of the state prediction error vector:

$$\mathbf{P}\left(k+1\right|k) = \boldsymbol{\Phi}\left(k,\tau\right)\mathbf{P}\left(k\left|k\right.\right)\boldsymbol{\Phi}^T\left(k,\tau\right) + \mathbf{Q}_d\left(k\right) \tag{4.50}$$

with:

$$\mathbf{F}(k) = \left.\frac{\partial \mathbf{f}\left(\mathbf{x}(t), \mathbf{u}_m(t), \boldsymbol{\theta}, t\right)}{\partial \mathbf{x}(t)}\right|_{\mathbf{x}=\hat{\mathbf{x}}_{k|k}} \qquad \boldsymbol{\Phi}(k,\tau) = e^{\mathbf{F}(k)\Delta t} \tag{4.51}$$

$$\mathbf{Q}_d\left(k+1|k\right) = \int_{t_k}^{t_{k+1}} \boldsymbol{\Phi}\left(t_{k+1},\tau\right)\mathbf{G}_k\mathbf{Q}_k\mathbf{G}_k^T\boldsymbol{\Phi}^T\left(t_{k+1},\tau\right) d\tau \tag{4.52}$$

3. Kalman gain:

$$\begin{aligned}\mathbf{K}(k+1) &= \mathbf{P}(k+1|k)\,\mathbf{H}^T(k+1)\times \\ &\times\left[\mathbf{H}(k+1)\,\mathbf{P}(k+1|k)\,\mathbf{H}^T(k+1)+\mathbf{R}(k+1)\right]^{-1}\end{aligned} \tag{4.53}$$

where $\mathbf{H}(k+1) = \left.\frac{\partial \mathbf{h}(\mathbf{x}(t),\mathbf{u}_m(t),\boldsymbol{\theta},t)}{\partial \mathbf{x}(t)}\right|_{\mathbf{x}=\boldsymbol{\eta}_1}$, which also holds for the next steps

4. measurement update step:

$$\boldsymbol{\eta}_2 = \hat{\mathbf{x}}(k+1|k) + \mathbf{K}(k+1)\left[\mathbf{z}(k+1) - \mathbf{h}(\boldsymbol{\eta}_1) - \mathbf{H}(k+1)\left(\hat{\mathbf{x}}(k+1|k) - \boldsymbol{\eta}_1\right)\right] \tag{4.54}$$

$$\varepsilon = \frac{\boldsymbol{\eta}_2 - \boldsymbol{\eta}_1}{\boldsymbol{\eta}_2} \tag{4.55}$$

as long as $|\varepsilon| > |\varepsilon_{\mathrm{crit}}|$, repeat steps 3 and 4 while after each iteration $\boldsymbol{\eta}_1 = \boldsymbol{\eta}_2$.[1]

5. update covariance matrix of state estimation error vector: as soon as $|\varepsilon| \leq |\varepsilon_{crit}|$:

$$\hat{\mathbf{x}}(k+1|k+1) = \boldsymbol{\eta}_2 \tag{4.56}$$

$$\begin{aligned}\mathbf{P}(k+1|k+1) &= \left[\mathbf{I} - \mathbf{K}(k+1)\,\mathbf{H}(k+1)\right]\mathbf{P}(k+1|k)\times \\ &\times\left[\mathbf{I} - \mathbf{K}(k+1)\,\mathbf{H}(k+1)\right]^T + \\ &+\mathbf{K}(k+1)\,\mathbf{R}(k+1)\,\mathbf{K}^T(k+1)\end{aligned} \tag{4.57}$$

where steps 3 and 4 are slightly deviating from the conventional EKF setup because of the additional optimization loop. Application of this procedure in an aircraft example has shown that this optimization loop is used only once in each one of the first ten time steps, after which no more additional correction is necessary with respect to the ordinary EKF.

Fig. 4.2 illustrates the working principle of the Iterated Extended Kalman Filter, which is an extension to the regular EKF. The correction step is performed iteratively, until the difference between two successive correction updates is below a predefined threshold. This iteration is needed when the observation model $\mathbf{h}$ contains significant nonlinearities such that its linearized counterpart $\mathbf{H}$ has a limited validity in a local area. For significant nonlinearities in the kinematics equations, another iteration procedure or other routines need to be incorporated, as illustrated in appendix C.

[1] In theory, this loop continues till the difference condition is satisfied, but in practice often a maximum number of iterations is specified in order to prevent an infinite loop.

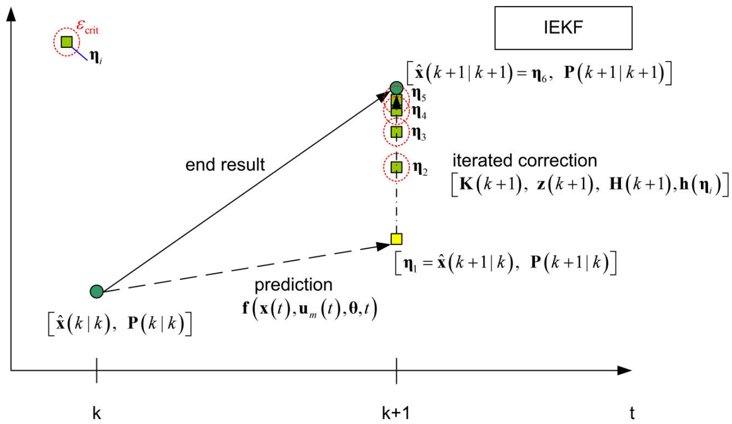

Figure 4.2: Working principle of the Iterated Extended Kalman Filter

Figures 4.3 present some estimation results for aircraft states, sensor biases and wind velocity components of a nominal non-damaged Boeing 747 simulation model. Estimation results for Matlab and Simulink calculation procedures are presented, and can be compared with the true uncontaminated state information from inside the simulation model as benchmark.

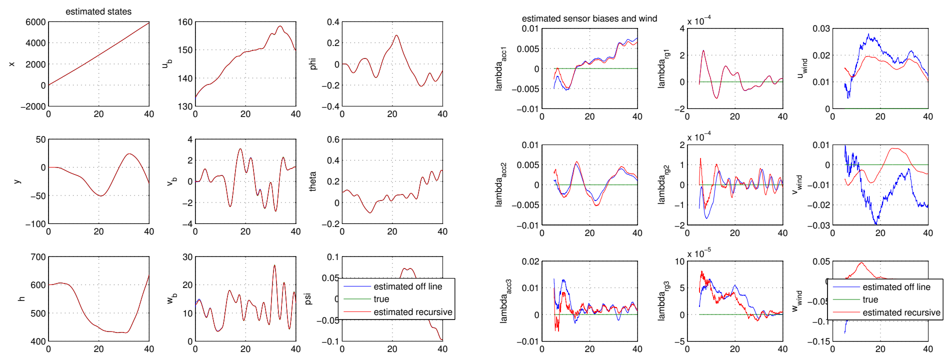

(a) estimation results of aircraft states

(b) estimation results of sensor biases and wind velocity conmponents

Figure 4.3: Aircraft state estimation phase results for a high-fidelity nominal non-damaged Boeing 747 simulation model

Convergence of Kalman Filter

Since the (extended) Kalman Filter is a gradient based optimization approach, there is no guarantee that a global optimum is reached for nonlinear systems. Only for (nearly) linear systems a global optimum can be guaranteed thanks to the convex optimization problem. In practice, it is possible for nonlinear systems to rely on the first measurement values to estimate the initial condition of the state vector. This prevents lack of convergence due to overcompensation in the correcting step of the Kalman Filter.

4.2 Aerodynamic Model Identification

The procedure of the second step is rather purpose dependent. For a pure in-flight identification task aiming at the construction of a precise mathematical aircraft model, the procedure must be as accurate as possible. However, in the case of an identification task for the purpose of fault tolerant flight control, the model structure has to be representative, where a trade off is made between accuracy versus computational speed, and thus model complexity. Since in this step the least square procedure is used, the model structure must be determined first, after which this regression method can be applied in order to estimate the aerodynamic model parameters. Another important issue is the determination of the aerodynamic model accuracy. Especially in the case of reconfiguring control, a reliable value for an uncertainty bound can be very useful in order to include some measure of robustness in the controller synthesis phase. Moreover, as will be shown in chapter 5, it is also useful in a model structure selection procedure.

4.2.1 Aerodynamic aircraft model

The input to the second step consists of two major parts. The first part are the sensor measurements (inertial, global positioning and air data system). The second are the estimated aircraft states, IMU bias errors and the wind components:

$$\mathbf{u}_m = \mathbf{u} + \boldsymbol{\lambda} + \mathbf{w} = [A_x, A_y, A_z, p, q, r]^T + [\lambda_x, \lambda_y, \lambda_z, \lambda_p, \lambda_q, \lambda_r]^T + \mathbf{w} \tag{4.58}$$

$$\begin{aligned}\mathbf{z}_m = \mathbf{z} + \mathbf{v} = [&x_{\text{INS}}, y_{\text{INS}}, z_{\text{INS}}, u_{\text{INS}}, v_{\text{INS}}, w_{\text{INS}}, \phi_{\text{INS}}, \theta_{\text{INS}}, \psi_{\text{INS}},\\ &V_{\text{TAS}}, \alpha_{\text{ADS}}, \beta_{\text{ADS}}]^T\end{aligned} \tag{4.59}$$

$$\mathbf{x} = [x_{\text{GS}}, y_{\text{GS}}, z_{\text{GS}}, u_{\text{AS}}, v_{\text{AS}}, w_{\text{AS}}, \phi, \theta, \psi]^T \tag{4.60}$$

$$\boldsymbol{\theta} = [\boldsymbol{\lambda}, \mathbf{V}_{\text{wind}}]^T = [\lambda_x, \lambda_y, \lambda_z, \lambda_p, \lambda_q, \lambda_r, u_{\text{wind}}, v_{\text{wind}}, w_{\text{wind}}]^T \tag{4.61}$$

With this available information, it is possible to correct the inertial measurements for their bias, but the noise contribution cannot be compensated for:

$$\begin{array}{ll} A_{x_{\mathrm{AMI}}} = A_{x_m} - \lambda_x = A_x + w_x & p_{\mathrm{AMI}} = p_m - \lambda_p = p + w_p \\ A_{y_{\mathrm{AMI}}} = A_{y_m} - \lambda_y = A_y + w_y & q_{\mathrm{AMI}} = q_m - \lambda_q = q + w_q \\ A_{z_{\mathrm{AMI}}} = A_{z_m} - \lambda_z = A_z + w_z & r_{\mathrm{AMI}} = r_m - \lambda_r = r + w_r \end{array} \tag{4.62}$$

Another preparation needed for the remainder of this step is the construction of the other aircraft states by means of the available state information above. These are necessary for the calculation of forces and moments and for their first order Taylor expansions. More precisely, two categories of quantities need to be determined:

- The states related to the air data, which are the aerodynamic flow angles and the true airspeed. As a matter of fact, they are already measured by the ADS. Nevertheless, with the formulas below using the aircraft states, they can be reconstructed more accurately since the measurements of these quantities are degraded by some instrumentation errors.

$$\alpha = \text{atan}\left(\frac{w_{AS}}{u_{AS}}\right) \quad \beta = \text{atan}\left(\frac{v_{AS}}{\sqrt{u_{AS}^2 + w_{AS}^2}}\right) \quad V = \sqrt{u_{AS}^2 + v_{AS}^2 + w_{AS}^2} \tag{4.63}$$

- The angular accelerations, which can be obtained by differentiating the noisy rotational rates, after having been corrected for their biases. An important condition for this manipulation is the fact that the measurement noise $\mathbf{w}(t)$ in the angular rate measurements should be small, since it will have a detrimental effect on the differentiation result. It should be noted that current generation ring laser gyroscope noise levels are low enough ($\sigma_{pqr} = 0.001°/s$) to permit differentiating these signals. An alternative approach for estimating the rotary accelerations can be the use of two accelerometers with a known distance between them or direct measurements using angular acceleration sensors[2].

$$\dot{p}_{\mathrm{AMI}}(k) = \frac{p_m(k+1) - p_m(k)}{\Delta t} \quad \dot{q}_{\mathrm{AMI}}(k) = \frac{q_m(k+1) - q_m(k)}{\Delta t} \quad \dot{r}_{\mathrm{AMI}}(k) = \frac{r_m(k+1) - r_m(k)}{\Delta t} \tag{4.64}$$

One key issue in this step is the determination of the forces and moments acting on the aircraft. These cannot be measured directly, however it is possible to construct them with the help of the measurements of specific aerodynamic forces acting on the aircraft and angular rates and accelerations of the aircraft, which have already been corrected above for the instrumentation errors (biases), which were estimated in the aircraft state estimation step. In this way the dimensionless forces and moments can be calculated:

[2]such as the IMAR Iodot, see www.imar-navigation.de [retrieved 13 Nov. 2009].

- dimensionless forces:

$$
\begin{aligned}
C_X &= \frac{X}{1/2\rho V^2 S} = \frac{mA_{x_{\mathrm{AMI}}}}{1/2\rho V^2 S} \\
C_Y &= \frac{Y}{1/2\rho V^2 S} = \frac{mA_{y_{\mathrm{AMI}}}}{1/2\rho V^2 S} \\
C_Z &= \frac{Z}{1/2\rho V^2 S} = \frac{mA_{z_{\mathrm{AMI}}}}{1/2\rho V^2 S}
\end{aligned}
\tag{4.65}
$$

- dimensionless moments:

$$
\begin{aligned}
C_l &= \frac{L}{1/2\rho V^2 S b} = \frac{\dot{p}_{\mathrm{AMI}} I_{xx} + q_{\mathrm{AMI}} r_{\mathrm{AMI}} \left(I_{zz} - I_{yy}\right) - \left(p_{\mathrm{AMI}} q_{\mathrm{AMI}} + \dot{r}_{\mathrm{AMI}}\right) I_{xz}}{1/2\rho V^2 S b} \\
C_m &= \frac{M}{1/2\rho V^2 S \bar{c}} = \frac{\dot{q}_{\mathrm{AMI}} I_{yy} + r_{\mathrm{AMI}} p_{\mathrm{AMI}} \left(I_{xx} - I_{zz}\right) + \left(p_{\mathrm{AMI}}^2 - r_{\mathrm{AMI}}^2\right) I_{xz}}{1/2\rho V^2 S \bar{c}} \\
C_n &= \frac{N}{1/2\rho V^2 S b} = \frac{\dot{r}_{\mathrm{AMI}} I_{zz} + p_{\mathrm{AMI}} q_{\mathrm{AMI}} \left(I_{yy} - I_{xx}\right) + \left(q_{\mathrm{AMI}} r_{\mathrm{AMI}} - \dot{p}_{\mathrm{AMI}}\right) I_{xz}}{1/2\rho V^2 S b}
\end{aligned}
\tag{4.66}
$$

Crucial for these calculations is the knowledge of mass and mass inertia. Moreover, one assumes the mass inertia $I_{yz} = 0$ and $I_{xy} = 0$ for symmetrical aircraft.

At this moment mass and inertia are treated as known constants, since one considers only damaged aircraft with changed aerodynamic properties but no mass property changes in this stage. In the absence of a structural failure, real time mass and inertia can be calculated by integrating fuel flow and subtracting it from the total take off values. Further research in chapter 6 is aimed at briefly evaluating the influence of changing mass, center of gravity and inertia due to the presence of structural failures. Air density can be deduced from altitude measurements. Decrease of measurement accuracy due to sensor failures in the air data system is ignored because of the assumed presence of sensor redundancy and sensor loss detection, which is usually the case.

4.2.2 Parameter estimator

As already mentioned above, the aerodynamic model structure must be defined before the model parameters are estimated by means of the least squares. This model structure has been set up by a first order Taylor series expansion with respect to the aircraft states which are relevant for each force and moment component separately. The resulting structures which have been chosen for the longitudinal and the lateral situation respectively are given as follows:

$$
\begin{aligned}
C_X &= C_{X_0} + C_{X_\alpha}\alpha + C_{X_{\alpha^2}}\alpha^2 + C_{X_q}\frac{q\bar{c}}{V} + C_{X_{\delta_{e_{ir}}}}|\delta_{e_{ir}}| + C_{X_{\delta_{e_{il}}}}|\delta_{e_{il}}| + C_{X_{\delta_{e_{or}}}}|\delta_{e_{or}}| \\
&+C_{X_{\delta_{e_{ol}}}}|\delta_{e_{ol}}| + C_{X_{i_h}}|i_h| + C_{X_{\delta_{sp_1}}}\delta_{sp_1} + ... + C_{X_{\delta_{sp_{12}}}}\delta_{sp_{12}} + C_{X_{\delta_{f_o}}}\delta_{f_o} + C_{X_{\delta_{f_i}}}\delta_{f_i} \\
&+C_{X_{EPR_1}}EPR_1 + ... + C_{X_{EPR4}}EPR_4 + \boxed{C_{X_\beta}\beta + C_{X_p}\frac{pb}{2V} + C_{X_r}\frac{rb}{2V}} \qquad (4.67)
\end{aligned}
$$

$$
\begin{aligned}
C_Z &= C_{Z_0} + C_{Z_\alpha}\alpha + C_{Z_q}\frac{q\bar{c}}{V} + C_{Z_{\delta_{e_{ir}}}}\delta_{e_{ir}} + C_{Z_{\delta_{e_{il}}}}\delta_{e_{il}} + C_{Z_{\delta_{e_{or}}}}\delta_{e_{or}} + C_{Z_{\delta_{e_{ol}}}}\delta_{e_{ol}} + \\
&+C_{Z_{i_h}}i_h + C_{Z_{\delta_{sp_1}}}\delta_{sp_1} + ... + C_{Z_{\delta_{sp_{12}}}}\delta_{sp_{12}} + C_{Z_{\delta_{f_o}}}\delta_{f_o} + C_{Z_{\delta_{f_i}}}\delta_{f_i} \\
&+C_{Z_{EPR_1}}EPR_1 + ... + C_{Z_{EPR4}}EPR_4 + \boxed{C_{Z_\beta}\beta + C_{Z_p}\frac{pb}{2V} + C_{Z_r}\frac{rb}{2V}} \qquad (4.68)
\end{aligned}
$$

$$
\begin{aligned}
C_m &= C_{m_0} + C_{m_\alpha}\alpha + C_{m_q}\frac{q\bar{c}}{V} + C_{m_{\delta_{e_{ir}}}}\delta_{e_{ir}} + C_{m_{\delta_{e_{il}}}}\delta_{e_{il}} + C_{m_{\delta_{e_{or}}}}\delta_{e_{or}} + C_{m_{\delta_{e_{ol}}}}\delta_{e_{ol}} + \\
&+C_{m_{i_h}}i_h + C_{m_{\delta_{sp_1}}}\delta_{sp_1} + ... + C_{m_{\delta_{sp_{12}}}}\delta_{sp_{12}} + C_{m_{\delta_{f_o}}}\delta_{f_o} + C_{m_{\delta_{f_i}}}\delta_{f_i} \\
&+C_{m_{EPR_1}}EPR_1 + ... + C_{m_{EPR4}}EPR_4 + \boxed{C_{m_\beta}\beta + C_{m_p}\frac{pb}{2V} + C_{m_r}\frac{rb}{2V}} \qquad (4.69)
\end{aligned}
$$

$$
\begin{aligned}
C_Y &= C_{Y_0} + C_{Y_\beta}\beta + C_{Y_p}\frac{pb}{2V} + C_{Y_r}\frac{rb}{2V} + C_{Y_{\delta_{a_{ir}}}}\delta_{a_{ir}} + C_{Y_{\delta_{a_{il}}}}\delta_{a_{il}} + C_{Y_{\delta_{a_{or}}}}\delta_{a_{or}} \\
&+C_{Y_{\delta_{a_{ol}}}}\delta_{a_{ol}} + C_{Y_{\delta_{r_u}}}\delta_{r_u} + C_{Y_{\delta_{r_l}}}\delta_{r_l} + C_{Y_{\delta_{sp_1}}}\delta_{sp_1} + ... + C_{Y_{\delta_{sp_{12}}}}\delta_{sp_{12}} \\
&+\boxed{C_{Y_\alpha}\alpha + C_{Y_q}\frac{q\bar{c}}{V}} + \boxed{C_{Y_{EPR_1}}EPR_1 + ... + C_{Y_{EPR4}}EPR_4} \qquad (4.70)
\end{aligned}
$$

$$
\begin{aligned}
C_l &= C_{l_0} + C_{l_\beta}\beta + C_{l_p}\frac{pb}{2V} + C_{l_r}\frac{rb}{2V} + C_{l_{\delta_{a_{ir}}}}\delta_{a_{ir}} + C_{l_{\delta_{a_{il}}}}\delta_{a_{il}} + C_{l_{\delta_{a_{or}}}}\delta_{a_{or}} + C_{l_{\delta_{a_{ol}}}}\delta_{a_{ol}} + \\
&+C_{l_{\delta_{r_u}}}\delta_{r_u} + C_{l_{\delta_{r_l}}}\delta_{r_l} + C_{l_{\delta_{sp_1}}}\delta_{sp_1} + ... + C_{l_{\delta_{sp_{12}}}}\delta_{sp_{12}} + \boxed{C_{l_\alpha}\alpha + C_{l_q}\frac{q\bar{c}}{V}} + \\
&+\boxed{C_{l_{EPR_1}}EPR_1 + ... + C_{l_{EPR4}}EPR_4} \qquad (4.71)
\end{aligned}
$$

$$
\begin{aligned}
C_n &= C_{n_0} + C_{n_\beta}\beta + C_{n_p}\frac{pb}{2V} + C_{n_r}\frac{rb}{2V} + C_{n_{\delta_{a_{ir}}}}\delta_{a_{ir}} + C_{n_{\delta_{a_{il}}}}\delta_{a_{il}} + C_{n_{\delta_{a_{or}}}}\delta_{a_{or}} \\
&+C_{n_{\delta_{a_{ol}}}}\delta_{a_{ol}} + C_{n_{\delta_{r_u}}}\delta_{r_u} + C_{n_{\delta_{r_l}}}\delta_{r_l} + C_{n_{\delta_{sp_1}}}\delta_{sp_1} + ... + C_{n_{\delta_{sp_{12}}}}\delta_{sp_{12}} \\
&+\boxed{C_{n_\alpha}\alpha + C_{n_q}\frac{q\bar{c}}{V}} + \boxed{C_{n_{EPR_1}}EPR_1 + ... + C_{n_{EPR4}}EPR_4} \qquad (4.72)
\end{aligned}
$$

From the above expressions, it can be seen that the aerodynamic model parameters, also known as the aerodynamic derivatives, are related to states as well as control inputs, namely control surface deflections and engine settings. One of the frequently used regressors in this structure is the time derivative of the angle of attack $\dot{\alpha}$. However, this regressor is most important for more agile aircraft than a large civil airliner which performs only benign manoeuvres with relatively small flight path angles. Moreover, without proper excitation (i.e. a looping for a jet fighter) collinearity risks exist with the already included regressor $\frac{q\bar{c}}{V}$. Therefore, the additional regressor $\dot{\alpha}$ has been ignored in this structure. More information about these considerations can be found in ref. [101]. It should be noted that the contributions indicated in boxes are the aerodynamic consequences of possible cross-couplings: they represent the contributions of longitudinal states on lateral forces and moments and vice versa. They appear due to possible asymmetries after structural failures. Moreover, also the aerodynamic derivatives related to the inputs have cross coupling effects, but these are presently assumed to be limited by the hardware constraints of the actuator hardware of each control surface type independently, present in the hardware logic block of the RECOVER simulation model. A description of this model can be found in appendix A. E.g. differential deflection of flaps is not possible[3]. For the Boeing 747 with the simulation model as given, the only cross coupling control inputs taken into account at the moment are the engine settings. Conventionally, all engine settings are identical and give only longitudinal steering capability, but they can provide also some lateral degree of controllability if differential thrust is applied. This is the model structure setup for the first version of model identification. More detailed cross-coupling terms which are even present in unfailed conditions, for example pitching moment terms due to rudder and aileron deflection, can be included in the model structure when more advanced types of control allocation are considered. However, special attention is then required in the field of separate surface excitation, in order to guarantee sufficient data richness and to prevent collinearities between control surface deflection measurements due to coupled surfaces. However, in a general perspective, this kind of cross couplings is completely dependent on the type of aircraft model under consideration.

Another important issue here is the choice how the control inputs are represented in the aerodynamics model as shown in equations (4.67) to (4.72). There are two alternatives for the control inputs, one being the pilot commands on control column δ_c, control wheel δ_w, pedals δ_p, etc., the other the actual control surface deflections, such as a.o. elevators δ_e, ailerons δ_a and rudder δ_r. When one considers the use of the former quantities, the advantage is that hardware failures are also taken into account, as illustrated in fig. 4.4. However, errors are introduced in the estimated parameter values, since hardware dynamics (such as actuator delays and position limits) are not taken into account in the aerodynamic model, although they are present between inputs and observation measurements. Moreover, the failure of an individual control surface cannot be observed specifically, since no individual measurements are used in the identification procedure. Therefore, it is better to use the measured actual control surface deflections, as shown in equations (4.67) to (4.72). Another alternative is the use of a mathematical model of the hardware dynamics, which allows to calculate the expected commanded control surface deflections based upon the pilot commands, and then to use these expected values. However, this would result in erroneous control efficiencies. Namely, these control efficiencies are aerodynamics related, and not

[3]According to the developers of the RECOVER simulation model, this hardware constraint is included since faulty differential deflection of flaps in low speed flight conditions cannot be compensated sufficiently by the ailerons and other control surfaces.

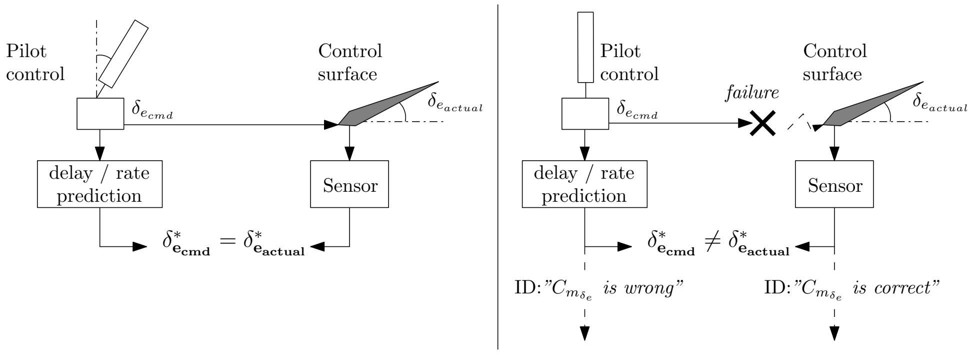

Figure 4.4: Consequence of using pilot commands instead of actual control surface deflections for parameter identification

hardware related. A hardware failure can be represented in another way. This can be done by considering an actuator health management system (AHMS). This system compares the measured actual control surface deflections with the expected commanded control surface deflections and can detect hardware failures when significant differences appear. Another advantage of this choice is that the physical nature of the approach is maintained, and the modularity is improved. Namely, aerodynamic failures are detected by means of the aerodynamic model identification step, hardware failures by the AHMS. This topic is discussed further in section 8.4.2.

As a final remark, it can be seen in equation (4.67) that absolute values of elevator and stabilizer deflections are considered. This is because of the fact that positive or negative control surface deflections have the same influence on the aerodynamic force in body X-direction, namely increasing drag. This requires the use of absolute values. Other control surface deflections in eq. (4.67) have only positive deflections.

For the online identification approach recursive least squares (RLS) have been implemented. Note that for each time instant, the covariance matrix from the covariance matrix update equation gives some information about the uncertainty and thus the reliability of the identified model parameters. It is common practice to apply a constant correction factor (typically 5 or 10) to the standard deviation computed from ordinary least-squares calculations to account for coloured residuals. Because this practice is a rough approximation, Klein and Morelli [159] emphasize the so-called coloured residual formula to compute the estimated parameter covariance matrix and standard deviations taking into account coloured noise. Despite being very useful, this is a postprocessing algorithm and is not applicable as such in this setup, however.

For the on-line identification approach recursive least squares have been implemented, resulting in three steps, which are similar to the set-up of the Kalman Filter:

1. update weighting matrix:

$$\mathbf{K}_{N+1} = \frac{\mathbf{P}_N \mathbf{x}_{n+1}}{\lambda + \mathbf{x}_{n+1}^T \mathbf{P}_N \mathbf{x}_{n+1}} \tag{4.73}$$

2. prediction error correction formula:

$$\hat{\boldsymbol{\theta}}_{N+1} = \hat{\boldsymbol{\theta}}_N + \mathbf{K}_{N+1} \left(\mathbf{y}_{n+1} - \mathbf{x}_{n+1}^T \hat{\boldsymbol{\theta}}_N \right) \tag{4.74}$$

3. corresponding covariance matrix update:

$$\mathbf{P}_{N+1} = \frac{1}{\lambda} \left(\mathbf{I} - \mathbf{P}_N \left(\frac{\mathbf{x}_{n+1} \mathbf{x}_{n+1}^T}{\lambda + \mathbf{x}_{n+1}^T \mathbf{P}_N \mathbf{x}_{n+1}} \right) \right) \mathbf{P}_N \tag{4.75}$$

where λ is the forgetting factor which is chosen equal to unity for the time being (no forgetting effect since the choice has been made not to discard useful information, see section 4.7). Note that the covariance matrix update equation (4.75) is rewritten by means of the matrix pseudo inversion lemma such that no cumbersome matrix inversion computation is needed. Because of this, identifiability of parameters is not an important issue here. The parameters which are not identifiable will not be updated.

As an example, figure 4.5 shows the least squares results of the identified aerodynamic derivatives for the moment M around the Y_b-axis. The constant line represents the off-line batch procedure result and serves as a benchmark for the time varying results, where the other lines are the on-line real time procedure in Simulink and the post flight recursive approach in Matlab. Differences between the last two lines are caused by rounding errors and approximation differences between Simulink and Matlab. It can be observed in figure 4.5 that there is not always an ”exact match” at the end of the time span between the off-line approach on the one side and the on-line and recursive approaches on the other side, despite the fact that both methods have the same amount of data available at the final moment. For this reason, two validation tests are explained in section 4.3. Both of them confirm the validity of these identification results.

4.3 Validation steps

After ASE and AMI phases have been completed, two validation tests are possible in order to check if the obtained result is correct. One is a short term validation of the AMI phase

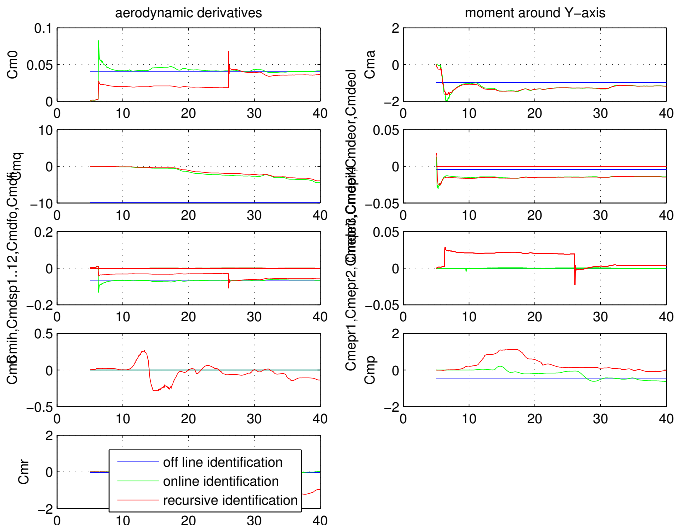

Figure 4.5: Aerodynamic derivatives of moment M around Y-axis

by considering the innovation of the least squares procedure. The other one is a global validation of both phases by reconstructing some of the INS/GPS measurements.

4.3.1 Innovation of the least squares procedure

The innovation can be calculated as the fit error between measured values and reconstructed values of the dependent variable. The results for these innovations are shown in figure 4.6 for all aerodynamic forces and moments.

From figure 4.6, it can be seen that the amplitude of the innovations is very small for batch as well as recursive approaches, and thus the least squares results obtained in the AMI step can be considered accurate, without significant difference. From the innovation signal, even more information can be extracted, but this will be discussed in section 4.7 about triggering for reconfiguration.

4.3.2 Reconstruction of INS/GPS measurements

The reconstruction of the measurements is performed in two steps. First the dimensionless forces and moments are reconstructed by means of the aerodynamic derivatives from the AMI step and the state information from the ASE step, which is done by using equations (4.67) till (4.72), of which the result is shown in fig 4.7, and which is compared with the original values for dimensionless forces and moments obtained with eq. (4.65) and (4.66).

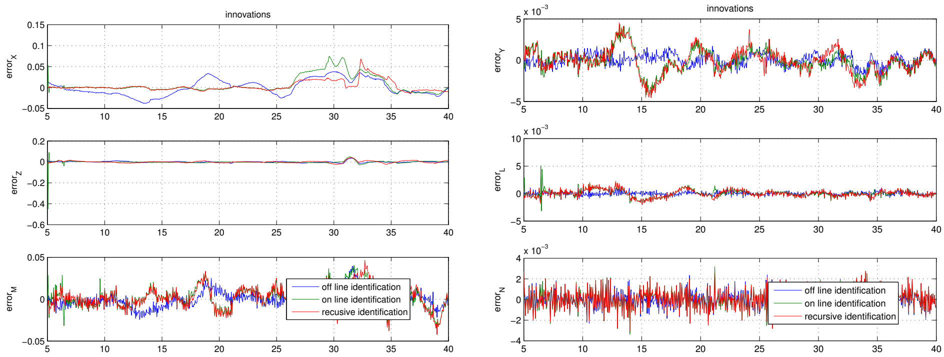

(a) least squares innovations for symmetric forces and moments

(b) least squares innovations for anti-symmetric forces and moments

Figure 4.6: Least squares innovations results for a high-fidelity nominal non-damaged Boeing 747 simulation model

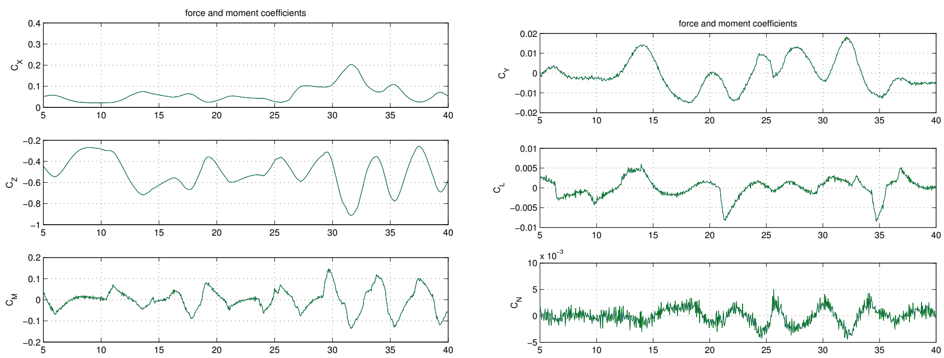

(a) reconstruction of dimensionless symmetric forces and moments

(b) reconstruction of dimensionless anti-symmetric forces and moments

Figure 4.7: Reconstruction of dimensionless forces and moments for a high-fidelity nominal non-damaged Boeing 747 simulation model

Consequently, these dimensionless forces and moments are used together with the available state information for the reconstruction of the INS/GPS measurements of airspeed components and angular rates. This is done by means of the following formulas, where values are calculated for the time derivatives of airspeed components and angular rates:

$$\dot{u} = \frac{C_X {}^1\!/\!_2 \rho V^2 S}{m} - g\sin\theta + rv - qw \tag{4.76}$$

$$\dot{v} = \frac{C_Y {}^1\!/\!_2 \rho V^2 S}{m} + g\cos\theta\sin\phi + pw - ru \tag{4.77}$$

$$\dot{w} = \frac{C_Z {}^1\!/\!_2 \rho V^2 S}{m} + g\cos\theta\cos\phi + qu - pv \tag{4.78}$$

$$\begin{aligned}\dot{p} = {} & \left(I_{xx} - \frac{I_{xz}^2}{I_{zz}}\right)^{-1} \left[C_l {}^1\!/\!_2 \rho V^2 Sb + \frac{I_{xz}}{I_{zz}} C_n {}^1\!/\!_2 \rho V^2 Sb - qr\left(I_{zz} - I_{yy} + \frac{I_{xz}^2}{I_{zz}}\right) + \right. \\ & \left. + pqI_{xz}\left(1 - \frac{I_{yy} - I_{xx}}{I_{zz}}\right)\right]\end{aligned} \tag{4.79}$$

$$\dot{q} = \frac{1}{I_{yy}}\left(C_m {}^1\!/\!_2 \rho V^2 Sc - rp\left(I_{xx} - I_{zz}\right) - \left(p^2 - r^2\right) I_{xz}\right) \tag{4.80}$$

$$\begin{aligned}\dot{r} = {} & \left(I_{zz} - \frac{I_{xz}^2}{I_{xx}}\right)^{-1} \left[C_n {}^1\!/\!_2 \rho V^2 Sb + \frac{I_{xz}}{I_{xx}} C_l {}^1\!/\!_2 \rho V^2 Sb - qrI_{xz}\left(1 + \frac{I_{zz} - I_{yy}}{I_{xx}}\right) + \right. \\ & \left. + pq\left(\frac{I_{xz}^2}{I_{xx}} - I_{yy} + I_{xx}\right)\right]\end{aligned} \tag{4.81}$$

The results are shown in fig. 4.8 and compared with the time derivatives of the original measurements of speed components and angular rates.

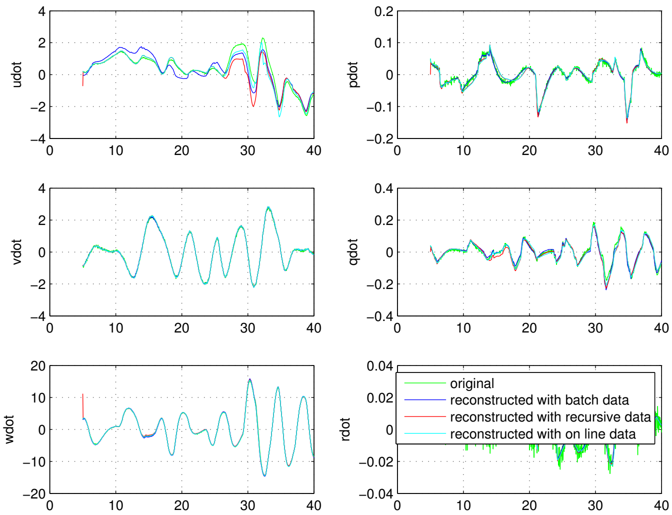

Figure 4.8: Reconstruction of GPS/INS measurements for a high-fidelity nominal non-damaged Boeing 747 simulation model

As a global conclusion, it can be stated that the validation tests have shown that the identification results obtained above are representative, accurate and reliable. Now that it has been confirmed that the procedure works satisfactorily for nominal non-damaged aircraft, the next topic is to analyse the performance of this identification procedure for damaged aircraft. This will be the subject of section 4.5.

4.4 Real Time Aerodynamic Model Identification

This above mentioned recursive two step method has been implemented in Simulink and combined with the conventional sensor output of a Cessna Citation simulator and a Boeing 747 simulator. A connected joystick provides the input. This allows performing real-time computer based identification calculations while performing flight manoeuvres by hand in a Simulink aircraft simulator. The progress of the identification process is continuously visualized on the computer display. The development of the aerodynamic derivatives is shown in a real-time developing box plot like representation, while also the time varying covariance of the aerodynamic derivatives is shown. The latter information provides some indication to the user if it is needed to adapt his manual input signal in order to reduce the uncertainty of the identification results.

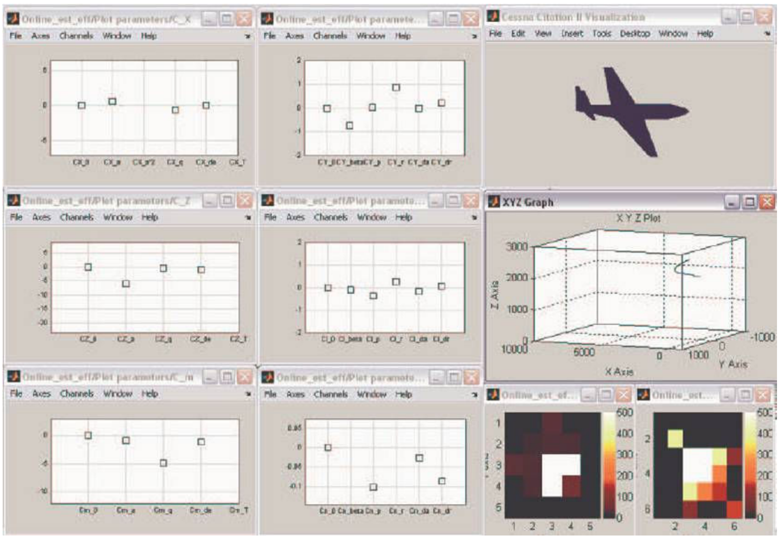

Figure 4.9: Overview of the operator information screen for real time identification. The left and middle columns in the screen give the aerodynamic derivative values, the right column gives (from top to bottom) aircraft attitude, trajectory and covariances for symmetrical (left) and asymmetrical (right) estimates.

4.5 Applications to the RECOVER simulation model

Two examples will be shown here for the two step method. One component failure, i.e. trim horizontal stabilizer runaway, and a structural failure, i.e. loss of the vertical tail. Both give a representative illustration of the two step method capabilities. In order to analyse the differences between the nominal and damaged models, the same control inputs must be applied. Moreover, satisfactory identification results can only be obtained if the control inputs excite all steering channels of the aircraft. Therefore, four different control inputs are consecutively applied, namely first a 3-2-1-1 input on the pitch channel (7–20s) and thereafter doublets on roll (26–30s), yaw (36–40s) and thrust (18–20s) respectively. Despite the fact that excitation of roll and yaw occur simultaneously in regular flights in order to perform coordinated turns, it has been chosen deliberately in this set-up to implement both control inputs consecutively. The reason for this is the fact that a simultaneous implementation may lead to undesirable correlations in the identification results. For the same reason, small doublet excitations have been imposed on every control surface individually. For each scenario, the identification result of the damaged simulation model is compared with the nominal non-damaged one, which is also given in each graph as a benchmark. It should be noted that the identification result for the failure scenario with horizontal stabilizer runaway does not last longer than 20 seconds of the total time span. The reason for this is the fact that the aircraft crashes after these 20 seconds, as illustrated by its trajectory in fig. 4.10.

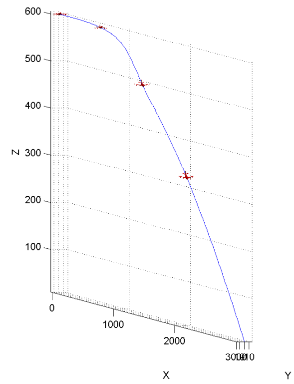

Figure 4.10: Trajectory of the aircraft for the stabilizer runaway scenario

4.5.1 Trim horizontal stabilizer (THS) runaway

The identification results of the stabilizer related aerodynamic derivatives are shown in fig. 4.11(a), where the deflection of the horizontal stabilizer is shown in fig. 4.11(b). For the nominal situation, the stabilizer remains fixed in its trim setting, except for a short excitation for identification purposes. In the runaway situation, the gradually deviating behaviour during the first 10 seconds is apparent. Mind that these plots in fig. 4.11(a) start from the 5th second onward, because the earlier identification results are not reliable since the first step of state estimation is not yet converged in this phase. It can be seen that there is no significant change between the failed and unfailed situation for the identification results. This can be explained by the fact that this is a hardware failure, without aerodynamic consequences.

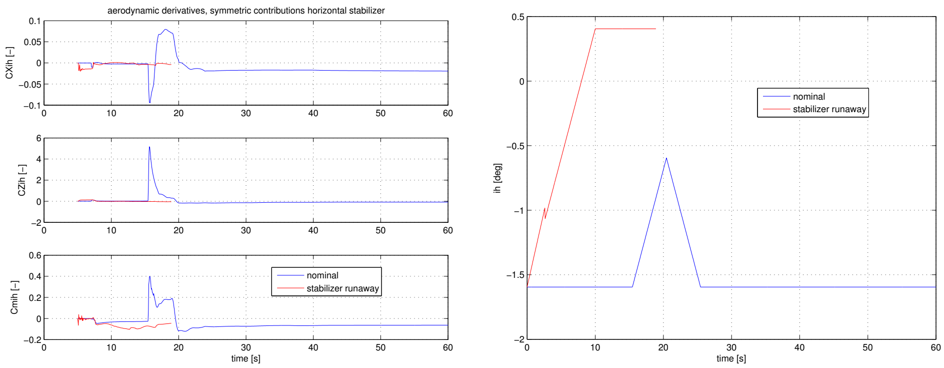

(a) identification of stabilizer related aerodynamic derivatives

(b) horizontal stabilizer runaway

Figure 4.11: Identification of stabilizer related aerodynamic derivatives for damaged Boeing 747 simulation model, horizontal stabilizer runaway scenario

4.5.2 Loss of the vertical tail

The identification results of the rudder related aerodynamic derivatives are shown in fig. 4.12(a), where the deflection of the rudder is shown in fig. 4.12(b). Since there is no rudder anymore in the situation of a vertical tail loss, the loss of yawing control should be visible in the identification result. For the nominal situation, the rudder makes a doublet movement. Mind that this doublet is not perfect, since the compensating influence of the yaw damper appears in this channel. In the vertical tail loss scenario, there is no deflection since the rudder is lost. Therefore, there is no convergence of the control derivatives. This is because persistent excitation is needed for a successful identification procedure. Another consequence of the tail loss scenario is the huge reduction of lateral static stability. This can be seen in the behaviour of the aerodynamic derivative C_{n_β}, as shown in fig. 4.13. A positive value for C_{n_β}, also known as Weathercock stability, points out for static directional stability. From fig. 4.13, it can be seen that the nominal aircraft is stable, but the damaged aircraft is observed to be lightly directionally statically unstable. This simulation shows also that there is no rudder deflection necessary to observe this, even a doublet on the roll channel (ailerons) induces some sideslip in order to make a static stability analysis. Summarizing, analysing both results, it can be stated that the loss of the tail surface can be identified by means of these identification results.

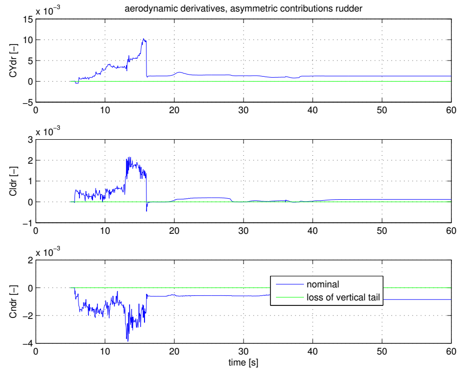

(a) identification of rudder related aerodynamic derivatives

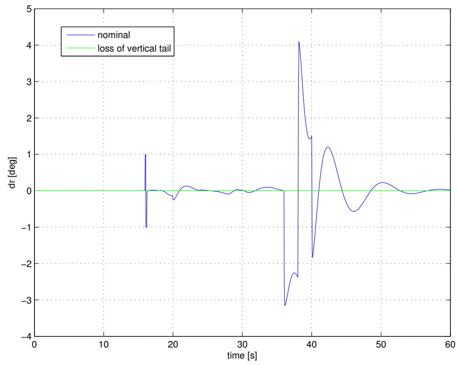

(b) rudder deflections for vertical tail loss scenario

Figure 4.12: Identification of rudder related aerodynamic derivatives for damaged Boeing 747 simulation model, vertical tail loss scenario

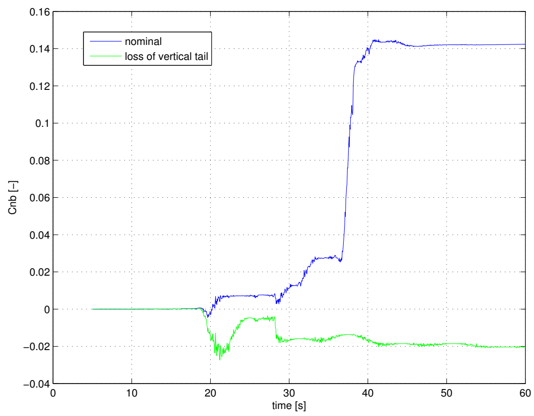

Figure 4.13: Directional stability C_{n_β} for vertical tail loss scenario

4.5.3 Validations for both failure scenarios

The identification results shown above focus specifically on relevant control surface related aerodynamic derivatives, but there are a lot more identification results. These are all presented in appendix D. In order to perform a validation of the accuracy of these identification results, the innovations can be calculated again, as already explained in section 4.3. These innovations can be found in figure 4.14. This shows that the least squares result is accurate. Also the reconstruction of linear and angular acceleration components confirm the accuracy of the identification results, these are shown in figure 4.15.

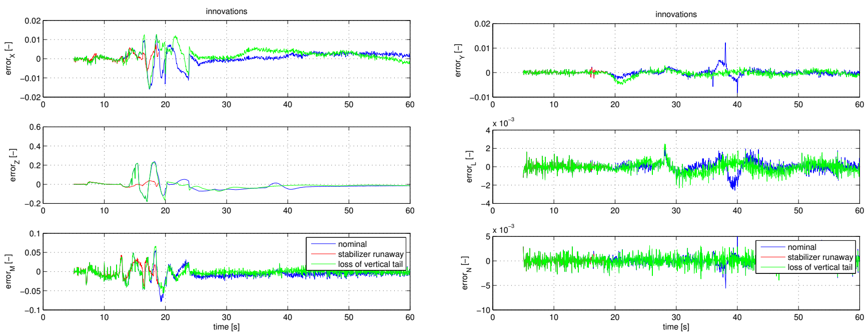

(a) least squares innovations for symmetric forces and moments of both failure scenarios

(b) least squares innovations for anti-symmetric forces and moments of both failure scenarios

Figure 4.14: Least squares innovations results for a high-fidelity damaged Boeing 747 simulation model for both failure scenarios

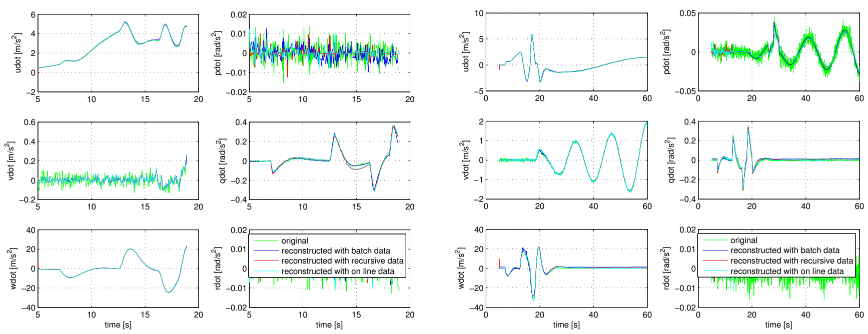

(a) reconstruction of airspeed components and angular rates for stabilizer runaway scenario

(b) reconstruction of airspeed components and angular rates for tail loss scenario

Figure 4.15: Reconstruction of GPS/INS measurements for the high-fidelity damaged Boeing 747 simulation models in both failure scenarios

4.6 Feedback of aircraft stability and control effector information to the pilot

The identified parameters contain valuable information about the physical state of the aircraft. The absolute value has less significance than its change compared to the initial value. Also, it requires a good understanding of flight dynamics and aerodynamic modeling to understand these parameters. For this reason, it is paramount to translate these values to a suitable format, which can be easily interpreted by the pilot. For example, the parameters C_{m_α} and C_{n_β} could be presented as "stability factors", while $C_{m_{\delta_e}}$, $C_{l_{\delta_a}}$, $C_{n_{\delta_r}}$ and $C_{X_{EPR}}$ could be presented as "elevator-", "aileron-", "rudder-" and "engine-effectiveness" respectively. It is worthwhile to investigate the possibility to present the parameters to the pilot in a proper way, giving him insight in the physical condition of the aircraft, as an example a possible visual presentation of this information on the multi-function display (MFD) to the pilot is given in fig. 4.16.

Figure 4.16: Example of visualisation of control effector effectiveness for the pilot, this information is based upon control effector effectiveness parameters, such as $C_{m_{\delta_e}}$, $C_{l_{\delta_a}}$, $C_{n_{\delta_r}}$ and $C_{X_{EPR}}$.

4.7 Triggering routine for reconfiguration

In order to ensure proper adaptivity of the identification routine for failure dynamics, there are two major options. One is to rely on a weighting factor λ in the recursive least squares procedure, the other is to incorporate a trigger for re-identification. In ref. [124], an evaluation has been made between both alternatives. Since the former has the disadvantage that older data, which might still contain useful information, are discarded progressively due to the limiting history horizon, the latter option has been preferred. This limiting history horizon has a major drawback during long periods of stationary flight with no control inputs, such as cruise, because the model is likely to become unstable due to the lack of significant excitations.

The concept of a reidentification trigger works by increasing the covariance matrix $\mathbf{P}$ artificially when the current model is not reliable anymore. In this way, no data will be lost during normal flight, maintaining the quality of the model also in constant flight conditions. In case an error occurs that affects the model, the aircraft will move [and this induced movement will be counteracted by the (auto)pilot], creating sufficient excitation data on the input channels to identify the new model within a limited time span. In [109], the authors describe a procedure to use the aforementioned innovation (see section 4.3) as a measure of the quality of the model. The whiteness of the innovation is used as a quality measure, because a perfect model would have a residual comparable to the noise present in the input signals. The residual (innovation) of the estimated aerodynamic model can be calculated as follows:

$$\mathbf{\Delta}(k) = \mathbf{z}(k) - \mathbf{X}(k)\,\hat{\boldsymbol{\theta}}_{RLS}(k) \tag{4.82}$$

in which $\mathbf{\Delta}(k)$ is the innovation, $\mathbf{z}(k)$ is the state measurement from the actual aircraft, $\mathbf{X}(k)$ is the data matrix and $\hat{\boldsymbol{\theta}}_{LS}(k)$ is the vector of estimated parameters. The faults, which change the system dynamics, also change the characteristics of $\mathbf{\Delta}(k)$ and make it different from white noise.

Three criteria, namely the autocorrelation criterion π_k, the moving average of the square innovation $\overline{\Delta}(k)$ and the spectral analysis σ^2_Δ have been analysed to decide whether this innovation is dominated by white noise, or contains a residual of an incorrect aerodynamic model. If the latter is the case, the reconfiguration of the model should be triggered. The former should be ignored in order to prevent false alarms. The triggering criterion candidates can be described as follows:

- autocorrelation function: $\pi_{k_{\text{gap}}} = \frac{1}{N}\sum\limits_{t=0}^{N-k_{\text{gap}}} \Delta(t)\,\Delta(t+k_{\text{gap}})$ where k_{gap} is a positive non-zero integer which needs to be selected. More information about the autocorrelation function can be found in [259].

- moving average of square innovation: $\bar{\Delta}(k) = \frac{1}{n_{\text{av}}}\sum\limits_{i=0}^{n_{\text{av}}} \Delta(k-i)^2$ where n_{av} is the number of samples over which this average is taken (a proper range is $25 - 100$ data samples, corresponding to $0.5s - 4s$).

- spectral analysis: $\sigma_{\Delta}^{2} = \frac{1}{N-1} \sum_{k=1}^{N} \left(\Delta \left(k \right) - \bar{\Delta} \right)^{2} \qquad \text{with :} \qquad \bar{\Delta} = \frac{1}{N} \sum_{k=1}^{N} \Delta \left(k \right)$

Analysis has revealed that the average value of the square innovation over a period of time is the preferable criterion since it has demonstrated in experiments to have the lowest false alarm rate for the failures considered in this research, [124]. For the triggering of the re-identification a threshold value has been chosen based on several simulated test flights, with and without failure.

Once the whiteness criterion has suggested the current model contains errors, the re-identification will take place. The covariance matrix $\mathbf{P}$ of the RLS procedure gives a measure for quality of the data that has entered the identification. Without forgetting factor, this ”data richness” can only improve, since all information from previous measurements is retained. This results in a gradual ”freezing” of the parameter values since every new data point is weighted less in the parameter identification. When it is concluded that the real-life situation has changed to such an extent that the identified model is not valid anymore, this old data should be disregarded. By artificially returning the covariance matrix to its initial state - a diagonal matrix with very large values (in the order of 10^6) - the parameter estimates are more influenced by new measurements and can be identified based on the flight data of the aircraft in its new, changed situation. Since each of the dimensionless forces and moments $[C_X \;\; C_Y \;\; C_Z \;\; C_l \;\; C_m \;\; C_n]^T$ has a separate innovation channel, the reconfiguration can be focused on the respective parameter set that triggers the reconfiguration. For this reason, six covariance matrices $\mathbf{P}$ are stored and updated separately. When for example the criterion value of roll-moment parameters C_l exceeds the threshold, only these parameters are triggered for re-identification. This prevents unnecessary destabilizing the aircraft model parts that are used in the control system.

4.8 Final note

Applications of the two step method to the RECOVER simulation model, as discussed in this chapter, have shown that this method can be used for identifying unfailed aircraft models, but also for aircraft with minor failures. In case of major structural failures, such as the engine separation scenario, the conventional aerodynamic model structure must be extended with additional terms. This topic will be elaborated in the next chapter.

Chapter 5

Taking into account aerodynamic property changes due to damage

In the methodology presented in chapter 4, some bottlenecks have been identified for applications to aircraft with major damage. One of them is the fact that the aerodynamic model structure is considered fixed when the aerodynamic derivatives are deduced by means of the recursive least squares procedure. The fixed structure considered here can be found in expressions (4.67) to (4.72). However, for failed situations, it is highly probable that this conventional model structure must be extended with additional non-linear and/or coupling terms and their accompanying derivatives. As an example, fig.5.1 shows the reconstruction of the airspeed components and the angular rates for a flight trajectory with high angles of attack. This validation shows that especially the reconstructed vertical speed component w and the pitch rate q deviate from the measurements, providing an indication that the estimated values for the longitudinal aerodynamic derivatives are not accurate. Higher order and coupling terms must be added to the model structure represented in eq. (4.67) to (4.72).

First, the need for structure selection and parameter estimation will be substantiated in section 5.1. This is done with a formal proof as well as a numerical example. Thereafter, two alternative methods for structure selection and parameter estimation will be discussed in detail, namely modified stepwise regression and adaptive recursive orthogonal least squares, respectively in sections 5.2 and 5.3. For both methods, numerical examples are shown. Finally, both methods are compared in section 5.4.

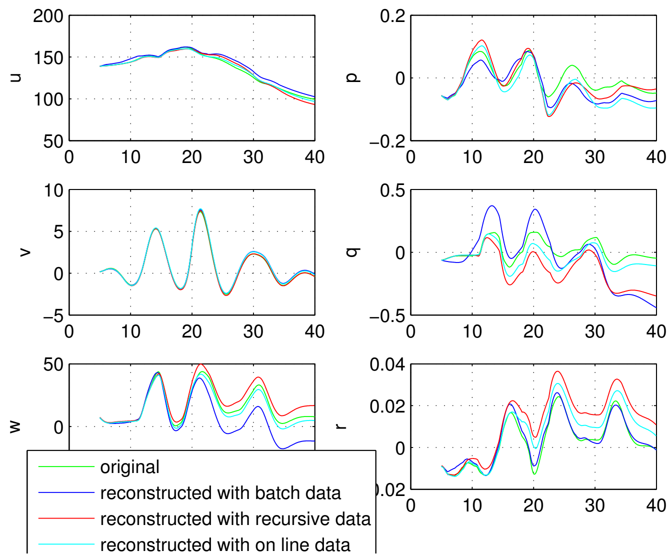

Figure 5.1: Reconstruction of airspeed components and angular rates for flight conditions with large angles of attack, using linear terms only

5.1 Substantiation of the need for structure selection and parameter estimation

In this kind of applications for damaged aircraft model identification, one is not certain which independent variables may or may not have a significant influence on the dependent variable, which makes it important to apply some measure of structure selection. There are some good reasons for this. First of all, it complies with the principle of parsimony.

Definition 1. *Principle of parsimony: if there are two mathematical models to represent the same system with equal accuracy, then the model with the fewest parameters is preferable.*

This principle promotes computational speed, which is especially important for on-line applications like here. Another fact is that including many insignificant data in the regressor set will lead to many small coefficients with large standard deviations due to ill-conditioning. Besides, these coefficients, although small but numerous, perturb the estimation of the coefficients for the significant regressors.

Proof. Suppose the true system can be described as: $\mathbf{z} = \mathbf{\Phi}_{\text{sign}}\boldsymbol{\theta}$. Due to a lack of model structure information, its approximation is defined as follows:

$$\mathbf{z} = \mathbf{\Phi}_{\text{sign}}\hat{\boldsymbol{\theta}}_{\text{sign}} + \mathbf{\Phi}_{\text{insign}}\hat{\boldsymbol{\theta}}_{\text{insign}} \tag{5.1}$$

where $\mathbf{\Phi}_{\text{sign}}$ contains the significant regressors and $\mathbf{\Phi}_{\text{insign}}$ is the collection of insignificant regressors. Premultiplying eq. (5.1) with $(\mathbf{\Phi}_{\text{sign}}^T\mathbf{\Phi}_{\text{sign}})^{-1}\mathbf{\Phi}_{\text{sign}}^T$ results in:

$$\hat{\boldsymbol{\theta}}_{\text{sign}} = \boldsymbol{\theta} - (\mathbf{\Phi}_{\text{sign}}^T\mathbf{\Phi}_{\text{sign}})^{-1}\mathbf{\Phi}_{\text{sign}}^T\mathbf{\Phi}_{\text{insign}}\hat{\boldsymbol{\theta}}_{\text{insign}} \tag{5.2}$$

which indicates a discrepancy between the parameter estimate $\hat{\boldsymbol{\theta}}_{\text{sign}}$ and the true parameter $\boldsymbol{\theta}$. This deviation becomes larger for $\hat{\boldsymbol{\theta}}_{\text{insign}}$ with larger size and if $\mathbf{\Phi}_{\text{sign}}$ and $\mathbf{\Phi}_{\text{insign}}$ are spanned in space by mutual linear dependent bases and if $\mathbf{\Phi}_{\text{sign}}$ is not well-defined. There is no deviation if $\mathbf{\Phi}_{\text{sign}}$ and $\mathbf{\Phi}_{\text{insign}}$ are mutually orthogonal, which is generally not the case. □

Therefore, proper identification, including structure selection, is *not* avoidable for damaged aircraft with changed aerodynamic properties. In this research, the aim of this routine is to perform adaptive structure selection and parameter estimation for an aerodynamic model of a structurally damaged aircraft. This allows to exploit the knowledge of these data for a model-based control technique, namely adaptive nonlinear dynamic inversion. In this way, safety and survivability will be enhanced.

There are many interesting structure selection and parameter estimation (SSPE) algorithms, like stepwise regression[81, 157], elaborated in section 5.2. It is a very physical and intuitive procedure, but besides being not (yet) recursive, its main drawback is that it includes addition and elimination criteria, and thus is less efficient than Orthogonal Least Squares, which involve only a forward selection procedure. Especially for on-line applications, this is an important advantage. Orthogonal Least Squares, described in section 5.3, have been used before for nonlinear modeling and roll derivatives estimation from flight data[277]. However, they have only been applied for batch data and not for damaged aircraft. For nonlinear aerodynamic modeling problems, the similar idea of generating multivariate orthogonal modeling functions from measured data, ranking those orthogonal functions by fit error reduction capability, and using the predicted square error metric (PSE) for model structure determination was originally developed by Morelli[159, 199, 200, 201]. The PSE metric was originally developed earlier by Barron[30]. Moreover, orthogonal functions were used earlier by Mulder[208] in the optimization of multidimensional input signals for dynamic flight test manoeuvres.

A possible alternative procedure of adding higher order and coupling terms that avoids the concept of structure selection is the fairly straightforward extension of the data matrix for the least squares routine, containing additional columns with all regressors that might possibly have an influence on the dimensionless forces and moments. The considered regressors are: $\alpha q, \alpha\delta_e, \alpha\beta^2, \alpha^m, \alpha\beta, \alpha p, \alpha r, \alpha^2\beta, \alpha^2 p, \alpha^2 r, \beta^n, \alpha\beta^3, \alpha^2\beta^3 \quad m = 2, \ldots, 8 \quad n = 2, \ldots, 5$. These nonlinear regressor candidates have been determined by means of the aerodynamical knowledge and have been found in ref. [157]. Fig. 5.2 shows the fitting result of this procedure on a measurement data set which is also used in the application example in section 5.2. The data fitting capabilities of this procedure seem superior on first sight, but analysing the numerical results gives a different insight. First of all, this computation gives singularity issues, since the extended data matrix containing the higher order regressors is ill-conditioned and suffer from (near-)collinearities, as already introduced in section 3.2.6. Secondly, taking a closer look at the resulting coefficient values in table 5.1 is worthwhile.

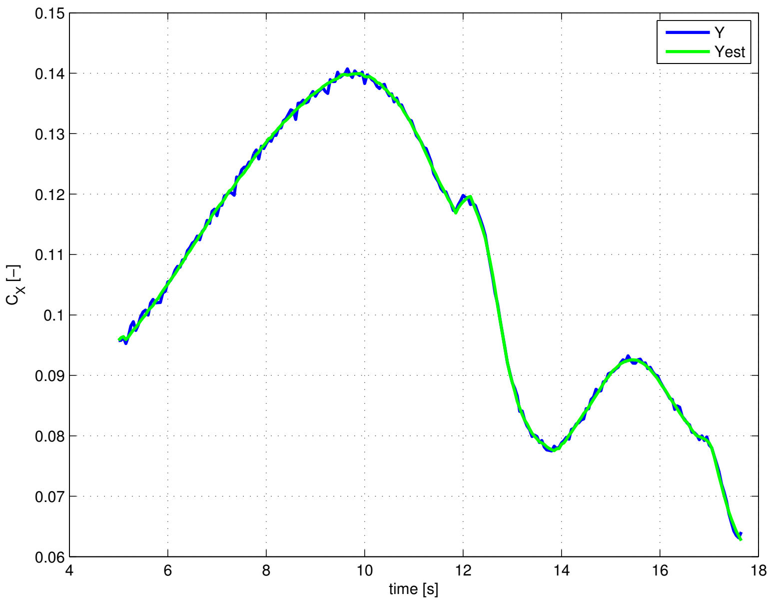

Figure 5.2: LS regression result with all nonlinear terms included in the data matrix

Inspecting table 5.1 shows that the higher order terms of α and β have a negative effect on the least squares operation. Since the magnitude of the higher order regressors is decreasing considerably (the angle unit is radians), coefficients of high order are necessary in order to play a significant role in the fitting procedure. Considering the orders of these coefficient values as well as their standard deviations in table 5.1, it can be seen that these numerical results are not trustworthy. These value magnitudes indicate also the presence of collinearities, as mentioned in section 3.2.6. Besides being unrealistically high, they imply a robustness risk. Despite its apparently satisfactory data fitting capacity, this combination of model structure and parameter values will lead to a problematic prediction capacity of the

Table 5.1: Result for the extended LS procedure for approximation of measured data set, see section 5.2

parameter	value	(σ)	parameter	value	(σ)
1	2.42	(29%)	α^5	$-3.27 \cdot 10^7$	(31%)
α	$-2.07 \cdot 10^2$	(36%)	α^6	$1.86 \cdot 10^8$	(30%)
α^2	$9.04 \cdot 10^3$	(36%)	α^7	$-5.86 \cdot 10^8$	(29%)
$\frac{q\bar{c}}{V}$	-7.48	(54%)	α^8	$7.82 \cdot 10^8$	(29%)
$\delta_{e_{IR}}$	$-3.51 \cdot 10^{-4}$	(66%)	$\alpha\beta$	-133	(73%)
δ_{sp_2}	$1.98 \cdot 10^5$	$(\approx 0\%)$	$\alpha\frac{pb}{2V}$	2.94	(1997%)
β	8.62	(73%)	$\alpha\frac{rb}{2V}$	-69.4	(82%)
$\frac{pb}{2V}$	1.05	(321%)	$\alpha^2\beta$	559	(69%)
$\frac{rb}{2V}$	4.07	(64%)	$\alpha^2\frac{pb}{2V}$	-14.8	(1676%)
$\alpha\frac{q\bar{c}}{V}$	79.4	(52%)	$\alpha^2\frac{rb}{2V}$	351	(86%)
$\alpha\delta_{e_{IL}}$	$9.69 \cdot 10^{-3}$	(25%)	β^3	-246	(81%)
$\alpha\delta_{sp_1}$	$6.92 \cdot 10^6$	(2225%)	β^4	$1.11 \cdot 10^3$	(142%)
$\alpha\beta^2$	90.9	(147%)	β^5	$4.97 \cdot 10^3$	(128%)
β^2	-6.67	(217%)	$\alpha\beta^3$	$4.31 \cdot 10^3$	(65%)
α^3	$-2.27 \cdot 10^5$	(34%)	$\alpha^2\beta^3$	$-1.25 \cdot 10^4$	(97%)
α^4	$3.47 \cdot 10^6$	(32%)			

dependent variable. Small errors in the state estimation routine will lead to larger deviations for the higher order values and thus also in the predicted value of the dependent variable. Moreover, since it is the intention to apply indirect adaptive control based upon this aircraft model, model robustness is an essential issue in this context. For this reason, it is not logical working with higher order terms from the start onward. Structure selection is required, moreover lower order terms should be given priority, since they provide the major contribution for data fitting purposes, as can be seen in Taylor series expansions and which will be discussed in section 5.2.4. Finally, two crucial criteria are the real time applicability and the computational efficiency. Whereas this method is without any problem real time applicable, the large size of the data matrix (for this example 31 columns), makes it computationally more intensive.

5.2 Modified stepwise regression

An interesting tool for joint structure selection and parameter estimation is the so-called Modified Stepwise Regression (MSWR) algorithm, which is based upon residual analysis. First the concept of stepwise regression is introduced, after which the slightly deviating principle of modified stepwise regression is derived as a development tool to determine model structures. Subsequently the monitoring criteria for this methodology are discussed.

The main power of the concept of stepwise regression[81, 159] is that it performs iteratively a least squares operation, where it selects step by step only the relevant regressors for a certain dependent variable, which is contaminated with noise, out of a set of candidate independent variables. In this way, it is avoided that the least squares operation is performed with irrelevant independent variables which disturb the result.

5.2.1 Principle

The procedure consists of the following steps:

1. Insert the regressor candidate with the highest partial correlation r_{jz} with the residual.
2. Check the significance of all the regressors included so far. This can be done by means of the partial F-test. If not all included regressors are significant, the regressor(s) with the lowest F_p-value(s) that do not pass a user specified threshold must be removed step by step.
3. Calculate monitoring criteria, such as the correlation coefficient R^2, $PRESS$ and PSE. These criteria are discussed later in this section.
4. Regress the remaining regressor candidates on the regressors already included. In this way the most significant contribution, perpendicular on the space spanned by the regressors already included, can be selected in the next step.
5. Go back to step 1.

The use of this stepwise regression procedure has been initiated in aeronautical identification applications, but in a slightly modified form [120, 157, 159, 208]. Stepwise regression is not interesting for aircraft model identification in near-steady and stationary flight conditions, where all relevant regressors are perfectly known thanks to the flight dynamics knowledge. It is more interesting to use the so-called modified stepwise regression procedure for significant non-linear flight regimes, for example at high angles of attack, spinning flight, and for unstable aircraft. In these flight phases, the classical linear regressors, familiar from flight dynamics, are inserted permanently in the first step. In the subsequent steps, nonlinear regressor candidates can be added, evaluated and subtracted by means of partial correlation and partial significance respectively. The permanently inserted linear regressors and the nonlinear regressor candidates have been determined by means of the aerodynamical knowledge. Linear regressors to be inserted permanently:
Longitudinal: $1, \alpha, q, \delta_e, \delta_T$ Lateral: $1, \beta, p, r, \delta_a, \delta_r$
Nonlinear regressors for the candidate set:
Longitudinal: $\alpha^2, \alpha q, \alpha\delta_e, \alpha\beta^2, \beta^2, \alpha^m \quad m = 3, \ldots, 8$
Lateral: $\alpha, \alpha\beta, \alpha p, \alpha r, \alpha\delta_a, \alpha\delta_r, \alpha^2, \alpha^2\beta, \alpha^2 p, \alpha^2 r, \alpha^2\delta_a, \alpha^2\delta_r, \alpha^3, \beta^n, \alpha\beta^3, \alpha^2\beta^3 \quad n = 2, \ldots, 5$

The reasoning behind the concept of modified stepwise regression applies also perfectly for the situation of damaged aircraft, which also can have non-linear behaviour. However, it should be noted that for asymmetrically damaged aircraft, the decoupling is not relevant anymore and as a result all nonlinear regressors should be grouped in one candidate set, together with the other set of linear regressors, which would not have been included in a decoupled situation for a symmetric aircraft.

5.2.2 Addition, Subtraction and Monitoring criteria

The criteria for adding and subtracting the candidate regressors are explained below, together with the criteria which are used to monitor the global progress of the stepwise regression routine. The regression equation is generally defined as follows: $\mathbf{z} = \mathbf{X}\boldsymbol{\theta} + \boldsymbol{\nu}$ where $\mathbf{z}$ is the dependent observed variable, $\mathbf{X}$ are the independent variables, $\boldsymbol{\theta}$ is the parameter vector and $\boldsymbol{\nu}$ is the disturbance vector.

- Addition criterion: the partial correlation r_{jz} is calculated by the following expression:

$$r_{jz} = \frac{S_{jz}}{\sqrt{S_{jj}S_{zz}}} \tag{5.3}$$

where:

$$\begin{aligned} S_{jz} &= \sum_N \left[x_j(i) - \bar{x}_j\right]\left[z(i) - \bar{z}\right], \quad S_{zz} = \sum_N \left[z(i) - \bar{z}\right]^2 \\ S_{jj} &= \sum_N \left[x_j(i) - \bar{x}_j\right]^2, \quad \bar{x}_j = \frac{1}{N}\sum_N x_j(i), \quad \bar{z} = \frac{1}{N}\sum_N z(i) \end{aligned} \tag{5.4}$$

- Subtraction criterion: the significance of each individual term of the regression is analysed through the partial F-test. For each independent variable inside the regression the value of F_p is calculated:

$$F_p = \frac{\hat{\theta}_j^2}{s_{\beta_j}^2} \tag{5.5}$$

where:

$$\hat{\boldsymbol{\theta}} = \left[\mathbf{X}^T\mathbf{X}\right]^{-1}\mathbf{X}^T\mathbf{z} \tag{5.6}$$

$$s^2 = \mathrm{diag}\left(\mathrm{Cov}\right) \tag{5.7}$$

$$\mathrm{Cov} = \frac{RSS}{N-p}\left(\mathbf{X}^T\mathbf{X}\right)^{-1} \quad \text{with } RSS = \sum_N \left[\varepsilon(i)\right]^2, \quad \boldsymbol{\varepsilon} = \mathbf{z} - \mathbf{X}\hat{\boldsymbol{\theta}} \tag{5.8}$$

Where $\hat{\boldsymbol{\theta}}$ is the estimated parameter vector, s is the standard error for each parameter, N is the number of measurements and p is the number of independent variables included in the regression.

- Some monitoring criteria are needed to check the proper development of the routine, and to judge when the iteration procedure must be interrupted. It is important to realize that this judgement is a trade-off between data fitting and prediction capabilities. More precisely, underfitting as well as overfitting must be avoided. Four interesting criteria are:

  - The predicted sum of squares $PRESS$, which are the residuals, normalized by prediction matrix diagonal elements:

    $$PRESS = \sum_{i=1}^{N} \left[\frac{\varepsilon(i)}{(1 - k_{ii})} \right]^2 \qquad k_{ii} = \text{diag}\left(\mathbf{X} \left(\mathbf{X}^T \mathbf{X} \right)^{-1} \mathbf{X}^T \right) \tag{5.9}$$

    It has to be noted that for a large set of data points $N \to \infty$, the diagonal elements of the prediction matrix k_{ii} asymptotically go to zero and the prediction sum of squares $PRESS$ equals the residual sum of squares RSS. With increasing data fitting properties of the regression operation, the $PRESS$ keeps decreasing.

  - The predicted square error PSE is a summation of two terms, the first one being the mean squared fit error $MSFE$, where the second one is an overfit penalty term, since it is proportional to the number of independent variables included in the regression:

    $$PSE = \frac{1}{N} \left(\boldsymbol{\varepsilon}^T \boldsymbol{\varepsilon} \right) + \sigma_{\max}^2 \frac{p}{N} \qquad \sigma_{\max}^2 = \frac{1}{N} \sum_{i=1}^{N} \left[z(i) - \bar{z} \right]^2 \tag{5.10}$$

    In this expression, $\sigma_{\max}$ is an a-priori upper bound estimate of the squared error between the future data and the model. It should be noted that the predicted square error PSE is particularly interesting for monitoring the progress of the routine, since it contains a data fitting as well as an overfit penalty term. This leads to a clear optimum, as illustrated in fig. 5.3.

  - The coefficient of determination R^2 takes a value between zero and one and is usually given as a percentage:

    $$R^2 = \frac{\hat{\boldsymbol{\theta}}^T \mathbf{X}^T \mathbf{z} - N\bar{z}^2}{\mathbf{z}^T \mathbf{z} - N\bar{z}^2} \tag{5.11}$$

    As long as significant regressors are being added, R^2 will keep increasing.

  - The fit error gives also an indication of the approximation of the regression

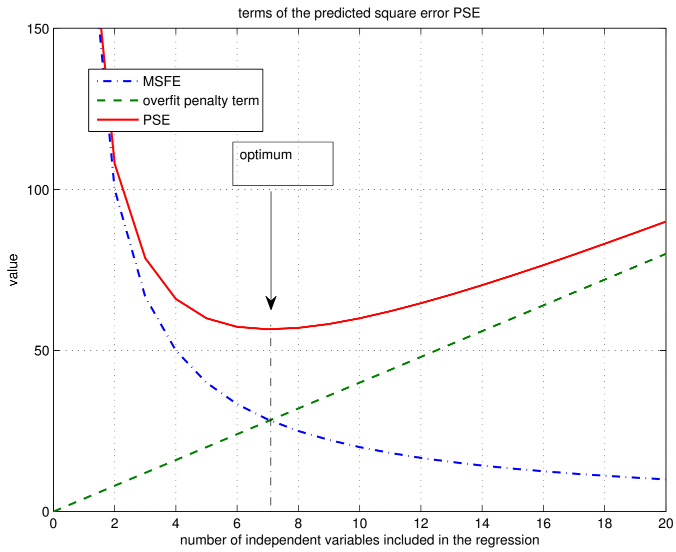

Figure 5.3: Breakdown of the predicted square error PSE in its data fitting and overfit penalty term. Source: Klein and Morelli[159].

operation and is calculated as follows:

$$\text{fit error} = \sqrt{\frac{RSS}{N-p}} \qquad RSS = \varepsilon^T\varepsilon \tag{5.12}$$

Each of these monitoring criteria has its own peculiarities to represent interesting information, either as ”fitting the data” criterion or as ”prediction” criterion. Therefore, it is important that a proper choice is made for selecting the most suitable criterion to terminate the iteration loop of the modified stepwise regression routine. The predicted square error PSE has been selected as criterion, because of its combined over- and underfitting detection qualities.

5.2.3 Least squares operation

In addition to the ordinary least squares operation, there are two variants that have specific advantages above the classical approach when there are disturbances in the independent variables or in the dependent variable. These are the weighted least squares and total least squares, described in section 3.3.3.3. Both are applied in the engine separation example.

5.2.4 Practical issues for the procedure

Experiments have shown that the Modified Stepwise Regression procedure is particularly sensitive to data collinearities, as any least squares operation. Therefore, some measures have been taken to perform some conditioning on the data-based regressor matrix $\mathbf{X}$ as well as the set of regressor candidates before the iteration procedure is started, in order to eliminate singularities without loosing general applicability of the method. Two actions have been performed: variables who remain constant (like the stabilizer incidence angle i_h in short time intervals) are detected and eliminated since they disturb the identification of the static aerodynamic derivatives like C_{X_0}, and variables who behave identically are identified and removed too. This holds for example for coupled surfaces, like some of the spoilers. This implies that surfaces deflecting identically are considered virtually as ”one surface”. The advantage is that this procedure does not limit general applicability of the method in case a separate surface excitation feature is added. Other experiments have shown that higher order terms of the candidate regressors, like α^6, can be included in the set of added regressors inappropriately. Considering the principle of Taylor expansions, like the different order expansions of $\sin(x)$ as shown in fig. 5.4, it can be seen that adding higher order candidate regressors only makes sense when the lower order terms already have been included.

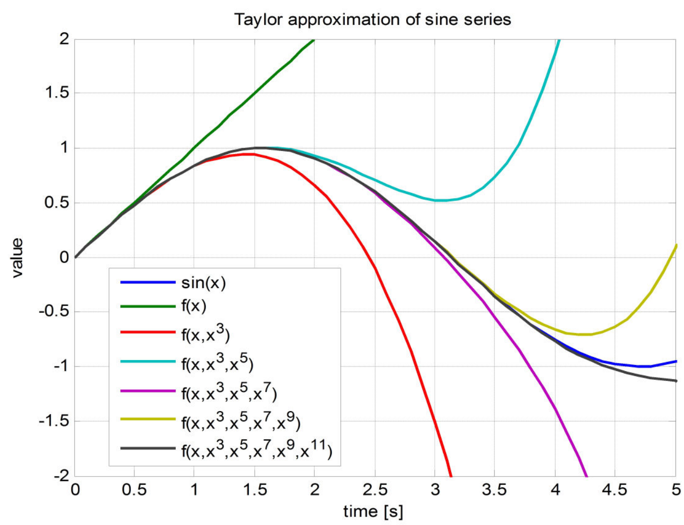

Figure 5.4: Different order Taylor approximations of a sine series

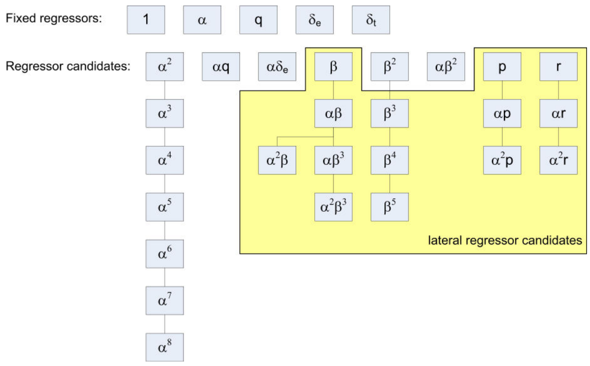

Figure 5.5: Priority scheduling for longitudinal forces and moments

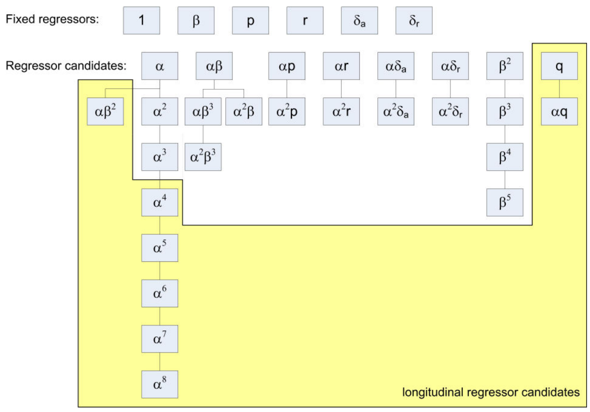

Figure 5.6: Priority scheduling for lateral forces and moments

This leads to the so-called choice of priority scheduling. Higher order terms can only be a regressor candidate when the relevant lower order terms have already been included in the regression operation. For example α^5 can only be a candidate if α up to α^4 are already present in the regression. The structure of this priority scheduling can be found in fig. 5.5 and 5.6. The last topic to be discussed in this section are the three criteria which can interrupt the iteration procedure:

- The loop has to be ended when the set of candidate regressors is empty.
- The procedure needs to stop when the new candidate regressor to be added is equal to the last removed regressor.
- The iteration must terminate and go back one step once the PSE criterion starts increasing.

These three criteria guarantee that the iteration procedure is halted when an optimal solution has been obtained. The next section will discuss the results of the application of the MSWR procedure on a failure scenario.

5.2.5 Engine separation scenario as an example for model structure development

The concept of Modified Stepwise Regression has been applied on the engine separation scenario described in section A.2.4. This failure scenario has been flown in the benchmark simulation program, resulting in the trajectory shown in fig. 5.7(a). All sensor information is logged and used to construct the dimensionless force coefficient in X-direction C_X. The time history of this coefficient is plotted in fig. 5.7(b).

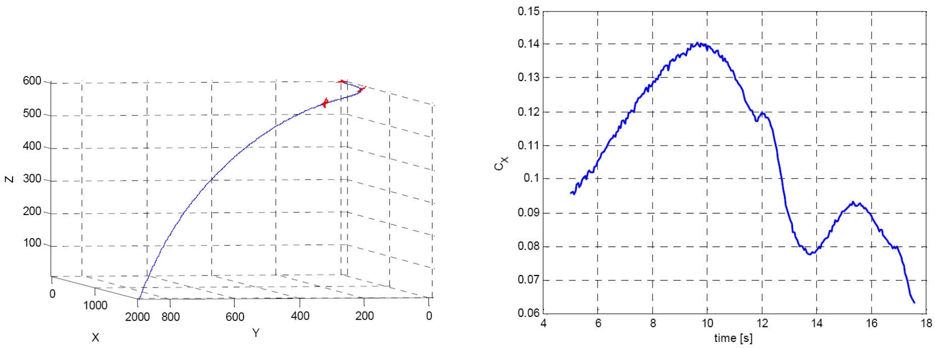

(a) trajectory of failed aircraft

(b) time history of the coefficient C_X

Figure 5.7: Simulation data of failed aircraft, EL AL scenario

The MSWR procedure as elaborated above has been used to approximate the time response of the coefficient C_X as shown in figure 5.8(b). Table 5.2 below presents the results obtained step by step by this procedure using ordinary least squares. The MSWR procedure has been applied on this scenario with three alternatives of least squares operation, namely ordinary least squares (OLS), weighted least squares (WLS) and total least squares (TLS). The results of these procedures can be found in table 5.3. Table 5.4 shows the final results for the monitoring criteria in all three procedures. There are no significant differences in the fitting properties, but WLS are found to result generally in smaller standard deviations for the estimated derivatives (except for a few irregularities), where TLS need a smaller amount of added regressors to achieve a similar fit, which leads to a significant lower final value for the PSE.

The figures below show the development of the procedure. Figure 5.8(a) shows the least squares regression result for the linear terms only, where fig. 5.8(b) shows the final

Table 5.2: Step by step results for the MSWR procedure for approximation of C_X, EL AL scenario

regressor	in/out	PRESS	PSE	fit error	R
$1, \alpha, \alpha^2, \frac{q\bar{c}}{V}, \delta_{e_{IR,IL,OR,OL}}, \delta_{sp_{2,10}}$	in	0.0012	$0.42 \cdot 10^{-5}$	0.0021	99.59%
$\frac{rb}{2V}$	in	0.0006	$0.23 \cdot 10^{-5}$	0.0015	99.79%
$\frac{pb}{2V}$	in	0.0003	$0.09 \cdot 10^{-5}$	0.0009	99.91%
$\alpha\frac{q\bar{c}}{V}$	in	0.0002	$0.08 \cdot 10^{-5}$	0.0009	99.92%
$\alpha\delta_{e_{IL}}$	in	0.0002	$0.08 \cdot 10^{-5}$	0.0009	99.92%
$\alpha\delta_{e_{OR}}$	in	0.0002	$0.06 \cdot 10^{-5}$	0.0008	$-$
$\alpha\frac{q\bar{c}}{V}$	out	$-$	$-$	$-$	99.95%
β^2	in	0.0002	$0.05 \cdot 10^{-5}$	0.0007	$-$
$\frac{pb}{2V}$	out	$-$	$-$	$-$	99.95%
$\alpha\beta^2$	in	0.0001	$0.05 \cdot 10^{-5}$	0.0007	99.95%
$\alpha\frac{q\bar{c}}{V}$	in	0.0001	$0.05 \cdot 10^{-5}$	0.0007	99.96%
β	in	0.0001	$0.04 \cdot 10^{-5}$	0.0007	99.96%
$\alpha\delta_{e_{IR}}$	in	0.0001	$0.04 \cdot 10^{-5}$	0.0006	$-$
$\alpha\delta_{e_{IR}}$	out	$-$	$-$	$-$	99.96%

Table 5.3: Final result for the different MSWR procedures for approximation of C_X, EL AL scenario

parameter	OLS		WLS		TLS	
	value	(σ)	value	(σ)	value	(σ)
1	-1.8373	(10%)	-1.7432	(7%)	-0.8828	(15%)
α	27.3024	(6%)	25.6535	(4%)	21.9603	(6%)
α^2	4.4212	(7%)	4.1049	(5%)	3.5746	(7%)
$\frac{q\bar{c}}{V}$	1.9673	(18%)	0.7801	(49%)	1.6622	(21%)
$\delta_{e_{IR}}$	-0.0021	(76%)	-0.0028	(36%)	0.0024	(67%)
$\delta_{e_{IL}}$	0.6345	(10%)	0.6040	(7%)	0.315	(15%)
$\delta_{e_{OR}}$	-1.0582	(10%)	-1.0007	(7%)	-0.5312	(14%)
$\delta_{e_{OL}}$	0.0025	(64%)	0.0028	(36%)	-0.0019	(84%)
δ_{sp_2}	-0.0002	(50%)	$4 \cdot 10^{-5}$	(250%)	-0.0003	(67%)
$\delta_{sp_{10}}$	-0.0002	(100%)	-0.0001	(100%)	-0.0005	(40%)
$\frac{rb}{2V}$	0.6992	(6%)	0.7107	(4%)	0.6145	(5%)
$\alpha\delta_{e_{IL}}$	-9.2575	(6%)	-8.6841	(4%)	-7.6195	(7%)
$\alpha\delta_{e_{OR}}$	15.1286	(6%)	14.1774	(4%)	11.8969	(6%)
β^2	1.9765	(14%)	2.2754	(10%)	0.3028	(14%)
$\alpha\beta^2$	-10.3953	(20%)	-11.6513	(14%)		
$\alpha\frac{q\bar{c}}{V}$	-34.2085	(15%)	-24.9563	(17%)	-17.8910	(27%)
β	0.0531	(23%)	0.0625	(17%)		
$\alpha\delta_{e_{IR}}$			0.0058	(24%)		

Table 5.4: Final result for monitoring data for the LS, TLS and WLS based MSWR procedures for approximation of C_X, EL AL scenario

parameter	LS MSWR	WLS MSWR	TLS MSWR
PRESS	0.0001	0.0001	0.0001
PSE	$4 \cdot 10^{-5}$	$4 \cdot 10^{-5}$	$5 \cdot 10^{-7}$
fit error	0.0006	0.0006	0.0007
R	99.96%	99.96%	99.95%

result after MSWR. Figure 5.8(c) shows the development of the monitoring criteria, where figure 5.8(d) shows the residual after the WLS based MSWR routine. It is apparent that the residual is very white noise like.

5.2.6 On-line adaptation of representative model structure

Since it has been found that Modified Stepwise Regression is a viable method to extend the model structure, the next step is to modify this routine to a piecewise sequential routine. Between two steps of the MSWR routine, RLS can still be used to evaluate the structure recursively. More precisely, the MSWR can be applied over fixed time intervals to determine the model structure, where its resulting structure and numerical results can be used as initial values and structure for the RLS procedure.

As illustrated in fig. 5.9, the first action after the occurrence of a failure is the continuation of the recursive least square calculations on every time instant measurement data are available, indicated by the dots. By ”resetting” the covariance matrices, as explained in section 4.7, in the recursive least squares calculation step of the two step method, new derivative values will be calculated in short term. When this recursive least square procedure does not lead to a better innovation signal after the least squares covariance matrices have converged to lower values, it can be concluded that no better result can be obtained with this fixed model structure. On that time instant, Δt seconds after the failure, all measurement data after the failure (indicated by the thick line and of which the starting point in time is marked by the above mentioned triggering) will be collected and analysed by the first modified stepwise regression calculation, indicated by the solid vertical thin line. After this calculation, a new model structure as well as new derivative values will be obtained. This structure will then be used from that point onward in the subsequent recursive least squares calculations (the subsequent dots). The MSWR calculated derivative values will serve as initial values for these subsequent recursive least squares calculations. Each time the covariance reset operation does not lead to an improved behaviour of the innovation signal, new MSWR calculations will be performed, indicated by the dashed vertical thin green lines. (However, this is not necessarily periodically.)

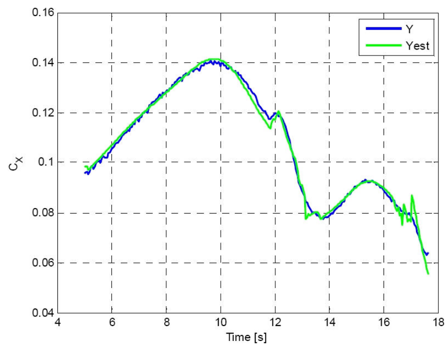

(a) WLS regression result, linear terms only

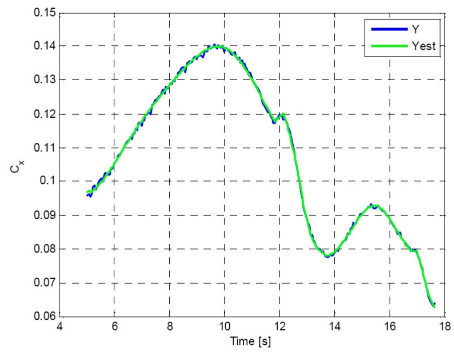

(b) WLS regression result after MSWR

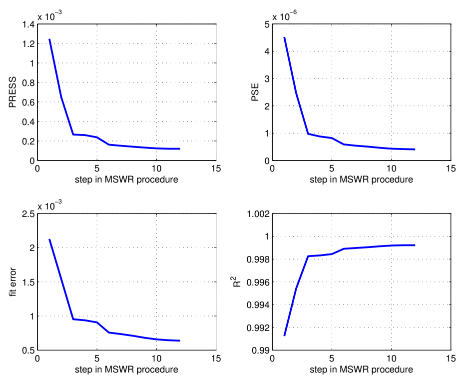

(c) monitoring criteria during WLS-MSWR

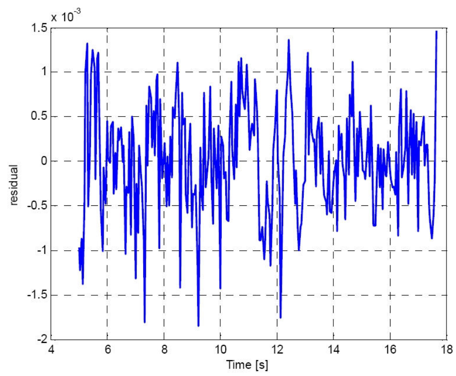

(d) residual after WLS-MSWR

Figure 5.8: Final result after WLS-MSWR based upon data of failed aircraft, EL AL scenario

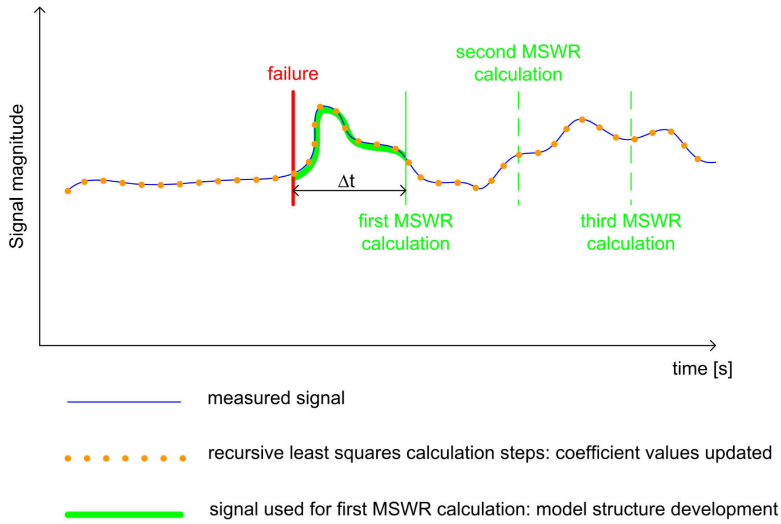

Figure 5.9: Illustration of the concept piecewise sequential modified stepwise regression

5.3 Adaptive recursive orthogonal least squares

An alternative algorithm for joint structure selection and parameter estimation is adaptive recursive orthogonal least squares (AROLS), which is based upon recursive orthogonal least squares. The concept of recursive orthogonal least squares has been introduced by Luo and Billings[94, 182, 183, 184], where the concept of structure selection has been highlighted. This is a very interesting and powerful routine, which can also be applied for damaged aircraft model identification, as explained above. However, for this aerospace application, some modifications are needed in the routine. Especially for on-line applications, it is important to include some protection against overfitting for computational speed and robustness considerations, which can be done by choosing an appropriate monitoring variable in the routine. Besides, in damaged situations, the physical system model changes abruptly and the routine must be rendered adaptive in order to deal with this varying structure. The objective of this section is to solve these problems and to elaborate a basic routine which is demonstrated for aerospace applications.

5.3.1 Principle of Orthogonal Least Squares

By augmenting the orthogonal decomposition techniques of Classical Gram-Schmidt and Modified Gram-Schmidt[63], simple and efficient SSPE algorithms that determine $\mathbf{\Phi}_s$, a subset of $\mathbf{\Phi}$, can be derived in a forward regression manner by choosing one column of $\mathbf{\Phi}$ for which the sum of squares of residuals is maximally reduced at a time in every step.

Assume that $\mathbf{\Phi}_s$ has m_s ($m_s \leq m$ and $m_s < n$) columns, where m and n are the numbers of columns and rows of $\mathbf{\Phi}$ respectively. Factorize $\mathbf{\Phi}_s$ into $\mathbf{Q}_s\mathbf{R}_s$, where $\mathbf{Q}_s$ is an $n \times m_s$ matrix consisting of m_s orthogonal columns and $\mathbf{R}_s$ is an $m_s \times m_s$ unit upper triangular matrix. This is commonly called a QR-factorization. The residuals are defined by

$$\hat{\boldsymbol{\xi}} = \begin{bmatrix} \hat{\xi}(1) \\ \vdots \\ \hat{\xi}(N) \end{bmatrix} = \mathbf{z} - \mathbf{\Phi}_s\hat{\boldsymbol{\theta}}_s = \mathbf{z} - \mathbf{Q}_s\left(\mathbf{R}_s\hat{\boldsymbol{\theta}}_s\right) = \mathbf{z} - \mathbf{Q}_s\mathbf{g}_s \tag{5.13}$$

Equation (5.13) can be rewritten as

$$\mathbf{z} = \mathbf{Q}_s\mathbf{g}_s + \hat{\boldsymbol{\xi}} \tag{5.14}$$

The sum of squares of the dependent variable $\mathbf{z}$ is therefore

$$\langle \mathbf{z}, \mathbf{z} \rangle = \sum_{i=1}^{M_s} g_i^2 \langle \mathbf{q}_i, \mathbf{q}_i \rangle + \left\langle \hat{\boldsymbol{\xi}}, \hat{\boldsymbol{\xi}} \right\rangle \tag{5.15}$$

The first term can be written as such thanks to the properties of the orthogonal columns of $\mathbf{Q}_s$. The error reduction ratio [err] due to $\mathbf{q}_i$ is thus defined as the proportion of the dependent variable variance explained by $\mathbf{q}_i$

$$[\mathrm{err}]_i = \frac{g_i^2 \langle \mathbf{q}_i, \mathbf{q}_i \rangle}{\langle \mathbf{z}, \mathbf{z} \rangle} = \frac{g_i^2 \langle \mathbf{q}_i, \mathbf{q}_i \rangle}{\sum_{i=1}^{M_s} g_i^2 \langle \mathbf{q}_i, \mathbf{q}_i \rangle + \left\langle \hat{\boldsymbol{\xi}}, \hat{\boldsymbol{\xi}} \right\rangle} \tag{5.16}$$

Equation (5.16) suggests a way of computing $\mathbf{Q}_s$ (and hence $\mathbf{\Phi}_s$) from $\mathbf{\Phi}$ by the CGS procedure. At the i^{th} stage, by interchanging the i to m columns of $\mathbf{\Phi}$ we can select a $\mathbf{p}_i$ which gives the largest $[\mathrm{err}]_i$ when orthogonalized into $\mathbf{q}_i$. The detailed procedure is as follows.

1. At the first step, for $1 \leq i \leq m$, compute

$$\mathbf{q}_1^{(i)} = \mathbf{p}_i \tag{5.17}$$

$$g_1^{(i)} = \frac{\left\langle \mathbf{q}_1^{(i)}, \mathbf{z} \right\rangle}{\left\langle \mathbf{q}_1^{(i)}, \mathbf{q}_1^{(i)} \right\rangle} \tag{5.18}$$

$$[\text{err}]_1^{(i)} = \frac{\left(g_1^{(i)}\right)^2 \left\langle \mathbf{q}_1^{(i)}, \mathbf{q}_1^{(i)} \right\rangle}{\langle \mathbf{z}, \mathbf{z} \rangle} \tag{5.19}$$

$$\text{Find } [\text{err}]_1^{(i_1)} = \max\left\{ [\text{err}]_1^{(i)},\ \ 1 \leq i \leq m \right\} \tag{5.20}$$

$$\text{Select } \mathbf{q}_1 = \mathbf{q}_1^{(i_1)} = \mathbf{p}_{i_1} \tag{5.21}$$

2. At the k^{th} step, where $k \geq 2$, compute for $1 \leq i \leq m, i \neq i_1, \ldots, i \neq i_{k-1}$

$$\left.\begin{array}{l} \alpha_{jk}^{(i)} = \frac{\mathbf{q}_j^T \mathbf{p}_i}{\mathbf{q}_j^T \mathbf{q}_j} \\ \mathbf{q}_k^{(i)} = \mathbf{p}_i - \sum_{j=1}^{k-1} \alpha_{jk}^{(i)} \mathbf{q}_j \end{array} \right\} \text{for } 1 \leq j < k \tag{5.22}$$

$$g_k^{(i)} = \frac{\left\langle \mathbf{q}_k^{(i)}, \mathbf{z} \right\rangle}{\left\langle \mathbf{q}_k^{(i)}, \mathbf{q}_k^{(i)} \right\rangle} \tag{5.23}$$

$$[\text{err}]_k^{(i)} = \frac{\left(g_k^{(i)}\right)^2 \left\langle \mathbf{q}_k^{(i)}, \mathbf{q}_k^{(i)} \right\rangle}{\langle \mathbf{z}, \mathbf{z} \rangle} \tag{5.24}$$

$$\text{Find } [\text{err}]_k^{(i_k)} = \max\left\{ [\text{err}]_k^{(i)},\ \ 1 \leq i \leq m, i \neq i_1, \ldots, i \neq i_{k-1} \right\} \tag{5.25}$$

3. Now select

$$\mathbf{q}_k = \mathbf{q}_k^{(i_k)} = \mathbf{p}_{i_k} - \sum_{j=1}^{k-1} \alpha_{jk}^{(i_k)} \mathbf{q}_j \tag{5.26}$$

4. The procedure is terminated at the m_s^{th} step when

$$1 - \sum_{j=1}^{m_s} [\text{err}]_j < \rho \tag{5.27}$$

where $0 < \rho < 1$ is the chosen tolerance. This leads to a subset model containing m_s basis functions in the descending order of dominance out of m total basis functions.

The term $1 - \sum_{j=1}^{m_s} [\text{err}]_j$ is the proportion of the unexplained dependent variable variance. The value of ρ determines how many terms will be included in the final submodel.

Generally the appropriate value of ρ is found by trial and error and can vary between different categories of data sample stretches and regressors.

5.3.2 Principle of Adaptive Recursive Orthogonal Least Squares

Recursive Orthogonal Least Squares are very similar to the classical OLS structure elaborated in section 5.3.1, but the procedure is rewritten in order to take into account a stepwise growing data matrix and vector of the dependent variable. SSPE by ROLS has been mentioned earlier by Luo, Billings et al[184], but the Adaptive Recursive Orthogonal Least Squares (AROLS) algorithm is a new development. In this chapter, the differences between ROLS and AROLS are shown. There are three crucial aspects which make AROLS different from regular ROLS. First another subset selection stopping criterion has been chosen instead of the normalized residual sum of squares $NRSS$. Reason for this change is the fact that the other criterion is better suited to protect against overfitting, as will be shown later. Secondly, the procedure has been modified in order to deal with possible collinearities between the several regressors. Finally, a last step has been added to make the routine adaptable for changes in the dynamics of the true system. The advantages of AROLS are also illustrated in the application examples, shown in sections 5.3.3 and 5.3.4.

This recursive procedure is based upon the property that the columns in the $\mathbf{R}$ matrix of a $\mathbf{QR}$ decomposition can be interchanged multiply and arbitrarily, as long as the product is compensated backwards by a proper permutation matrix.

This property can be proven as follows.

Proof. Suppose that $\mathbf{\Phi} = \mathbf{QR}$ and define $\mathbf{R}^{(1)} = \mathbf{R\Pi}_1$, where permutation matrix $\mathbf{\Pi}_1$ is orthonormal, so $\mathbf{\Pi}_1^{-1} = \mathbf{\Pi}_1^T$. Correspondingly

$$\mathbf{R} = \mathbf{R}^{(1)}\mathbf{\Pi}_1^{-1} = \mathbf{R}^{(1)}\mathbf{\Pi}_1^T \tag{5.28}$$

Since $\mathbf{R}^{(1)}$ is not purely upper triangular, it can be decomposed as

$$\mathbf{R}^{(1)} = \mathbf{Q}_N\mathbf{R}_N^{(1)} \tag{5.29}$$

Substituting all this for the original data matrix $\mathbf{\Phi}$ results in:

$$\mathbf{\Phi} = \mathbf{QR}^{(1)}\mathbf{\Pi}_1^T = \underbrace{\mathbf{QQ}_N}_{\mathbf{Q}^{(1)}}\mathbf{R}_N^{(1)}\mathbf{\Pi}_1^T \tag{5.30}$$

Now define the second permutation:

$$\mathbf{R}_N^{(2)} = \mathbf{R}_N^{(1)}\mathbf{\Pi}_2 \tag{5.31}$$

Correspondingly

$$\mathbf{R}_N^{(1)} = \mathbf{R}_N^{(2)}\mathbf{\Pi}_2^T \quad (5.32)$$

Since $\mathbf{R}_N^{(2)}$ is not purely upper triangular, it can once again be decomposed as

$$\mathbf{R}_N^{(2)} = \mathbf{Q}_{2N}\mathbf{R}_{2N}^{(2)} \quad (5.33)$$

Substituting all this for the original data matrix $\mathbf{\Phi}$ results in:

$$\mathbf{\Phi} = \underbrace{\mathbf{Q}^{(1)}\mathbf{Q}_{2N}}_{\mathbf{Q}^{(2)}}\mathbf{R}_{2N}^{(2)}\underbrace{\mathbf{\Pi}_2^T\mathbf{\Pi}_1^T}_{\mathbf{\Pi}_{\mathrm{tot}}^T} \quad (5.34)$$

The principle holds by recursion for more permutations. □

Exploiting this property, the ROLS algorithm works generally as itemized below. For each item, references are given to the steps of the detailed procedure which is given later.

- recursive orthogonalization (steps 1–2)
- ranking according to capability for fit error reduction and stepwise addition to the subset (steps 3–4)
- subset selection stopping criterion (step 5)
- subset parameter estimation (steps 6–7)
- subset selection necessity check (step 8)
- re-initialization necessity check (step 9)

In this general overview, it is important to realize that the criterion in step 8 triggers steps 4–6. If not needed, the subset selection steps are omitted and the algorithm focuses on the parameter estimation task in step 7. On the other hand, steps 3–5 form a structure ranking iteration procedure which is terminated by the criterion in step 5. A visual overview of the procedure can be found in fig. 5.10, where a clear distinction is made between the 'standard' steps to be performed under any circumstance, on the left, and the 'optional' steps on the right, of which the execution is triggered when needed. The detailed procedure of this algorithm is split up between an initialization phase and a recursive phase to be repeated for every time step.

INITIALIZATION

Generally the QR decomposition works as follows:

$\mathbf{z}(t) = \mathbf{\Phi}(t)\boldsymbol{\theta}(t) + \boldsymbol{\nu}(t)$

$\mathbf{\Phi}(t) = \mathbf{Q}(t)\mathbf{R}(t)$ with $\mathbf{Q}^T(t)\mathbf{Q}(t) = \mathbf{I}$ with $\mathbf{I}$ the identity matrix and $\mathbf{R}(t)$ upper triangular

Calculate: $\mathbf{v}(t) = \mathbf{Q}^T(t)\mathbf{z}(t)$ since $\mathbf{v}(t) = \mathbf{Q}^T(t)\mathbf{z}(t) = \mathbf{R}(t)\boldsymbol{\theta}(t) + \mathbf{Q}^T(t)\boldsymbol{\nu}(t)$

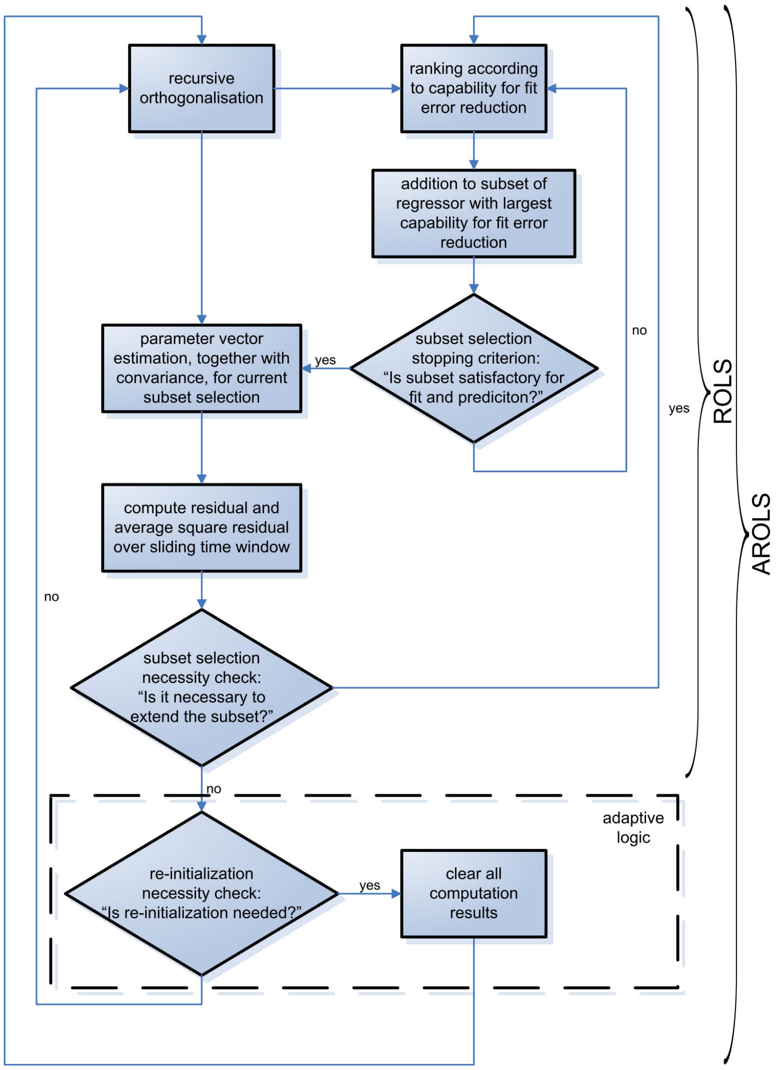

Figure 5.10: Overview of the steps of the AROLS procedure

As initialization, the following initial values can be defined: $\mathbf{R}(t-1) = \mathbf{I}_m$ and $\mathbf{v}_m(t-1) = \mathbf{0}_{m\times 1}$
Construct the augmented matrix:
$\mathbf{R}_{\text{aug}}(t-1) = \begin{bmatrix} \mathbf{R}(t-1) & \mathbf{v}_m(t-1) \\ \mathbf{0}_1 & \mathbf{0}_2 \end{bmatrix}$
$\mathbf{\Pi}_0 = \mathbf{I}_{m+1}$
TO BE REPEATED FOR EVERY TIME STEP

1. Multiply this augmented matrix with forgetting factor $\lambda^{1/2}$ and put the new data in a new row:

$$\mathbf{R}_{\text{aug}}(t) = \begin{bmatrix} \begin{bmatrix} \lambda^{1/2}\mathbf{R}(t-1) & \lambda^{1/2}\mathbf{v}_m(t-1) \end{bmatrix} \\ \begin{bmatrix} \phi_1(t), \ldots, \phi_m(t) & z(t) \end{bmatrix} \mathbf{\Pi}_{\text{tot}} \end{bmatrix} \tag{5.35}$$

2. Using Givens rotations produce the new augmented matrix:

$$\mathbf{R}_{\text{aug}_{\text{new}}}(t) = \begin{bmatrix} \mathbf{R}(t) & \mathbf{v}_m(t) \\ \mathbf{0}_1 & \mathbf{0}_2 \end{bmatrix} \tag{5.36}$$

3. When the j^{th} regressor is being selected, compute $v^2_{m(p)}(t), p = j, \ldots, m, j \geq 1$ based upon the updated values $\mathbf{v}_m(t)$ in equation (5.36) and choose the k^{th} optimal regressor with the maximum $v^2_{m(p)}(t), p = j, \ldots, m$ for the j^{th} position by earmarking the appropriate column of $\mathbf{R}(t)$.

4. This step can be skipped in the case that $j = k$.
According to the result from the previous step, as the k^{th} variable has been selected, exchange the positions of the current j^{th} and k^{th} columns of $\mathbf{R}(t)$ and then retriangularize $\mathbf{R}(t)$ and rotate $\mathbf{v}_m(t)$ via $\mathbf{QR}$.[1] Mind that $j \leq k$. Define permutation matrix $\mathbf{\Pi}_{jk}$ accordingly:
$$\mathbf{\Pi}_{jk} = \begin{bmatrix} \mathbf{I}_{j-1,j-1} & & & & \mathbf{0}_{j-1,m-k+1} \\ & 0_{j,j} & & 1_{j,k} & \\ & & \mathbf{I}_{k-j,k-j} & & \\ & 1_{k,j} & & 0_{k,k} & \\ \mathbf{0}_{m-k+1,j-1} & & & & \mathbf{I}_{m-k+1,m-k+1} \end{bmatrix}$$
and compute the total permutation matrix as the product of all individual permutation matrices $\mathbf{\Pi}_{\text{tot}} = \prod(\mathbf{\Pi}_{jk})$

5. Evaluate a subset selection stopping criterion and perform the next step if this condition is satisfied, otherwise return to step 3 to select more regressors. There are some

[1] Mind that calculating $\mathbf{Q}$ is not necessary here. All required information is contained in the upper triangular $\mathbf{R}$. This saves a considerable amount of computational load, since the size of $\mathbf{Q}$ increases with the number of data samples and the dimensions of $\mathbf{R}(t)$ are invariant.

alternatives for this subset selection stopping criterion, and this subject is elaborated further in a later stage.

6. Suppose that m_s regressors have been selected, then the computational augmented matrix is:

$$\mathbf{R}_{\text{aug}}(t) = \begin{bmatrix} r_{11}(t) & \cdots & \cdots & r_{1,m_s}(t) & \cdots & r_{1,m-1}(t) & v_1(t) \\ 0 & \ddots & & \vdots & & \vdots & \vdots \\ \vdots & \ddots & \ddots & \vdots & & \vdots & \vdots \\ \vdots & & 0 & r_{m_s,m_s}(t) & & \vdots & v_{m_s}(t) \\ \vdots & & & 0 & \ddots & \vdots & \vdots \\ \vdots & & & \vdots & \ddots & r_{m-1,m-1}(t) & v_m(t) \\ 0 & \cdots & \cdots & 0 & \cdots & 0 & 0 \end{bmatrix} \tag{5.37}$$

7. Using back-substitution solve for the parameters $\hat{\theta}_i(t), i = 1, \ldots, m_s$ from $\mathbf{R}_{m_s}(t)$, which is the top-left triangular portion of the final $\mathbf{R}_{\text{aug}}(t)$, and $\mathbf{v}_{m_s}(t)$ which consists of the first m_s elements of $\mathbf{v}_m(t)$. The standard deviation can be calculated by exploiting the property that $\left(\mathbf{\Phi}_s^T \mathbf{\Phi}_s\right)^{-1} = \left(\mathbf{R}_{m_s}^T \mathbf{Q}_s^T \mathbf{Q}_s \mathbf{R}_{m_s}\right)^{-1} = \left(\mathbf{R}_{m_s}^T \mathbf{R}_{m_s}\right)^{-1}$

8. Compute the residual at the time instant t, $\boldsymbol{\varepsilon}(t) = \mathbf{z}(t) - \sum_{i=1}^{m_s} \boldsymbol{\phi}_i(t)\hat{\theta}_i(t)$. This result is used to calculate the average square residual in the sliding time window M_s: $\overline{\varepsilon_{M_s}^2}(t) = \frac{1}{M_s} \sum_{i=0}^{M_s-1} \varepsilon^2(t-i)$, with typically $M_s = 20 - 100$ (choice here: 50). If the average square residual is below the predefined threshold $\overline{\varepsilon_{M_s}^2}(t) \leq \xi_{M_{s_1}} = 0.2$, then steps 4 to 6 can be omitted and m_s remains unchanged. If average residual exceeds predefined threshold, steps 4 to 6 need to be performed again.

9. If average square residual exceeds second more relaxed threshold $\overline{\varepsilon_{M_s}^2}(t) \geq \xi_{M_{s_2}} = 0.3$ and if the standard deviation of all coefficients is below a predefined third threshold $\sigma_j < {\xi_{M_{s_3}}}^2$, then all previous measurement data can be ignored and the procedure has to start over again. The motivation for this is the fact that for higher values of standard deviations, structure selection is most appropriate. If the standard deviations are low and the average square residual exceeds a predefined threshold, one obtains an indication that the true system dynamics have changed compared to the previous situation.

[2]This indicates a low level of uncertainty. Based upon the data content used until now, an accurate estimate has been obtained.

The last step can be omitted when one considers invariant nonlinear systems, like an aircraft performing a rapid manoeuvre in the same region of the flight envelope. However, when the nonlinear system can change suddenly in time, e.g. a damaged aircraft, one should ignore the data before the change, since they are not representative anymore for the actual current nonlinear system. This is the purpose of the last step.

The last remaining topic in this algorithm setup to be discussed is the subset selection stopping criterion. Several criteria can be used for this purpose. Section 5.2 mentioned in this respect already the predicted sum of squares $PRESS$, the predicted square error PSE, the coefficient of determination R^2 and the fit error. In section 5.2, these metrics have been evaluated, and it has been found that the Predicted Square Error PSE was preferable for off-line applications of subset selection and parameter estimation on batch stretches of data because of its clear optimum and its transparent breakup in an underfitting and an overfitting penalty term.

Verification if $PSE_{j-1} - PSE_j$ remains below a certain criticality threshold $\varepsilon_{\text{crit}_1}$ (here chosen as $\varepsilon_{\text{crit}_1} = 1 \cdot 10^{-5}$) serves here too as a satisfactory subset selection termination criterion. Use of this criterion for on-line applications has shown to work well for examples with a known structure and for dimensionless forces of a significant magnitude (such as C_Z in the example in section 5.3.4). However, it has been found that dimensionless moments (such as C_l and C_n in the example in section 5.3.4) generally have lower orders of magnitude, leading to even lower $MSFE$ values in the PSE criterion from the start onward. As a result, it has been observed in the experiments that the overfit penalty term has a higher relative weight and use of the PSE for these types of dependent variables leads generally to an underfitted solution for the subset selection.

Therefore, an alternative criterion has been searched for, which still has the same structure of a data fitting and an overfitting penalty term. Miller[196] gives a good overview of candidate critics. Possible candidates are:

- Akaike's Information Criterion AIC[16, 17, 18]:

$$AIC_j(\alpha) = N \ln(MSFE_j) + \alpha p, \qquad \alpha > 0 \tag{5.38}$$

- Schwarz criterion or Bayesian Information Criterion BIC[237] can be considered as a specific case of the AIC where $\alpha = \ln(N)$, which is defined under the assumptions that the data distribution is in the exponential family. The BIC's penalty term for additional parameters is stronger than that of the AIC.

$$BIC_j(\alpha) = N \ln(MSFE_j) + p \ln(N) \tag{5.39}$$

Because of its stronger penalty term, the BIC has been preferred for application in the

AROLS algorithm. Experiments have shown that this criterion does not suffer from the previously mentioned underfitting tendency for the dimensionless moments, as occurs for the PSE. The same threshold principle has been used for this metric as explained previously for the PSE.

The potential of this routine is shown in a few examples in the next sections. First, the algorithm procedure is illustrated on a dataset with a known system structure in section 5.3.3 using the PSE. Subsequently, AROLS is applied on an aerodynamic model data set in section 5.3.4 with the BIC.

5.3.3 Application to a data set from a known system structure

Three examples illustrate the possibilities of AROLS. The first involves a non-changing model. The second is a gradually changing model where the final is an abrupt changing model. There is a significant difference between both how the AROLS system deals with them.

5.3.3.1 The case of a non-changing model

The true system is defined as follows:

$$\begin{aligned} y_{\text{meas}} &= -0.5x_0 - x_1 + 5x_2 + 2x_1x_2 + 3x_2x_4 + 0.02x_2^2 + v \\ v &= 5\% \text{ white noise} \end{aligned} \tag{5.40}$$

The following regressors are included as candidate regressors in the data matrix $\mathbf{\Phi}$:

- linear: x_0, x_1, x_2, x_3, x_4,
- nonlinear: $x_5 = x_1x_2$, $x_6 = x_2x_4$, $x_7 = x_1x_3$, $x_8 = x_1x_4$, $x_9 = x_2^2$

Applying the AROLS routine to this data set leads to the results as shown in fig. 5.11. As can be seen in this figure, the fit is very accurate. The optimal residual, which is updated over the entire time history at every time step, resembles white noise very closely. The real residual is the actual residual at every time step, without a posteriori update. Except for two major exceptions, it confirms the accuracy too. Significant deviations are visible in two time intervals, namely initially up to step 50 and between steps 200 and 300. The first interval is needed for initialisation. During the second interval, the regressors which are only significant in the longer term become apparent. In this interval, the structure selection procedure is activated, as will be shown later. The lowest subfigure shows the coefficient estimates and their standard deviations, which is also shown in table 5.5. These estimates are indeed very accurate. Only regressor x_2^2 is left out, since its influence is too small to be

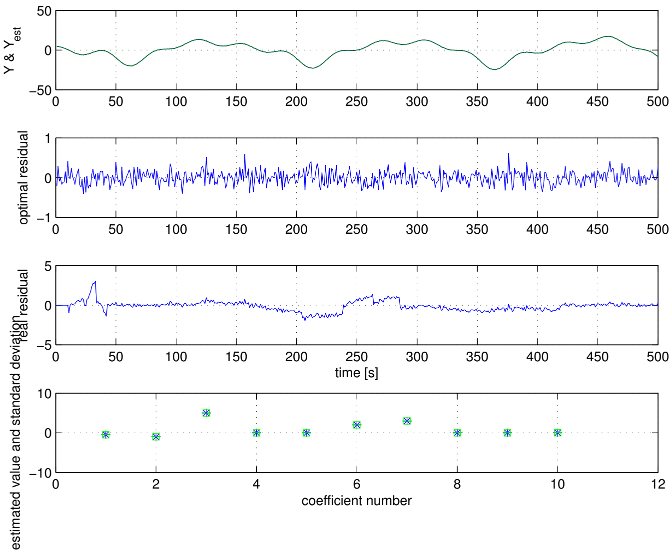

Figure 5.11: Results AROLS for non changing model

Table 5.5: SSPE results for non changing model

regressor	true	estimated	(σ)
x_0	-0.5	-0.4754	(5%)
x_1	-1	-1.0015	(1%)
x_2	5	5.0087	$(\approx 0\%)$
x_3	–	–	–
x_4	–	–	–
x_1x_2	2	2.0001	$(\approx 0\%)$
x_2x_4	3	2.9863	(1%)
x_1x_3	–	–	–
x_1x_4	–	–	–
x_2^2	0.02	–	–

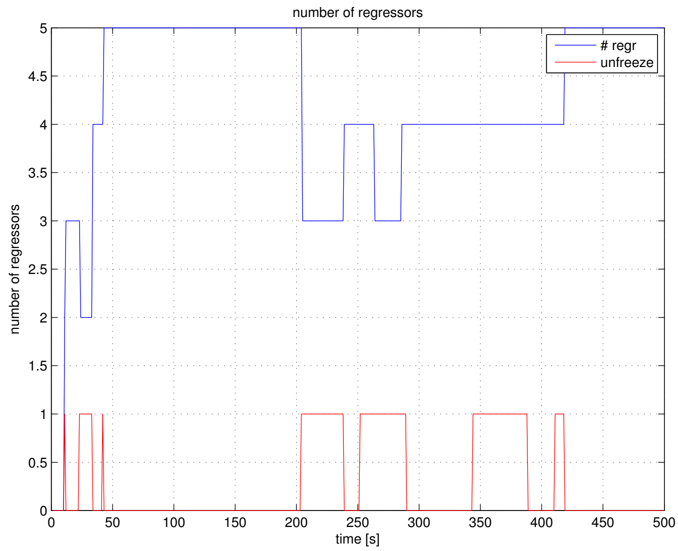

Figure 5.12: Number of regressors included

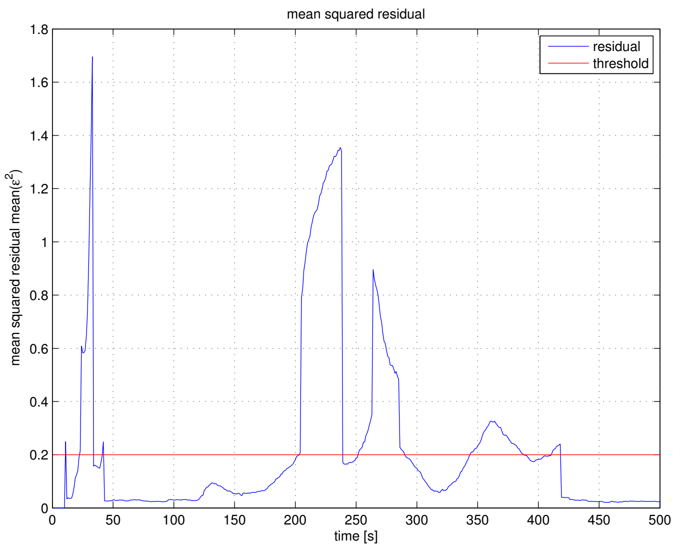

Figure 5.13: Triggering of structure selection procedure

sensible. This confirms the compliance with the principle of parsimony: the model is made as compact as possible.

Figure 5.12 shows the number of regressors that have been included in the regression at every time instant. It also illustrates at which time instants the structure selection procedure is active. Comparing these structure selection windows with the average square residual in fig. 5.13 shows the corresponding triggering. From fig. 5.12 it can be that there are two major structure selection time intervals, namely the initial 50 steps and the steps between 200 and 300.

Analysis of the required computational time for every time step has shown that the structure selection procedure is indeed much more computationally intensive, and thus should be resticted to the time windows only when it is strictly needed. This advocates the use of the PSE criterion to activate steps 3 to 6 in the routine instead of running them straightaway at every time step. This saves a lot of computational time. Moreover, validation tests have confirmed the accuracy of the $\mathbf{QR}$ approximation of the data matrix after these repeated permutations.

Figures 5.14 show the results of the statistical consistency analysis. These figures give the fitting errors between the true parameters and the parameter estimates $\epsilon_i = x_i - \hat{x}_i$, for $i = 1, \ldots, 10$, together with the standard deviations of the parameter estimates σ_i. From the plots 5.14(a) and 5.14(c), it can be seen that the conventional method to analyse the consistency of the estimates, i.e. the fit errors should be inside the standard deviation bounds for 67% of the time, holds only after the structure selection process has been terminated. In figures 5.14(b) and 5.14(d), it can be observed that the parameter estimates are consistent in this phase, except for ϵ_{10}, which is not included in the selected structure.

The beneficial influence of the structure selection algorithm is also visible in the degree of ill-conditioning of the Fisher matrix, as introduced in chapter 3. The covariance matrix condition number of the complete corresponding data matrix, thus without structure selection, is $\kappa_{\text{full}} = 194.55$. On the other hand, after structure selection, the corresponding condition number for the reduced data matrix with only 5 columns is $\kappa_{\text{structsel}} = 35.31$. Comparing these values illustrates that structure selection eliminates ill-conditioning issues.

Finally, a statistical error analysis has been performed, by investigating the stochastic properties of the innovation or residual $\boldsymbol{\epsilon} = \mathbf{z} - \Phi\hat{\boldsymbol{\theta}}$. Two residuals can be found in this setup: the real residual ϵ_{real} and the optimal residual $\epsilon_{\text{optimal}}$, as defined previously. The real residual has the following values for mean and standard deviations: $\mu_{\text{real}} = -0.1208$ and $\sigma_{\text{real}} = 0.6133$ respectively. Since the optimal residual is optimized over the entire time span, its statistical properties are significantly improved compared to the real residual, $\mu_{\text{optimal}} = -6.4726 \cdot 10^{-17}$ and $\sigma_{\text{optimal}} = 0.1705$. The optimal residual resembles white noise closely. As a benchmark, the statistical properties of the process noise in this process are: $\mu_{\text{noise}} = -0.0146$ and $\sigma_{\text{noise}} = 0.1696$. Figures 5.15 show the probability distribution of real and optimal residual, based upon a histogram as well as a bell curve defined by the aforementioned mean and standard deviation values. As a comparison basis, figure 5.16

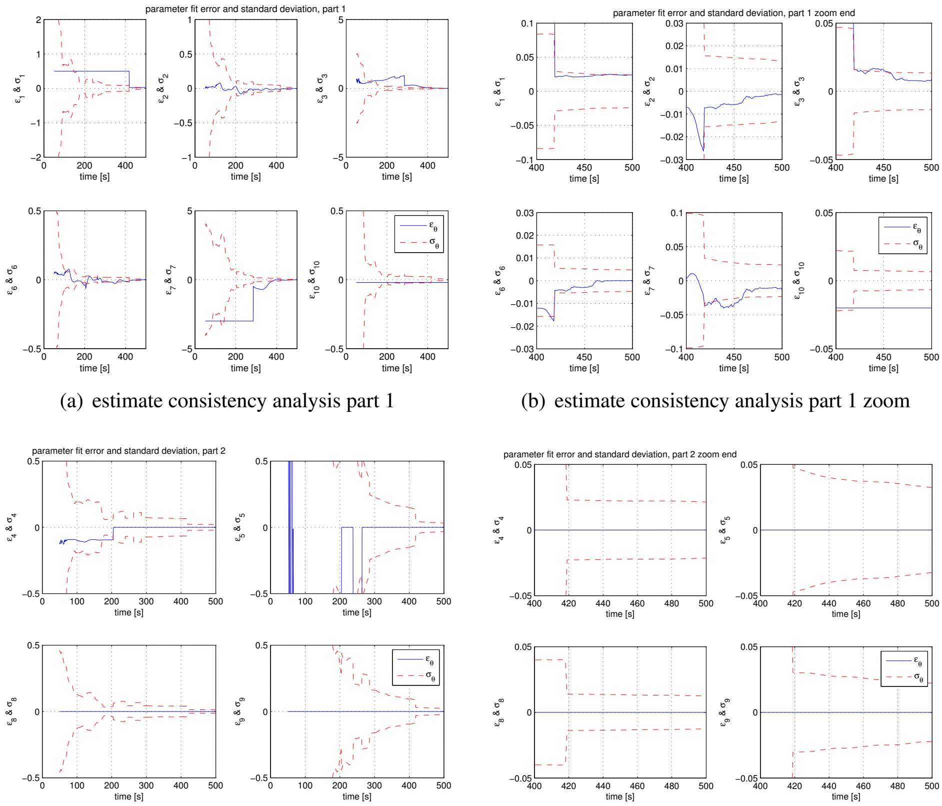

(a) estimate consistency analysis part 1

(b) estimate consistency analysis part 1 zoom

(c) estimate consistency analysis part 2

(d) estimate consistency analysis part 2 zoom

Figure 5.14: Analysis of the statistical consistency of the estimates

shows the probability distribution of the process noise. There is only a small difference between the distributions for the process noise and the optimal residual in figures 5.16 and 5.15(b) respectively.

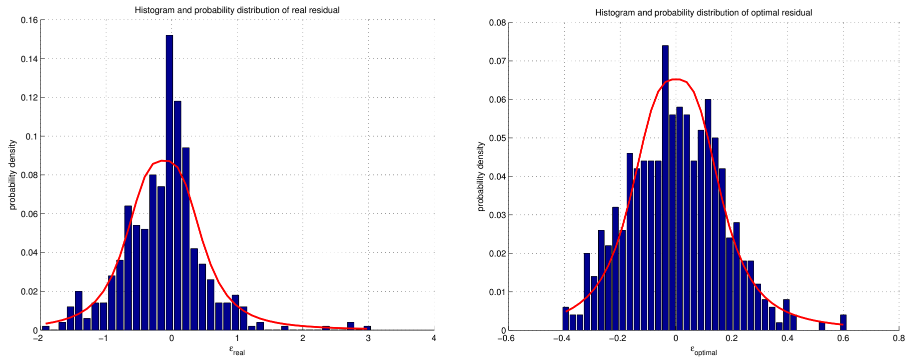

(a) real residual probability distribution (b) optimal residual probability distribution

Figure 5.15: Statistical error analysis

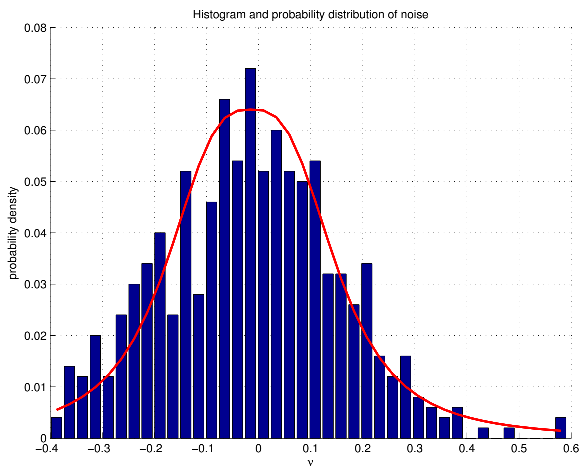

Figure 5.16: Noise probability distribution

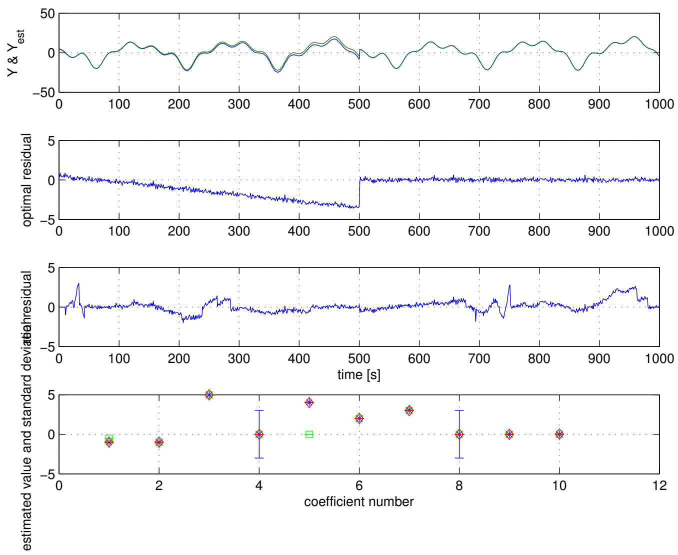

Figure 5.17: Results AROLS for gradually changing model

5.3.3.2 The case of a gradually changing model

The same true system is used as previously defined, but after 500s the model structure changes gradually. This means that the initial model structure is capable to fit the new model well until the difference exceeds the sensitivity threshold. This gradual change is caused by regressor x_4, which is linear. The model structure and estimation result can be seen in table 5.6. The model change is activated at timestep 500, but the gradually increasing influence of this regressor is only detected close to timestep 700, as can be seen in fig. 5.18. However, analysis of the optimal residual in fig. 5.17 reveals the true time instant when the change occurred. Mind that the trend in the optimal residual before time instant 500 is caused by the change in the model structure: this residual is calculated over the entire time span with the final identified model. The true residual confirms the linear influence of regressor x_4 between timesteps 500 and 700. Figure 5.19 confirms the triggering routine. The gradual inflow of excitation data promotes the decrease in the standard deviation, which ends up below threshold $\xi_{M_{s_3}}$ after timestep 400. The change starting at timestep 500 starts building up in the average squared residual and crosses the second higher sensitivity threshold $\xi_{M_{s_2}}$ close to timestep 700. The choice of the thresholds is a tradeoff between sensitivity and computational load.

The statistical consistency analysis plots in figure 5.20 focus on the time span after change, since the situation before the change is identical as in the previous example. Most of the parameter estimates are consistent, although there is only a very little time span available

Table 5.6: SSPE results for gradually changing model

		prior change			post change	
	true	estimated	(σ)	true	estimated	(σ)
x_0	-0.5	-0.4754	(5%)	$-\mathbf{1}$	-1.0004	(2%)
x_1	-1	-1.0015	(1%)	-1	-1.0064	(2%)
x_2	5	5.0087	$(\approx 0\%)$	5	4.9723	$(\approx 0\%)$
x_3	–	–	–	–	–	–
x_4	–	–	–	$\mathbf{4}$	4.0279	(1%)
x_1x_2	2	2.0001	$(\approx 0\%)$	2	(1.9986)	$(\approx 0\%)$
x_2x_4	3	2.9863	(1%)	3	(3.0357)	(1%)
x_1x_3	–	–	–	–	–	–
x_1x_4	–	–	–	–	–	–
x_2^2	0.02	–	–	0.02	–	–

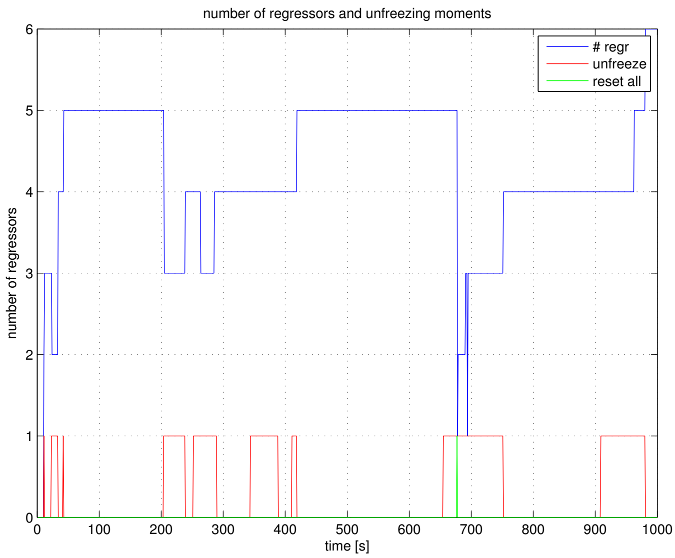

Figure 5.18: Number of regressors included

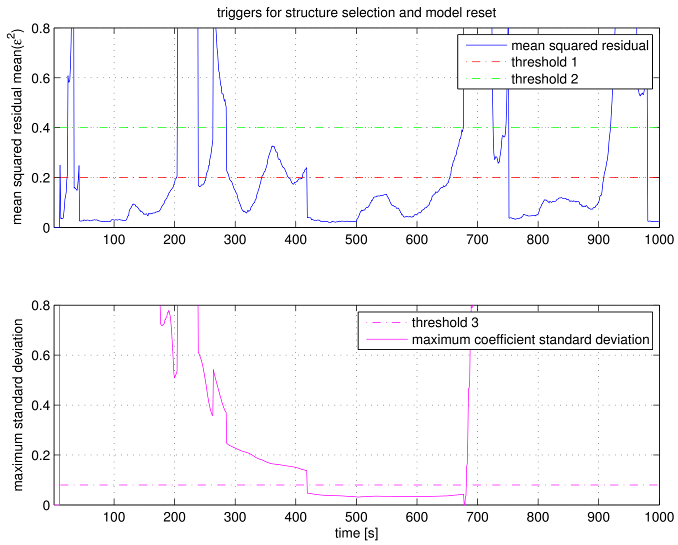

Figure 5.19: Triggering of structure selection procedure

to perform this analysis, since the structure selection procedure takes until approximately $t = 980s$, as can be seen in figure 5.18.

The improvement that structure selection brings in the ill-conditioning of the data matrices can be analysed by means of the condition number of the covariance matrices, similarly as done previously: $\kappa_{\text{full}} = 2.3775 \cdot 10^6$ and $\kappa_{\text{structsel}} = 197.3723$. The statistical error analysis provides the following numerical results for both residuals: $\mu_{\text{real}} = 0.0111$ and $\sigma_{\text{real}} = 0.7614$ and $\mu_{\text{optimal}} = 0.0072$ and $\sigma_{\text{optimal}} = 0.1725$. The probability distributions of the residuals are presented in fig. 5.21 in an analogous way as for the previous example.

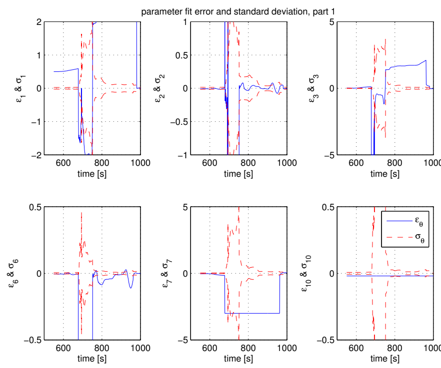

(a) estimate consistency analysis part 1

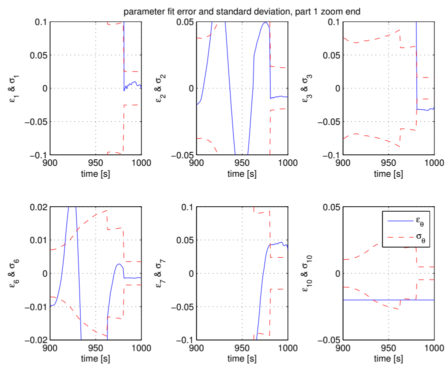

(b) estimate consistency analysis part 1 zoom

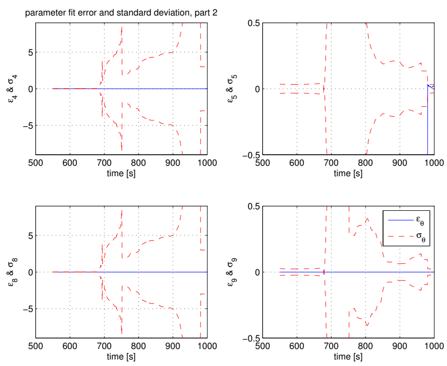

(c) estimate consistency analysis part 2

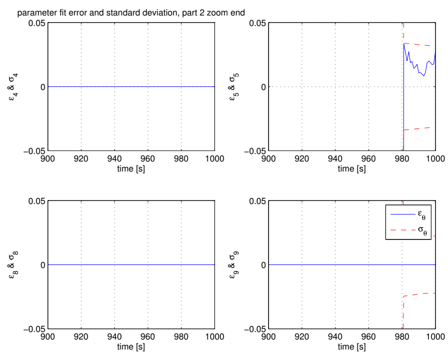

(d) estimate consistency analysis part 2 zoom

Figure 5.20: Analysis of the statistical consistency of the estimates

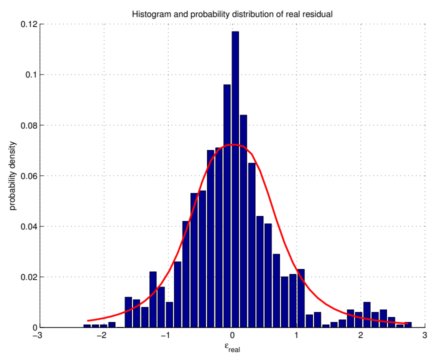

(a) real residual probability distribution

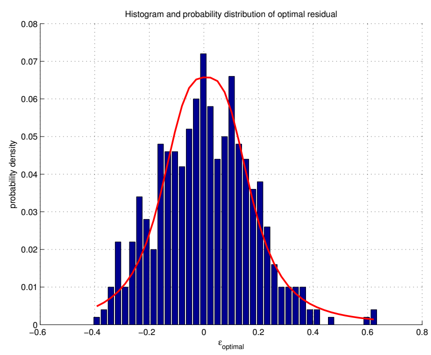

(b) optimal residual probability distribution

Figure 5.21: Statistical error analysis

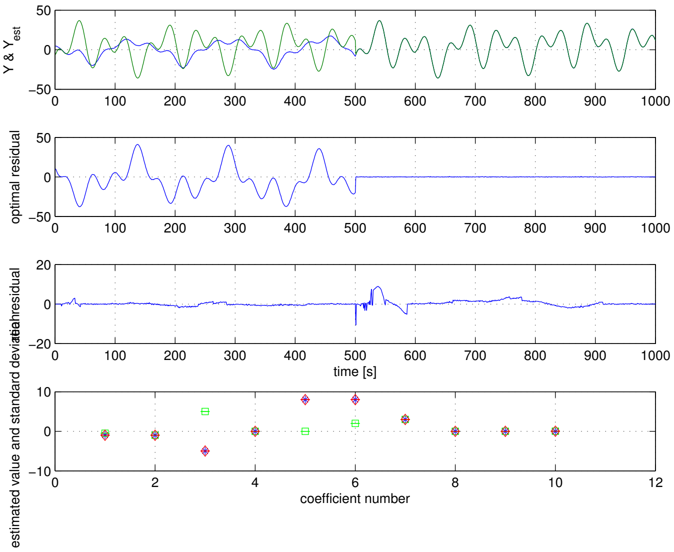

Figure 5.22: Results AROLS for abrupt changing model

5.3.3.3 The case of an abruptly changing model

The same true system is used as previously defined, but after 500s the model structure changes abruptly. This means that the initial model structure is not capable to fit the new model anymore from the first time step after the change since the difference exceeds the sensitivity threshold immediately. This abrupt change is caused by the combined influence of regressors x_2, x_4, and x_1x_2 which is nonlinear. The model structure and estimation result are shown in table 5.7. The model change is activated at timestep 500, and is detected immediately, as can be seen in fig. 5.23. Mind that the non-white noise behaviour in the optimal residual before time instant 500 is caused by the change in the model structure: this residual is calculated over the entire time span with the final identified model. The true residual confirms the adaptation to the new model structure between timesteps 500 and 600. Figure 5.24 confirms the triggering routine, where the average squared residual crosses the second higher sensitivity threshold $\xi_{M_{s_2}}$ immediately after the change, in contrast with the slow increase in fig. 5.19. Also here, the estimated parameter values are accurate and the amount of parameters is parsimonial.

The statistical consistency analysis plots in figure 5.25 focus on the time span after change, analogously as in the previous example. Most of the parameter estimates are consistent.

Table 5.7: SSPE results for abrupt changing model

	prior change			post change		
	true	estimated	(σ)	true	estimated	(σ)
x_0	-0.5	-0.4754	(5%)	$-\mathbf{1}$	-0.9751	(2%)
x_1	-1	-1.0015	(1%)	-1	-1.0015	(1%)
x_2	5	5.0087	$(\approx 0\%)$	$-\mathbf{5}$	-4.9902	$(\approx 0\%)$
x_3	–	–	–	–	–	–
x_4	–	–	–	$\mathbf{8}$	8.0005	$(\approx 0\%)$
x_1x_2	2	2.0001	$(\approx 0\%)$	$\mathbf{8}$	8.0001	$(\approx 0\%)$
x_2x_4	3	2.9863	(1%)	3	2.9846	$(\approx 0\%)$
x_1x_3	–	–	–	–	–	–
x_1x_4	–	–	–	–	–	–
x_2^2	0.02	–	–	0.02	–	–

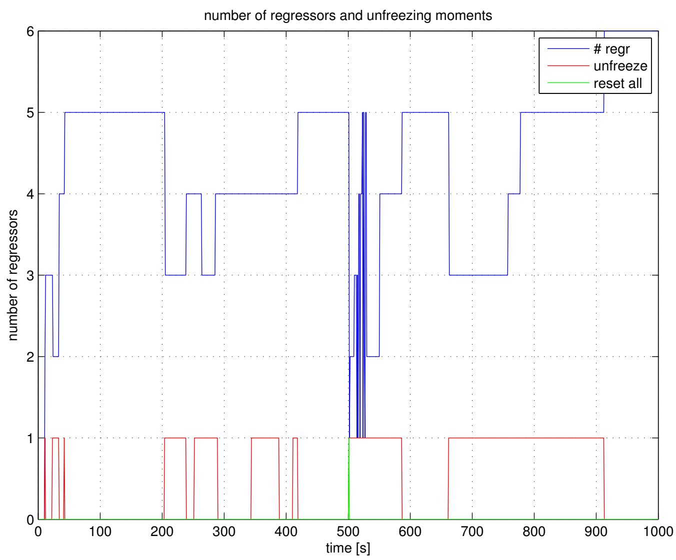

Figure 5.23: Number of regressors included

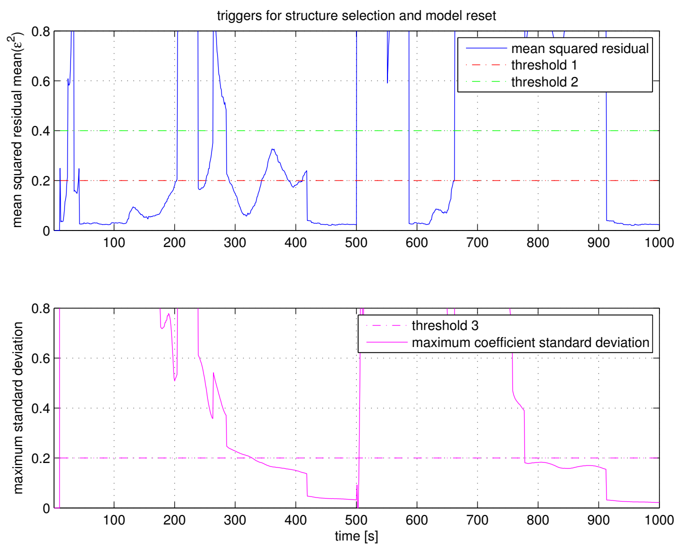

Figure 5.24: Triggering of structure selection procedure

The improvement that structure selection brings in the ill-conditioning is illustrated similarly as done previously: $\kappa_{\text{full}} = 157.25$ and $\kappa_{\text{structsel}} = 61.55$. The statistical error analysis provides the following numerical results for both residuals: $\mu_{\text{real}} = 0.1677$ and $\sigma_{\text{real}} = 1.5652$ and $\mu_{\text{optimal}} = -4.114 \cdot 10^{-4}$ and $\sigma_{\text{optimal}} = 0.1705$. The probability distributions of the residuals are presented in fig. 5.26 similarly as for the previous examples.

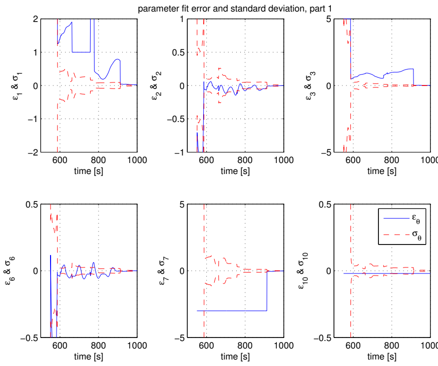

(a) estimate consistency analysis part 1

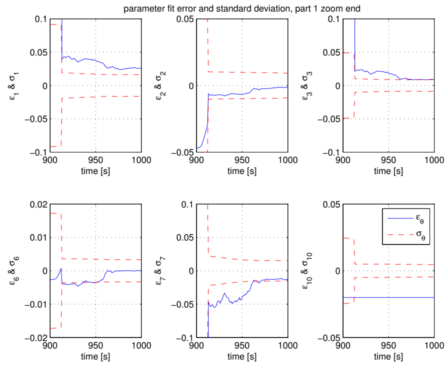

(b) estimate consistency analysis part 1 zoom

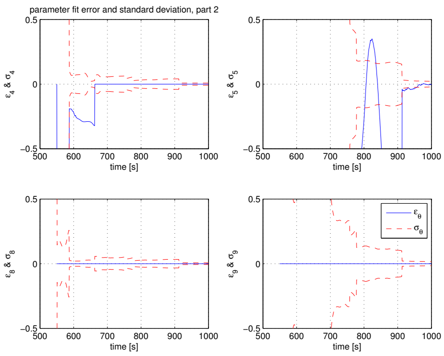

(c) estimate consistency analysis part 2

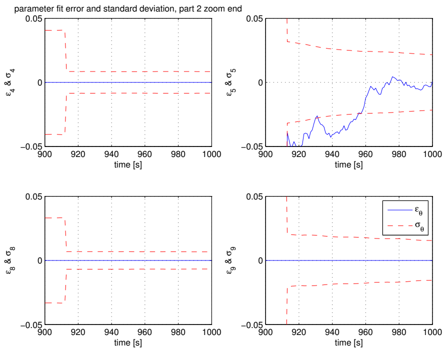

(d) estimate consistency analysis part 2 zoom

Figure 5.25: Analysis of the statistical consistency of the estimates

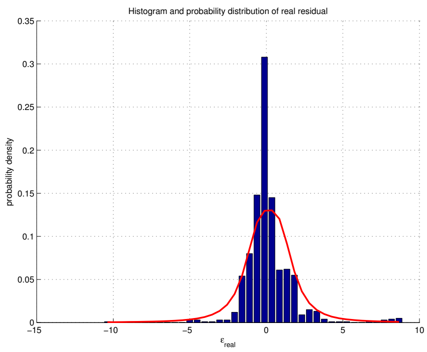

(a) real residual probability distribution

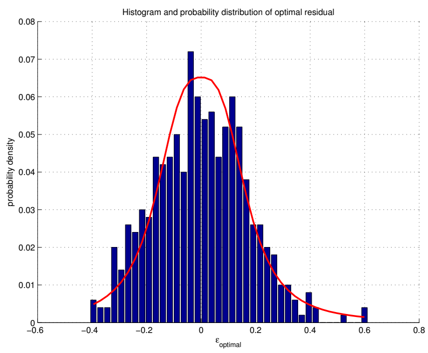

(b) optimal residual probability distribution

Figure 5.26: Statistical error analysis

5.3.4 Application to an aerodynamic model data set

As for the MSWR example, also AROLS has been applied on the engine separation scenario. As already mentioned above, the aerodynamic model structure must be selected while the model parameters are being estimated. This is one of the main advantages of the recursive orthogonal least squares. Before this model structure selection can be set up, a pool of regressor candidates needs to be defined, i.e. independent variables which are candidates to be included in the structure.

As an example, the dimensionless force coefficient in the body Z-axis can be analysed. Following the literature[157], the following aircraft state based independent variables can be treated as model regressor candidates. Besides the usual linear independent variables which occur also in the regular aerodynamic models, there are also nonlinear symmetrical regressor candidates. In case of asymmetric damage, also asymmetrical nonlinear regressor candidates need to be taken into account. These categories contain the following regressors:

- conventional linear independent variables: 1, α, $\frac{q\bar{c}}{V}$ and control surface deflections such as δ_e
- nonlinear symmetrical regressor candidates: $\alpha^2, \alpha^m, \alpha\frac{q\bar{c}}{V}, \alpha\delta_e \quad m = 3, \ldots, 8$
- asymmetrical nonlinear regressor candidates:
  $\beta, \frac{pb}{2V}, \frac{rb}{2V}, \alpha\beta, \alpha\beta^2, \alpha^2\beta, \alpha\beta^3, \alpha^2\beta^3, \alpha\frac{pb}{2V}, \alpha\frac{rb}{2V}, \alpha^2\frac{pb}{2V}, \alpha^2, \frac{rb}{2V}, \beta^n \quad n = 2, \ldots, 5$

Also the dimensionless moment coefficients C_l and C_n can be analysed. Taking into account the same categorization as previously, but this time for the lateral setup, one obtains:

- conventional linear independent variables: β, $\frac{pb}{2V}$, $\frac{rb}{2V}$ and control surface deflections such as δ_a and δ_r
- nonlinear asymmetrical regressor candidates:
  $\alpha\beta, \alpha\beta^2, \alpha^2\beta, \alpha\beta^3, \alpha^2\beta^3, \alpha\frac{pb}{2V}, \alpha\frac{rb}{2V}, \alpha^2\frac{pb}{2V}, \alpha^2\frac{rb}{2V}, \beta^n \quad n = 2, \ldots, 5$
- symmetrical nonlinear regressor candidates: 1, α, $\frac{q\bar{c}}{V}, \alpha^2, \alpha^m, \alpha\frac{q\bar{c}}{V}, \alpha\delta_e \quad m = 3, \ldots, 8$

Especially in the case of aircraft with a large set of control surfaces, like the Boeing 747, it is possible that control surfaces deflect identically or linear dependently, e.g. $\delta_{e_{ol}} = \delta_{e_{or}}$ and $\delta_{e_{il}} = \delta_{e_{ir}}$. Nevertheless, all must be included in the regressor set, since the linear dependency can be lost after a control surface failure. Therefore, all of them are included in the candidate regressor set, but the maximum $v^2_{m(p)}(t), p \in \mathcal{P}$ in step 3 of the ROLS algorithm is only selected out of a subset $\mathcal{P}$, consisting of the columns corresponding with the remaining entries in a row reduced echelon form of the upper triangular matrix. In this way, one can avoid collinearities in the identification result.

Fig. 5.27 shows the time histories of the calculated dimensionless forces and moments coefficients together with the corresponding trajectory of the simulated engine separation scenario. These data will be used for the application of AROLS in the subsequent sections. The engine separation failure is triggered 50s after the simulation started. Note that engine related contributions in forces and moments are not included here. This study focuses solely on the aerodynamic effects.

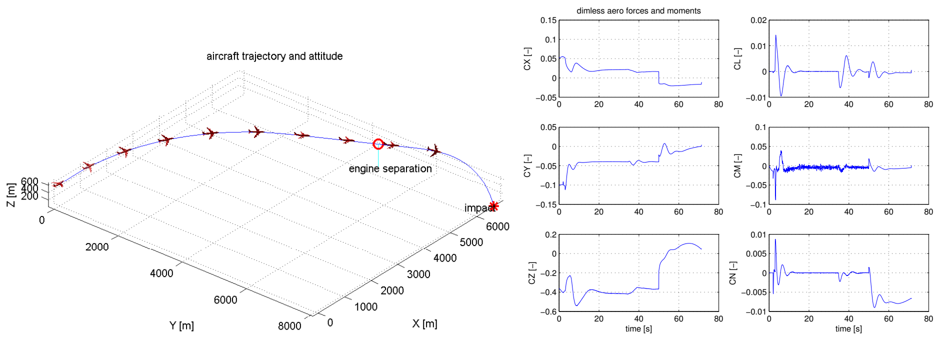

(a) Simulation trajectory of engine separation scenario

(b) Calculated dimensionless forces and moments coefficients during simulation

Figure 5.27: Simulation information of the engine separation scenario

As an example, the dimensionless force coefficient in Z-direction and the dimensionless moment coefficients C_l and C_n, as shown in fig. 5.27(b), have been selected as dependent variables to demonstrate the AROLS algorithm.

5.3.4.1 Dimensionless force coefficient C_Z

In this example, the dimensionless force coefficient C_Z is considered. First, the need for structure selection is illustrated. Predicting the dependent variable in post failure conditions based upon identification results in the unfailed situation leads to the result as shown in fig. 5.28(a). From this figure, it can be observed that the values related to the situation prior to the failure do not hold post-failure. Therefore, fig. 5.28(b) illustrates the situation with updated parameter value estimation restricted to the data after the failure, but keeping the fixed conventional model structure which was successful for fitting the data before the failure. This figure illustrates that values are re-estimated, but the algorithm is not successful in fitting the data set accurately without structure adaptation. This structure adaptation is exactly the purpose of adaptive recursive orthogonal least squares (AROLS), which will be illustrated in the remainder of this section.

Applying the AROLS routine to this stretch of simulation data leads to the results as shown in fig. 5.29. Fig. 5.29(a) shows the results prior to failure, while fig. 5.29(b) focuses

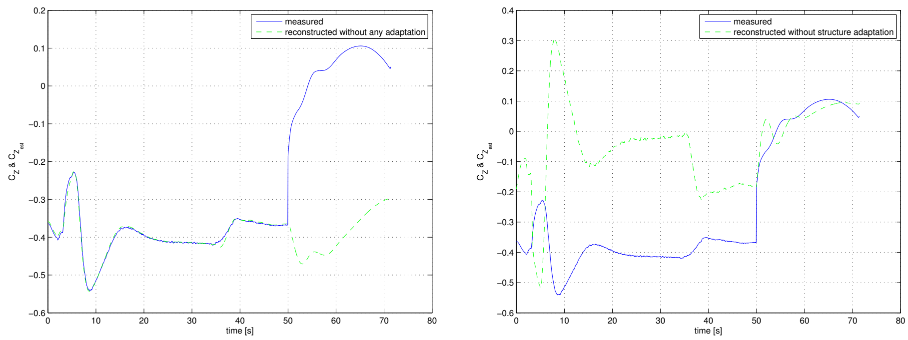

(a) fitting with originally selected structure and estimated parameter values for the unfailed situation

(b) fitting with originally selected structure for the unfailed situation but with updated estimated parameter values for the failed situation

Figure 5.28: Fitting of complete data set of C_Z without full adaptation for the post-failure characteristics

on the post-failure situation. As can be seen in this figure, the fit is accurate. The optimal residual, which is updated over the entire time history at every time step, is minimal. The real residual, which is not updated a posteriori, gives an indication of the reduction in the residual over the time interval. Fig. 5.29(a) reveals the initial large residual due to initialization. Fig. 5.29(b) shows the initial large residual caused by the failure. This is minimized in very short term, but starts increasing thereafter due to slow dynamics which become dominant. Between 55s and 60s, the residual is again minimized, thanks to the incorporation of these slow dynamics in the aerodynamic model.

The parameter estimation results, together with their standard deviations, can be found in table 5.8. These results highlight the difference between the situations before and after failure. Because there is no anomaly before the failure, the important independent variables for the vertical force are the conventional ones, namely a constant, the angle of attack α and pitch rate $\frac{q\bar{c}}{V}$. However, after the failure a violent roll-dive manoeuvre follows. The influence of the damage on the change in aerodynamics is represented by additional contributions by sideslip β and roll rate $\frac{pb}{2V}$. These are a consequence of the asymmetric damage, as a result of which the decoupling of longitudinal and lateral regressors does not hold anymore in this scenario.

The development of the structure selection algorithm can be seen in fig. 5.30. Fig. 5.30(a) shows the number of regressors which have been included and fig. 5.30(b) displays the time history of the monitoring criteria. The first few seconds of the simulation, the initialization takes place while there is no significant excitation or dynamics, after which only

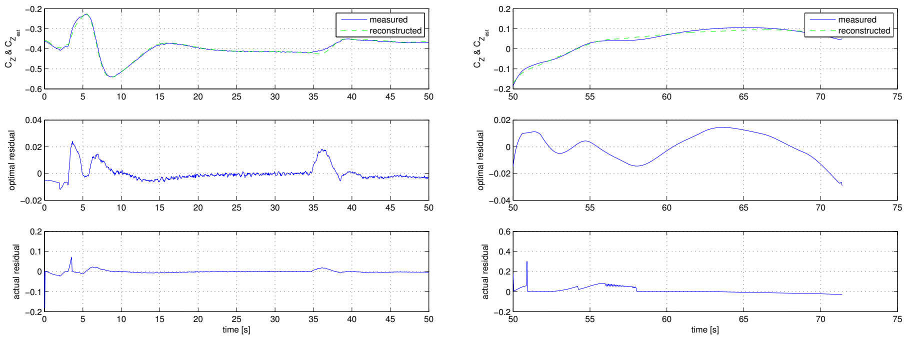

(a) AROLS structure selection and parameter estimation result for C_Z prior to failure

(b) AROLS structure selection and parameter estimation result for C_Z after failure

Figure 5.29: AROLS structure selection and parameter estimation results for C_Z before and after the failure

Table 5.8: SSPE results for C_Z for engine separation scenario, before and after failure

	prior failure		post failure	
	estimated	(σ)	estimated	(σ)
1	-0.1583	(1%)	-0.4131	(2%)
α	-4.4016	$(\approx 0\%)$	4.9047	(1%)
$\frac{q\bar{c}}{V}$	-1.6124	(22%)	105.1966	(1%)
β	–	–	4.2319	(1%)
$\frac{pb}{2V}$	–	–	9.4708	$(\approx 0\%)$
$\frac{rb}{2V}$	–	–	–	–
all others	–	–	–	–

one regressor, being the constant, is selected which is sufficient to represent the aerodynamic model during these first few seconds. Between 5 and 10s, a dynamic right hand turn is executed, which leads to an extension of the model structure because of the significant excitation. Soon after the start of the turn a repetition of the structure selection phase is triggered and at the end the three conventional regressors are retained. Since the mean squared residual, shown in fig. 5.30(b), does not cross the first threshold $\xi_{M_{s_1}}$ anymore afterwards, the structure selection is frozen after this phase, which saves a considerable amount of computational load and time. When the engines separate, $\overline{\varepsilon^2_{M_s}}(t)$ increases dramatically while the maximum standard deviation remains below its threshold $\xi_{M_{s_3}}$. This triggers step 9 in the ROLS algorithm and the identification procedure is reset, ignoring all data collected before since they have become irrelevant for the new configuration. During the first few seconds, there is a brief transient, since the algorithm tries first to fit the new aircraft behaviour by extending the regressor subset without resetting the data content. But thereafter the reinitialization is triggered and only two regressors are retained, namely $\frac{q\bar{c}}{V}$ and $\frac{pb}{2V}$ are included, since they represent the fastest dynamics which are dominant in the short term. However, slower dynamics are not yet present at that time instant but become apparent in the subsequent seconds, from 53s onward. This influence makes the mean squared residual increase and triggers the structure selection routine again around $t = 58s$, since the standard deviation values are too large to warrant a new reinitialization. In the subsequent structure selection steps, the slower regressors 1, α and β are included simultaneously. After this, the structure selection procedure freezes again completely, since $\overline{\varepsilon^2_{M_s}}(t)$ becomes extremely small, well below threshold $\xi_{M_{s_1}}$. However, it can once again be seen that, towards the end the mean squared residual increases again, due to new slower dynamics which become influential, and will unfreeze the selection once again. However, the aircraft impacts terrain and the simulation is terminated before this new structure selection step is triggered.

Figure 5.31 shows the AROLS results over the complete time span. The optimal residual is updated over the entire time history at every time step, as explained before. The real residual on the contrary is the actual residual at every time step, without a posteriori update. Except for two major exceptions, namely initializations in the beginning of the simulation and after failure, this real residual is very small and confirms the accuracy of structure and parameter estimates. However, the optimal residual has an additional monitoring purpose. For this specific example, there is an abrupt change and the change in model structure is relatively quickly detected by means of the monitoring criteria, which reveals also when the failure occurred approximately (here at $t = 52s$). However, it is also possible that some gradual developing failures occur. The time instant when the reset operation is triggered by the monitoring criteria can be significantly later, hiding the true time instant when the failure occurred. In these scenarios, the optimal residual has an additional advantage, since it will reveal when the failure occurred. More precisely, the time instant where the optimal residual changes from substantial to extremely small corresponds to the moment of failure.

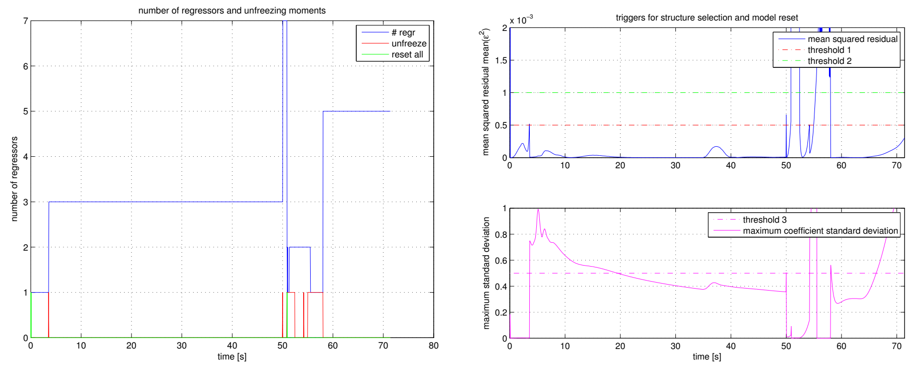

(a) Number of regressors included for C_Z

(b) AROLS structure selection and parameter estimation result after failure for C_Z

Figure 5.30: Number of regressors included and triggering of structure selection procedure for C_Z

In figure 5.31, this corresponds to $t = 50s$.

Figure 5.32 serves as an additional validation test where the vertical specific force A_z is calculated with the SSPE result before and after the failure, and compared with the measured value. Note that these results have been obtained without mass updates, but with the original values which are biased in post failure conditions. This validation confirms the accuracy of the achieved identification result including structure selection. Moreover, the significant difference between the situations before and after failure can be observed in this figure.

5.3.4.2 Dimensionless moment coefficient C_l

Applying the AROLS routine to this stretch of simulation data leads to the results as shown in fig. 5.33. Also for this example, the fit is accurate. Especially after the failure, the real residual illustrates that the structure selection procedure is triggered whenever it deviates significantly from zero.

The parameter estimation results, together with their standard deviations, can be found in table 5.9. These results highlight the difference between the situations before and after failure. Because there is no anomaly before the failure, the important independent variables for the rolling moment are the conventional ones, namely the angle of sideslip β, roll rate $\frac{pb}{2V}$, and the ailerons as control effectors. Recall that the inner left aileron $\delta_{a_{IL}}$ is not included, since its deflection is collinear with another aileron surface. This is achieved by considering the row reduced echelon form. However, after the failure a violent roll-dive

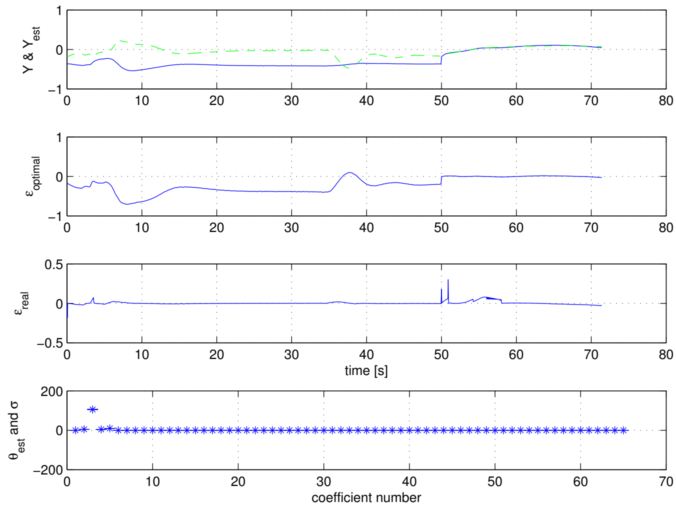

Figure 5.31: Results AROLS over complete time span for C_Z

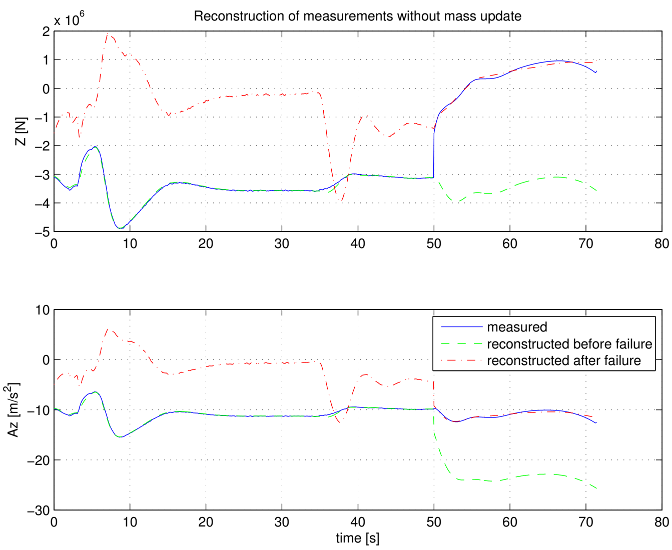

Figure 5.32: Reconstruction of the vertical specific force A_z with the SSPE result

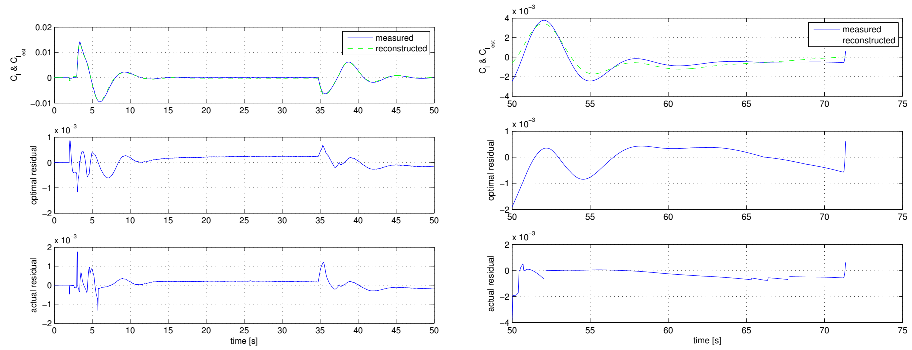

(a) AROLS structure selection and parameter estimation result for C_l prior to failure

(b) AROLS structure selection and parameter estimation result for C_l after failure

Figure 5.33: AROLS structure selection and parameter estimation results for C_l before and after the failure

manoeuvre follows, as illustrated previously. The influence of the damage on the change in aerodynamics is represented by an additional contribution from pitch rate $\frac{q\bar{c}}{V}$, since decoupling of longitudinal and lateral regressors does not hold anymore in this scenario. It should also be noted that the ailerons are no significant regressors after the failure. This is because they cannot move anymore as can be seen in fig. A.9 in appendix A. A few spoilers remain effective, but these are not sufficiently excited by the classical control system in this short time span to allow a successful identification of their individual control efficiencies. Therefore, separate surface excitation (SSE) is needed[112, 287]. In combination with the SSPE algorithm, this will provide reliable values for the primary control efficiencies. Subsequently, this information can be used by the model based control algorithm, such as adaptive nonlinear dynamic inversion (ANDI).

The development of the structure selection algorithm is again displayed in fig. 5.34. Fig. 5.34(a) shows the number of regressors which have been included and fig. 5.34(b) displays the time history of the monitoring criteria. Between 5 and 10s, when the dynamic right hand turn is executed, the rolling moment is excited significantly and the model structure is extended accordingly. Soon after the start of the turn a repetition of the structure selection phase is triggered and at the end of the turn the structure is frozen and will not change anymore till the failure occurs. When the engines separate, $\overline{\varepsilon^2_{M_s}}(t)$ increases dramatically while the maximum standard deviation shows no significant increase. This triggers step 9 in the ROLS algorithm and the identification procedure is reset, ignoring all data collected before since they have become irrelevant for the new configuration. The reinitialization is triggered and after some model development updates only three regressors are retained,

Table 5.9: SSPE results for C_l for engine separation scenario, before and after failure

	prior failure		post failure	
	estimated	(σ)	estimated	(σ)
β	-0.1130	(1%)	-0.1673	(1%)
$\frac{pb}{2V}$	-0.3109	$(\approx 0\%)$	-0.3065	(1%)
$\frac{rb}{2V}$	–	–	–	–
$\delta_{a_{IR}}$	-0.0005	(2%)	–	–
$\delta_{a_{IL}}$	–	–	–	–
$\delta_{a_{OR}}$	-0.0004	(1%)	–	–
$\delta_{a_{OL}}$	0.0003	(1%)	–	–
1	–	–	–	–
α	–	–	–	–
$\frac{q\bar{c}}{V}$	–	–	-0.4706	$(\approx 0\%)$
all others	–	–	–	–

namely β, $\frac{pb}{2V}$ and $\frac{q\bar{c}}{V}$ are included, since they represent the most important dynamics which are dominant in the longer term. Initially, also the yaw rate $\frac{rb}{2V}$ is included, but its relevance, together with its coefficient, decrease over time, and the regressor becomes redundant from 68s onward. After this, the structure selection procedure freezes again , since $\overline{\varepsilon^2_{M_s}}(t)$ becomes smaller again, but not far below threshold $\xi_{M_{s_1}}$, pointing out that an optimal fit has not yet been achieved. Towards the end, it can also be seen that the mean squared residual increases again, due to new slower dynamics which become influential. These dynamics would unfreeze the selection once again if the aircraft would not have hit terrain.

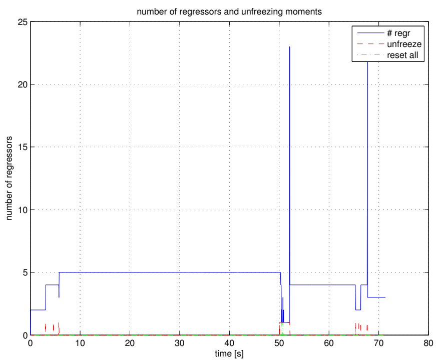

(a) Number of regressors included for C_l

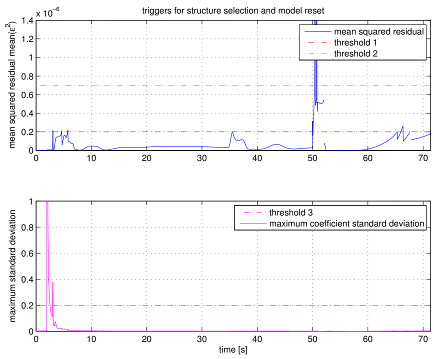

(b) AROLS structure selection and parameter estimation result after failure for C_l

Figure 5.34: Number of regressors included and triggering of structure selection procedure for C_l

Figure 5.35 shows the AROLS results over the complete time span. The optimal and real residual have been defined in the previous example. The upper graph illustrating the true signal and its final approximation, after failure and at the moment of impact, fits the post-failure data well, but not the stretch of data before the failure. This illustrates the significant difference in model properties before and after failure, and thus the extent of the damage and its influence on the aircraft behaviour.

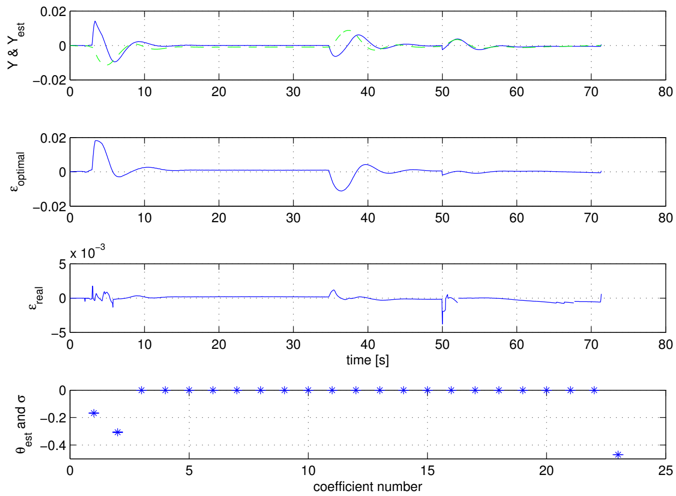

Figure 5.35: Results AROLS over complete time span for C_l

An additional validation test is provided in Figure 5.36, where the roll acceleration $\dot{p}$ is calculated by means of the SSPE result before and after the failure, and compared with the measured value. Note that these results have been obtained without post failure mass updates. The accuracy of the achieved identification result is confirmed by this test. Moreover, in comparison with the previous application example, there is still some difference between the situations before and after failure, as can be observed in this figure, but the difference is less significant. The largest difference can be observed immediately after failure.

5.3.4.3 Dimensionless moment coefficient C_n

Figure 5.37 shows the results of AROLS applied to this stretch of data. As can be seen in this figure, the fit is accurate once again. The parameter estimation results, together with their standard deviations, can be found in table 5.10. Before the failure, the important independent variables for the yawing moment are the conventional ones, namely the angle of sideslip β, roll rate $\frac{pb}{2V}$, yaw rate $\frac{rb}{2V}$ and the ailerons and rudder as control effectors. The rudder is the most efficient yawing control effector, and this can be seen in the estimated

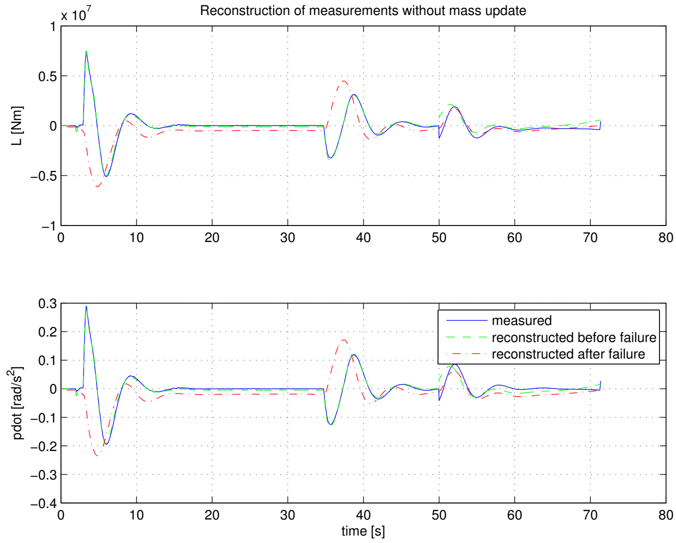

Figure 5.36: Reconstruction of the roll acceleration $\dot{p}$ with the SSPE result

value, which is an order of magnitude larger compared to the aileron effectiveness. After the failure a violent roll-dive manoeuvre follows, but there is no difference in model structure between the situations before and after failure. Comparing the estimated values before and after failure shows that there is little change in the influence of the independent variables on the yawing moment. From these observations, it follows that the influence of the damage can be found primarily in the rolling moment L, and it is minimal on the yawing moment N. Recall that asymmetric thrust is not taken into account here, only the aerodynamic moment is considered. Wing damage has more effect on the rolling moment L than on the yawing moment N. The latter can be influenced more effectively by damage to the vertical tail, for example.

The development of the structure selection algorithm can be seen in fig. 5.38. No special observations occur here. During the right hand turn, the model structure is selected and does not change anymore afterward till impact with terrain. This is underpinned by the time history of the value of the mean squared residual, which remains small at any time.

Figure 5.39 shows the AROLS results over the complete time span. The upper graph confirms that there is no significant change in the yawing moment characteristics between situations before and after damage. The fitting result at the end fits the complete data set very well, from the initial situation till the end. This confirms that an SSPE procedure is not needed for this specific dependent variable, which is taken into account by the AROLS

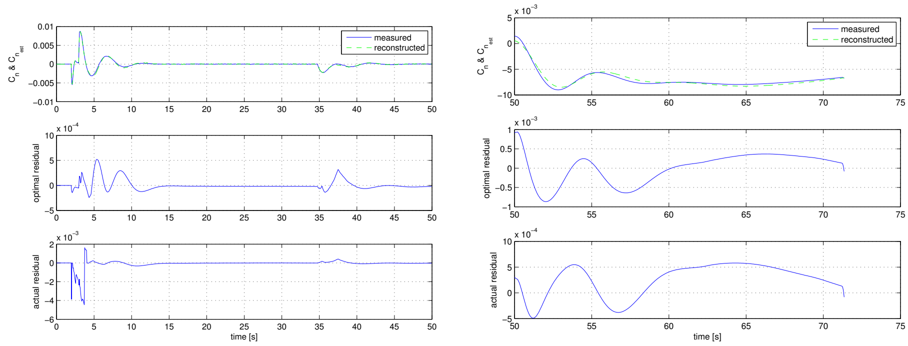

(a) AROLS structure selection and parameter estimation result for C_n prior to failure

(b) AROLS structure selection and parameter estimation result for C_n after failure

Figure 5.37: AROLS structure selection and parameter estimation results for C_n before and after the failure

Table 5.10: SSPE results for C_n for engine separation scenario, before and after failure

	prior failure		post failure	
	estimated	(σ)	estimated	(σ)
β	0.1385	$(\approx 0\%)$	0.1257	$(\approx 0\%)$
$\frac{pb}{2V}$	-0.0249	$(\approx 0\%)$	-0.0252	$(\approx 0\%)$
$\frac{rb}{2V}$	-0.1953	$(\approx 0\%)$	-0.1763	$(\approx 0\%)$
$\delta_{a_{IR}}$	-0.0001	$(\approx 0\%)$	-0.0002	$(\approx 0\%)$
$\delta_{a_{IL}}$	–	–	–	–
$\delta_{a_{OR}}$	-0.0001	(14%)	$2.7 \cdot 10^{-7}$	(10370%)
$\delta_{a_{OL}}$	$-1.2 \cdot 10^{-6}$	(108%)	$-2.1 \cdot 10^{-5}$	(90%)
δ_{r_L}	-0.0015	(1%)	-0.0015	(3%)
δ_{r_U}	–	–	–	–
all others	–	–	–	–

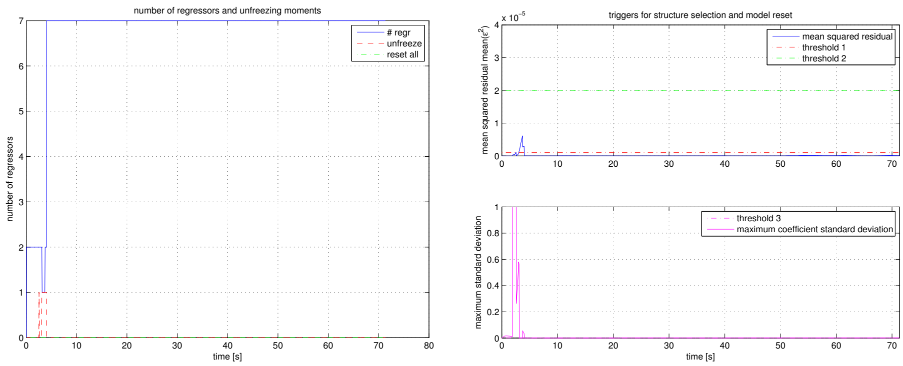

(a) Number of regressors included for C_n

(b) AROLS structure selection and parameter estimation result after failure for C_n

Figure 5.38: Number of regressors included and triggering of structure selection procedure for C_n

algorithm since a re-initialization is not activated.

Analogously as in the previous examples, Figure 5.40 serves as validation. It is most important to take into account the important thrust contribution for N in this test. Note that these results too have been obtained without post-failure mass updates. Once again, the accuracy of the achieved identification result is confirmed by this test. Moreover, in contrast with the previous application examples, there is no significant difference between the situations before and after failure, as can be observed in this figure. This confirms the absence of any need for structure selection, as already observed in the previous results of this third application example.

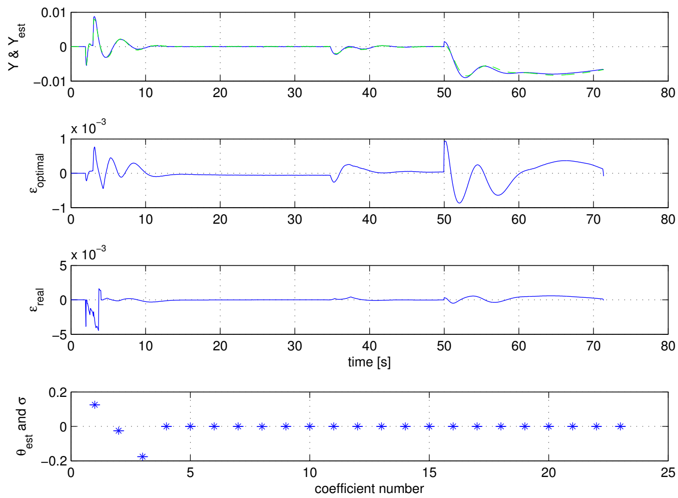

Figure 5.39: Results AROLS over complete time span for C_n

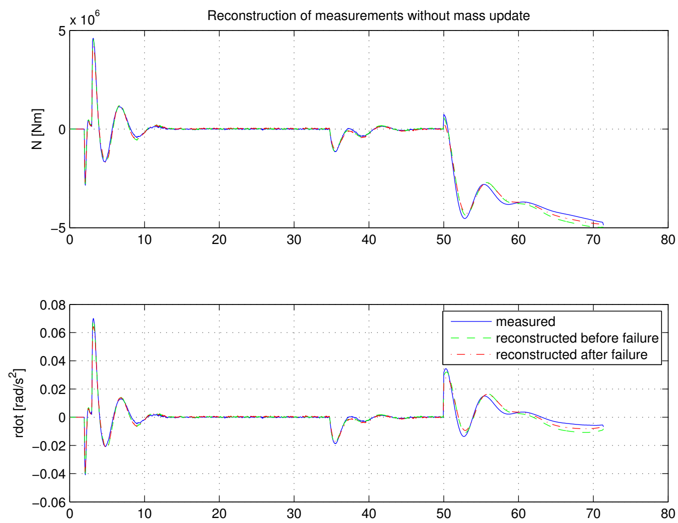

Figure 5.40: Reconstruction of the yaw acceleration $\dot{r}$ with the SSPE result

5.3.5 Computational efficiency and real time application

As can be observed from the working principle in section 5.3.2, AROLS is a recursive algorithm. This makes it suitable for on-line applications. However, real time applicability depends on computational efficiency.

Several measures have been taken to make this algorithm computationally efficient. Adding data for every time step results in a stepwise growing data matrix $\mathbf{\Phi}$. However, its orthogonal decomposition results in a stepwise growing orthogonal $\mathbf{Q}$ matrix and a fixed size triangular $\mathbf{R}$ matrix. Therefore, the computations have been optimized by making exclusive use of the triangular $\mathbf{R}$ matrix, which contains all necessary information for the AROLS algorithm. In this way, the computational load is independent of the time instant. Moreover, the structure selection phase is restricted to the time span where it is useful by considering a stopping criterion in step 3 and a starting criterion in step 8 in the working principle in section 5.3.2. In this way, computational efficiency is enhanced as can be observed in figure 5.41. In this figure, computational time of AROLS is presented for the calculations for every time step applied on the data set discussed in section 5.3.3.3, where re-initialization occurs at $t = 500s$. Structure selection is applied in specific intervals, namely at $t = 200 - 300s$, around $t = 400s$, at $t = 500 - 600s$ and $t = 700 - 900s$. The computational load caused by the structure selection steps (priority ranking, adding and evaluating) is visible in these time spans. Only relative comparisons of computational time values are useful here, since they reflect the computational load in the Matlab® environment. It is expected that translation of the algorithm into C-code will significantly improve the computational load, such that it will be real time applicable to perform the calculations at frequencies ranging from 20Hz-100Hz on a PC with a Pentium 4 processor.

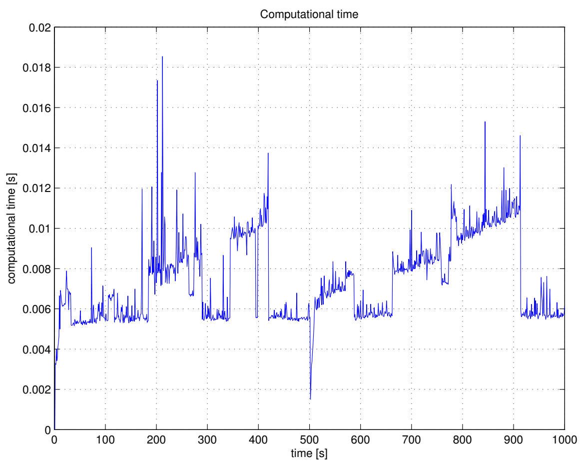

Figure 5.41: Computational load of AROLS for every time step applied on the data set discussed in section 5.3.3.3

5.4 Comparison of both structure selection and parameter estimation procedures

Comparing both structure selection and parameter estimation procedures gives a clear advantage to the adaptive recursive orthogonal least squares algorithm. First of all because of its recursive and computationally efficient nature which makes it suitable for real-time online applications. Compared with the modified stepwise regression procedure, it only needs a forward sweep, instead of combined addition and elimination criteria which apply for the latter. Moreover, the results show other arguments. Classical stepwise regression can be made suitable for aerodynamic applications with some major modifications. As an example, significant linear regressors are initially ”enforced” to appear in the selected structure (hence the term modified in the name). Higher order candidate regressors also require the use of priority scheduling. AROLS, on the other hand, is suitable for aerodynamics applications without any of these modifications. The reason for this is that its addition criterion is better suited for this specific kind of applications. In MSWR the selection of regressors is based on the largest similarity between the candidate regressors and the residual (via the partial correlation). For AROLS the selection is based upon the capability to minimize the residual as much as possible (via the fit error reduction capability). Considering all these arguments, adaptive recursive orthogonal least squares are preferable above modified stepwise regression.

Chapter 6

Taking into account mass property changes due to damage

Next to aerodynamic model structure changes, there is another bottleneck which has been identified in the methodology presented in chapter 4 for applications to damaged aircraft. Namely, this baseline methodology assumes that the mass properties (mass, center of gravity and mass inertia) are known and that the aircraft can be considered as mass symmetric, which results in the simplification $I_{yz} = 0$ and $I_{xy} = 0$.

In the specific case where mass properties change, but aerodynamic forces and moments are known, it is possible to estimate the mass parameters based upon the force and moment values. Then the mass can be estimated by e.g. dividing the forces Z over the specific force in the corresponding direction A_z. The mass inertia can be estimated by means of the moments $L,\ M,\ N$, by the following regression expressions:

$$L = I_{xx}\,\dot{p} - (I_{yy} - I_{zz})\,q\,r - I_{xz}(\dot{r} + p\,q) \tag{6.1}$$

$$M = I_{yy}\,\dot{q} - (I_{zz} - I_{xx})\,r\,p - I_{xz}(r^2 - p^2) \tag{6.2}$$

$$N = I_{zz}\,\dot{r} - (I_{xx} - I_{yy})\,p\,q - I_{xz}(\dot{p} - q\,r) \tag{6.3}$$

In this setup, it is possible to estimate $m,\ I_{xx},\ I_{yy},\ I_{zz}$ and I_{xz} individually, on the condition that direct measurements of forces and moments are available. This is not a realistic assumption, except when a database is available for the aerodynamic coefficients, which allows to reconstruct the forces and moments without the knowledge of mass properties.

However, this simplified approach is not realistic for damaged aircraft, since aerodynamic and mass property changes often occur simultaneously as a result of significant structural damage. Therefore, a different approach is needed. In this chapter, the general influence of mass property changes on aircraft forces and moments is described. This is done with respect to the linear as well as the angular accelerations.

6.1 Influence of mass property changes on aircraft forces and moments

When structural damage occurs to an aircraft, such as loss of a part of the wing, the mass properties of the aircraft change. More precisely, the total aircraft mass decreases, the center of gravity moves, and the mass inertia will change too. Generally mass inertia values decrease after a structural loss. An aircraft can experience symmetric as well as asymmetric damage. In the former situation, the center of gravity moves in the plane of symmetry, but also a lateral shift will occur in the latter scenario. Especially the longitudinal position of the center of gravity has an influence on the stability margin of an aircraft. Stability problems of a damaged aircraft can be caused by mass as well as aerodynamic property changes. Moreover, loss of mass symmetry results also in additional non-zero mass inertia $I_{yz} \neq 0$ and $I_{xy} \neq 0$. In the next sections linear and angular accelerations are analysed in the presence of mass property changes. For the aerodynamic forces, the linear acceleration must be considered. The angular momentum, on the other hand, is to be incorporated in the expressions for the aerodynamic moments. The latter will be discussed in depth after the former.

6.1.1 Forces via linear acceleration

The standard equations for the linear accelerations as defined from equation (4.15) till (4.17) need to be expanded for the fact that the origin of the frame of reference does not coincide with the center of gravity after its shift, as shown in fig. 6.1. The expanded equations for the aerodynamic forces are defined as follows in vector form:

$$
\begin{aligned}
\mathbf{F} &= (m + \Delta m)\,\mathbf{a}_{I,O} - \mathbf{W} - \Delta\mathbf{W} && (6.4)\\
&= (m + \Delta m)\left(\frac{d\mathbf{V}_{B,O}}{dt} + \frac{d\boldsymbol{\Omega}}{dt} \times \boldsymbol{\Delta}\mathbf{r} + \boldsymbol{\Omega} \times (\mathbf{V}_{B,O} + \boldsymbol{\Omega} \times \boldsymbol{\Delta}\mathbf{r})\right) - \mathbf{W} - \Delta\mathbf{W} && (6.5)
\end{aligned}
$$

with the inertial kinematic acceleration vector: $\mathbf{a}_{I,O} = [\ a_x \quad a_y \quad a_z\ ]^T$, the body fixed velocity vector $\mathbf{V}_{B,O} = [\ u \quad v \quad w\ ]^T$, the angular rate vector $\boldsymbol{\Omega} = [\ p \quad q \quad r\ ]^T$, the

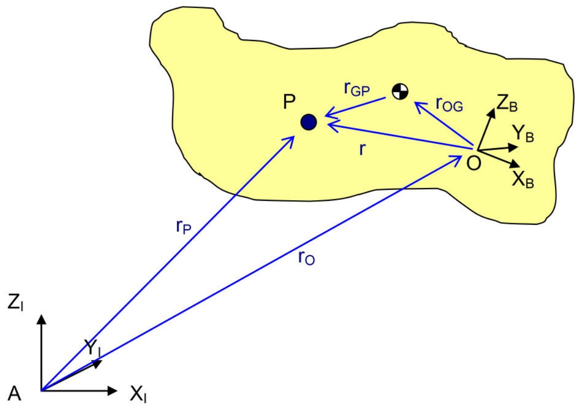

Figure 6.1: Non coinciding reference frame origin and center of gravity

distance between the center of gravity and the origin $\mathbf{\Delta r} = [\ \Delta x \quad \Delta y \quad \Delta z\ ]^T$, the weight $\mathbf{W} = mg[\ -\sin\theta \quad \cos\theta\sin\phi \quad \cos\theta\cos\phi\ ]^T$ and the weight change $\Delta\mathbf{W} = \Delta mg[\ -\sin\theta \quad \cos\theta\sin\phi \quad \cos\theta\cos\phi\ ]^T$. The derivation of this expression can be found in appendix E.1. In this derivation, the terms $\Delta\dot{\mathbf{r}}$ and $\Delta\dot{m}$ can be significant when they represent an impulse force over a short time due to instantaneous changes in the center of gravity position and mass. However, they have been neglected here, since post damage flight dynamics are considered here.

Writing out the vector equation results in the following force equations:

$$\begin{aligned} X &= (m+\Delta m)\left(\dot{u} + qw - rv - \left(q^2+r^2\right)\Delta x + (pq-\dot{r})\,\Delta y + (\dot{q}+pr)\,\Delta z + \right. \\ &\quad \left. +g\sin\theta\right) \qquad (6.6) \\ Y &= (m+\Delta m)\left(\dot{v} + ru - pw + (\dot{r}+pq)\,\Delta x - \left(p^2+r^2\right)\Delta y + (qr-\dot{p})\,\Delta z + \right. \\ &\quad \left. -g\cos\theta\sin\varphi\right) \qquad (6.7) \\ Z &= (m+\Delta m)\left(\dot{w} + pv - qu + (pr-\dot{q})\,\Delta x + (\dot{p}+qr)\,\Delta y - \left(p^2+q^2\right)\Delta z + \right. \\ &\quad \left. -g\cos\theta\cos\varphi\right) \qquad (6.8) \end{aligned}$$

where the additional contributions from the mass change and the shift in the center of gravity are clear. From these expressions, it can be found that the angular accelerations have an influence on the aerodynamic forces when the center of gravity is shifted away from the fixed reference location. These expressions correspond to those derived in ref. [26].

6.1.2 Moments via angular acceleration

The standard equations for the aerodynamic moments as defined in section 4.2 need to be expanded for the fact that the origin of the frame of reference does not coincide with the center of gravity after its shift.

As a result, the expanded equations for the aerodynamic moments are defined as follows in vector form:

$$M_a = \mathbf{I}\dot{\mathbf{\Omega}} + m\Delta\mathbf{r} \times \dot{\mathbf{V}}_0 + \mathbf{\Omega} \times \mathbf{I\Omega} - m\Delta\mathbf{r} \times (\mathbf{V}_0 \times \mathbf{\Omega}) - \mathbf{\Delta r} \times (mg\mathbf{\Theta}) \tag{6.9}$$

with the inertia matrix: $I = \begin{bmatrix} I_{xx} & -I_{xy} & -I_{xz} \\ -I_{xy} & I_{yy} & -I_{yz} \\ -I_{xz} & -I_{yz} & I_{zz} \end{bmatrix}$, the body fixed velocity vector $\mathbf{V}_O = [\ u \quad v \quad w\ ]^T$, the angular rate vector $\mathbf{\Omega} = [\ p \quad q \quad r\ ]^T$, the distance between the center of gravity and the origin $\mathbf{\Delta r} = [\ \Delta x \quad \Delta y \quad \Delta z\ ]^T$, the weight $mg\mathbf{\Theta} = mg[\ -\sin\theta \quad \cos\theta\sin\phi \quad \cos\theta\cos\phi\ ]^T$. The derivation of this expression can be found in appendix E.2.

Substituting and working out leads to:

$$\begin{aligned} L &= \dot{p}I_{xx} + (pr - \dot{q})\,J_{xy} - (pq + \dot{r})\,J_{xz} + \left(r^2 - q^2\right)J_{yz} + qr\,(I_{zz} - I_{yy}) + \\ &\quad +m\,(\dot{w} - qu + pv - g\cos\phi\cos\theta)\,\Delta y - m\,(\dot{v} + ru - pw - g\cos\theta\sin\phi)\,\Delta z \\ M &= -(\dot{p} + qr)\,J_{xy} + \dot{q}I_{yy} + (pq - \dot{r})\,J_{yz} + \left(p^2 - r^2\right)J_{xz} + pr\,(I_{xx} - I_{zz}) + \\ &\quad -m\,(\dot{w} + pv - qu - g\cos\theta\cos\phi)\,\Delta x + m\,(\dot{u} - rv + qw + g\sin\theta)\,\Delta z \quad (6.10) \\ N &= (qr - \dot{p})\,J_{xz} - (\dot{q} + pr)\,J_{yz} + \dot{r}I_{zz} + \left(q^2 - p^2\right)J_{xy} + pq\,(I_{yy} - I_{xx}) + \\ &\quad +m\,(\dot{v} - pw + ru - g\sin\phi\cos\theta)\,\Delta x - m\,(\dot{u} + qw - rv + g\sin\theta)\,\Delta y \quad (6.11) \end{aligned}$$

These equations indicate that the changes in the mass properties effectively create additional moment contributions. These expressions correspond also to those derived in ref. [26].

6.1.3 Couplings between aerodynamic forces and moments due to center of gravity shift

Moreover, the shift in center of gravity also creates additional contributions to the moments by the forces:

$$C_{l_{\text{tot}}} = C_l + C_y\frac{2\Delta z}{b} - C_z\frac{2\Delta y}{b} \tag{6.12}$$

$$C_{m_{\text{tot}}} = C_m - C_x\frac{\Delta z}{\bar{c}} + C_z\frac{\Delta x}{\bar{c}} \tag{6.13}$$

$$C_{n_{\text{tot}}} = C_n + C_x\frac{2\Delta y}{b} - C_y\frac{2\Delta x}{b} \tag{6.14}$$

6.2 Final note

In appendix E.3 to E.6, a mass sensitivity analysis of forces and moments has been performed, together with an initial investigation how mass changes can be represented in the kinematics and observation models and in the aerodynamic model.

This topic is subject to further research activities in identification of damaged aircraft models. In this research project, it has been found in chapters 7 and 8 that considering mass and inertia as known constants, without post-damage updates, leads to satisfactory performance of the fault tolerant flight control algorithms in the failure scenarios considered here.

Chapter 7

Baseline Flight Controller Synthesis

As motivated in section 2.12, a model based control method has been chosen for the reconfiguring flight control synthesis phase. One of the valid approaches is the so-called concept of adaptive nonlinear dynamic inversion. Nonlinear dynamic inversion is a popular control approach in the literature for flight control and aircraft guidance, see ref. [27, 58, 224, 231, 282], where two of its main advantages are the absence of any need of gain scheduling over the flight envelope and a complete decoupling between input-output relations. In ref. [225], enhanced incremental NDI strategies have been applied for reconfigurable flight control in the case of stuck or missing effectors. The enhancement is made by weighting position and rate with nonlinear functions in order to minimize control rate and position to prevent control saturation. However, this reference mentions the need for relatively noise free critical measurements and uses only one NDI loop with a position/angle allocator. Other applications of adaptive NDI are mentioned in [38, 51, 83, 235, 241, 261, 289]. The application discussed in this section however, can deal with noisy measurements thanks to the presence of a robust identification routine acting on the measurements. Moreover, a dual NDI loop has been implemented here, with inner loop body angular rate and outer loop aerodynamic angle tracking properties. This overall combination increases greatly the ability to reconfigure the aircraft in the presence of component as well as structural failures.

After discussing the theoretical background, the detailed ANDI setup is explained, for use in manual as well as autopilot control. For autopilot control, two alternative NDI setups have been developed.

7.1 Theoretical background

First, the concept of dynamic inversion will be introduced by means of the concept of Lie derivatives. Then, the concept of multiloop NDI is elaborated by means of the time scale separation principle. Finally, a short stability analysis is provided for the case of non-ideal or imperfect dynamic inversion.

7.1.1 The concept of NDI

The general idea of nonlinear dynamic inversion is as follows. Consider the nonlinear MIMO system dynamic model, which is assumed to be affine in the input:

$$\dot{\mathbf{x}} = \mathbf{f}(\mathbf{x}) + \mathbf{G}(\mathbf{x})\mathbf{u} \tag{7.1}$$

The output $\mathbf{y}$ of the system is then expressed as a function $\mathbf{h}$ of the aircraft state vector $\mathbf{x}$:

$$\mathbf{y}(\mathbf{x}) = \mathbf{h}(\mathbf{x}) \tag{7.2}$$

Defining the matrix $\nabla\mathbf{h}\left(\mathbf{x}\right)$ as the Jacobian matrix:

$$\frac{\partial \mathbf{h}(\mathbf{x})}{\partial \mathbf{x}} = \nabla\mathbf{h}(\mathbf{x}) \tag{7.3}$$

the time derivatives of the outputs in eq. (7.2) can be expressed as:

$$\frac{d\mathbf{y}}{dt} = \nabla\mathbf{h}\left(\mathbf{x}\right)\left[\mathbf{f}(\mathbf{x}) + \mathbf{G}(\mathbf{x})\mathbf{u}\right] = L_f^1\mathbf{h}\left(\mathbf{x}\right) + L_g\mathbf{h}\left(\mathbf{x}\right)\mathbf{u} \tag{7.4}$$

where $L_f^1\mathbf{h}\left(\mathbf{x}\right) = \nabla\mathbf{h}\left(\mathbf{x}\right)\mathbf{f}(\mathbf{x})$ denotes the first order Lie derivative vector and the $L_g\mathbf{h}\left(\mathbf{x}\right) = \nabla\mathbf{h}\left(\mathbf{x}\right)\mathbf{G}(\mathbf{x})$. If the second term of eq. (7.4) is zero, more time derivatives of eq. (7.4) are required, generally until the second term of eq. (7.4) is nonzero. This nonzero time derivative order is defined as "relative degree". In general, as the elements within the output vector $\mathbf{y}(\mathbf{x})$ may have different relative degrees, it is convenient to write the time derivative for each output as:

$$\frac{d^{r_i}y_i}{dt^{r_i}} = \frac{d^{r_i}h_i\left(\mathbf{x}\right)}{dt^{r_i}} = L_f^{r_i}h_i\left(\mathbf{x}\right) + \sum_{j=1}^{m} L_{g_j}L_f^{r_i-1}h_i\left(\mathbf{x}\right)u_j \tag{7.5}$$

In eq. (7.5), r_i is the relative degree for the i^{th} output. A collection of all differentiated (r_i^{th} order) outputs yields:

$$\mathbf{y}^r\left(\mathbf{x}\right) = \mathbf{l}\left(\mathbf{x}\right) + \mathbf{M}\left(\mathbf{x}\right)\mathbf{u} \tag{7.6}$$

with:

$$\mathbf{y}^r(\mathbf{x}) = \begin{bmatrix} \frac{d^{r_1} h_1(\mathbf{x})}{dt^{r_1}} \\ \vdots \\ \frac{d^{r_m} h_m(\mathbf{x})}{dt^{r_m}} \end{bmatrix} \tag{7.7}$$

$$\mathbf{l}(\mathbf{x}) = \begin{bmatrix} L_f^{r_1} h_1(\mathbf{x}) \\ L_f^{r_2} h_2(\mathbf{x}) \\ \vdots \\ L_f^{r_m} h_m(\mathbf{x}) \end{bmatrix} \tag{7.8}$$

and

$$\mathbf{M}(\mathbf{x}) = \begin{bmatrix} L_{g_1} L_f^{r_1-1} h_1(\mathbf{x}) & L_{g_2} L_f^{r_1-1} h_1(\mathbf{x}) & \cdots & L_{g_m} L_f^{r_1-1} h_1(\mathbf{x}) \\ L_{g_1} L_f^{r_2-1} h_2(\mathbf{x}) & L_{g_2} L_f^{r_2-1} h_2(\mathbf{x}) & \cdots & L_{g_m} L_f^{r_2-1} h_2(\mathbf{x}) \\ \vdots & \vdots & \vdots & \vdots \\ L_{g_1} L_f^{r_m-1} h_m(\mathbf{x}) & L_{g_2} L_f^{r_m-1} h_m(\mathbf{x}) & \cdots & L_{g_m} L_f^{r_m-1} h_m(\mathbf{x}) \end{bmatrix} \tag{7.9}$$

Solving for $\mathbf{u}$ if the total relative degree $r = r_1 + r_2 + \ldots + r_m = n$, with n the number of states of the system, by introducing a virtual outer loop control input vector $\boldsymbol{\nu}$, which consists of time derivatives of control variables $cv_i(\mathbf{x})$ up to the corresponding relative degree r_i :

$$\mathbf{u} = \mathbf{M}^{-1}(\mathbf{x})\,[\boldsymbol{\nu} - \mathbf{l}(\mathbf{x})] \tag{7.10}$$

with:

$$\boldsymbol{\nu}(\mathbf{x}) = \begin{bmatrix} \frac{d^{r_1} cv_1(\mathbf{x})}{dt^{r_1}} \\ \vdots \\ \frac{d^{r_m} cv_m(\mathbf{x})}{dt^{r_m}} \end{bmatrix} \tag{7.11}$$

then this results in a closed-loop system with a linear and decoupled input-output relation:

$$\mathbf{y}^r(\mathbf{x}) = \begin{bmatrix} \frac{d^{r_1} h_1(\mathbf{x})}{dt^{r_1}} \\ \vdots \\ \frac{d^{r_m} h_m(\mathbf{x})}{dt^{r_m}} \end{bmatrix} = \boldsymbol{\nu} = \begin{bmatrix} \frac{d^{r_1} cv_1(\mathbf{x})}{dt^{r_1}} \\ \vdots \\ \frac{d^{r_m} cv_m(\mathbf{x})}{dt^{r_m}} \end{bmatrix} \tag{7.12}$$

Thus the control law for tracking tasks

$$\frac{d^{r_i} cv_i}{dt^{r_i}} = \frac{d^{r_i} h_{i_d}}{dt^{r_i}} - k_{0_i} e - k_{1_i} \dot{e} - \ldots - k_{(r_i-1)_i} e^{(r_i-1)} \;\text{ with }\; e = y_{i_d}(t) - y_i(t) \tag{7.13}$$

for $i = 1, \ldots, m$ with the k_js chosen so that $p^n + k_{n-1}p^{n-1} + \ldots + k_1 p$ is a stable polynomial, leads to the exponentially stable tracking dynamics for $i = 1, \ldots, m$:

$$e^{(r_i)} + k_{(r_i-1)_i} e^{(r_i-1)} + \ldots + k_{1_i} \dot{e} + k_{0_i} e = 0 \;\text{ with }\; e(t) \to 0 \tag{7.14}$$

By making use of Nonlinear Dynamic Inversion (NDI), the nonlinear aircraft dynamics can be cancelled out such that the resulting system behaves like a pure single r-th order integrator. In eq. (7.10), $\mathbf{l}(\mathbf{x})$ represents the airframe/engine model and $\mathbf{M}(\mathbf{x})$ is the so-called effector blending model. Note that the effector blending model $\mathbf{M}(\mathbf{x})$ needs to be inverted. See also ref. [65, 244].

7.1.2 Multiloop NDI and time scale separation

In this setup, the multiloop NDI concept has been applied, based on time scale separation. The time scale separation principle states the following. When a moment acts on an object, then primarily the angular rates change, whereas the attitude angles remain approximately the same for small time steps. This concept is commonly used in aircraft control, for example in Reiner et al. [231]. As a consequence of the time scale separation principle, it is sufficient for each subsystem to consider the first order Lie derivative to find the relevant control input, and the local "relative degree" is one. In theory, this separation principle involves some stability issues, however, practice has shown that the bandwidths of angular rates and attitude angles are sufficiently separated to prevent the risk for instabilities due to interactions. In the remainder of the discussions, first order systems will be considered.

7.1.3 Stability analysis for non-ideal or imperfect dynamic inversion

The closed loop system as given above assumes perfect knowledge of the accurate system model through the "certainty equivalence principle". However, this is frequently not the case, even with aerodynamic model identification present. In practice, numerical experiments have shown that nonlinear dynamic inversion can deal with minor misfits in the identified system model. Moreover, it has been found that NDI without aerodynamic model identification can cope with mild failures which are not destabilizing. The following reasoning gives an explanation for these observations. Therefore the consequences are analysed for misfits in the airframe information in $\mathbf{l}(\mathbf{x})$ as well as in the control efficiencies in $\mathbf{M}(\mathbf{x})$. In case of a misfit in the aerodynamic model information due to a change in the true system dynamics, this becomes:

$$\dot{\mathbf{y}} = [\mathbf{l}(\mathbf{x}) + \mathbf{\Delta l}(\mathbf{x})] + \mathbf{M}(\mathbf{x})\,\mathbf{u} \tag{7.15}$$

with the not updated control law as given in eq. (7.10) resulting in:

$$\dot{\mathbf{y}} = \boldsymbol{\nu} + \mathbf{\Delta l}(\mathbf{x}) \tag{7.16}$$

As can be seen, this misfit leads to an error term which is independent of the input. Consequently, compared to the nominal situation this can be considered as a bias error term which can be compensated for in certain conditions by including integral action in the outer loop linear controller. This can be shown as follows. The tracking error of this closed loop system, including bias error term, can be defined as follows:

$$\mathbf{e}\left(t\right)=\mathbf{y}_{d}\left(t\right)-\mathbf{y}\left(t\right)=\mathbf{y}_{d}\left(t\right)-\int_{t_0}^{t_{\mathrm{end}}}\left(\boldsymbol{\nu}\left(t\right)+\boldsymbol{\Delta}\mathbf{l}\left(\mathbf{x}(t)\right)\right)dt \tag{7.17}$$

Rewriting in the Laplace domain this becomes:

$$\mathbf{e}\left(s\right)=\mathbf{y}_{d}\left(s\right)-\frac{1}{s}(\boldsymbol{\nu}\left(s\right)+\boldsymbol{\Delta}\mathbf{l}\left(\mathbf{x}(s)\right)) \tag{7.18}$$

And the control law for a linear PI-controller is as follows:

$$\boldsymbol{\nu}\left(s\right)=K_{P}\mathbf{e}\left(s\right)+\frac{K_{I}}{s}\mathbf{e}\left(s\right) \tag{7.19}$$

with K_P and K_I the proportional and integral control gains respectively. Substituting eq. (7.19) in eq. (7.18) results in the following expression for the tracking error:

$$\mathbf{e}\left(s\right)=\frac{s\left(s\mathbf{y}_{d}\left(s\right)-\boldsymbol{\Delta}\mathbf{l}\left(\mathbf{x}(s)\right)\right)}{s^{2}+K_{P}s+K_{I}} \tag{7.20}$$

Applying the final value theorem, which holds only for proper transfer functions (satisfied in eq. (7.20) for second order $\mathbf{y}_d\left(s\right)$ and first order $\boldsymbol{\Delta}\mathbf{l}\left(\mathbf{x}(s)\right)$) with all poles inside the closed left half plane (satisfied in eq. (7.20) for strictly positive $K_P > 0$, $K_I > 0$ and stable $\mathbf{y}_d\left(s\right)$ and $\boldsymbol{\Delta}\mathbf{l}\left(\mathbf{x}(s)\right)$), results in the following requirement in order to achieve asymptotic stable tracking:

$$\lim_{t\to\infty}\mathbf{e}(t)=\lim_{s\to 0}\frac{s^{2}\left(s\mathbf{y}_{d}\left(s\right)-\boldsymbol{\Delta}\mathbf{l}\left(\mathbf{x}(s)\right)\right)}{s^{2}+K_{P}s+K_{I}} \tag{7.21}$$

From this equality, it can be stated that

$$\lim_{t\to\infty}\mathbf{e}(t)=0 \tag{7.22}$$

on a few conditions. First of all, it is needed that K_I is nonzero. This substantiates the need for integral action to counteract additive inversion errors $\boldsymbol{\Delta}\mathbf{l}(\mathbf{x}(t))$. Moreover, it can be observed in eq. (7.21) that $\mathbf{y}_d$ can be tracked up to second order signals and additive errors $\boldsymbol{\Delta}\mathbf{l}(\mathbf{x}(t))$ up to first order can be dealt with. Moreover, both must be stable. If any of the above conditions is not satisfied, the linear controller must be replaced by a robust controller in order to achieve stable tracking. However, an unstable additive inversion error $\boldsymbol{\Delta}\mathbf{l}(\mathbf{x}(t))$ will not appear in this setup, since instabilities are always identifiable in the setup described in chapter 4. Reason for this fact is their inherent property of being persistently exciting. This latter property is also the argument why model identification is necessary in this setup. Without identification, one cannot deal with failures leading to an unstable damaged aircraft model.

As an example, consider the situation where the aerodynamic derivative C_{m_α} is not correctly identified, then there is a small misfit ΔC_{m_α} between the true derivative and the identified one. This results in an additive inversion error: $\mathbf{\Delta l}(\mathbf{x}(t)) = [0 \ \ \Delta C_{m_\alpha}\alpha(t) \ \ 0]^T$. Substituting the equation for the pitching moment, commanding the pitch rate $q(t)$, in eq. (7.21) results in:

$$\begin{aligned} \lim_{t\to\infty} e(t) &= \lim_{s\to 0} \frac{s^3 \mathbf{y}_d(s)}{s^2 + K_P s + K_I} - \lim_{s\to 0} \frac{s^2 \mathbf{\Delta l}(\mathbf{x}(s))}{s^2 + K_P s + K_I} \\ &= \lim_{s\to 0} \frac{s^3 q_{\mathrm{ref}}(s)}{s^2 + K_P s + K_I} - \lim_{s\to 0} \frac{s^2 \Delta C_{m_\alpha}\alpha(s)}{s^2 + K_P s + K_I} \end{aligned}$$

It can be observed that both limits asymptotically converge to zero on the condition that K_P and K_I are strictly positive and, as stated earlier, that $q_{\mathrm{ref}}(s)$ represents stable reference pitch rate signals up to second order and angles of attack $\alpha(s)$ are up to first order. Moreover, the smaller the ratio $\frac{\Delta C_{m_\alpha}\alpha(s)}{K_I}$, and thus the smaller ΔC_{m_α} is, the faster the limit converges to zero. This indicates that identification is still needed, since it provides smaller misfits and thus faster convergence.

In case of a combined misfit in the control effectivity and aerodynamic model terms due to a change in the true system dynamics, this becomes:

$$\dot{\mathbf{y}} = \mathbf{l}(\mathbf{x}) + \mathbf{\Delta l}(\mathbf{x}) + [\mathbf{M}(\mathbf{x}) + \mathbf{\Delta M}(\mathbf{x})]\,\mathbf{u} \tag{7.23}$$

with the not updated control law as given in eq. (7.1) resulting in:

$$\begin{aligned} \dot{\mathbf{y}} &= \boldsymbol{\nu} + \mathbf{\Delta l}(\mathbf{x}) + \mathbf{\Delta M}(\mathbf{x})\,\mathbf{M}^{-1}(\mathbf{x})\,[\boldsymbol{\nu} - \mathbf{l}(\mathbf{x})] & (7.24) \\ &= \left[1 + \mathbf{\Delta M}(\mathbf{x})\,\mathbf{M}^{-1}(\mathbf{x})\right]\boldsymbol{\nu} + \mathbf{\Delta l}(\mathbf{x}) \\ &\quad - \mathbf{\Delta M}(\mathbf{x})\,\mathbf{M}^{-1}(\mathbf{x})\,\mathbf{l}(\mathbf{x}) & (7.25) \end{aligned}$$

As can be seen, this misfit leads not only to a double bias error term, but also an additional scaling error term on the virtual input. The latter disturbance cannot be handled by the linear controller. This can be illustrated as follows. In a similar procedure as for the additive error earlier, the expression for the tracking error in the Laplace domain becomes here:

$$\begin{aligned} \mathbf{e}(s) &= \left(s^2 + \left[1 + \mathbf{\Delta M}(\mathbf{x}(s))\,\mathbf{M}^{-1}(\mathbf{x}(s))\right](K_P s + K_I)\right)^{-1} \cdot \\ &\quad \left(s\left[s\mathbf{y}_d(s) - \mathbf{\Delta l}(\mathbf{x}(s)) + \mathbf{\Delta M}(\mathbf{x}(s))\,\mathbf{M}^{-1}(\mathbf{x}(s))\,\mathbf{l}(\mathbf{x}(s))\right]\right) & (7.26) \end{aligned}$$

In this case, the final value theorem leads to the following limit value:

$$\lim_{t\to\infty} \mathbf{e}(t) = \left(\left[1 + \Delta\mathbf{M}(\mathbf{x}(0))\,\mathbf{M}^{-1}(\mathbf{x}(0))\right] K_I\right)^{-1} \tag{7.27}$$

This result indicates that the presence of $\mathbf{\Delta M}\left(\mathbf{x}(0)\right)\mathbf{M}^{-1}\left(\mathbf{x}(0)\right)$ in this equality leads to perturbations. Consequently, accurate model identification is required with respect to $\mathbf{M}(\mathbf{x})$ in order to deal successfully with the disturbance. However, the control derivatives in $\mathbf{M}(\mathbf{x})$ are well identifiable due to the control surface excitations which are steered directly. Moreover, no state estimation results are needed for this part, avoiding additional risk for estimation errors.

7.2 Reconfiguring flight control with adaptive non-linear dynamic inversion

Equation (7.10) can be rewritten for an aircraft by considering the dynamic equation of an aircraft:

$$\dot{\mathbf{x}} = \begin{bmatrix} \dot{p} \\ \dot{q} \\ \dot{r} \end{bmatrix} = \mathbf{I}^{-1}\begin{bmatrix} L \\ M \\ N \end{bmatrix} - \mathbf{I}^{-1}\begin{bmatrix} p \\ q \\ r \end{bmatrix} \times \left(\mathbf{I}\begin{bmatrix} p \\ q \\ r \end{bmatrix}\right) \tag{7.28}$$

where $\begin{bmatrix} p & q & r \end{bmatrix}^T$ are the rotational rates and $\begin{bmatrix} L & M & N \end{bmatrix}^T$ the angular moments acting on the aircraft. The inertia matrix $\mathbf{I}$ stands for:

$$\mathbf{I} = \begin{bmatrix} I_{xx} & -I_{xy} & -I_{xz} \\ -I_{yx} & I_{yy} & -I_{yz} \\ -I_{zx} & -I_{zy} & I_{zz} \end{bmatrix} \tag{7.29}$$

where the moments of inertia I_{xy}, I_{yx}, I_{yz} and I_{zy} are assumed to be zero. These angular moments can be seen as functions of different state and control variables. NDI cancels out all non-linear parts, in order to obtain a system which behaves as a pure integrator, regardless of the state. This pure integrator can be controlled by a linear controller which produces the virtual control input $\begin{bmatrix} \nu_p & \nu_q & \nu_r \end{bmatrix}^T$. The aircraft dynamics in eq. (7.28) can be rewritten in the form of eq. (7.10). Here it should be noted that the aerodynamic moment equations can be split into a part describing the contribution of the states and a contribution of the control surface settings.

Note that for inverting the effector blending model $\mathbf{M}(\mathbf{x})$, some simplifications have been made concerning the control channels. First of all, in this stage engine thrust is not used to generate moments, therefore the contribution of the throttle setting can be seen as a state, which does not occur in the effector blending model. The same principle holds for the stabilizer and flaps. Moreover, the individual control derivatives of the different aileron, elevator, rudder and spoiler surfaces from the identification step have been combined into equivalent global control derivatives which are used in the effector blending model of the control phase.

$$
\begin{aligned}
\begin{bmatrix} C_l \\ C_m \\ C_n \end{bmatrix} &= \begin{bmatrix} C_{l_0} + C_{l_\beta}\beta + C_{l_p}\frac{pb}{2V} + C_{l_r}\frac{rb}{2V} + C_{T_c}T_c \\ C_{m_0} + C_{m_\alpha}\alpha + C_{m_q}\frac{q\bar{c}}{V} + C_{m_{i_h}} i_h + C_{m_{\delta_{f_o}}}\delta_{f_o} + C_{m_{\delta_{f_i}}}\delta_{f_i} + C_{m_{T_c}}T_c \\ C_{n_0} + C_{n_\beta}\beta + C_{n_p}\frac{pb}{2V} + C_{n_r}\frac{rb}{2V} + C_{n_{T_c}}T_c \end{bmatrix} \\
&\quad + \begin{bmatrix} \tilde{C}_{l_{\delta_a}} & 0 & \tilde{C}_{l_{\delta_r}} \\ 0 & \tilde{C}_{m_{\delta_e}} & 0 \\ \tilde{C}_{n_{\delta_a}} & 0 & \tilde{C}_{n_{\delta_r}} \end{bmatrix} \begin{bmatrix} \delta_a \\ \delta_e \\ \delta_r \end{bmatrix} && (7.30) \\
&= \begin{bmatrix} C_{l_\text{states}} \\ C_{m_\text{states}} \\ C_{n_\text{states}} \end{bmatrix} + \begin{bmatrix} \tilde{C}_{l_{\delta_a}} & 0 & \tilde{C}_{l_{\delta_r}} \\ 0 & \tilde{C}_{m_{\delta_e}} & 0 \\ \tilde{C}_{n_{\delta_a}} & 0 & \tilde{C}_{n_{\delta_r}} \end{bmatrix} \begin{bmatrix} \delta_a \\ \delta_e \\ \delta_r \end{bmatrix} && (7.31)
\end{aligned}
$$

where:

$$
\begin{aligned}
\tilde{C}_{l_{\delta_a}} &= -C_{l_{\delta_{a_{ir}}}} + C_{l_{\delta_{a_{il}}}} - C_{l_{\delta_{a_{or}}}} + C_{l_{\delta_{a_{ol}}}} - C_{l_{\delta_{sp_1}}} - ... - C_{l_{\delta_{sp_5}}} + \\
&\quad + C_{l_{\delta_{sp_8}}} + ... + C_{l_{\delta_{sp_{12}}}} && (7.32) \\
\tilde{C}_{n_{\delta_a}} &= -C_{n_{\delta_{a_{ir}}}} + C_{n_{\delta_{a_{il}}}} - C_{n_{\delta_{a_{or}}}} + C_{n_{\delta_{a_{ol}}}} - C_{n_{\delta_{sp_1}}} - ... - C_{n_{\delta_{sp_5}}} + \\
&\quad + C_{n_{\delta_{sp_8}}} + ... + C_{n_{\delta_{sp_{12}}}} && (7.33) \\
\tilde{C}_{m_{\delta_e}} &= C_{m_{\delta_{e_{ir}}}} + C_{m_{\delta_{e_{il}}}} + C_{m_{\delta_{e_{or}}}} + C_{m_{\delta_{e_{ol}}}} && (7.34) \\
\tilde{C}_{l_{\delta_r}} &= C_{l_{\delta_{r_u}}} + C_{l_{\delta_{r_l}}} && (7.35) \\
\tilde{C}_{n_{\delta_r}} &= C_{n_{\delta_{r_u}}} + C_{n_{\delta_{r_l}}} && (7.36)
\end{aligned}
$$

Inserting this into eq. (7.28) and solving for the control inputs $\begin{bmatrix} \delta_a & \delta_e & \delta_r \end{bmatrix}^T$, results in a similar structure as in eq. (7.10):

$$
\begin{aligned}
\begin{bmatrix} \delta_a \\ \delta_e \\ \delta_r \end{bmatrix} &= \begin{bmatrix} b\tilde{C}_{l_{\delta_a}} & 0 & b\tilde{C}_{l_{\delta_r}} \\ 0 & \bar{c}\tilde{C}_{m_{\delta_e}} & 0 \\ b\tilde{C}_{n_{\delta_a}} & 0 & b\tilde{C}_{n_{\delta_r}} \end{bmatrix}^{-1} \cdot \\
&\quad \left\{ \frac{\mathbf{I}}{\frac{1}{2}\rho V^2 S} \left(\begin{bmatrix} \nu_p \\ \nu_q \\ \nu_r \end{bmatrix} + \mathbf{I}^{-1} \begin{bmatrix} p \\ q \\ r \end{bmatrix} \times \left(\mathbf{I} \begin{bmatrix} p \\ q \\ r \end{bmatrix} \right) \right) - \begin{bmatrix} bC_{l_\text{states}} \\ \bar{c}C_{m_\text{states}} \\ bC_{n_\text{states}} \end{bmatrix} \right\} && (7.37)
\end{aligned}
$$

where the virtual inputs $\begin{bmatrix} \nu_p & \nu_q & \nu_r \end{bmatrix}^T$ are the time derivatives of the rotational rates of the aircraft, which are selected to be the control variables in order to obtain rate control. The first part of eq. (7.37) performs the control inversion, while the second part contains the state inversion.

Subsequently, the different aileron, elevator, rudder and spoiler surfaces are coupled and deflect in a fixed coordinated way, as illustrated by eq. (7.32) till eq. (7.36). All four ailerons and ten spoilers deflect simultaneously. The same holds for the four elevator surfaces and the upper and lower rudder. A more flexible control allocation algorithm is considered in chapter 8. Nevertheless, the results shown here prove that this simplification has no serious detrimental effect on the performance of the FTFC module.

The weakness of classical NDI, its sensitivity to modeling errors which leads to erroneous inversion and thus a possibly unstable result, is circumvented here by making use of the real time identified physical model, which has a greater accuracy than an a priori model. As a result, one obtains an adaptive NDI routine which renders the aircraft behaviour like a pure integrator in situations before and after the failure. The NDI based closed loop system is composed of two loops as explained in section 7.1.2. The inner loop allows for rate control on roll and pitch steering. Yaw control is achieved by sideslip control. This is the proposed way of manual control for the human pilot. The outer loop adds another NDI routine for angle control on heading, flight path angle and sideslip. This is the so-called concept of angle control, where it should be noted that the angles of the groundspeed velocity vector and not the aircraft angles are controlled. These three quantities form an ideal basis for the design of the classical autopilot modes.

Research has revealed that this adaptive model based control approach has an important advantage since a very representative aerodynamic model is available by means of the two step method described earlier. In this way, a fault tolerant control scheme has been obtained which is virtually capable of handling any aircraft failure, as long as it is identified and represented correctly by the on-line aircraft model.

There are some implementation issues that need further elaboration. Especially for fault tolerant flight control using NDI, two issues arise. First of all, there is the problem of robustness: if the real time identification routine is not able to make an accurate fit of the aircraft model, the possibility exists that classical NDI leads to an unsatisfactory result. Therefore, robust NDI could be considered for application in this context, but real time applicability is a major concern here and the stability analysis given in section 7.1.3 has shown that the control setup has sufficient robustness against non-ideal dynamic inversion on some conditions, which are satisfied in this setup and in these experiments. Moreover, there is the underdetermination problem due to the large amount of control surfaces. This is the domain of control allocation, which is considered in chapter 8.

The principle of Adaptive NDI (ANDI) has been applied on two levels. The lower level is manual control, which has been verified by means of workload evaluation runs in the Simona Research Simulator, as presented in chapter 9. The upper level is full automatic autopilot control, which has been evaluated by the assessment criteria as defined in appendix B. For both control alternatives, the same inner loop has been established, which focuses on pure body fixed angular rate control as elaborated in equation (7.37) and as illustrated in fig. 7.1. The distinction between the inner and outer loop has been based upon the time

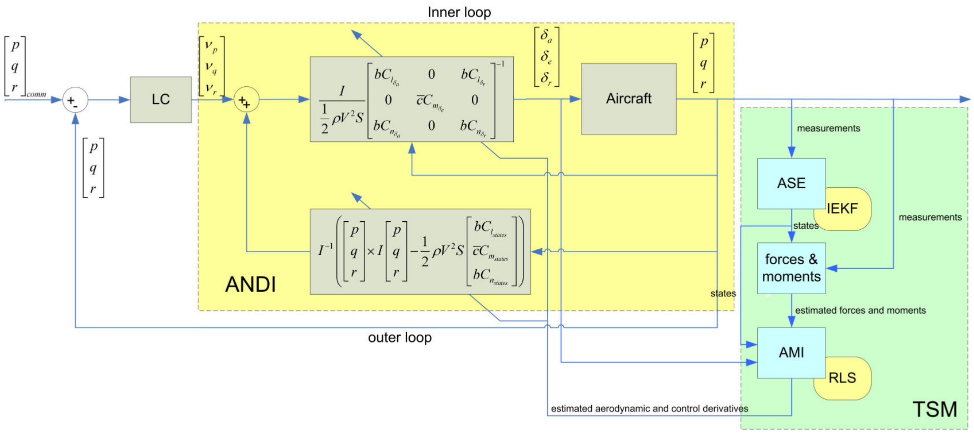

Figure 7.1: NDI rate control inner loop

scale separation principle as mentioned earlier in section 7.1.2. Mind that in each approach, the two step method is operational and supplying the real time identified model parameters, including failure characteristics when relevant.

7.2.1 Manual Control

For manual control, an outer loop is needed in order to convert the pilot pedals input towards a sideslip β command rather than a yaw rate r command. A pure classical feedback loop works for unfailed aircraft, but this will not perform adequately for asymmetrically damaged aircraft, where a certain steady non-zero sideslip angle β and/or roll angle ϕ are necessary to compensate for the asymmetry. Therefore, this loop must also be NDI-based, where the feedback path makes use of the lateral specific force A_y (which is related to the sideslip angle), the roll angle ϕ and the commanded roll rate p_{comm}.

The control law can be deduced analogously as for the inner loop described earlier, where at this stage a relation must be found between the sideslip angle β and the body fixed angular rates. From [159], the sideslip angle β can be written as follows:

$$v = V \sin \beta \tag{7.38}$$

Rewriting for β and differentiating and inserting the equation for $\dot{v}$ from the nonlinear aircraft kinematics yields:

$$\begin{aligned}\dot{\beta} &= \frac{d}{dt}\left(\arcsin\frac{v}{V}\right) = \frac{1}{\sqrt{V^2-v^2}}\cdot\dot{v} \\ &= \frac{1}{\sqrt{V^2-v^2}}\cdot\left[A_y + g\cos\theta\sin\phi\right] + \begin{bmatrix}\frac{w}{\sqrt{V^2-v^2}} & 0 & \frac{-u}{\sqrt{V^2-v^2}}\end{bmatrix}\begin{bmatrix}p\\q\\r\end{bmatrix}\end{aligned} \tag{7.39}$$

Since controlling the sideslip β is implemented by the rudder δ_r via primarily the yaw rate r, given $u \gg w$, equation (7.39) can be rewritten for the NDI loop command for r in the rate control loop where the virtual input is $\nu_\beta = \dot{\beta}$ and where p_{comm} is the commanded roll rate by the pilot, which tracks the cockpit roll wheel deflection:

$$r = \left(\frac{-u}{\sqrt{V^2-v^2}}\right)^{-1}\cdot\left\{\nu_\beta - \frac{1}{\sqrt{V^2-v^2}}\left[A_y + g\cos\theta\sin\phi + wp_{\mathrm{comm}}\right]\right\} \tag{7.40}$$

As a result, fig. 7.2 shows the manual control outer loop architecture. In this set-up the pilot's controls work as follows. Control wheel steering supplies a reference roll rate, pitch rate tracks the control column and the pedals give the commanded sideslip angle, which is limited between $+5°$ and $-5°$. Moreover, in order to ensure comfortable aircraft responses to the pilot inputs, some first order low pass filters have been added in the input channel. In the inner loop, the linear controllers involve proportional-integral control, and gains have been selected in order to ensure favourable handling qualities by means of damping ratio ζ and natural frequency ω_n. Currently, the outer loop gains have been determined heuristically. Subsequent research has focused on controller gain optimization by means of multi-objective optimization, as presented in chapter 8.

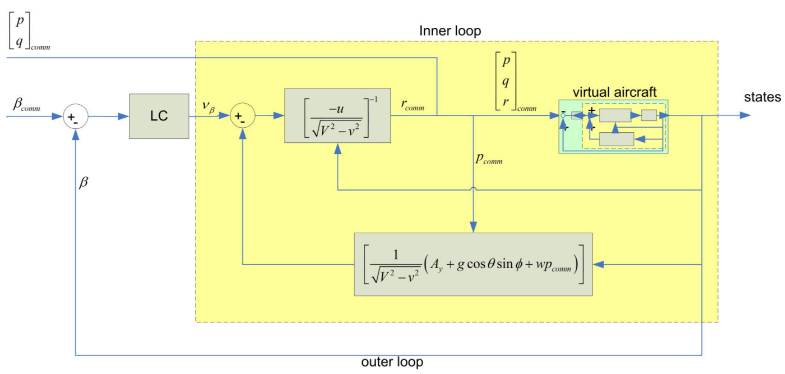

Figure 7.2: NDI manual control outer loop

This manual control setup has been applied and extensively validated in the SIMONA (SImulation, MOtion and NAvigation) Research Simulator (SRS). An evaluation campaign has been set up to evaluate the handling qualities and to assess the pilot workload of the manual variant of the fault tolerant controller, compared to the classical manual control setup. This experiment setup, together with the observations, is presented in chapter 9.

7.2.2 Autopilot Control

For autopilot control, a double loop is needed over the inner loop rate control described earlier. As mentioned for the manual control lay-out, a pure classical feedback loop works for unfailed aircraft, but this will not perform adequately for asymmetrically damaged aircraft, where a certain steady non-zero sideslip angle β and/or roll angle ϕ are necessary to compensate for the asymmetry. Therefore, also both loops considered here must be NDI-based. The middle loop quantities are the aerodynamic angles, namely roll angle ϕ, angle of attack α and sideslip angle β. The equation for sideslip angle β is already available from the manual control part. The equations for roll angle ϕ and angle of attack α remain to be derived.

First, in order to obtain roll angle control, an equation needs to be found which expresses the change in roll angle in terms of the required rotational rates. Reference [159] provides:

$$\frac{d\phi}{dt} = \dot{\phi} = p + (q \sin\phi + r \cos\phi) \tan\theta \tag{7.41}$$

Separating the rotational rates $\begin{bmatrix} p & q & r \end{bmatrix}^T$ yields:

$$\dot{\phi} = \begin{bmatrix} 1 & \sin\phi \tan\theta & \cos\phi \tan\theta \end{bmatrix} \begin{bmatrix} p \\ q \\ r \end{bmatrix} \tag{7.42}$$

Second, the angle of attack must be represented in a similar way, in terms of the required rotational rates. Since:

$$\dot{\alpha} \approx \dot{\theta} - \dot{\gamma} \tag{7.43}$$

this problem boils down to finding equations for $\dot{\theta}$ and $\dot{\gamma}$. The glideslope angle γ is the angle between the total velocity vector and its vertical component in the earth fixed reference frame:

$$\begin{aligned} \sin\gamma &= \frac{w_e}{V} \\ \gamma &= \arcsin\left(\frac{w_e}{V}\right) \end{aligned} \tag{7.44}$$

A descent $(w_e > 0)$ results in a positive glideslope angle. Differentiating eq. (7.44) results in:

$$\begin{aligned}\dot{\gamma} &= \frac{1}{\sqrt{1-\frac{w_e^2}{V^2}}}\frac{\dot{w}_e}{V} = \frac{\dot{w}_e}{\sqrt{V^2-w_e^2}} \\ &= \frac{1}{\sqrt{V^2-w_e^2}} \cdot [-A_x \sin\theta + A_y \sin\phi\cos\theta + A_z \cos\phi\cos\theta + g] \end{aligned} \tag{7.45}$$

This equation is obtained by rotating the vertical acceleration A_z from the earth into the body reference frame. Note that no rotational rates can be found in this equation. On the other hand, the time derivative of the pitch angle $\dot{\theta}$ depends on the rates in the following way:

$$\dot{\theta} = q\cos\phi - r\sin\phi \tag{7.46}$$

Separating the rates yields:

$$\dot{\theta} = \begin{bmatrix} 0 & \cos\phi & -\sin\phi \end{bmatrix} \begin{bmatrix} p \\ q \\ r \end{bmatrix} \tag{7.47}$$

Combining eq. (7.43), (7.45) and (7.47) results in the NDI equation for the angle of attack α:

$$\begin{aligned}\dot{\alpha} \approx \dot{\theta} - \dot{\gamma} &= -\frac{1}{\sqrt{V^2-w_e^2}} \cdot [-A_x \sin\theta + A_y \sin\phi\cos\theta + A_z \cos\phi\cos\theta + g] + \\ &+ \begin{bmatrix} 0 & \cos\phi & -\sin\phi \end{bmatrix} \begin{bmatrix} p \\ q \\ r \end{bmatrix} \end{aligned} \tag{7.48}$$

The different controls for roll angle ϕ, angle of attack α and sideslip angle β can now be combined and the resulting equation can now be rewritten for the required rotational velocities:

$$\begin{aligned}\begin{bmatrix} p \\ q \\ r \end{bmatrix} &= \begin{bmatrix} 1 & \sin\phi\tan\theta & \cos\phi\tan\theta \\ 0 & \cos\phi & -\sin\phi \\ \frac{w}{\sqrt{V^2-v^2}} & 0 & \frac{-u}{\sqrt{V^2-v^2}} \end{bmatrix}^{-1} \cdot \\ & \left\{ \begin{bmatrix} \dot{\phi} \\ \dot{\alpha} \\ \dot{\beta} \end{bmatrix} - \begin{bmatrix} 0 \\ -\frac{1}{\sqrt{V^2-w_e^2}} \cdot [-A_x \sin\theta + A_y \sin\phi\cos\theta + A_z \cos\phi\cos\theta + g] \\ \frac{1}{\sqrt{V^2-v^2}} \cdot [A_y + g\cos\theta\sin\phi] \end{bmatrix} \right\} \end{aligned} \tag{7.49}$$

The outer loop quantities to be controlled in this setting are the true airspeed V_{TAS}, the flight path angle γ and the course χ. It should be noted that these quantities allow total control over the velocity vector, respectively regarding magnitude, elevation and azimuth in the polar coordinates. Ref. [54] explains the conventional coupling between the course χ and the roll angle ϕ. Regarding the demanded flight path angle γ_{comm}, this one can be rewritten in terms of the required angle of attack α. It has been found that the expression $\alpha \approx \theta - \gamma_{\mathrm{comm}}$ is not accurate enough for this purpose, and therefore a more elaborate expression is deduced from ref. [257]:

$$\begin{aligned} \sin\gamma &= a\sin\theta - b\cos\theta \\ &\text{with:} \quad \begin{cases} a = \cos\alpha\cos\beta \\ b = \sin\phi\sin\beta + \cos\phi\sin\alpha\cos\beta \end{cases} \end{aligned} \tag{7.50}$$

This equation has been rewritten for α, where it has been assumed that $a = \cos\alpha\cos\beta \approx 1$:

$$\sin\alpha = -\frac{\sin\gamma}{\cos\phi\cos\beta\cos\theta} + \left(\frac{\tan\theta}{\cos\phi\cos\beta} - \tan\phi\tan\beta\right) \tag{7.51}$$

For thrust control, an NDI loop has been added parallel to the middle loop which inverts the velocity V_{TAS}. This velocity can be expressed as:

$$V_{TAS} = \sqrt{u_b^2 + v_b^2 + w_b^2} \tag{7.52}$$

Differentiating eq. (7.52):

$$\begin{aligned} \dot{V}_{TAS} &= \frac{1}{2}\left(u_b^2 + v_b^2 + w_b^2\right)^{-\frac{1}{2}}\left(2u_b\dot{u}_b + 2v_b\dot{v}_b + 2w_b\dot{w}_b\right) \\ &= \frac{1}{\sqrt{u_b^2 + v_b^2 + w_b^2}}\left(g\left(-u_b\sin\theta + \cos\theta\left(v_b\sin\phi + w_b\cos\phi\right)\right) + \right. \\ &\quad \left. + \frac{\rho V^2 S}{2m}\left(u_b\tilde{C}_x + v_b\tilde{C}_y + w_b\tilde{C}_z\right)\right) + \\ &\quad + \frac{1}{\sqrt{u_b^2 + v_b^2 + w_b^2}}\frac{\rho V^2 S}{2m}\left(u_b C_{x_T} + v_b C_{y_T} + w_b C_{z_T}\right) T_c \end{aligned} \tag{7.53}$$

Rewriting for the thrust lever input T_c results in:

$$\begin{aligned} T_c &= \left(\frac{\rho V S}{2m}\left(u_b C_{x_T} + v_b C_{y_T} + w_b C_{z_T}\right)\right)^{-1} \cdot \\ &\quad \left(\dot{V}_{TAS} - \left(\frac{g}{V}\left(-u_b\sin\theta + \cos\theta\left(v_b\sin\phi + w_b\cos\phi\right)\right) + \right.\right. \\ &\quad \left.\left. + \frac{\rho V S}{2m}\left(u_b\tilde{C}_x + v_b\tilde{C}_y + w_b\tilde{C}_z\right)\right)\right) \end{aligned} \tag{7.54}$$

wherein:

$$\tilde{C}_x = C_{X_0} + C_{X_\alpha}\alpha + C_{X_{\alpha^2}}\alpha^2 + C_{X_q}\frac{q\bar{c}}{V} + C_{X_{\delta_{e_{ir}}}}\delta_{e_{ir}} + C_{X_{\delta_{e_{il}}}}\delta_{e_{il}} + \\ + C_{X_{\delta_{e_{or}}}}\delta_{e_{or}} + C_{X_{\delta_{e_{ol}}}}\delta_{e_{ol}} + C_{X_{i_h}} i_h + C_{X_{\delta_{f_o}}}\delta_{f_o} + C_{X_{\delta_{f_i}}}\delta_{f_i} \tag{7.55}$$

$$\tilde{C}_y = C_{Y_0} + C_{Y_\beta}\beta + C_{Y_p}\frac{pb}{2V} + C_{Y_r}\frac{rb}{2V} + C_{Y_{\delta_{a_{ir}}}}\delta_{a_{ir}} + C_{Y_{\delta_{a_{il}}}}\delta_{a_{il}} + C_{Y_{\delta_{a_{or}}}}\delta_{a_{or}} + \\ + C_{Y_{\delta_{a_{ol}}}}\delta_{a_{ol}} + C_{Y_{\delta_{r_u}}}\delta_{r_u} + C_{Y_{\delta_{r_l}}}\delta_{r_l} + C_{Y_{\delta_{sp_1}}}\delta_{sp_1} + \ldots + C_{Y_{\delta_{sp_{12}}}}\delta_{sp_{12}} \tag{7.56}$$

$$\tilde{C}_z = C_{Z_0} + C_{Z_\alpha}\alpha + C_{Z_q}\frac{q\bar{c}}{V} + C_{Z_{\delta_{e_{ir}}}}\delta_{e_{ir}} + C_{Z_{\delta_{e_{il}}}}\delta_{e_{il}} + C_{Z_{\delta_{e_{or}}}}\delta_{e_{or}} + C_{Z_{\delta_{e_{ol}}}}\delta_{e_{ol}} + \\ + C_{Z_{i_h}} i_h + C_{Z_{\delta_{f_o}}}\delta_{f_o} + C_{Z_{\delta_{f_i}}}\delta_{f_i} \tag{7.57}$$

As a result, fig. 7.3 shows the autopilot control outer loop architecture. In this set-up the outer loop quantities V_{TAS}, γ and χ can provide the connection to the Mode Control Panel, operated by the human pilot, on which he can set up specific values for these quantities to be tracked. Alternatively, and as used in the experiments considered here, the same quantities can be used to implement waypoint control, where these quantities can be calculated from the distance between the last and next waypoint in the three cartesian coordinate components using trigonometry. Finally, two more remarks must be added concerning fig. 7.3. The acronym 'LC' stands for linear controller. Moreover, some requirements have been implemented on the roll angle, which is limited between $+45°$ and $-45°$. These maximum roll angles should be adapted in post failure conditions, dependent upon the extent of the damage suffered by the aircraft, and thus how far the safe flight envelope has been reduced.

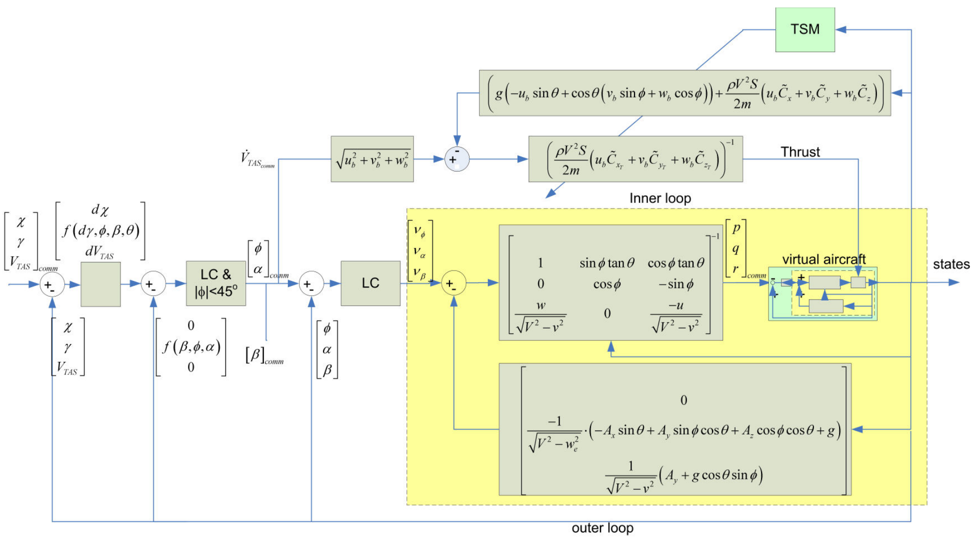

Figure 7.3: NDI autopilot outer loop, featuring V_{TAS}, γ and χ control

The evaluation of the autopilot FTFC strategy is based upon desktop based off-line evaluations for stabilizer runaway, rudder loss and the engine separation Bijlmermeer accident. The requirements which apply on the time histories of these states are based upon a predefined benchmark scenario, given in appendix section A.1.3 and ref. [249]. In this scenario, desired and adequate value ranges have been defined for the most important states. An elaborate discussion on how these specifications have been determined can be found in appendix B and ref. [178]. In order to save space, the first two scenarios are discussed jointly below.

7.2.2.1 Stabilizer Runaway and Rudder Loss

First of all, a comparison has been made between the unfailed and the failed trajectory, as can be seen in fig. 7.4(a). It can be seen that there is almost no difference in the trajectory between the unfailed and the stabilizer runaway situation. For the rudder loss scenario, there is a significant difference. The reason for this is that the maximum safe roll angle without rudder is limited to $20°$. This is related to the issue of the post-failure safe flight envelope. Currently, these manoeuvre limits have been defined heuristically following evaluating simulation runs for this analysis. Future research will investigate the use of safe flight envelope prediction in order to derive these manoeuvre limits based on the model estimation parameters. Two benchmark trajectory phases have been analysed for this control setup, namely straight flight and right hand turn. The straight flight is the time span between the failure occurrence and the first waypoint. The phase between first and second waypoint is classified as the right hand turn manoeuvre. Besides, the beneficial influence of the repeated identification procedure after failure is illustrated in fig. 7.4(b). As can be seen in this figure, the NDI controller is not capable to fly properly from the second waypoint towards the third one without identifying the new aircraft dynamics. As a matter of fact, loss of the rudder is a drastic structural failure, as already illustrated in section 4.5.2, and the NDI controller is not able fulfill the mission profile with the new aircraft configuration if the mathematical model used by the controller is not updated post-failure.

Concerning the straight flight phase, the states as well as the specific forces have been analysed in fig. 7.5. The state requirements are all satisfied, and also the specific forces seem acceptable. It is apparent that there is no significant influence from the stabilizer runaway in any of the graphs. The rudder loss effect is visible in the lateral specific force A_y time history. However, the force scale shows that this is not a significant issue. Also for the right turn, the state requirements are satisfied as can be seen in fig. 7.6. Due to the more stringent roll angle limitation from 30 to 20 degrees after rudder loss, it takes a longer time to execute the turn in the different scenarios, which explains the time difference in figures 7.6(a) and 7.6(b). The same issue holds for the kinematic acceleration requirements in fig. 7.7. Only body roll and yaw rates together with sideslip angle suffer small violations of the specifications, this is connected to the behaviour explained below, together with the analysis of the lateral kinematic acceleration. Analysing the kinematic accelerations in fig.

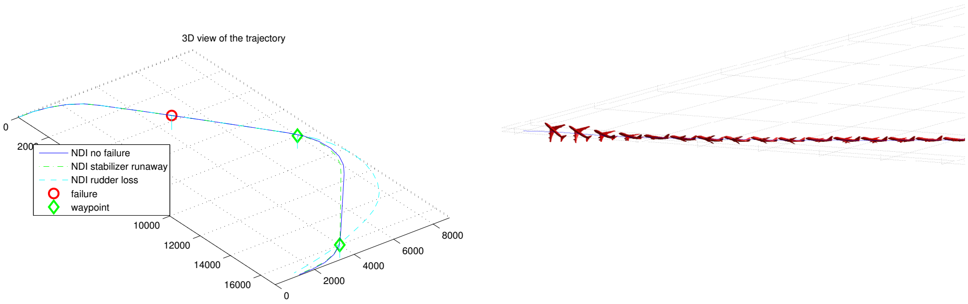

(a) aircraft trajectory with FTFC autopilot along three waypoints in the scenario's unfailed, stabilizer runaway and rudder loss

(b) part of aircraft trajectory with FTFC autopilot between two final waypoints in the scenario rudder loss without identification

Figure 7.4: Aircraft trajectory with FTFC autopilot along three waypoints

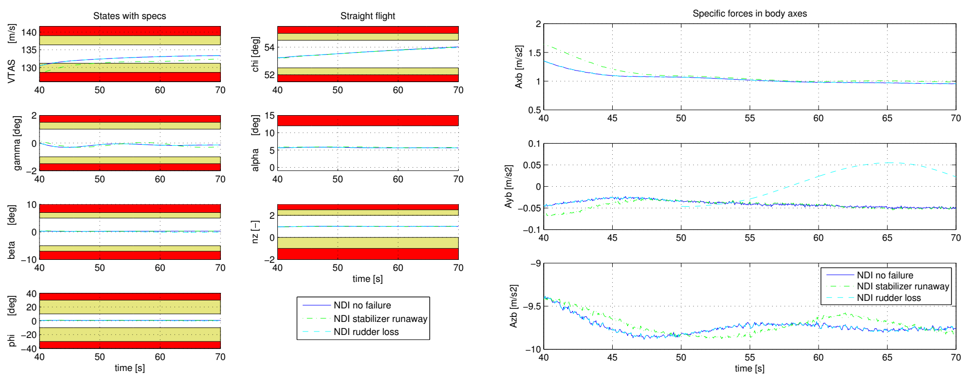

(a) states

(b) specific forces

Figure 7.5: Straight flight phase performance check with assessment criteria for stabilizer runaway and rudder loss

7.7 shows that only the lateral kinematic acceleration a_y is not satisfied. This is caused by the directional stability problem, due to the missing rudder surface. This missing rudder eliminates directional stability, as shown in fig. 4.13. Consequently, lateral damping is insufficient during the turn, and after ending the right hand turn, the aircraft also has the tendency to continue a slipping flight, which is indicated by the time history of this quantity. This problem can be solved by incorporating differential thrust in order to promote artificial lateral damping, this is one of the points for further work.

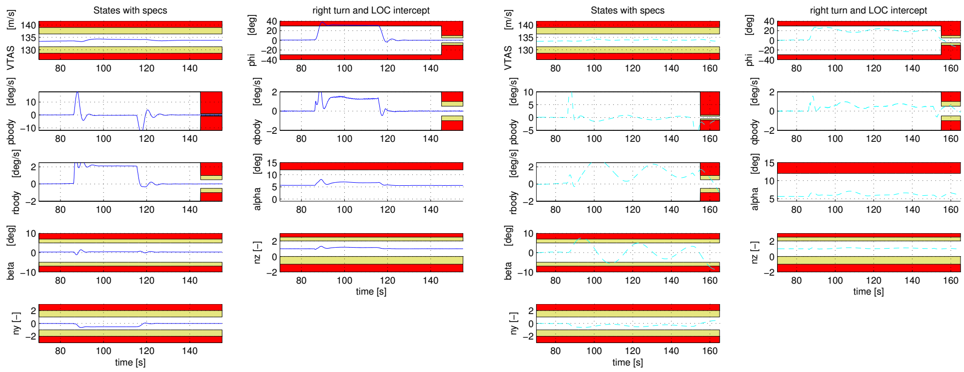

(a) states nominal and stabilizer runaway (b) states rudder loss

Figure 7.6: Right turn flight phase states performance check with assessment criteria for stabilizer runaway and rudder loss

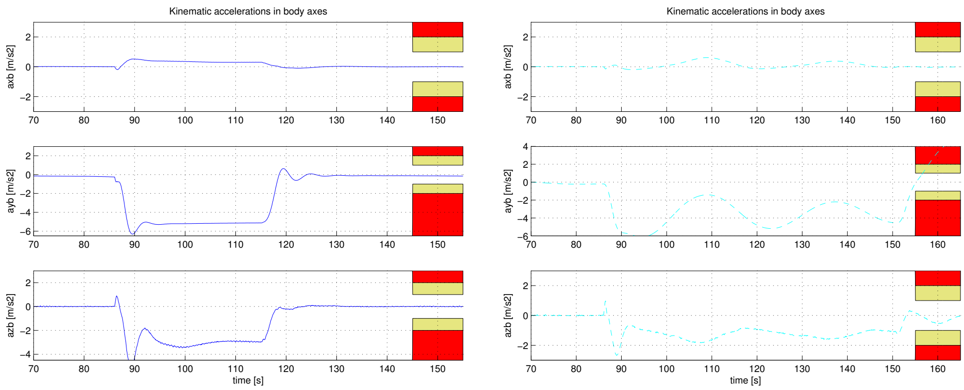

(a) states nominal and stabilizer runaway (b) states rudder loss

Figure 7.7: Right turn flight phase kinematic accelerations performance check with assessment criteria for stabilizer runaway and rudder loss

The control surface deflections are shown and compared hereafter. Fig. 7.8 shows the control surface deflections commanded by the fault tolerant flight control system in a nominal unfailed scenario. On the contrary, fig. 7.9 gives the same deflections in the stabilizer runaway scenario. In this figure, it can be seen that the elevators compensate for the disturbing stabilizer failure. Finally, fig. 7.10 represents the control surface deflections in the vertical tail loss scenario. There are no rudder deflections anymore after the failure, since the aircraft lacks the complete rudder. On the contrary, aileron and spoiler deflections indicate that they are more active compared to the unfailed scenario, since they are compensating for the lack of rudder input.

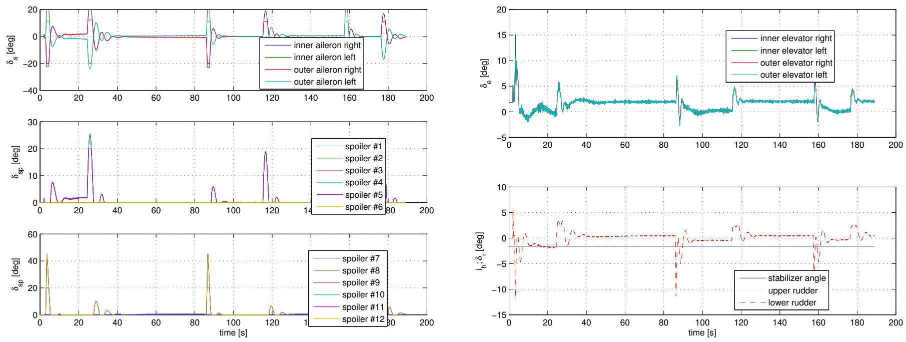

(a) ailerons and spoilers (b) elevators, stabilizer and rudders

Figure 7.8: Nominal scenario flight control surface deflections

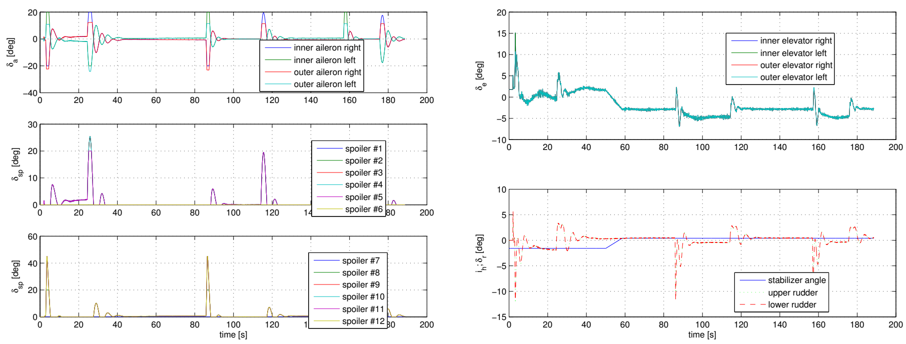

(a) ailerons and spoilers (b) elevators, stabilizer and rudders

Figure 7.9: Stabilizer runaway scenario flight control surface deflections

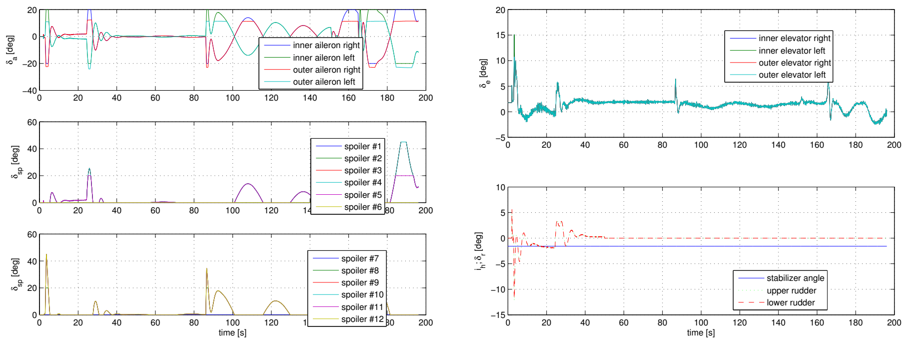

(a) ailerons and spoilers (b) elevators, stabilizer and rudders

Figure 7.10: Vertical tail loss scenario flight control surface deflections

7.2.2.2 Engine separation Bijlmermeer accident

Comparing the unfailed and failed trajectories for the engine separation scenario leads to the result shown in fig. 7.11. The classic controller is by no means capable of handling the failure, while the nonlinear dynamic inversion based fault tolerant controller can. It is important to be aware that both control alternatives have the same hardware constraints on the control authority of the actuators, but FTFC does not employ the same proportional couplings in the control allocation scheme between the several control surfaces, like inner ailerons, outer ailerons and spoilers, or the four elevators, as the classic autopilot controller. Despite its failure accommodation qualities, there is a difference in the trajectory between the unfailed and the NDI failed situation. The reason for this is again that the maximum safe roll angle with right wing damage, lost right wing engines and only half the hydraulics is limited to 20°, again due to the post-failure safe flight envelope. The same two benchmark trajectory phases have been analysed for this scenario too. The straight flight is the time span between the failure occurrence and the first waypoint. The phase between first and second waypoint is classified as the right hand turn manoeuvre.

Concerning the straight flight phase, the states as well as the specific forces have been analysed in fig. 7.12.

The state requirements are satisfied, and also the specific forces seem acceptable in fig. 7.12. In the state graphs, it can be seen that proper energy management is important in this failed situation, only altitude or speed can be maintained. The choice has been made to increase initial speed up to 170m/s and then to allow the speed to decrease down to 133.8m/s, after which the throttle is opened. The initial speed of 170 m/s is shown in fig. 7.12(a). The most significant decrease towards 130 m/s occurs during the right hand turn as can be seen in fig. 7.13(b).

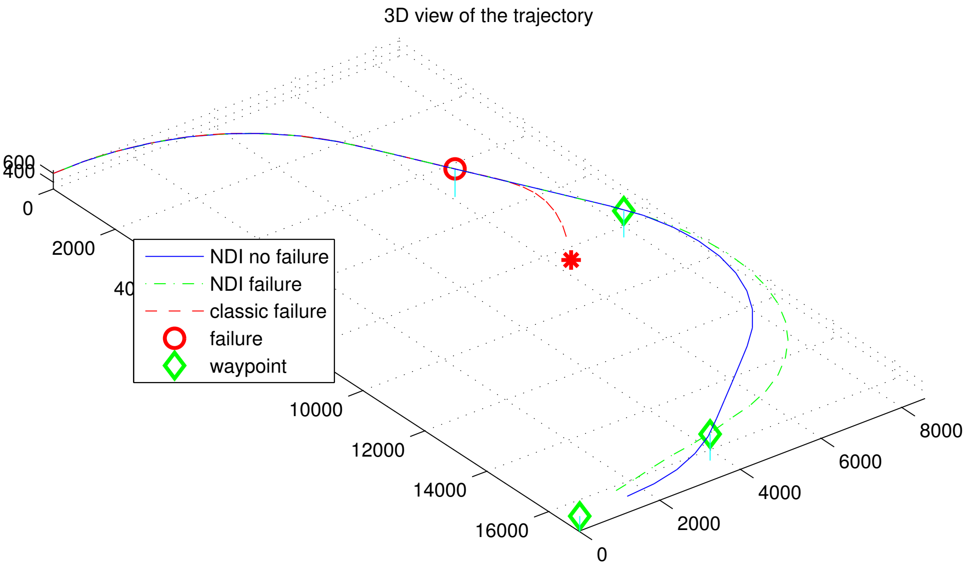

Figure 7.11: Aircraft trajectory with autopilot along three waypoints in the scenario's FTFC controlled no failure, FTFC controlled with failure, classically controlled with failure

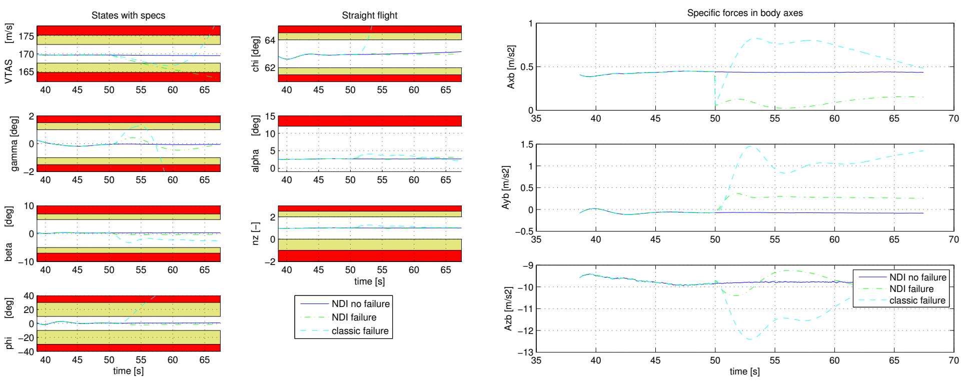

(a) states

(b) specific forces

Figure 7.12: Straight flight phase performance check with assessment criteria for the three scenarios involving engine separation

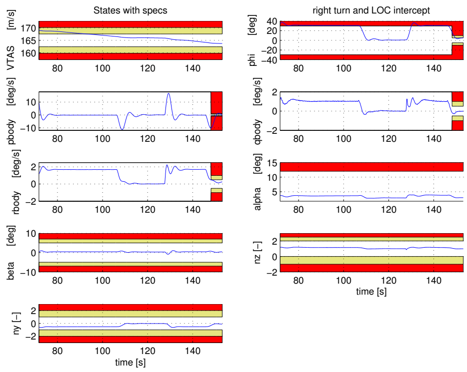

(a) states nominal

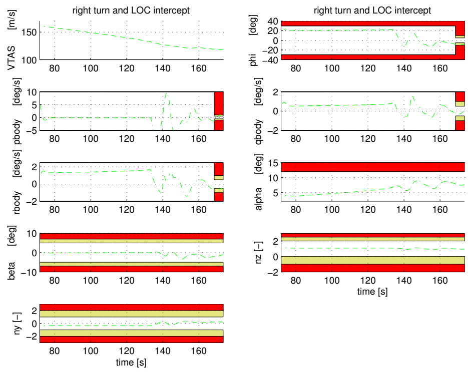

(b) states engine separation

Figure 7.13: Right turn flight phase states performance check with assessment criteria for the three scenarios involving engine separation

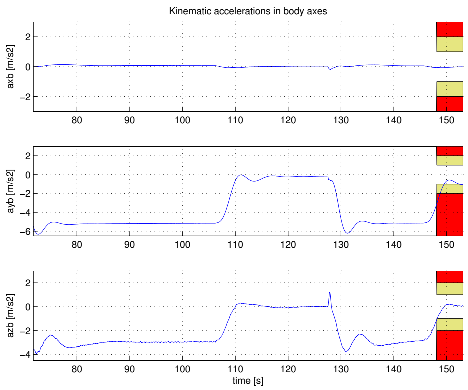

(a) kinematic accelerations nominal runaway

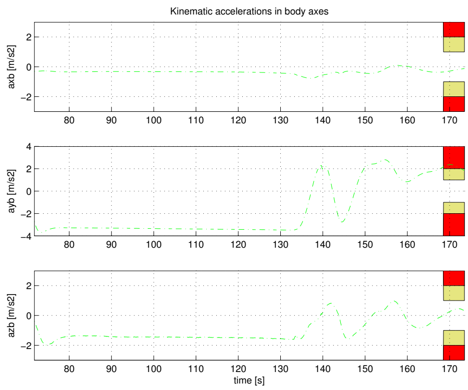

(b) kinematic acceleration engine separation

Figure 7.14: Right turn flight phase kinematic accelerations performance check with assessment criteria for the three scenarios invovling engine separation

From fig. 7.13 and 7.14, the same conclusions can be drawn. Due to the more stringent roll angle limitation from 30 to 20 degrees after the engine separation failure, it takes a longer time to execute the turn in the failed scenario, which explains the time difference. All requirements in fig. 7.13 and 7.14 are satisfied. In the failed situation the requirements on the lateral kinematic acceleration a_y are not completely met. This is due to the asymmetric damage. A certain non-zero roll angle ϕ, sideslip angle β and thus lateral kinematic acceleration a_y are needed to keep the aircraft in equilibrium.

The control surface deflections are shown and compared hereafter. Fig. 7.15 shows the control surface deflections commanded by the fault tolerant flight control system in a nominal unfailed scenario. Fig. 7.16 gives the same deflections in the engine separation scenario. In this figure, it can be seen that quite some control surfaces are inoperative due to the partial loss of hydraulics. However, the remaining operative control surfaces, like two of the four elevators and a small subset of ailerons and spoilers, are able to steer the aircraft along the predefined waypoints. Finally, fig. 7.17 represents the control surface deflections for the same engine separation scenario, but with the classical controller with less control authority. The simulation ends considerably sooner compared with fig. 7.15 and 7.16, this is because the aircraft hits the terrain.

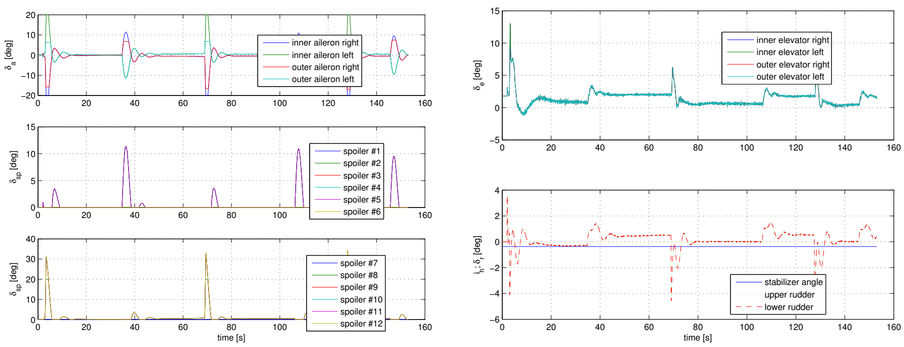

(a) ailerons and spoilers (b) elevators, stabilizer and rudders

Figure 7.15: Nominal scenario flight control surface deflections

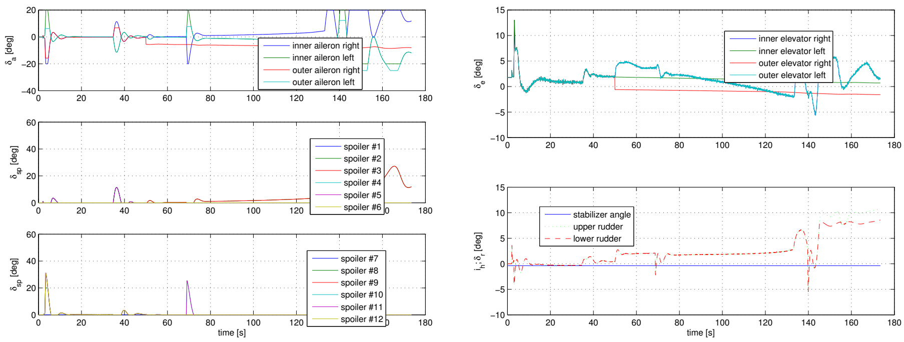

(a) ailerons and spoilers (b) elevators, stabilizer and rudders

Figure 7.16: Engine separation scenario with fault tolerant controller flight control surface deflections

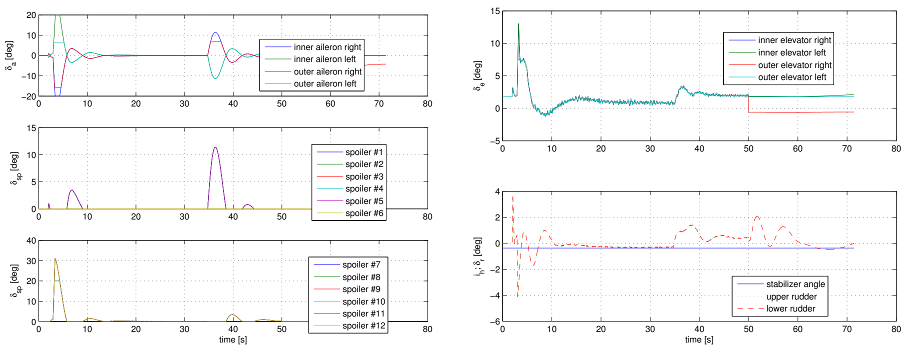

(a) ailerons and spoilers (b) elevators, stabilizer and rudders

Figure 7.17: Engine separation scenario with classic controller flight control surface deflections

Chapter 8

Improvements of the baseline flight controller synthesis

Several improvements can be made to the baseline flight controller presented in chapter 7, as already announced in that chapter. Four major topics will be discussed in this chapter. First, the outer NDI loop of the reconfiguring controller will be revisited, since this loop can be included in the NDI set-up as well. Secondly, Multi-Objective Parameter Synthesis can be used to optimize the gain tuning in the control structure. Moreover, Pseudo Control Hedging is worthwhile to include. This adapts the reference model for the system output in case of unachievable commands due to control saturation. Finally, as already mentioned in chapter 7, it is possible to optimize the distribution of the required control moments over the different control effectors, taking into account their aerodynamic efficiency and the actuator health status. All these topics are discussed in this chapter.

8.1 Reconfiguring Flight Control: outer NDI loop revisited

As a matter of fact, also the navigational dynamics can be incorporated in a dynamic inversion loop, instead of converting these demand signals towards the aerodynamic reference angles as done in chapter 7.

8.1.1 Third dynamic inversion loop: navigational dynamics

The procedure used in this step is inspired by the method used in [121, 122], although the application for this project implies some important deviations compared to the conventional method, since an adaptive model needs to be taken into account. Main crux in this deviating approach is that this inversion loop constitutes of two separate steps. First, the kinematics based virtual inputs are transformed towards the roll angle and the symmetric aerodynamic forces through a physically interpretable nonlinear mapping. Consequently, the aforementioned force components are translated into commanded angle of attack and dimensionless thrust values via a classical NDI-setup as used before, which involves a local gradient determination step. The derivation of these control laws is elaborated below.

8.1.1.1 Nonlinear mapping of virtual inputs towards roll angle and symmetric force components

The trajectory dynamics of the aircraft can be expressed in the kinematic frame of reference, where the origin is located in the airplane center of gravity, the X_k-axis coincides with the groundspeed velocity vector, Z_k-axis lies in the plane of symmetry of the aircraft, and finally the Y_k-axis is oriented perpendicular on the plane spanned by the origin and both the X_k and Z_k axes.

According to this definition, the kinematic (groundspeed) velocity vector is defined as follows in this frame of reference:

$$\mathbf{V}_k = \begin{bmatrix} V_k \\ 0 \\ 0 \end{bmatrix} \tag{8.1}$$

This velocity vector is differentiated as follows and put equal to the sum of aerodynamic and gravity forces:

$$\begin{aligned} \frac{d\mathbf{V}_k}{dt} &= \frac{\partial \mathbf{V}_k}{\partial t} + \mathbf{\Omega}_{ke}^{k} \times \mathbf{V} = \begin{pmatrix} \dot{V}_k \\ 0 \\ 0 \end{pmatrix} + \mathbf{\Omega}_{ke}^{k} \times \begin{pmatrix} V_k \\ 0 \\ 0 \end{pmatrix} & (8.2) \\ &= \frac{1}{m} \begin{pmatrix} 1 & 0 & 0 \\ 0 & \cos\mu & -\sin\mu \\ 0 & \sin\mu & \cos\mu \end{pmatrix} \Sigma \mathbf{F}_{A_{\text{aero}}} + \mathbf{\Theta}_{kg} \begin{pmatrix} 0 \\ 0 \\ g \end{pmatrix} & (8.3) \end{aligned}$$

$$\mathbf{\Omega}_{ke}^{k} = \begin{pmatrix} -\sin\gamma \cdot \dot{\chi} \\ \dot{\gamma} \\ \cos\gamma \cdot \dot{\chi} \end{pmatrix} \tag{8.4}$$

$$\mathbf{\Theta}_{kg} = \begin{pmatrix} \cos\gamma & 0 & -\sin\gamma \\ 0 & 1 & 0 \\ \sin\gamma & 0 & \cos\gamma \end{pmatrix} \begin{pmatrix} \cos\chi & \sin\chi & 0 \\ -\sin\chi & \cos\chi & 0 \\ 0 & 0 & 1 \end{pmatrix} \tag{8.5}$$

In equation (8.3), the rotation around the aerodynamic roll angle μ corresponds to the transformation from the aerodynamic reference frame towards the kinematic frame of reference, as elaborated in appendix F. In the same way, transformation matrix $\mathbf{\Theta}_{kg}$ defined in eq. (8.5) represents the conversion from the earth fixed frame of reference towards the same aforementioned kinematic reference frame. Finally, the angular velocity vector $\mathbf{\Omega}_{ke}^{k}$ in eq. (8.4) depicts the rotational rate of the kinematic reference frame with respect to the earth fixed reference frame, expressed in terms of the kinematic frame of reference. This expression is determined by means of two consecutive rotations, as elaborated in [212]:

1. Rotation χ_k kinematic azimuth angle about the Z_e axis;
2. Rotation γ_k kinematic flight path angle about the Y_k axis.

Expressed in matrix form as follows:

$$\mathbf{\Omega}_{ke}^{k} = \begin{pmatrix} \cos\gamma & 0 & -\sin\gamma \\ 0 & 1 & 0 \\ \sin\gamma & 0 & \cos\gamma \end{pmatrix} \begin{bmatrix} 0 \\ 0 \\ \dot{\chi}_k \end{bmatrix} + \begin{bmatrix} 0 \\ \dot{\gamma}_k \\ 0 \end{bmatrix} = \begin{pmatrix} -\sin\gamma \cdot \dot{\chi} \\ \dot{\gamma} \\ \cos\gamma \cdot \dot{\chi} \end{pmatrix} \tag{8.6}$$

Combining all previous information leads to the expression:

$$\frac{d\mathbf{V}_k}{dt} = \begin{pmatrix} \dot{V}_k \\ 0 \\ 0 \end{pmatrix} + \begin{pmatrix} -\sin\gamma \cdot \dot{\chi} \\ \dot{\gamma} \\ \cos\gamma \cdot \dot{\chi} \end{pmatrix} \times \begin{pmatrix} V_k \\ 0 \\ 0 \end{pmatrix} = \begin{pmatrix} \dot{V}_k \\ V_k \cdot \cos\gamma \cdot \dot{\chi} \\ -V_k \cdot \dot{\gamma} \end{pmatrix} \tag{8.7}$$

$$= \frac{1}{m} \begin{pmatrix} 1 & 0 & 0 \\ 0 & \cos\mu & -\sin\mu \\ 0 & \sin\mu & \cos\mu \end{pmatrix} \begin{pmatrix} F_{A_X} \\ F_{A_Y} \\ F_{A_Z} \end{pmatrix} + \begin{pmatrix} -g\sin\gamma \\ 0 \\ g\cos\gamma \end{pmatrix} \tag{8.8}$$

Rewriting this result for $\dot{V}_k$, $\dot{\gamma}$ and $\dot{\chi}$:

$$\dot{V}_k = \frac{1}{m} F_{A_X} - g\sin\gamma \tag{8.9}$$

$$\dot{\chi} = \frac{1}{mV_k \cdot \cos\gamma} \left(\cos\mu \cdot F_{A_Y} - \sin\mu \cdot F_{A_Z}\right) \tag{8.10}$$

$$\dot{\gamma} = \frac{1}{-mV_k} \left(\sin\mu \cdot F_{A_Y} + \cos\mu \cdot F_{A_Z}\right) - \frac{g\cos\gamma}{V_k} \tag{8.11}$$

Finally, these expressions need to be rewritten for the roll angle μ and the symmetric aerodynamic forces F_{A_X} and F_{A_Z}. This process is by no means unique, and several ways have been explored to do so. Comparing two mathematical inversions and one goniometrical inversion has pointed out that the latter is preferable, since it is physically intuitive and it does not require solving a quadratic polynomial, in contrast to the two former procedures.

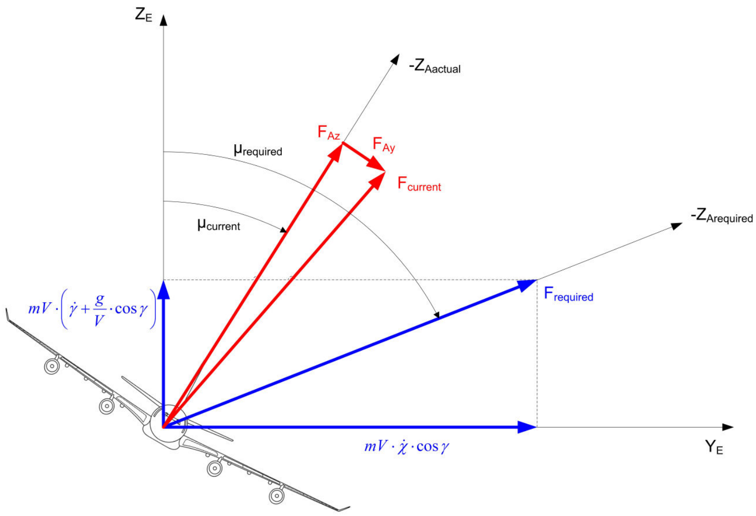

Figure 8.1: Forces acting on the refererence frame axes in the plane perpendicular on the velocity vector

Figure 8.1 illustrates the forces acting on the reference frame axes perpendicular on the velocity. The magnitude of the total required force, $|F_{\text{required}}|$ and the required roll angle μ_{required} can be derived from this figure. Given that

$$|F_{\text{required}}| = \sqrt{F^2_{\text{horizontal}} + F^2_{\text{vertical}}} \tag{8.12}$$

$$\tan \mu_{\text{required}} = \frac{F_{\text{horizontal}}}{F_{\text{vertical}}} \tag{8.13}$$

where these force components are expressed with respect to the earth fixed reference frame. From eq. (8.9) – (8.11) these can be written as follows:

$$F_{\text{horizontal}} = mV_k \dot{\chi} \cos\gamma \tag{8.14}$$

$$F_{\text{vertical}} = mV_k \dot{\gamma} + mg\cos\gamma = mV_k \left(\dot{\gamma} + \frac{g}{V_k}\cos\gamma\right) \tag{8.15}$$

Combining this information, while taking into account the contribution from the lateral sideforce F_{A_y} results in the required set of quantities:

$$F_{A_X} = m\left(\dot{V} + g\sin\gamma\right) \tag{8.16}$$

$$\begin{aligned} F_{A_Z} &= \sqrt{F^2_{\text{required}} - F^2_{A_Y}} \\ &= -\cos\gamma\sqrt{m^2\left[\left(g + \frac{V\dot{\gamma}}{\cos\gamma}\right)^2 + (V\dot{\chi})^2\right] - \left(\frac{F_{A_Y}}{\cos\gamma}\right)^2} \end{aligned} \tag{8.17}$$

$$\mu = \arctan\left(\frac{\dot{\chi}\cos\gamma}{\dot{\gamma} + g\frac{\cos\gamma}{V}}\right) \tag{8.18}$$

where μ is in fact μ_{required}. Note that the minus sign for F_{A_Z} is needed for the purpose of convention (positive Z-axis downward).

8.1.1.2 Translation of force components into commanded angle of attack and dimensionless thrust values

Since the aerodynamic forces are available in the body fixed reference frame, they must be converted towards the aerodynamic reference frame, involving a rotation around the angle of attack α and the sideslip angle β:

$$F_A = \begin{pmatrix} \cos\alpha & 0 & \sin\alpha \\ 0 & 1 & 0 \\ -\sin\alpha & 0 & \cos\alpha \end{pmatrix}\begin{pmatrix} \cos\beta & \sin\beta & 0 \\ -\sin\beta & \cos\beta & 0 \\ 0 & 0 & 1 \end{pmatrix} F_B \tag{8.19}$$

$$\begin{pmatrix} F_{A_X} \\ F_{A_Y} \\ F_{A_Z} \end{pmatrix} = \bar{q}S\begin{pmatrix} \cos\alpha\cos\beta\cdot C_X + \cos\alpha\sin\beta\cdot C_Y + \sin\alpha\cdot C_Z \\ -\sin\beta\cdot C_X + \cos\beta\cdot C_Y \\ -\sin\alpha\cos\beta\cdot C_X - \sin\alpha\sin\beta\cdot C_Y + \cos\alpha\cdot C_Z \end{pmatrix} \tag{8.20}$$

The dimensionless force coefficients in the three axes are expanded as follows:

$$C_X = C_{X_0} + C_{X_\alpha}\alpha + C_{X_{\alpha^2}}\alpha^2 + C_{X_q}\frac{q\bar{c}}{V} + C_{X_{\delta_e}}\delta_e + C_{X_{T_c}}T_c \tag{8.21}$$

$$\approx C_{X_0} + C_{X_\alpha}\alpha + C_{X_{\alpha^2}}\alpha^2 + C_{X_{T_c}}T_c \tag{8.22}$$

$$C_Y = C_{Y_0} + C_{Y_\beta}\beta + C_{Y_p}\frac{pb}{2V} + C_{Y_r}\frac{rb}{2V} + C_{Y_{\delta_a}}\delta_a + C_{Y_{\delta_r}}\delta_r \tag{8.23}$$

$$C_Z = C_{Z_0} + C_{Z_\alpha}\alpha + C_{Z_q}\frac{q\bar{c}}{V} + C_{Z_{\delta_e}}\delta_e + C_{Z_{T_c}}T_c \approx C_{Z_0} + C_{Z_\alpha}\alpha \tag{8.24}$$

It should be noted that the above expansions have been simplified in order to reduce complexity. First of all, the first order Taylor series expansion has been limited to the most important independent variables. For the X-force, these are the constant term, angle of attack α and its square α^2 and the dimensionless thrust coefficient T_c. For the Z-force, only the constant term and angle of attack α are relevant. Although being a considerable simplification, this is justifiable. First of all, angular rates and control surface deflections have a primary influence on the aerodynamic moments. The aerodynamic forces, which always have some delay compared to the moments, depend primarily on the aerodynamic angles and thrust. Moreover, taking out these dependencies eliminates an implicit feedback loop of angular rates and deflections, which would increase the complexity unnecessarily. In case of serious aerodynamic failures, additional regressors can become relevant in these force expressions, but these possible influences can be taken into account selectively by means of Adaptive Recursive Orthogonal Least Squares AROLS, see chapter 5. Finally, the contribution of the sideslip angle β in F_{A_X}, F_{A_Y} and F_{A_Z} is not discounted via the dimensionless coefficient C_Y, but through the specific force A_Y. Reason for this is that this expression does not need to be rewritten towards β. Consequently, the dimensionless Y-force coefficient can be calculated by means of the specific force in the relevant direction:

$$Y_{\text{aero}} = mA_Y = \bar{q}SC_Y \quad \Rightarrow \quad C_Y = \frac{mA_Y}{\bar{q}S}$$

Combining this information in eq. (8.20) results in the following expressions:

$$F_{A_X} = \bar{q}S\left(\cos\alpha\cos\beta\cdot C_X(\alpha,T_C) + \cos\alpha\sin\beta\cdot\frac{mA_Y}{\bar{q}S} + \sin\alpha\cdot C_Z(\alpha)\right) \tag{8.25}$$

$$F_{A_Y} = \bar{q}S\left(-\sin\beta\cdot C_X(\alpha,T_C) + \cos\beta\cdot\frac{mA_Y}{\bar{q}S}\right) \tag{8.26}$$

$$F_{A_Z} = \bar{q}S\left(-\sin\alpha\cos\beta\cdot C_X(\alpha,T_C) - \sin\alpha\sin\beta\cdot\frac{mA_Y}{\bar{q}S} + \cos\alpha\cdot C_Z(\alpha)\right) \tag{8.27}$$

This system of equations must be rewritten towards the quantities angle of attack α and the dimensionless thrust coefficient T_c. However, this cannot be done as easily as in the previous section, since higher order influences are present in this system of equations, which is moreover overdetermined. Although it could be argued to ignore the influences of the lateral force in the Y-direction on these symmetric quantities for unfailed aircraft, this simplification does not hold here, due to the fact that this control law needs to be applicable for asymmetrically damaged aircraft, possibly flying with nonzero sideslip angle $\beta \neq 0$. Despite the presence of these higher order influences, they are still gradual and relatively small. Therefore, they can be treated globally as linear influences on these forces in the aerodynamic frame of reference:

$$F_{A_X} \approx F_{A_{X_0}} + F_{A_{X_\alpha}}\alpha + F_{A_{X_{Tc}}}Tc \tag{8.28}$$

$$F_{A_Y} \approx F_{A_Y} + F_{A_{Y_\alpha}}\alpha + F_{A_{Y_{Tc}}}Tc \tag{8.29}$$

$$F_{A_Z} \approx F_{A_{Z_0}} + F_{A_{Z_\alpha}}\alpha + F_{A_{Z_{Tc}}}Tc \tag{8.30}$$

These force coefficients are calculated on-line for a realistic range of values for angle of attack and dimensionless thrust, while avoiding collinearities between both ranges. This on-line calculation procedure is called "Local Gradient Determination" (LGD). Extensive validations have shown that these approximations are sufficiently accurate. Finally, the aforementioned structure allows to rewrite the system for angle of attack and dimensionless thrust in the usual structure as used for nonlinear dynamic inversion.

$$\begin{pmatrix} \alpha \\ T_C \end{pmatrix} = \begin{pmatrix} F_{A_{X_\alpha}} & F_{A_{X_{T_C}}} \\ F_{A_{Y_\alpha}} & F_{A_{Y_{T_C}}} \\ F_{A_{Z_\alpha}} & F_{A_{Z_{T_C}}} \end{pmatrix}^{\dagger} \left[\begin{pmatrix} F_{A_{X\mathrm{comm}}} \\ F_{A_Y} \\ F_{A_{Z\mathrm{comm}}} \end{pmatrix} - \begin{pmatrix} F_{A_{X_0}} \\ F_{A_{Y_0}} \\ F_{A_{Z_0}} \end{pmatrix} \right] \tag{8.31}$$

where the symbol † denotes the left inverse.

Summarizing, the global setup of the third dynamic inversion loop can be found in figure 8.2. The integration of the second and third inversion loop is illustrated in figure 8.3.

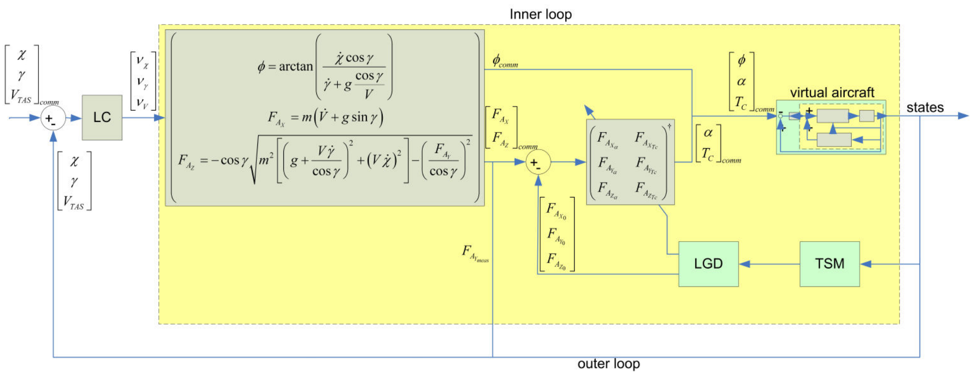

Figure 8.2: Third NDI autopilot loop, featuring V_{TAS}, γ and χ control. LGD stands for local gradient determination. TSM represents the two step method model identification block elaborated in detail earlier.

8.1.1.3 Adaptation of second level NDI loop

Moreover, a minor adaptation has been implemented in the second level of the NDI loop, more precisely with respect to the angle of attack α. Since the following expression holds:

$$\alpha = \arcsin\left(\frac{w_b}{V}\right) \tag{8.32}$$

$$\dot{\alpha} = \frac{1}{\sqrt{V^2 - w_b^2}} \dot{w}_b = \frac{1}{\sqrt{V^2 - w_b^2}} \left(A_z + g\cos\theta\cos\phi + q u_b - p v_b\right) \tag{8.33}$$

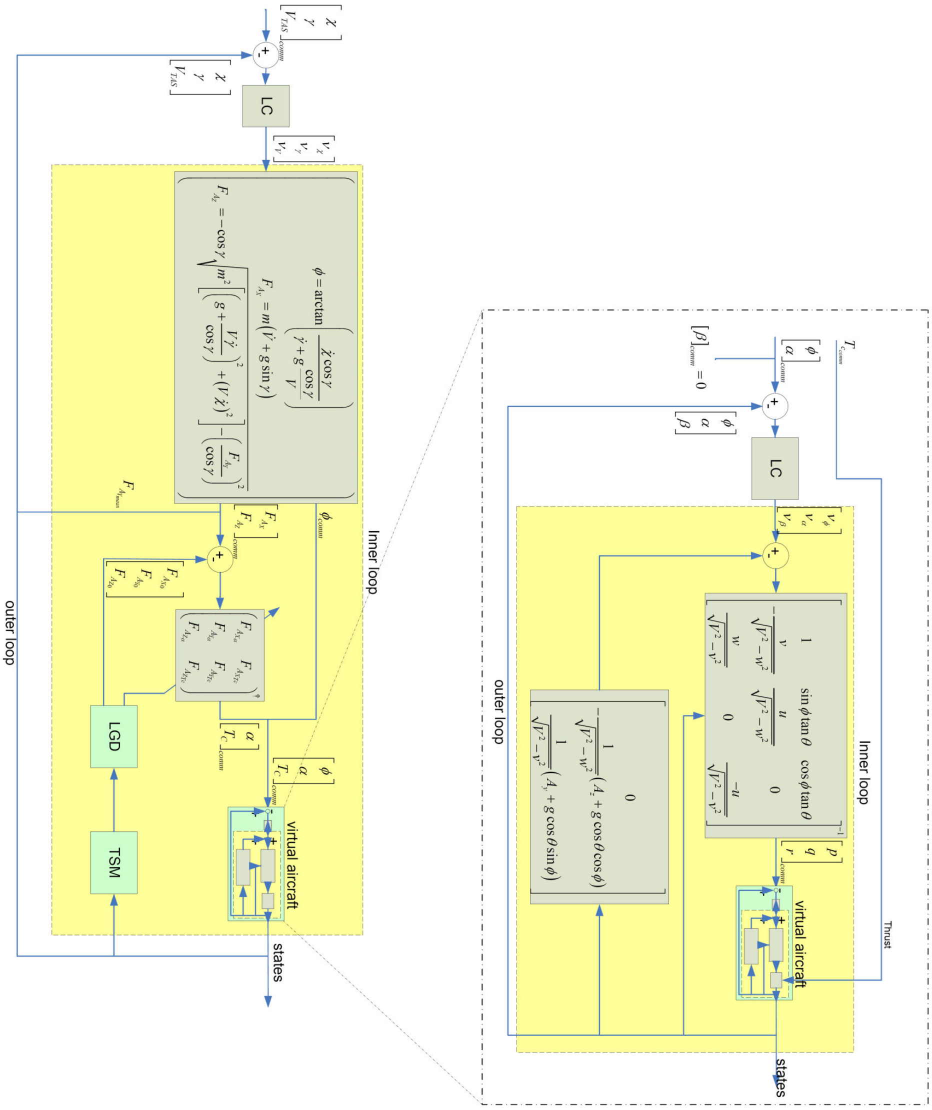

Figure 8.3: Assembled NDI autopilot setup, with second and third NDI loop portrayed in detail.

This expression is more globally valid compared to eq. (7.48), since it is no approximation. The overall second level NDI control law becomes then:

$$\begin{bmatrix} p \\ q \\ r \end{bmatrix} = \begin{bmatrix} 1 & \sin\phi\tan\theta & \cos\phi\tan\theta \\ -\frac{v_b}{\sqrt{V^2-w_b^2}} & \frac{u_b}{\sqrt{V^2-w_b^2}} & 0 \\ \frac{w_b}{\sqrt{V^2-v_b^2}} & 0 & \frac{-u_b}{\sqrt{V^2-v_b^2}} \end{bmatrix}^{-1} \cdot$$
$$\left\{ \begin{bmatrix} \nu_{\dot{\phi}} \\ \nu_{\dot{\alpha}} \\ \nu_{\dot{\beta}} \end{bmatrix} - \begin{bmatrix} 0 \\ -\frac{1}{\sqrt{V^2-w_b^2}}\left(A_z + g\cos\theta\cos\phi\right) \\ \frac{1}{\sqrt{V^2-v_b^2}}\left(A_y + g\cos\theta\sin\phi\right) \end{bmatrix} \right\} \tag{8.34}$$

8.1.1.4 Flying with nonzero sideslip angle to counteract asymmetric damage

As can be seen in fig. 8.3, the commanded sideslip angle β_{comm} is zero in all circumstances. However, for asymmetric damage, it might be necessary to fly with a non-zero sideslip angle in order to reach an equilibrium condition. This control setup and the concept of time scale separation take this issue automatically into account. First of all, the yaw rate behaviour r of an aircraft is much faster than its slipping behaviour in β. Therefore, after the asymmetric damage abruptly occurs, like in the engine separation scenario, the aircraft will start yawing towards the lost engines and the inner loop will counteract for this response at once. At second instance, while the yawing rotational rate is being reduced to zero, nonzero sideslip is building up gradually. In a classical linear control setup for the middle loop without NDI, this behaviour would prevent that a new equilibrium condition could be achieved, because of the continuous nonzero commanded yaw rate $r_{\text{comm}} = -K_\beta \beta_{\text{meas}}$. However, thanks to the presence of NDI control in the middle loop, this problem does not occur here, as the commanded yaw rate is calculated as follows:

$$r_{\text{comm}} \approx \left(-\frac{u}{\sqrt{V^2-v^2}}\right)^{-1} \cdot \left[-K_\beta \beta_{\text{meas}} - \frac{1}{\sqrt{V^2-v^2}}\left(A_y + g\cos\theta\sin\phi\right)\right] \tag{8.35}$$

It should be noted that this equation is simplified for transparency by ignoring the contribution from the virtual roll angle input $\nu_{\dot{\phi}}$. This contribution is in fact small compared to the other terms, but in the control setup this input does contribute effectively, as can be seen in fig. 8.3. Eq. (8.35) shows that r_{comm} returns to zero when the nonzero values of sideslip β_{meas}, lateral specific force A_y and roll angle ϕ come in balance, after the faster dynamics of the yaw rate have damped out.

8.1.2 Linear controller structure and selected controller gains

The linear controllers, as shown in fig. 8.2 and 8.3, comprise proportional and integral action. However, these controllers have a slightly different architecture compared to a clas-

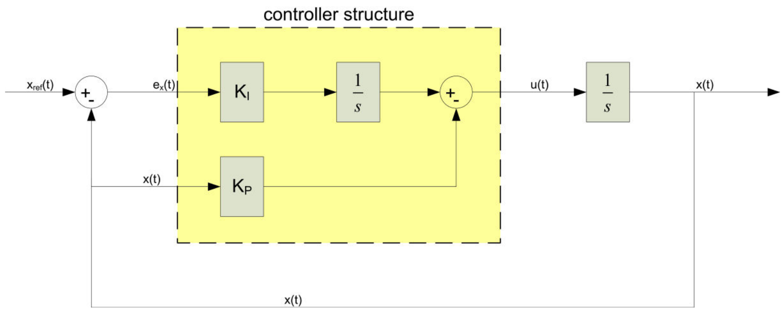

Figure 8.4: Controller structure involving PI-action without closed loop zero

sical PI-controller. This architecture is illustrated in fig. 8.4, where this type of controller is applied on a single integrator. The advantage of this controller structure can be analysed by considering the closed loop transfer function of the block diagram in fig. 8.4:

$$\frac{X(s)}{X_{\text{ref}}(s)} = \frac{K_I}{(s^2 + K_p s + K_I)} \tag{8.36}$$

Comparing with the closed loop transfer function for the classical linear controller setup:

$$\frac{X(s)}{X_{\text{ref}}(s)} = \frac{K_p s + K_I}{(s^2 + K_p s + K_I)} \tag{8.37}$$

This adapted setup eliminates the closed loop zero, thus avoiding overshoot and other transient disturbances in the closed loop system. Furthermore, the static gain of the closed loop system remains equal to unity, as for the classical setup. The initial controller gains have been selected as shown in table 8.1. The principle of time scale separation is visible. Linear controllers in inner loops have higher control gains, resulting in increased controller authority to track the inner loop reference signal quicker before tracking the outer loop reference signal.

Table 8.1: Selected controller gains for three linear controller levels in NDI control structure

inner	middle	outer
$k_p = 2$	$k_\phi = 0.8$	$k_\chi = 0.15$
		$k_{\chi_I} = 0.01$
$k_q = 3$	$k_\alpha = 0.8$	$k_\gamma = 0.7$
$k_{q_I} = 4$		$k_{\gamma_I} = 0.09$
$k_r = 2$	$k_\beta = 0.8$	$k_V = 0.15$
		$k_{V_I} = 0.01$

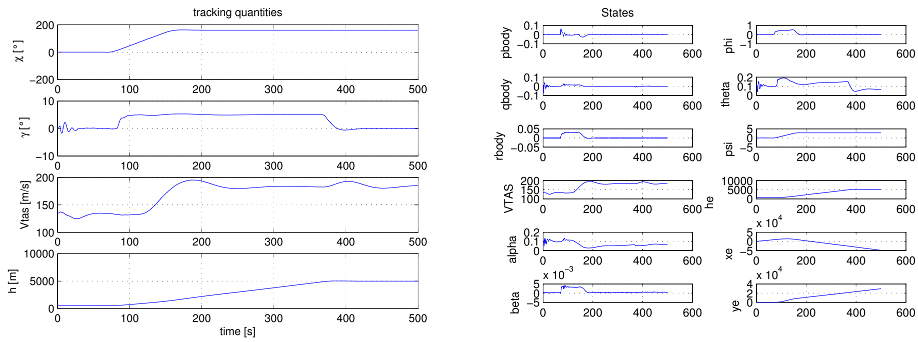

(a) tracking quantities

(b) states

Figure 8.5: Tracking quantities and states for the unfailed scenario

8.1.3 Simulation Results

Implementation of the improvements mentioned above results in the controller performance illustrated in the following simulation results. Besides the unfailed scenario the following failures have been investigated: stabilizer runaway, vertical tail loss and engine separation. In each scenario, the failure occurs exactly at $t = 50s$.

8.1.3.1 Unfailed scenario

A complex manoeuvre is performed to evaluate the performance of the fault tolerant controller. Three joint commands are given, more precisely a course change of $\Delta\chi = 160°$ at $t = 70s$, an altitude change towards $h = 5000m$ at $t = 80s$ and a velocity change of $\Delta V = 50m/s$ around $t = 110s$. This scenario allows to evaluate the performance as well as eventual inadvertent couplings between the different channels. The tracking of the reference signals is satisfactory and couplings are minimal to even non-existent, as can be seen in fig. 8.5. In the control surface deflection time histories in figures 8.6 and 8.7(a), it can be seen that the elevators compensate first for the vertical lift component loss induced by the turn, and then initiate the altitude change. Ailerons and rudders cooperate in order to achieve a coordinated turn. It can be seen that the spoilers assist the ailerons to set the turn up. The specific forces in fig. 8.7(b) indicate an acceptable behaviour. The responses of the unfailed aircraft will serve as a comparison basis to evaluate the performance of the controller in failed situations.

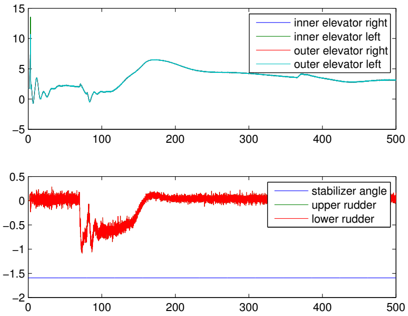

(a) deflections of elevators, stabilizer and rudders

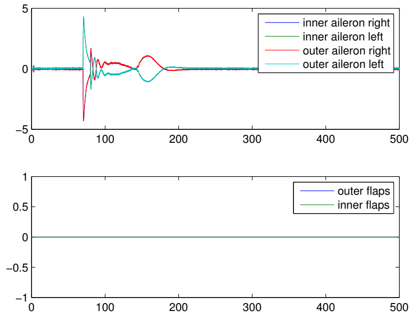

(b) deflections of ailerons and flaps

Figure 8.6: Deflections of elevators, stabilizer, rudders, ailerons and flaps for the unfailed scenario

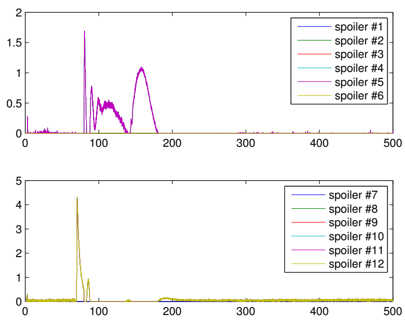

(a) deflections of spoilers

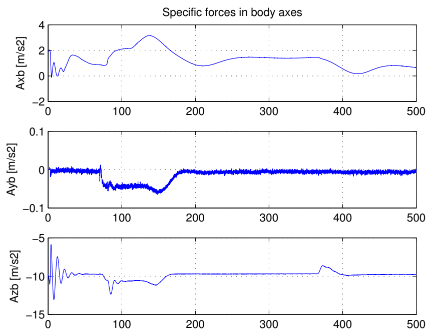

(b) specific forces

Figure 8.7: Deflections of spoilers and specific forces for the unfailed scenario

8.1.3.2 Stabilizer runaway

It has been found that this failure does not represent a major challenge for the control system. As can be seen in fig. 8.9(a), the stabilizer suffers a leading edge upward shift, as described in section A.2.1, and the elevators compensate immediately for this disturbing moment. Due to the fast reaction of the control system, there is no noticeable deterioration in the performance of the aircraft while performing the requested manoeuvre, as can be seen in figures 8.8 and 8.10.

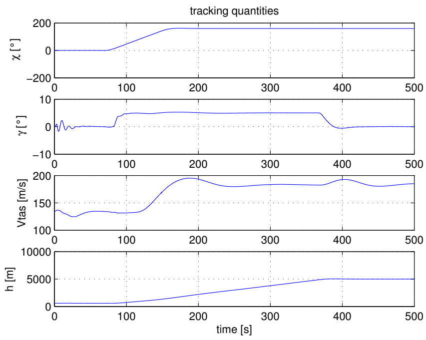

(a) tracking quantities

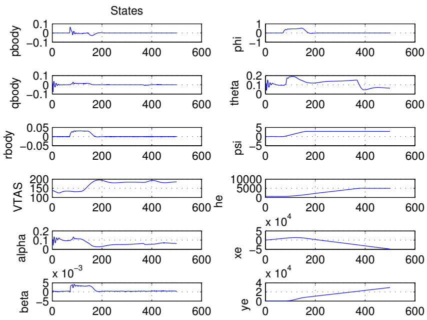

(b) states

Figure 8.8: Tracking quantities and states for the stabilizer runaway scenario

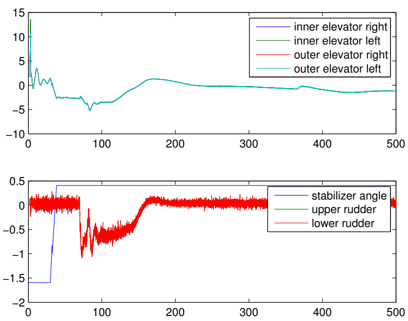

(a) deflections of elevators, stabilizer and rudders

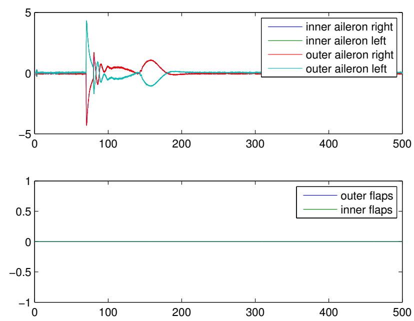

(b) deflections of ailerons and flaps

Figure 8.9: Deflections of elevators, stabilizer, rudders, ailerons and flaps for the stabilizer runaway scenario

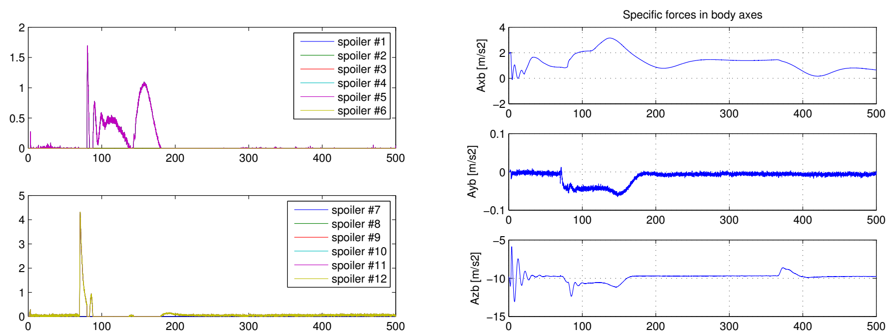

(a) deflections of spoilers (b) specific forces

Figure 8.10: Deflections of spoilers and specific forces for the stabilizer runaway scenario

8.1.3.3 Vertical tail loss

For this failure scenario, the reference signals have been slightly adapted. No speed change is requested here, because this situation is more demanding for the control surfaces. When the speed increase is maintained, the increasing aerodynamic damping reduces the disturbing effect of the failure. The altitude capture has been changed accordingly to $1500m$, in order to prevent throttle saturation. Aerodynamic damping is the very reason why, in practice, control laws actually work with calibrated airspeed CAS. In this way the control actions are related to the dynamic pressure and control surface efficiency is maintained.

Figure 8.12(b) reveals the compensating behaviour of the ailerons which takes into account the loss of the vertical tail and the cessation of rudder functioning after failure, as can be seen in fig. 8.12(a). It can be observed that the ailerons effectively take over the function of yaw damper, assisted by the spoilers in fig. 8.13(a), since the rudders are lost. Figure 8.13(b) shows that the oscillation in the lateral specific force A_y is only damped in the longer term, which can be explained by the fact that ailerons and spoilers have no direct influence on the yawing moment, but on the rolling moment.

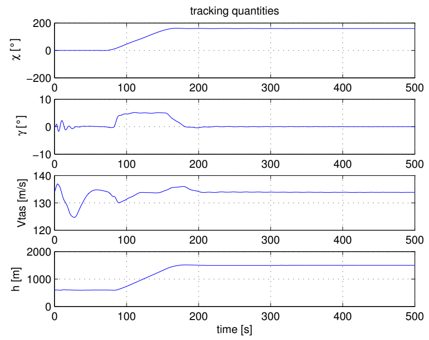

(a) tracking quantities

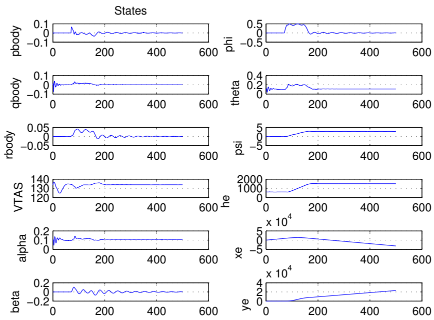

(b) states

Figure 8.11: Tracking quantities and states for the tail loss scenario

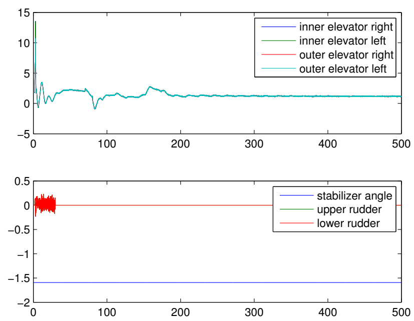

(a) deflections of elevators, stabilizer and rudders

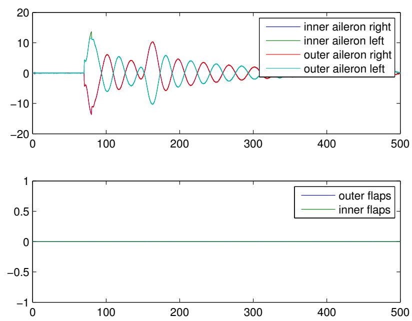

(b) deflections of ailerons and flaps

Figure 8.12: Deflections of elevators, stabilizer, rudders, ailerons and flaps for the tail loss scenario

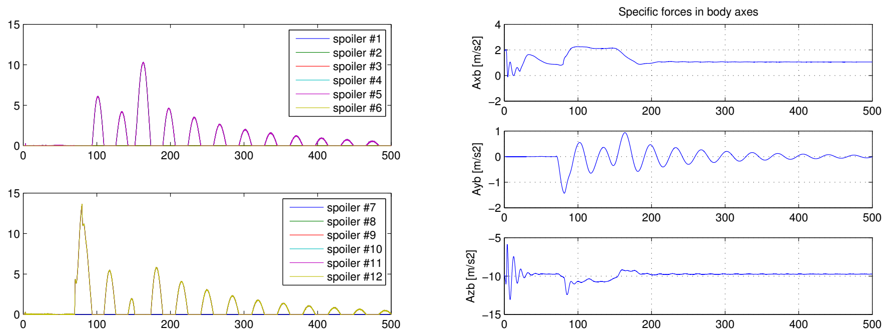

(a) Deflections of spoilers (b) specific forces

Figure 8.13: Deflections of spoilers and specific forces for the tail loss scenario

8.1.3.4 Engine separation

The engine separation scenario is a very sensitive situation to combine commands in heading, altitude and speed simultaneously. Crucial in this context is to avoid engine throttle saturation. Therefore, in this experiment only a heading change has been considered, as shown in fig. 8.14(a). Moreover, a limited maximum roll angle has been imposed, due to the restricted safe flight envelope as explained in the previous chapter. It has been found that altitude and speed changes are also feasible separately, but these are not discussed in this section.

The time histories of the states in fig. 8.14(b) reveal that the aircraft in post failure conditions flies with a small nonzero roll angle and sideslip angle, due to the asymmetric damage, despite a zero commanded sideslip angle. This phenomenon is explained in section 8.1.1.4. The control surface deflections in figures 8.15 and 8.16(a) confirm the cessation of functioning of the control surfaces which are powered by the hydraulic circuits connected to engines number 3 and 4, as illustrated in fig. A.9. The remaining operative surfaces are successful in keeping the aircraft in equilibrium, although with restricted authority. The nonzero lateral specific force in fig. 8.16(b) is a consequence of the sideslipping flight.

Two additional interesting quantities to investigate are the throttle setting and the average square innovation, which triggers the re-identification routine as explained in section 4.7. Figure 8.17(a) confirms that the throttle setting does not saturate, however the remaining control margins in order to remain inside the safe flight envelope are severely restricted. This is due to the asymmetric thrust which needs to be compensated by the control surfaces. The spike at $t = 50s$ is caused by the feedforward path in the controller, which is needed to compensate for the instantaneous thrust loss of the two lost engines. No feedback configuration can be designed which is fast enough to compensate for the speed loss in this low

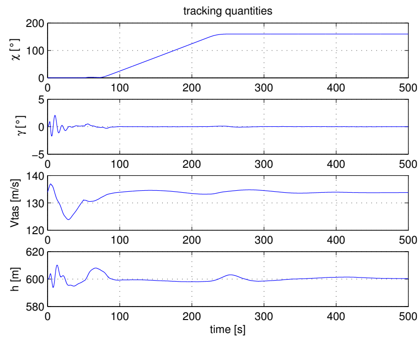

(a) tracking quantities

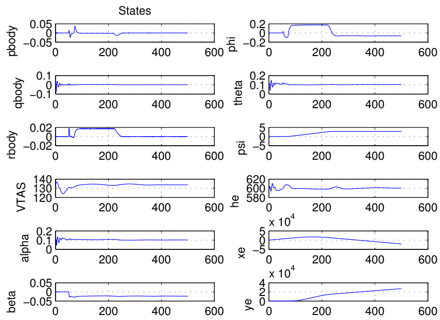

(b) states

Figure 8.14: Tracking quantities and states for the engine separation scenario

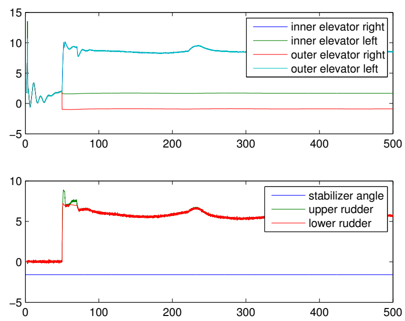

(a) deflections of elevators, stabilizer and rudders

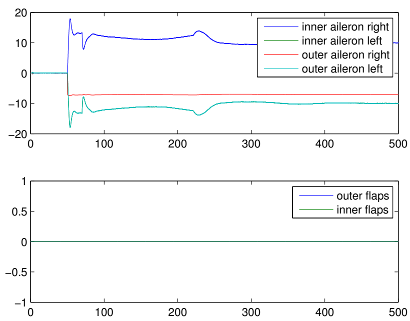

(b) deflections of ailerons and flaps

Figure 8.15: Deflections of elevators, stabilizer, rudders, ailerons and flaps for the engine separation scenario

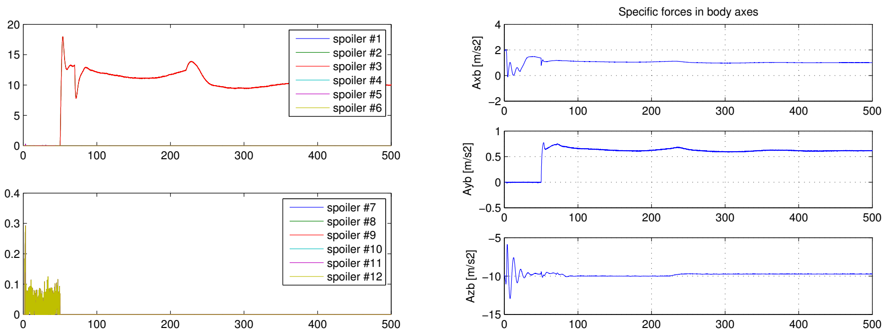

(a) deflections of spoilers (b) specific forces

Figure 8.16: Deflections of spoilers and specific forces for the engine separation scenario

speed flight condition. The only valid alternative is starting the simulation with a higher initial airspeed, such as done for the example in section 7.2.2.2. Figure 8.17(b) depicts the values for the average square innovation for each force and moment channel separately. At $t = 50s$, it can be seen that the threshold for $\overline{\Delta}_X$ is exceeded, and a re-identification procedure is triggered for C_X. It has become necessary to include the sideslip angle $|\beta|$ as an additional regressor in the identification procedure, because it has become significant due to the sideslipping flight. This leads to a successful new identification procedure which is performed extremely quickly as can be seen in this figure. This result confirms the beneficial contribution from the identification routine in this fault tolerant flight control setup.

8.2 Multi-Objective Parameter Synthesis gain tuning on the control structure

The use of Multi-Objective Parameter Synthesis (MOPS), developed over the years at the Institute of Robotics and Mechatronics (RM) of the German Aerospace Center DLR and still under further development, has been found to be beneficial for structural tuning of the controller gains in the three linear controllers of this control setup, as will be shown below.

8.2.1 Motivation

It should be noted that the application of perfect NDI in theory renders the need for gain tuning superfluous, since the gains of a two degree of freedom controller for a pure in-

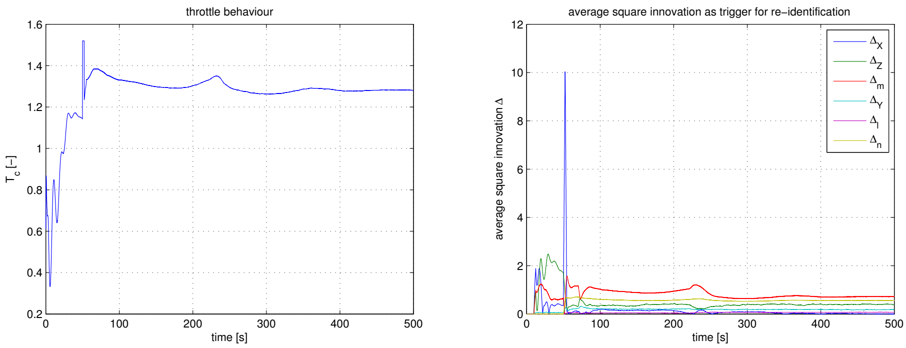

(a) throttle behaviour

(b) average square innovation as trigger for re-identification

Figure 8.17: Throttle behaviour and innovation monitoring for the engine separation scenario

tegrator system can be defined in a straightforward manner by means of pole placement. However, this holds only in theory, and especially not for aircraft applications. There are several reasons for this, which are all the consequence of the fact that the application of NDI on three levels, as done here, does not result in a perfect third order integrator. First of all, it is probable that there will be small model fit errors in the identification procedure which contaminate the inversion operation, as already discussed in section 7.1.3. Moreover, there are other disturbances which make the resulting behaviour deviate from a pure higher order integrator, namely the presence of rate and saturation limits in the actuators of the aircraft, as given in figure A.1.2.1 for this specific aircraft model, possible small couplings between the different linear controllers, despite the assumption of the time scale separation principle, and finally the physical nature of an aircraft does not allow NDI to fully decouple the different degrees of freedom of an aircraft. For example, a pitch manoeuvre certainly leads to bleeding off airspeed, and a nonzero angle of sideslip β always induces a certain (small) nonzero roll angle ϕ if one wants zero body angular rates (i.e. an equilibrium condition). All these reasons make it useful and worthwhile to apply MOPS for the final tuning of the controller gains for these three feedback loops.

8.2.2 Working principle of MOPS

Ref. [181] gives a brief introduction in the formulation of the basic optimisation problem, as follows. For each control loop in the controller design procedure, the problem of tuning and compromising between the different criteria is formulated as a weighted min-max optimisation problem, comprising all active criteria, over all sub-tasks, over all selected model parameter cases per sub-task:

$$\min_{T} \max_{ijk \in S_m} \{c_{ijk}(T, p_{ij}) / d_{ijk}\} \tag{8.38}$$

$$c_{ijk}(T, p_{ij}) \leq d_{ijk}, \quad ijk \in S_i \tag{8.39}$$

$$c_{ijk}(T, p_{ij}) = d_{ijk}, \quad ijk \in S_e \tag{8.40}$$

$$T_{\min,l} \leq T_l \leq T_{\max,l} \tag{8.41}$$

where there are three sets of criteria, classified according to their purpose: S_m is the set of criteria to be minimized, S_i is the set of inequality constraints, and S_e is the set of equality constraints. T is a vector containing the tuning parameters T_l to be optimised, lying between the user-specified upper and lower bounds $T_{\min,l}$ and $T_{\max,l}$, respectively. $c_{ijk}/d_{ijk} \in S_m$ is the k^{th} normalized criterion of the j^{th} model parameter case in the i^{th} optimisation sub-task (e.g. tracking for roll control, angle of attack and sideslip angle) where d_{ijk} is the corresponding demand value, which serves as a criterion weight. p_{ij} denotes a parameter vector of the i^{th} sub-task, defining the j^{th} model case. The criteria $c_{ijk} \in S_i,\ S_e$ are used as inequality and equality constraints respectively. The affiliation of criteria to one of the groups S_m, S_i or S_e respectively, can be changed depending on the phase considered in the design process. This is done for example when switching from inner and middle control loops towards outer control loops. Minimization criteria for the inner and middle loops, serve as inequality constraints for the outer loop, while the inner and middle loop optimized gains are used as initial values for the outer loop optimization process. This allows the outer loop performance to be improved while the demanded level of performance of the inner and middle loops is allowed to deteriorate to the level of the demanded criteria values (d_{ijk}). The optimisation problem described by eq. (8.38) to (8.41) is formulated automatically by the MOPS environment. Adding optimisation sub-tasks or model cases, and setting properties of criteria can be done with the help of a graphical user interface, or alternatively via scripts [140]. The min-max optimisation problem is solved by reformulating it as a standard Nonlinear Programming (NLP) problem with equality, inequality and simple bound constraints. The latter apply for the controller gains which serve as tuning values for the optimisation algorithm. This reformulation is done fully automatically, after which the NLP problem is solved by using one of several available powerful solvers implementing local and global search strategies. Besides efficient gradient-based solvers, also gradient-free direct search-based solvers (usually more robust, but somewhat less efficient) are available to address problems with non-smooth criteria. Solvers based on statistical methods or genetic algorithms are available as well. For the joint inner-middle and outer control loop optimization procedures, a pattern search method has been applied, which turned out to cope better with the inequality constraints than the gradient based methods, like sequential quadratic programming (SQP).

8.2.3 Definition of optimization constraints for middle and inner loop

Optimization has been split up over two phases. In a first stage, the inner rate control loop and middle aerodynamic angle control loop have been optimized jointly. Thereafter, the navigational loop has been optimized.

Partly inspired by ref. [181], the optimization constraints as shown in table 8.2 have been defined for the first optimisation step for this specific application.

Table 8.2: Selected optimization constraints for linear controller gain tuning in inner and middle loop of NDI control structure

requirement	calculation	quantity		
risetime	$10\% \rightarrow 90\%$	ϕ	α	β
overshoot		ϕ	α	β
settling time	5%	ϕ	α	β
damping ratio	$\min\{\zeta_i\}$ perfect NDI assumed	-		
control activity	$\max\left\{\left\|\dot{\delta}_{\text{cs}}(t)\right\|\right\}$	δ_a	δ_e	δ_r
input energy	$\int_{t_0}^{t_{\text{end}}} \left(\sum \Delta\delta_{\text{cs}}^2(t)\right) dt$	δ_a	δ_e	δ_r
disturbance rejection	$\frac{1}{\Delta t}\int_{t_0}^{t_{\text{end}}} \left(X_{\text{ref}}(t) - X(t)\right)^2 dt$	α, β	ϕ, β	ϕ, α
maximum deviations	$\max\{\|\Delta X(t)\|\}$	α, β	ϕ, β	ϕ, α
extreme values	$\max\{\|X(t)\|\}$	α, β	ϕ, β	ϕ, α
maximum command effort	$\max\left\{\left\|\dot{X}_{\text{ref}}(t)\right\|\right\}$	p_{ref}	q_{ref}	r_{ref}
gain order for time scale separation	$\frac{\|K_{\text{inner}}\|}{\|K_{\text{outer}}\|} > \varepsilon_1$ $\|K_{\text{inner}}\| - \|K_{\text{outer}}\| > \varepsilon_2$	$K_{p,q,r}$ $K_{\phi,\alpha,\beta}$	$K_{p,q,r}$ $K_{\phi,\alpha,\beta}$	$K_{p,q,r}$ $K_{\phi,\alpha,\beta}$

The requirements concerning risetime, overshoot and settling time evaluate the reference tracking capability of the closed loop system. Damping ratio evaluation has been used as stability analysis criterion, which has been found to be necessary in order to prevent MOPS to follow destabilizing gradients during the tuning procedure of the controller gains. The calculations of control activity and input energy have been chosen to apply on the tracking relevant input only for each relevant channel, and to ignore the disturbance rejection activity and energy. In this way both efforts are decoupled and there is no contamination possible during optimization. Disturbance rejection constraints at the other hand apply for the disturbance quantities only, since the tracking quantities exhibit significant instantaneous but irrelevant peaks for this criterion at the moment when the step reference input takes place.

Overshoot, settling time, control action and input energy serve as minimization criteria, all the other requirements serve as inequality constraints.

Finally, some important notes should be made. In order to guarantee a smooth procedure, the sensor noise has been eliminated in the MOPS optimization schedule. Otherwise, this noise would cause an inconsistency between the different evaluations and thus perturb the optimization results. Finally, the chosen optimization solver is the pattern search method, which is not gradient based. This solver is more robust for ill-posed problems, but on the other hand requires more time to perform the routine.

8.2.4 Results for middle and inner loop

As already introduced, a pattern search method has been used, which is not gradient based. Consequently, this method is more robust but somewhat less efficient. This procedure resulted in 41 iterations and 155 evaluations, with the final results shown in table 8.3.

Table 8.3: MOPS optimized linear controller gains for inner and middle loops in NDI control structure, solver: PSRCH, initial values shown between brackets

inner	middle
$k_p = 1.3947 \ \ (2)$	$k_\phi = 0.64712 \ \ (0.8)$
$k_q = 1.8887 \ \ (3)$	$k_\alpha = 0.77962 \ \ (0.8)$
$k_{q_I} = 4.0395 \ \ (4)$	
$k_r = 1.2654 \ \ (2)$	$k_\beta = 0.98241 \ \ (0.8)$

Time domain simulations have confirmed that these findings are satisfactory. Results of this optimisation procedure are shown in fig. 8.18, 8.19 and 8.20. Fig. 8.18 shows how all minimization criteria and ineqality contraints have been satisfied or not for the different optimisation steps. Fig. 8.19 and 8.20 present the time responses of the most important aircraft states for the different tracking commands for the different optimisation steps. The thick line shows the end result in all figures.

8.2.5 Definition of optimization constraints for outer loop

Building further on the inner and middle loop constraints, the optimization constraints as shown in table 8.4 have been defined for the outer loop. It should be noted that the inner loop inequality constraints still hold, while minimization criteria for the inner loop become inequality constraints for the outer loop optimization problem. Furthermore, inner and middle loop controller gains are subject to this optimization scheme too, while optimal controller gain values for inner and middle loop, obtained from the previous step, are set here as their initial values.

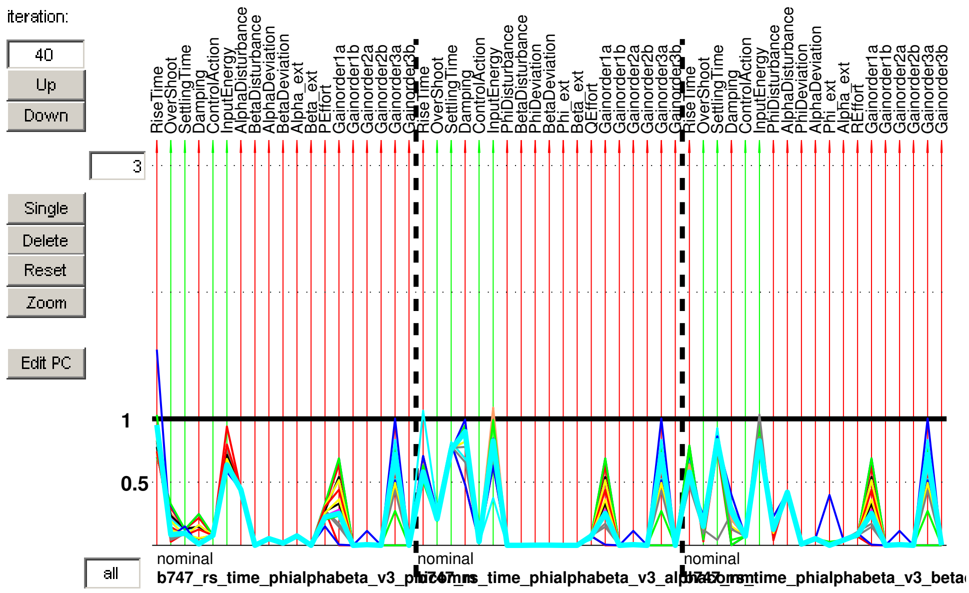

Figure 8.18: Scaled criteria in parallel coordinates for the ϕ, α and β tracking commands. Scaled criteria values below the horizontal unity line satisfy demanded values. The thick line shows the end result.

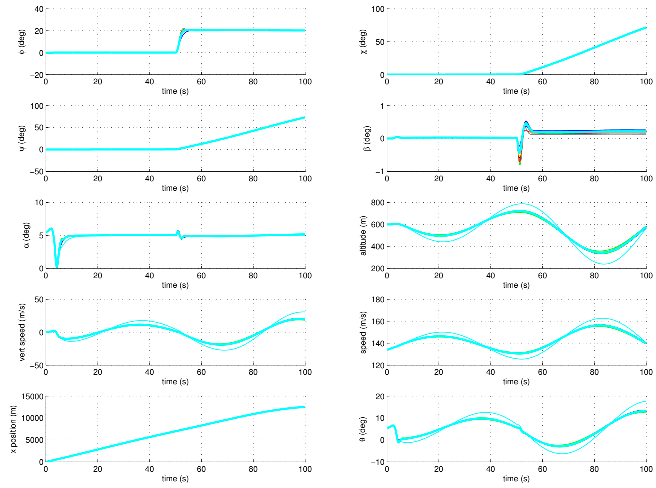

(a) Time responses for roll tracking command

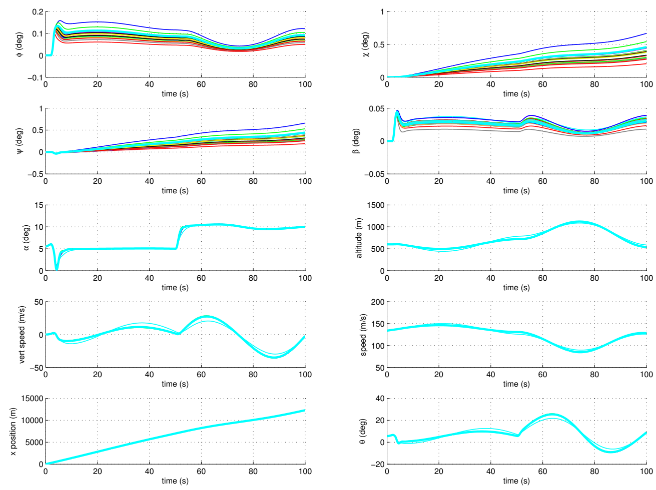

(b) Time responses for angle of attack tracking command

Figure 8.19: Time responses for the different tracking commands, including the results for the different optimization steps, part 1. The thick line shows the end result.

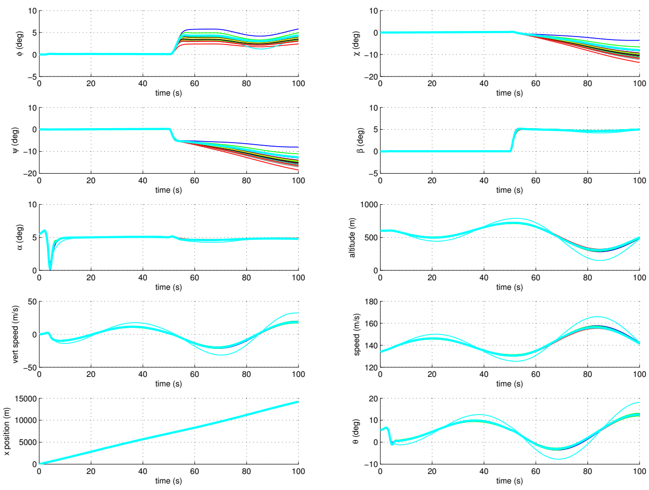

(a) Time responses for angle of sideslip tracking command

Figure 8.20: Time responses for the different tracking commands, including the results for the different optimization steps, part 2. The thick line shows the end result.

8.2.6 Results for outer loop

As for the previous loops, a pattern search method has been used. The final results of the procedure for the outer loop are shown in table 8.5. The time scale separation principle is visible in the results. One assumes that the larger control authority in the inner loops allows them to converge to the steady state value before the outer loops do.

The optimization result leads to the tracking performances shown in fig. 8.21(a) and the corresponding trajectory given in fig. 8.21(b). All constraints and criteria are satisfied, and comparing this optimized result with the initial performance shown in fig. 8.5(a) shows subtle improvements, e.g. in the speed disturbance rejections. Thanks to the good initial choice of control gain values according to the principle of time scale separation, no major improvement can be made in the field of gain tuning. However, Multiobjective Parameter Synthesis is still capable to enforce small improvements in the tuning so that optimal performance can be achieved with respect to the defined criteria.

Table 8.4: Selected optimization constraints for linear controller gain tuning in outer loop of NDI control structure

requirement	calculation	quantity		
risetime	$10\% \rightarrow 90\%$	χ, ϕ	γ, α	V
overshoot		χ	γ	V
settling time	5%	χ, ϕ	γ, α	V
damping ratio	$\min\{\zeta_i\}$ perfect NDI assumed	-		
control activity	$\max\left\{\left\|\dot{\delta}_{\text{cs}}(t)\right\|\right\}$	δ_a	δ_e	δ_{th}
input energy	$\int_{t_0}^{t_{\text{end}}} \left(\sum \Delta\delta_{\text{cs}}^2(t)\right) dt$	δ_a	δ_e	δ_{th}
disturbance rejection	$\frac{1}{\Delta t}\int_{t_0}^{t_{\text{end}}} \left(X_{\text{ref}}(t) - X(t)\right)^2 dt$	γ, V, α, β	χ, V, ϕ, β	$\chi, \gamma, \phi, \alpha, \beta$
maximum deviations	$\max\{\|\Delta X(t)\|\}$	γ, V, α, β	χ, V, ϕ, β	$\chi, \gamma, \phi, \alpha, \beta$
extreme values	$\max\{\|X(t)\|\}$	γ, α, β	χ, ϕ, β	$\chi, \gamma, \phi, \alpha, \beta$
maximum command effort	$\max\left\{\left\|\dot{X}_{\text{ref}}(t)\right\|\right\}$	$p_{\text{ref}}, \phi_{\text{ref}}$	$q_{\text{ref}}, \alpha_{\text{ref}}$	$-$
gain order for time scale separation	$\frac{\|K_{\text{inner}}\|}{\|K_{\text{outer}}\|} > \varepsilon_1$ $\|K_{\text{inner}}\| - \|K_{\text{outer}}\| > \varepsilon_2$	$K_{p,q,r}$ $K_{\phi,\alpha,\beta}$ $K_{\chi,\gamma,V}$	$K_{p,q,r}$ $K_{\phi,\alpha,\beta}$ $K_{\chi,\gamma,V}$	$K_{p,q,r}$ $K_{\phi,\alpha,\beta}$ $K_{\chi,\gamma,V}$

Table 8.5: MOPS optimized linear controller gains for the three loops in NDI control structure, solver: PSRCH, initial values shown between brackets

inner	middle	outer
$k_p = 2.2524\ (2)$	$k_\phi = 0.61039\ (0.8)$	$k_\chi = 0.19449\ (0.15)$
		$k_{\chi_I} = 0.015372\ (0.01)$
$k_q = 2.2844\ (3)$	$k_\alpha = 1.1608\ (0.8)$	$k_\gamma = 0.64224\ (0.7)$
$k_{q_I} = 4.0628\ (4)$		$k_{\gamma_I} = 0.1163\ (0.09)$
$k_r = 2.4036\ (2)$	$k_\beta = 0.48744\ (0.8)$	
		$k_V = 0.39055\ (0.15)$
		$k_{V_I} = 0.022684\ (0.01)$

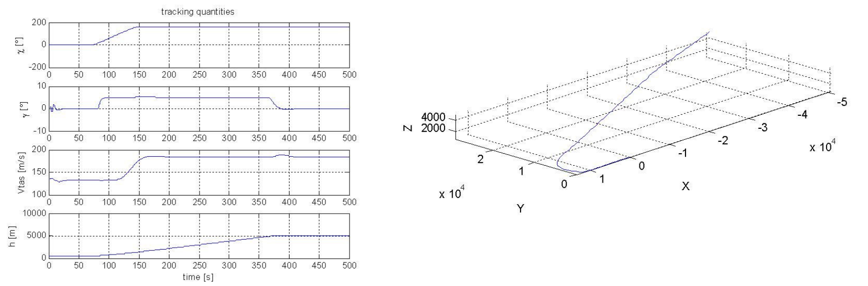

(a) Time responses for tracking commands

(b) Trajectory for tracking task

Figure 8.21: Time responses and corresponding trajectory for the different simultaneous tracking tasks.

8.3 Pseudo Control Hedging

An important issue that has not been discussed so far is how to deal with unachievable commands. Despite successful control reconfiguration in case of failures, the reachable flight envelope will likely be reduced. Therefore, fault tolerant control should not focus exclusively on control reconfiguration to compensate for the failure dynamics, but attention should also be paid to the eventually needed ”downscaling” of reference signals. Namely, the signal magnitude of the virtual input should take into account the maximum achievable limits, before as well as after failure. This promotes the reaction speed of the system, since saturation of actuators is prevented upstream by limiting the magnitude of the virtual input. The need for this downscaling has already been found in the examples given in sections 8.1.3.3 and 8.1.3.4, where it was found that changes to the reference signals were needed in order to prevent throttle saturation.

First the principle of Pseudo Control Hedging will be introduced. Thereafter, some evaluation results will be shown by applying the PCH algorithm on the RECOVER simulation model.

8.3.1 Pseudo Control Hedging (PCH) principle

The concept of Pseudo Control Hedging (PCH) was initially developed in [136, 137]. Aim is to compensate the reference model signal for input characteristics such as actuator position limits, actuator rate limits, and linear input dynamics. In [122], this concept has been applied in an adaptive control setup based upon nonlinear dynamic inversion. An additional advantage of PCH is that the relative order of the dynamic inversion operation can be reduced by one degree. NDI inverts the aircraft dynamics, but not the input behaviour, represented by the actuators, which are usually modelled as first order lag components. The use of PCH provides an alternative for an eventual additional inversion loop for these dynamics, although this has been no point of concern in the research setup presented here. Nevertheless, input saturation is a concern here, as discussed in section 8.1.3.

The principle of Pseudo Control Hedging works as follows. For system dynamics of the form: $\dot{\mathbf{x}} = \mathbf{a}(\mathbf{x}) + \mathbf{b}(\mathbf{x})\,\boldsymbol{\delta}_{\text{comm}}$, where $\mathbf{a}(\mathbf{x})$ contains aerodynamic model information and $\mathbf{b}(\mathbf{x})$ represents control effectivity, the NDI control law is structured as follows: $\boldsymbol{\delta}_{\text{comm}} = \mathbf{b}^{-1}(\mathbf{x})\,[\boldsymbol{\nu} - \mathbf{a}(\mathbf{x})]$, resulting in: $\dot{\mathbf{x}} = \boldsymbol{\nu}$, where $\boldsymbol{\nu}$ is defined as the virtual input. Due to the control effector characteristics, such as actuator position and rate limits, the actual control displacement $\boldsymbol{\delta}_{\text{act}}$ is not identical to the commanded control displacement $\boldsymbol{\delta}_{\text{comm}}$. Subsequently, the estimated virtual input $\hat{\boldsymbol{\nu}}$ can be calculated, which is based upon the actual control displacement $\boldsymbol{\delta}_{\text{act}}$:

$$\hat{\boldsymbol{\nu}} = \mathbf{a}(\mathbf{x}) + \mathbf{b}(\mathbf{x})\,\boldsymbol{\delta}_{\text{act}} \tag{8.42}$$

Finally, the PCH signal $\boldsymbol{\nu}_h$ is obtained by subtracting the estimated from the commanded virtual input:

$$\boldsymbol{\nu}_h = \boldsymbol{\nu} - \hat{\boldsymbol{\nu}} \tag{8.43}$$

This signal serves as compensation signal which is fed back to the reference model and which is subtracted from $\dot{\mathbf{x}}_{\text{ref}}$. The reference signal at the output of the reference model becomes:

$$\mathbf{x}_{\text{comm}} = \frac{1}{s}\left(\mathbf{K}_{\text{ref}}\left(\mathbf{x}_{\text{ref}} - \mathbf{x}_{\text{comm}}\right) - \boldsymbol{\nu}_h\right) \tag{8.44}$$

The overview of the Pseudo Control Hedging setup can be seen in fig. 8.22. This figure shows that PCH scales (hedges) the commanded signal down to a level that is achievable by the actuator dynamics.

The advantage of this setup is that for adaptive NDI, damage information in the identified aerodynamic model as well as in the control surface deflections is automatically taken into account while calculating the estimated virtual input $\hat{\boldsymbol{\nu}}$ and subsequently the PCH signal $\boldsymbol{\nu}_h$. The beneficial influence of PCH for this purpose is illustrated in the evaluation results presented next.

8.3.2 Evaluation Results

As explained in section 8.1, the improved control setup consists of three consecutive NDI loops. This means that PCH can be implemented on these three levels as well. Application is rather straightforward by combining the PCH laws in eq. (8.42), (8.43) and (8.44) from the previous section and the NDI control laws as given in eq. (7.37), (8.34) and (8.18) combined with (8.31) for the inner, middle and outer loops respectively. Two application

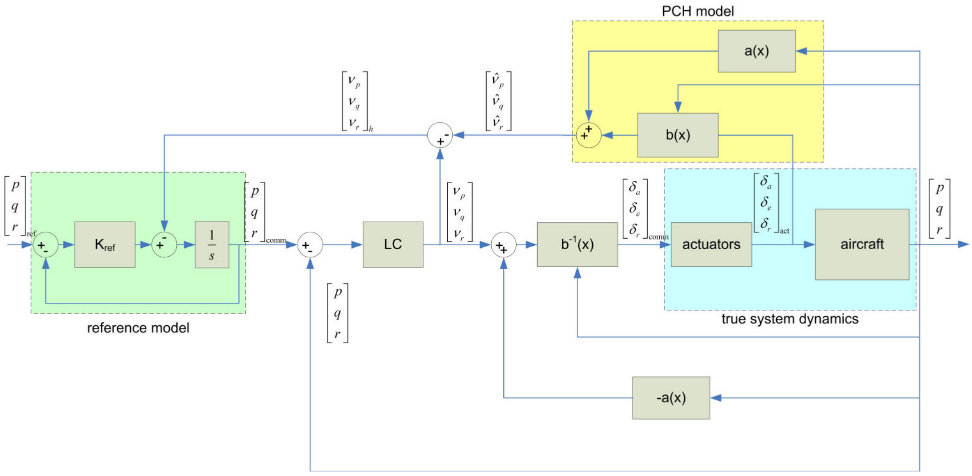

Figure 8.22: Setup of the Pseudo Control Hedging structure

examples are given below, a pitch rate example in the inner loop and a velocity example in the outer loop.

8.3.2.1 PCH applied on inner loop: pitch rate example

In the first example, a doublet command is given on the pitch rate channel, while two of the elevators are defective. Figure 8.23 illustrates the consequences of actuator saturation without pseudo-control hedging. Fig. 8.23(b) shows that elevator deflection angle limit saturation (see also figure A.1.2.1) occurs between $60s$ and $65s$. As a consequence, the reference pitch rate cannot be achieved by the measured pitch rate, as shown in fig. 8.23(a). The beneficial influence of PCH is visualized in figure 8.24. The protecting effect of the PCH signal in the reference model can be seen in fig. 8.24(a), where the hedged reference signal $q_{\mathrm{ref}_{\mathrm{PCH}}}$ differs from the regular doublet reference signal q_{ref}. It can be seen in figure 8.24(b) that the control surface does not saturate anymore, and as a consequence the measured pitch rate q_{meas} matches the compensated reference signal $q_{\mathrm{ref}_{\mathrm{PCH}}}$ in fig. 8.24(a). Comparing figures 8.23 and 8.24 illustrates that actuator rate saturation is responsible for the initial hedging signal, later on augmented by the position saturation.

This basic example illustrates the use of PCH in the control loop. However, it is possible to implement this algorithm on all control layers, and this application is illustrated by the following example.

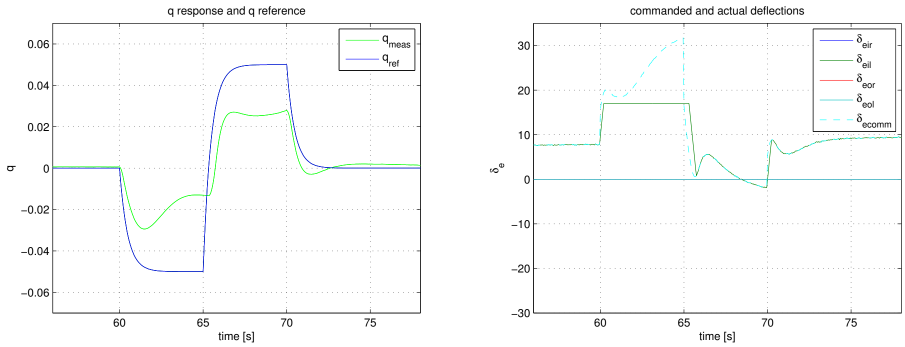

(a) pitch rate response and pitch rate reference (b) commanded and actual deflections

Figure 8.23: Pitch rate doublet command without PCH

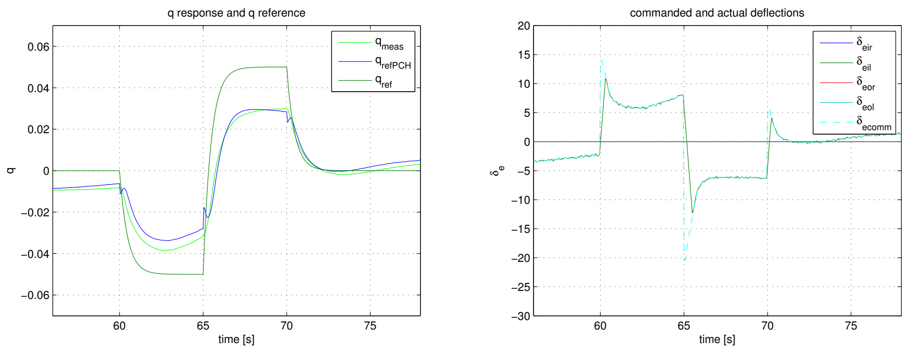

(a) pitch rate response and pitch rate reference (b) commanded and actual deflections

Figure 8.24: Pitch rate doublet command with PCH

8.3.2.2 PCH applied on outer loop: velocity example

In this example, a step command is given on the velocity channel combined with the altitude change, while some performance degrading restrictions apply on the engine parameters, i.e. they react slower and can give less maximum thrust. As a consequence, for the situation without PCH in figure 8.25(a), it can be seen that the slower engine reactions lead to a longer rise time and considerable overshoot. Comparing thrust command and actual thrust values in fig. 8.25(b) shows that saturation occurs over sustained periods of time. In contrast, figure 8.26 shows the effect of PCH. In figure 8.26(a), PCH provides a corrected reference signal $V_{\mathrm{ref}_{\mathrm{PCH}}}$ which is reachable in the present configuration. The hedging effect on the reference signal is caused by the simultaneous altitude change, which requires an amount of the restricted available remaining thrust authority to achieve. As soon as the altitude change has been achieved, between 400 and 500s, the hedging influence disappears. However, figure 8.26(b) shows that thrust saturation still occurs, although the level of saturation and its time span are considerably reduced, as can be seen by comparing with fig. 8.25(b). Further analysis has shown that saturation occurs in the time intervals when relatively small fit errors occur in the local gradient calculation of the third NDI loop, described in section 8.1.1.2. This result shows that very accurate identification results are needed for accurate PCH which eliminates all saturation in the controls. However, even with small misfits in the local gradient determination results, the beneficial influence of PCH is still visible as can be seen by comparing figures 8.25(b) and 8.26(b).

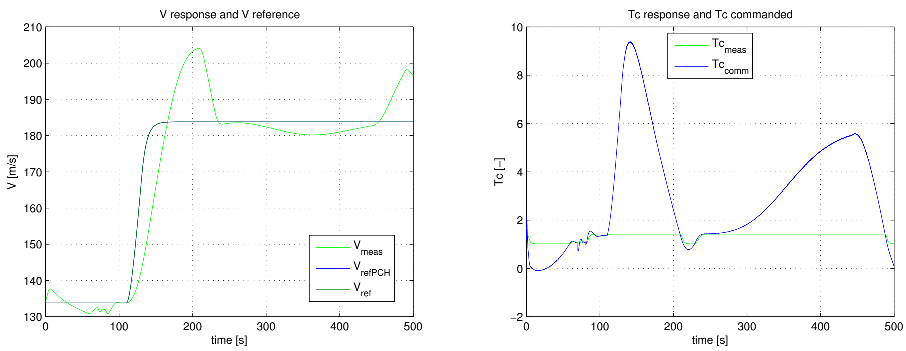

(a) velocity response and velocity reference

(b) commanded and actual thrust

Figure 8.25: Velocity change command with engine limitations without PCH

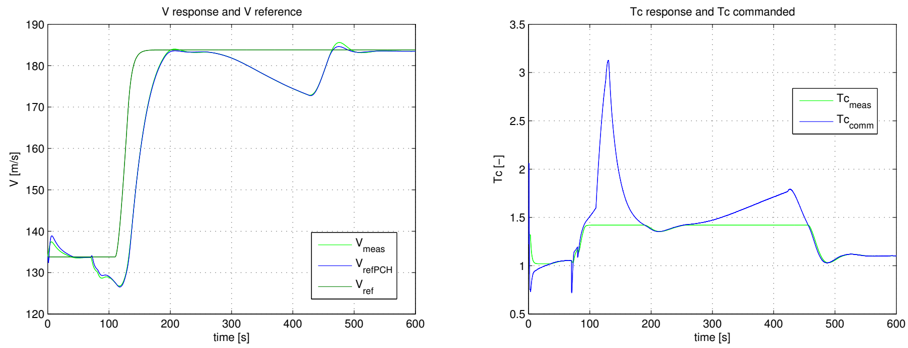

(a) velocity response and velocity reference

(b) commanded and actual thrust

Figure 8.26: Velocity change command with engine limitations with PCH

8.4 Control Allocation (CA)

Another important issue needs to be taken into account in the control setup, in order to improve performance compared to the baseline NDI controller. Namely, static control allocation in the $\mathbf{b}^{-1}(\mathbf{x})$ function of the NDI control law should be rendered dynamic by taking into account control effectiveness information from the identification procedure and to exploit this information by redistributing the command over the most effective control effectors. In this respect, it is important to take into account not only control effectiveness from the aerodynamic identification procedure, but also actuator performance, which can be observed through an actuator health monitoring system. E.g. a failed elevator actuator with the physical elevator surface still attached will not be detected by the aerodynamic model identification algorithm, since the aerodynamic contribution is still present, although constant. The monitoring system serves for this specific purpose, which detects that the control surface deflection does not follow the commanded signal. On the other hand, when part of the elevator surface is lost, with the elevator servo still operative, this failure will not be detected by the monitoring system, but by the aerodynamic identification procedure, due to its reduced aerodynamic contribution. This kind of control surface failure has occurred previously. A British Airways Concorde lost part of its rudder control surface in mid flight over the Tasman sea in 1989, see figure 8.27(a) and ref. [2], and in 2005 an Air Transat Airbus A310 lost its entire rudder in mid flight, South of Miami, see figure 8.27(b) and ref. [8]. An important issue in this matter is that collinearities between the measurement signals of the control surface deflections should be avoided here, otherwise it is impossible for the identification algorithm to distinguish which control surface is stricken.

A wealth of control allocation methods exists, as discussed in section 2.5 in the literature survey. The control allocation method selected here is an optimization based method. First,

(a) partial rudder loss of the British Airways Concorde, source: concordesst.com

(b) complete rudder loss of Air Transat Airbus A310, source: [8]

Figure 8.27: Examples of the loss of (part of) the rudder control surface

the underlying theories of the chosen control allocation approach, namely Control Distributor Concept (CDC), and the concepts of Actuator Health Monitoring System (AHMS) and seperate surface excitation (SSE) will be elaborated, which are needed in this setup. Finally, some baseline examples illustrate the usefulness of this control setup.

8.4.1 Control Distributor Concept (CDC)

Given the motivation presented above, a control allocation method is needed which integrates control action updates taking into account aerodynamic changes as well as actuator hardware failures. A valid approach for this purpose is the control distributor concept (CDC), presented in ref. [123]. The principle of this approach is as follows. Consider the system described by

$$\dot{\mathbf{x}} = \mathbf{F}\mathbf{x} + \mathbf{G}\boldsymbol{\delta} \tag{8.45}$$

where $\mathbf{x}$ is the state vector, $\mathbf{F}$ is the system matrix, $\mathbf{G}$ is the control matrix, and $\boldsymbol{\delta}$ is the actual control motion (such as surface deflection). The total control effort is given by $\mathbf{G}\boldsymbol{\delta}$. Let $\mathbf{M}$ be the command distributor matrix that apportions the commanded control input $\mathbf{u}$ efficiently over the set of available control effectors $\boldsymbol{\delta}$:

$$\boldsymbol{\delta} = \mathbf{M}\mathbf{u} \tag{8.46}$$

The aim of control allocation is to ensure that the total control effort after a control failure approximates the total effort before the failure as good as possible:

$$\mathbf{G}_f\boldsymbol{\delta}_f \approx \mathbf{G}\boldsymbol{\delta} \tag{8.47}$$

$$\mathbf{G}_f\mathbf{M}_f\mathbf{u} \approx \mathbf{G}\mathbf{M}\mathbf{u} \tag{8.48}$$

where $\mathbf{G}_f$ represents the control efficiencies after failure, provided by the identification algorithm in chapter 4. The objective of CDC is to minimize the ℓ_2 norm of the total control effort based cost function:

$$\mathbf{J} = \|\mathbf{G}_f \mathbf{M}_f - \mathbf{G}\mathbf{M}\|_2 \tag{8.49}$$

resulting in the minimum norm formulation for the new command distributor matrix $\mathbf{M}_f$:

$$\mathbf{M}_f = \mathbf{G}_f^{\dagger} \mathbf{G}\mathbf{M} \tag{8.50}$$

where $\mathbf{G}_f^{\dagger}$ is the pseudo inverse of $\mathbf{G}_f$. Ref. [123] suggests the use of the Penrose pseudo-inverse. However, for the application in this context, where one needs to take into account actuator hardware failures too, it is preferable to rely on the weighted pseudo inverse as mentioned in ref. [73]. In this manner, one obtains an integrated control allocation method which is capable to deal with both types of failures. More precisely, this weighted pseudo inverse is calculated as follows:

$$\mathbf{G}_f^{\dagger} = \mathbf{W}_f \mathbf{G}_f^T \left(\mathbf{G}_f \mathbf{W}_f \mathbf{G}_f^T\right)^{-1} \tag{8.51}$$

where $\mathbf{W}_f$ is a diagonal matrix with unity values on the diagonal, for unfailed situations equal to the identity matrix, and in case of actuator failures updated with information obtained from an actuator fault detection flag monitoring algorithm, such that the appropriate channel is cut out of the control distribution procedure by putting the corresponding diagonal element in $\mathbf{W}_f$ equal to zero. This actuator fault detection monitoring algorithm is also called an Actuator Health Monitoring System (AHMS).

CDC relies on a set of assumptions. Primarily, it assumes the presence of a relative large amount of similar control surfaces in order to distribute the control tasks (control redundancy), and that the mutual couplings between the different surfaces are not too large. Secondarily, it needs control efficiency information of each individual control surface, also after failure, in order to define $\mathbf{G}_f$. Another issue is that it only compensates for actuator and control surface failures. The regular dynamic inversion setup, presented earlier, deals with changes in the system dynamics, represented in the $\mathbf{F}$ matrix. Moreover, it does not take into account eventual control saturation. However, for the failure scenarios considered in the RECOVER model, it has been observed that control surface saturation is not a major issue to take into account in the control allocation algorithm.

The Actuator Health Monitoring System (AHMS) and the determination of control efficiency information of each individual control surface are briefly discussed in the next sections.

8.4.2 Actuator Health Monitoring System (AHMS)

There are several ways to determine the health status of the actuators, and this field forms a research discipline on its own. Due to the dynamic actuator response, comparison of actuator input and output is not a valid approach. Transients would lead to many false failure alarms, except for an unacceptably high failure detection threshold. Since actuator properties are usually well known, a popular way is to consider a mathematical actuator model which predicts the actuator behaviour and to analyse the residual between the measured true actuator position and the calculated actuator model output, as shown in fig. 8.28.

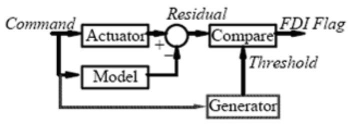

Figure 8.28: Actuator Health Management System, source: [73].

In case of a failure, this residual will deviate from zero and a failure can be declared in the respective steering channel. Nominal measurement errors can be accommodated by using a non-zero decision threshold for comparison with the residual. However, residuals can be quite different from zero in the presence of significant modelling errors. In order to minimize this type of false alarms, higher constant threshold values can be used. However, these lead also to a higher missed detection risk. Therefore, adaptive thresholds are preferable. This adaptive threshold can be dependent on input amplitude to deal with linear actuator models. However, limiting causes nonlinearities in the actuator model and necessitates the use of a composite signal, which at each time sample is the maximum of the real-time and delayed versions of the command. More information about this adaptive threshold can be found in ref. [73].

An alternative method for this adaptive threshold for residual evaluation is mentioned in ref. [276], where the evaluation signal is a general composite signal:

$$\theta(t) = \alpha r^2(t) + \beta \int_{t-T}^{t} r^2(\tau) d\tau \tag{8.52}$$

where α and β are appropriate weightings for the instantaneous and long-term contributions, $r(t)$ is the residual signal and T is the width of the observation window. By tuning α and β, emphasis can be shifted between the current values of the residual signals (β small) and persistent faults (α small). Again, a threshold must be defined for $\theta(t)$. Ref. [275] considers the use of least order residual generators for this purpose, applied on a Boeing 747-100/200 aircraft, making use of the same RECOVER simulation model as used in this study.

However, implementation of these AHMS algorithms has been deemed to be outside the scope of this thesis. It is assumed that they are present and that they are providing FDI results with respect to actuator failures to the $\mathbf{W}_f$ matrix in the CDC control allocation algorithm.

8.4.3 Control effectiveness evaluation of the control surfaces

In order to assess the control efficiencies of the individual control surfaces, a few alternative methods exist. Possible methods that can be used for effectiveness evaluation of the control surfaces are separate surface excitation (SSE) [112, 287] and multivariate orthonormal input functions [208]. Due to the mutual orthogonal input design, the latter method allows an efficient and faster identification of the individual control surface efficiencies, especially in the case of a large number of control surfaces (in the Boeing 747 case one has 22 primary control surfaces: four elevators, four ailerons, twelve spoilers and two rudders). Speed of identification is extremely important after failure, since survivability might depend on it. Separate surface excitation is applied consecutively on each control surface individually, and takes significantly more time. The procedure has been applied in flight tests a.o. on the X-31A ([287]). While orthonormal input functions are preferable for practical applications from an efficiency point of view, the SSE method has been applied in this specific example, since this procedure allows distinctive analysis of the estimation of the control efficiencies, as shown in figures 8.29 and 8.30 presenting results for elevators and ailerons respectively.

Four consecutive doublets have been applied on the elevators, one on each as shown in figure 8.29(a), after trim settings have been obtained. The corresponding identification results are presented in fig. 8.29(b). These results converge to the same value. The residual is very small.

The same procedure has been applied on the ailerons, as shown in fig. 8.30(a). Closer analysis of these deflections reveals that the dynamic inversion controller compensates immediately for the disturbing surface excitations. This reduces the disturbing movements of

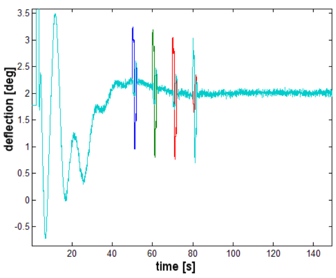

(a) separate doublet deflections of the four elevators

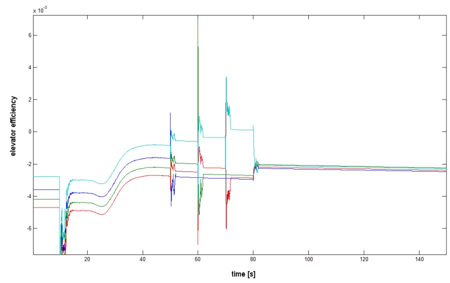

(b) identified control efficiencies following separate elevator deflections

Figure 8.29: Separate surface excitation for the elevators

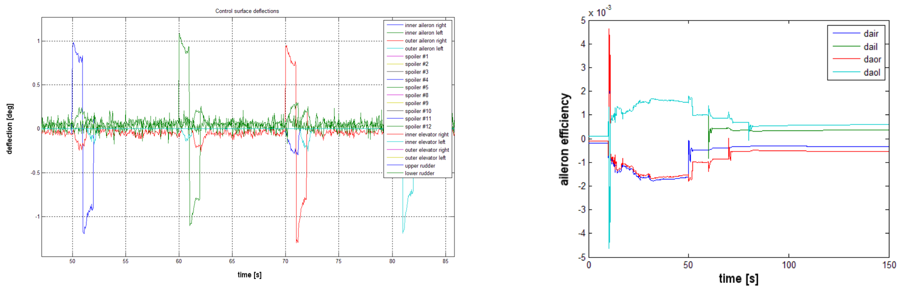

(a) separate doublet deflections of the four ailerons

(b) identified control efficiencies following separate aileron deflections

Figure 8.30: Separate surface excitation for the ailerons

the aircraft as it responds to the control excitations, while correlation levels are not compromising the identification results. The identification results in fig. 8.30(b) have opposite signs between left and right hand side. The outer ailerons have larger efficiency values, because of their longer moment arms.

8.4.4 Application examples

Two channels have been considered as application cases of the AHMS-SSPE-CDC control setup, namely the elevator and the aileron. In case of the elevator, actuator as well as aerodynamic failures have been considered, the latter focusses on actuator failures. All examples are applied on the RECOVER model data.

8.4.4.1 Elevators

First example are the elevator actuator failures, which are taken into account in the control allocation algorithm through the matrix $\mathbf{W}_f$. One considers the four elevators on the Boeing 747, as illustrated in fig. A.4. Test results are summarized in table 8.6.

Table 8.6: Actuator failures for the four elevators of the Boeing 747

elevator control efficiency $C_{m_{\delta_e}}$	δ_{eOL} $-3.2 \cdot 10^{-3}$	δ_{eIL} $-3.2 \cdot 10^{-3}$	δ_{eIR} $-3.2 \cdot 10^{-3}$	δ_{eOR} $-3.2 \cdot 10^{-3}$
command distribution unfailed	1	1	1	1
command distribution failure 1	$\emptyset$	1.33	1.33	1.33
command distribution failure 2	$\emptyset$	$\emptyset$	2	2
command distribution failure 3	$\emptyset$	$\emptyset$	$\emptyset$	4

From the results in table 8.6, it can be seen that the commands are effectively redistributed over the remaining control surfaces, while actuator failure information is taken into account. These results are rather straightforward due to the equal efficiency values for the different control surfaces.

As a next example, variations in the aerodynamic control efficiency of the individual elevators are considered. These are identified by the real time identification algorithm and taken into account in the post failure control efficiency matrix $\mathbf{G}_f$. Again, the four elevators on the Boeing 747 are considered. Test results are summarized in table 8.7.

Table 8.7: Reduced control efficiency for the four elevators of the Boeing 747

elevator	$\delta_{e_{OL}}$	$\delta_{e_{IL}}$	$\delta_{e_{IR}}$	$\delta_{e_{OR}}$
control efficiency unfailed	$-3.2 \cdot 10^{-3}$	$-3.2 \cdot 10^{-3}$	$-3.2 \cdot 10^{-3}$	$-3.2 \cdot 10^{-3}$
command distribution unfailed	1	1	1	1
control efficiency failure 1	$-3.2 \cdot 10^{-4}$	$-3.2 \cdot 10^{-3}$	$-3.2 \cdot 10^{-3}$	$-3.2 \cdot 10^{-3}$
command distribution failure 1	0.1329	1.3289	1.3289	1.3289
control efficiency failure 2	$-1.2 \cdot 10^{-4}$	$-1.2 \cdot 10^{-4}$	$-3.2 \cdot 10^{-3}$	$-3.2 \cdot 10^{-3}$
command distribution failure 2	0.3846	0.3846	1.9231	1.9231
control efficiency failure 3	0	0	$-1.6 \cdot 10^{-3}$	$-3.2 \cdot 10^{-3}$
command distribution failure 3	0	0	1.6	3.2

The results in table 8.7 show that control commands are also rescaled over the control surfaces, taking into account their individual control efficiency in post failure conditions.

8.4.4.2 Ailerons

The second example focuses on the aileron actuator failures. An important difference with the elevators is that the ailerons have different control efficiency values. The outer ailerons are more effective due to their longer moment arm, as illustrated in fig. A.4. Test results are summarized in table 8.8.

Table 8.8: Actuator failures for the four ailerons of the Boeing 747

elevator	$\delta_{a_{OL}}$	$\delta_{a_{IL}}$	$\delta_{a_{IR}}$	$\delta_{a_{OR}}$
control efficiency $C_{l_{\delta_a}}$	$-0.6 \cdot 10^{-3}$	$-0.4 \cdot 10^{-3}$	$0.4 \cdot 10^{-3}$	$0.6 \cdot 10^{-3}$
command distribution unfailed	1.15	0.77	-0.77	-1.15
command distribution failure 1	$\emptyset$	1.18	-1.18	-1.76
command distribution failure 2	$\emptyset$	$\emptyset$	-1.54	-2.31
command distribution failure 3	$\emptyset$	$\emptyset$	$\emptyset$	-3.33

Table 8.8 confirms that the control distribution concept works also for non-uniform control efficiencies.

8.4.5 Final note

The discussion about Control Allocation presented in this section summarizes the preliminary results of an initial study in this field. However, more extensive research is being undertaken currently to explore this field of research further, including applications in a full set of RECOVER failure simulations.

8.5 Comparison of baseline version NDI controller versus improvements

Based upon initial evaluation results obtained with the baseline flight controller in chapter 7, a selection of improvements have been implemented in chapter 8. Comparing simulation results from both versions in sections 7.2.2 and 8.1.3 shows significant improvements for the latter. The fact that the improved version has an additional inversion loop and relies on less assumptions, makes that it has more control authority and there is a larger flight envelope where it is capable to keep the aircraft under control compared with the baseline controller. However, a major conclusion from these simulations is that avoiding control saturation, especially with respect to the throttles, is a crucial aspect to guarantee survivability in post failure conditions. For this purpose, Pseudo Control Hedging has been implemented. Control Allocation on the other hand allows to maximize control authority on the side of available individual efficiencies of the different control surfaces. All these additional features provide important improvements in the global setup.

Chapter 9

Piloted simulator evaluation of the manual reconfiguring controller

Two versions of a fault tolerant controller have been designed, namely an automatic and a manual one, as discussed in chapter 7. If the system takes the form of a manual fault tolerant flight control algorithm, as opposed to a fully automatic system, there are some specific requirements, related to human-machine interactions, which need to be taken into account, namely handling qualities and pilot workload. The system must provide the pilot with good handling qualities in normal flight conditions and acceptable handling qualities in failed conditions. This chapter discusses the results of a piloted simulator evaluation, conducted in the SIMONA Research Simulator of Delft University of Technology. The control algorithm considered in this evaluation is the manual nonlinear dynamic inversion based controller as discussed in section 7.2.1. The objective of the piloted evaluation is to assess the real-time aircraft failure accommodation capabilities, following a potentially catastrophic failure. This will be done in terms of aircraft failure recovery capabilities, stabilisation, controllability and required pilot workload to conduct a survivable approach and landing. Comparison with the conventional classical controller provides a benchmark which allows to analyse the improvements achieved by the fault tolerant controller. The performance measurement of the latter control algorithm has been conducted in two ways:

- Qualitative: by means of subjective handling qualities ratings
- Quantitative: by means of objective pilot workload measurements

These measurements allow an initial assessment of the achieved performance of the fault tolerant control algorithm in a real-time operational environment using (subjective) pilot ratings that are correlated with objective (quantitative) data of pilot control activity as a measure of workload.

Pilot evaluations of Fault Tolerant Controllers have been organised before, as discussed in ref. [51, 97]. In ref. [51], handling quality evaluations have been discussed of a reconfigurable control law on the X-36 tailless advanced fighter aircraft (TAFA) for a pitch capture, bank capture and a 360° roll manoeuvre task. In ref. [97], handling qualities as well as workload have been analysed for a pitch down manoeuvre in order to evaluate Fault Detection, Isolation and Reconfiguration Algorithms for a Civil Transport Aircraft. However, the handling quality and workload assessment in this chapter is based upon a more elaborate experiment, involving a realistic complete approach manoeuvre. Besides, a significant part of the chapter focuses also on the experiment setup and the simulator equipment used, in order to put the results in the correct perspective.

The used aircraft model has been introduced in appendix A. This appendix shows that a high fidelity simulation model has been used in this research, including failure modes of which some have been validated on flight data obtained from digital flight data recorders. Subsequently, the manual fault tolerant flight control method which has been tested here for its post-failure handling qualities and workload has been elaborated in section 7.2.1. The experiment setup and evaluation procedure are discussed in section 9.1. Section 9.2 focuses on the observations and the analysis of the simulation results, concerning handling qualities and pilot workload, more precisely physical as well as compensatory workload. Finally, concluding remarks are presented.

9.1 Experiment method

The method for the piloted evaluation was based on procedures for human factors experiments. Some procedures were shortened to remain within the available time frame. The number of pilots and repetitions were smaller than required for a full statistical analysis of the experiment, but are sufficient to observe certain trends.

9.1.1 Design

The baseline condition for comparison was the conventional flight control system, which was manually flown. The controller considered in this research is set up such that the pilot could manually manoeuvre the aircraft, much like the conventional manual control strategy. In this case, the perceived dynamics were modified by the fly-by-wire algorithm to a rate command/hold scheme. During the evaluation, the aircraft was flown in the manual classical (mechanical) flight control system mode and in FTFC mode. In the former configuration, aircraft control was achieved via the mechanical and hydraulic system architecture modeled after the real aircraft. In the latter configuration, all control surfaces were commanded via the FTFC module. The interface design was modular, as illustrated in figure 9.1, such that switching from classical to FTC controller could be done in a relative straightforward manner.

The failures were flown in a fixed order with half of the pilots first flying with classical control and the other half with the FTFC under investigation. At the start of the session the

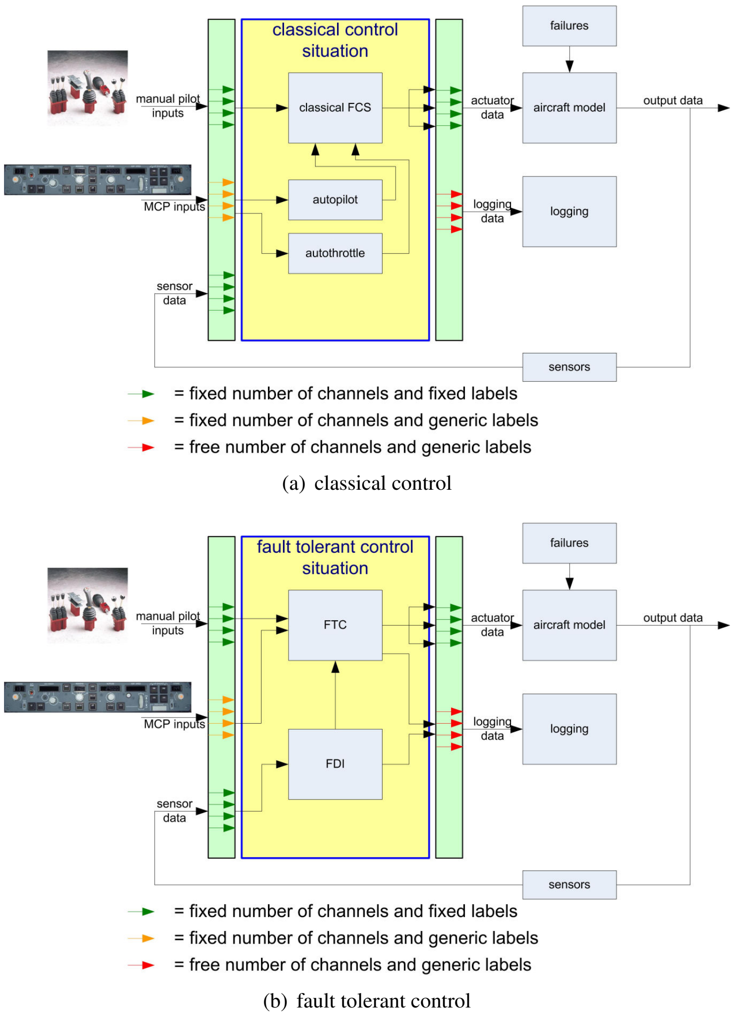

Figure 9.1: Interface design in simulation model to allow switching between classical and fault tolerant controllers.

pilot was given some time to familiarize himself with the simulator, experiment procedure and rating scales in the classical control mode.

9.1.2 Dependent measures

The controller was assessed on two types of dependent measures: implementation and operational.

9.1.2.1 Implementation

One measure of a controller's practical applicability is the computational load on the Flight Control Computer. The amount of additional calculations necessary for fault-tolerant control must be sufficiently low to enable actual introduction within the foreseeable future. The computational load was measured in the simulator software environment without a pilot in the loop. For comparison purposes a standard desktop PC (AMD Athlon$^{\mathrm{TM}}$ X2 5600+ processor) was used to measure the time needed by the algorithm to perform a single integration step. The simulation software was used to time the invocation of the controller's main function. This function included some overhead of getting the input data from other parts of the simulation and publishing the results, but this overhead was minimal (typically around $20\mu s$). This measurement can help in identifying the relative impact of the controller design on the computational load.

9.1.2.2 Operational variables

The operational variables were concerned with the interaction between the controller and pilot. Objective (for example, measured pilot control activity) and subjective (for example, handling qualities rating) operational variables were measured. The objective measurements in the evaluation consisted of the pilot's control inputs and the states of the aircraft. For the subjective measurement, the Cooper-Harper handling qualities rating scale was used (see appendix G and ref [70]). This rating scale is commonly used to provide a framework in assessing the handling qualities of a particular aircraft (or configuration) and the required workload and performance in a particular task. The performance of the reconfigured aircraft was assessed in a series of six flight phases, most of which were explicitly rated by the pilot. These flight phases were:

- Straight and level flight (not rated)
- Altitude changes
- Bank angle captures
- Right-hand turn (not rated)

- Localizer intercept
- Glideslope intercept

The wording on the scale is geared towards use during the development program of a new aircraft type. For an aircraft with structural or mechanical failures, it was sometimes tempting to take the degradations into account in the rating and not rate it as a fully functional aircraft ready to go into production. In such a case the pilot sometimes seemed to be willing to give a low (good) rating, even though the required workload and degraded performance would be totally unacceptable in daily operations. It was stressed however that the rating should be given to the aircraft ”as is” without taking the mitigating circumstances of the failure into account. Only in this way a fair comparison can be made between the nominal aircraft and the failed aircraft, as well as between the classical and fault-tolerant control schemes. To increase the validity of the rating, especially for inexperienced pilots, they were advised for every evaluation to explicitly follow the decision tree of the rating scale and correlate the attained performance with the experienced workload. Saving time by directly choosing a pilot rating number or not relating the rating with the actual performance would have seriously degraded the quality of the recorded ratings. In the evaluation, a number of tasks and performance criteria were defined. In general the lateral and longitudinal handling qualities were given separate ratings. Also, in some cases the task direction would be influenced by the specific failure, so these were split up as well, e.g. right and left bank angle capture or up and down altitude captures. Table 9.1 summarizes the tasks that were to be rated, along with the adequate and required performance criteria.

The pilots were given feedback on their performance before filling in the rating scales, as described in section 9.1.5.

9.1.3 Participants

Familiarity with the flown aircraft is one of the main requirements for the participants in a piloted evaluation. Some flight test or evaluation experience is also beneficial, especially when using standard rating scales.

In this campaign five professional airline pilots with an average experience of about 15000 flight hours, participated in the evaluation. They were all type rated for the Boeing 747 aircraft, and had experience in HQ evaluations and the rating method used. Table 9.2 shows information on the individual background and experience of the experiment pilots.

9.1.4 Apparatus

The evaluation was performed on the SIMONA Research Simulator (SRS, Figure 9.2) at Delft University of Technology. The SRS is a 6-DOF research flight simulator, with configurable flight deck instrumentation systems, wide-view outside visual display system, hydraulic control loading and motion system. The middleware software layer called DUECA

Table 9.1: Performance criteria divided by manoeuvre type

Manoeuvre	Description	Lateral performance	Longitudinal performance
Altitude capture	Intercept the new altitude with a climb or sink rate of at least 1000 feet/minute and without over- or undershoots outside of the required performance band. Maintain heading and airspeed within the required performance bands.	Required: - heading: $\pm 2°$ Adequate: - heading: $\pm 4°$	Required: - altitude: $\pm$ 50 feet - speed: $\pm$ 5 knots Adequate: - altitude: $\pm$ 100 feet - speed: $\pm$ 10 knots
Bank angle capture	Attain a 20 degree bank angle as quickly and precisely as possible and hold it stable. Maintain altitude and airspeed within the required performance bands.	Required: - bank: $20 \pm 1°$ Adequate: - bank: $20 \pm 2°$	Required: - altitude: $\pm$ 50 feet - speed: $\pm$ 5 knots Adequate: - altitude: $\pm$ 100 feet - speed: $\pm$ 10 knots
Localizer intercept	Intercept and follow the localizer. Maintain altitude and airspeed within the required performance bands.	Required: - offset: $\pm$ 0.5 dot Adequate: - offset: $\pm$ 1 dot	Required: - altitude: $\pm$ 50 feet - speed: $\pm$ 5 knots Adequate: - altitude: $\pm$ 100 feet - speed: $\pm$ 10 knots
Glideslope intercept	Intercept and follow the glide slope and localizer. Maintain airspeed with the required performance band.	Required: - localizer offset: $\pm$ 0.5 dot Adequate: - localizer offset: $\pm$ 1 dot	Required: - glideslope offset: $\pm$ 0.5 dot - speed: $\pm$ 5 knots Adequate: - glideslope offset: $\pm$ 1 dot - speed: $\pm$ 10 knots

Table 9.2: Experiment pilots flight experience and aircraft type rating

pilot no.	age	flight hours	type rating
1	64	13000	Boeing 747-200/300/400, Cessna Citation II, DC-3, DC-8
2	51	14000	Boeing 747-400
3	43	15000	Boeing 747-300, Boeing 767
4	54	18000	Boeing 747-400, Boeing 737, DC-10, DC-9, Fokker F-28
5	40	12000	Boeing 747-400, Boeing 737

(Delft University Environment for Communication and Activation) allows rapid-access for programming of the SRS, relieving the user of taking care of the complexities of network communication, synchronization, and real-time scheduling of the different simulation modules [272].

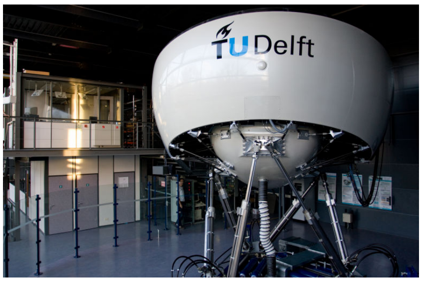

(a) outside view

(b) cockpit view

Figure 9.2: The SIMONA (SImulation, MOtion and NAvigation) Research Simulator (SRS) at Delft University of Technology, photo by Joost Ellerbroek

9.1.4.1 Flight deck instrumentation

The flight deck of the SRS was set up to resemble a generic, 2 person cockpit as found in many modern airliners. The installed hardware consisted of two aircraft seats, a conventional control column and wheel with hydraulically powered control loaders (captain's position) and rudder pedals, and an electrically actuated sidestick (1st officer's position, not used in this experiment), a B777 control pedestal, 4 LCD screens to display the flight instruments (60Hz refresh rate), and a B737 mode control panel (MCP). The displays were based on the B747-400 Electronic Flight Instrumentation System (EFIS, see Figure 9.3). They were shown on the LCD panels mounted in front of the pilot at the ergonomically correct locations. Although not all display functionality was incorporated, the pilot had all the information available to fly the given trajectory. One notable omission was the Flight Director (FD), which normally gives steering commands to the pilot. Especially during the localizer and glide slope capture and tracking, the use of "raw ILS data" instead of the FD added somewhat to the pilot workload. To help the pilots assess the controller's actions, the surface deflections of the elevators (left/right), ailerons (left/right, inner/outer) and rudders (upper/lower) were shown in the upper right hand corner of the Engine Indication and Crew Alerting System Display (EICAS).

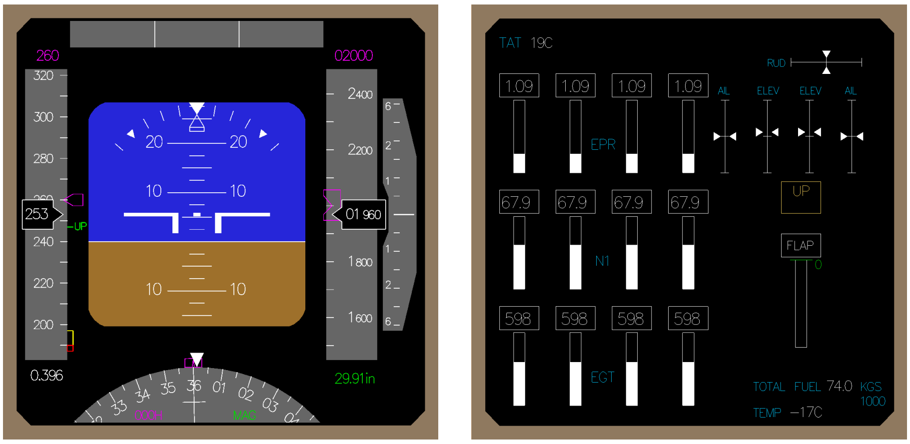

(a) Primary Flight Display

(b) Engine Indication and Crew Alerting System Display. AIL, ELEV and RUD on the EICAS indicate aileron, elevator and rudder deflections respectively

Figure 9.3: The PFD and EICAS flight deck displays presented to the pilot during the simulation runs

9.1.4.2 Outside visual system

The SRS has a wide field-of-view collimated outside visual system to give the pilot attitude information, as well as to induce a sense of motion through the virtual world. Three LCD projectors produce computer generated images on a rear-projection screen, which was viewed by the pilots through the collimating mirror. The resulting visual has a field of view of 180 x 40, with a resolution of 1280 x 1024 pixels per projector. Update rate of the visual was the same as the main simulation at 100 Hz, while the projector refresh rate was 60 Hz [260]. For this evaluation, a visual representation of Amsterdam Airport Schiphol was used. All runways and major taxiways were in their correct location, complemented with the most important buildings on the airfield. The surrounding area was kept simpler, with a textured ground plane showing a rough outline of the Dutch coast and North Sea.

9.1.4.3 Control loading feel system

The pilot used a conventional control column and wheel with hydraulically powered control loaders. The simulated dynamics of the controls were a constant mass-spring-damper system with parameters representative of the aircraft in the evaluated condition. The simulation model did not allow for feedback of surface forces to the controls, a feature that normally would have been present in a B747 aircraft (through the aircraft's q-feel system). This absence of surface deflection feedback forces may have reduced pilot control efficiency, especially in the mechanical failure cases.

Table 9.3: Control loading feel system characteristics

	pitch	roll
arm	$0.714m$	$0.17m$
spring constant	$474Nm/rad$	$5.416Nm/rad$
inertia	$5.577Nms^2/rad$	$0.478Nms^2/rad$
damping	$195.3Nms/rad$	$1.116Nms/rad$
break-out	$11.1Nm$	$0.1313Nm$
stiction/friction	$11.1Nm$	$0.1313Nm$

9.1.4.4 Motion system

The motion system of the SRS is a hydraulic hexapod with six degrees of freedom. Its cueing algorithm or washout filters can be easily adjusted to fit new aircraft dynamics or manoeuvres. For this evaluation the severity of the motion was tuned down somewhat to allow for the sometimes violent manoeuvres of the failures without reaching the limits of the motion base. The cueing algorithm was of the classical washout design, with high-pass filters on all degrees of freedom and a tilt coordination channel to simulate low frequency surge and sway cues by tilting the simulator. The sway tilt was especially apparent in some failure cases where large sideslip angles and sideforces were persistently present.

9.1.5 Procedure

The geometry of the flight scenario (Figure 9.4) was based on the 1992 Amsterdam Bijlmermeer aircraft accident profile [247, 248]. The scenario consisted of a number of phases. In every scenario, the pilot starts flying at an altitude of 2000 ft and with a speed of 260 kts towards the North. During this phase the controller should stabilize the aircraft, identify and correct for any deviations from the nominal trimmed aircraft condition, and give the pilot a sense of its non-failed handling qualities. After the normal flight phase, which included a 90 degree right turn and acceleration from 260 to 270 knots, the simulator operator introduced

Table 9.4: SRS motion system (adapted from [260])

DOF	Kinematics		Motion cueing algorithm				
	minimum deflection	maximum deflection	gain	high-pass filter order	high-pass break frequency	low-pass break frequency	damping
surge	$-0.981m$	$1.259m$	0.5	2	$2.0rad/s$	$4.0rad/s$	1.0
sway	$-1.031m$	$1.031m$	0.5	2	$2.0rad/s$	$4.0rad/s$	1.0
heave	-0.363	$0.678m$	0.4	3	$2.0rad/s$	-	1.0
roll	$-25.9°$	$25.9°$	0.5	1	$2.0rad/s$	-	-
pitch	$-23.7°$	$24.3°$	0.5	1	$2.0rad/s$	-	-
yaw	$-41.6°$	$41.6°$	0.5	1	$1.0rad/s$	-	-

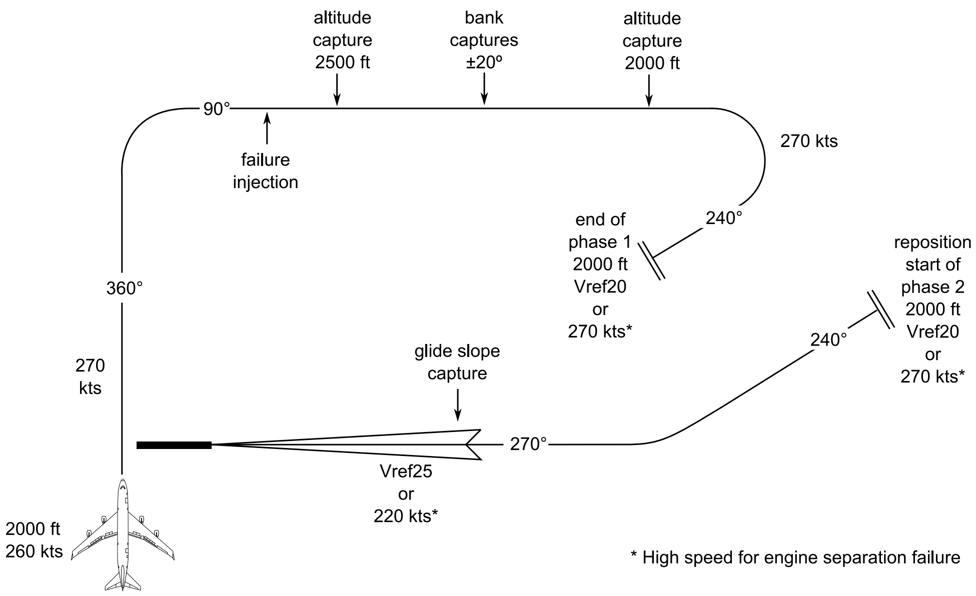

Figure 9.4: The definition of the experiment scenario as it was flown in the flight simulator

the failure (see Appendix A for a complete list of the available failure modes). For evaluation purposes, the pilot (but not the control system) was informed of the type of failure and the moment of its occurrence. This decision reflects the desire to examine the post-failure handling qualities and not the initial reaction to the failure and (in the manual control case) the pilot's surprise and fault identification behaviour. Initial tests of the fault-tolerant controller showed virtually no additional pilot action or compensation being required during and immediately after the failure, in stark contrast to the classical control configuration. Here the pilot spent considerable effort in recovering from the initial upset and developing a new control strategy to cope with the failure. By informing the pilot and thereby partly removing these tasks in the final evaluation, the pilot could better observe the failure and recovery and focus on the relative handling qualities in the post-failure configuration. It was felt this led to a fairer comparison between the classical and augmented configurations with less bias towards the latter.

The time span after the failure where control was recovered and the aircraft was brought back to a stable state, was called the recovery phase. In this phase the pilot could try different strategies to bring the aircraft back under control using classical manual control. If an FTFC algorithm was active, this system could identify the problem and reconfigure itself to the new situation.

If this recovery was successful, the aircraft should again be in a stable flight condition. After recovery, an optional identification phase could be introduced during which the flying capabilities of the aircraft could be assessed. This allowed for a complete parameter identification of the model for the faulty aircraft. The knowledge gained during this identification phase could be used by the controller to improve the chances of a safe and survivable landing. For the controller evaluated, no explicit identification phase was necessary, because the controller identified and reconfigured the aircraft and flight control system during the initial recovery and, if needed, continuously during later phases, thanks to its automatic reconfiguration capabilities discussed in section 4.7. In principle, the flight control system was fully reconfigured to allow safe flight after the identification phase.

During the straight and level flight after the failure, the pilot could assess the workload necessary to maintain the aircraft in a stable condition. Once stable at 2000ft, the pilot was asked to make a rapid and precise altitude capture to 2500ft. During the climb, airspeed and heading had to be kept constant. This manoeuvre was meant to examine the longitudinal handling qualities of the new aircraft configuration. At the new altitude the pilot was asked to perform bank angle captures of 20 degrees to the left and right. Again the goal was to make these captures as rapid and precise as possible, while maintaining altitude and speed. Banking the aircraft in this way was included in the experiment to expose undesirable lateral handling qualities.

After the bank angle captures, a new altitude capture was executed to bring the airplane back to 2000ft. Speed and heading were maintained during the descent. Finally, a right hand turn towards 240 degrees was performed which brought the aircraft on an intercept heading to the ILS localizer of runway 27 at Amsterdam Airport Schiphol (AMS). For all failures, except the El Al Flight 1862 failure, the pilot was asked to decelerate to 174kts, which was Vref20[1] for this configuration. Once stable on the new heading and airspeed, the simulator was paused to give the pilot the opportunity to fill in the rating scales.

To assist in providing Cooper-Harper ratings, the pilot was presented with time histories of the relevant parameters, along with their adequate and desired performance boundaries as defined in Table 9.1. An example of these plots is shown in Figure 9.5.

To maintain a constant approach geometry between runs, the aircraft was then repositioned at a point before the localizer intercept. To allow for some time for restabilization after the simulator ”unfreeze”, a point 5NM along track from the intercept point was used. This intercept point was also moved back 5 NM from the standard intercept point to allow for more time to capture the localizer. Especially for the El Al Flight 1862 failure case this was helpful because the intercept was performed with abnormally high speed (270kts as opposed to 174kts).

To capture the localizer, the pilot used raw ILS data on his display. The localizer was captured at an altitude of 2000ft with an airspeed of 174kts for all scenarios except the El Al Flight 1862 which used the higher speed of 270kts. After some time on the localizer, the aircraft intercepted the glide slope and the pilot started to descend. During the deceleration and glideslope capture, the normal configuration changes of flaps and landing gear were executed, except in the El Al Flight 1862 case. For this scenario, the aircraft model was identified only for the configuration with flaps 1 and gear up. It was not known how the aircraft would have reacted to other configurations and the validity of the model with those configurations was also unknown, so these were not used for the evaluation.

At an altitude of 500ft the run was stopped and the pilot filled in the rating scales for the second part of the flight. Again, he had access to the attained performance through the plots in Figure 9.6.

The landing itself was not part of the benchmark, because a realistic aerodynamic model of the damaged aircraft in ground effect and gear down was not available. However, it was assumed that if the aircraft was brought to the threshold in a stable condition and within the runway boundaries, the pilot would likely have been able to perform the final flare and landing as well.

[1]Reference speed for flaps set at 20 degrees.

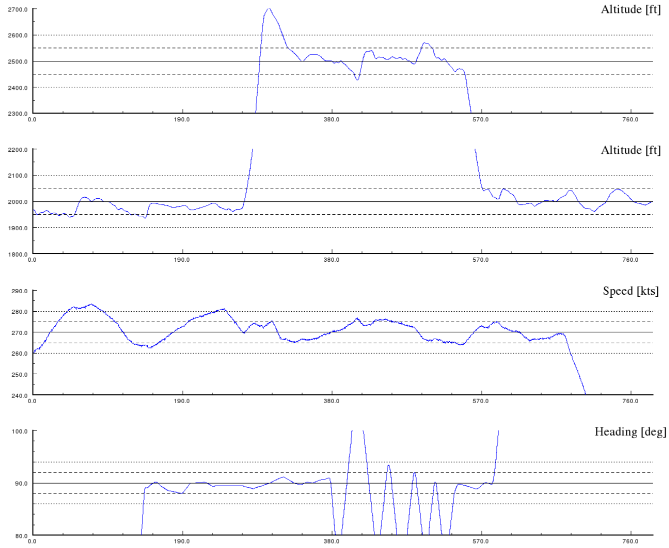

(a) altitude captures for 2000ft and 2500ft

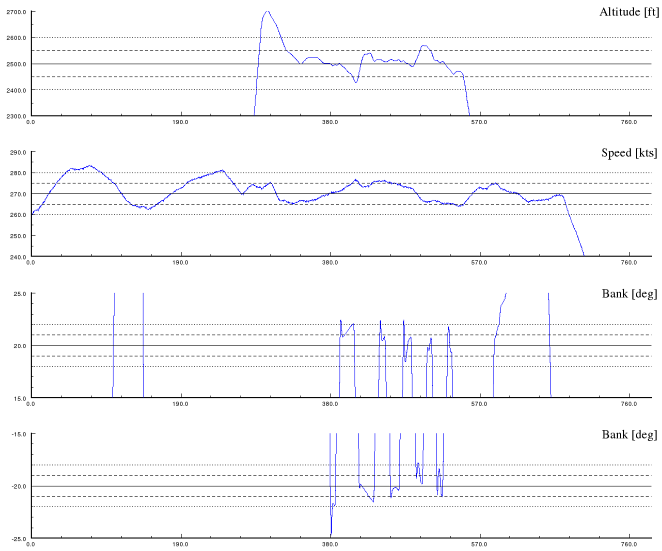

(b) bank angle captures for 20° and $-20°$

Figure 9.5: Performance plots: altitude captures and bank angle captures

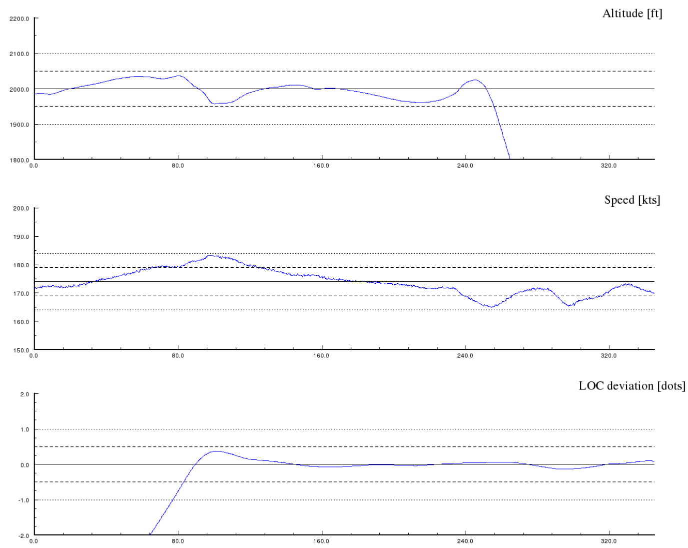

(a) localizer captures

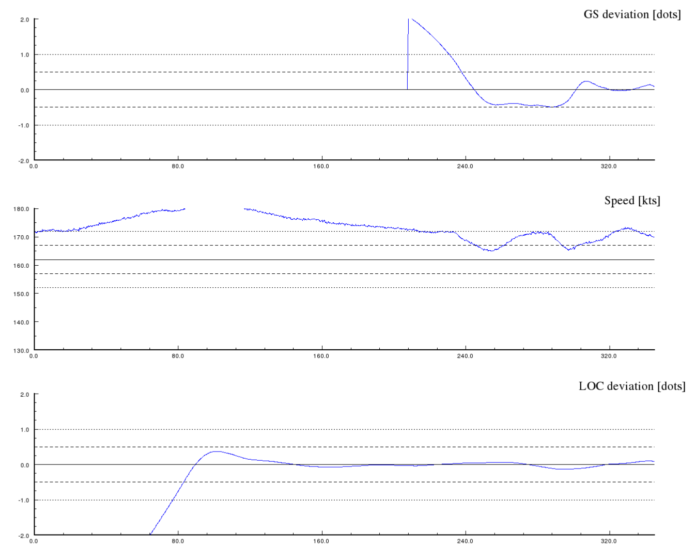

(b) glideslope captures

Figure 9.6: Performance plots: localizer captures and glideslope captures

9.2 Results

In this section, handling qualities and workload results are given on the manually flown Real-Time Model Identification and Nonlinear Dynamic Inversion Controller. First the time histories of the pilot inputs, a selection of aircraft states, and the control surface deflections are analysed. Subsequently, focus is placed on the analysis of handling qualities and pilot workload calculations.

9.2.1 FTC and pilot performance analysis results: time histories

The adaptive NDI control system has been validated on three failure scenarios besides the unfailed flight. The flown damaged scenarios have been selected in the simulation model's failure mode library, see appendix A, based upon relevance and practical value. The engine separation failure and the rudder runaway scenarios have been inspired by realistic accidents which have happened before, see chapter 1. The stabilizer runaway is another example of practical value and of interest for civil airliner manufacturers. Considering the restricted available time, the evaluation phase has concentrated on these three scenarios.

Figure 9.7(a) shows the pilot control deflections for the unfailed situation. This figure shows that there is no significant difference in required control deflections between both control alternatives in unfailed conditions, but this graph serves as a benchmark for the subsequent analysis for the different failure cases. Figure 9.7(b) shows that no sustained pitch deflection is necessary to compensate for the failure in the FTFC case, in contrast to the classic control case, which occurs at approximately at t = 150s. No significant differences are visible in the roll and yaw channel, because the failure has only consequences for the longitudinal controls. In fact, this behaviour can also be called 'autotrim', because all unrequested pitch rates are automatically canceled out. During the simulation run, the pilot stated that there was no noticeable difference between the FTFC controlled aircraft suffering stabilizer runaway and an unfailed aircraft.

In the Flight 1862 failure mode scenario, both right-wing engines (no. 3 and 4) are separated simultaneously resulting in substantial structural wing damage and partial loss of hydraulics. In this particular case, the aircraft dynamics closely match the flight data as obtained from the digital flight data recorder (DFDR). Figure 9.7(c) illustrates that the failure mode is highly demanding for the pilot to compensate for. The pilot has to use all available steering channels (roll by the steering wheel, pitch by the column and yaw by the pedals) in order to keep the aircraft under control in the classical control system configuration. The separation of the right-wing engines occurs around t = 200s into the flight for both the classical and ANDI control system. For the classical control system configuration, some pilots were not able to maintain control of the aircraft while trying to recover and stabilise after the separation of the right-wing engines. Due to the characteristics of this failure, the demand for the pilot is dependent upon the speed regime where the damaged aircraft is flying. At high speed (above approximately 260 KTS) and at a weight of 317.000 kg, the aircraft appears to be controllable, while at lower speeds larger control deflections are needed until control is lost around 200 KTS in a gliding condition (almost idle thrust on the remaining engines no. 1 and 2). Several other interesting observations were made for this failure scenario. For all pilots, the separation of both right-wing engines and the subsequent damage to the aircraft necessitated the use of both hands on the control wheel throughout most of the flight to keep the aircraft under control (Figure 9.8(a)). The sustained control forces, both to control bank angle and yaw, resulted in significant physical workloads as commented by the pilots afterwards and confirmed by their ratings. Additionally, most pilots commented about the obstruction of the primary flight instruments by the control wheel deflected at large angles required for lateral control (Figure 9.8(b)). The lateral control capabilities of the damaged aircraft with the classical control system showed that approaching approximately 260 knots in level flight, controlling left bank angles towards the operating engines became progressively sluggish requiring up to almost full control wheel deflection while applying full rudder pedal. For a right turn into the separated engines, the baseline aircraft had a tendency to overbank up to the point where control was lost (Figure 9.9). It was furthermore observed that lateral control capabilities were improved at increasing sink rates while intercepting the glideslope and decelerating and stabilising for a gliding condition towards the runway. Reason for this is the decreasing thrust effect. However, for a successful landing, the pilot requires knowledge concerning the aircrafts minimum control speed under the prevailing conditions in order to remain within the degraded safe flight envelope boundaries. After control reconfiguration by the fly-by-wire ANDI control law, following a real-time identification of the damaged aircraft dynamics, the experiment showed that conventional control strategies were restored allowing normal use of the control wheel, column and pedal to conduct a successful landing (Figure 9.10). Aircraft recovery transients and stabilisation by the ANDI fault tolerant control laws, immediately after the separation of the engines, proved to be acceptable (almost a non-event as commented by the pilots). Comparing the classical control system and the fault tolerant control algorithms in Figure 9.7(c) shows that the ANDI control laws require no more control effort from the pilot on the roll, pitch and yaw steering channels than before the failure. Only near the end of this particular simulation run for the FTFC configuration a major pilot control action in the lateral axis can be seen at about t=900s resulting in a saturation of the ailerons. This appeared to be a corrective action by the pilot as the damaged aircraft accidently decelerated below the (unavailable) minimum control speed during final approach. More information about this will be given later, see also fig. 9.13. This event highlights how information about the remaining pilot authority and the restricted safe flight envelope would contribute significantly to the pilot's situational awareness.

The rudder runaway is the most challenging failure from the pilot perspective. The failure occurs shortly before t = 200s. In this scenario, both upper and lower rudder surfaces are deflected uncommanded towards the aerodynamic blowdown limit (dependent on airspeed). As can be seen in Figure 9.7(d), the pilot has to use all available steering channels (roll by the steering wheel, pitch by the column and yaw by the pedals) to keep the aircraft under control in the case of classical control. This is remarkable, since only two channels (roll and pitch) retain their efficiency. Rudder demands via the pedal inputs have no use in this failure scenario, nevertheless it can be seen that the pilot is still tempted to use the pedals as a natural (trained) reaction, despite being aware of the failure characteristics via the pre-flight briefing. The aircraft failure transient behaviour following a sudden rudder hardover of the classical control system appeared to be rather critical. As can be seen in Figure 9.11, providing a visualisation of the simulator data, the baseline aircraft attains an initial large roll upset following a left rudder hardover without immediate pilot compensation. Most pilots were able to recover and stabilise the aircraft by manually applying differential thrust following the failure (Figure 9.12(d)). However, the application of differential thrust to stabilise the aircraft and improve lateral control margins resulted in difficulties controlling airspeed as commented by some of the pilots. The ANDI control algorithm, on the other hand, requires no more control effort from the pilot on these steering channels as before the failure. The pedals for instance, need no pilot input at all to minimize the sideslip of the aircraft in the case of FTFC. Only at the very end, a small pedal input is given by the pilot in order to line the aircraft up with the runway a few seconds before touchdown. It should also be noted that, to ensure sufficient lateral controllability, differential thrust must be applied. For the current FTFC control algorithm, differential thrust has been applied manually by the pilot during the recovery and stabilisation phase which appeared to be less critical immediately after reconfiguration.

Generally, comparing classical and fault tolerant control in the failure scenarios above shows that a fault tolerant flight controller requires no more control effort from the pilot on these steering channels than before the failure. The pedals for instance, need no pilot input at all to minimize the sideslip of the aircraft in the case of FTFC. Finally, some comments are given concerning the time scale. No timing requirements have been given to the pilot, resulting in some variations in time scales, depending on failure and control system.

Fig. 9.11 and 9.13 show the time histories of a selection of the most important aircraft states. These confirm the evaluation trajectory as outlined in fig. 9.4. Moreover, altitude and roll angle plots illustrate the altitude and roll angle captures executed by the test pilot to evaluate the post-failure handling qualities of the aircraft. Fig. 9.13 gives some additional information about the situation where the safe flight envelope boundary has been exceeded. The velocity graph shows that airspeed in the fault tolerant control case is allowed to reduce significantly lower than for the classical control case. At some point, the minimum controllable airspeed is exceeded, slightly above 100 m/s, and the aircraft exhibits a rolling tendency to the right which is almost impossible to counteract. Opening throttles for increasing airspeed even aggravates this behaviour, since only the left hand engines are providing thrust. After some major effort, the test pilot succeeds to stabilize the aircraft

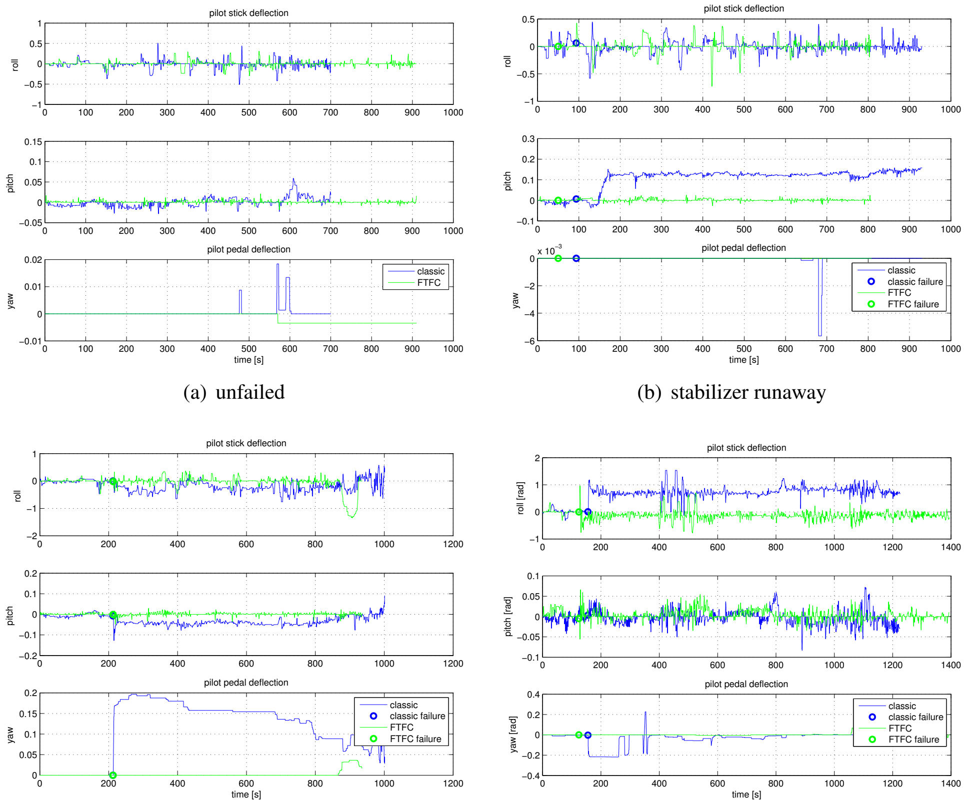

(a) unfailed

(b) stabilizer runaway

(c) engine separation scenario

(d) rudder runaway

Figure 9.7: The pilot control actions during the different scenarios which were flown manually. Range of available pilot control deflections: roll ± 1.536 rad, pitch ± 0.221 rad, yaw ± 0.244 rad

(a) Pilot (left) requiring both hands for lateral control after separation of both right-wing engines without control reconfiguration

(b) Pilot's head position (left) to scan primary flight instruments while applying left control wheel deflection to counteract roll without control reconfiguration

Figure 9.8: Pilot control activity after separation of both right-wing engines for classical hydro-mechanical control system configuration

again, but altitude and speed conditions do not permit to line up the aircraft successfully with the runway.

Fig. 9.14 shows the time histories of the control surface deflections for the different scenarios. These graphs demonstrate that the ANDI-controller uses the remaining active control surfaces in a way similar to what a human pilot would do. However, for the classical control system, the control surface deflections are proportional to the pilot's commands whereas in the fly-by-wire ANDI case, there is no direct coupling anymore. In fig. 9.14(b), for instance, it can be seen that the disturbing influence of the stabilizer runaway is counteracted by means of the elevators, however, without command from the pilot as can be seen in fig. 9.7(b). The same principle holds for the other scenarios. Another difference between the classical control system and the ANDI algorithm is visible in the application of the elevator for the nominal (unfailed) and rudder hardover cases as shown in fig. 9.14(a) and 9.14(d). The ANDI algorithm uses the elevator as an 'auto-trim' feature that automatically compensates for a mistrimmed stabilizer.

Information regarding control reconfiguration status by the ANDI algorithm was available to the pilot via the engine indicating and crew alerting system (EICAS) display in the cockpit. Figures 9.15(a) and 9.15(b) illustrate the EICAS display before and after the separation of the right-wing engines. As shown in the figures, the asymmetric physical loss of the engines is recovered and compensated by allocation of control to the remaining surfaces. For this scenario, the inboard ailerons are only half operational, supported by the remaining spoilers, as already mentioned by the damage information in appendix A, and this is also visible in fig. 9.14(c). This figure shows also that the FTFC algorithm exploits the full control authority of the rudder, where the human pilot relies less on rudder control input. As a consequence, slightly less aileron deflections are needed in the FTFC case compared

(a) Aircraft intercepting localiser

(b) Aircraft capturing localiser

(c) Aircraft overbanking to the right. Full aileron and rudder applied to compensate roll

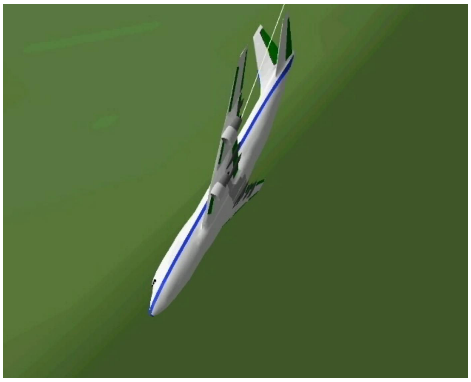

(d) Loss of lateral control

Figure 9.9: Piloted simulation showing separated right-wing engines and loss of lateral control due to overbank tendency without control reconfiguration and automatic stabilisation (flight animation by Rassimtech AVDS©)

Figure 9.10: Piloted simulator demonstration of approach and landing after separation of both right-wing engines using fly-by-wire ANDI control reconfiguration (courtesy of RTL4 Television, The Netherlands)

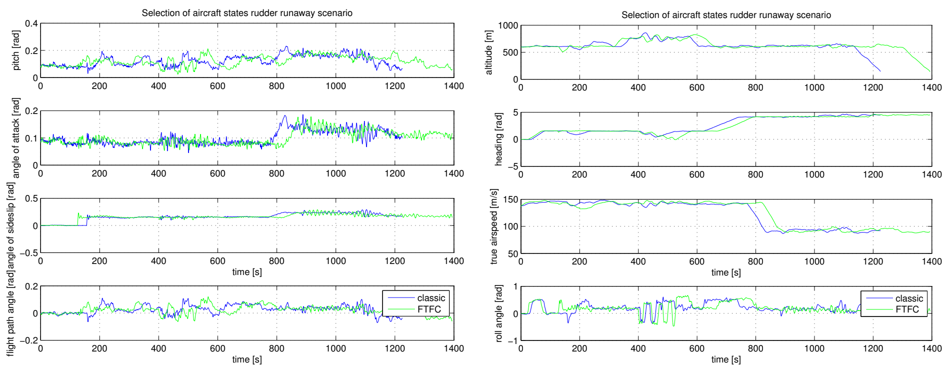

Figure 9.11: Comparison of a selection of aircraft states for the rudder runaway scenario

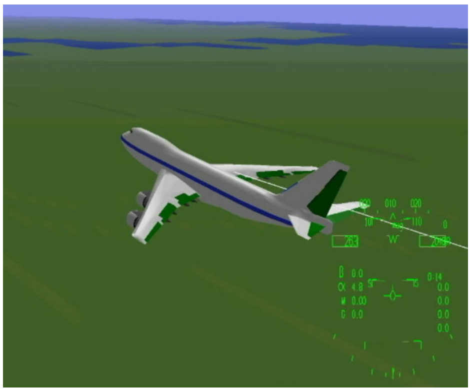

(a) Aircraft stabilised before failure. Altitude 2000 feet, Airspeed 260 KTS, Sideslip 0 deg, Bank angle 0 deg

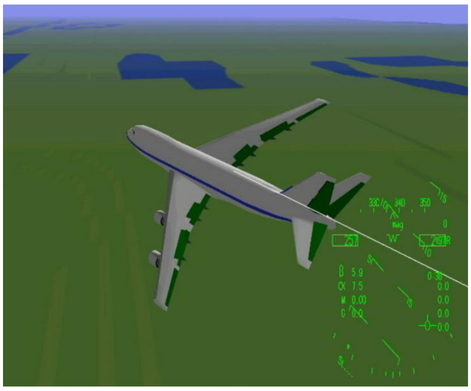

(b) Left rudder hardover to blowdown limit. Altitude 2000 feet, Airspeed 260 KTS, Maximum sideslip excursion 11.8 deg, Maximum bank angle 40 deg

(c) Pilot standing-by before failure insertion

(d) Pilot applies full right-wing down control wheel deflection and differential thrust for aircraft recovery

Figure 9.12: Piloted simulation of left rudder hardover inducing a large upset of the aircraft without ANDI reconfigurable control laws (flight animation by Rassimtech AVDS©)

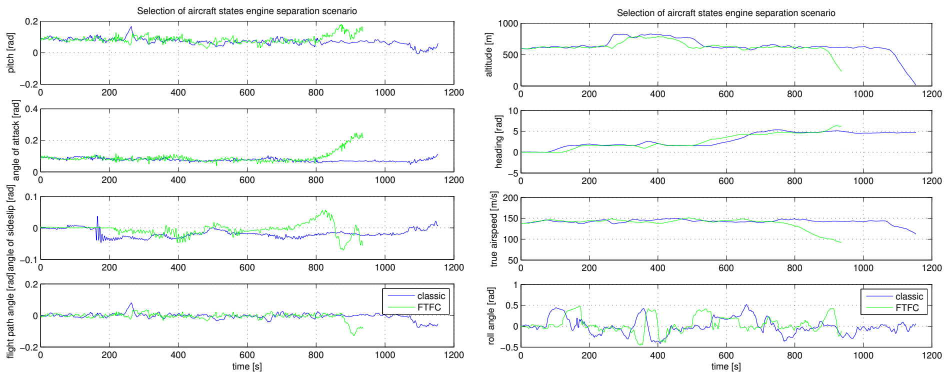

Figure 9.13: Comparison of a selection of aircraft states for the engine separation scenario

to classic control. The balance between aileron and rudder use can be improved by means of further optimisation of the control allocation scheme.

The reconfiguration status of the ANDI algorithm for a sudden rudder hardover, as presented to the pilot, is illustrated in Figures 9.15(c) and 9.15(d). Following the failure, lateral and directional control is allocated to the ailerons and spoilers providing roll and yaw compensation while any longitudinal trim offsets, due to the failure, are compensated by the elevators. In fig. 9.14(d), the faulty rudder behaviour illustrates the aerodynamic blowdown effect which is taken into account in the RECOVER simulation model. As a result the maximum rudder deflection is slightly below $15°$ for an airspeed around 270 knots, and even close to $25°$ (the physical maximum deflection limit imposed by the rudder control system structure) for an airspeed of 165 knots. The maximum physical deflections for all control surfaces are enumerated in fig. A.1.2.1 to support the results in fig. 9.14.

Based upon these simulation runs, handling qualities as well as pilot workload have been analysed, as is shown next. Simulations have shown that the stabilizer runaway was the least challenging from a pilot point of view, as explained earlier. Therefore, the subsequent discussions focus primarily on engine separation and rudder hardover, since these are the most interesting scenarios from a pilot point of view.

9.2.2 Handling qualities analysis results: CH ratings

The experiment pilots were asked to rate both the baseline aircraft with the hydro-mechanical control system configuration and the fly-by-wire ANDI reconfigurable control laws using the Cooper-Harper handling qualities rating scale, see appendix G. Both the rudder runaway scenario and Flight 1862 engine separation scenario were rated. As a comparison basis, the classical flight control system and fly-by-wire ANDI control algorithms were rated for the

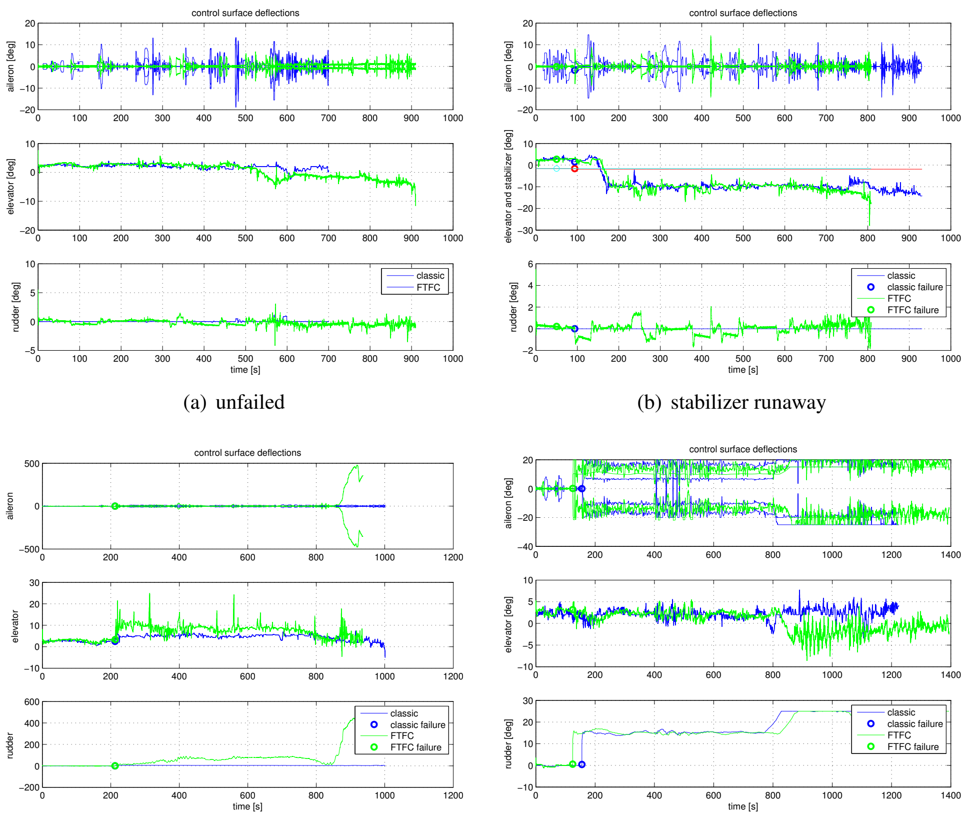

(a) unfailed

(b) stabilizer runaway

(c) engine separation scenario

(d) rudder runaway

Figure 9.14: Time histories of the control surface deflections involved in the different scenarios which were flown manually

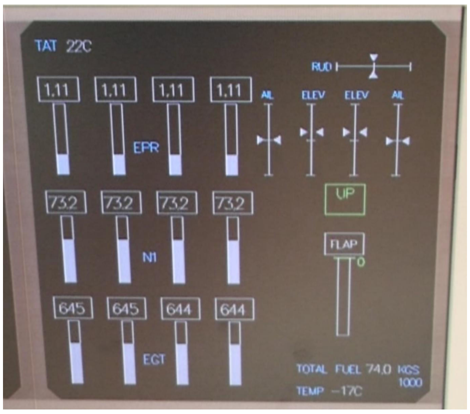

(a) EICAS display before failure

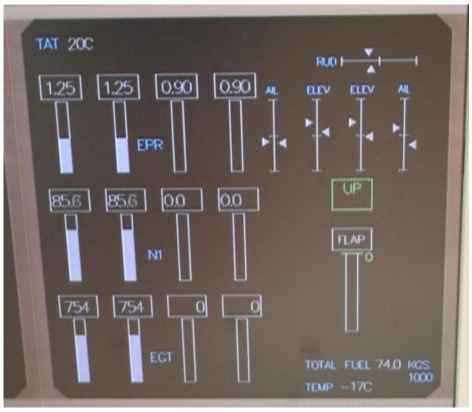

(b) EICAS display showing control surface reconfiguration after separation of right-wing engines

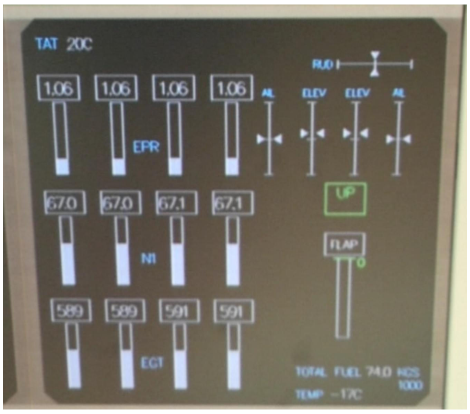

(c) EICAS display before failure

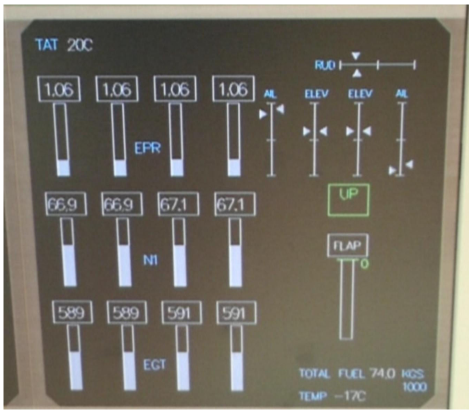

(d) EICAS display showing control surface reconfiguration after rudder hardover to blowdown limit

Figure 9.15: Engine indicating and crew alerting system (EICAS) display providing control reconfiguration status of ANDI control algorithm

nominal flight conditions (no failure modes). This also provided the opportunity to familiarise the pilots with the different baseline control strategies.

The handling qualities analysis results are illustrated in Figures 9.16 and 9.17. For all evaluation tasks, pilot handling qualities ratings were provided for both longitudinal and lateral task performance. For the evaluated control algorithm, the piloted evaluation tasks included altitude capture, bank angle acquisition and localizer capture up to the intercept of the glideslope. The bank angle capture task was subdivided into an evaluation of left and right bank acquisition capabilities to account for asymmetric failure modes. Figures 9.16 and 9.17 show the individual ratings, horizontally separated as classical (left) and fault tolerant (right), and from top to bottom the tasks altitude capture, left bank capture, right bank capture and localizer intercept respectively.

The experiment results show that both the baseline (classical) and fly-by-wire ANDI (FBW-ANDI) aircraft configuration were rated Level 1 (Rating 1-3) by most pilots for the unfailed condition. This provides a comparison basis when analysing pilot performance in degraded conditions for the different flight control system configurations. The trends of the pilot ratings for the ANDI reconfigurable control algorithm show that, especially for the Flight 1862 engine separation scenario, conventional flight control was restored up to acceptable handling qualities levels (upper Level 1) following a failure. In these conditions, no significant task performance degradations occurred as compared to the unfailed fly-by-wire aircraft while physical and mental workload was reduced as indicated by an analysis of the aggregated control forces and pilot comments. After incurring significant damage due to the loss of the right-wing engines, the pilot ratings for the conventional aircraft with classical control system show that in all conditions, above the minimum control speed, Level 2 handling qualities existed. The reconfigured aircraft (FBW-ANDI) is able to improve the handling qualities back towards the upper Level 1 region. This was substantiated by the measured pilot control activities, representative of workload, indicating no sustained pilot compensation after control reconfiguration.

The rudder hardover scenario appears to be more critical from a handling qualities perspective. As with the Flight 1862 case, Level 2 handling qualities were obtained in most conditions for the classical control system. However, the lateral control tasks were observed to induce severely coupled longitudinal and lateral dynamics resulting in further degradation of the handling qualities to Level 3. For the reconfigured aircraft, the handling qualities ratings remain about Level 2 after control reconfiguration despite no required sustained control inputs by the pilot. Most likely, the main reason for the inferior rating is caused by the fact that the fault tolerant controller is a rate controller, it minimizes disturbances in angular rates, but not the disturbed angle itself. As a consequence, rudder hardover results in a yaw rate to the left which is eliminated by the controller, but the heading angle change built-up meanwhile is not eliminated automatically, and is left to the pilot to compensate. Later on in this chapter, a solution will be proposed for this problem.

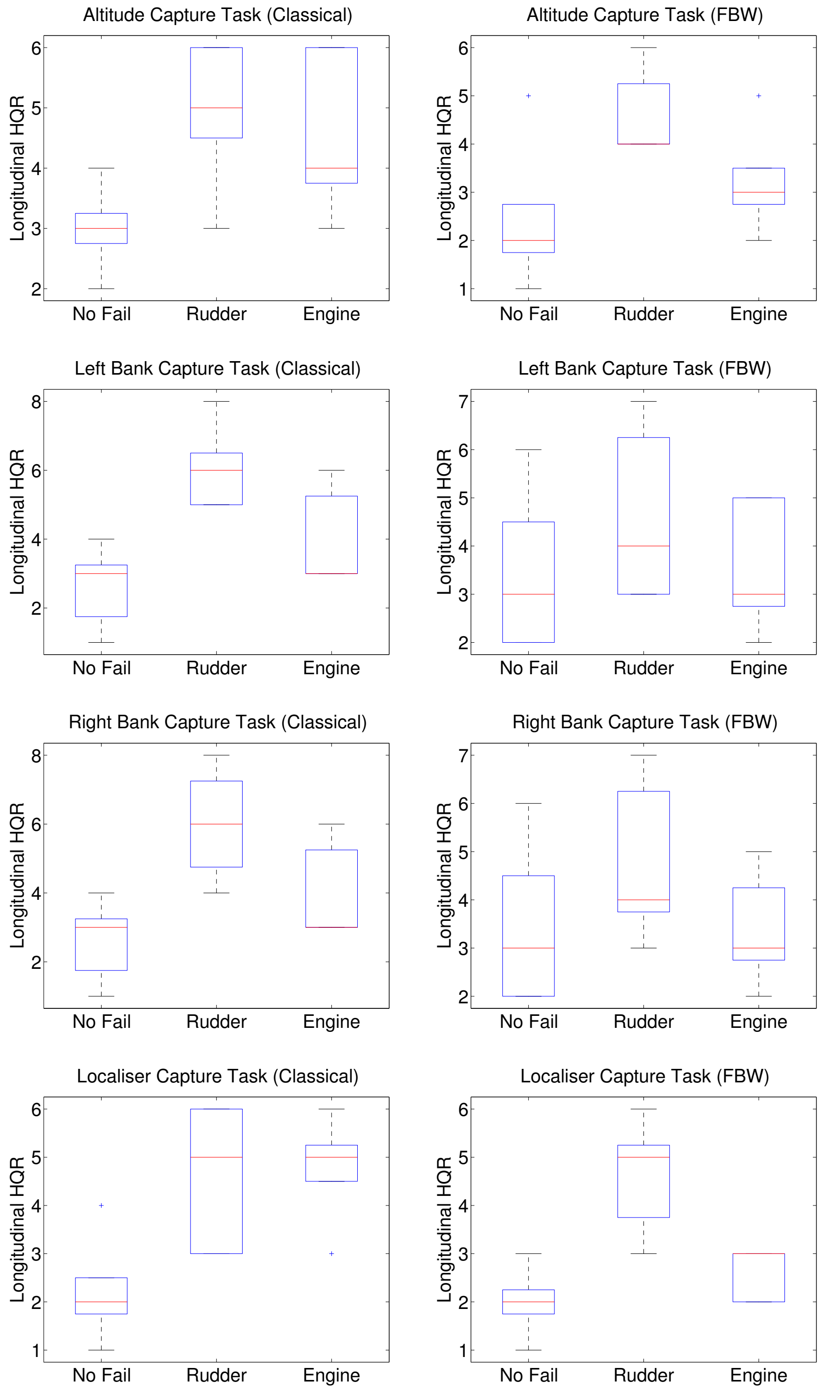

Figure 9.16: Pilot longitudinal handling qualities ratings of classical and FTFC flight control system configurations for the different aircraft failure scenarios.

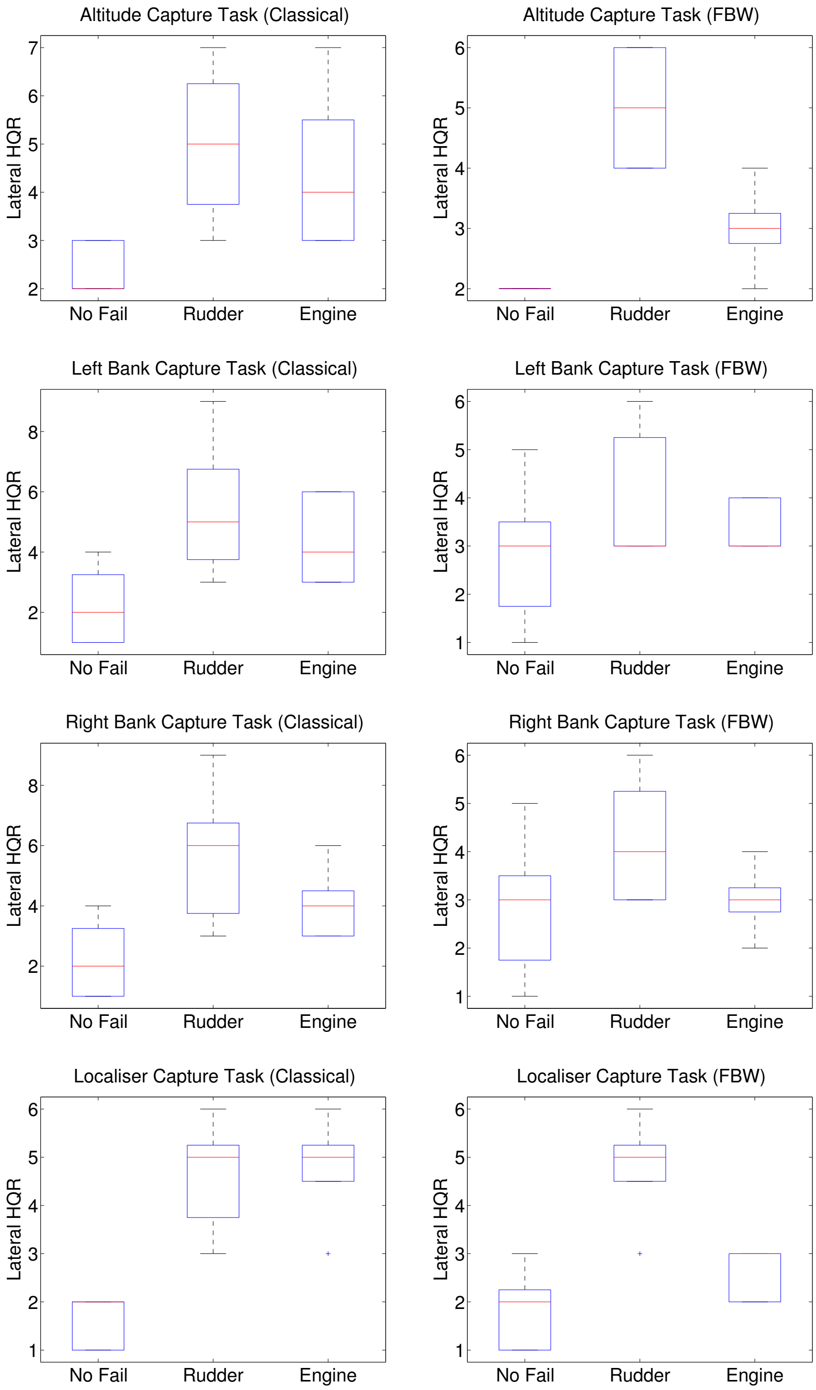

Figure 9.17: Pilot lateral handling qualities ratings of classical and FTFC flight control system configurations for the different aircraft failure scenarios.

9.2.3 Pilot work analysis results

Handling quality ratings are only one means to evaluate the performance of a flight control system, and despite use of the Cooper Harper Rating Scale, they still involve some pilot subjectivity, although this is eliminated as much as possible. On the other hand, there is the quantifiable pilot workload analysis. This subsection focuses on the latter part of the study.

Specific metrics exist in order to analyse the specific workload properties of a flight control system, excluding possible secondary influences, like the control loading system characteristics, as described in section 9.1.4.3. The workload of the pilot while controlling the aircraft can be divided into physical workload and compensatory workload. Especially during failure conditions, the pilot may be required to apply prolonged control inputs to maintain controllability of the damaged aircraft. For the Flight 1862 scenario, for instance, the asymmetric aircraft configuration caused by the separation of both right-wing engines and subsequent damage to the right wing requires sustained large control wheel deflections and the application of full rudder pedal throughout the flight. It can be observed that in these conditions the physical effort exerted by the pilot to maintain control of the aircraft can be significant and fatiguing. To maintain stability of the (damaged) aircraft, the pilot is required to apply compensatory workload by making constant adjustments to achieve task objectives (e.g. capturing a heading). The quantities studied here allow a distinctive analysis of physical workload and compensatory workload. The former is represented by average force and root mean square of the pilot control deflections, as illustrated in section 9.2.3.1. The latter can be observed by analysing the root mean square of the pilot control deflection rates or the pilot control power, as done in section 9.2.3.2.

This pilot workload figures have been calculated for two different phases, namely the specific part of the localizer intercept phase (left), which is defined as the time span between the triggering of the LOC valid flag and the GS valid flag, and secondarily the total simulation run (right). For the latter, the time span is defined as follows. Unfailed situations are considered from start to end of the simulation run. Scenarios including failures are restricted to the time span after the failure till the end. The localizer intercept phase work levels are comparable, since the time intervals are almost identical, thanks to the well-defined start and end points and the prescribed airspeed and trajectory. However, for the total simulation run, there are considerable variations in the time span from beginning till end, as can be seen in figures 9.7 and 9.14, which makes the absolute workload values not comparable. Therefore, average workload levels have been calculated for the total simulation run. In each graph, a distinction is made between roll, pitch and yaw channel, as illustrated by the three graphs separated vertically. In each control channel, six cases have been studied, namely unfailed, engine separation and rudder runaway, each time with classical and fault tolerant control. In each case, the workload figure of each of the five pilots is represented individually by means of bar plots, after which the mean and standard deviations are superimposed on these bar plots for every case, in order to facilitate mutual comparisons. Note that no data are available for pilot 1 in the localizer intercept phase for the engine separation failure with fault tolerant controller, this is because the safe flight envelope boundary has been exceeded before the GS valid flag was raised, leading to unreliable results since they are not representative.

9.2.3.1 Physical workload

The physical workload quantifies the physical effort a pilot has to exert in order to accomplish the requested mission profile. This workload can be represented in the first place by the aggregate of the applied control force (wheel, column and pedal) or the average value of the absolute forces. Alternatively the root mean square of the pilot control deflections can be used, which is calculated as follows:

$$RMS_{\text{defl}} = \frac{\|\delta_{\text{ctrl}}\|_2}{\sqrt{n}} \tag{9.1}$$

where δ_{ctrl} is the pilot control deflection under consideration and n is the length of the recorded data sample. Note that both measures are set up in such a way that variations in data sample lengths are automatically taken into account, which is important for the total simulation run data. Figures 9.18 and 9.19 illustrate the physical workload analysis results in the presentation as was introduced earlier. Figure 9.18 depicts the average pilot forces, and figure 9.19 portrays the root mean square of the pilot control deflections.

Both figures lead to the same observations regarding the measured physical workload during the experiment. The unfailed conditions confirm that this is a sound comparison basis between classic and FTFC, since both have the same ratings. Significant physical

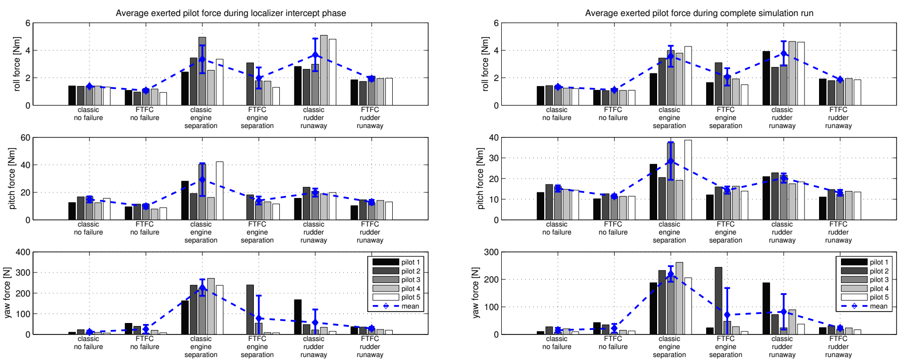

(a) localizer intercept phase (b) complete simulation run

Figure 9.18: Total average pilot force during localizer intercept phase (left) and during complete simulation run (right)

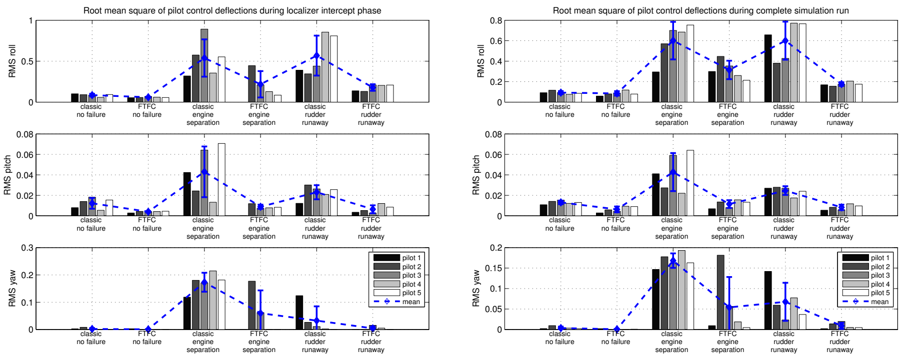

(a) localizer intercept phase (b) complete simulation run

Figure 9.19: Root mean square of pilot control deflections during localizer intercept phase (left) and during complete simulation run (right)

workload can be seen for the different failure scenarios to maintain control of the damaged aircraft. Especially for the Flight 1862 engine separation scenario, the data shows that for the complete duration of the flight and during the individual tasks, compensation of the failure was required in all control axes (roll, pitch and yaw). For the rudder hardover scenario, compensation is especially apparent in the roll channel, while the other channels require less compensation. For the reconfigured aircraft, utilising the ANDI control algorithms, the control forces are reduced significantly indicating that use of the pilot controls was decreased. Additionally, the data shows more consistency amongst the pilots in most cases for the FTFC configuration as represented by the standard deviations in the graphs. Only the applied rudder pedal force for the FTFC engine separation case is an exception to this trend, but it can be seen that this is caused by test pilot 2 who exhibits significantly higher and above-average control behaviour as compared to the other subjects. This was partly based on a misunderstanding of the pilot regarding the implemented control strategy of the controller in which the pedals directly command sideslip angle. For the rudder hardover scenario, the data shows that almost all pilots had a natural tendency to react to the failure by applying rudder pedal despite being briefed that rudder was not available. The minimum overlap of the errorbars of workload, for the limited number of subjects, between the classical and ANDI control system confirms that the observed trends are significant.

Summarizing, it can be stated that average absolute force as well as pilot control deflections RMS confirm that the FTFC reduces the physical workload considerably, compared to classical control.

9.2.3.2 Compensatory workload: RMS of pilot control deflections

The compensatory workload is an indication of the correcting or stabilizing efforts applied by the pilot. The most frequently used variable to quantify this type of workload is the root mean square of the pilot control deflection rates. These are presented in fig. 9.20.

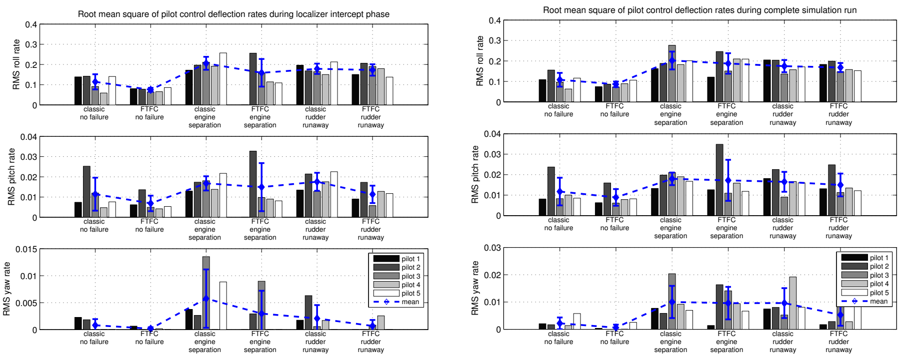

(a) localizer intercept phase (b) complete simulation run

Figure 9.20: Root mean square of pilot control deflection rates during localizer intercept phase (left) and during complete simulation run (right)

These results show no decisive confirmation about any changes in the workload. This can be partly explained by the nature of the experiment. In order to be able to draw the right conclusions about the compensatory workload based upon the RMS of the deflection rates, one needs to make the test pilots feel familiar with the system. Because of a lack of training in these specific experiments and the absence of repetitions, this causes a lot of spread in the data, as can be seen in the relatively large standard deviations in fig. 9.20. Each pilot was still in the process of determining his control strategy, which differs from pilot to pilot. With enough experience, after sufficient repetitions, these control strategies would converge again. However, including more training for the pilots disagrees with the setup of the experiment to confront the pilots with failures they are unfamiliar with.

An alternative method to represent compensatory workload is the power level required by the pilot to control and stabilise the aircraft. The pilot power takes into account both the applied physical control forces and compensating deflection rates. For the total simulation run, the power level is again averaged over the time interval and has been calculated as follows:

$$P = \int_{t=t_0}^{t_{\text{end}}} F(t) \cdot \frac{d\delta_{\text{ctrl}}(t)}{dt} dt \tag{9.2}$$

$$P_{\text{av}} = \frac{1}{T_{\text{tot}}} \int_{t=t_0}^{t_{\text{end}}} F(t) \cdot \frac{d\delta_{\text{ctrl}}(t)}{dt} dt \tag{9.3}$$

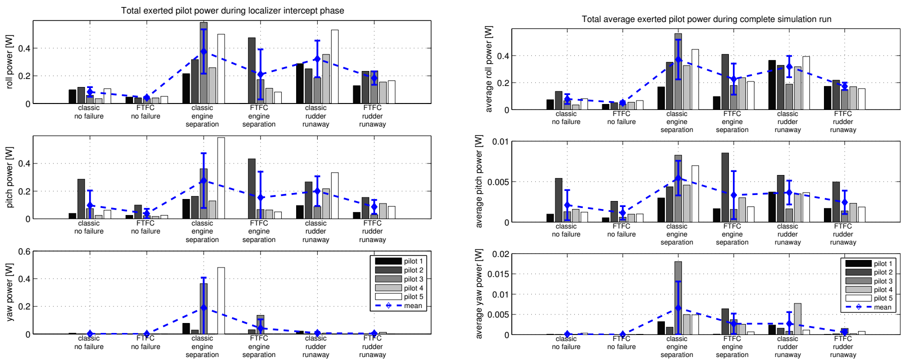

(a) localizer intercept phase

(b) complete simulation run

Figure 9.21: Average pilot power during localizer intercept phase (left) and during complete simulation run (right)

These power values are depicted in fig. 9.21. Although not as decisive as for the physical workload, the trends are still visible. The unfailed conditions confirm that this is a good comparison basis between classic and FTFC, since both have the same ratings. Taking into account the different behaviour of pilot no 2, causing a higher spread in the data, the workload shows more consensus between the subjects. The yaw power values should ideally be zero in the rudder failure case, since the pedals have no effective use. As a matter of fact, the pilots still had the natural intuitive tendency to use the pedals to compensate for the disturbance. Some pilots realized this fact after a while, others were aware of it from the start. As a consequence, some yaw power values are zero where others are nonzero but still relatively small.

In summary, there are indications that the pilot's compensatory workload is also made easier by the fault tolerant control, although these indications may not be as decisive as for his physical workload. It should be noted that this manual FTFC algorithm has not yet been fully optimized for HQ ratings. This is partly the reason for these less clear observations. As a final remark, it can be noted that all workload assessment figures confirm a significant improvement in both types of pilot workload increase for the rudder runaway scenario, although this is not clear from the pilot's appreciation through the Cooper Harper Handling Qualities assessment. Most likely, the reason for the lower rating is caused by the fact that the fault tolerant controller is a rate controller, it minimizes disturbed angular rates, but not the disturbed angle itself. A possible solution for this is the implementation of a rate control attitude hold algorithm, as shown in fig. 9.22. The beneficial effect of this feature can possibly be tested in a new campaign.

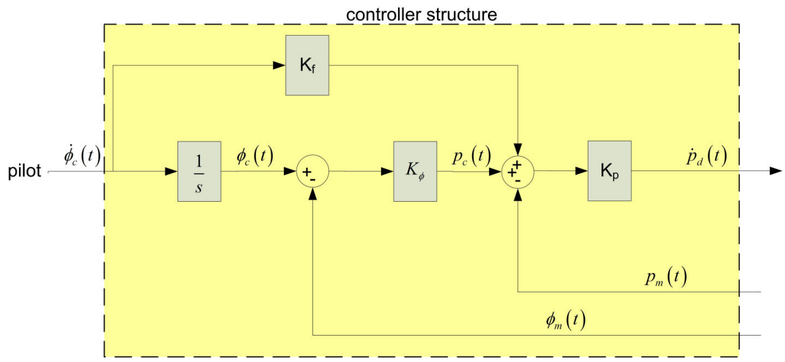

Figure 9.22: Input structure setup for a rate control attitude hold controller

9.3 Concluding remarks

As part of an experimental campaign in the SIMONA Research Simulator, the manually operated Adaptive Nonlinear Dynamic Inversion (ANDI) based controller using Online Physical Model Identification was evaluated for a damaged aircraft during a piloted simulator assessment. The scenarios for the evaluation were selected based on their criticality to the operation of the aircraft and available flight data for the validation of the damaged aircraft dynamics.

The experiment results show that the controller is successful in recovering the ability to control damaged aircraft after incurring a physical loss of two right-wing engines or a sudden hardover of the rudder. Simulation results have shown that the handling qualities of the fault tolerant controller devaluate less for most failures, indicating improved task performance. Moreover, it has been found that the average increase in workload after failure is considerably reduced for the fault tolerant controller, compared to the classical controller. The data shows more consistency amongst the pilots in most cases for the FTFC configuration. These observations apply for physical as well as compensatory (mental) workload.

For the rudder runaway scenario, physical workload was reduced with the ANDI reconfiguration algorithm, but the lack of a rate control/attitude hold control scheme caused a negative effect on aircraft handling. To allow a fully automatic reconfiguration of failure modes that affect the lateral control axes, the fault tolerant flight control laws should include a rate control/attitude hold control scheme.

Analysis of the control surface deflections has shown that their behaviour is similar for both the conventional hydro-mechanical control system and FTFC control laws. The major difference is that in the latter situation these commands do not come from the pilot directly. This is a significant advantage of the physical approach which has been followed in this method. Future research in control allocation schemes for the ANDI control algorithm will optimize the balance between the use of the different control surfaces.

Due to the automatic failure recovery and stabilisation capabilities of reconfigurable control, it is expected that the pilot is able to land the aircraft sooner due to the reduction of the time consuming learning phase for the pilot to understand the new basic principles of the damaged aircraft's flying characteristics. Although control reconfiguration can utilise the control effectors in an optimal manner for stabilisation, the experiment has shown that information regarding the safe flight envelope should be an integral part of a fault tolerant flight control scheme to assist the pilot in controlling the aircraft.

For both the Flight 1862 and rudder hardover case, as part of the scenarios surveyed in this research, the pilots demonstrated the ability to fly the damaged aircraft, following control reconfiguration, back to the airport and conduct a survivable approach and landing.

Chapter 10

Conclusions and recommendations

10.1 Conclusions

10.1.1 Global overview of the modular physical approach

In the research project described in this thesis, a modular physical approach has been used to achieve fault tolerant flight control. The global overview of this modular approach is given in fig. 10.1. Globally, the overall architecture consists of three major assemblies, namely the controlled system, the Fault Detection and Identification (FDI) assembly and the Fault Tolerant Flight Control (FTFC) assembly. Each of them will be discussed in depth.

The controlled system consists of the aircraft model and the actuator hardware. Possible failures in this controlled system are structural failures in the former block and actuator hardware failures in the latter. Sensor failures have not been considered in this research, since it has been assumed that effects of these failures can be minor thanks to sensor redundancy and sensor loss detection. However, the latter component is part of recommended future research.

The Fault Detection and Identification (FDI) architecture consists of several components. The core of this assembly is the two step method (TSM) module. This module consists of a separate aircraft state estimation step followed by an aerodynamic model identification step, where the latter is a joint structure selection and parameter estimation (SSPE) procedure, see also chapter 5. The state estimator is an Iterated Extended Kalman Filter, described in section 4.1.2. The preferred SSPE algorithm is Adaptive Recursive Orthogonal

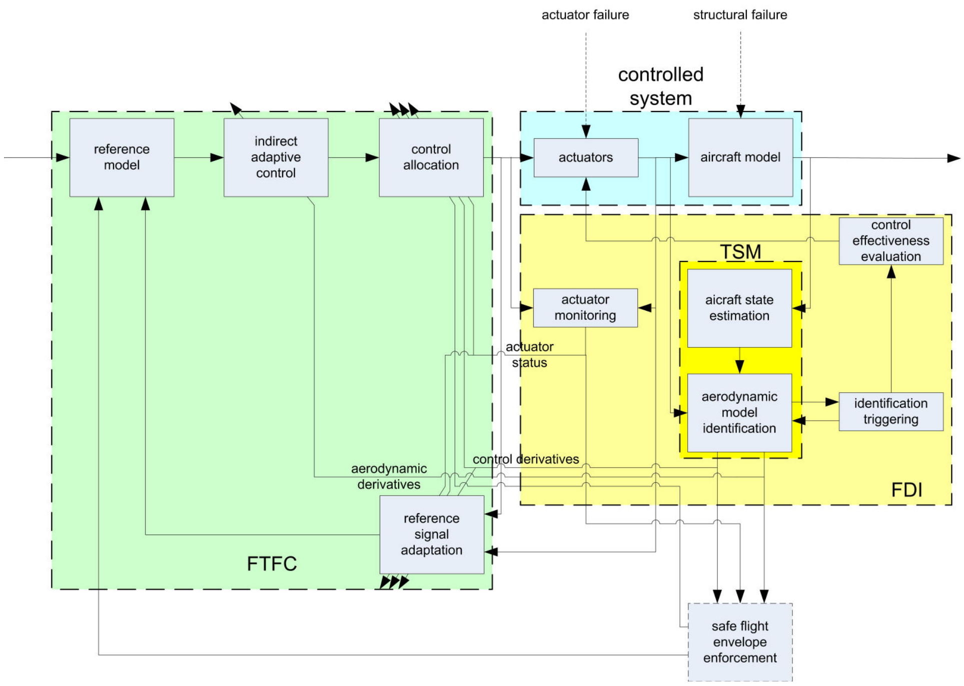

Figure 10.1: Overview of the modular physical approach for fault tolerant flight control

Least Squares and is described in section 5.3. In case a structural failure occurs (in the aircraft structure or in one of the control surfaces), re-identification is triggered when the average square innovation exceeds a predefined threshold, as described in section 4.7. For successful identification of the control derivatives of every individual control surface, control effectiveness evaluation is needed after failure, as described in section 8.4.3. This can be done by inserting multivariate orthogonal input signals in the actuators, described in ref. [208]. Although this must be done carefully such that the damaged aircraft cannot be destabilized, it is necessary in order to obtain sufficient control surface efficiency information for the control allocation module, to be discussed later. A valid approach might be to introduce these evaluation signals only when strictly needed, i.e. when successful reconfiguration is not possible due to a lack of this control efficiency information. The two step method is ideally suited to deal with structural failures, but for the detection of actuator failures a separate actuator monitoring algorithm is needed, such as an Actuator Health Monitoring System (AHMS), discussed in section 8.4.2. There is a remarkable analogy between this FDI group and the general steps in an aircraft system identification procedure as shown in a block diagram in Fig. 3.1. The control effectiveness evaluation block is part of the experiment design block, the TSM core block corresponds to the central block "model structure determination and parameter and state estimation", and the identification triggering serves as a model validation test. Identification triggering as well as actuator monitoring are typical fault detection blocks.

Four other blocks can be grouped to form the Fault Tolerant Flight Control (FTFC) assembly. The core blocks for this group are indirect adaptive control and control allocation. Indirect adaptive control can be achieved by adaptive nonlinear dynamic inversion (ANDI), as described in chapters 7 and 8. The advantage of ANDI is that it removes the need for gain scheduling over different operating conditions and it effectively decouples input-output relationships. Moreover, the NDI control algorithm automatically involves some form of control allocation, due to the structure of the control law. This structuring allows a clear separation how different failure types are dealt with. Structural failures independent of the control surfaces are detected by the TSM and this damage information is supplied to the ANDI algorithm by means of the aerodynamic derivatives. On the other hand control surface related failures, aerodynamics or actuator related, are identified by the TSM or the actuator monitoring algorithm respectively. This information is sent to the adaptive control allocation block. The preferred control allocation approach is found to be the control distributor concept (CDC), combined with the weighted pseudo inverse (WPI), as discussed in section 8.4. This approach fits in the modular setup of the global procedure, where the CDC principle takes into account aerodynamic changes and the WPI provides the adaptivity with reference to actuator failures. Furthermore, a reference model defines the reference signal that the closed loop configuration has to track. However, this reference model needs to be adaptive such that its signals are limited based upon the achievable performance of the damaged closed loop configuration. This reference signal adaptation can be achieved

Table 10.1: Preferred methods for FTFC modules

component	preferred method	section
aircraft state estimation	Iterated Extended Kalman Filter	4.1.2
aerodynamic model identification	Adaptive Recursive Orthogonal Least Squares	5.3
identification triggering	average square innovation & threshold	4.7
control effectiveness evaluation	multivariate orthogonal input functions	8.4.3
control allocation	Control Distributor Concept & Weighted Pseudo Inverse	8.4
indirect adaptive control	triple layer Adaptive Nonlinear Dynamic Inversion	7.2.1,8.1
actuator monitoring	Actuator Health Monitoring System	8.4.2
reference signal adaptation	Pseudo Control Hedging	8.3.1
safe flight envelope enforcement	*recommended future work*	–

by Pseudo Control Hedging, as explained in section 8.3.1. This modulation is based upon the difference between the demanded input signal and the achieved input signal by the actuators. This reference signal adaptation is primarily driven by saturation effects. Besides, this hedging operation takes into account the updated model information via actuator status, aerodynamic derivatives and control derivatives. In this way, one makes sure that no unreachable reference signals are given to the closed loop configuration. This PCH operation can be considered as a first degree of safe flight envelope enforcement, based upon input saturation effects and updated model information.

During this research, it has been found that safe flight envelope enforcement is a crucial aspect in this control setup, and it is part of recommended future research. This protection algorithm, based upon the achievable performance which can be estimated based upon actuator status, aerodynamic derivatives and control derivatives, should contribute on two levels. On one hand, it has to assist the PCH algorithm by limiting the reference model output appropriately. Moreover, the output of the control allocation block, and thus the input to the actuators, should be limited based upon this reachable flight envelope information.

A tabular overview of the preferred method for every component in the global overview of the fault tolerant flight control setup can be found in table 10.1.

10.1.2 Certainty equivalence principle

The main limitation of the indirect adaptive control approach is that it relies on the certainty equivalence principle. This means that the controller parameters are computed from the estimates of the plant parameters as if they were the true ones. However, it has been shown in section 7.1.3 that this assumption is not absolutely necessary when applied to ANDI. More precisely, it has been found that that the combination of ANDI and a linear controller in the outer loop is asymptotically insensitive for misfits in the estimates of the aerodynamic derivatives, especially thanks to the presence of integral action in the linear controller. On the other hand, this robustness does not hold for identification errors in the control derivative values. However, these estimates are well identifiable due to the control surface excitations which are steered directly.

10.1.3 Experiments on the SIMONA Research Simulator

In this research, an automatic as well as a manually operated fault tolerant flight controller have been developed in sections 8.1 and 7.2.1 respectively. The automatic controller satisfied most performance requirements and succeeded to keep the aircraft under control, as shown in sections 7.2.2 and 8.1.3. The manual controller has been evaluated extensively in the SIMONA Research Simulator, as discussed in chapter 9, and it has been found that the fault tolerant controller was successful in recovering the ability to control the damaged aircraft scenarios investigated in this research project. Simulation results have shown that the handling qualities of the fault tolerant controller devaluate less for most failures, indicating improved task performance. Moreover, it has been found that the average increase in workload after failure is considerably reduced for the fault tolerant controller, compared to the classical controller. The data shows more consistency amongst the pilots in most cases for the FTFC configuration. These observations apply for physical as well as compensatory (mental) workload. It has been stated in [105] that these extensive evaluations have led to the technology increasing in its Technology Readiness Level scale (TRL) level from 3/4 to 5/6, see also picture 10.2.

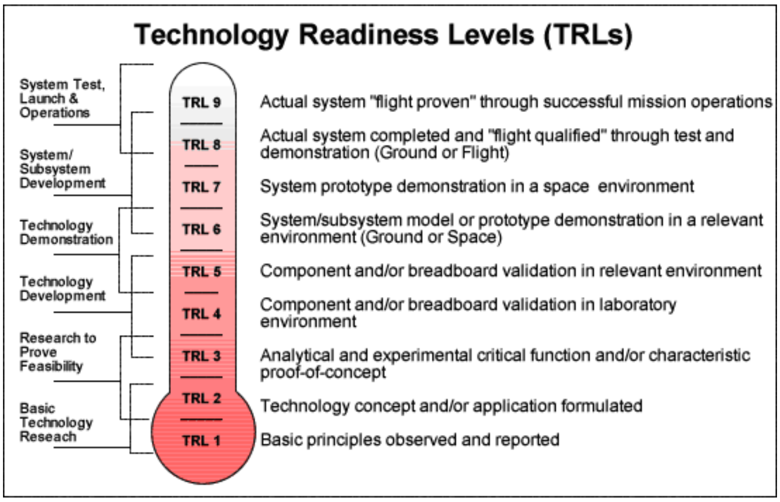

Figure 10.2: Technology Readiness Level scheme, source: NASA

10.1.4 Comparative studies and optimization procedures

During this research project, some comparative studies have been performed for the SSPE algorithm and for the ANDI setup, together with an optimization procedure for the outer loop linear controller gains in the ANDI setup. Some conclusions with respect to these subjects will be presented here.

With respect to the SSPE procedure, two algorithms have been compared in chapter 5, namely Modified Stepwise Regression (MSWR) and Adaptive Recursive Orthogonal Least Squares (AROLS). Comparing both structure selection and parameter estimation procedures gives a clear advantage to the AROLS algorithm. First of all because of its recursive and computationally efficient nature which makes it suitable for real-time on-line applications. Compared with the modified stepwise regression procedure, it only needs a forward sweep, instead of combined addition and elimination criteria which apply for the latter. Moreover, no major modifications are required to AROLS for damaged aircraft applications, as opposed to MSWR which needs priority scheduling among the candidate regressors. Considering all these arguments, adaptive recursive orthogonal least squares are preferable above modified stepwise regression.

In the ANDI setup, a baseline control structure has been defined in chapter 7, consisting of a double NDI loop, and an improved control structure was developed in section 8.1, consisting of a triple NDI loop. Comparing simulation results from both versions in sections 7.2.2 and 8.1.3 shows significant improvements for the latter. The fact that the improved version has an additional inversion loop and relies on less assumptions, makes that it has more control authority and results in a larger flight envelope where it is capable to keep the aircraft under control compared with the baseline controller.

A multi-objective optimization procedure has been used in section 8.2 for parameter synthesis of the linear controller gains. This allowed to improve the controller gains based upon predefined optimization criteria while taking into account inequality constraints. Comparing this optimized result with the initial performance shows subtle improvements, especially in the speed disturbance rejections. Thanks to the good initial choice of control gain values according to the principle of time scale separation, no major improvement can be made in the field of gain tuning. However, Multiobjective Parameter Synthesis is still capable to enforce small improvements in the tuning so that optimal performance can be achieved with respect to the defined criteria.

10.1.5 Contributions

There are five major contributions from this thesis.

- First of all, the fault tolerant control setup described in this thesis is based on a **physical approach**, where focus is placed on the use of mathematical representations based on flight dynamics. All quantities and variables which appear in the model have a physical meaning and thus are interpretable in this approach, and one avoids so-called black and grey box models where the content has no clear physical meaning. Besides the fact that this is a more transparent approach, allowing the designers and engineers to interpret data in each step, it is assumed that these physical models will facilitate certification for eventual future real life applications, since monitoring of data is more meaningful.

- Secondly, an **all-in modular approach** has been developed for fault tolerant flight control. The global overview of this set-up can be found in figure 10.1. This control approach has been **applied successfully on a high fidelity simulation model**, including several failure scenarios. One of the failure scenarios has been validated with real accident data, obtained from a digital flight data recorder. In the beginning of the research project, there was some concern that the adaptation rate of this indirect control approach might not be fast enough to compensate for sudden drastic structural damage, and it was expected that some "composite/combined" control structure would be needed, see ref. [168], where a quicker direct control algorithm would be needed temporarily to bridge the gap until the indirect approach would reach satisfactory performance. However, experiment results shown in section 8.1.3 have shown that the indirect approach is fast enough such that a direct intermediate step is not needed.

- Moreover, an **on-line joint structure selection and parameter estimation algorithm** has been developed for aerodynamic model identification, including adaptivity to take into account structural failures. This developed algorithm is called adaptive recursive orthogonal least squares (AROLS), and has been described in section 5.3.

- In addition, it has been found that **Pseudo Control Hedging**, developed earlier by [136, 137], can serve as a **safe flight envelope enforcement feature** of the first degree, scaling the reference signal down to reachable values based upon input saturation and updated model information, as shown in section 8.3.1.

- Finally, the simulator evaluation campaign presented in chapter 9 has led to the technology **increasing in its Technology Readiness Level** scale (TRL) level from 3/4 to 5/6.

10.2 Recommendations and the road ahead...

Based upon the results which have been obtained during this research project, some recommendations can be given to extend the work reported in this thesis. These recommendations can be divided over short and long term work.

The short term work is described first. The research results presented in this thesis include the topics of control allocation, actuator health monitoring and control effectiveness evaluation. These topics were discussed only briefly, and a more extensive comparative analysis of alternative methods can be an interesting recommendation for future research. As a matter of fact, current research at the author's research organization is exploring alternative ways of control allocation. Conclusions of that research will contribute to this project. However, as has been found in the course of this research project, one of the most important aspects in a fault tolerant flight control setup is the concept of safe flight envelope enforcement. This applies for manual as well as for automatic control. During the automatic control design procedure, described in section 7.2.2, it has been observed that some limitations must be imposed on e.g. roll angle, and that these limitations become significantly more stringent after structural damage, like in the Flight 1862 scenario. This specific scenario has also consequences for the maximum thrust level in engines no. 1 and 2 after failure. Also in the manual control setup, described in section 7.2.1 and evaluated in chapter 9, it has been observed that for a successful landing, the pilot requires knowledge concerning the aircrafts minimum control speed under the prevailing conditions in order to remain within the degraded safe flight envelope boundaries. Although control reconfiguration can utilise the control effectors in an optimal manner for stabilisation, the experiment has shown that information regarding the safe flight envelope should be an integral part of a fault tolerant flight control scheme to assist the pilot in controlling the aircraft. Reason for this is the fact that control reconfiguration, next to its advantages, reduces partly the situational awareness of the pilot, since he does not feel the gradual reduction in control authority of the pilot controls, which would be felt in a classical mechanical control setup. This all motivates the need to present information regarding the safe flight envelope to the pilot. An important part of the safe flight envelope is determined by the saturation limits of the control inputs. The dynamic inversion process is only successful without control input saturation. Therefore, pseudo control hedging has been applied, as discussed in section 8.3.1, in order to scale back reference signals such that control input saturation is prevented. In this context, this signal hedging can be considered as safe flight envelope enforcement of the first degree. However, a more elaborate investigation of on-line safe flight envelope enforcement is an important point for future research.

Longer term research work involves two major aspects, namely the consideration of sensor failures in the modular setup, and validation and verification of the newly developed technologies on relevant flight platforms. One important category of failures has not been considered in this research project, namely sensor failures. In this project, sensor failure effects are considered minor in the presence of sensor redundancy and sensor loss detection, which is usually the case. As an example, in each aircraft at least three inertial reference units are installed, and the same applies for air data sensors etc. With three operational units, the median of the measurements is calculated. If one unit fails and is isolated, only two operational units remain, which is the minimum amount according to the MMEL (Master Minimum Equipment List). Of these two remaining measurements, the average is then calculated. Both set-ups have different results in the case of a non-isolated misreading in

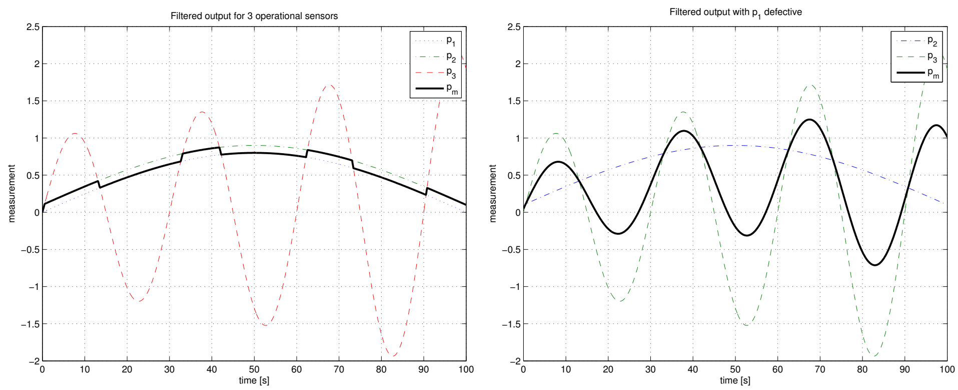

(a) Normal filtered sensor output in normal conditions (b) Filtered sensor output with one failed sensor

Figure 10.3: Filtered sensor output in normal conditions and with sensor failure

one sensor. The two scenarios are illustrated in fig. 10.3. The normal operation is shown in fig. 10.3(a). In this setup, a non-isolated misreading is successfully compensated. In case of an isolated sensor, an additional non-isolated misreading cannot be compensated for successfully as shown in fig. 10.3(b).

Despite this redundant sensor setup, recent airliner accidents have indicated that sensor malfunctions can be critical failures. Four recent accidents underpin this statement, namely a catastrophic takeoff of a Northrop Grumman B-2 stealth bomber of the US Air Force, the in-flight upset of a Qantas Airbus A330, the crash of a Turkish Airlines New Generation Boeing 737 during final approach and the in-flight loss of an Air France Airbus A330.

Figure 10.4: US Air Force B-2 Spirit

Northrop Grumman B-2 [61]: On 23 February 2008, a Northrop Grumman B-2A, tailnumber 89-0127 nicknamed ”Spirit of Kansas”, assigned to the 509th Bomb Wing at Whiteman Air Force Base (AFB), Missouri, crashed during initial takeoff from Andersen AFB, Guam. This was a scheduled return from Andersen AFB to Whiteman AFB concluding a 4-month continuous bomber presence deployment. The two-person crew successfully ejected from the aircraft during the mishap.

It was found, through clear and convincing evidence, that distorted data introduced into the flight control computers caused an uncommanded 30 degrees nose-high pitch-up on takeoff resulting in a stall and subsequent crash. Moisture in the port transducer units (PTUs) of the aircraft during an air data calibration caused an unnecessarily large correction bias to the air data system. Using this ’moisture distorted data’, the flight computers calculated inaccurate airspeed and a negative angle of attack which contributed to an early rotation and uncommanded pitch-up during takeoff. Loss of all air data resulted in degraded flight controls response and degraded stability of the aircraft involved. The nose-high attitude and heavy gross weight of the aircraft resulted in deterioration of airspeed. The end result was a low-altitude stall, culminating in a roll and yaw to the left. The lack of airspeed and altitude denied the pilot the ability to recover the aircraft. As the left wing made contact with the ground, the crew succesfully ejected. The aircraft impacted the ground and was destroyed by fire.

Qantas Airbus A330 [9]: On 7 October 2008, a Qantas Airbus A330-303 aircraft, registered VH-QPA, departed Singapore on a scheduled passenger transport service to Perth, Australia. On board the aircraft, operating as flight number QF72, were 303 passengers, nine cabin crew and three flight crew. While the aircraft was cruising at 37,000 ft, the autopilot disconnected, simultaneously there were various aircraft system failure indications. While the crew was evaluating the situation, the aircraft abruptly pitched nose-down. The aircraft reached a maximum pitch angle of about 8.4 degrees nose-down and descended 650 ft during the event. As a consequence of the flight upset, there were 11 occupants seriously injured and many others experienced less serious injuries. After returning the aircraft to 37,000 ft, the crew commenced actions to deal with multiple failure messages. A few moments later, the aircraft commenced a second uncommanded pitch-down event. The aircraft reached a maximum pitch angle of about 3.5 degrees nose-down, and descended about 400 ft during this second event. The aircraft subsequently landed at Learmonth, after declaring an emergency.

Figure 10.5: Qantas Airbus A330-303, VH-QPA, ©Andrew Hunt - Airteamimages, via airlines.net

The investigation to date has identified two significant safety factors related to the pitch-down movements. Firstly, immediately prior to the autopilot disconnect, one of the air data inertial reference units (ADIRUs) started providing erroneous data (spikes) on many parameters to other aircraft systems. The other two ADIRUs continued to function correctly. Secondly, some of the spikes in angle of attack data were not filtered by the flight control computers, and the computers subsequently commanded the pitch-down movements. Two other occurrences have been identified involving similar anomalous ADIRU behaviour, but in neither case was there an in-flight upset. The investigation is continuing at the time of writing. So far, no clear cause has been found for the anomalous ADIRU behaviour. Given the lack of evidence of a problem with the system, the ATSB (Australian Transport Safety Bureau) is considering - among other avenues of inquiry - the possibility of a 'single event effect', generated by particle impact from cosmic radiation.

Figure 10.6: Turkish Airlines 737-800 TC-JGE, ©Peter de Jong, via airliners.net

Turkish Airlines Boeing B737 [12]: On February 25th 2009, the Boeing 737-800 of Turkish Airlines, registered TC-JGE, departed Istanbul International Ataturk Airport, Turkey for a flight to Amsterdam Airport Schiphol, the Netherlands. The flight crew consisted of three pilots, involving a first officer carrying out a line flight under supervision (LFUS). The aircraft was directed by Air Traffic Control towards runway 18R for an instrument landing system (ILS) approach and landing. The crew performed the approach with one of the two autopilots (autopilot B) and autothrottle engaged. The aircraft descended to 2000 feet above mean sea level (amsl) and was vectored towards the localiser. The autothrottle system receives information about the altitude from the left radio altimeter during approach and landing. The recorded value on the digital flight data recorder was 8191 feet (this is the maximal value the digital flight data recorder has registered) during the most part of the flight. When the aircraft during approach descended below 8191 feet, the recorded value remained fixed at 8191 feet. At approximately 1950 feet the recorded value suddenly changed to -8 feet and remained at that value up until shortly before impact. According to the data recorded by the cockpit voice recorder several aural landing configuration warnings sounded earlier during the flight. The warnings sounded because the computer systems receive their data from the left radio altimeter, amongst others, which erroneously transmitted that the aircraft was near the ground. The values of the right radio altimeter and pressure altimeter were correct during approach. Preliminary investigation results have shown that erroneous autopilot and autothrottle commands were given, due to the faulty altimeter information supplied, resulting in a too low airspeed. The crew seemed to detect this failure only in an advanced stage and was unsuccessful to intervene in time and to prevent an imminent stall and early contact with the terrain 1.5 km before the runway threshold.

Air France Airbus A330 [11]: On 31 May 2009, Air France flight AF447 took off from Rio de Janeiro Galeao airport bound for Paris Charles de Gaulle, with 12 crew members and 216 passengers on board. The airplane, an Airbus A330-203 registered F-GZCP, was in contact with the Brazilian ATLANTICO ATC centre on the INTOL SALPU ORARO route at FL350. There were no further communications with the crew after passing the INTOL point.

At 2 h 10, a position message and some maintenance messages were transmitted by the ACARS automatic system, after which any further ground station attempts to contact the aircraft proved unsuccessful. Bodies and airplane parts were found from 6 June 2009 onwards by the French and Brazilian navies during a large scale sea search operation in the South Atlantic. At the time of writing, underwater sea search operations were still under way to try to locate and recover the Flight Data Recorder and Cockpit Voice Recorder.

Figure 10.7: Air France Airbus A330-203 F-GZCP, ©Gabriel Widyna, via airliners.net

At the moment of writing, the following facts have been established during the investigation:

- no distress messages were received by the control centres or by other airplanes,
- there were no satellite telephone communications between the airplane and the ground,
- the last radio exchange between the crew and Brazilian ATC occurred at 1 h 35 min 15 s. The airplane arrived at the edge of radar range of the Brazilian control centres,
- at 2 h 01, the crew tried, without success for the third time, to connect to the Dakar ATC ADS-C system,
- up to the last automatic position point, received at 2 h 10 min 35 s, the flight had followed the route indicated in the flight plan,
- the meteorological situation was typical of that encountered in the month of June in the inter-tropical convergence zone, there were powerful cumulonimbus clusters on the route. Some of them could have been the centre of some notable turbulence,
- several airplanes that were flying before and after AF 447, at about the same altitude, altered their routes in order to avoid cloud masses,
- twenty-four automatic maintenance messages were received between 2 h 10 and 2 h 15 via the ACARS system. These messages show inconsistency between the measured speeds as well as the associated consequences,
- before 2 h 10, no flight performance related maintenance messages had been received.
- the operators and the manufacturers procedures mention actions to be undertaken by the crew when they have doubts as to the speed indications,

– the last ACARS message was received towards 2 h 14 min 28 s,

– visual examination showed that the airplane was not destroyed in flight ; it appears to have struck the surface of the sea in a straight line with high vertical acceleration.

With the limited information available at the time of writing, it has been observed that erroneous airspeed measurements from the pitot probes were a contributing factor in the accident. However, this information is far from complete and these measurement errors cannot be considered as the single cause that resulted in the accident. More information will follow pending further technical investigations.

Motivated by the sensor output averaging principle and the recent airliner accidents discussed above, it can be stated that sensor malfunctions are worthwhile to be considered in a fault tolerant flight control setup. This aspect is part of a European FP7 funded research project, called ADDSAFE (Advanced Fault Diagnosis for Safer Flight Guidance and Control), in which many of the Garteur FM-AG(16) partners are involved, including the faculty of Aerospace Engineering from Delft University.

In the longer term, further developments should also be aimed at increasing the current TRL stage of the fault tolerant control technology. This includes validation and verification of the newly developed technologies on relevant flight platforms. Current state of the art experimental research aircraft can serve as test platforms for this. In the USA as well as in Europe, several test vehicles exist with the necessary on-board equipment for this purpose.

In the USA, several research aircraft suitable for the in flight validation of fault tolerant flight control can be found at NASA. The ones known by the author are enumerated here:

Dynamically scaled Generic Transport Model (GTM),[144]: This is an extremely sophisticated and complex airframe and is a 5.5% dynamically scaled generic transport model (identical to the Boeing 757), [145]. This airframe has a takeoff weight of approximately 25 kg, a wingspan of 2 m and is powered by two small turbine engines. This specialized airframe was designed and built at Langley Research Center. By adhering to the properties of similitude, the properties of an object of one size (a subscale airplane) can be mathematically related to the properties of an object of another size (a full airplane), [95, 290]. For a scale factor of K equal to 0.055, the subscale response is related to the full scale response by a factor of $\sqrt{K}$, or approximately 4.26. That is, the subscale model will respond 4.26 times faster than the full scale airframe. The 5.5% scale factor was chosen based on a number of factors including the existence of a large database of wind tunnel data for this scale airframe and a feasibility study which was conducted that determined the

Figure 10.8: NASA Generic Transport Model in flight, source: [144]

structural and payload requirements for a research vehicle could be met at that scale. For the experiments that the AirSTAR testbed can be used for, such as loss-of-control flight due to high angles-of-attack and sideslip, the flow around the aircraft becomes separated and fluid effects associated with Reynolds number scaling may be minimized, [93]. For more benign flight conditions, Reynolds number effects can be significant and the aerodynamics of the model would not be representative of the full scale aircraft for certain manoeuvres.

AirSTAR S2,[144]: This is a commercial-off-the-shelf (COTS) transport model (inspired by the Lockheed Tristar), powered by a single turbine engine integrated in the vertical tail. It weighs approximately 22 kg and has a wingspan of 2.2 m. While this model is not dynamically scaled, it was designed to have favourable flying qualities at this size and weight. Because this is a commercially available airframe kit, it has significantly reduced costs and maintenance, compared to the GTM, and thus is an ideal test platform for the validation of new hardware and software, before installing these in the GTM. Recently, the airframe has been used for real-time parameter identification, modeling, and fault detection research experiments.

Figure 10.9: NASA AirSTAR S2 research aircraft during flight testing, source: [144]

McDonnell Douglas F-15: NASA's Dryden Flight Research Center, Edwards, Calif., used a modified F-15B aircraft as a testbed for a variety of flight research experiments. Dryden's F-15B is a two-seat version of the F-15 tactical fighter aircraft built by the McDonnell Aircraft and Missile Systems division of the Boeing Company. The aircraft was obtained in 1993 from the Hawaii Air National Guard. Bearing NASA tail number 836, the F-15B is about 20 m long and has a wingspan of just under 13 m. It is powered by two Pratt and Whitney F100-PW-100 turbofan engines which can produce almost 11,000 kg of thrust each in full afterburner. It is capable of dash speeds of Mach 2.3, at altitudes of 12,000 to 18,000 m. In 1997, installation of a new data acquisition system in the aircraft added an additional research capability. An on-board video system monitored from the rear seat of the cockpit provides a high-speed airborne video and photo capability that can be downlinked to researchers on the ground. The data system includes a research air data system for the aircraft itself, as well as a GPS navigation package, a radome with a nose boom which contains an air data probe, a dig-

Figure 10.10: NASA Dryden F-15B tail number 836, source: NASA Multimedia libary, Photo by: J. Ross

ital data recorder, and telemetry antennas. This aircraft has been used extensively in the intelligent flight control system (IFCS) project, as described in sections 1.3.5 and 2.9.2.

McDonnell Douglas F/A-18: NASA's F-18 #853 is a former Navy F/A-18A fighter plane modified by Dryden technicians that now performs research duties. This versatile research aircraft serves in many capacities, one of them being adaptive flight controls. The advantage of this research aircraft is that it is extensively instrumented, it contains a comprehensive sensor suit and a quadruplex research flight control system (RFCS), including an on-board excitation system and the capability to simulate failures, such as Single Surface Lock, Multi-Surface Lock, Throttle-Steering-Only, so-called Damaged Wing and other user-specified failures. This capability will be used extensively in NASA's IRAC project (Integrated Resilient Aircraft Control), as part of the NASA aviation safety program, involving several US partners from industry and academia.

Figure 10.11: NASA Dryden's highly-modified Active Aeroelastic Wing F/A-18A ; source: NASA Dryden Flight Research Center Photo Collection, Photo by: J. Ross

McDonnell Douglas C-17: Besides the UAV's and the fighter-based research aircraft, also larger aircraft are used as test vehicles. A U.S. Air Force C-17 transport aircraft, tail number 0025, is being used by NASA Dryden and other NASA centers, the U.S. Air Force, Boeing, and Pratt & Whitney in the Propulsion Health Management (PHM) portion of the Integrated Vehicle Health Management (IVHM) program. The program is using a USAF C-17 transport in an effort to enhance aircraft safety by enabling early electronic detection of potential problems with aircraft engines and associated systems. The McDonnell Douglas C-17 Globemaster III is a strategic/tactical airlifter for the USAF, which is also used by a number of military export customers. Besides tactical airlift, the aircraft can perform medical evacuations (MEDEVAC) and airdrop missions. In the NASA research, the aforementioned C-17 serves as a test vehicle for various research programs just like one of the MD-11 prototypes was used in the PCA project.

Figure 10.12: C-17 in flight over the California desert; source: NASA Dryden Flight Research Center Photo Collection, Photo by: J. Ross

In Europe, on the other hand, another collection of several research aircraft can be found. However, these are not all affiliated to one research organization, but to many national organizations.

UAV testbed "Barracuda": The Barracuda is a single-engine UAV developed by EADS-Germany of 8.25 m length, 7.2 m wing span and a take-off weight of 3250 kg. It has been designed to fly up to M 0.85 and it representative for high-performance UAV's. In terms of control surfaces there are ailerons, elevators and a double v-shaped rudder. All surfaces themselves are coupled, i.e. they are not split into 2 independently driven surfaces. The actuators have some BIT (built in test) capability. The flight sensors supply angle of attack α, sideslip angle β, and the load factors in three axes n_x, n_y, n_z. Due to the coupled surfaces, surface lock failure scenarios are more difficult to investigate, but a possible alternative is looking to the reconfiguration of high level mission automation functions (Autopilot, FMS, Flight Planning) following to a wider failure scenario set involving other main aircraft subsystems. This will possibly be the subject for a follow-on research project in the GARTEUR framework under the title "Fault Tolerant Integrated Aircraft Management System".

Figure 10.13: EADS Barracude in flight; source: EADS Multimedia library

VFW-614 ATTAS (Advanced Technologies Testing Aircraft System)[194]: The German Aerospace Center (DLR) operates the flying test-bed ATTAS (Advanced Technologies Testing Aircraft System). ATTAS is based on a VFW 614, a 44-passenger civil transport aircraft with two Rolls-Royce turbofan engines, a wing span of 21.5 m and a length of 25 m. The original conventional mechanical control system of the basic aircraft was supplemented by the German aerospace industry (MBB) and the DLR with an electrical flight control system (Fly-By-Wire). If the ATTAS electronic flight control system is used, the safety pilot can go back to the mechanical control system at any time. Thus, the safety pilot is the central instance of the ATTAS safety concept. The mechanical control system of the basic aircraft is the backup system of the electric flight control system. Due to its size, its relatively spacious cabin, its additional load capacity and its flight characteristics the VFW 614 is an ideal flying test-bed for various applications. The full fueled aircraft can load 3.5 tons of test equipment. Additional to the standard control surfaces ATTAS

Figure 10.14: DLR VFW-614 ATTAS in flight; source: DLR

has six direct lift control (DLC) flaps at the trailing edge of the landing flaps. These flaps permit a very fast influence on the lift. ATTAS has a maximum cruising altitude amounts to 25000 feet (7620 m) and its maximum cruising speed is 288 knots (148.2 m/s, CAS). Furthermore, ATTAS has a very low landing speed of about 100 knots (51.4 m/s). Active flight control is one of the most sophisticated fields of research of ATTAS, research results have been presented in ref. [32, 180]. Recently, Flight Test Results on ATTAS of Fault-Tolerant Model Predictive Control have been presented in [19]. However, this research aircraft is gradually approaching the end of its service life and will be replaced in the near future by the following research aircraft.

Airbus A320-232 (Advanced Technology Research Aircraft) "D-ATRA": The Airbus A320-232 "D-ATRA", the latest and largest addition to the research fleet, will be deployed by the German Aerospace Center (Deutsches Zentrum fr Luft- und Raumfahrt; DLR) in the near future. ATRA (Advanced Technology Research Aircraft) is a flexible flight test platform for European aerospace research. ATRA is the successor to DLR's VFW 614 ATTAS (Advanced Technologies Testing Aircraft System) research aircraft. The Airbus has considerably better flight performance than the veteran VFW 614. ATRA will be deployed for an extensive range of research fields, one of them being research into flight control commands a.o. in the field of autonomous flight, and many more disciplines. Initial planned research with the aircraft focuses on the implementation of a fuel cell system for auxiliary power supply, wake vortex research, and high-lift research for efficient take-off and landing phases.

Figure 10.15: DLR A320 ATRA on the ground; source: DLR

Delft University of Technology/NLR Cessna Citation II CE-550 PH-LAB [295]: The Faculty of Aerospace Engineering of the Delft University of Technology co-operates a Cessna Citation II laboratory aircraft, in cooperation with the NLR. The aircraft is equipped with an in-house developed advanced flight test instrumentation system (FTIS), including an air sensor equipped nose boom and is used for research and student educational flights. The aircraft has a conventional reversible control system, combined with an analog electric automatic control system. To accommodate new research projects a novel fly-by-wire control system has been

Figure 10.16: DUT/NLR Cessna Citation II CE-550 PH-LAB; photo P. Zaal

developed for this airframe. The fly-by-wire system is based on the original automatic control system of the aircraft, reducing the impact on the original flight controls, minimizing aircraft modifications, and inheriting the safety features of the original control system. As a result, the complexity of the certification process and costs could be significantly reduced. The new system will be used for research into novel flight control algorithms, optimal input signals for aircraft model identification, the identification of multimodal pilot control behaviour, and novel human-machine interfaces.

Royal Netherlands Air Force F-16 research aircraft "Orange Jumper" [258]: This test aircraft is a dedicated F-16 airframe. The RNLAF developed the requirements and specification, but the NLR, the national aerospace laboratory in the Netherlands, developed the modifications. The aircraft is commonly called "Orange Jumper", referring to the orange test wiring installed in the aircraft. It was modified at Woensdrecht Air Base when it went through the mid-life update (MLU) program. A key RNLAF requirement was that the modifications should not affect the aircrafts operational capabilities. (Modifications to the previous F-16 test aircraft made it unsuitable for operational use.) To meet that requirement, the aircrafts dedicated instrumentation system is compact in size with some detachable systems. As a result, only a few external features on the F-16 test jet distinguish it as a test aircraft, the most catching feature on the aircraft is an extended pitot tube with sideslip vanes. The backseat cockpit serves as the flight test office. A separate computer has been installed in the rear cockpit to control the instrumentation. The computers display above the front panel can be copied on the right multifunction display in the front cockpit. The aircraft features an onboard telemetry system that allows the flight test engineer to monitor test results in-flight and in real-time, increasing test flight efficiency. All flight data can be stored on a test data recorder located in the left side panel. The front cockpit features a few minor modifications as well. Repetition of the real-time data in the front cockpit, such as angle of attack and sideslip, assists the pilot in applying control inputs during certain test profiles. The aircraft can also be fitted with cameras in the chaff/flare launchers, on the wingtip stations, and in a small blister just aft of the cockpit, to record wing flutter and separation tests. This aircraft is used frequently for certifying new weapons systems and sensors on the F-16 and evaluating new hard- and software, also for foreign aeronautics companies.

Figure 10.17: Royal Netherlands Air Force F-16 research aircraft "Orange Jumper"; source: DACO

As can be seen in the above lists, there are several research aircraft worldwide which can serve as test platforms for the validation and verification of fault tolerant control techniques. This is a crucial next step in the development of these new technologies in order to enhance safety in aviation. Over the recent years, a wealth of different control approaches have been developed, see a.o. [87] and chapter 2, with varying complexity and capabilities. However, at the current stage, demonstrating these approaches practically in a realistic environment is the next logical step in the development process.

The interest of society in this scientific discipline is illustrated by another development contract which has been awarded recently. Air Transport Intelligence news (24/12/2009, by John Croft) reported recently that ”NASA has awarded Boeing a contract worth up to $2.1 million to design, implement and demonstrate an aircraft health evaluation system that will monitor in real-time propulsion, flight control, airframe and software systems to identify an ’adverse event’. Once detected, the vehicle level reasoning system (VLRS) will then diagnose the cause, predict the effect on the remaining useful life of the vehicle and take appropriate steps to mitigate the event. Included in the adverse effects the system is meant to identify and correct are ”system, subsystem or component faults or failures due to damage, degradation or environmental hazards. Under the contract, deliverables must be adaptable to legacy and next generation civil and military aircraft.”

All these developments will bring the current status at a higher technology readiness level (TRL) on the scale as presented in fig. 10.2 and will contribute in the development process such that this technology will be part of the standard equipment for all aircraft in the future.

A few final notes of the author

Although the presented adaptive control techniques have demonstrated to be very promising for application in future aircraft, there is an important technical factor in this perspective, namely the available processor capacity on-board. For the simulation results shown in this thesis, specific processors have been used. Desktop simulations in chapters 7 and 8 have been peformed using an Intel Pentium 4 processor with a computational capacity of 3.2 GHz. The Simona evaluations in chapter 9 were based on an Athlon 64 processor of 2.2 GHz. However, state of the art processor technology in recent aircraft designs has a considerable lower computational capacity. The reason for this is the fact that processors can only be used in aerospace applications if they have statistically proven low failure rates. As an illustration, the Airbus A340, which flew first in 1991, relies on AMD486-processors of 32 MHz. The Boeing 777 design, with first flight in 1994, uses HI-29KII-processors having a computational capacity of 50 MHz. Finally 66 MHz PowerPC's have been built in the A380, the most recent civil airliner design with the widely advertised initial flight of the first prototype in 2005. These trends show that it will take some time before computationally more expensive adaptive control techniques can be built in serial production aircraft, because of the conservatism with respect to new computer hardware driven by safety considerations. As a matter of fact, simplified Kalman Filters can be applied in current flight control computers, but the structure selection and parameter estimation algorithms are more time consuming for the current generation of processor hardware in the aerospace industry.

As a last remark, it is crucial to understand that fault tolerant flight control is intended as an additional safety feature on-board of aircraft. If some part of the plane fails, fault tolerant control has a more extended authority to keep the vehicle under control and to allow a safe emergency landing. However, it is *not* intended as an instrument which allows to shorten the master minimum equipment list (MMEL). This list states the minimum amount of equipment which needs to be functioning properly and flawless. In some cases, it is possible to defer maintenance for non-essential aircraft components, possibly due to redundancy. These components are no part of the MMEL. Economic arguments can motivate reducing the MMEL in the presence of a FTFC, because more failures or more serious damage can be compensated for by this control system without the need for e.g. hardware redundancy. However, this does not correspond with the original purpose the control system is intended for, since reducing the MMEL leads also to a decrease in adaptive control authority of the control system in case a failure occurs.

Appendix A

RECOVER simulation model

A simulation benchmark has been developed specifically for the assessment of new fault tolerant flight control techniques. The benchmark was developed initially based on the reconstructed aircraft model representing the validated Flight 1862 accident scenario, as described in section 1.2.4. This benchmark has been developed by the Dutch Aerospace Laboratory NLR in the GARTEUR (Group for Aeronautical Research and Technology in Europe) framework, as part of the fault tolerant flight control research activities in action group FM-AG(16). The basic architecture of the GARTEUR REconfigurable COntrol for Vehicle Emergency Return (RECOVER) simulation benchmark is based on the Delft University Aircraft Simulation and Analysis Tool (DASMAT). The DASMAT package was developed by Delft University of Technology in order to meet the requirements for computer assisted design (CAD) using Matlab/Simulink and the evaluation of flight control systems, [267]. The DASMAT tool was further enhanced with a full nonlinear simulation of the Boeing 747-100/200 aircraft (Flightlab747/FTLAB747), including hydromechanical flight control system architecture, for the Flight 1862 accident study as conducted by Delft University of Technology, see ref. [247, 248]. This simulation environment was subsequently enhanced to the 2003 FTLAB747 version 6.5. This version was developed at the University of Minnesota within the context of the NASA Aviation Safety Project (AvSP), [190]. The FTLAB747v6.5 has been used in the US during the last 7 years to assess model and data based aircraft FDI and FTC approaches under the auspices of NASA by many research groups from industry and universities. Previous research that used this version of the simulation model can be found in [96, 117, 186, 191, 193, 192, 300]. Finally, it has evolved in Europe under GARTEUR's impulse to become a significant and realistic FDI/FTC aircraft benchmark, [249, 245]. The simulation benchmark is now freely available for research use and can be found in ref. [87]. The majority of the information presented in this appendix comes from [246].

A.1 RECOVER benchmark model description

The GARTEUR RECOVER software package is equipped with several simulation and analysis tools, all centered around a generic nonlinear aircraft model for six-degree-of-freedom nonlinear aircraft simulations. This package has been integrated as a toolbox in the computing environment Matlab/Simulink. The tools of the RECOVER benchmark include trimming and linearization for linear (adaptive) flight control design, nonlinear off-line (interactive) simulations, simulation data analysis and 3D aircraft and pilot interface visualization. In conjunction with the Matlab/Simulink Real-Time Workshop, the model is suitable for integration on simulation platforms for piloted hardware in the loop testing. The software architecture of the RECOVER simulation benchmark comprises a generic model of the aircraft (DASMAT architecture) with aircraft specific modules including aerodynamics, flight control system and engines. The specific aerodynamic coefficients are taken from [116], which have been obtained from extensive wind tunnel experiments, simulations and test flights. The technical data have been obtained from NASA [115, 116]. The baseline flight control system model reflects the hydro-mechanical system architecture of the Boeing 747-100/200 aircraft. All modeled control surfaces are subjected to aerodynamic effects (aerodynamic blowdown) and mechanical limitations (position/rate limits) throughout the flight envelope to account for actuator force limitations and control surface floating in the case of (multiple) hydraulic system failures. From the previous information, it is clear that much effort has been paid in order to make the RECOVER simulation model as realistic and truthful as possible. However, an important extension has been made to the flight controls as inputs. Two versions of input controls have been developed. One one hand, the original model of the RECOVER benchmark was based on the classical hydro-mechanical flight control system of the Boeing 747-100/200 aircraft, with the pilot cockpit controls as inputs, see fig. A.1(a). This situations has been retained in order to provide a reference basis to compare the fault tolerant control simulation results with. On the other hand, a fly-by-wire version of the Boeing 747-100/200 aircraft was created where all 25 aerodynamic control surfaces and the four engines can be controlled individually, see fig. A.1(b). This was needed because the classical control capabilities would be too limiting for the purpose of FTC research. This fly-by-wire version allows modern fault tolerant controllers to have the capability to completely reconfigure the available flight controls individually.

A.1.1 Implementation

Figure A.2 provides a schematic overview of the GARTEUR RECOVER benchmark including relationships between the different model components of the benchmark. The basic

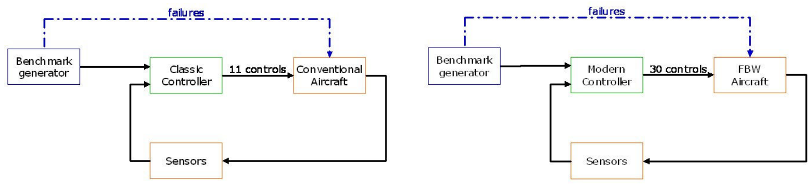

(a) Original benchmark model with classic controller and pilot controls

(b) RECOVER benchmark model including modern controller and separate control surfaces

Figure A.1: Adaptation of original benchmark model for simulation of fly-by-wire aircraft

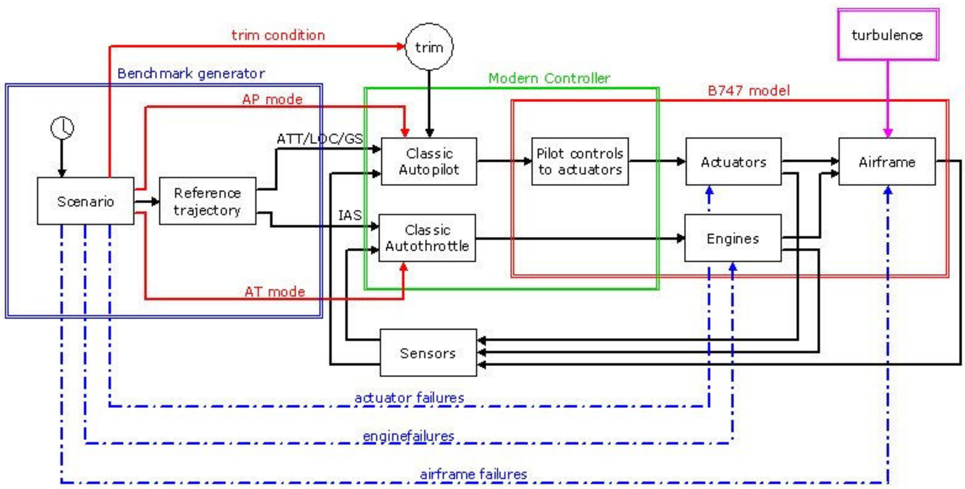

Figure A.2: Detailed schematic of the GARTEUR RECOVER benchmark showing model component relationships including test manoeuvre and failure scenario generation and fault injection, source: [246]

aircraft model contains the airframe, actuator, engine and turbulence models as grouped in the right part of the diagram under the label *B747 model*. As described earlier, the inputs to this model are the pilot's control inputs (steering wheel, control column, pedals,...) in the classical control configuration, which have a fixed linkage to the separate control surfaces like elevators, ailerons, rudders, spoilers, etc. The reconfigurable control algorithms require to control the surfaces separately, and therefore this fixed linkage has been grouped in the pilot controls to actuators block, which can be separated from the baseline aircraft model for the fault tolerant control case. Mind that all inherent hardware limitations of the control surfaces (a.o. position and rate limits) have been retained in the actuators block, but the fixed control distribution scheme from pilot demands to the different aerodynamic control surfaces, which is scheduled by means of a.o. dynamic pressure and Mach number, does not apply in the FTC setting. Mind that this implies that features like wing load relief and minimization of drag due to control surface deflections are not implemented in the fault tolerant control setup unless explicitly taken into account in the fault tolerant controller itself. In the control approach elaborated in this thesis, these features are not considered. There is a good reason for this, namely, the major concern after critical damage has occurred is to bring the aircraft back to the ground quickly and safely. Wing load relief or drag minimization is of secondary importance in these situations. These features can be included in the control allocation component of the fault tolerant control setup as discussed in this thesis. However, since these features are only relevant from an operational and practical point of view, and since this research serves mainly to provide a proof of concept, they have not been considered as essential in the focus of this research. It is also desired to have a basic classical controller available in the benchmark, based on the Boeing 747 classical Sperry autopilot, including autothrottle, to serve as a reference standard for the new adaptive control algorithm developments. A new FTFC controller design, to be evaluated with the benchmark model, replaces the classic autopilot and autothrottle and drives the separate control surface deflections and engines directly. This is indicated in the diagram by the group block *Modern Controller*. In order to operate the benchmark, a scenario and failure mode generator have been added. The scenario consists of commands fed into the autopilot and autothrottle, while the failures are directly introduced into the airframe, flight control system and propulsion models as indicated by the broken lines in fig. A.2.

A.1.2 Aircraft characteristics

The Boeing 747 aircraft (Figure A.3) is a wide-body commercial jet airliner designed for long range operations, with the popular nickname "jumbo jet". It was the first wide-body ever produced, manufactured by Boeing Commercial Airplanes in Seattle. First flight was on February 9, 1969. It made its first commercial flight in 1970 with Pan Am. The four-engine 747 uses a double deck configuration for part of its length, which makes it well recognizable. It is available in passenger, freighter, combi and other configurations and has been built in several versions, the most recent one is the Boeing 747-400, and the Boeing 747-8 and 747-8F are currently on the drawing board and in prototype assembly phase respectively. Total number produced exceeded 1400 by August 2009. The variant considered here is the Boeing 747-100/200, since it is the variant involved in the Bijlmermeer accident, see section 1.2.4. All electrical and hydraulic systems aboard the aircraft are powered by the four turbofan jet engines that deliver the required thrust. Through a mechanical gearbox underneath each engine, the engine high pressure shaft (N2) is connected with pressure and electricity generating units. In addition, engine compressor bleed air is taken from the engine for pneumatic air supply. Four independent hydraulic systems deliver all necessary pressure to the hydraulic users. Pressure is generated from hydraulic pumps located in the engine gearbox. The hydraulic users comprise the entire B747 flight control system and landing gear systems.

Figure A.3: Cargo B Airlines Boeing 747-209F/SCD OO-CBB, ©Thomas Lombaerts

A.1.2.1 Control surface information

Figure A.4 illustrates the large amount of aerodynamic control surfaces of the Boeing 747-100/200, namely four elevators, four ailerons, twelve spoilers and two rudders. Control surfaces with lower deflection rates are one stabilizer and two sets of flaps, divided over inner and outer flaps. Besides, there are four engines and the landing gear, bringing the number of independent control inputs to thirty. This illustrates the significant redundancy of control effectors to steer the aircraft around three axes and to accelerate/decelerate. As a consequence, this Boeing 747-100/200 simulation model is a testbed platform par excellence to investigate the possibilities and the beneficial contributions of Fault Tolerant Flight Control.

Figure A.4 shows the location of the different control surfaces. This drawing provides already an indication of the coupling effects of the control surfaces. There are, for example, pitching contributions due to rudder deflection (located significantly above the center of gravity) and inboard or outboard aileron deflections. The pitching moment due to outboard aileron deflection can be particularly significant due to wing sweepback. These coupling effects can augment, although in a limited way, the control authority redundancy levels of the different segregated control surfaces of each category. A complete overview of these coupling effects can be found in table A.1.

However, there are still some limitations with respect to control surface deflections in the hardware logic in the actuator dynamics. As an example, the flaps cannot be deflected

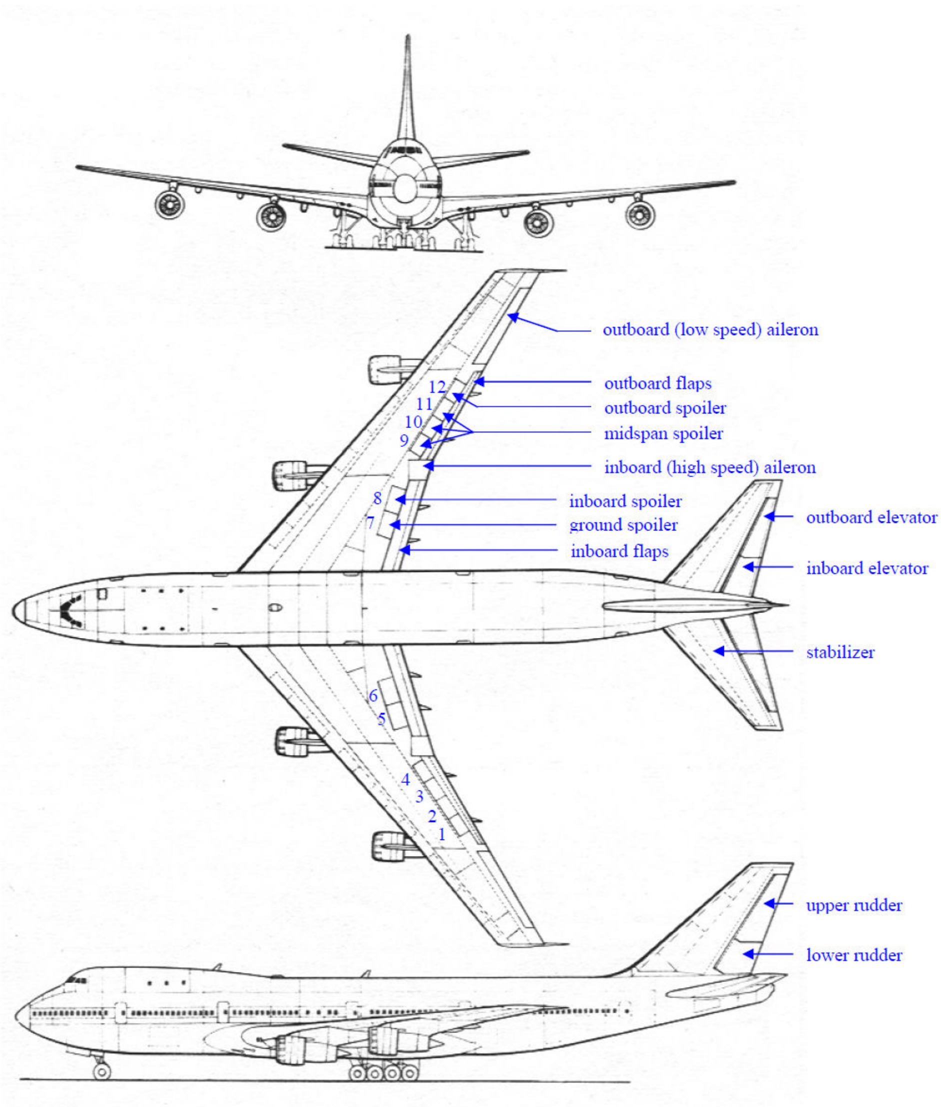

Figure A.4: Boeing 747-200 and locations of control surfaces, source: [175]

Table A.1: Coupling effects of the control effectors in the four axes, $\oplus$ means primary influence and conventional steering channel, $\sim$ means minor coupling effect, + points out major coupling effects and 0 indicates the absence of any (significant) coupling.

δ	δ_a	δ_e	δ_r	δ_{sp}	i_h	f_i	f_o	EPR
#	4	4	2	12	1	1	1	4
L	$\oplus$	0	$\sim$	$\oplus$	0	0	0	+
M	$\sim$	$\oplus$	$\sim$	$\sim$	$\oplus$	$\sim$	$\sim$	$\sim$
N	+	0	$\oplus$	+	0	0	0	+
ΔV	0	0	0	$\oplus$	$\oplus$	$\oplus$	$\oplus$	$\oplus$

in a differential way for directional control. Reason for this is the fact that, according to the information of the RECOVER simulation model developers, this hardware constraint is incorporated by the designers in the Boeing 747 since faulty differential deflection of flaps in low speed flight conditions cannot be compensated sufficiently by the ailerons and other control surfaces. The physical limitations (deflection angle and rate limits) of the different control surfaces in the simulation model are presented in figure A.1.2.1.

A.1.2.2 Sensor information

The RECOVER simulation model contains also a realistic and truthful sensor model. Three groups of sensors are included, namely a GPS assisted inertial reference system (ARS), an air data computer (ADC) and an instrument landing system (ILS) so that it is possible to make automatic landings. All these sensor measurements are contaminated by random noise with a realistic covariance level. The complete set of available sensor measurements, 35 in total, is given in table A.2.

A.1.3 Flight scenario

The geometry of the GARTEUR RECOVER benchmark flight scenario is roughly modeled after the Flight 1862 accident profile, see figure A.6 and section 1.2.4.

The scenario consists of a number of phases. First, it starts with a short section of normal flight, after which the fault occurs, which is in turn followed by a recovery phase. If this recovery is successful, the aircraft should again be in a stable flight condition, although not necessarily at the original altitude and heading. After recovery, an optional identification phase is introduced during which the flying capabilities of the aircraft can be assessed. This allows for a complete parameter identification of the model for the damaged aircraft as well as the identification of the safe flight envelope. The aim is that the knowledge gained during this identification phase can be used by the controller to improve the chances for a safe landing. In principle, the flight control system is then reconfigured to allow safe flight. The

control surface	symbol	maximum displacement	normal operation (full boost) rate	one hydraulic system failure rate
		[deg]	*[deg/s]*	*[deg/s]*
elevators				
• inboard	δ_{EI}	+17 / -23	+37 / -37	+30 / -26
• outboard	δ_{EO}	+17 / -23	+37 / -37	-(1)
stabilizer	Δ_{FRL}	+3 / -12	0.5 → 0.2	0.25 → 0.1
ailerons				
• inboard	δ_{AI}	+20 / -20	+40 / -45	+27 / -35
• outboard	δ_{AO}	+15 / -25	+45 / -55	+22 / -45
spoilers(2)	δ_{SP}			
• inboard (5, 8)		+20 / 0	+75 / -75	-
• midspan (2, 3, 4, 9, 10, 11)		+45 / 0	+75 / -75	-
• outboard (1, 12)		+45 / 0	+75 / -75	-
• ground (6, 7) (speedbrakes)		+20 / 0	+75 / -75	-
flaps				
• inboard	δ_{FI}	+113(3) / 0	+1.83 / -1.83	-
• outboard	δ_{FO}	+113(3) / 0	+1.83 / -1.83	-
rudder				
• upper	δ_{RU}	+25 / -25	+50 / -50	+40 / -40
• lower	δ_{RL}	+25 / -25	+50 / -50	+40 / -40
yaw damper(4)				
• upper	δ_{YU}	+3.6 / -3.6	+15 / -15	-
• lower	δ_{YL}	+3.6 / -3.6	+15 / -15	-

Notes:
positive (negative) values indicate downward (upward) deflections, except for spoilers
for locations of control surfaces, see drawing in figure 3.
(1): in reality outboard elevators half boost rate as inboard counterparts, but not included in model
(2): all spoilers except ground spoilers are spoiler ailerons as well as speedbrakes by a special scheduling
(3): (theoretical) maximum displacement, calculation based upon maximum flap screw travel
(4): the yaw damper uses the rudder surfaces to damp the Dutch roll, but these surfaces are steered through its own actuators with their own limitations. This explains the separate additional information for the yaw damper.

Figure A.5: Physical limitations of the different control surfaces in the simulation model (maximum deflection angle and rate), source: [175]

Table A.2: Standard sensor information in the RECOVER model

source	variable(s)	symbol(s)	noise
IRS	body angular rates	p, q, r	$1.73 \cdot 10^{-4}$
	specific forces	A_x, A_y, A_z	$1 \cdot 10^{-2}$
	attitude angles	ϕ, θ, ψ	$1.73 \cdot 10^{-4}$
	track angle	χ	$1.73 \cdot 10^{-4}$
	baro-inertial altitude	h_{bi}	$1 \cdot 10^{-2}$
	geometrical distance	x_{geo}, y_{geo}	$1 \cdot 10^{-2}$
	velocity components	V_x, V_y, V_z	$1 \cdot 10^{-2}$
ADC	pressure altitude	h	$1 \cdot 10^{-1}$
	true airspeed	V_{TAS}	$1 \cdot 10^{-1}$
	aerodynamic angles	α, β	$1.73 \cdot 10^{-3}$
	derivative of true airspeed	$\dot{V}_{\text{TAS}}$	$1 \cdot 10^{-2}$
	indicated airspeed	V_{IAS}	$1 \cdot 10^{-1}$
	calibrated airspeed	V_{CAS}	$1 \cdot 10^{-1}$
	rate of climb	$\dot{h}$	$1 \cdot 10^{-1}$
	Mach number	M	$1 \cdot 10^{-3}$
	static and total pressure	p_s, p_t	$1 \cdot 10^{0}$
	static and total air temperature	T_s, T_t	$1 \cdot 10^{-1}$
	air density	ρ	$1 \cdot 10^{-3}$
ILS	distance to threshold	DME	$1 \cdot 10^{-1}$
	glideslope deviation and valid signal	Γ	$1.22 \cdot 10^{-3}$
	localizer deviation and valid signal	λ	$1.05 \cdot 10^{-3}$

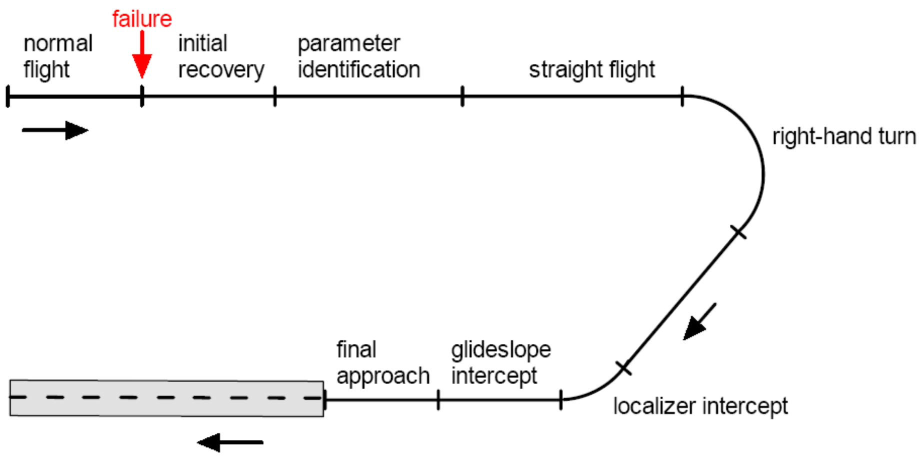

Figure A.6: GARTEUR RECOVER benchmark flight scenario for qualification of fault tolerant flight control strategies for safe landing of a damaged transport aircraft performance of the reconfigured aircraft is subsequently assessed in a series of five flight phases. These consist of straight and level flight, a right-hand turn to a course intercepting the localizer beam, localizer intercept, glideslope intercept and the final approach. The landing itself is not part of the benchmark, because a realistic aerodynamic model of the damaged aircraft with ground effect is not available. However, it is believed that if the aircraft is brought to the threshold in a stable condition, the pilot will certainly be able to take care of the final flare and landing. The RECOVER benchmark scenario and in particular the definition of the fault tolerant flight control assessment criteria are further elaborated in appendix B.

A.2 Failure scenarios

Based on an aircraft accident and incident survey, conducted in GARTEUR action group FM-AG(16), a number of realistic fault cases were selected for the GARTEUR RECOVER benchmark. All selected fault scenarios have proven to be critical in recent aircraft accident and incident cases and include stuck or erroneous control surface positions as well as structural damage. An additional requirement was the availability of sufficient information or flight test data for the modeling and validation of the failure modes. The list of selected fault cases is shown in table A.3 and A.4. Although the first four failure cases in the table are serious, it might be expected that continued flight to the destination would be possible. That is not the case for the last two fault cases which are extremely serious and critical, the major concern after these failures occurred is to land at the nearest airport. The failure scenarios stabilizer runaway, rudder runaway, vertical tail loss and engine separation are used in the computer based or piloted simulator evaluations and elaborated further in the next sections.

A.2.1 Stabilizer runaway

This damage scenario is inspired by feedback from aircraft manufacturers. In case of stabilizer runaway, the horizontal stabilizer suffers a nose upward shift of 2 degrees, resulting in a diving effect of the aircraft, as illustrated in figure A.7.

A.2.2 Rudder runaway

This failure case is inspired by the accidents described in section 1.2.5. In the rudder hardover scenario, the rudder deflects to the left, inducing a yawing tendency of the aircraft to the left. The rudder deflection limit in this scenario depends on the flight speed, since aerodynamic blowdown is taken into account in the RECOVER simulation model. As a result the maximum rudder deflection is slightly below 15° for an airspeed around 270 knots, and even close to 25° (the physical maximum deflection limit imposed by the rud-

Table A.3: Failure Mode test matrix, part 1

	failure mode	description	reconfiguration	assessment	criticality
0.	No failure	Baseline undamaged aircraft			
1.	Stuck elevators	All elevator surfaces are stuck in a faulty position with an offset from trim.	Remaining surfaces: stabiliser, ailerons (symmetric), differential thrust	Transient behaviour (load factor); Controllability (authority); Continued safe flight and landing	Major
2.	Stuck aileron	All aileron surfaces are stuck in a faulty position with an offset from trim.	Remaining surfaces: ailerons (other), spoilers	Transient behaviour (load factor); Controllability (authority); Continued safe flight and landing	Major
3.	Stabilizer runaway*	The stabiliser surface moves quickly to an extreme position	Remaining surfaces: elevator (bad stabiliser), ailerons (symmetric), flaps, differential thrust	Transient behaviour (load factor); Controllability (authority); Continued safe flight and landing	Critical
4.	Rudder runaway*	All rudder surfaces move quickly to an extreme position.	Remaining surfaces and asymmetric thrust	Transient behaviour (load factor); Controllability (authority); Continued safe flight and landing	Critical
5.	Stuck elevators (with turbulence)	All elevator surfaces are stuck in a faulty position with an offset from trim.	Remaining surfaces: stabiliser, ailerons (symmetric), differential thrust	No false FDI detection; Transient behaviour (load factor); Controllability (authority); Continued safe flight and landing	Major
6.	Stuck aileron (with turbulence)	All aileron surfaces are stuck in a faulty position with an offset from trim.	Remaining surfaces: stabiliser, ailerons (symmetric), differential thrust	No false FDI detection; Transient behaviour (load factor); Controllability (authority); Continued safe flight and landing	Major

*used in computer based or piloted simulator evaluations

Table A.4: Failure Mode test matrix, part 2

	failure mode	description	reconfiguration	assessment	criticality
7.	Stabilizer runaway (with turbulence)	The stabiliser surface moves quickly to an extreme position	Remaining surfaces: elevator (bad stabiliser), ailerons (symmetric), flaps, differential thrust	No false FDI detection; Transient behaviour (load factor); Controllability (authority); Continued safe flight and landing	Critical
8.	Rudder runaway (with turbulence)	All rudder surfaces move quickly to an extreme position.	Remaining surfaces and asymmetric thrust	No false FDI detection; Transient behaviour (load factor); Controllability (authority); Continued safe flight and landing	Critical
9.	Loss of vertical tail*	The loss of the vertical tail leads to the loss of all rudder control surfaces as well as the loss of all damping in the roll and yaw axes.	Remaining surfaces and asymmetric thrust	Transient behaviour (load factor); Controllability (authority); Continued safe flight and landing	Catastrophic
10.	Engine separation & resulting structural damage (El Al Flight 1862)*		Real time control law reconfiguration; Remaining surfaces; Remaining engines; Remaining sensors	Transient behaviour (load factor); Stability; Controllability (authority); Continued safe flight and landing	Catastrophic

*used in computer based or piloted simulator evaluations

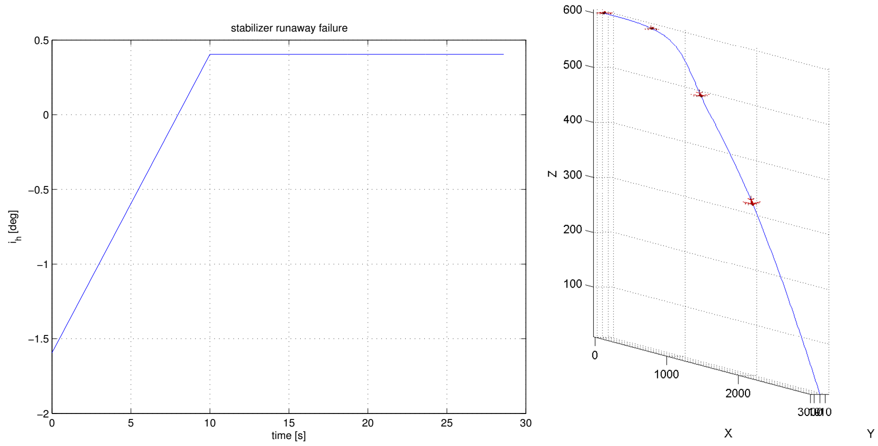

(a) stabilizer deflection (b) uncompensated trajectory

Figure A.7: Stabilizer deflection and uncompensated trajectory of the Boeing 747 with stabilizer runaway failure

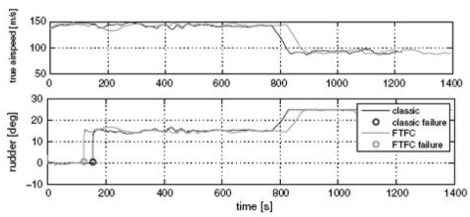

Figure A.8: Rudder deflection in rudder runaway failure scenario

der control system structure) for an airspeed of 165 knots. This blowdown effect is clearly visible in figure A.8.

A.2.3 Vertical tail loss

This damage scenario renders the aircraft directionally unstable due to the loss of the vertical tail and rudder controls. Moreover, yaw damping is not available anymore to counteract Dutch roll behaviour. This scenario is similar to an aircraft accident case in which a loss of the vertical tail occurred, see section 1.2.2, although it is not intended to be an accurate representation. In the true accident, also all hydraulics halted functioning, as explained in section 1.2.2. However, after this accident, the manufacturer included some safety measures in the hydraulic circuit to prevent the total loss of all hydraulics in the future in similar scenarios. This led to the benchmark design choice to include the vertical tail loss in the RECOVER accident scenarios list without considering the total loss of hydraulics.

A.2.4 Engine separation

The El Al engine separation scenario is an accurate DFDR[1] data validated simulation of flight 1862, as explained in section 1.2.4, where the loss of hydraulics is taken into account. This is the most important and most complicated failure scenario in the failure library of the simulation model. It consists of a combination of both system and structural failure modes. This scenario concerns the situation where an EL AL Boeing 747 lost both starboard engines due to metal fatigue in the engine pylons. This resulted in more extended damage to the starboard wing and to the hydraulic systems, as shown in fig. A.9. The separation of both right wing engines will result in a loss of hydraulic systems no 3 and 4 and a loss of control surfaces according to the B747-100/200 hydraulics systems architecture as described in [116]. Additional effects due to center of gravity shift and estimated weight loss due to the missing engines are all taken into account. The estimated aerodynamic contribution due to the loss of right wing leading edge structure, based on accident flight data, are calculated in a separate model and added to the baseline aerodynamic coefficients. More information about how these failure characteristics have been incorporated in the simulation model can be found in ref. [247, 248].

Figure A.9 provides an overview of the sustained damage to the flight 1862 aircraft's structure and onboard systems after the separation of both right wing engines. Due to the

[1]DFDR = digital flight data recorder

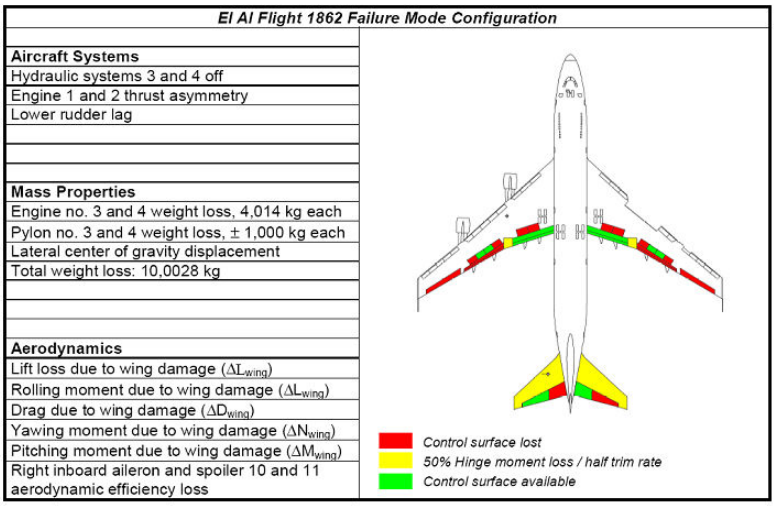

Figure A.9: Failure modes and structural damage configuration of the Flight 1862 accident aircraft, suffering right wing engine separation, partial loss of hydraulics and change in aerodynamics, [245] loss of engines no 3 and 4, not only hydraulic systems no 3 and 4 were lost, but also the mass properties were changed drastically, as illustrated in table A.5.

Table A.5: Mass property changes in the El Al Flight 1862 scenario

variable	original	change
mass	$m_0 = 3.17 \cdot 10^5 kg$	$\Delta m = -1.0028 \cdot 10^4 kg$
center of gravity	$y_{cg_0} = 0m$	$\Delta y_{cg} = 0.5426m$
inertia	$I_{xx_0} = 2.6144 \cdot 10^7 kgm^2$	$\Delta I_{xx} = -4.329 \cdot 10^5 kgm^2$
	$I_{yy_0} = 4.6734 \cdot 10^7 kgm^2$	$\Delta I_{yy} = -8.644 \cdot 10^5 kgm^2$
	$I_{zz_0} = 6.9822 \cdot 10^7 kgm^2$	$\Delta I_{zz} = -8.876 \cdot 10^5 kgm^2$
	$I_{xz_0} = 1.457 \cdot 10^6 kgm^2$	$\Delta I_{xz} = -6.108 \cdot 10^4 kgm^2$

The physical loss of the engines from the right wing caused also considerable damage to the wing's leading edge, resulting in significantly altered aerodynamic properties, i.e. increased drag and loss of lift force, together with a wing damage induced rolling, pitching and yawing moment. All these effects have been incorporated in the simulation model, and comparison of simulation results with the accident data recorded by the DFDR has shown that this simulation model accurately describes the flight dynamics of the damaged aircraft. As a result, the RECOVER simulation model is a unique facility for the validation of FTFC design and development.

Appendix B

Assessment criteria

To obtain a quantitative measure of predicted FTFC system performance in degraded modes, specifications need to be defined to assess proper functioning under realistic operational flight conditions. The goal of the benchmark specifications modelling, as described in this appendix, is to create a set of assessment criteria in order to evaluate the quality of the performance of fault detection and identification (FDI) and reconfigurable control algorithms. The lay-out of this appendix is as follows. First, the specifications modelling process is introduced by discussing the benchmark scenario. Subsequently, the general evaluation criteria will be considered by defining two classes of test manoeuvres. Thereafter, focus is placed on the test manoeuvres for FTFC qualification, which is the major topic of this appendix. After the discussion on how the assessment quantities of interest can be divided in two categories, four qualification test manoeuvres are discussed in depth. These include straight flight, right turn and localizer intercept, glideslope intercept and final approach with sidestep. Finally, a summary of the specified assessment quantities is given for the different FTFC qualification test manoeuvres. These criteria have also been published in ref. [177].

B.1 Specification modelling

The goal of specifications modelling is to create a set of assessment criteria in order to evaluate the quality of the performance of fault detection and identification (FDI) and controller reconfiguration algorithms. A schematic overview of the benchmark scenario, as introduced in appendix A, is provided in figure A.6. Obviously, after the introduction of a failure to the aircraft, a total catastrophe is to be avoided. Therefore, it is necessary that a failure is detected promptly. Furthermore, a new trim condition, or quasi-trim condition, must be established quickly for safe continuation of the flight. This phase is called initial recovery, as illustrated in fig. A.6, and needs to be completed as soon as possible, even before firm flight control reconfiguration takes place. The normal operating limits of the non-crippled aircraft, i.e. maximum and minimum velocity, maximum g-load, can be seen as worst-case bounds on the allowable manoeuvres during all subsequent phases. After fault identification and reconfiguration, the four qualification manoeuvres are performed according to the scenario as shown in fig. A.6.

The FTFC assessment criteria are defined for two different phases during the flight control reconfiguration process. First, criteria are enumerated for the Fault Detection and Identification phase. After control reconfiguration has taken place, some test manoeuvres for qualification have been selected for which specifications have been defined. These criteria enable to assess the correct functioning of the reconfigured control system under realistic operational conditions.

B.1.1 General evaluation criteria

For the assessment of Fault Detection and Identification algorithms, it is customary to define the following list of criteria, as can be found in ref. [109]:

- the time needed to detect a failure;
- the ratio of successful detection of failures vs. the number of false alarms;
- the time needed to give a first reaction or control input and re-establish trim;
- the operating limits of the aircraft may not be exceeded after failure introduction;
- the ability to reconfigure the controller such that the aircraft states are controlled with adequate performance, and preferably with desired performance.

The above criteria are usually applied for FDI in general. However, for the RECOVER benchmark emphasis is placed on operational assessment criteria that impose constraints on the total flight trajectory instead of the technical FDI criteria only. Therefore, the operational criteria have been defined by using the FDI requirements, as mentioned above, as a basis. The result of this study can be found in the remainder of this appendix.

Some graphic examples of the applied operational assessment criteria, which hold for one of the aircraft states or variables, are depicted in figures B.1 and B.2. Figure B.1 applies for test manoeuvres with trajectory constraints, where figure B.2 applies for test manoeuvres with end-point position constraints.

The specifications apply to certain variables which are relevant and critical for each flight phase, e.g. position information, linear rates, angular rates, linear accelerations, angular accelerations and g-forces, each in the three axes of the aircraft reference system. The

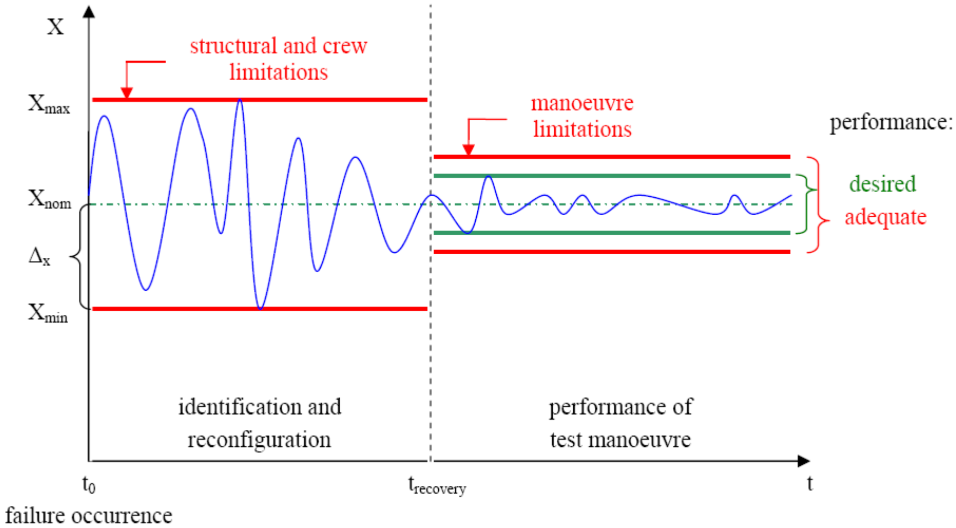

Figure B.1: Graphic representation of FDI and control reconfiguration assessment criteria representing test manoeuvre with trajectory constraints

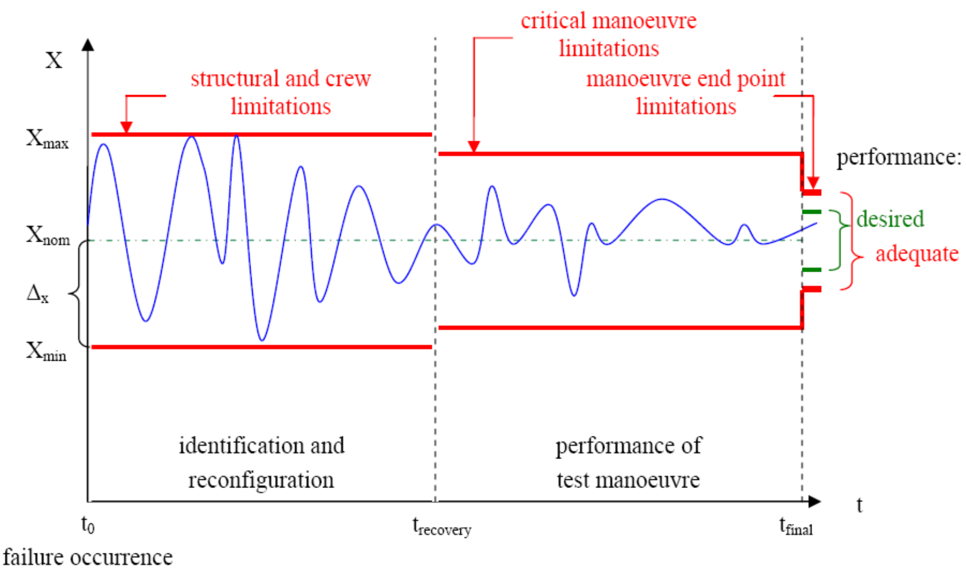

Figure B.2: Graphic representation of FDI and control reconfiguration assessment criteria representing test manoeuvre with end-point position constraints

list of relevant assessment quantities will be enumerated later for each test manoeuvre separately. These variables have to comply with certain operational limitations, which can be divided over two categories, according to the relevant part of the time span. When a failure occurs at time t_0, the flight control systems have some time for identification and reconfiguration up to the moment t_{recovery}, whereafter a test manoeuvre is performed in order to analyse if the reconfiguration was successful.
In the first part, where identification and reconfiguration take place, the variables are limited by structural and crew capability (human performance) boundaries. After t_{recovery} the qualification test manoeuvre is performed. In the case of a test manoeuvre with trajectory constraints, some fairly stringent manoeuvre limitations are defined for the relevant assessment quantity values from t_{recovery} onward till the end of the test manoeuvre. These limitations define a box which specifies if the manoeuvre performance is desired or adequate (figure B.1). On the other hand, when a test manoeuvre is considered with end-point position constraints, the relevant assessment quantity values are restricted to a larger range defined by slightly reduced safe flight boundaries as initial trajectory constraints (critical manoeuvre limitations, figure B.2). More stringent boundaries to evaluate the manoeuvre quality are then defined at the end point t_{final}, where the boundaries represent a limitation box specifying whehter the manoeuvre performance is desired or adequate. The aircraft must be in (quasi) steady state at t_{final}, otherwise the performance criteria cannot be guaranteed persistently.

A possible definition of adequate and desired performance boxes for the benchmark flight phases including straight flight, right turn and localizer intercept, glideslope intercept and final approach with sidestep down to decision height will be discussed later in this appendix. The performance limitations may depend on many other variables, like indicated airspeed of the aircraft and altitude. Therefore, it is important to define one representative reference trajectory with fixed altitude and velocity as initial conditions, because in that way the complexity is already reduced considerably. Here, most interest is in low altitudes because of the small margins there.

The manoeuvres are a very important aspect in this work. It should be noted that there are two kinds of manoeuvres. The first kind are manoeuvres for parameter identification that take place in the identification and reconfiguration phase, before t_{recovery} in figures B.1 and B.2, these are facultative manoeuvres. The other kind of manoeuvres are test manoeuvres for qualification which are performed during the second part of the time span in figures B.1 and B.2, after t_{recovery}. These are mandatory for qualification of the fault tolerant flight control system.

B.1.2 Test manoeuvres for qualification

As discussed in the foregoing paragraph, four qualification test manoeuvres have been defined which are mandatory and will be used to obtain the RECOVER benchmark criteria. The straight flight and glideslope intercept are two manoeuvres with trajectory constraints. On the other hand, right turn with localizer intercept and final approach with sidestep have end-point position constraints. The motivation for this is that there are no critical requirements on the turn and the approach themselves, as long as the aircraft ends up at the right location at the end of the manoeuvre. The straight flight and final approach test manoeuvres have longitudinal as well as lateral constraints. The other two manoeuvres deal only with one axis at a time. As such, the right turn manoeuvre has only lateral constraints where the glideslope intercept has only longitudinal constraints.
The aircraft should be in (quasi-)equilibrium at t_{final} for the end-point position constraints and after t_{recovery} for the trajectory constraints. To achieve this requirement for all four test manoeuvres, all angular rates (p,q,r) as well as the three linear acceleration components (a_x,a_y,a_z) should be as small as possible within certain boundaries. For any failure scenario, the time to reach equilibrium is a very important criterium.
The assessment variables can be defined in two different categories, namely specification boundary variables and competitiveness variables. Specification boundary quantities provide limits which cannot be exceeded, like safe flight boundaries and performance boxes. On the other hand, competitiveness criteria have been defined that allow to distinguish between the performances of different reconfigurable control strategies. For any manoeuvre, the time to accomplish the manoeuvre is a very important competitiveness criterion. In some situations, assessment variables can belong to both categories simultaneously. For each test manoeuvre, a list of relevant quantities is enumerated in table B.2, B.3, B.4 and B.5. In the first two columns of each table, an indication is given about the category the quantity belongs to. The abbreviations 'sb' and 'cc' represent specification boundary and competitiveness variables respectively.

The initial conditions for the benchmark qualification test manoeuvres are defined in table B.1. A distinction is made between a nominal flight scenario, a heavy weight Flight 1862 scenario and a low weight Flight 1862 scenario, since each of the Flight 1862 scenarios has a different aircraft weight value. In the nominal situation, the aircraft weight is approximately 263 tons and the touchdown speed is 165 knots. As the Flight 1862 accident happened just after take off, the aircraft weight was considerably higher, namely 317 tons (after separation of the right-wing engines). This resulted into the fact that the crew had to maintain a high speed of about 260 knots, which reduced the chances for a survivable landing significantly. Based on the Flight 1862 performance capability analysis [249], the aircraft was able to maintain level flight in order to reduce the landing weight by dumping fuel. A weight reduction due to fuel jettison down to approximately 263 tons would have led to a more survivable landing at a speed of about 210 knots.

Table B.1: Initial conditions for the three benchmark scenario's: nominal flight, **heavy weight Flight 1862** and *low weight Flight 1862*

manoeuvre	straight flight	right turn LOC int	GS int	final approach
h [m]	600	600	600	90
V [m/s]	92.6/**133.8**	92.6/**133.8**	92.6/**133.8**	85/**133.8**/*108*
flap setting	20/**1**	20/**1**	20/**1**	25/**1**/*1*
landing gear	up	up	down	down

With the flap setting stuck at 1 and an aircraft weight of 317 tons, the minimum speed is limited to the relatively high value of 133.8 m/s. The stuck flap setting at position 1 in case of the Flight 1862 accident scenario results into a minimum allowable speed of 108 m/s in the final approach phase at a weight of 263 tons in the case of fuel jettison.

The benchmark qualification test manoeuvres are based on operational procedures in order to approximate realistic flight conditions as much as possible. To achieve this, some manoeuvres have been based upon the instrument approach chart to runway 27 of Amsterdam airport Schiphol (ICAO-code EHAM). This chart is included at the end of this appendix. In this chart, a red line marks the trajectory of the flight 1862 accident aircraft. Indicated in green in this chart is the approximate trajectory of the proposed benchmark scenario. Note that closely following this trajectory is not part of the benchmark criteria. The end-point is more relevant than the trajectory in this set-up.

B.1.2.1 Straight flight

The first benchmark qualification test manoeuvre is performing a straight flight downwind, with the presence of some turbulence. Analysing the closed loop system time responses of course χ and flight path angle γ allows to compare the quality of the different reconfiguring control strategies. During this test manoeuvre, the aircraft should remain in a predefined box, like a virtual tunnel in the sky. In order to analyse this manoeuvre, the assessment quantities of interest are defined in table B.2. The abbreviations sb and cc in the first two columns of the table represent *specification boundary (sb)* and *competitiveness criteria (cc)* respectively.

Applying the above mentioned specifications and criteria to the benchmark simulation model with the classical (mechanical) flight control system results in the plots shown in fig. B.4. The performance of each fault tolerant control design can be assessed by generating similar plots for the relevant outputs. The routines to generate the performance plots are an integral part of the benchmark simulation software package.

Table B.2: Specified assessment quantities for the straight flight qualification manoeuvre

sb	cc	symbol	quantity
✓	✓	V	velocity
✓	✓	χ	course or track angle
✓	✓	γ	flight path angle
✓		α	angle of attack
✓	✓	β	sideslip angle
✓	✓	n_z	load factor
✓	✓	ϕ	roll angle

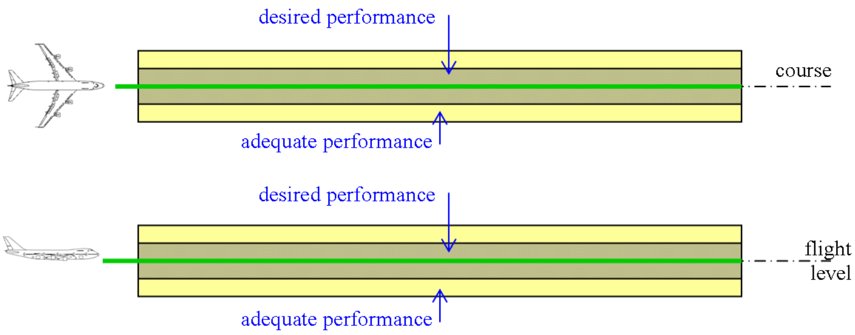

Figure B.3: Definition of performance boxes for straight flight qualification manoeuvre

In figure B.4, competitiveness criteria apply on all shown states, except for the angle of attack α. The yellow regions indicate where the desired performance is not met, where failure to achieve adequate performance is indicated by the red regions. It is clear that for the straight flight phase, trajectory constraints apply. Figure B.4 shows that the baseline aircraft model, with classical control system, satisfies all assessment criteria for the straight flight phase with considerable margins.

B.1.2.2 Right turn and localizer intercept

The second benchmark test manoeuvre starts by performing a right turn, with the presence of some turbulence. After 10 seconds of straight flight, a right turn is initiated in order to reach the localizer (LOC) intercept course. No special limitations are imposed on the turn manoeuvre itself[1], except for the fact that the time necessary to complete the turn is a competitiveness criterion. The specific lateral force A_y and altitude changes Δ_h during this manoeuvre should be minimal for the sake of passenger comfort and trajectory accuracy

[1] E.g. also a left turn is allowed, as can be seen in fig. B.5

respectively. The localizer intercept manoeuvre is performed with a $45°$ heading change, where $\pm 5°$ deviation is still acceptable and velocity should be close to the reference value. After this manoeuvre, the aircraft should be on the localizer beam. In order to analyse this final position and the equilibrium at the end of this manoeuvre, an end phase for evaluation is defined. This end phase starts on the moment the aircraft crosses a vertical plane at 15 km distance from the runway threshold. From this moment onward, the end phase lasts for the following 10 seconds, during which angular rates and linear accelerations should remain within their predefined equilibrium limits to show that the aircraft is fully stabilized. The relevant assessment quantities during the complete manoeuvre are enumerated in table B.3. The abbreviations sb and cc in the first two columns of the table represent *specification boundary (sb)* and *competitiveness criteria (cc)* respectively. As illustrated by the perfor-

Table B.3: Specified assessment quantities for the right turn and localizer intercept qualification manoeuvre

sb	cc	symbol	quantity
✓		x_{runway}	distance from runway threshold
✓	✓	λ	localizer deviation during end phase
		Λ	LOC intercept angle
✓	✓	V	velocity
✓		ϕ	roll angle during turn
✓	✓	ϕ	roll angle during end phase
	✓	p	roll rate during end phase
	✓	q	pitch rate during end phase
	✓	r	yaw rate during end phase
	✓	a_x	longitudinal acceleration during end phase
	✓	a_y	lateral acceleration during end phase
	✓	a_z	vertical acceleration during end phase
✓		α	angle of attack
✓	✓	β	sideslip angle
✓	✓	A_y	lateral specific force
✓	✓	n_z	load factor
✓	✓	Δ_h	altitude deviation

mance box in figure B.5, it is clear that the allowed cross track deviation is presented as the localizer angular deviation, while the longitudinal deviation is linear. The roll angle ϕ is an assessment quantity to verify if the aircraft rolled out properly to end the turn manoeuvre. As the localiser and glideslope are presented to the pilot on an uncalibrated scale, the deviations are indicated in "dots" (1 dot is $1.25°$). During tracking of the localizer, 0.5 dot localiser deviation is allowed as a maximum, see also fig.B.6. The right turn and localizer intercept performance criteria are as follows:

Applying the above mentioned specifications and criteria to the benchmark simulation model with the classical control system results in the plots shown in fig. B.7.

In figure B.7, competitiveness criteria apply on all shown states, except for the angle of attack α. The yellow regions indicate where the desired performance is not met, where failure to achieve adequate performance is indicated by the red regions. It is clear that end-point position constraints can be found for certain states in the right turn and localizer intercept phase. It can be seen in figure B.7 that not all criteria are met. More precisely, the roll angle ϕ the aircraft achieves is slightly too large. However, for comfort reasons, it is advisable to enforce that the fault tolerant flight control designs satisfy this requirement.

B.1.2.3 Glideslope intercept

The third benchmark test manoeuvre is the interception of the glideslope in the presence of some turbulence. Note that also in actual practice, localizer intercept occurs before glideslope intercept according to operational practices. After 10 seconds of straight flight, the glideslope interception point is met at 11.5 km from the runway threshold and the aircraft starts following the 3° glideslope downward. After the interception point, the aircraft should remain within a predefined box, like a virtual funnel in the sky. In order to analyse this final position and the equilibrium at the end of the manoeuvre, an end phase for evaluation is defined. This end phase starts on the moment the aircraft intercepts the extension of the runway center line at 11.5 km distance from the threshold. From this moment onward, the end phase lasts for the following 10 seconds during which angular rates and linear accelerations should remain within their predefined equilibrium limits. For this manoeuvre, assessment quantities of interest are included in table B.4. The abbreviations sb and cc in the first two columns of the table represent *specification boundary (sb)* and *competitiveness criteria (cc)* respectively. The deviation from the glideslope is also expressed in dots, where one dot

Table B.4: Specified assessment quantities for the glideslope intercept qualification manoeuvre

sb	cc	symbol	quantity
✓		x_{runway}	longitudinal distance from runway threshold
✓	✓	V	velocity
✓	✓	Γ	glideslope deviation during end phase
✓		α	angle of attack
	✓	p	roll rate during end phase
	✓	q	pitch rate during end phase
	✓	r	yaw rate during end phase
	✓	a_x	longitudinal acceleration during end phase
	✓	a_y	lateral acceleration during end phase
	✓	a_z	vertical acceleration during end phase
✓	✓	n_z	load factor
✓	✓	λ	localizer deviation

equals $0.35°$. An illustration for this can be found in fig. B.8.

The angle of attack α is a primary assessment quantity of interest because it is an important parameter in order to keep the aircraft within its stall limits. As illustrated in figure B.9, it is clear that vertical deviation is expressed in an angular way, analogously as the right turn and localizer intercept scenario.

Applying the above mentioned specifications and criteria to the benchmark simulation model with the classical control system results in the plots shown in fig. B.10.

In figure B.10, competitiveness criteria apply on all shown aircraft states, except for the angle of attack α. As with the foregoing specifications, the yellow regions indicate where the desired performance is not met and failure to comply with adequate performance is indicated by the red regions. For this test phase, end-point constraints apply after the glideslope interception point. For this particular example with the baseline classical control system, the aircraft satisfies all assessment criteria for the glideslope intercept phase with considerable margins, except for the localizer error angle λ. However, this maximum localizer deviation can still be used as a design guideline for the fault tolerant control designs. Since these latter have more freedom to control the aircraft, it can be expected that they are capable to meet this requirement.

B.1.2.4 Final approach with sidestep

The last benchmark test manoeuvre is the final approach down to decision height, with a 300 feet lateral offset around half a nautical mile from the runway threshold. Some turbulence is included during this manoeuvre. No special limitations are imposed on the approach manoeuvre itself, except for the fact that the time necessary to complete the approach is a competitiveness criterion. Additionally, lateral specific force A_y and glideslope deviations Γ during this manoeuvre should be minimal for the sake of passenger comfort and trajectory accuracy respectively. However, after this manoeuvre, the aircraft should arrive in a predefined performance box on decision height above the runway (note that the flare manoeuvre is not included in this study). The origin of the reference frame for these performance boxes is placed at decision height on the centerline of the runway above the runway threshold and is defined as the end-point. It is assumed that the aircraft ends up in the vicinity of this point at the end of the manoeuvre. In order to analyse this final position and the equilibrium at the end of this manoeuvre, an end phase for evaluation is defined. This end phase starts 10 seconds before the aircraft reaches the runway threshold and ends on the moment the aircraft crosses the threshold. During this test phase, angular rates and linear accelerations should remain within their predefined equilibrium limits. To analyse the complete manoeuvre, the assessment quantities of interest are enumerated in table B.5. The abbreviations sb and cc in the first two columns of the table represent the *specification boundary (sb)* and *competitiveness criteria (cc)* respectively. As can be seen from the illustration of the performance box in figure B.11, the allowed cross track deviation Δy is more restricted than the wider longitudinal Δx range. Also in this phase, the roll angle ϕ is an assessment

Table B.5: Specified assessment quantities for the final approach with sidestep qualification manoeuvre

sb	cc	symbol	quantity
✓	✓	Δx	longitudinal deviation at end-point
✓	✓	Δy	lateral deviation at end-point
✓	✓	u	forward velocity
✓	✓	w	vertical velocity
✓	✓	χ	track angle
✓		ψ	heading angle
✓	✓	ϕ	roll angle at end-point
✓	✓	v_r	transversal velocity above runway at end-point
	✓	p	roll rate during end phase
	✓	q	pitch rate during end phase
	✓	r	yaw rate during end phase
	✓	a_x	longitudinal acceleration during end phase
	✓	a_y	lateral acceleration during end phase
	✓	a_z	vertical acceleration during end phase
✓		α	angle of attack
✓	✓	n_z	load factor

quantity to verify if the aircraft rolled out properly to end the turn manoeuvre. The vertical speed w can be deduced from the glideslope angle γ and forward speed u. The heading ψ is a measure of the alignment of the aircraft with the runway. A measure of the alignment of the velocity vector with the runway is indicated by the track angle χ. Because arriving at the runway is the main challenge, the track should be aligned with the runway and not necessarily the heading. The heading deviates from the track angle due to the wind components. Normally the aircraft will align the heading with the runway to put the landing gear wheels in the direction of the ground velocity. This is called a decrab manoeuvre, but this is not a strictly necessary practice during Boeing 747 crosswind landings according to the Aircraft Operation Manual, so it is not considered here. However, it should be noted that decrab is still required for other types of aircraft. For the Boeing 747 aircraft, the roll angle ϕ should be kept small close to the ground in order to prevent one of the outboard engines and/or wingtips hitting the runway. For this reason, a roll angle deviation of maximum $\pm 8°$ is acceptable. Lateral velocity v_r with reference to the runway is also relevant here, since lateral velocity is not consistent with sideslip angle β in the presence of turbulence. Also the angular rates p, q, r (pitch, roll and yaw) should be minimal in order to guarantee a smooth touchdown. Finally the angle of attack α should be well within its stall limits.

Applying the above mentioned specifications and criteria on the simulation model with the classical controller results in the plots shown in fig. B.12.

In figure B.12, competitiveness criteria apply on all shown states, except for the angle of attack α. Again, the yellow regions indicate where the desired performance is not met, and adequate performance failure is indicated by the red regions. It is clear that for this phase, end-point position constraints apply. For this particular example with the baseline aircraft model including classical control system, quite some criteria have been violated. However, these requirements can still be used as a design guideline for the fault tolerant control systems. Since these advanced control systems have more freedom to control the aircraft, it can be expected that they are capable to meet these requirements.

B.2 Discussion

The proposed assessment criteria, as discussed in this appendix, can be used to evaluate the performances of the different fault tolerant control methods and strategies. By making a distinction between the described four different qualification test manoeuvres, instead of considering one global sequence of manoeuvres, it is possible to identify particular advantages and disadvantages of each FTFC method. The test scenarios have been integrated in the FTFC benchmark simulation environment for analytical evaluation purposes. A final assessment using piloted simulation (as conducted on the Simona research simulator of Delft University of Technology as part of this study) will provide pilot opinions on the operational acceptability of the designed FTFC methodologies. Real-time piloted simulation also makes it possible to analyse objectively the failure accommodation capabilities and handling qualities of reconfigurable flight control systems for aircraft subjected to critical structural and system failure modes. By flying the benchmark scenario with the baseline non-damaged aircraft model, a comparison can be made to determine the overall quality of all control algorithms with reference to the standard situation.

As a final remark, it should be noted that the assessment criteria, as described in this appendix for each qualification test manoeuvre, are an evaluation tool. However, they should be put in the right perspective. The ultimate goal is to perform a survivable recovery of the damaged aircraft and this is also the final and paramount evaluation criterion.

Table B.6 shows a summary of all the benchmark assessment variables and an indication for which qualification test manoeuvre they are relevant.

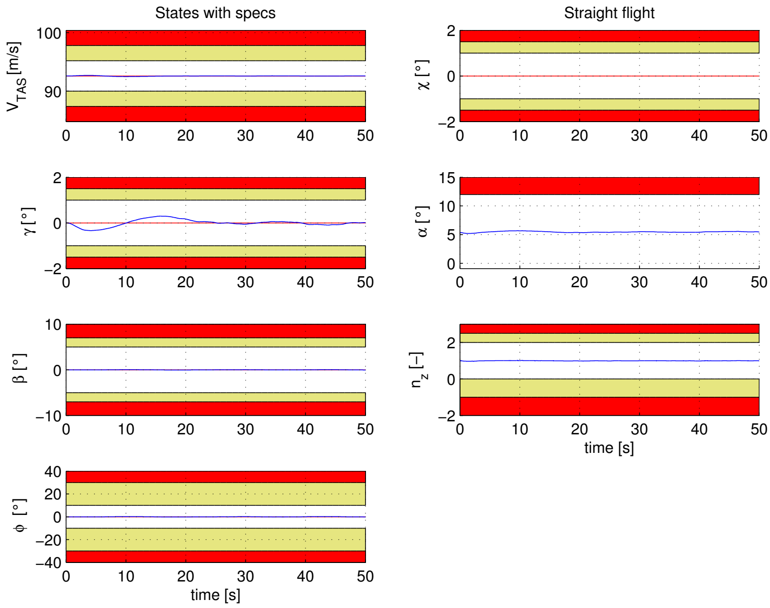

(a) aircraft states

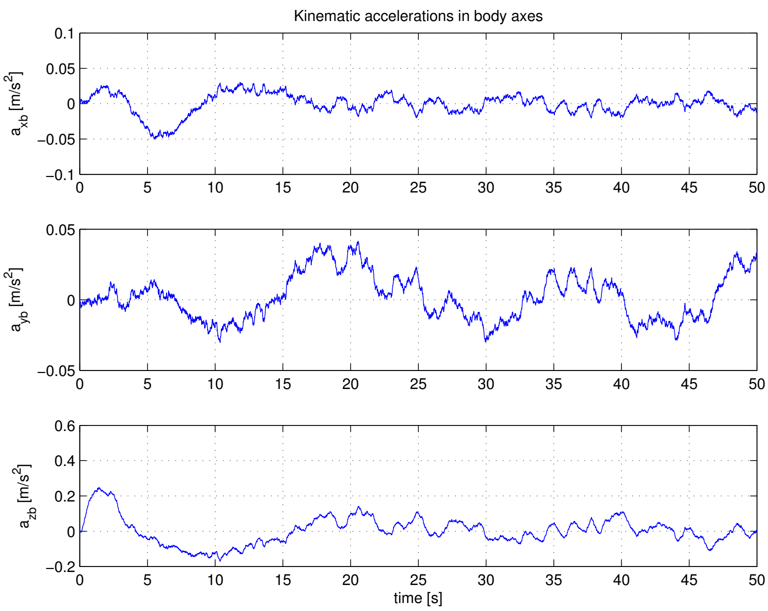

(b) kinematic accelerations

Figure B.4: Specifications on the aircraft states for the downwind straight flight qualification manoeuvre

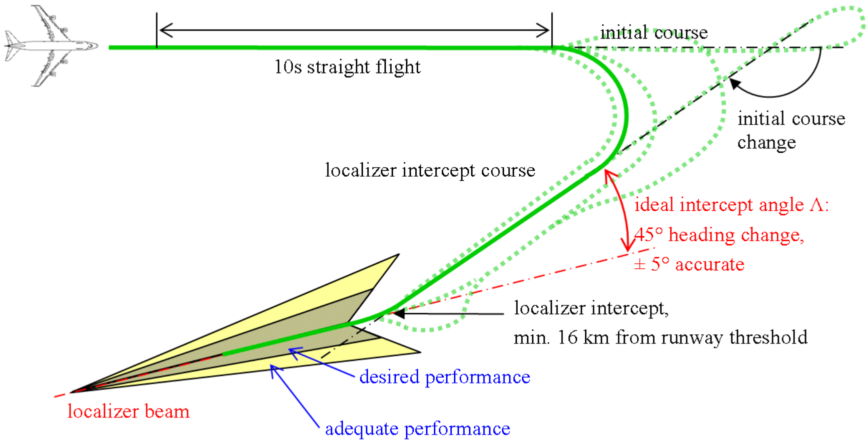

Figure B.5: Definition of performance boxes for right turn and localizer intercept

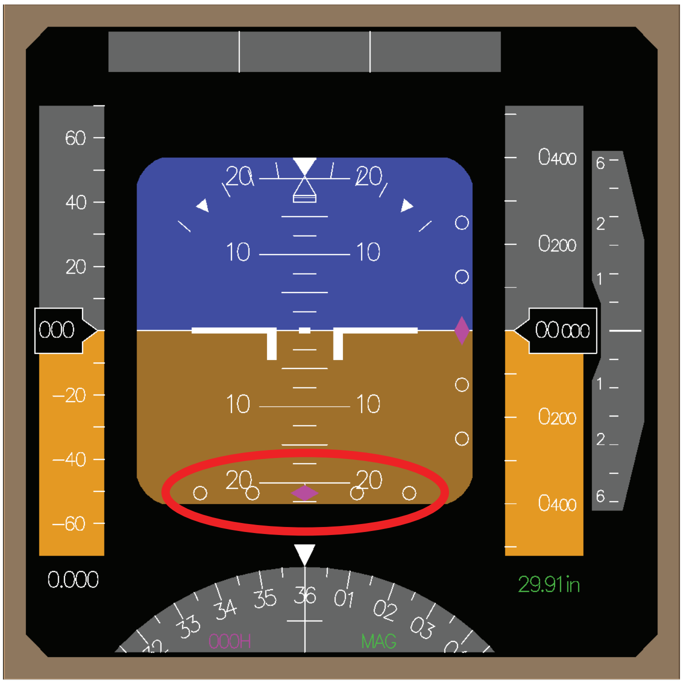

Figure B.6: Primary Flight Display (PFD) with the Localizer (LOC) deviation scale and magenta diamond shaped LOC signal indicator in the middle of the scale

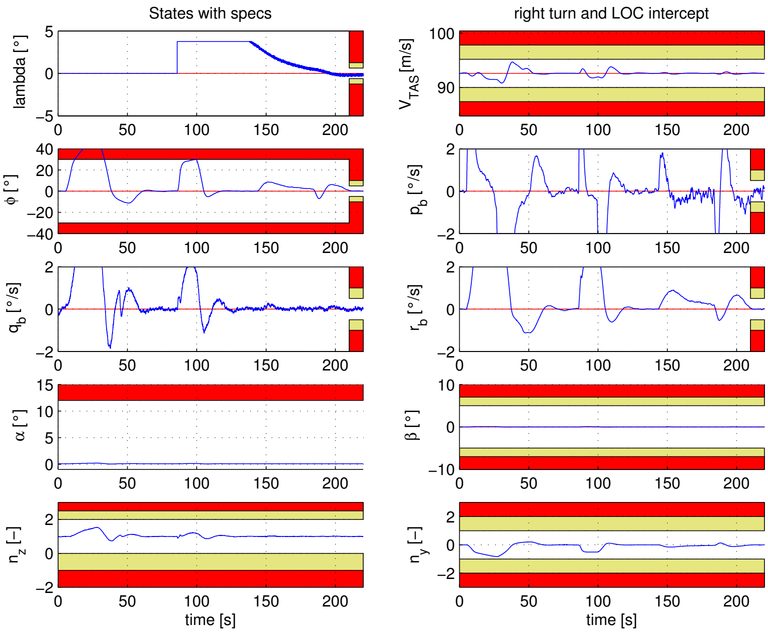

(a) aircraft states

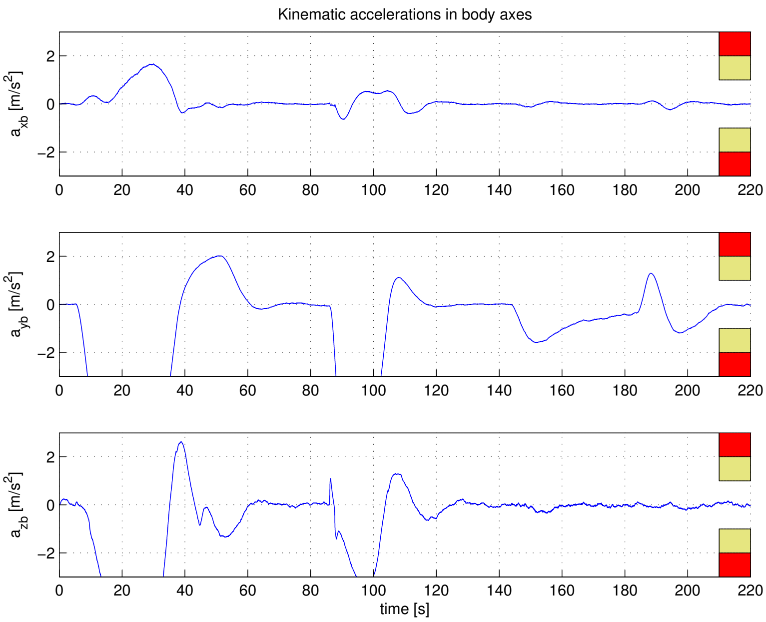

(b) kinematic accelerations

Figure B.7: Specifications on the aircraft states for the right hand turn and localizer intercept flight qualification manoeuvre

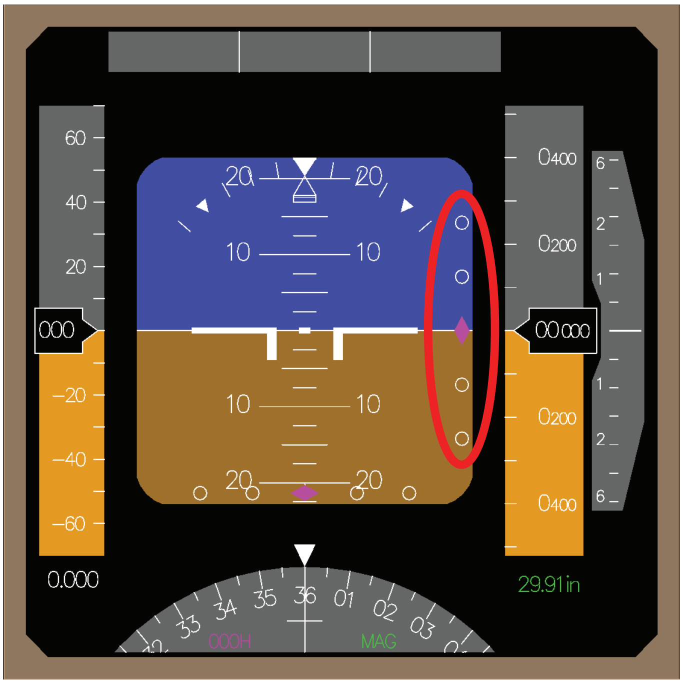

Figure B.8: Primary Flight Display (PFD) with the Glideslope (GS) deviation scale and magenta diamond shaped GS signal indicator in the middle of the scale

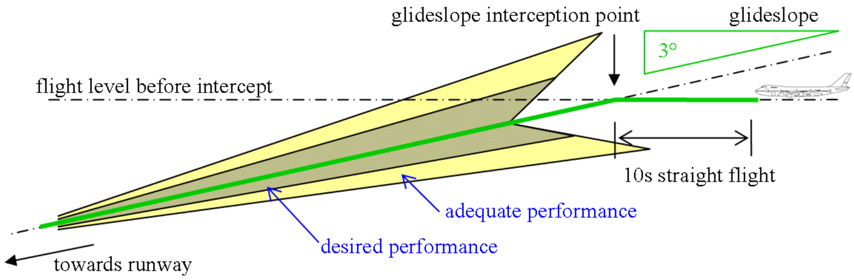

Figure B.9: Definition of performance boxes for glideslope intercept qualification manoeuvre

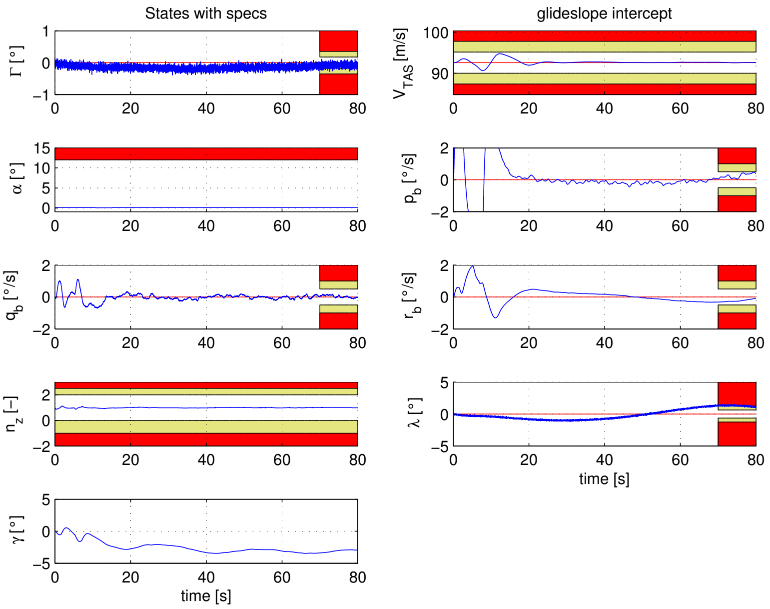

(a) aircraft states

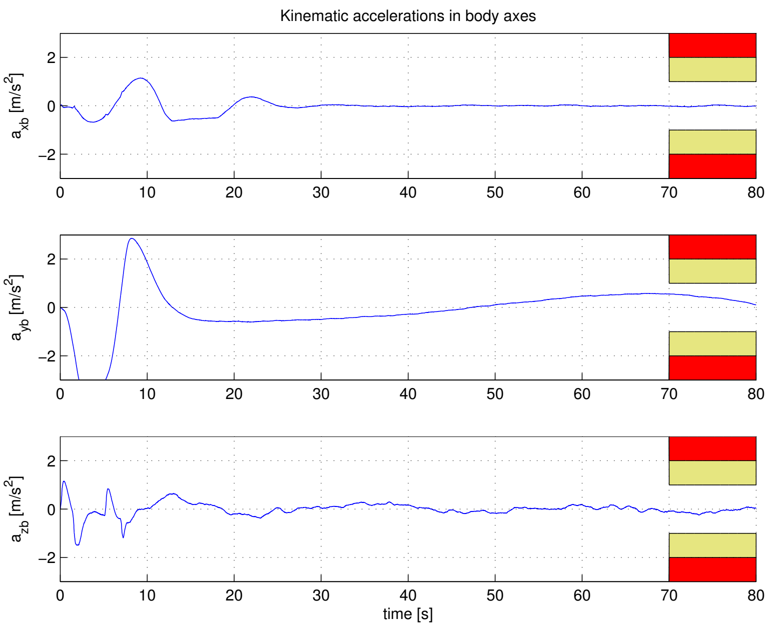

(b) kinematic accelerations

Figure B.10: Specifications on the aircraft states for the glideslope intercept qualification manoeuvre

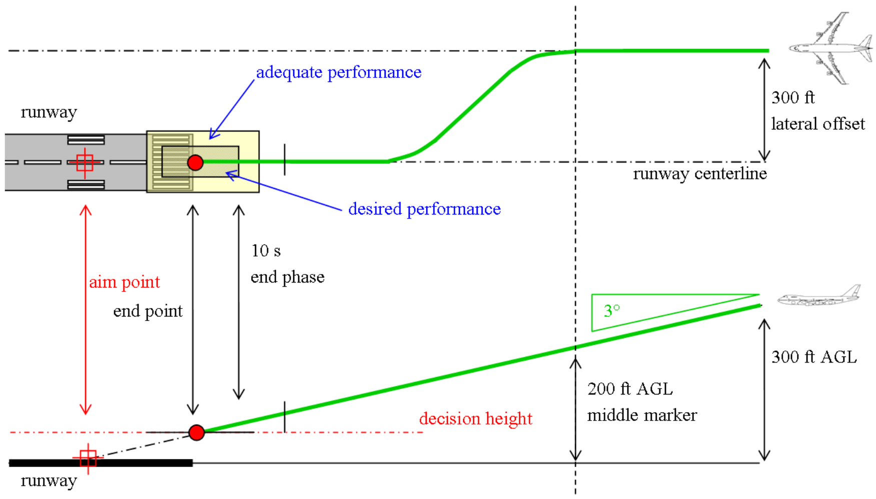

Figure B.11: Definition of performance boxes for approach with sidestep qualification manoeuvre

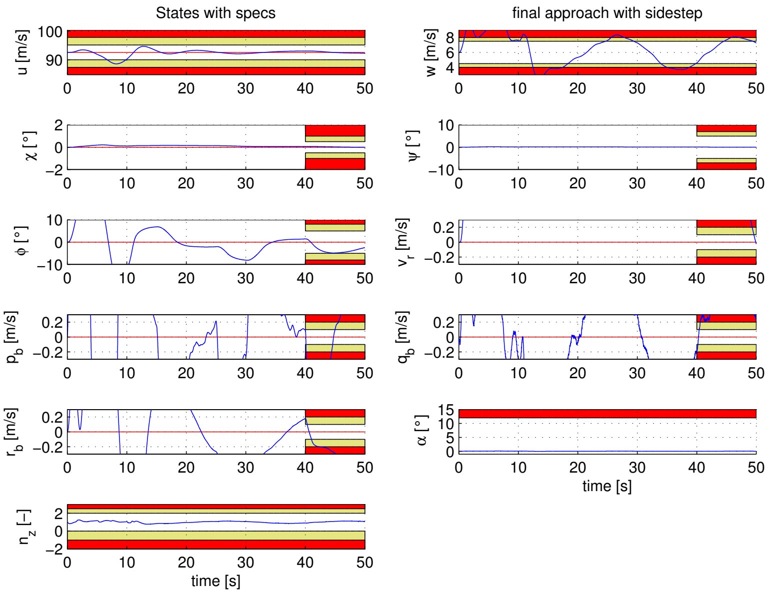

(a) aircraft states

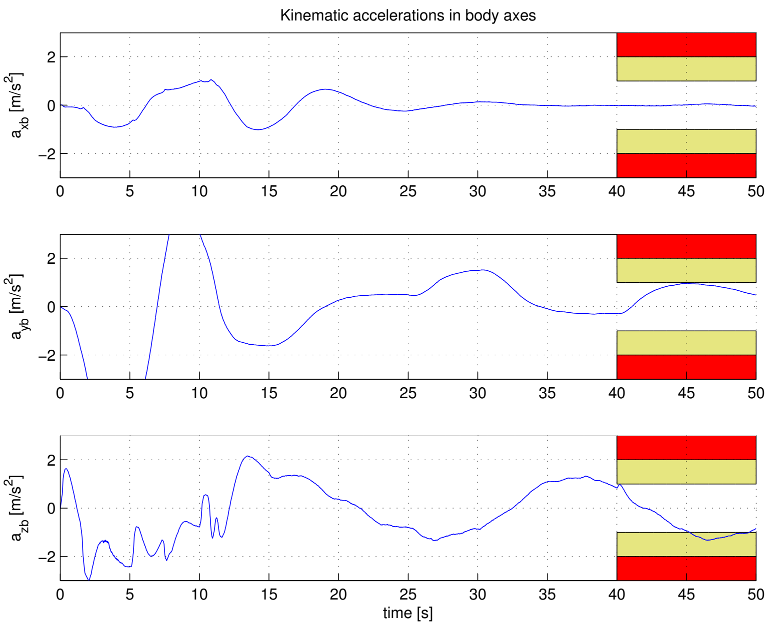

(b) kinematic accelerations

Figure B.12: Specifications on the aircraft states for the final approach with sidestep qualification manoeuvre

Table B.6: Summary of all benchmark assessment quantities and their relevance for each qualification test manoeuvre

symbol	description	straight flight	right turn LOC int	glideslope intercept	final approach
x_{runway}	longitudinal distance from runway threshold		✓	✓	
x	longitudinal position				✓
y	lateral position				✓
Δx	longitudinal deviation at end-point				✓
Δy	lateral deviation at end-point				✓
Δh	altitude deviation		✓		
u	forward velocity				✓
v_r	transversal velocity above runway at end-point				✓
w	vertical velocity				✓
V	velocity	✓	✓	✓	
ϕ	roll angle	✓	✓		✓
θ	pitch attitude angle				
ψ	heading angle				✓
p	roll rate during end-phase	✓	✓	✓	✓
q	pitch rate during end-phase	✓	✓	✓	✓
r	yaw rate during end-phase	✓	✓	✓	✓
a_x	longitudinal acceleration during end-phase	✓	✓	✓	✓
a_y	lateral acceleration during end-phase	✓	✓	✓	✓
a_z	vertical acceleration during end-phase	✓	✓	✓	✓
α	angle of attack	✓	✓	✓	✓
β	sideslip angle	✓	✓		
γ	flight path angle	✓			
χ	track angle	✓			✓
λ	localizer deviation		✓	✓	
Γ	glideslope deviation			✓	
Λ	LOC intercept angle		✓		
A_y	lateral specific force		✓		
n_z	load factor	✓	✓	✓	✓
t	time	✓	✓	✓	✓

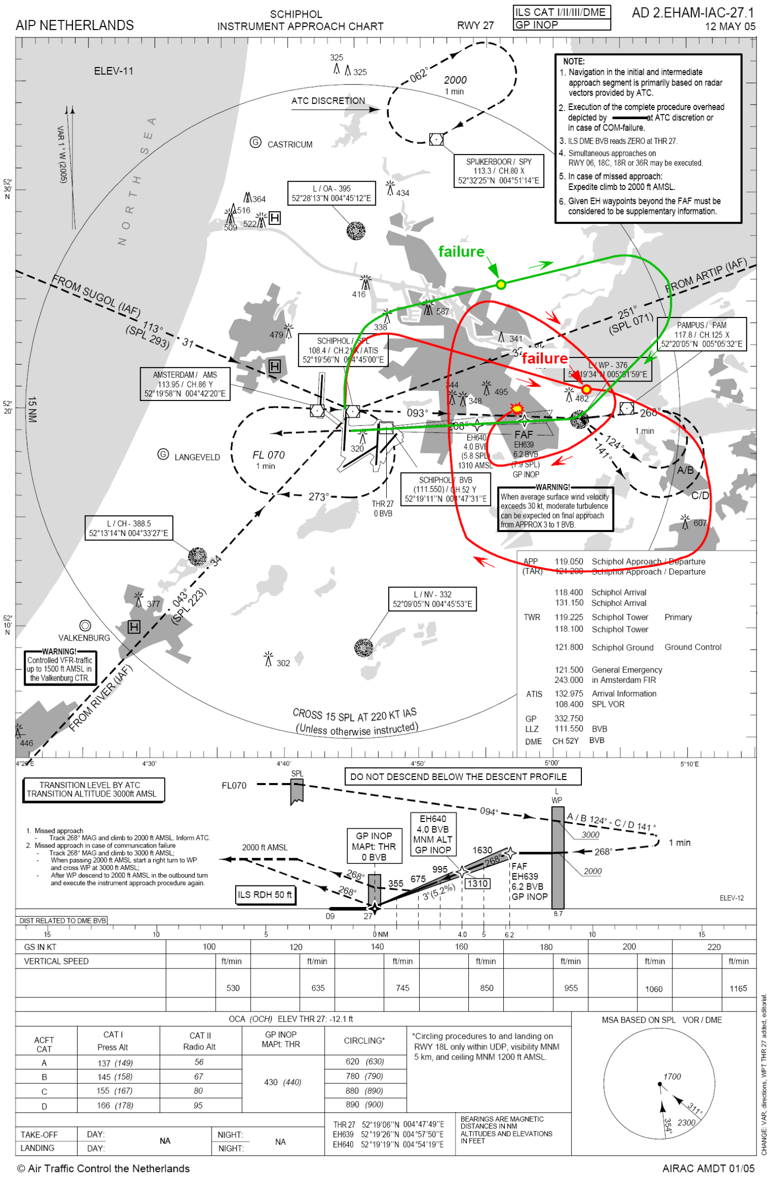

: flight path of the El Al flight 1862 accident aircraft

: proposed benchmark scenario

Appendix C

Iterated Linear Filter Smoother and Unscented Kalman Filter

As described in section 3.3, the Kalman filtering algorithm has been designed to estimate the state vector for linear systems. In practice however, the system and measurement equations turn out to be nonlinear most of the time, especially in aerospace applications. If the model turns out to be nonlinear, the Extended Kalman Filter (EKF), which is a form of the Kalman Filter ”extended” to nonlinear dynamical systems, can be applied to estimate the state vector, as described in section 3.3.2.2. The Iterated Extended Kalman Filter (IEKF), described in section 4.1.2, contains an iteration procedure in the correction step in order to deal with significant nonlinearities in the observation model, which cannot be captured by means of the first order gradient in the EKF. Analogously, a modification is needed when also the kinematics model contains significant nonlinearities. The algorithms suitable for this purpose are the Iterated Linear Filter Smoother ILFS and the Unscented Kalman Filter UKF.

C.1 Iterated linear filter smoother, source: [35]

1. one step ahead prediction (time propagation):

$$\boldsymbol{\xi}_1 = \hat{\mathbf{x}}(k\,|k) \qquad \boldsymbol{\xi}_i = \boldsymbol{\xi}_2 \tag{C.1}$$

$$\mathbf{x}^*(k+1;\boldsymbol{\xi}_i) = \boldsymbol{\xi}_i + \int\limits_k^{k+1} \mathbf{f}(\boldsymbol{\xi}_i, \mathbf{u}_m(t), \boldsymbol{\theta}, t)\,dt \tag{C.2}$$

$$\begin{aligned}\boldsymbol{\eta}_1 &= \hat{\mathbf{x}}(k+1\,|k) \\ &= \mathbf{x}^*(k+1;\boldsymbol{\xi}_i) + \boldsymbol{\Phi}(k+1,k;\boldsymbol{\xi}_i)\left[\hat{\mathbf{x}}(k\,|k) - \boldsymbol{\xi}_i\right]\end{aligned} \tag{C.3}$$

2. prediction of covariance matrix of the state prediction error vector:

$$\begin{aligned}\mathbf{P}(k+1|\,k) &= \boldsymbol{\Phi}(k+1,k;\boldsymbol{\xi}_i)\,\mathbf{P}(k\,|k)\,\boldsymbol{\Phi}^T(k+1,k;\boldsymbol{\xi}_i) + \\ &\quad + \mathbf{Q}_d(k+1)\end{aligned} \tag{C.4}$$

3. Kalman gain

$$\begin{aligned}\mathbf{K}(k+1) &= \mathbf{P}(k+1\,|k)\,\mathbf{H}^T(k+1;\boldsymbol{\eta}_i) \times \\ &\quad \times \left[\mathbf{H}(k+1;\boldsymbol{\eta}_i)\,\mathbf{P}(k+1\,|k)\,\mathbf{H}^T(k+1;\boldsymbol{\eta}_i) + \mathbf{R}(k+1)\right]^{-1}\end{aligned} \tag{C.5}$$

where:

$$\mathbf{H}(k) = \left.\frac{\partial \mathbf{h}(\mathbf{x}(t), \mathbf{u}_m(t), \boldsymbol{\theta}, t)}{\partial \mathbf{x}(t)}\right|_{\mathbf{x}=\boldsymbol{\eta}_i} \tag{C.6}$$

4. measurement update step

$$\begin{aligned}\boldsymbol{\eta}_2 &= \hat{\mathbf{x}}(k+1\,|k) + \mathbf{K}(k+1)\left[\mathbf{z}(k+1) - \mathbf{h}(\boldsymbol{\eta}_1) + \right. \\ &\quad \left. -\mathbf{H}(k+1;\boldsymbol{\eta}_1)(\hat{\mathbf{x}}(k+1\,|k) - \boldsymbol{\eta}_1)\right]\end{aligned} \tag{C.7}$$

$$\mathbf{S}(k;\boldsymbol{\xi}_i) = \mathbf{P}(k|k)\,\boldsymbol{\Phi}^T(k+1,k,\boldsymbol{\xi}_i)\,\mathbf{P}^{-1}(k+1|k) \tag{C.8}$$

$$\boldsymbol{\xi}_2 = \hat{\mathbf{x}}(k\,|k) + \mathbf{S}(k;\boldsymbol{\xi}_i)\left[\boldsymbol{\eta}_2 - \hat{\mathbf{x}}(k+1\,|k)\right] \tag{C.9}$$

$$\varepsilon_1 = \frac{\|\boldsymbol{\eta}_2 - \boldsymbol{\eta}_1\|}{\|\boldsymbol{\eta}_2\|},\ \varepsilon_2 = \frac{\|\boldsymbol{\xi}_2 - \boldsymbol{\xi}_1\|}{\|\boldsymbol{\xi}_2\|} \tag{C.10}$$

repeat steps 1 till 4 as long as $|\epsilon| > |\epsilon_{crit}|$
As soon as $|\epsilon| \le |\epsilon_{crit}|$:

$$\hat{\mathbf{x}}(k+1\,|k+1) = \boldsymbol{\eta}_2 \tag{C.11}$$

5. update covariance matrix of state estimation error vector

$$\begin{aligned}\mathbf{P}\left(k+1|\,k+1\right) &= \left[\mathbf{I}-\mathbf{K}\left(k+1\right)\mathbf{H}\left(k+1\right)\right]\mathbf{P}\left(k+1\,|k\right)\times \\ &\quad \times\left[\mathbf{I}-\mathbf{K}\left(k+1\right)\mathbf{H}\left(k+1\right)\right]^{T}+ \\ &\quad +\mathbf{K}\left(k+1\right)\mathbf{R}\left(k+1\right)\mathbf{K}^{T}\left(k+1\right)\end{aligned} \tag{C.12}$$

where:

$$\mathbf{H}(k)=\left.\frac{\partial\mathbf{h}\left(\mathbf{x}(t),\mathbf{u}_m(t),\boldsymbol{\theta},t\right)}{\partial\mathbf{x}(t)}\right|_{\mathbf{x}=\hat{\mathbf{x}}_{k|k}} \tag{C.13}$$

The Iterated Linear Filter Smoother, illustrated in fig. C.1, is one step further than the IEKF in the scale of complexity and iteration loops. This filter is ideally suited for situations where not only the observation model, but also the kinematics model has significant nonlinearities which cannot be captured by one local derivative $\mathbf{F}$ alone. The first step of the ILFS shows major similarities with the regular EKF, except for the fact that the difference between the predicted one step ahead state estimate and the final result, together with the sensitivity $\mathbf{S}$, determines a correction on the initial state estimate at time step k, as can be seen in fig. C.1(a). In the subsequent steps, a prediction is made in two steps, based upon the corrected initial state estimate at time step k, where the extent of the second prediction step is determined by the extent of the initial state estimate correction at time step k, as is illustrated in fig. C.1(b). Subsequent correction operations are analogous as in step 1. Both iteration procedures continue until the difference between two successive correction updates for $\boldsymbol{\xi}$ as well as $\boldsymbol{\eta}$ are below a predefined threshold.

C.2 Unscented Kalman filter

Initialize with:

$$\begin{aligned}\hat{\mathbf{x}}_0 &= E\left[\mathbf{x_0}\right] \\ \mathbf{P}_0 &= E\left[\left(\mathbf{x_0}-\hat{\mathbf{x}}_0\right)\left(\mathbf{x_0}-\hat{\mathbf{x}}_0\right)^T\right] \\ \hat{\mathbf{x}}_0^a=E\left[\mathbf{x}_0^a\right] &= \begin{bmatrix}\hat{\mathbf{x}}_0^T & 0 & 0\end{bmatrix}^T \\ \mathbf{P}_0^a=E\left[\left(\mathbf{x}_0^a-\hat{\mathbf{x}}_0^a\right)\left(\mathbf{x}_0^a-\hat{\mathbf{x}}_0^a\right)^T\right] &= \begin{bmatrix}\mathbf{P}_0 & 0 & 0\\ 0 & \mathbf{P}_v & 0\\ 0 & 0 & \mathbf{P}_n\end{bmatrix}\end{aligned} \tag{C.14}$$

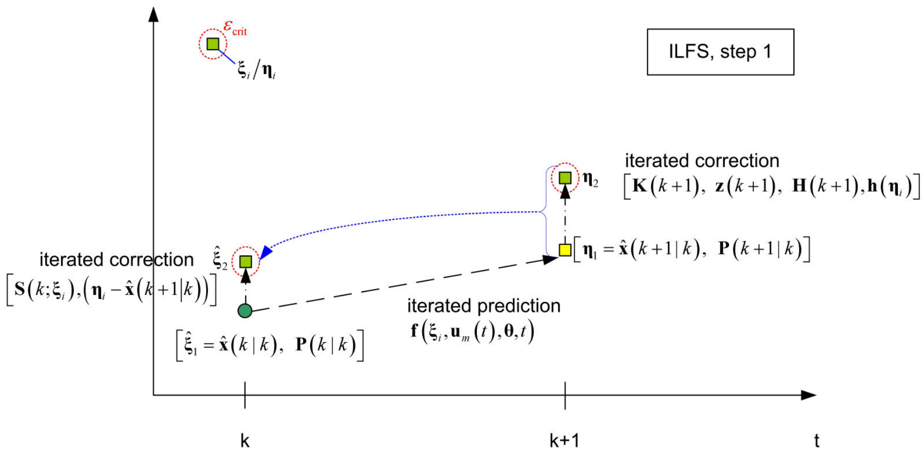

(a) ILFS working principle step 1

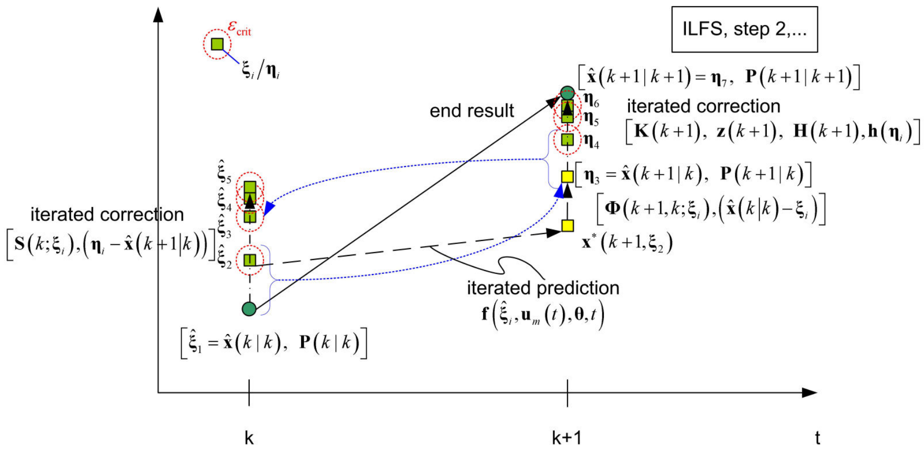

(b) ILFS working principle step 2 etc.

Figure C.1: Working principle of the Iterated Linear Filter Smoother

For $k \in \{1, \ldots, \infty\}$,
Calculate sigma points:

$$\boldsymbol{\mathcal{X}}^a_{k-1} = \left[\hat{\mathbf{x}}^a_{k-1} \ \ \hat{\mathbf{x}}^a_{k-1} \pm \sqrt{(L+\lambda)\mathbf{P}^a_{k-1}}\right] \tag{C.15}$$

Time update:

$$
\begin{aligned}
\boldsymbol{\mathcal{X}}^x_{k|k-1} &= \mathbf{F}\left[\boldsymbol{\mathcal{X}}^x_{k-1}, \boldsymbol{\mathcal{X}}^v_{k-1}\right] && \text{(C.16)}\\
\hat{\mathbf{x}}^-_k &= \sum_{i=0}^{2L} W_i^{(m)} \mathcal{X}^x_{i,k|k-1} && \text{(C.17)}\\
\mathbf{P}^-_k &= \sum_{i=0}^{2L} W_i^{(c)} \left[\mathcal{X}^x_{i,k|k-1} - \hat{\mathbf{x}}^-_k\right]\left[\mathcal{X}^x_{i,k|k-1} - \hat{\mathbf{x}}^-_k\right]^T && \text{(C.18)}\\
\boldsymbol{\mathcal{Y}}_{k|k-1} &= \mathbf{H}\left[\boldsymbol{\mathcal{X}}^x_{k-1}, \boldsymbol{\mathcal{X}}^n_{k-1}\right] && \text{(C.19)}\\
\hat{\mathbf{y}}^-_k &= \sum_{i=0}^{2L} W_i^{(m)} \mathcal{Y}_{i,k|k-1} && \text{(C.20)}
\end{aligned}
$$

Measurement update equations:

$$
\begin{aligned}
\mathbf{P}_{\tilde{\mathbf{y}}_k\tilde{\mathbf{y}}_k} &= \sum_{i=0}^{2L} W_i^{(c)} \left[\mathcal{Y}_{i,k|k-1} - \hat{\mathbf{y}}^-_k\right]\left[\mathcal{Y}_{i,k|k-1} - \hat{\mathbf{y}}^-_k\right]^T && \text{(C.21)}\\
\mathbf{P}_{\mathbf{x}_k\mathbf{y}_k} &= \sum_{i=0}^{2L} W_i^{(c)} \left[\mathcal{X}_{i,k|k-1} - \hat{\mathbf{x}}^-_k\right]\left[\mathcal{Y}_{i,k|k-1} - \hat{\mathbf{y}}^-_k\right]^T && \text{(C.22)}\\
\mathcal{K} &= \mathbf{P}_{\mathbf{x}_k\mathbf{y}_k}\mathbf{P}^{-1}_{\tilde{\mathbf{y}}_k\tilde{\mathbf{y}}_k} && \text{(C.23)}\\
\hat{\mathbf{x}}_k &= \hat{\mathbf{x}}^-_k + \mathcal{K}(\mathbf{y}_k - \hat{\mathbf{y}}^-_k) && \text{(C.24)}\\
\mathbf{P}_k &= \mathbf{P}^-_k - \mathcal{K}\mathbf{P}_{\tilde{\mathbf{y}}_k\tilde{\mathbf{y}}_k}\mathcal{K}^T && \text{(C.25)}
\end{aligned}
$$

where $\mathbf{x}^a = \begin{bmatrix}\mathbf{x}^T & \mathbf{v}^T & \mathbf{n}^T\end{bmatrix}^T$, $\boldsymbol{\mathcal{X}}^a = \begin{bmatrix}(\boldsymbol{\mathcal{X}}^x)^T & (\boldsymbol{\mathcal{X}}^v)^T & (\boldsymbol{\mathcal{X}}^n)^T\end{bmatrix}^T$, λ = composite scaling parameter, L = dimension of augmented state, $\mathbf{P}_v$ = process noise covariance, $\mathbf{P}_n$ = measurement noise covariance, W_i = weights calculated as follows:

$$
\begin{aligned}
W_0^{(m)} &= \frac{\lambda}{L+\lambda}\\
W_0^{(c)} &= \frac{\lambda}{L+\lambda} + (1-\alpha^2+\beta)\\
W_i^{(m)} &= W_i^{(c)} = \frac{1}{2(L+\lambda)} \quad i = 1,\ldots,2L
\end{aligned}
$$

where $\lambda = \alpha^2(L+\kappa) - L$ is a scaling parameter. α determines the spread of the sigma points around $\overline{\mathbf{x}}$ and is usually set to a small positive value (e.g., 1e-3). κ is a secondary scaling parameter which is usually set to 0, and β is used to incorporate prior knowledge of the distribution of $\mathbf{x}$ (for Gaussian distributions, $\beta = 2$ is optimal).

The Unscented Kalman Filter is an alternative for systems with considerable nonlinearities in the models. Its working principle is illustrated in fig. C.2. Thanks to the use of a

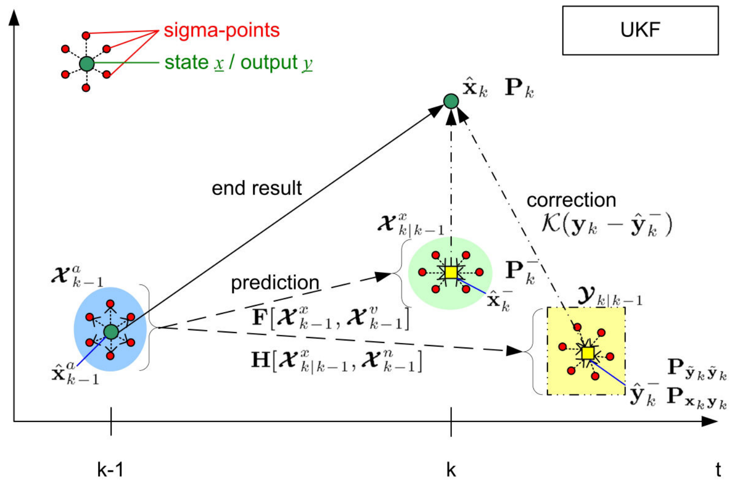

Figure C.2: Working principle of the Unscented Kalman Filter

local grid of so-called sigma-points, the method is less sensitive for the occurrence of local minima. Moreover, the working principle of this filter avoids the need to calculate time derivatives $\mathbf{F}$ and $\mathbf{H}$ of the kinematics $\mathbf{f}$ and observation $\mathbf{h}$ models respectively. For the initial state estimate, a number of sigma points is determined, dependent on the number of process and observation noise signals. State as well as sigma points are used to calculate predictions of one step ahead state estimates as well as observations. Taking the weighted average of these mapped sigma points results in estimates of the one step ahead state estimation and observation. These, combined with the actual measured output, can be used for the correction step. However, each additional source of process and observation noise leads to the necessity of an additional sigma point. This makes that for realistic flight path reconstruction applications, a considerable amount of sigma points must be determined, which on its turn causes the method to work considerably more slowly than the ILFS.

Appendix D

Complete set of identification results from section 4.5

Figures D.1 and D.2 show the effect of these failure scenarios on the different aerodynamic derivatives. One of the observations is that a longitudinal failure, like the stabilizer run-away, has no significant influence on the aerodynamic derivatives of the asymmetric force and moments in figure D.2, as well as vice versa for the influence of the tail loss on the symmetrical aerodynamic forces and moment derivatives in figure D.1. Note also that there is no asymmetric damage for both failures, leading to no significant identification results for the cross coupling contributions.

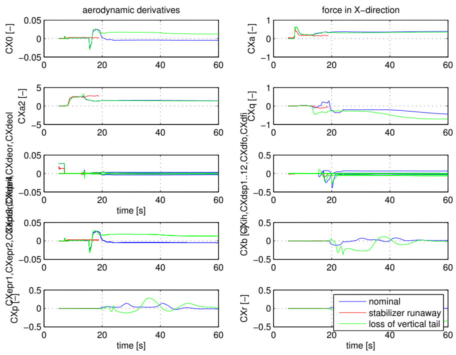

(a) aerodynamic derivatives of force X

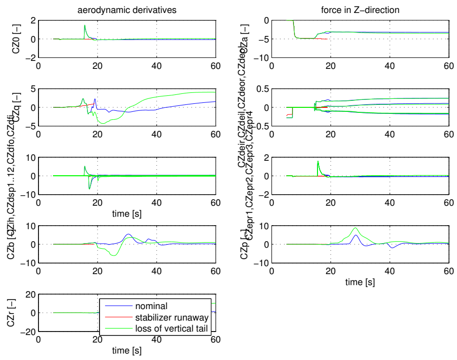

(b) aerodynamic derivatives of force Z

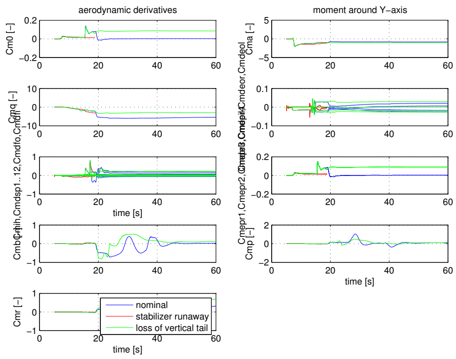

(c) aerodynamic derivatives of moment M around Y-axis

Figure D.1: Aerodynamic derivatives of symmetric forces and moments for a high-fidelity damaged Boeing 747 simulation model for both failure scenarios

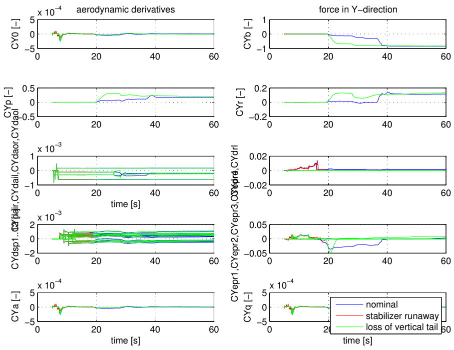

(a) aerodynamic derivatives of force Y, part 1

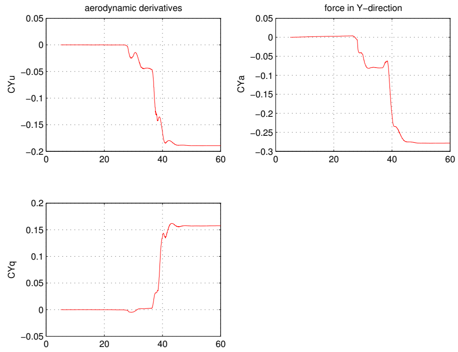

(b) aerodynamic derivatives of force Y, part 2

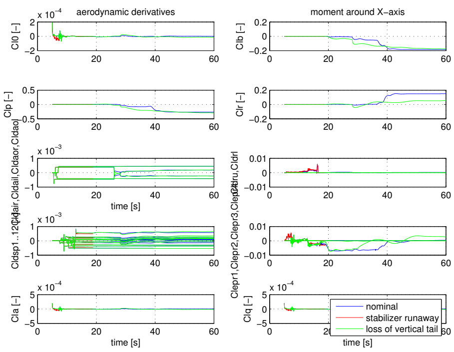

(c) aerodynamic derivatives of moment L around X-axis, part 1

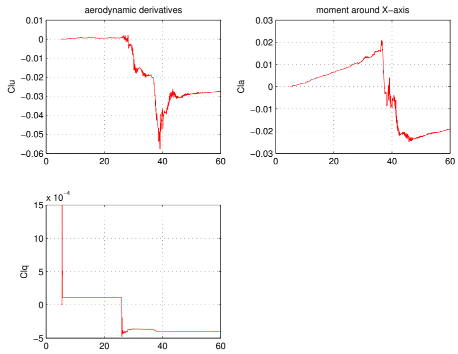

(d) aerodynamic derivatives of moment L around X-axis, part 2

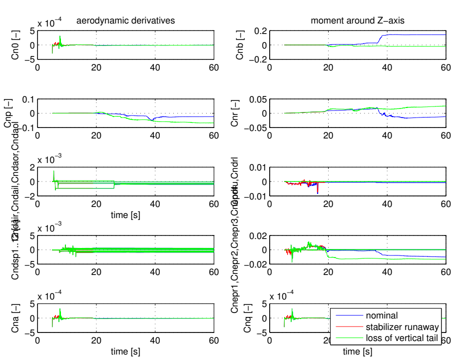

(e) aerodynamic derivatives of moment N around Z-axis, part 1

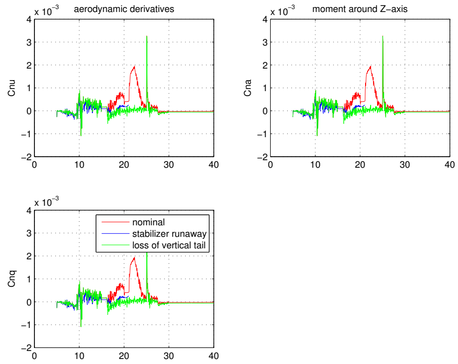

(f) aerodynamic derivatives of moment N around Z-axis, part 2

Figure D.2: Aerodynamic derivatives of asymmetric forces and moments for a high-fidelity damaged Boeing 747 simulation model for both failure scenarios

Appendix E

Update of equations of motion for changing mass properties

The definitions of the different reference frames and vectors for non coinciding reference frame origin and center of gravity are shown in fig. E.1. This nomenclature is used throughout the appendix.

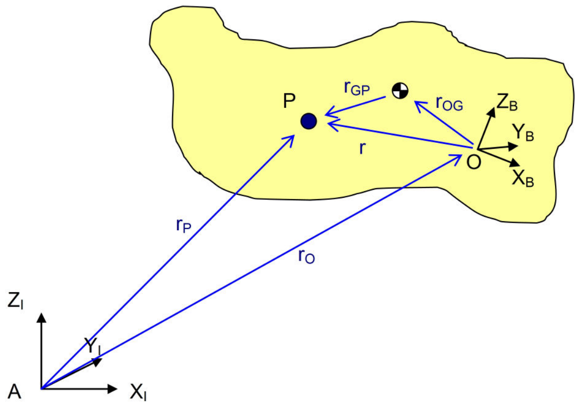

Figure E.1: Definition of reference frames and vectors

E.1 Translational acceleration with changing mass properties

The standard equations for the linear accelerations as defined from (4.15) till (4.17) need to be expanded for the fact that the origin of the frame of reference does not coincide with the center of gravity after its shift.

A force acting on a point mass is equal to the change of momentum of that point mass in time:

$$d\mathbf{F}_P = \frac{d}{dt}\left(dm\mathbf{V}_{I,P}\right)^I$$

Where $d\mathbf{F}_P$ is the exerted force vector, dm is the mass of the point mass P and $\mathbf{V}_{I,P}$ is the time varying inertial velocity vector of point mass P. For a body, the summation of the external forces is equal to the integration of the momenta of each point mass in the body: $\sum\limits_P d\mathbf{F}_{\text{ext}_\text{P}} = \frac{d}{dt}\left(\int\limits_m \mathbf{V}_{I,P}dm\right)^I$ where the velocity vector of the point mass P can be defined as (see figure E.1): $\frac{d\mathbf{r}_P^I}{dt} = \frac{d\mathbf{r}_O^I}{dt} + \frac{d\mathbf{r}^I}{dt} \quad \rightarrow \quad \mathbf{V}_{I,P} = \mathbf{V}_{I,O} + \frac{d\mathbf{r}^I}{dt}$ which results in:

$$\sum_P d\mathbf{F}_{\text{ext}_\text{P}} = \frac{d}{dt}\left(\int\limits_m \left\{\mathbf{V}_{I,O} + \frac{d\mathbf{r}^I}{dt}\right\} dm\right)^I$$

wherein:

$$\begin{aligned}
\int\limits_m \left\{\mathbf{V}_{I,O} + \tfrac{d\mathbf{r}^I}{dt}\right\} dm &= \int\limits_m \mathbf{V}_{I,O}dm + \int\limits_m \tfrac{d\mathbf{r}^I}{dt}dm \\
&= \mathbf{V}_{I,O}\int\limits_m dm + \int\limits_m \tfrac{d\mathbf{r}^I}{dt}dm \\
&= \mathbf{V}_{I,O}m + \int\limits_m \tfrac{d\mathbf{r}^I}{dt}dm
\end{aligned}$$

Combining both previous results:

$$\sum_P d\mathbf{F}_{\text{ext}_\text{P}} = \frac{d}{dt}\left(\mathbf{V}_{I,O}m + \int\limits_m \frac{d\mathbf{r}^I}{dt}dm\right)^I$$

Considering instantaneous mass changes and thus $\frac{dm}{dt} = 0$:

$$\sum_P d\mathbf{F}_{\text{ext}_\text{P}} = m\left(\frac{d\mathbf{V}_{I,O}}{dt}\right)^I + \frac{d}{dt}\left(\int\limits_m \frac{d\mathbf{r}^I}{dt}dm\right)^I$$

Mind that all variables in this expression are inertial.

Generally, a conversion of a time derivative of vector $\mathbf{r}$ between 2 different frames of reference can be defined as: $\left(\frac{d\mathbf{r}}{dt}\right)^2 = \left(\frac{d\mathbf{r}}{dt}\right)^1 + \mathbf{\Omega}_{12}^1 \times \mathbf{r}$

Implementing for $\mathbf{V}$ and $\mathbf{r}$ in the conversion from inertial to body for the above inertial expression:

$$\sum_P d\mathbf{F}_{\mathrm{ext_P}} = m\left(\frac{d\mathbf{V}_{B,O}}{dt}\right)^B + m\mathbf{\Omega}_{BI}^B \times \mathbf{V}_{B,O} + \frac{d}{dt}\left(\int\limits_m \left(\frac{d\mathbf{r}^B}{dt} + \mathbf{\Omega}_{BI}^B \times \mathbf{r}^B\right) dm\right)^I$$

wherein $\frac{d\mathbf{r}^B}{dt} = 0$, since the body is considered to be rigid, thus:

$$\sum_P d\mathbf{F}_{\mathrm{ext_P}} = m\left(\frac{d\mathbf{V}_{B,O}}{dt}\right)^B + m\mathbf{\Omega}_{BI}^B \times \mathbf{V}_{B,O} + \frac{d}{dt}\left(\int\limits_m \mathbf{\Omega}_{BI}^B \times \mathbf{r}^B dm\right)^I$$

For continuous differentiable functions hold:

$$\sum_P d\mathbf{F}_{\mathrm{ext_P}} = m\left(\frac{d\mathbf{V}_{B,O}}{dt}\right)^B + m\mathbf{\Omega}_{BI}^B \times \mathbf{V}_{B,O} + \int\limits_m \frac{d}{dt}\left(\mathbf{\Omega}_{BI}^B \times \mathbf{r}^B\right)^I dm$$

where:

$$\begin{aligned} \frac{d}{dt}\left(\mathbf{\Omega}_{BI}^B \times \mathbf{r}^B\right)^I &= \frac{d}{dt}\left(\mathbf{\Omega}_{BI}^B \times \mathbf{r}^B\right)^B + \mathbf{\Omega}_{BI}^B \times \left(\mathbf{\Omega}_{BI}^B \times \mathbf{r}^B\right) \\ &= \frac{d\mathbf{\Omega}_{BI}^B}{dt} \times \mathbf{r}^B + \mathbf{\Omega}_{BI}^B \times \underbrace{\frac{d\mathbf{r}^B}{dt}}_{=0} + \mathbf{\Omega}_{BI}^B \times \left(\mathbf{\Omega}_{BI}^B \times \mathbf{r}^B\right) \\ &= \frac{d\mathbf{\Omega}_{BI}^B}{dt} \times \mathbf{r}^B + \mathbf{\Omega}_{BI}^B \times \left(\mathbf{\Omega}_{BI}^B \times \mathbf{r}^B\right) \end{aligned}$$

which leads to the following expression:

$$\sum_P d\mathbf{F}_{\mathrm{ext_P}} = m\left(\frac{d\mathbf{V}_{B,O}}{dt}\right)^B + m\mathbf{\Omega}_{BI}^B \times \mathbf{V}_{B,O} + \frac{d\mathbf{\Omega}_{BI}^B}{dt} \times \int\limits_m \mathbf{r}^B dm + \mathbf{\Omega}_{BI}^B \times \left(\mathbf{\Omega}_{BI}^B \times \int\limits_m \mathbf{r}^B dm\right)$$

Since it can be seen in the picture that $\mathbf{r}^B = \mathbf{r}_{OG}^B + \mathbf{r}_{GP}^B$ it follows that: $\int\limits_m \mathbf{r}^B dm = \int\limits_m \mathbf{r}_{OG}^B dm + \underbrace{\int\limits_m \mathbf{r}_{GP}^B dm}_{=0} = \mathbf{r}_{OG}^B \int\limits_m dm = \mathbf{r}_{OG}^B m$ since $\mathbf{r}_{OG}$ is constant for all mass elements P.

Define now $\mathbf{r}_{OG}^{B} = \mathbf{\Delta r} = \begin{bmatrix} \Delta x \\ \Delta y \\ \Delta z \end{bmatrix}$: $\int\limits_m \mathbf{r}^B dm = m\mathbf{\Delta r}$. This leads to the final result:

$$\sum_P d\mathbf{F}_{\mathrm{ext_P}} = m\left(\frac{d\mathbf{V}_{B,O}}{dt}\right)^B + m\mathbf{\Omega}_{BI}^B \times \mathbf{V}_{B,O} + m\frac{d\mathbf{\Omega}_{BI}^B}{dt} \times \mathbf{\Delta r} + m\mathbf{\Omega}_{BI}^B \times \left(\mathbf{\Omega}_{BI}^B \times \Delta r\right)$$

This expression simplifies to the conventional translational acceleration formulation for $\mathbf{r}_{OG} = \mathbf{\Delta r} = 0$.

The final result corresponds to the standard expression in the inertial reference frame, showing that

$$\sum_P d\mathbf{F}_{\mathrm{ext_P}} = m\mathbf{a}_{I,O}$$

It can be seen that the situation for changing mass properties is an extension to the standard situation.

Summarizing, one can write the following expression combining both previous one:

$$\mathbf{a}_{I,O} = \frac{d\mathbf{V}_{B,O}}{dt} + \frac{d\mathbf{\Omega}}{dt} \times \Delta\mathbf{r} + \mathbf{\Omega} \times (\mathbf{V}_{B,O} + \mathbf{\Omega} \times \Delta\mathbf{r})$$

with: $\mathbf{a}_{I,O} = \begin{bmatrix} a_x \\ a_y \\ a_z \end{bmatrix}$, $\mathbf{V}_{B,O} = \begin{bmatrix} u \\ v \\ w \end{bmatrix}$, $\mathbf{\Omega} = \begin{bmatrix} p \\ q \\ r \end{bmatrix}$, $\mathbf{\Delta r} = \begin{bmatrix} \Delta x \\ \Delta y \\ \Delta z \end{bmatrix}$ substituting and working out leads to:

$$\begin{aligned}
\begin{bmatrix} a_x \\ a_y \\ a_z \end{bmatrix} &= \begin{bmatrix} \dot{u} \\ \dot{v} \\ \dot{w} \end{bmatrix} + \begin{bmatrix} \dot{p} \\ \dot{q} \\ \dot{r} \end{bmatrix} \times \begin{bmatrix} \Delta x \\ \Delta y \\ \Delta z \end{bmatrix} + \begin{bmatrix} p \\ q \\ r \end{bmatrix} \times \begin{bmatrix} u \\ v \\ w \end{bmatrix} + \begin{bmatrix} p \\ q \\ r \end{bmatrix} \times \begin{bmatrix} p \\ q \\ r \end{bmatrix} \times \begin{bmatrix} \Delta x \\ \Delta y \\ \Delta z \end{bmatrix} \\
&= \begin{bmatrix} \dot{u} \\ \dot{v} \\ \dot{w} \end{bmatrix} + \begin{bmatrix} \dot{q}\Delta z - \dot{r}\Delta y \\ \dot{r}\Delta x - \dot{p}\Delta z \\ \dot{p}\Delta y - \dot{q}\Delta x \end{bmatrix} + \begin{bmatrix} qw - rv \\ ru - pw \\ pv - qu \end{bmatrix} + \begin{bmatrix} p \\ q \\ r \end{bmatrix} \times \begin{bmatrix} q\Delta z - r\Delta y \\ r\Delta x - p\Delta z \\ p\Delta y - q\Delta x \end{bmatrix} \\
&= \begin{bmatrix} \dot{u} \\ \dot{v} \\ \dot{w} \end{bmatrix} + \begin{bmatrix} qw - rv \\ ru - pw \\ pv - qu \end{bmatrix} + \begin{bmatrix} \dot{q}\Delta z - \dot{r}\Delta y \\ \dot{r}\Delta x - \dot{p}\Delta z \\ \dot{p}\Delta y - \dot{q}\Delta x \end{bmatrix} + \begin{bmatrix} pq\Delta y - q^2\Delta x - r^2\Delta x + pr\Delta z \\ qr\Delta z - r^2\Delta y - p^2\Delta y + pq\Delta x \\ pr\Delta x - p^2\Delta z - q^2\Delta z + qr\Delta y \end{bmatrix} \\
&= \begin{bmatrix} \dot{u} + qw - rv - \left(q^2 + r^2\right)\Delta x + (pq - \dot{r})\,\Delta y + (\dot{q} + pr)\,\Delta z \\ \dot{v} + ru - pw + (\dot{r} + pq)\,\Delta x - \left(p^2 + r^2\right)\Delta y + (qr - \dot{p})\,\Delta z \\ \dot{w} + pv - qu + (pr - \dot{q})\,\Delta x + (\dot{p} + qr)\,\Delta y - \left(p^2 + q^2\right)\Delta z \end{bmatrix}
\end{aligned}$$

$$\text{with } \mathbf{F}_{\text{tot}} = \mathbf{F}_A + \mathbf{F}_G$$

$$m\mathbf{a}_{I,O} = m\mathbf{A}_{I,O} + mg\mathbf{\Theta} \qquad \mathbf{\Theta} = \begin{bmatrix} -\sin\theta \\ \cos\theta\sin\phi \\ \cos\theta\cos\phi \end{bmatrix}$$

$$\mathbf{a}_{I,O} = \mathbf{A}_{I,O} + g\mathbf{\Theta} \quad \text{or} \quad \mathbf{A}_{I,O} = \mathbf{a}_{I,O} - g\mathbf{\Theta}$$

$$\begin{cases} A_x = a_x + g\sin\theta \\ A_y = a_y - g\cos\theta\sin\phi \\ A_z = a_z - g\cos\theta\cos\phi \end{cases}$$

$$\begin{cases} A_x = \dot{u} + qw - rv - \left(q^2 + r^2\right)\Delta x + (pq - \dot{r})\,\Delta y + (\dot{q} + pr)\,\Delta z + g\sin\theta \\ A_y = \dot{v} + ru - pw + (\dot{r} + pq)\,\Delta x - \left(p^2 + r^2\right)\Delta y + (qr - \dot{p})\,\Delta z - g\cos\theta\sin\phi \\ A_z = \dot{w} + pv - qu + (pr - \dot{q})\,\Delta x + (\dot{p} + qr)\,\Delta y - \left(p^2 + q^2\right)\Delta z - g\cos\theta\cos\phi \end{cases}$$

This can be used for the kinematics model as well as for the aerodynamic forces, by rewriting towards the time derivatives of the body velocity components:

$$\begin{cases} \dot{u} = A_x - g\sin\theta - qw + rv + \left(q^2 + r^2\right)\Delta x - (pq - \dot{r})\,\Delta y - (\dot{q} + pr)\,\Delta z \\ \dot{v} = A_y + g\cos\theta\sin\phi - ru + pw - (\dot{r} + pq)\,\Delta x + \left(p^2 + r^2\right)\Delta y - (qr - \dot{p})\,\Delta z \\ \dot{w} = A_z + g\cos\theta\cos\phi - pv + qu - (pr - \dot{q})\,\Delta x - (\dot{p} + qr)\,\Delta y + \left(p^2 + q^2\right)\Delta z \end{cases}$$

The measured values and their corrections for biases and noise must be substituted for specific forces and angular rates:

$$\begin{aligned}
\dot{u} &= (A_{x_m} - \lambda_x - w_x) - g\sin\theta - (q_m - \lambda_q - w_q)\,w + (r_m - \lambda_r - w_r)\,v + \\
&\quad + \left((q_m - \lambda_q - w_q)^2 + (r_m - \lambda_r - w_r)^2\right)\Delta x + \\
&\quad - \left((p_m - \lambda_p - w_p)\,(q_m - \lambda_q - w_q) - (\dot{r}_m - \dot{w}_r)\right)\Delta y + \\
&\quad - \left((\dot{q}_m - \dot{w}_q) + (p_m - \lambda_p - w_p)\,(r_m - \lambda_r - w_r)\right)\Delta z \\
\dot{v} &= (A_{y_m} - \lambda_y - w_y) + g\cos\theta\sin\phi - (r_m - \lambda_r - w_r)\,u + (p_m - \lambda_p - w_p)\,w + \\
&\quad - \left((\dot{r}_m - \dot{w}_r) + (p_m - \lambda_p - w_p)\,(q_m - \lambda_q - w_q)\right)\Delta x + \\
&\quad + \left((p_m - \lambda_p - w_p)^2 + (r_m - \lambda_r - w_r)^2\right)\Delta y + \\
&\quad - \left((q_m - \lambda_q - w_q)\,(r_m - \lambda_r - w_r) - (\dot{p}_m - \dot{w}_p)\right)\Delta z \\
\dot{w} &= (A_{z_m} - \lambda_z - w_z) + g\cos\theta\cos\phi - (p_m - \lambda_p - w_p)\,v + (q_m - \lambda_q - w_q)\,u + \\
&\quad - \left((p_m - \lambda_p - w_p)\,(r_m - \lambda_r - w_r) - (\dot{q}_m - \dot{w}_q)\right)\Delta x + \\
&\quad - \left((\dot{p}_m - \dot{w}_p) + (q_m - \lambda_q - w_q)\,(r_m - \lambda_r - w_r)\right)\Delta y + \\
&\quad + \left((p_m - \lambda_p - w_p)^2 + (q_m - \lambda_q - w_q)^2\right)\Delta z
\end{aligned}$$

The knowledge of the center of gravity position can be used to calculate the aerodynamic force components:

$$\begin{cases} X_a = m\left(\dot{u} + qw - rv - \left(q^2 + r^2\right)\Delta x + \left(pq - \dot{r}\right)\Delta y + \left(\dot{q} + pr\right)\Delta z + g\sin\theta\right) \\ Y_a = m\left(\dot{v} + ru - pw + \left(\dot{r} + pq\right)\Delta x - \left(p^2 + r^2\right)\Delta y + \left(qr - \dot{p}\right)\Delta z - g\cos\theta\sin\phi\right) \\ Z_a = m\left(\dot{w} + pv - qu + \left(pr - \dot{q}\right)\Delta x + \left(\dot{p} + qr\right)\Delta y - \left(p^2 + q^2\right)\Delta z - g\cos\theta\cos\phi\right) \end{cases}$$

By considering the specific forces the unknown mass is not needed:

$$\begin{cases} A_{X_a} = \dot{u} + qw - rv - \left(q^2 + r^2\right)\Delta x + \left(pq - \dot{r}\right)\Delta y + \left(\dot{q} + pr\right)\Delta z + g\sin\theta \\ A_{Y_a} = \dot{v} + ru - pw + \left(\dot{r} + pq\right)\Delta x - \left(p^2 + r^2\right)\Delta y + \left(qr - \dot{p}\right)\Delta z - g\cos\theta\sin\phi \\ A_{Z_a} = \dot{w} + pv - qu + \left(pr - \dot{q}\right)\Delta x + \left(\dot{p} + qr\right)\Delta y - \left(p^2 + q^2\right)\Delta z - g\cos\theta\cos\phi \end{cases}$$

E.2 Angular momentum with changing mass properties

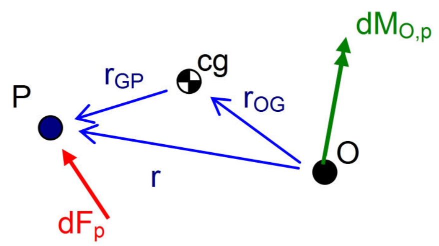

Figure E.2: Moment about center of mass due to force on point mass

A moment $d\mathbf{M}_{O,P}$ generated by a force $d\mathbf{F}_P$ around reference point O is equal to the cross product between the force vector $d\mathbf{F}_p$ and the relative distance vector $\mathbf{r}$:

$$d\mathbf{M}_{O,P} = \mathbf{r}^I \times d\mathbf{F}_P = \mathbf{r}^I \times \frac{d}{dt}\left(dm\mathbf{V}_{I,P}\right)^I$$

Furthermore, define the angular momentum as: $d\mathbf{B}^I_{O,P} = \mathbf{r}^I \times \left(\mathbf{V}_{I,P}dm\right)$. Differentiating the angular momentum leads to:

$$\begin{aligned} \frac{d\left(d\mathbf{B}^I_{O,P}\right)}{dt} &= \frac{d}{dt}\left(\mathbf{r}^I \times \left(\mathbf{V}_{I,P}dm\right)\right)^I \\ &= \frac{d\mathbf{r}^I}{dt} \times \left(\mathbf{V}_{I,P}dm\right) + \mathbf{r}^I \times \left(\frac{d\left(\mathbf{V}_{I,P}dm\right)}{dt}\right)^I \end{aligned}$$

Considering figure E.1, it can be seen that: $\frac{d\mathbf{r}^I}{dt} = \frac{d\mathbf{r}^I_P}{dt} - \frac{d\mathbf{r}^I_O}{dt} = \mathbf{V}_{I,P} - \mathbf{V}_{I,O}$. Substituting this in the above equation:

$$\frac{d\left(d\mathbf{B}_{O,P}^{I}\right)}{dt} = \left(\mathbf{V}_{I,P} - \mathbf{V}_{I,O}\right) \times \left(\mathbf{V}_{I,P}dm\right) + \mathbf{r}^{I} \times \left(\frac{d\left(\mathbf{V}_{I,P}dm\right)}{dt}\right)^{I}$$

Since $\mathbf{V}_{I,P} \times \mathbf{V}_{I,P} = 0$, this expression can be simplified to:

$$\frac{d\left(d\mathbf{B}_{O,P}^{I}\right)}{dt} = -\mathbf{V}_{I,O} \times \mathbf{V}_{I,P}dm + \mathbf{r}^{I} \times \left(\frac{d\left(\mathbf{V}_{I,P}dm\right)}{dt}\right)^{I}$$

This equation can be rewritten in:

$$\mathbf{r}^{I} \times \left(\frac{d\left(\mathbf{V}_{I,P}dm\right)}{dt}\right)^{I} = \frac{d\left(d\mathbf{B}_{O,P}^{I}\right)}{dt} + \mathbf{V}_{I,O} \times \mathbf{V}_{I,P}dm$$

This can be substituted in the definition of the moment:

$$d\mathbf{M}_{O,P} = \mathbf{r}^{I} \times d\mathbf{F}_{P} = \mathbf{r}^{I} \times \frac{d}{dt}\left(dm\mathbf{V}_{I,P}\right)^{I} = \frac{d\left(d\mathbf{B}_{O,P}^{I}\right)}{dt} + \mathbf{V}_{I,O} \times \mathbf{V}_{I,P}dm$$

Integrating over all mass elements leads to:

$$\begin{aligned}
\int\limits_{m} d\mathbf{M}_{O,P} &= \int\limits_{m} \left(\frac{d\left(d\mathbf{B}_{O,P}^{I}\right)}{dt} + \mathbf{V}_{I,O} \times \mathbf{V}_{I,P}dm\right) \\
\mathbf{M}_{O_{\text{ext}}} &= \frac{d}{dt}\left(\int\limits_{m} d\mathbf{B}_{O,P}^{I}\right) + \int\limits_{m} \mathbf{V}_{I,O} \times \mathbf{V}_{I,P}dm \\
&= \frac{d\mathbf{B}_{O}^{I}}{dt} + \int\limits_{m} \mathbf{V}_{I,O} \times \mathbf{V}_{I,P}dm
\end{aligned}$$

Since $\mathbf{V}_{I,O}$ is independent of the mass elements P, it is possible to write:

$$\begin{aligned}
\int\limits_{m} \mathbf{V}_{I,O} \times \mathbf{V}_{I,P}dm &= \mathbf{V}_{I,O} \times \int\limits_{m} \mathbf{V}_{I,P}dm \qquad \text{where :} \quad \mathbf{V}_{I,P} = \mathbf{V}_{I,O} + \frac{d\mathbf{r}^{I}}{dt} \\
&= \mathbf{V}_{I,O} \times \int\limits_{m} \left(\mathbf{V}_{I,O} + \frac{d\mathbf{r}^{I}}{dt}\right) dm \\
&= \underbrace{\mathbf{V}_{I,O} \times \mathbf{V}_{I,O}}_{=0} \int\limits_{m} dm + \mathbf{V}_{I,O} \times \int\limits_{m} \frac{d\mathbf{r}^{I}}{dt} dm
\end{aligned}$$

Moreover, since it can be seen in the picture that $\mathbf{r}^I = \mathbf{r}^I_{OG} + \mathbf{r}^I_{GP}$ it follows that:

$$\begin{aligned}
\int\limits_m \frac{d\mathbf{r}^I}{dt} dm &= \frac{d}{dt}\int\limits_m \mathbf{r}^I dm = \frac{d}{dt}\int\limits_m \mathbf{r}^I_{OG} dm + \frac{d}{dt}\underbrace{\int\limits_m \mathbf{r}^I_{GP} dm}_{=0} = \frac{d}{dt}\mathbf{r}^I_{OG}\int\limits_m dm = \\
&= \frac{d\mathbf{r}^I_{OG}}{dt} m = \left(\underbrace{\frac{d\mathbf{r}^B_{OG}}{dt}}_{=0} + \mathbf{\Omega}^B_{BI}\times\mathbf{r}^B_{OG}\right) m = \mathbf{\Omega}^B_{BI}\times\mathbf{r}^B_{OG} m
\end{aligned}$$

since $\mathbf{r}_{OG}$ is constant for all mass elements P and an instantaneous mass and center of gravity change are considered. This leads to the expression:

$$\mathbf{M}_{O_{\text{ext}}} = \frac{d\mathbf{B}^I_O}{dt} + \mathbf{V}_{I,O}\times\frac{d\mathbf{r}^I_{OG}}{dt} m = \frac{d\mathbf{B}^I_O}{dt} + \mathbf{V}_{I,O}\times\left(\mathbf{\Omega}^B_{BI}\times\mathbf{r}^B_{OG} m\right)$$

The angular momentum is defined as follows: $\mathbf{B}^I_O = \int\limits_m \mathbf{r}^I \times \mathbf{V}_{I,P} dm$

Since $\mathbf{V}_{I,P} = \mathbf{V}_{I,O} + \frac{d\mathbf{r}^I}{dt} = \mathbf{V}_{I,O} + \underbrace{\frac{d\mathbf{r}^B}{dt}}_{=0} + \mathbf{\Omega}^B_{BI}\times\mathbf{r}^B = \mathbf{V}_{I,O} + \mathbf{\Omega}^B_{BI}\times\mathbf{r}^B$ it follows that:

$$\begin{aligned}
\mathbf{B}^I_O &= \int\limits_m \mathbf{r}^I\times\left(\mathbf{V}_{I,O} + \mathbf{\Omega}^B_{BI}\times\mathbf{r}^B\right) dm \\
&= \int\limits_m \mathbf{r}^I\times\mathbf{V}_{I,O} dm + \int\limits_m \mathbf{r}^I\times\left(\mathbf{\Omega}^B_{BI}\times\mathbf{r}^B\right) dm
\end{aligned}$$

wherein:

$$\int\limits_m \mathbf{r}^I\times\mathbf{V}_{I,O} dm = -\int\limits_m \mathbf{V}_{I,O}\times\mathbf{r}^I dm = -\mathbf{V}_{I,O}\times\int\limits_m \mathbf{r}^I dm$$

Since it can be seen in the picture that $\mathbf{r}^I = \mathbf{r}^I_{OG} + \mathbf{r}^I_{GP}$ it follows that:

$$\int\limits_m \mathbf{r}^I dm = \int\limits_m \mathbf{r}^I_{OG} dm + \underbrace{\int\limits_m \mathbf{r}^I_{GP} dm}_{=0} = \mathbf{r}^I_{OG}\int\limits_m dm = \mathbf{r}^I_{OG} m$$

since $\mathbf{r}_{OG}$ is constant for all mass elements P. Define now $\mathbf{r}^I_{OG} = \mathbf{\Delta r} = \begin{bmatrix} \Delta x \\ \Delta y \\ \Delta z \end{bmatrix}$:

$\int_m \mathbf{r}^I dm = m\Delta r$, then it can be seen that:

$$
\begin{aligned}
\int_m \mathbf{r}^I \times \mathbf{V}_{I,O} dm &= -\mathbf{V}_{I,O} \times m\mathbf{\Delta r} \\
&= m\mathbf{\Delta r} \times \mathbf{V}_{I,O}
\end{aligned}
$$

Substituting this result in the expression for the angular momentum:

$$
\begin{aligned}
\mathbf{B}_O^I &= m\mathbf{\Delta r} \times \mathbf{V}_{I,O} + \int_m \mathbf{r}^I \times \left(\mathbf{\Omega}_{BI}^B \times \mathbf{r}^B \right) dm \\
&= m\mathbf{\Delta r} \times \mathbf{V}_{I,O} + I_O \mathbf{\Omega}_{BI}^B
\end{aligned}
$$

Expressed with respect to the body fixed frame of reference, this becomes:

$$
\mathbf{B}_O^B = m\mathbf{\Delta r} \times \mathbf{V}_{B,O} + I_O \mathbf{\Omega}_{BI}^B
$$

Now, the moment expression can be rewritten in the body fixed reference frame as follows:

$$
\mathbf{M}_{O_{\text{ext}}} = \frac{d\mathbf{B}_O^B}{dt} + \mathbf{\Omega}_{BI}^B \times \mathbf{B}_O^B + \mathbf{V}_{B,O} \times \left(\mathbf{\Omega}_{BI}^B \times m\mathbf{\Delta r} \right)
$$

Substituting $\mathbf{B}_O^B = m\mathbf{\Delta r} \times \mathbf{V}_{B,O} + I_O \mathbf{\Omega}_{BI}^B$ results in:

$$
\begin{aligned}
\mathbf{M}_{O_{\text{ext}}} &= m\mathbf{\Delta r} \times \frac{d\mathbf{V}_{B,O}}{dt} + I_O \frac{d\mathbf{\Omega}_{BI}^B}{dt} + \mathbf{\Omega}_{BI}^B \times (m\mathbf{\Delta r} \times \mathbf{V}_{B,O}) + \\
&\quad + \mathbf{\Omega}_{BI}^B \times I_O \mathbf{\Omega}_{BI}^B + \mathbf{V}_{B,O} \times \left(\mathbf{\Omega}_{BI}^B \times m\mathbf{\Delta r} \right)
\end{aligned}
$$

Relying on the Jacoby identity $\mathbf{a} \times (\mathbf{b} \times \mathbf{c}) + \mathbf{b} \times (\mathbf{c} \times \mathbf{a}) + \mathbf{c} \times (\mathbf{a} \times \mathbf{b}) = 0$, the following equality holds:

$$
\mathbf{\Omega}_{BI}^B \times (m\mathbf{\Delta r} \times \mathbf{V}_{B,O}) + \mathbf{V}_{B,O} \times \left(\mathbf{\Omega}_{BI}^B \times m\mathbf{\Delta r} \right) = -m\mathbf{\Delta r} \times \left(\mathbf{V}_{B,O} \times \mathbf{\Omega}_{BI}^B \right)
$$

Substituting this in the moment expression leads to the following result:

$$
\mathbf{M}_{O_{\text{ext}}} = m\mathbf{\Delta r} \times \frac{d\mathbf{V}_{B,O}}{dt} - m\mathbf{\Delta r} \times \left(\mathbf{V}_{B,O} \times \mathbf{\Omega}_{BI}^B \right) + I_O \frac{d\mathbf{\Omega}_{BI}^B}{dt} + \mathbf{\Omega}_{BI}^B \times I_O \mathbf{\Omega}_{BI}^B
$$

For $\mathbf{r}_{OG} = \mathbf{\Delta r} = 0$, this expression simplifies to the standard expression for the angular moment:

$$
\mathbf{M}_{\text{tot}} = \mathbf{I}\dot{\mathbf{\Omega}} + \mathbf{\Omega} \times \mathbf{I}\mathbf{\Omega}
$$

Summarizing, the following result has been obtained:

$$
\begin{aligned}
\mathbf{M}_{\text{tot}} &= \mathbf{M}_a + \mathbf{M}_g = \mathbf{M}_a + \boldsymbol{\Delta}\mathbf{r} \times \mathbf{W} \\
&= \mathbf{I}\dot{\boldsymbol{\Omega}} + m\Delta\mathbf{r} \times \dot{\mathbf{V}}_0 + \boldsymbol{\Omega} \times \mathbf{I}\boldsymbol{\Omega} - m\Delta\mathbf{r} \times (\mathbf{V}_0 \times \boldsymbol{\Omega}) \\
M_a &= \mathbf{I}\dot{\boldsymbol{\Omega}} + m\Delta\mathbf{r} \times \dot{\mathbf{V}}_0 + \boldsymbol{\Omega} \times \mathbf{I}\boldsymbol{\Omega} - m\Delta\mathbf{r} \times (\mathbf{V}_0 \times \boldsymbol{\Omega}) - \boldsymbol{\Delta}\mathbf{r} \times (mg\boldsymbol{\Theta})
\end{aligned}
$$

Substituting and working out leads to:

$$
\begin{aligned}
L &= \dot{p}I_{xx} + (pr - \dot{q})\,J_{xy} - (pq + \dot{r})\,J_{xz} + \left(r^2 - q^2\right) J_{yz} + qr\,(I_{zz} - I_{yy}) + \\
&\quad +m\,(\dot{w} - qu + pv - g\cos\phi\cos\theta)\,\Delta y - m\,(\dot{v} + ru - pw - g\cos\theta\sin\phi)\,\Delta z
\end{aligned} \tag{E.1}
$$

$$
\begin{aligned}
M &= -\,(\dot{p} + qr)\,J_{xy} + \dot{q}I_{yy} + (pq - \dot{r})\,J_{yz} + \left(p^2 - r^2\right) J_{xz} + pr\,(I_{xx} - I_{zz}) + \\
&\quad -m\,(\dot{w} + pv - qu - g\cos\theta\cos\phi)\,\Delta x + m\,(\dot{u} - rv + qw + g\sin\theta)\,\Delta z
\end{aligned} \tag{E.2}
$$

$$
\begin{aligned}
N &= (qr - \dot{p})\,J_{xz} - (\dot{q} + pr)\,J_{yz} + \dot{r}I_{zz} + \left(q^2 - p^2\right) J_{xy} + pq\,(I_{yy} - I_{xx}) + \\
&\quad +m\,(\dot{v} - pw + ru - g\sin\phi\cos\theta)\,\Delta x - m\,(\dot{u} + qw - rv + g\sin\theta)\,\Delta y
\end{aligned} \tag{E.3}
$$

This system of equations can be simplified by considering the specific forces in the center of gravity $A_{x_{cg}}$, $A_{y_{cg}}$ and $A_{z_{cg}}$:

$$
\begin{aligned}
L &= \dot{p}I_{xx} + (pr - \dot{q})\,J_{xy} - (pq + \dot{r})\,J_{xz} + \left(r^2 - q^2\right) J_{yz} + qr\,(I_{zz} - I_{yy}) + \\
&\quad +mA_{z_{cg}}\Delta y - mA_{y_{cg}}\Delta z
\end{aligned} \tag{E.4}
$$

$$
\begin{aligned}
M &= -\,(\dot{p} + qr)\,J_{xy} + \dot{q}I_{yy} + (pq - \dot{r})\,J_{yz} + \left(p^2 - r^2\right) J_{xz} + pr\,(I_{xx} - I_{zz}) + \\
&\quad -mA_{z_{cg}}\Delta x + mA_{x_{cg}}\Delta z
\end{aligned} \tag{E.5}
$$

$$
\begin{aligned}
N &= (qr - \dot{p})\,J_{xz} - (\dot{q} + pr)\,J_{yz} + \dot{r}I_{zz} + \left(q^2 - p^2\right) J_{xy} + pq\,(I_{yy} - I_{xx}) + \\
&\quad +mA_{y_{cg}}\Delta x - mA_{x_{cg}}\Delta y
\end{aligned} \tag{E.6}
$$

E.3 Mass sensitivity analysis

Force and moment equations can be grouped in known kinematic terms and unknown mass property components:

$$\begin{bmatrix} X \\ Y \\ Z \end{bmatrix} = \begin{bmatrix} \dot{u} + qw - rv + g\sin\theta & -\left(q^2 + r^2\right) & (pq - \dot{r}) & (\dot{q} + pr) \\ \dot{v} + ru - pw - g\cos\theta\sin\phi & (\dot{r} + pq) & -\left(p^2 + r^2\right) & (qr - \dot{p}) \\ \dot{w} + pv - qu - g\cos\theta\cos\phi & (pr - \dot{q}) & (\dot{p} + qr) & -\left(p^2 + q^2\right) \end{bmatrix} \begin{bmatrix} m \\ m\Delta x \\ m\Delta y \\ m\Delta z \end{bmatrix}$$

$$\begin{bmatrix} L \\ M \\ N \end{bmatrix} = \begin{bmatrix} \dot{p} & -qr & qr & (pr - \dot{q}) & -(pq + \dot{r}) & \left(r^2 - q^2\right) \\ pr & \dot{q} & -pr & -(\dot{p} + qr) & \left(p^2 - r^2\right) & (pq - \dot{r}) \\ -pq & pq & \dot{r} & \left(q^2 - p^2\right) & (qr - \dot{p}) & -(\dot{q} + pr) \end{bmatrix} \begin{bmatrix} I_{xx} \\ I_{yy} \\ I_{zz} \\ J_{xy} \\ J_{xz} \\ J_{yz} \end{bmatrix} +$$

$$+ \begin{bmatrix} 0 & A_{z_{cg}} & -A_{y_{cg}} \\ -A_{z_{cg}} & 0 & A_{x_{cg}} \\ A_{y_{cg}} & -A_{x_{cg}} & 0 \end{bmatrix} \begin{bmatrix} m\Delta x \\ m\Delta y \\ m\Delta z \end{bmatrix}$$

where the mass and inertia can be split in their original value and the change. This holds also for the forces and the moments. The original values are in equilibrium, which allows to leave them out:

$$\begin{bmatrix} \Delta X \\ \Delta Y \\ \Delta Z \end{bmatrix} = \begin{bmatrix} A_{x_{cg}} & -\left(q^2 + r^2\right) & (pq - \dot{r}) & (\dot{q} + pr) \\ A_{z_{cg}} & (\dot{r} + pq) & -\left(p^2 + r^2\right) & (qr - \dot{p}) \\ A_{z_{cg}} & (pr - \dot{q}) & (\dot{p} + qr) & -\left(p^2 + q^2\right) \end{bmatrix} \begin{bmatrix} \Delta m \\ (m_0 + \Delta m)\,\Delta x \\ (m_0 + \Delta m)\,\Delta y \\ (m_0 + \Delta m)\,\Delta z \end{bmatrix}$$

$$\begin{bmatrix} \Delta L \\ \Delta M \\ \Delta N \end{bmatrix} = \begin{bmatrix} \dot{p} & -qr & qr & (pr - \dot{q}) & -(pq + \dot{r}) & \left(r^2 - q^2\right) \\ pr & \dot{q} & -pr & -(\dot{p} + qr) & \left(p^2 - r^2\right) & (pq - \dot{r}) \\ -pq & pq & \dot{r} & \left(q^2 - p^2\right) & (qr - \dot{p}) & -(\dot{q} + pr) \end{bmatrix} \begin{bmatrix} \Delta I_{xx} \\ \Delta I_{yy} \\ \Delta I_{zz} \\ \Delta J_{xy} \\ \Delta J_{xz} \\ \Delta J_{yz} \end{bmatrix} +$$

$$+ \begin{bmatrix} 0 & A_{z_{cg}} & -A_{y_{cg}} \\ -A_{z_{cg}} & 0 & A_{x_{cg}} \\ A_{y_{cg}} & -A_{x_{cg}} & 0 \end{bmatrix} \begin{bmatrix} (m_0 + \Delta m)\,\Delta x \\ (m_0 + \Delta m)\,\Delta y \\ (m_0 + \Delta m)\,\Delta z \end{bmatrix}$$

where $\Delta m < 0$, no absolute judgement can be made about the inertia, but generally $\Delta I < 0$.

E.4 Mass sensitivity analysis of forces and moments

A sensitivity analysis can be performed of the forces and moments for variations in mass, inertia and center of gravity. The equations below present additional contributions to forces and moments due to these variations, as derived in appendix E.3:

$$\begin{bmatrix} \Delta X \\ \Delta Y \\ \Delta Z \end{bmatrix} = \begin{bmatrix} A_{x_{cg}} & -\left(q^2+r^2\right) & (pq-\dot{r}) & (\dot{q}+pr) \\ A_{y_{cg}} & (\dot{r}+pq) & -\left(p^2+r^2\right) & (qr-\dot{p}) \\ A_{z_{cg}} & (pr-\dot{q}) & (\dot{p}+qr) & -\left(p^2+q^2\right) \end{bmatrix} \cdot \begin{bmatrix} \Delta m \\ (m_0+\Delta m)\,\Delta x \\ (m_0+\Delta m)\,\Delta y \\ (m_0+\Delta m)\,\Delta z \end{bmatrix}$$

$$\begin{bmatrix} \Delta L \\ \Delta M \\ \Delta N \end{bmatrix} = \begin{bmatrix} \dot{p} & -qr & qr & (pr-\dot{q}) & -(pq+\dot{r}) & \left(r^2-q^2\right) \\ pr & \dot{q} & -pr & -(\dot{p}+qr) & \left(p^2-r^2\right) & (pq-\dot{r}) \\ -pq & pq & \dot{r} & \left(q^2-p^2\right) & (qr-\dot{p}) & -(\dot{q}+pr) \end{bmatrix} \begin{bmatrix} \Delta I_{xx} \\ \Delta I_{yy} \\ \Delta I_{zz} \\ \Delta J_{xy} \\ \Delta J_{xz} \\ \Delta J_{yz} \end{bmatrix} +$$

$$+ \begin{bmatrix} 0 & A_{z_{cg}} & -A_{y_{cg}} \\ -A_{z_{cg}} & 0 & A_{x_{cg}} \\ A_{y_{cg}} & -A_{x_{cg}} & 0 \end{bmatrix} \cdot \begin{bmatrix} (m_0+\Delta m)\,\Delta x \\ (m_0+\Delta m)\,\Delta y \\ (m_0+\Delta m)\,\Delta z \end{bmatrix}$$

These equations have been derived in appendix E.3 and are useful for analysis purposes in simulations, where the changes in mass, inertia and center of gravity location are known.

This sensitivity analysis has been applied on two scenarios. The first one is a small mass property change, namely a temporary lateral shift in center of gravity $\Delta_{cg_y} = 1.5m$ for $t = 20s - 60s$. The results of this analysis can be found in fig. E.3. These results show that the impact of the center of gravity shift on the forces and longitudinal moment is negligible. For the lateral moments, however, there is a very significant change and as a result the relative errors become larger than 100%. As soon as the shift disappears, also the errors dissipate. It can be seen that even a small mass property change can have a major impact on the moments.

The second scenario is more severe, being the El Al Flight 1862 scenario. The loss of the two engines on the right wing leads to significant changes in the mass properties, as illustrated in table E.1.

Table E.1: Mass property changes in the El Al Flight 1862 scenario

variable	original	change
mass	$m_0 = 3.17 \cdot 10^5 kg$	$\Delta m = -1.0028 \cdot 10^4 kg$
center of gravity	$y_{cg_0} = 0m$	$\Delta y_{cg} = 0.5426m$
inertia	$I_{xx_0} = 2.6144 \cdot 10^7 kgm^2$	$\Delta I_{xx} = -4.329 \cdot 10^5 kgm^2$
	$I_{yy_0} = 4.6734 \cdot 10^7 kgm^2$	$\Delta I_{yy} = -8.644 \cdot 10^5 kgm^2$
	$I_{zz_0} = 6.9822 \cdot 10^7 kgm^2$	$\Delta I_{zz} = -8.876 \cdot 10^5 kgm^2$
	$I_{xz_0} = 1.457 \cdot 10^6 kgm^2$	$\Delta I_{xz} = -6.108 \cdot 10^4 kgm^2$

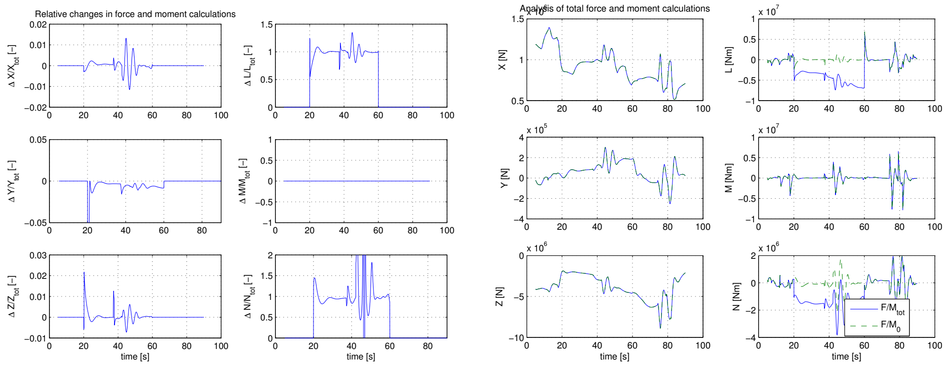

(a) relative errors in force and moment calculations

(b) comparison between uncorrected and total force and moment calculations

Figure E.3: Mass sensitivity analysis for temporary lateral shift in center of gravity $\Delta y_{cg} = 1.5m$ for $t = 20s - 60s$

The results of this second analysis can be found in fig.E.4. These results show that the impact of the changes in the mass properties is again negligible for the forces, since they have the same order of magnitude as in the previous scenario. However, the rolling and yawing moments change due to the corresponding combined mass, center of gravity and inertia changes. This failure makes the aircraft roll over to the right, this tendency being induced by the asymmetric thrust and drag. The gravity component in the lateral specific aerodynamic force builds up gradually, due to the larger than normal roll angle. This gradual build up can be found in the Y-force change.

This mass sensitivity analysis has shown that especially the aerodynamic moments are susceptible to mass property changes. However, this analysis has been performed on open loop configurations, and most part of the moment changes have been caused by the excessive uncontrolled angular rates. The control actions in closed loop configurations limit the magnitude of these rates and thus also the changes in the moments.

E.5 Taking mass changes into account in the kinematics and observation model: cg shift

The shift in the center of gravity location is the only mass property parameter which has an influence on the aircraft kinematics. The kinematics and observation model are rewritten such that this cg shift is taken into account.

The models must be defined with respect to a specific reference point. It has been chosen to define the kinematics with respect to the center of gravity, which is the conventional

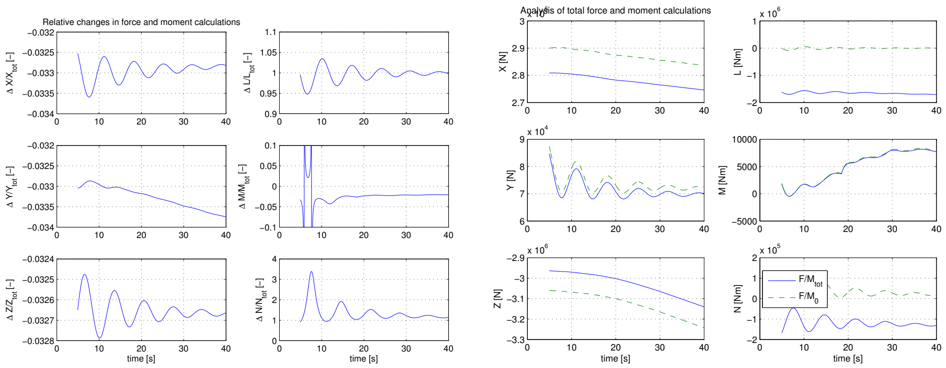

(a) relative errors in force and moment calculations

(b) comparison between uncorrected and total force and moment calculations

Figure E.4: Mass sensitivity analysis for El Al Flight 1862 scenario

approach. The observation model, on the other hand, includes a transformation from the actual center of gravity towards the origin reference point. This needs to be done because of the fixed location of the sensors, which can be compensated for the fixed misalignment with respect to this origin of the reference frame, but which will be perturbed in case of a shift in the center of gravity. This perturbation is taken into account in the aforementioned transformation.

Thus, the kinematics are defined with respect to the center of gravity, but this requires a correction for the specific force measurements, which are defined with respect to the origin and need to be transformed towards the center of gravity:

$$\dot{\mathbf{x}}_{GS_{cg}} = \mathbf{v}_{GS_{cg}} = \mathbf{\Omega}_{\text{tot}}\mathbf{v}_{AS_{cg}} + \mathbf{v}_{\text{wind}} \tag{E.7}$$

$$\dot{\mathbf{v}}_{AS_{cg}} = \mathbf{A}_{cg} - \mathbf{\Omega}_{\phi}\mathbf{\Omega}_{\theta}\begin{bmatrix} 0 \\ 0 \\ g \end{bmatrix} - \boldsymbol{\omega}_b \times \mathbf{v}_{AS_{cg}} \tag{E.8}$$

$$= \left(\mathbf{A}_0 - \dot{\boldsymbol{\omega}}_b \times \mathbf{\Delta r} - \boldsymbol{\omega}_b \times (\boldsymbol{\omega}_b \times \mathbf{\Delta r})\right) - \mathbf{\Omega}_{\phi}\mathbf{\Omega}_{\theta}\begin{bmatrix} 0 \\ 0 \\ g \end{bmatrix} - \boldsymbol{\omega}_b \times \mathbf{v}_{AS_{cg}} \tag{E.9}$$

$$\dot{\mathbf{\Theta}} = \dot{\mathbf{\Theta}}\left(\boldsymbol{\omega}_b\right) \tag{E.10}$$

On the other hand, the observation equations are defined with respect to the origin, and they are based on the states which are defined with respect to center of gravity, this requires a transformation over the cg shift:

$$
\begin{aligned}
\mathbf{x}_{INS_0} &= \mathbf{x}_{GS_{cg}} + \mathbf{\Omega}_{\mathrm{tot}}\mathbf{\Delta r} + \nu_1 && \text{(E.11)}\\
\mathbf{v}_{INS_0} &= \mathbf{\Omega}_{\mathrm{tot}}\mathbf{v}_{AS_0} + \mathbf{v}_{\mathrm{wind}} + \nu_2 && \text{(E.12)}\\
&= \mathbf{\Omega}_{\mathrm{tot}}\left(\mathbf{v}_{AS_{cg}} + \boldsymbol{\omega}_b \times \mathbf{\Delta r}\right) + \mathbf{v}_{\mathrm{wind}} + \nu_2 && \text{(E.13)}\\
\mathbf{\Theta}_{INS_0} &= \mathbf{\Theta} + \nu_3 && \text{(E.14)}\\
V_{TAS_0} &= \left\|\mathbf{v}_{AS_{cg}} + \boldsymbol{\omega}_b \times \mathbf{\Delta r}\right\|_2 && \text{(E.15)}\\
\alpha_0 &= \mathrm{atan}\frac{\left(w_{AS_{cg}} - p\Delta y + q\Delta x\right)}{\left(u_{AS_{cg}} - q\Delta z + r\Delta y\right)} && \text{(E.16)}\\
\beta_0 &= \mathrm{atan}\frac{\left(v_{AS_{cg}} - r\Delta x + p\Delta z\right)}{\sqrt{\left(u_{AS_{cg}} - q\Delta z + r\Delta y\right)^2 + \left(w_{AS_{cg}} - p\Delta y + q\Delta x\right)^2}} && \text{(E.17)}
\end{aligned}
$$

Next step is to take into account the mass property changes on the angular momentum. This will be discussed in the next section.

E.6 Taking mass changes into account in the aerodynamic model: cg, mass, inertia

The angular momentum, on the other hand, is to be incorporated in the expressions for the aerodynamic moments. The standard equations for the aerodynamic moments as defined in section 4.2 need to be expanded for the fact that the origin of the reference frame does not coincide with the center of gravity after its shift, as has been done previously in appendix E.2.

It should be noted that not enough information is available to calculate the moments, like in the conventional two step method procedure. More precisely mass m, center of gravity shift Δ_x, Δ_y, Δ_z, inertias J_{xz} and J_{yz} can appear. Moreover the values of the conventionally used inertias I_{xx}, I_{yy}, I_{zz} and I_{xz} can change.

From appendix E.2, it is known that the following equations hold:

$$
\begin{aligned}
L &= \dot{p}I_{xx} + (pr - \dot{q})\,J_{xy} - (pq + \dot{r})\,J_{xz} + \left(r^2 - q^2\right)J_{yz} + qr\,(I_{zz} - I_{yy}) + \\
&\quad + mA_{z_{cg}}\Delta y - mA_{y_{cg}}\Delta z && \text{(E.18)}\\
M &= -(\dot{p} + qr)\,J_{xy} + \dot{q}I_{yy} + (pq - \dot{r})\,J_{yz} + \left(p^2 - r^2\right)J_{xz} + pr\,(I_{xx} - I_{zz}) + \\
&\quad - mA_{z_{cg}}\Delta x + mA_{x_{cg}}\Delta z && \text{(E.19)}\\
N &= (qr - \dot{p})\,J_{xz} - (\dot{q} + pr)\,J_{yz} + \dot{r}I_{zz} + \left(q^2 - p^2\right)J_{xy} + pq\,(I_{yy} - I_{xx}) + \\
&\quad + mA_{y_{cg}}\Delta x - mA_{x_{cg}}\Delta y && \text{(E.20)}
\end{aligned}
$$

A possible solution is to rewrite these equations in a structure which is linear in the parameters, splitting unknown parameters from the known or measured ones. This can be done by rewriting the expressions above as functions of the angular accelerations $\dot{p}$, $\dot{q}$ and $\dot{r}$:

$$
\begin{aligned}
\dot{p}\,(t) \quad = \quad & \left(I_{xx}I_{yy}I_{zz} - I_{xx}I_{yz}^2 - I_{xy}^2 I_{zz} - 2I_{xy}I_{xz}I_{yz} - I_{xz}^2 I_{yy}\right)^{-1} \cdot \\
& \left[L(t)\left(-I_{yz}^2 + I_{yy}I_{zz}\right) + \right. \\
& +M(t)\left(I_{xz}I_{yz} + I_{xy}I_{zz}\right) + \\
& +N(t)\left(I_{xy}I_{yz} + I_{xz}I_{yy}\right) + \\
& +p^2\,(t)\left(I_{yz}\left(I_{xy}^2 - I_{xz}^2\right) + I_{xy}I_{xz}\left(I_{yy} - I_{zz}\right)\right) + \\
& +q^2\,(t)\left(-I_{yz}\left(I_{xy}^2 + I_{yz}^2\right) + I_{yy}\left(I_{zz}I_{yz} - I_{xy}I_{xz}\right)\right) + \\
& +r^2\,(t)\left(I_{yz}\left(I_{xz}^2 + I_{yz}^2\right) + I_{zz}\left(I_{xy}I_{xz} - I_{yy}I_{yz}\right)\right) + \\
& +p\,(t)\,q\,(t)\left(I_{xz}\left(I_{yy}\left(I_{xx} - I_{yy} + I_{zz}\right) - 2I_{yz}^2\right) + I_{xy}I_{yz}\left(I_{xx} - I_{yy} - I_{zz}\right)\right) + \\
& +q\,(t)\,r\,(t)\left(I_{yy}\left(I_{zz}\left(I_{yy} - I_{zz}\right) - I_{yz}^2 - I_{xz}^2\right) + I_{zz}\left(I_{yz}^2 + I_{xy}^2\right)\right) + \\
& +p\,(t)\,r\,(t)\left(I_{yz}\left(I_{xz}\left(-I_{xx} + I_{yy} + I_{zz}\right) + 2I_{xy}I_{yz}\right) + I_{xy}I_{zz}\left(-I_{xx} - I_{yy} + I_{zz}\right)\right) + \\
& +A_{x_{cg}}(t)\left(-\left(I_{xy}I_{zz} + I_{xz}I_{yz}\right)m\Delta z + \left(I_{xy}I_{yz} + I_{xz}I_{yy}\right)m\Delta y\right) + \\
& +A_{y_{cg}}(t)\left(-\left(I_{xz}I_{yy} + I_{xy}I_{yz}\right)m\Delta x + \left(I_{yy}I_{zz} - I_{yz}^2\right)m\Delta z\right) + \\
& \left. +A_{z_{cg}}(t)\left(\left(I_{xy}I_{zz} + I_{xz}I_{yz}\right)m\Delta x + \left(I_{yy}I_{zz} - I_{yz}^2\right)m\Delta y\right)\right]
\end{aligned}
\tag{E.21}
$$

$$
\begin{aligned}
\dot{q}\,(t) \quad = \quad & \left(I_{xx}I_{yy}I_{zz} - I_{xx}I_{yz}^2 - I_{xy}^2 I_{zz} - 2I_{xy}I_{xz}I_{yz} - I_{xz}^2 I_{yy}\right)^{-1} \cdot \\
& \left[L(t)\left(I_{xy}I_{zz} + I_{xz}I_{yz}\right) + \right. \\
& +M(t)\left(I_{xx}I_{zz} - I_{xz}^2\right) + \\
& +N(t)\left(I_{xx}I_{yz} + I_{xy}I_{xz}\right) + \\
& +p^2\,(t)\left(I_{xy}\left(I_{xy}I_{xz} + I_{xx}I_{yz}\right) + I_{xz}\left(I_{xz}^2 - I_{xx}I_{zz}\right)\right) + \\
& +q^2\,(t)\left(I_{xz}\left(I_{yz}^2 - I_{xy}^2\right) + I_{xy}I_{yz}\left(I_{zz} - I_{xx}\right)\right) + \\
& +r^2\,(t)\left(-I_{xz}\left(I_{yz}^2 + I_{xz}^2\right) + I_{zz}\left(I_{xx}I_{xz} - I_{xy}I_{yz}\right)\right) + \\
& +p\,(t)\,q\,(t)\left(I_{yz}\left(I_{xx}\left(I_{xx} - I_{yy} - I_{zz}\right) + 2I_{xz}^2\right) + I_{xy}I_{xz}\left(I_{xx} - I_{yy} + I_{zz}\right)\right) + \\
& +q\,(t)\,r\,(t)\left(I_{xz}\left(I_{yz}\left(-I_{xx} + I_{yy} - I_{zz}\right) - 2I_{xy}I_{xz}\right) - I_{xy}I_{zz}\left(-I_{xx} - I_{yy} + I_{zz}\right)\right) + \\
& +p\,(t)\,r\,(t)\left(I_{xx}\left(I_{zz}\left(-I_{xx} + I_{zz}\right) + I_{yz}^2 + I_{xz}^2\right) - I_{zz}\left(I_{xz}^2 + I_{xy}^2\right)\right) + \\
& +A_{x_{cg}}(t)\left(-\left(I_{xx}I_{yz} + I_{xy}I_{xz}\right)m\Delta y + \left(I_{xx}I_{zz} - I_{xz}^2\right)m\Delta z\right) + \\
& +A_{y_{cg}}(t)\left(\left(I_{xx}I_{yz} + I_{xy}I_{xz}\right)m\Delta x - \left(I_{xy}I_{zz} + I_{xz}I_{yz}\right)m\Delta z\right) + \\
& \left. +A_{z_{cg}}(t)\left(\left(I_{xy}I_{zz} + I_{xz}I_{yz}\right)m\Delta y - \left(I_{xx}I_{zz} - I_{xz}^2\right)m\Delta x\right)\right]
\end{aligned}
\tag{E.22}
$$

$$
\begin{aligned}
\dot{r}\left(t\right) \;=\;& \left(I_{xx}I_{yy}I_{zz}-I_{xx}I_{yz}^{2}-I_{xy}^{2}I_{zz}-2I_{xy}I_{xz}I_{yz}-I_{xz}^{2}I_{yy}\right)^{-1}\cdot\\
&\left[L(t)\left(I_{xy}I_{yz}+I_{xz}I_{yy}\right)+\right.\\
&+M(t)\left(I_{xx}I_{yz}+I_{xy}I_{xz}\right)+\\
&+N(t)\left(I_{xx}I_{yy}-I_{xy}^{2}\right)+\\
&+p^{2}\left(t\right)\left(-I_{xy}\left(I_{xy}^{2}+I_{xz}^{2}\right)+I_{xx}\left(I_{xy}I_{yy}-I_{xz}I_{yz}\right)\right)+\\
&+q^{2}\left(t\right)\left(I_{xy}\left(I_{xy}^{2}+I_{yz}^{2}\right)+I_{yy}\left(I_{xz}I_{yz}-I_{xx}I_{xy}\right)\right)+\\
&+r^{2}\left(t\right)\left(I_{xy}\left(I_{xz}^{2}-I_{yz}^{2}\right)+I_{xz}I_{yz}\left(I_{xx}-I_{yy}\right)\right)+\\
&+p\left(t\right)q\left(t\right)\left(I_{yy}\left(I_{xx}\left(I_{xx}-I_{yy}\right)+I_{xy}^{2}+I_{xz}^{2}\right)-I_{xx}\left(I_{yz}^{2}+I_{xy}^{2}\right)\right)+\\
&+q\left(t\right)r\left(t\right)\left(I_{xz}\left(I_{yy}\left(-I_{xx}+I_{yy}-I_{zz}\right)+2I_{xy}^{2}\right)-I_{xy}I_{yz}\left(-I_{xx}-I_{yy}+I_{zz}\right)\right)+\\
&+p\left(t\right)r\left(t\right)\left(I_{xy}\left(I_{xz}\left(-I_{xx}-I_{yy}+I_{zz}\right)-2I_{xy}I_{yz}\right)-I_{xx}I_{yz}\left(I_{xx}-I_{yy}-I_{zz}\right)\right)+\\
&+A_{x_{cg}}(t)\left(\left(I_{xx}I_{yy}-I_{xy}^{2}\right)m\Delta y-\left(I_{xx}I_{yz}+I_{xy}I_{xz}\right)m\Delta z\right)+\\
&+A_{y_{cg}}(t)\left(-\left(I_{xx}I_{yy}-I_{xy}^{2}\right)m\Delta x+\left(I_{xy}I_{yz}+I_{xz}I_{yy}\right)m\Delta z\right)+\\
&\left.+A_{z_{cg}}(t)\left(\left(I_{xx}I_{yz}+I_{xy}I_{xz}\right)m\Delta x-\left(I_{xy}I_{yz}+I_{xz}I_{yy}\right)m\Delta y\right)\right]
\end{aligned}
\tag{E.23}
$$

where $A_{x_{cg}}$, $A_{y_{cg}}$ and $A_{z_{cg}}$ are the specific forces in the center of gravity. However, these quantities are not available, since the accelerometer measurements are not corrected for the true center of gravity after the shift. Therefore, a correction is needed according to the following transformation as obtained in appendix E.1:

$$A_{x_{cg}} = A_{x_a}+\left(q^2+r^2\right)\Delta x-\left(pq-\dot{r}\right)\Delta y-\left(\dot{q}+pr\right)\Delta z \tag{E.24}$$

$$A_{y_{cg}} = A_{y_a}-\left(\dot{r}+pq\right)\Delta x+\left(p^2+r^2\right)\Delta y-\left(qr-\dot{p}\right)\Delta z \tag{E.25}$$

$$A_{z_{cg}} = A_{z_a}-\left(pr-\dot{q}\right)\Delta x-\left(\dot{p}+qr\right)\Delta y+\left(p^2+q^2\right)\Delta z \tag{E.26}$$

A possible solution is to implement the latter expressions in the former and to write this out. Although the length of the equations increases significantly, their structure with reference to the known parameters remains unchanged.

It should be noted that in expressions (E.21) to (E.23), all mass properties are considered as unknowns, where the angular rates and the specific forces are known or derivable from the state estimation phase. Hence, they serve as mass property regressors of which the additional ones compared to (4.81) become only relevant in case of a mass property change. The fixed and candidate mass property regressors are arranged for each dependent variable in table E.2.

A drawback of this approach is that no distinction can be made between individual values of mass inertias, but the advantage is that the choice of the dependent variable and this structure correspond directly with the setup of the NDI control approach as elaborated in chapter 7, adding to the transparency of the global approach.

Table E.2: Fixed and candidate mass property regressors for angular accelerations serving as dependent variables

dependent variable	fixed regressors	candidate regressors
$\dot{p}$	$L\ N\ qr\ pq$	$M\ p^2\ q^2\ r^2\ pr\ A_x\ A_y\ A_z$
$\dot{q}$	$M\ pr\ \left(p^2 - r^2\right)$	$L\ N\ p^2\ q^2\ r^2\ pq\ qr\ A_x\ A_y\ A_z$
$\dot{r}$	$L\ N\ qr\ pq$	$M\ p^2\ q^2\ r^2\ pr\ A_x\ A_y\ A_z$

Appendix F

Frame conversions

Figure F.1 illustrates the matrix transformations which are needed to make the conversions from one reference frame to the other.

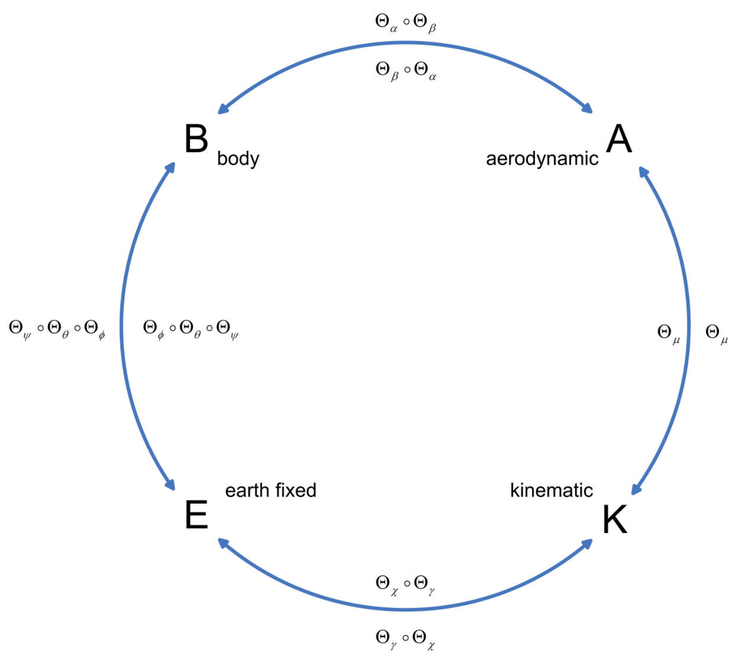

Figure F.1: Reference frame conversions. Inner sequences apply for clockwise directions, outer for counterclockwise directions

Appendix G

Cooper Harper handling quality rating scale

The rating scale for handling qualities according to Cooper and Harper works as illustrated here. The ratings can be divided in three levels. Level one ratings contain rating numbers 1 till 3, numbers 4 till 6 are level 2 ratings and all higher numbers can be grouped in level 3.

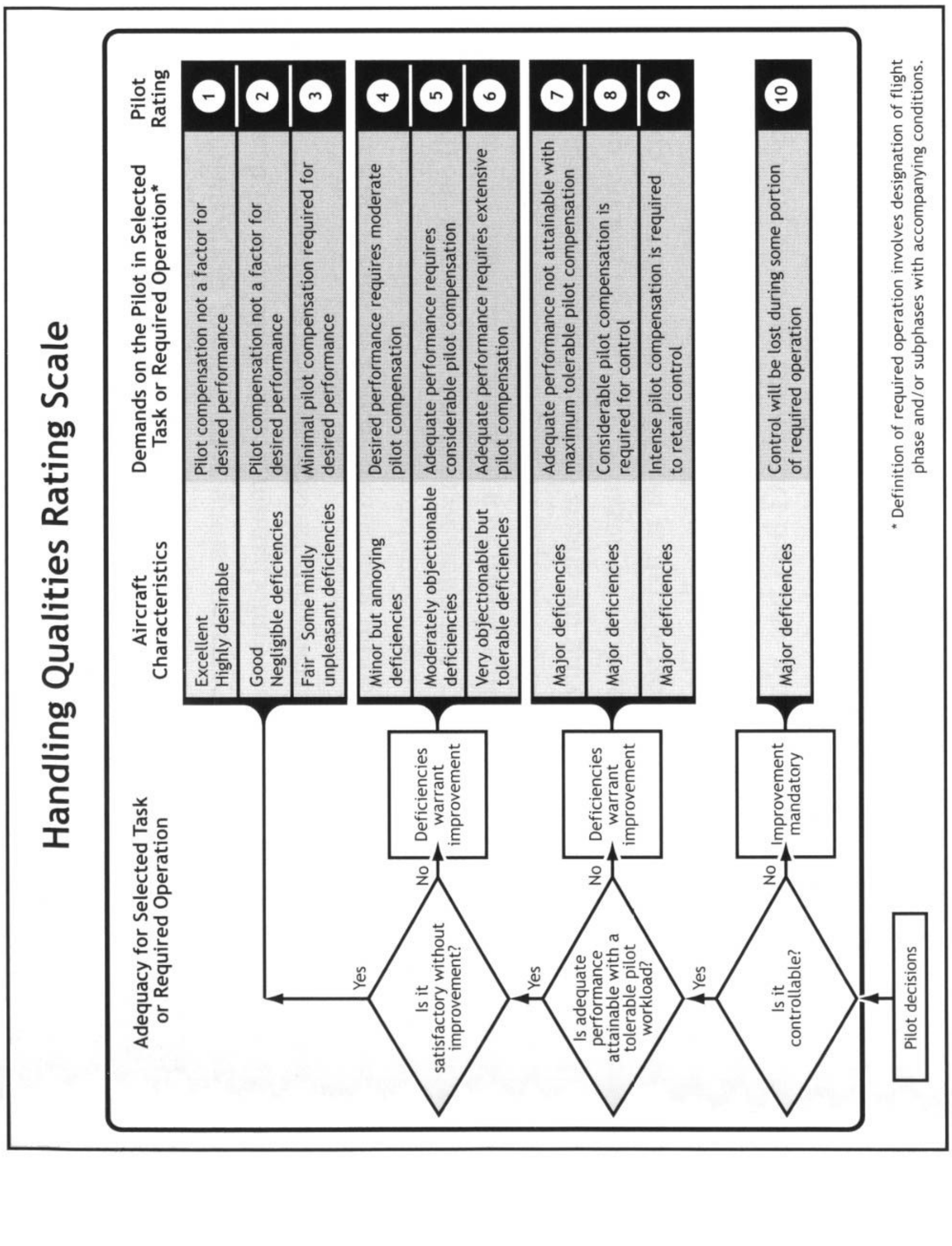
Handling Qualities Rating Scale
Adequacy for Selected Task or Required Operation
Aircraft Characteristics
Demands on the Pilot in Selected Task or Required Operation*
Pilot Rating
Excellent Highly desirable
Pilot compensation not a factor for desired performance
1
Good Negligible deficiencies
Pilot compensation not a factor for desired performance
2
Fair - Some mildly unpleasant deficiencies
Minimal pilot compensation required for desired performance
3
Minor but annoying deficiencies
Desired performance requires moderate pilot compensation
4
Moderately objectionable deficiencies
Adequate performance requires considerable pilot compensation
5
Very objectionable but tolerable deficiencies
Adequate performance requires extensive pilot compensation
6
Major deficiencies
Adequate performance not attainable with maximum tolerable pilot compensation
7
Major deficiencies
Considerable pilot compensation is required for control
8
Major deficiencies
Intense pilot compensation is required to retain control
9
Major deficiencies
Control will be lost during some portion of required operation
10
Is it satisfactory without improvement?
Deficiencies warrant improvement
Is adequate performance attainable with a tolerable pilot workload?
Deficiencies warrant improvement
Is it controllable?
Improvement mandatory
Yes
No
Yes
No
Yes
No
Pilot decisions
* Definition of required operation involves designation of flight phase and/or subphases with accompanying conditions.

References

[1] Applying lessons learned from accidents. http://faalessons.workforceconnect.org/.

[2] Report on the accident to concorde 102 g-boaf, over the tasman sea, about 140 nm east of sydney, australia on 12 april 1989. Technical Report 6/89, Air Accidents Investigation Branch, 1989.

[3] Rotorcraft system identification. Technical Report AGARD-AR-280, AGARD, 1991.

[4] Aircraft accident report united airlines flight 585 boeing 737-291, n999ua uncontrolled collision with terrain for undetermined reasons 4 miles south of colorado springs municipal airport colorado springs, colorado march 3, 1991. Technical report, National Transportation Safety Board (NTSB), 1992.

[5] Aircraft accident report uncontrolled descent and collision with terrain usair flight 427 boeing 737-300, n513au near aliquippa, pennsylvania september 8, 1994. Technical report, National Transportation Safety Board NTSB, 1999.

[6] Intelligent flight control: Advanced concept program. Final Report BOEING-STL 99P0040, The Boeing Company, 1999.

[7] Integrated resilient aircraft control - stability, maneuverability and safe landing in the presence of adverse conditions. Technical report, National Aeronautics and Space Administration, Aeronautics Research Mission Directorate, April 2007. Aviation Safety Program.

[8] Loss of rudder in flight air transat airbus a310-308 c-gpat, miami, florida, 90 nm s, 6 march 2005. Technical Report A05F0047, Transportation Safety Board of Canada, 2007.

[9] Atsb transport safety report: In-flight upset 154 km west of learmonth, wa 7 october 2008 vh-qpa airbus a330-303. Technical report, Australian Transport Safety Bureau, 2008.

[10] Civil aviation safety data 1993-2007. Technical report, Civil Aviation Authority of the Netherlands (CAA-NL), 2008.

[11] Interim report on the accident on 1st june 2009 to the airbus a330-203 registered f-gzcp operated by air france flight af 447 rio de janeiro paris. Technical report, Bureau dEnqutes et dAnalyses pour la scurit de laviation civile, 2009.

[12] preliminary accident report: Turkish boeing 737 25 february 2009. Technical report, The Dutch Safety Board, 2009.

[13] Aircraft accident report: Uncontrolled descent and collision with terrain united airlines flight 585 boeing 737-200, n999ua 4 miles south of colorado springs municipal airport colorado springs, colorado, march 3, 1991. Technical report, National Transportation and Safety Board, March 27, 2001.

[14] Zainal Abidin. *Adaptive Self-Tuning Flight Control Systems The Multiple Model Approach*. PhD thesis, Delft University of Technology, 1998.

[15] D.M. Acosta and S. Joshi. Adaptive nonlinear dynamic inversion control of an autonomous airship for the exploration of titan. In *AIAA Guidance, Navigation and Control Conference and Exhibit*, number AIAA-2007-6502, August 2007.

[16] Hirotugu Akaike. Fitting autoregressive models for prediction. *Annals of Statistics and Mathematics*, pages 243–247, 1969.

[17] Hirotugu Akaike. A new look at the statistical model identification. *IEEE Transactions on Automatic Control*, AC-19(6):716–723, December 1974.

[18] Hirotugu Akaike. Stochastic theory of minimal realization. *IEEE Transactions on Automatic Control*, AC-19(6):667–674, December 1974.

[19] F.A. de Almeida and D. Leiling. Fault-tolerant model predictive control with flight test results on attas. In *AIAA Guidance, Navigation, and Control Conference*, number AIAA 2009-5621, 2009.

[20] Halim Alwi. *Fault Tolerant Sliding Mode Control Schemes with Aerospace Applications*. PhD thesis, University of Leicester, February 2008.

[21] E. Ammons. F-16 flight control system redundancy concepts. In *Guidance and Control Conference*, Boulder, Colorado, August 1979.

[22] B. Anderson and T. Bedos. X-38 v201 avionics architecture. Technical Report N20000086667, NASA, February 1999.

[23] A.N. Andry, E.Y. Shapiro, and J.C. Chung. Eigenstructure assignment for linear systems. *IEEE Transactions on Aerospace Electronic Systems*, 19(5), September 1983.

[24] A. Arabian. Afti/f-16 digital flight control computer design. In *NAECOn 1983*, Dayton, Ohio, 1983.

[25] K.J. Astrom and B. Wittemark. *Adaptive Control*. Addison-Wesley Publishing Company, second edition edition, 1995.

[26] B.J. Bacon and I.M. Gregory. General equations of motion for a damaged asymmetric aircraft. In *AIAA Atmospheric Flight Mechanics Conference and Exhibit*, number AIAA-2007-6306, 2007.

[27] G. Balas, W. Garrard, and J. Reiner. Robust dynamic inversion control laws for aircraft control. In *Proceedings of the AIAA Guidance, Navigation and Control Conference*, pages 192–205, Washington, DC, 1992. AIAA.

[28] G.J. Balas. Linear, parameter-varying control and its application to a turbofan engine. *International Journal of Robust and Nonlinear Control*, 12:763–796, 2002.

[29] G.J. Balas. Flight control law design: An industry perspective. *European Journal of Control, special issue*, 9(2–3):207–226, 2003.

[30] A. R. Barron. Predicted squared error: a criterion for automatic model selection. In S. J. Farlow, editor, *Self-Organizing Methods in Modeling*, volume 54, pages 87–103, New York, 1984. Marcel Dekker.

[31] D.G. Bates and I. Postlethwaite. *Robust Multivariable Control of Aerospace Systems*. Series 03, Control and Simulation 08. Delft University Press, DUP Science, Delft, The Netherlands, December 2002.

[32] J.-M. Bauschat, D. Monnich, W. Willemsen, and Looye G. Flight testing robust autoland control laws. In *AIAA Guidance, Navigation, and Control Conference and Exhibi*, number AIAA 2001-4208, 2001.

[33] D.A. Belsley, E. Kuh, and R.E. Welsh. *Regression Diagnostics: Identifying Influential Data and Sources of Collinearity*. Wiley, New York, 1980.

[34] S. Bennani, R. van der Sluis, G. Schram, and J.A. Mulder. Control law reconfiguration using robust linear parameter varying control. In *Proceedings of the AIAA Guidance, Navigation and Control Conference*, number AIAA-1999-4137, 1999.

[35] R. J. M. Bennis. Non-linear state estimation techniques with application to dynamic modelling of angle of attack vane from cessna citation ii flight data. Master's thesis, Delft University of Technology, August 1998.

[36] R. J. M. Bennis, Q. P. Chu, and J. A. Mulder. Non-stationary noise estimation with adaptive filters. In *AIAA Guidance, Navigation, and Control Conference and Exhibit, Collection of Technical Papers*, volume 3, pages 1769–1782, 1999.

[37] M. Bodson. Evaluation of optimization method for control allocation. In *Proceedings of AIAA Guidance, Navigation and Control Conference*, number AIAA-2001-4223, August 2001.

[38] M. Bodson. Reconfigurable nonlinear autopilot. *AIAA Journal of Guidance, Control and Dynamics*, 26(5):719–727, 2003.

[39] M. Bodson and J.E. Groszkiewicz. Multivariable adaptive algorithms for reconfigurable flight control. *IEEE Transactions on Control Systems Technology*, 5(2):217–229, March 1997.

[40] L. Boldue. Redundancy management for the x-33 vehicle and mission computer. In *19th Digital Avionics Systems Conference*, Philadelphia, Pennsylvania, October 2000.

[41] K. Bordignon and J. Besselo. Control allocation for the x-35b. In *Proceedings of the Biennial International Powered Lift Conference and Exhibit*, number AIAA-2002-6020, November 2002.

[42] B. Boskovich and R.E. Kaufmann. Evolution of the honeywell first-generation adaptive autopilot and its applications to f-94, f-101, x-15, and x-20 vehicles. *Journal of Aircraft*, 3(4):296–304, July-August 1966.

[43] J.D. Boskovich, S.E. Bergstrom, R.K. Mehra, James M. Urnes, M. Hood, and Y. Lin. Fast on-line actuator reconfiguration enabling (flare) system. In *Proceedings of the AIAA Guidance, Navigation and Control Conference and Exhibit*, number AIAA-2005-6339, 2005.

[44] J.D. Boskovich, S.E. Bergstrom, R.K. Prasanth, and R.K. Mehra. A multi-layer intelligent loss-of-control prevention system (lps) for flight control applications. In *Proceedings of the AIAA Guidance, Navigation and Control Conference and Exhibit*, number AIAA-2005-6340, 2005.

[45] J.D. Boskovich, R.K. Prasanth, and R.K. Mehra. Reconfigurable fault-tolerant flight control: Algorithms, implementation and metrics. In *Proceedings of the AIAA Guidance, Navigation and Control Conference and Exhibit*, number AIAA-2006-6549, 2006.

[46] J.T. Bosworth. Flight results of the nf-15b intelligent flight control system (ifcs) aircraft with adaptation to a longitudinally destabilized plant. In *Proceedings of the AIAA Conference on Guidance, Navigation and Control*, number AIAA-2008-6985, 2008.

[47] John A. Bowlus, Dieter Multhopp, and Siva S. Banda. Challenges and opportunities in tailless aircraft stability and control. In *AIAA Guidance, Navigation, and Control Conference, collection of technical papers*, volume 3, 1997.

[48] D. Brekke, N. Giere, Schlosser R., M. Slavich, D. Tabor, and B. Turner. Next generation fault-tolerant guidance and navigation unit for the inertial upper stage. In *Rocky Mountain Guidance and Control Conference*, Keystone, Co, February 1995.

[49] D. Briere and P. Traverse. Airbus a320/a330/a340 electrical flight controls - a family of fault tolerant systems. In *IEEE Conference*, 1993.

[50] J.S. Brinker and K.A. Wise. Nonlinear simulation analysis of a tailless advanced fighter aircraft reconfigurable flight control law. In *AIAA Guidance, Navigation and Control Conference and Exhibit*, number AIAA-99-4040, Portland, OR, August 1999.

[51] J.S. Brinker and K.A. Wise. Flight testing of reconfigurable control law on the x-36 tailless aircraft. *Journal of Guidance, Control and Dynamics*, 24(5):903–909, September 2001.

[52] P.D. Bruce and M.G. Kellett. Modelling and identification of non-linear aerodynamic functions using b-splines. *Proceedings of the Institution of Mechanical Engineers, Part G: Journal of Aerospace Engineering*, 214:27–40, 2000.

[53] A.E. Bryson and Y. Ho. *Applied Optimal Control – Optimization, Estimation and Control*. Hemisphere Publishing Corporation, Washington DC, USA, 1975. revised printing.

[54] A.E. Jr. Bryson. *Control of Spacecraft and Aircraft*. Princeton University Press, 1994.

[55] J.J. Burken, T.A. Maine, F.W. Burcham, and J.A. Kahler. Longitudinal emergency control system using thrust modulation demonstrated on an md-11 airplane. In *AIAA, ASME, SAE, and ASEE, Joint Propulsion Conference and Exhibit, 32nd*, Lake Buena Vista, FL, July 1996.

[56] A.J. Calise, S. Lee, and M. Sharma. Direct adaptive reconfigurable control of a tailless fighter aircraft. In *AIAA Guidance, Navigation and Control conference*, Boston, MA, August 1998.

[57] Anthony J. Calise, Seungjae Lee, and Manu Sharma. Development of a reconfigurable flight control law for the x-36 tailless fighter aircraft. *AIAA Journal of Guidance, Control and Dynamics*, 24(5):896–902, 2001.

[58] Giampiero Campa, Brad Seanor, Yu Gu, and Marcello R. Napolitano. Nldi guidance control laws for close formation flight. In *American Control Conference*, Portland, OR, USA, June 8-10 2005.

[59] C. Cao and N. Hovakimyan. Design and analysis of a novel $\mathcal{L}_1$ adaptive controller, part i: Control signal and asymptotic stability. In *Proceedings of the 2006 American Control Conference*, pages 3397–3402, 2006.

[60] C. Cao and N. Hovakimyan. Design and analysis of a novel $\mathcal{L}_1$ adaptive controller, part ii: Guaranteed transient performance. In *Proceedings of the 2006 American Control Conference*, pages 3403–3408, 2006.

[61] Floyd L. Carpenter. Summary of facts b-2 accident on 23 february 2008. Technical report, Accident Investigation Board, USAF, 2008.

[62] P.R. Chandler, M. Pachter, and M. Mears. System identification for adaptive and reconfigurable control. *AIAA Journal of Guidance, Control and Dynamics*, 18(3):516–524, May–June 1995.

[63] S. Chen, S.A. Billings, and W. Luo. Orthogonal least squares methods and their application to non-linear system identification. *International Journal of Control*, 50(5):1873–1896, 1989.

[64] Q. P. Chu. *Maximum Likelihood Parameter Identification of Flexible Spacecraft*. PhD thesis, Delft University of Technology, 1987.

[65] Q.P. Chu. *Lecture Notes AE4-394, Modern Flight Test Technologies and System Identification*. Delft University of Technology, Faculty of Aerospace Engineering, 2007.

[66] Q.P. Chu, J.A. Mulder, and J.K. Sridhar. Decomposition of aircraft state and parameter estimation problems. In *Proceedings of fhe 10th IFAC Sympium on System Identifiation*, volume Vol. 3, pages pp. 61–66, 1994.

[67] Q.P. Chu, J.A. Mulder, and P.Th.L.M. Van Woerkom. Aircraft flight path reconstruction with nonlinear adaptive filters. In *Proceedings of the American Control Conference*, volume 2, pages 1196–1200, Seattle, 1995. ACC.

[68] Q.P. Chu, J.A. Mulder, and P.Th.L.M. Van Woerkom. Modified recursive maximum likelihood adaptive filter for nonlinear aircraft flight path reconstruction. *AIAA Journal of Guidance, Control and Dynamics*, 19(6):1285–1295, 1996.

[69] Q.P. Chu, A. Verbass, J.A. Mulder, and P.Ph. van den Broek. Nonlinear adaptive filtering with application to spaceplane flight path reconstruction. In *Proceedings of the 2nd ESA International Conference on Guidance, Navigation and Control Systems*, pages 107–116, Noordwijk, April 1994. ESTEC, ESTEC Conference Bureau.

[70] G.E. Cooper and R.P. Jr. Harper. The use of pilot rating in the evaluation of aircraft handling qualities. Technical Report TN D-5153, NASA, 1969.

[71] John H. Corvin, William J. Havern, Stephen E. Hoy, Kevin F. Norat, James M. Urnes, and Edward A. Wells. Self-repairing flight control systems, volume i: Flight test evaluation on an f-15 aircraft. Final Report WL-TR-91-3025, 1991.

[72] R.R. da Costa, Q. P. Chu, and J. A. Mulder. Re-entry flight controller design using nonlinear dynamic inversion. *Journal of Spacecraft and Rockets*, 40(1):64–71, 2003.

[73] J.B. Davidson, F.J. Lallman, and W.T. Bundick. Real-time adaptive control allocation applied to a high performance aircraft. In *5th SIAM Conference on Control & Its Applications*, 2001.

[74] J.J. D'Azzo and C.H. Houpis. *Linear Control System Analysis and Design, conventional and modern*. McGraw-Hill New York, 1995.

[75] C.C. de Visser, Q. P. Chu, and J. A. Mulder. A new approach to linear regression with multivariate splines. *Automatica*, 2009. accepted for publication.

[76] C.C. de Visser, J. A. Mulder, and Q. P. Chu. Global aerodynamic modeling with multivariate splines. In *Proceedings of AIAA Modeling and Simulation Technologies Conference and Exhibit*, number AIAA-2008-7500, 2008.

[77] C.C. de Visser, J. A. Mulder, and Q. P. Chu. Global nonlinear aerodynamic model identification with multivariate splines. In *Proceedings of AIAA Atmospheric Flight Mechanics Conference and Exhibit*, number AIAA-2009-5726, 2009.

[78] E. de Weerdt, Q.P. Chu, and J.A. Mulder. Neural network aerodynamic model identification for aerospace reconfiguration. In *Proceedings of the AIAA Conference on Guidance, Navigation and Control*, number AIAA-2005-6448, 2005.

[79] V. Dobrokhodov, I. Kitsios, I. Kaminer, K.D. Jones, E. Xargay, N. Hovakimyan, C. Cao, M.I. Lizarraga, and I.M. Gregory. Flight validation of a metrics driven $\mathcal{L}_1$ adaptive control. In *Proceedings of the AIAA Guidance, Navigation and Control Conference and Exhibit*, number AIAA-2008-6987, 2008.

[80] J.C. Doyle, K. Glover, P.P. Khargonekar, and A. Francis, B. State-space solutions to standard $\mathcal{H}_2$ and $\langle_\infty$ control problems. *IEEE Transactions on Automatic Control*, AC–34(8):831–847, 1989.

[81] N. Draper and H. Smith. *Applied Regression Analysis*. John Wiley & Sons, Inc., 1981.

[82] K. Driscoll and K. Hoyme. The airplane information management system, an integrated real-time flight deck control system. In *Real-Time System Symposium*, December 1992.

[83] G.J.J. Ducard. *Fault-Tolerant Flight Control and Guidance Systems, practical methods for small unmanned aerial verhicles*. Springer, 2009.

[84] W.C. Durham. Computationally efficient control allocation. *Journal of Guidance, Control and Dynamics*, 24(3):519–524, May-June 2001.

[85] B.C. Dutoi, N.D. Richards, N. Gandhi, D.G. Ward, and J.R. Leonard. Hybrid robust control and reinforcement learning for optimal upset recovery. In *Proceedings of the AIAA Guidance, Navigation and Control Conference and Exhibit*, number AIAA-2008-6502, 2008.

[86] EASA. *Certification Specifications for Large Aeroplanes*. EASA. CS-25.

[87] C. Edwards, T.J.J. Lombaerts, and M.H. Smaili. *Fault tolerant control a benchmark challenge*. Lecture Notes in Control and Information Sciences. Springer-Verlag, 2009. To be published.

[88] D. Enns. Control allocation approaches. In *Proceedings of the AIAA GNC Conference*, number AIAA-98-4109, pages 98–108, 1998.

[89] P. Eykhoff. *System Identification*. John Wiley & Sons, second edition edition, 1974.

[90] Federal Aviation Administration FAA. *Airworthiness Standards: Transport Category Airplane*. Federal Aviation Administration FAA. title 14, part 25.

[91] J. Farrell, M. Sharma, and M. Polycarpou. Backstepping-based flight control with adaptive function approximation. *AIAA Journal of Guidance, Control and Dynamics*, 28(6):1089–1102, November–December 2005.

[92] W. Favoreel. *Subspace methods for identification and control of linear and bilinear systems*. PhD thesis, Faculty of Engineering, K.U. Leuven, Belgium, 1999.

[93] J.V. Foster, K. Cunningham, C.M. Fremaux, G.H. Shah, E.C. Stewart, R.A. Rivers, J.E. Wilborn, and W. Gato. Dynamics modeling and simulation of large transport airplanes in upset conditions. In *AIAA Guidance, Navigation and Control Conference and Exhibit*, number AIAA-2005-5933, 2005.

[94] C.F. Fung, S.A. Billings, and W. Luo. On-line supervised adaptive training using radial basis function networks. *neural networks*, 9(9):1597–1617, 1996.

[95] T.G. Gainer and S. Hoffman. Summary of transformation equations and equations of motion used in free-flight and wind tunnel data reduction and analysis. Technical Report SP-3070, NASA, 1972.

[96] S. Ganguli, A. Marcos, and G.J. Balas. Reconfigurable lpv control design for boeing 747-100/200 longitudinal axis. In *American Control Conference*, pages 3612–3617, 2002.

[97] S. Ganguli, G. Papageorgiou, S. Glavaski, and Elgersma M. Piloted simulation of fault detection, isolation and reconfiguration algorithms for a civil transport aircraft. In *AIAA Guidance, Navigation and Control Conference and Exhibit*, number AIAA-2005-5936, San Francisco, CA, August 2005.

[98] S. Ganguli, G. Papageorgiou, S. Glavaski, and Elgersma M. Aircraft fault detection, isolation and reconfiguration in the presence of measurement errors. In *AIAA Guidance, Navigation and Control Conference and Exhibit*, number AIAA-2006-6551, Keystone, Co, August 2006.

[99] V. Gavrilets. Damage tolerant flight control systems for unmanned aircraft. In *ICAS/ATIO Conference*, 2008.

[100] A. Gelb, editor. *Applied Optimal Estimation*. MIT Press, 1974.

[101] O.H. Gerlach. *Analyse van een mogelijke methode voor het meten van prestaties en stabiliteits- en besturingseigenschappen van een vliegtuig in niet-stationaire, symmetrische vluchten*. PhD thesis, Technische Hogeschool Delft Vliegtuigbouwkunde, 1964.

[102] A.K. Ghosh and S.C. Raisinghani. Parameter estimation from flight data of an unstable aircraft using neural networks. *AIAA Journal of Aircraft*, 39(5):892–894, 2000.

[103] G.C. Goodwin and R.L. Payne. *Dynamic System Identification: Experiment Design and Data Analysis*. Academic Press, 1977.

[104] P. Goupil. Airbus overview of fault tolerant control. In *Garteur AG-16 Workshop*, 4-5 April 2006.

[105] P. Goupil and A. Marcos. *Fault Tolerant Flight Control – A Benchmark Challenge*, chapter Industrial review, pages 517–532. Springer-Verlag, 2010.

[106] I.M. Gregory, C. Cao, E. Xargay, N. Hovakimyan, and X. Zou. $\mathcal{L}_1$ adaptive control design for nasa airstar flight test vehicle. In *Proceedings of the AIAA Guidance, Navigation and Control Conference and Exhibit*, number AIAA-2009-5738, 2009.

[107] J.E. Groszkiewicz and M. Bodson. Flight control reconfiguration using adaptive methods. In *Proceedings of the 34th Conference on Decision and Control*, pages 1159–1164, 1995.

[108] B. Gunston. *Modern Fighters*. Salamander Books ltd., London, 1988.

[109] Chingiz Hajiyev and Fikret Caliskan. *Fault Diagnosis and Reconfiguration in Flight Control Systems*, volume 2 of *Cooperative Systems*. Kluwer Academic Publishers, 2003.

[110] R. Hallouzi. *Multiple-Model based Diagnosis for Adaptive Fault-Tolerant Control*. PhD thesis, Delft University of Technology, 2008.

[111] R. Hallouzi and M. Verhaegen. Fault-tolerant subspace predictive control applied to a boeing 747 model. *AIAA Journal of Guidance, Control and Dynamics*, 31:873–883, 2008.

[112] P.G. Hamel and R.J. Jategaonkar. Evolution of flight vehicle system identification. *Journal of Aircraft*, 33(1):9–28, January-February 1996.

[113] R. Hammett. Design by extrapolation: an evaluation of fault tolerant avionics. *Aerospace and Electronic Systems Magazine, IEEE*, 17(4):17–25, April 2002.

[114] J.F. Hanaway and R.W. Moorehead. Space shuttle avionics system. Technical Report SP-504, NASA, 1989.

[115] C. Hanke. The simulation of a large jet transport aircraft. volume i: Mathematical model. Technical Report CR-1756, NASA and the Boeing company, 1971.

[116] C. Hanke and D. Nordwall. The simulation of a jumbo jet transport aircraft. volume ii: Modelling data. Technical Report CR-114494/D6-30643-VOL2, NASA and the Boeing company, 1970.

[117] M. Harefors and D.G. Bates. Integrated propulsion-based flight control system design for a civil transport aircraft. In *Proceedings of the 2002 IEEE International Conference on Control Applications*, pages 132–137, 2002.

[118] O. Harkegard. *Backstepping and Control Allocation with Applications to Flight Control*. PhD thesis, Linkoping University, Sweden, 2003.

[119] R.A. Hess and S.R. Wells. Sliding mode control applied to reconfigurable flight control design. *AIAA Journal of Guidance, Control and Dynamics*, 26(3):452–462, May-June 2003.

[120] J.C. Hoff and M.V. Cook. Initial evaluation of the modified stepwise regression procedure to estimate aircraft stability and control parameters from flight test data. College of Aeronautics report No. 9313, Cranfield University, October 1993.

[121] Florian Holzapfel. Dynamic inversion based control concept with application to an unmanned aerial vehicle. In *AIAA Guidance, Navigation, and Control Conference and Exhibit*, number AIAA-2004-4907, 2004.

[122] Florian Holzapfel. *Nichtlineare adaptive Regelung eines unbemannten Fluggerätes*. PhD thesis, Lehrstuhl für Flugmechanik und Flugregelung, Technische Universität München, 2004.

[123] C. Huang. Analysis and simulation of control distributor concept for a control- reconfigurable aircraft. In *AIAA Guidance, Navigation and Control Conference*, pages 726–735, Minneapolis, MN; USA, 15-17 August 1988.

[124] H.O. Huisman. Fault tolerant flight control based on real-time physical model identification and nonlinear dynamic inversion. Master's thesis, Delft University of Technology, Faculty of Aerospace Engineering, Control and Simulation Division, June 20 2007.

[125] P. A. Ioannou and P.V. Kokotovic. *Adaptive systems with reduced models*. Springer-Verlag, 1983.

[126] Petros A. Ioannou and Jing Sun. *Robust Adaptive Control*. Prentice-Hall, Inc., Upper Saddle River, NJ, USA, 1995.

[127] C. R. Jarvis and K. J. Szalai. Ground and flight test experience with a triple redundant digital fly by wire control system. Technical Report 19810010480, NASA, 1981.

[128] Ravindra Jategaonkar. *Flight Vehicle System Identification: A Time Domain Methodology*, volume 216 of *Progress in Astronautics and Aeronautics Series*. AIAA, first edition, 2006.

[129] Ravindra Jategaonkar and E. Plaetschke. Maximum likelihood estimation of parameters in linear systems with process and measurement noise. Technical Report Forschungsbericht 87-20, DFVLR, 1978.

[130] A.H. Jazwinksi. *Stochastic Processes and Filtering Theory*. Academic Press, New York, 1970.

[131] Dennis R. Jenkins. *Hypersonics Before the Suttle*. Number SP-2000-4518 in Monographs in Aerospace History. NASA, June 2000.

[132] J. Jiang. Fault-tolerant control systems – an introductory overview. *ACTA Automatica Sinica*, 31(1):161–174, January 2005.

[133] Mufeed Mahmoud Jin, Jin Jiang, and Youmin Zhang. Optimal control law for fault tolerant control systems.

[134] Macarthur Job. *Air Disaster*, volume 2. Aerospace Publications Pty Ltd, 1996.

[135] E.H. Johnson, A.J. Calise, H.A. El-Shirbiny, and R.T. Rysdyk. Feedback linearization with neural network augmentation applied to x-33 attitude control. In *Proceedings of the AIAA Guidance, Navigation and Control Conference and Exhibit*, number AIAA-2000-4157, 2000.

[136] Eric. N. Johnson. *Limited Authority Adaptive Flight Control*. PhD thesis, Georgia Institute of Technology, November 2000.

[137] Eric N. Johnson and Anthony J. Calise. pseudo-control hedging: a new method for adaptive control. In *Advances in Navigation Guidance and Control Technology Workshop*, 2000.

[138] Colin N. Jones. Reconfigurable flight control, first year report. Technical report, University of Cambridge, March 2005.

[139] H.L. Jonkers. Application of the kalman filter to flight path reconstruction from flight test data including estimation of instrumental bias error corrections. Technical Report VTH-162, Delft University of Technology, Department of Aerospace Engineering, February 1976.

[140] Hans-Dieter Joos, Johann Bals, Gertjan Looye, Klaus Schnepper, and Andras Varga. A multi-objective optimisation-based software environment for control systems design. In *Proceedings of the IEEE International Symposium on Computer Aided Control System Design*, pages 7–14, Glasgow, Scotland, UK, September 2002.

[141] D.A. Joosten, T.J.J. van den Boom, and T.J.J. Lombaerts. Effective control allocation in fault-tolerant flight control with mpc and feedback linearization. In *Proceedings of the European Conference on Systems and control*, pages 3552–3559, Kos, Greece, July 2007.

[142] D.A. Joosten, T.J.J. van den Boom, and T.J.J. Lombaerts. Computationally efficient use of mpc and dynamic inversion for reconfigurable flight control. In *AIAA Guidance, Navigation and Control Conference and Exhibit*, number AIAA-2008-7431, Honolulu, HI, August 18-21 2008.

[143] D.A. Joosten, T.J.J. van den Boom, and T.J.J. Lombaerts. Fault-tolerant control using dynamic inversion and model-predictive control applied to an aerospace benchmark. In *the Proceedings of the 17th IFAC world congress*, volume 17, pages 12030–12035, 2008.

[144] T.L. Jordan and R.M. Bailey. Nasa langley's airstar testbed - a subscale flight test capability for flight dynamics and control system experiments. In *AIAA Guidance, Navigation and Control Conference and Exhibit*, number AIAA-2008-6660, Honolulu, Hawaii, 18 – 21 August 2008.

[145] T.L. Jordan, W.M. Langford, and J.S. Hill. Airborne subscale transport aircraft research testbed - aircraft model development. In *AIAA Guidance, Navigation and Control Conference*, number AIAA-2005-6432, 2005.

[146] S. Juliana, Q.P. Chu, J.A. Mulder, and T. Van Baten. The analytical derivation of nonlinear dynamic inversion control for parametric uncertain system. In *AIAA Guidance, Navigation, and Control Conference and Exhibit*, number AIAA-2005-5849, August 2005.

[147] R. Kadali, B. Huang, and A. Rossiter. A data driven subspace approach to predictive controller design. *Control Engineering Practice*, 11(3):261–278, 2003.

[148] M.M. Kale and A.J. Chipperfield. Stabilized mpc formulations for robust reconfigurable flight control. *Control Engineering Practice*, 13(6):771–788, 2005.

[149] R. Kalman. A new approach to linear filtering and prediction problems. *Transactions of the ASME*, 82:35–45, 1960. Series D.

[150] R. Kalman and R. Bucy. New results in linear filtering and prediction theory. *Journal of Basic Engineering, series D*, 83:95–108, 1961.

[151] S. Kanev. *Robust fault-tolerant control*. PhD thesis, University of Twente, 2004.

[152] T. Keviczky and G.J. Balas. Software enabled receding horizon control for autonomous unmanned aerial vehicle guidance. *AIAA Journal of Guidance, Control and Dynamics*, 29(3):680–694, 2006.

[153] K. Kim, K. Lee, and Y. Kim. Reconfigurable flight control system design using direct adaptive method. *AIAA Journal of Guidance, Control and Dynamics*, 26(4):543–550, July–August 2003.

[154] I. Kitsios, V. Dobrokhodov, I. Kaminer, K.D. Jones, E. Xargay, N. Hovakimyan, C. Cao, M.I. Lizarraga, I.M. Gregory, N.T. Nguyen, and K. KrishnaKumar. Experimental validation of a metrics driven $\mathcal{L}_1$ adaptive control in the presence of general unmodeled dynamics. In *Proceedings of the AIAA Guidance, Navigation and Control Conference and Exhibit*, number AIAA-2009-6188, 2009.

[155] V. Klein. Aircraft parameter estimation in the frequency domain. In *Proceedings of the AIAA Atmospheric Flight Mechanics Conference and Exhibit*, number AIAA-1978-1344, 1978.

[156] V. Klein. Maximum likelihood method for estimating airplane stability and control parameters from flight data in frequency domain. Technical Report TP-1637, NASA, 1980.

[157] V. Klein, J.G. Batterson, and P.C. Murphy. Determination of airplane model structure from flight data by using modified stepwise regression. Technical Report TP-1916, NASA, October 1981.

[158] V. Klein and D.A. Keskar. Frequency domain identification of a linear system using maximum likelihood estimation. In *5th IFAC Symposium on Identification and System Parameter Estimation*, volume 2, pages 1039–1046. Pergamon Press, 1979.

[159] Vladislav Klein and Eugene A. Morelli. *Aircraft System Identification, Theory and Practice*. AIAA Education Series, pp.141-158, 2006.

[160] K. KrishnaKumar and K. Gundy-Burlet. Intelligent control approaches for aircraft applications. Technical report, NeuroEngineering Laboratory, NASA Ames Research Center.

[161] K. KrishnaKumar, S. Rickard, and S. Bartholomew. Adaptive neuro-control for spacecraft attitude control. *Neurocomputing*, 9:131–148, 1995.

[162] M. Krstic, I. Kanellakopoulos, and P. V. Kokotovic. *Nonlinear and Adaptive Control Design*. John Wiley & Sons, 1995.

[163] J.F. Kuhlberg, J. Kniat, D.M. Newirth, J.C. Jamison, and J.R. Switalski. Transport engine control design. In *AIAA, SAE and ASME, Joint Propulsion Conference, 18th*, Cleveland, Ohio, June 1982.

[164] M. Laban. Online aircraft state and parameter estimation. Technical Report AGARD-CP-519, paper 29, AGARD, May 1992.

[165] M. Laban. *Online aircraft aerodynamic model identification*. PhD thesis, Delft University of Technology, 1994.

[166] M. Laban and K. Masui. Total least squares estimation of aerodynamic model parameters from flight data. *Journal of Aircraft*, 30(1):150–152, 1993.

[167] M. Laban and J.A. Mulder. Online identification of aircraft aerodynamic model parameters. In *9th IFAC/IFORS Symposium on "Identification and System Parameter Estimation"*, Budapest, Hungary, July 1991.

[168] E. Lavretsky. Combined / composite model reference adaptive control. In *Proceedings of the AIAA Guidance, Navigation and Control Conference and Exhibit*, number AIAA-2009-6065, 2009.

[169] X. Le Tron. Airbus fly-by-wire: An integrated system design. In *Garteur AG-16 Workshop*, 4-5 April 2006.

[170] D. Learmount. Missile attack, great escape. *Flight International*, pages 34 – 38, 21/12/2004 - 03/01/2005.

[171] S. Lee, C. Ha, and B.S. Kim. Adaptive nonlinear control system design for helicopter robust command augmentation. *Aerospace Science and Technology*, 9:241–251, 2005.

[172] B. Lemaignan. Flying with no flight controls: Handling qualities analyses of the baghdad event. In *AIAA-2005-5907*, 2005.

[173] D. Li, N. Hovakimyan, and C. Cao. $\mathcal{L}_1$ adaptive controller in the presence of input saturation. In *Proceedings of the AIAA Guidance, Navigation and Control Conference and Exhibit*, number AIAA-2009-6064, 2009.

[174] L. Ljung. *System Identification, Theory for the user*. Prentice Hall, Upper Saddle River, NJ, USA, second edition edition, 1999.

[175] T.J.J. Lombaerts and J. Breeman. Garteur ag-16 benchmark model: Boeing 747 model and control surface information. Technical report, Delft University of Technology and Dutch Aerospace Laboratory NLR, September 2005. for the Group for Aeronautical Research and Technology in Europe GARTEUR, Action Group of Fault Tolerant Flight Control FM-AG(16).

[176] T.J.J. Lombaerts, Q.P. Chu, and J.A. Mulder. *Lecture Notes AE4-301, Automatic Flight Control System Design*. Delft University of Technology, Faculty of Aerospace Engineering, Delft, The Netherlands, January 2005.

[177] T.J.J. Lombaerts, D.A. Joosten, J.A. Breeman, M.H. Smaili, A.J.J. van den Boom, Q.P. Chu, J.A. Mulder, and M. Verhaegen. Assessment criteria as specifications for reconfiguring control. In *AIAA-2006-6331*, 2006.

[178] T.J.J. Lombaerts, D.A. Joosten, J.H.Breemand, H.M. Smaili, Q.P Chu, T.J.J. van den Boom, J.A. Mulder, and M. Verhaegen. Assessment criteria as specifications for reconfiguring control. In *proceedings of the AIAA Guidance, Navigation, and Control Conference and Exhibit*, number AIAA-2006-6331, Keystone, CO, August 2006.

[179] T.J.J. Lombaerts, J.A. Mulder, G.M. Voorsluijs, and R. Decuypere. Design of a robust flight control system for a mini-uav. In *Proceedings of the AIAA Guidance, Navigation and Control Conference and Exhibit*, number AIAA-2005-6408, 2005.

[180] G. Looye and H.-D. Joos. Design of autoland controller functions with multiobjective optimization. *AIAA Journal of Guidance, Control and Dynamics*, 29(2):475–484, March-April 2006.

[181] G.H.N. Looye. *An Integrated Approach to Aircraft Modelling and Flight Control Law Design*. PhD thesis, Delft University of Technology, 2007.

[182] W. Luo and S.A. Billings. Adaptive model selection and estimation for nonlinear systems using a sliding data window. *Signal Processing*, 46:179–202, 1995.

[183] W. Luo and S.A. Billings. Structure selective updating for nonlinear models and radial basis function neural networks. *International Journal of Adaptive Control and Signal Processing*, 12:325–345, 1998.

[184] W. Luo, S.A. Billings, and K.M. Tsang. On-line structure detection and parameter estimation with exponential windowing for nonlinear systems. *European Journal of Control*, 2:291–304, 1996.

[185] J.M. Maciejowski. *Predictive control with constraints*. Prentice Hall, 2002.

[186] J.M. Maciejowski and Colin N. Jones. Mpc fault-tolerant flight control case study: Flight 1862. In *Proceedings of the 5th IFAC Symposium on Fault Detection, Supervision and Safety of Technical Processes SAFEPROCESS*, pages 121–126, Washington DC, USA, June 2003.

[187] R.E. Maine and K.W. Illif. Agard flight test techniques series, volume 3 on identification of dynamic systems - application to aircraft, part 1: The output error approach. Technical report, AGARDograph, 1986.

[188] Gerard Maoui, editor. *Cockpits by Airbus Industrie*. Cherche midi entreprise, 1998.

[189] A. Marcos. A linear parameter varying model of the boeing 747-100/200 longitudinal motion. Master's thesis, University of Minnesota, 2001.

[190] A. Marcos and G. Balas. Linear parameter varying model of the boeing 747-100/200 longitudinal motion. In *Proceedings of the AIAA Guidance, Navigation and Control Conference and Exhibit*, number AIAA-2001-4347, 2001.

[191] A. Marcos and G. Balas. A boeing 747100/200 aircraft fault tolerant and diagnostic benchmark. Technical Report AEMUoM20031, Department of Aerospace and Engineering Mechanics, University of Minnesota, 2003.

[192] A. Marcos and G. Balas. A robust integrated controller/diagnosis aircraft application. *International Journal of Robust and Nonlinear Control*, 15:531–551, 2005.

[193] A. Marcos, S. Ganguli, and G.J. Balas. An application of $\mathcal{H}_\infty$ fault detection and isolation to a transport aircraft. *Control Engineering Practice*, 13:105–119, 2005.

[194] M. Martin Gestwa, D. Leiling, and J.M. Bauschat. The software development environment of the flying test-bed attas. In *AIAA Modeling and Simulation Technologies Conference and Exhibit*, number AIAA 2005-6211, 2005.

[195] J.M. Mendel. *Lessons in Estimation Theory for Signal Processing, Communications, and Control*. Prentice Hall, 1995.

[196] Allan J. Miller. *Subset Selection in Regression*. Chapman & Hall/CRC, 2002.

[197] T.R. Moes, H. Smith, and E.A. Morelli. Flight investigation of prescribed simultaneous independent surface excitations for real-time parameter identification. Technical Report TM-2003-212029, NASA, 2003.

[198] T.R. Moes, H. Smith, and E.A. Morelli. Flight investigation of prescribed simultaneous independent surface excitations for real-time parameter identification. In *Proceedings of the AIAA Atmospheric Flight Mechanics Conference and Exhibit*, number AIAA-2003-5702, 2003.

[199] E.A. Morelli. Nonlinear aerodynamic modeling using multivariate orthogonal functions. In *AIAA Atmospheric Flight Mechanics Conference*, Monterey, CA, August 1993.

[200] E.A. Morelli. Global nonlinear aerodynamic modeling using multivariate orthogonal functions. *Journal of Aircraft*, 32(2):270–277, March-April 1995.

[201] E.A. Morelli. Global nonlinear parametric modeling with application to f-16 aerodynamics. In *American Control Conference*, number WP04-2, Philadelphia, PA, June 1998. Paper ID i-98010-2.

[202] E.A. Morelli. In-flight system identification. In *Proceedings of the AIAA Atmospheric Flight Mechanics Conference and Exhibit*, number AIAA-1998-4261, 1998.

[203] E.A. Morelli. Real-time parameter estimation in the frequency domain. *Journal of Guidance, Control and Dynamics*, 23(5):812–818, 2000.

[204] E.A. Morelli and M.S. Smith. Real-time dynamic modeling - data information requirements and flight test results. In *AIAA Atmospheric Flight Mechanics Conference and Exhibit*, 2008.

[205] W. Morse and K. Ossman. Model-following reconfigurable flight control system for the afti/f-16. *AIAA Journal of Guidance, Control and Dynamics*, 13(6):969–976, 1990.

[206] H. Muhammad. *identification of turboprop thrust from flight test data*. PhD thesis, Delft University of Technology, December 1995.

[207] J.A. Mulder. Estimation of thrust and drag in nonsteady flight. In *Proceedings of the 4th IFAC Symposium, Identification and System Parameter Estimation*, Tbilisi, 1976.

[208] J.A. Mulder. *Design and evaluation of dynamic flight test manoeuvers*. PhD thesis, TU Delft, Faculty of Aerospace Engineering, 1986.

[209] J.A. Mulder. Design and evaluation of dynamic flight test manoeuvers. Technical Report LR-497, Delft University of Technology, Delft, the Netherlands, 1986.

[210] J.A. Mulder, Q.P. Chu, J.K. Sridhar, J.H. Breeman, and M. Laban. Non-linear aircraft flight path reconstruction review and new advances. *Progress in Aerospace Sciences*, 35(7):673–726, 1999.

[211] J.A. Mulder, H.L. Jonkers, J.J. Horsten, J.H. Breeman, and J.L. Simons. Analysis of aircraft performance, stability and control measurements. In *AGARD Lecture Series*, number 104, 1979.

[212] J.A. Mulder, W.H.J.J. van Staveren, J.C. van der Vaart, and E. de Weerdt. *Lecture Notes AE3-302, Flight Dynamics*. Delft University of Technology, Faculty of Aerospace Engineering, Delft, The Netherlands, January 2006.

[213] J.A. Mulder, J.K. Sridhar, and J.H. Breeman. Identification of dynamic systems, applications to aircraft, part 2: nonlinear analysis and manoeuvre design. volume 3 part 2 300, AGARDograph, 1986.

[214] P.C. Murphy and V. Klein. Estimation of aircraft unsteady aerodynamic parameters from dynamic wind tunnel testing. *AIAA*, 4016:1–9, June 2001.

[215] P.C. Murphy and V. Klein. Validation of methodology for estimating aircraft unsteady aerodynamic parameters from dynamic wind tunnel tests. In *Proceedings of the AIAA Atmospheric Flight Mechanics Conference and Exhibit*, number AIAA-2003-5397, 2003.

[216] N.E. Nahi. *Estimation Theory and Applications*. John Wiley & Sons, 1969.

[217] K.S. Narendra and A.M. Annaswamy. A new adaptive law for robust adaptation without persistent excitation. *IEEE Transactions on Automatic Control*, AC-32(2):134–145, February 1987.

[218] K.S. Narendra and J. Balakrishnan. Adaptive control using multiple models. *IEEE Transactions on Automatic Control*, 42(2):171–187, February 1997.

[219] N.T. Nguyen and K. KrishnaKumar. Hybrid intelligent flight control with adaptive learning parameter estimation. *Journal of Aerospace Computing, Information and Communication*, 6:171–186, March 2009.

[220] N.T. Nguyen, K. KrishnaKumar, and J. Boskovich. An optimal control modification to model-reference adaptive control for fast adaptation. In *Proceedings of the AIAA Guidance, Navigation and Control Conference and Exhibit*, number AIAA-2008-7283, 2008.

[221] N.T. Nguyen, K. KrishnaKumar, J. Kaneshige, and P. Nespeca. Flight dynamics and hybrid adaptive control of damaged aircraft. *AIAA Journal of Guidance, Control and Dynamics*, 31(3):751–764, May–June 2008.

[222] J. Oliveira, Q. P. Chu, J. A. Mulder, H.M.N.K. Balini, and W.G.M. Vos. Output error method and two step method for aerodynamic model identification. In *Proceedings of the AIAA Guidance, Navigation and Control Conference and Exhibit*, number AIAA-2005-6440, 2005.

[223] M.W. Oppenheimer and D.B. Doman. Efficient reconfiguration and recovery from damage for air vehicles. In *Proceedings of the AIAA Guidance, Navigation and Control Conference and Exhibit*, number AIAA-2006-6552, 2006.

[224] Aaron J Ostroff and Barton J Bacon. Force and moment approach for achievable dynamics using nonlinear dynamic inversion. In *Proceedings of the AIAA Guidance, Navigation and Control Conference and Exhibit*, number AIAA-1999-4001, pages 424–434, 1999.

[225] Aaron J Ostroff and Barton J Bacon. Enhanced ndi strategies for reconfigurable flight control. In *Proceedings of the American Control Conference*, Anchorage, AK, May 8-10 2002.

[226] R.J. Patton. Fault tolerant control systems: The 1997 situation. In *Proceedings of IFAC Symposium on SAFEPROCESS*, pages 1033–1055, HULL, UK, August 1997.

[227] J. Prakash, S. Narasimhan, and S.C. Patwardhan. Integrating model based fault diagnosis with model predictive control. *Industrial & Engineering Chemistry Research*, 44(12):4344–4360, 2005.

[228] R.W. Pratt. *Flight Control Systems, practical issues in design and implementation*. IEE/AIAA, Stevenage, UK/Reston, USA, 2000.

[229] Viswanath Ramakrishna, L.R. Hunt, and G. Meyer. Parameter variations, relative degree, and stable inversion. *Automatica*, 37:871–880, 2001.

[230] K. J. Åström. Maximum likelihood and prediction error methods. *Automatica*, 16(5):551–574, September 1980.

[231] Jacob Reiner, Gary J. Balas, and William L. Garrard. Flight control design using robust dynamic inversion and time-scale separation. *Automatica*, 32(11):1493–1504, 1996.

[232] M. Rodrigues, D. Theilliol, S. Aberkane, and D. Sauter. Fault tolerant control design for polytopic lpv systems. *International Journal of Applied Mathematics and Computer Science*, 17:27–37, 2007.

[233] A.P. Sage and J.L. Melsa. *Estimation Theory with Applications to Communications and Control*. McGraw-Hill, 1971.

[234] Shankar Sastry and Marc Bodson. *Adaptive Control: stability, convergence and robustness*. Prentice Hall, Inc., 1989.

[235] J.D. Schiermann, D.G. Ward, J.R. Hull, N. Gandhi, M.W. Oppenheimer, and D.B. Doman. Integrated adaptive guidance and control for re-entry vehicles with flight-test results. *AIAA Journal of Guidance, Control and Dynamics*, 27(6):975–988, November-December‘ 2004.

[236] G. Schram, G.J.C. Copinga, P.M. Bruijn, and H.B. Verbruggen. Failure-tolerant control of aircraft; a fuzzy logic approach. In *Proceedings of the American Control Conference*, pages 2281–2285, Philadelphia, Pennsylvania, June 1998.

[237] G. Schwarz. Estimating the dimension of a model. *Annals of Statistics*, 14(3):416–464, 1978.

[238] F.C. Schweppe. *Uncertain Dynamic Systems*. Prentice Hall, Upper Saddle River, NJ, 1973.

[239] J. Shin and C.M. Belcastro. Performance analysis on fault tolerant control system. *IEEE Transactions on Control Systems Technology*, 14:920–925, 2006.

[240] J. Shin, N.E. Wu, and C.M. Belcastro. Adaptive linear parameter varying control synthesis for actuator failure. *Journal of Guidance, Control and Dynamics*, 27:787–794, 2004.

[241] Y. Shin, A.J. Calise, and M.D. Johnson. Adaptive control of advanced fighter aircraft in nonlinear flight regimes. *AIAA Journal of Guidance, Control and Dynamics*, 31(f5):1464–1477, September–October 2008.

[242] Y. Shtessel, J. Buffington, and S. Banda. Tailless aircraft flight control using multiple time scale reconfigurable sliding modes. *IEEE Transactions on Control Systems Technology*, 10(3):288–296, May 2002.

[243] Y.B. Shtessel and J. Buffington. Multiple time scale flight control using reconfigurable sliding modes. *AIAA Journal of Guidance, Control and Dynamics*, 22(6):873–883, November-December 1999.

[244] Jean-Jacques E. Slotine and Weiping Li. *Applied Nonlinear Control*. Prentice Hall, 1991.

[245] H.M. Smaili, J. Breeman, and T.J.J. Lombaerts. A simulation benchmark for aircraft survivability assessment. In *Proceedings of the International Congress of Aeronautical Sciences*, number 2008-9.3.2, 2008.

[246] H.M. Smaili, J. Breeman, T.J.J. Lombaerts, and D.A. Joosten. *Fault Tolerant Flight Control – a Benchmark Challenge*, chapter RECOVER: A Benchmark for Integrated Fault Tolerant Control Evaluation, pages 171–212. Springer-Verlag, 2009.

[247] M.H. Smaili. Flight Data Reconstruction and Simulation of EL AL Flight 1862. Final thesis, T.U. Delft, November 1997.

[248] M.H. Smaili. Flight data reconstruction and simulation of the 1992 amsterdam bijlmermeer airplane accident. In *AIAA-2000-4586*, August 2000.

[249] M.H. Smaili, J. Breeman, T.J.J. Lombaerts, and D.A. Joosten. A simulation benchmark for integrated fault tolerant flight control evaluation. In *Proceedings of the AIAA Modelling and Simulation Technologies Conference and Exhibit*, number AIAA-2006-6471, 2006.

[250] M.R. Smith, T.R. Moes, and E.A. Morelli. Real-time stability and control derivative extraction from f-15 flight data. Technical Report TM-2003-212027, NASA, 2003.

[251] M.S. Smith, T.R. Moes, and E.A. Morelli. Real-time stability and control dervitative extraction from f-15 flight data. In *Proceedings of the AIAA Atmospheric Flight Mechanics Conference and Exhibit*, number AIAA-2003-5701, 2003.

[252] M.W. Soijer. Sequential computation of total least-squares parameter estimates. *AIAA Journal of Guidance, Control and Dynamics*, 27(3):501–503, 2004.

[253] A. Sollazzo, G. Morani, and A. Giovanni. *Fault Tolerant Flight Control – a Benchmark Challenge*, chapter An Adaptive Fault-Tolerant FCS for a Large Transport Aircraft, pages 265–283. Springer-Verlag, 2009.

[254] L. Sonneveldt, Q.P. Chu, and J.A. Mulder. Nonlinear flight control design using constrained adaptive backstepping. *AIAA Journal of Guidance, Control and Dynamics*, 30(2):322–336, March–April 2007.

[255] L. Sonneveldt, E.R. van Oort, Q.P. Chu, and J.A. Mulder. Nonlinear adaptive trajectory control applied to an f-16 model. *AIAA Journal of Guidance, Control and Dynamics*, 32(1):25–39, January–February 2009.

[256] R. Srichander and B.K. Walker. Stochastic stability analysis for continuous-time fault tolerant control systems. *International Journal of Control*, 57(2):433–452, 1993.

[257] B.L. Stevens and F.L. Lewis. *Aircraft Control and Simulation*. Wiley Europe, Printed in Chichester, second edition, 2003.

[258] E. Stijger. Mlu testing at leeuwarden. *Code One magazine*, 17(2), second quarter 2002.

[259] P. Stoica. A test for whiteness. *IEEE transactions on automatic control*, AC-22(6):992–993, December 1977.

[260] O. Stroosma, M.M. Van Paassen, and M. Mulder. Using the simona research simulator for human-machine interaction research. In *AIAA Modeling and Simulation Conference and Exhibit*, number AIAA-2003-5525, August 2003.

[261] N. Tanaka, S. Suzuki, K. Masui, and H. Tomita. Restructurable guidance and control for aircraft with failures considering gust effects. *AIAA Journal of Guidance, Control and Dynamics*, 29(3):635–642, May–June 2006.

[262] G Tao, S. Chen, and S. Joshi. An adaptive actuator failure compensation controller using output feedback. *IEEE Transactions on Automatic Control*, 47(3):506–511, 2002.

[263] M.B. Tischler and R.K. Remple. *Aircraft and Rotorcraft System Identification, Engineering Methods with Flight Test Examples*. AIAA Education Series, 2006.

[264] H. Toutenburg. *Prior Information in Linear Models*. Wiley Europe, London, 1982.

[265] T.J.J. van den Boom and T.C.P.M. Backx. Model predictive control. lecture notes for the course SC 4060, January 2005. Delft University of Technology.

[266] T.J.J. van den Boom and S. Bennani. Reconfigurable handling & flying qualities for degraded flight systems using model predictive control, stw research proposal. Technical report, Delft University of Technology, January 2004.

[267] C.A.A.M. van der van der Linden. *DASMAT – Delft University Aircraft Simulation Model and Analysis Tool, A Matlab/Simulink Environment for Flight Dynamics and Control Analysis*. Series 03, Control and Simulation 03. Delft University Press, DUP Science, Delft, The Netherlands, 1998.

[268] R. van der Sluis, G. Schram, S. Bennani, and J.A. Mulder. Stability analysis of nonlinearly scheduled fault tolerant control system with varying structure. In *Proceedings of the AIAA Guidance, Navigation and Control Conference*, number AIAA-2000-37158, 2000.

[269] S. Van Huffel and J. Vandewalle. The total least squares problem: Computational aspects and analysis. In *Society for Industrial and Applied Mathematics*, pages 27–39, Philadelphia, PA, 1991.

[270] E. van Kampen, Q.P. Chu, and J.A. Mulder. Continuous adaptive critic flight control aided with approximated plant dynamics. In *Proceedings of the AIAA Guidance, Navigation and Contol Conference and Exhibit*, number AIAA-2006-6429, 2006.

[271] E.R. van Oort, Q.P. Chu, J.A. Mulder, and T.J.J. van den Boom. Robust model predictive control of a feedback linearized nonlinear f-16/matv aircraft model. In *Proceedings of the AIAA Guidance, Navigation and Control Conference and Exhibit*, number AIAA-2006-6318, 2006.

[272] M.M. Van Paassen and O. Stroosma. Dueca - data-driven activation in distributed real-time computation. In *AIAA Modeling and Simulation Conference and Exhibit*, number AIAA-2000-4503. AIAA, August 2000.

[273] W.R. van Soest, Q. P. Chu, and J. A. Mulder. Combined feedback linearization and model predictive control for re-entry flight. *AIAA Journal of Guidance, Control and Dynamics*, 29(2):427–434, 2006.

[274] J.C. van Tooren. Fuzzy aerodynamic modeling and identification. Master's thesis, Delft University of Technology, 2006.

[275] A. Varga. Design of least order residual generators for fault detection and isolation with application to monitoring actuator/surface faults for a boeing 747-100/200 aircraft. Technical report, German Aerospace Center (DLR), 2007.

[276] A. Varga and S. Hecker. Methods for threshold selection for robust residual evaluation. Technical report, German Aerospace Center (DLR), 2004.

[277] E. Vathsal, A.K. Sarkar, and J. Umakant. Nonlinear modeling and roll derivatives estimation from flight data using ols. In *AIAA Atmospheric Flight Mechanics Conference and Exhibit*, Providence, Rhode Island, August 16-19 2004.

[278] M. Verhaegen and V. Verdult. *Filtering and system identification: an introduction*. Cambridge University Press, 2007.

[279] H. Vicente de Castro and T.J.J. Lombaerts. Lecture notes robust flight control. AE4-303, May 2005.

[280] K.Y. Volyanskyy, W.M. Haddad, and A.J. Calise. A new neuroadaptive control architecture for nonlinear uncertain dynamical systems: Beyond $\sigma-$ and $e-$modifications. In *Proceedings of the 47th IEEE Conference on Decision and Control*, pages 80–85, 2008.

[281] S.J.W. Waelkens, Q. P. Chu, and J. A. Mulder. Aerodynamic model identification from flight data for the eclipse 500 very light jet. In *Proceedings of the AIAA Guidance, Navigation and Control Conference and Exhibit*, number AIAA-2005-6261, 2005.

[282] G.P. Walker and D.A. Allen. X-35b stovl flight control law design and flying qualities. In *Proceedings of the Biennial International Powered Lift Conference and Exhibit*, number AIAA-2002-6018, 2002.

[283] X. Wang, B. Huang, and T. Chen. Data driven predictive control for solid oxide fuel cells. *Journal of Process Control*, 17(2):103–114, 2007.

[284] D.G. Ward and A. R. Barron. Real-time parameter identification for self-designing flight control. In *Proc. Nat'l Aerospace and Electronics Conf. (NAECON)*, Dayton, OH, May 1994.

[285] D.G. Ward and R.L. Barron. A self-designing receding horizon optimal flight controller. In *Proceedings of the American Control Conference*, Seattle, Washington, June 1995.

[286] K. Watanabe. *Adaptive Estimation and Control: Partitioning Approach*. Prentice Hall, London, 1991.

[287] Susanne Weiss, Holger Friehmelt, Ermin Plaetschke, and Detlef Rohlf. X-31a system identification using single-surface excitation at high angles of attack. *Journal of Aircraft*, 33(3):485–490, May–June 1996.

[288] P.S. Williams-Hayes. Flight test implementation of a second generation intelligent flight control system. In *Infotech@Aerospace*, 2005.

[289] K.A. Wise, J.S. Brinker, A.J. Calise, D.F. Enns, M.R. Elgersma, and P. Voulgaris. Direct adaptive reconfigurable flight control for a tailless advanced fighter aircraft. *International Journal of Robust and Nonlinear Control*, 9(14):999–1022, December 1999.

[290] C. H. Wolowicz, Jr. Brown, J. S., and W. P. Gilbert. Similitude requirements and scaling relationships as applied to model testing. Technical Report TP-1435, NASA, 1979.

[291] B.R. Woodley, J.P. How, and R.L. Kosut. Subspace based direct adaptive $\mathcal{H}_\infty$ control. *International Journal of Adaptive Control and Signal Processing*, 15:535–561, 2001.

[292] F. Wu. A generalized lpv system analysis and control synthesis framework. *International Journal of Control*, 74:745–759, 2001.

[293] Y.C. Yeh. Triple-triple redundant 777 primary flight computer. In *IEEE Aerospace Application Conference*, pages 293–307, Aspen, Colorado, 1996.

[294] T. Yucelen, A.J. Calise, W.M. Haddad, and K.Y. Volyanskyy. A comparison of a new neuroadaptive controller architecture with the $\sigma-$ and $e-$modification architectures. In *Proceedings of the AIAA Guidance, Navigation and Control Conference and Exhibit*, number AIAA-2009-6060, 2009.

[295] P.M.T. Zaal, D.M. Pool, F.N. Postema, A.C. in t Veld, M. Mulder, M.M. van Paassen, and J.A. Mulder. Design and certification of a fly-by-wire system with minimal aircraft modifications. *Journal of Guidance, Control And Dynamics*, 2010. Submitted and under review.

[296] Y. Zhang and J. Jiang. Integrated design of reconfigurable fault-tolerant control systems. *AIAA Journal of Guidance, Control and Dynamics*, 24(1):133–136, 2000.

[297] Y. Zhang and J. Jiang. Active fault-tolerant control system against partial actuator failures. *IEEE Proceedings in Control Theory Application*, 149(1):95–104, January 2001.

[298] Y. Zhang and J. Jiang. Integrated active fault-tolerant control using imm approach. *IEEE Transactions on Aerospace and Electronic Systems*, 37(4):1221–1235, October 2001.

[299] Y. Zhang and J. Jiang. Bibliographical review on reconfigurable fault-tolerant control systems. In *5th IFAC Symposium on Fault Detection, Supervision and Safety for Technical Processes*, pages 265–275, Washington DC, USA, June 9-11 2003.

[300] K. Zhou, P.K. Rachinayani, N. Liu, Z. Ren, and J. Aravna. Fault diagnosis and reconfigurable control for flight control systems with actuator failures. In *43rd IEEE Conference on Decision and Control*, Bahamas, 2004.

Index

Samenvatting

Fouttolerante vliegtuigbesturing, een aanpak gebaseerd op fysische modellen

Thomas Lombaerts

Veiligheid is van kapitaal belang in alle vervoerssystemen, maar vooral in de burgerluchtvaart. Alle ontwikkelingen in de burgerluchtvaart concentreren zich daarom op de verbetering van de veiligheid en het verminderen van risico's op ongelukken. Wanneer men de recentste statistieken van ongelukken in de burgerluchtvaart analyseert, dan onderscheidt men twee belangrijke categorieën van ongevallen die aan één enkele primaire oorzaak kunnen worden toegeschreven, namelijk ”botsing met de grond” en ”verlies van besturing tijdens de vlucht”. In de eerste categorie, ook wel gecontroleerde vlucht in het terrein genoemd, raakt een volledig functioneel vliegtuig het terrein, toe te schrijven aan oriëntatieverlies van de piloot. Deze oorzaak ligt aan de basis van 26 % van de ongevallen. Dit percentage is in de loop van de jaren verminderd dankzij de onophoudelijke evolutie van de hoeveelheid informatie in de cockpit, en de manier waarop die gepresenteerd wordt. De tweede belangrijkste categorie is ”verlies van besturing tijdens de vlucht”, wat kan worden toegeschreven aan stuurfouten van de piloot of wat te wijten is aan technische defecten of verstoringen. Tot deze categorie behoort 17% van alle vliegtuigongevallen. Dit aantal vermindert niet.

De analyse van een groot deel van de ongevallen in de laatstgenoemde categorie heeft geleid tot een algemene conclusie: vanuit het perspectief van de vluchtdynamica, met de huidige beschikbare technologie en rekencapaciteit, zou het mogelijk geweest zijn om de vliegtuigen en hun passagiers in veel van deze scenario's in veiligheid te brengen, op voorwaarde dat niet-conventionele controlestrategieën gebruikt zouden zijn. Deze niet-conventionele controlestrategieën impliceren het zogenaamde concept van actieve fouttole-

rante vliegtuigbesturing (FTFC), waar het besturingssysteem in staat is om de verandering in het vliegtuiggedrag te ontdekken en het stuurgedrag overeenkomstig aan te passen zodat het overweg kan met de verstoorde vliegtuigdynamica. De vroegere onderzoeksprojecten in FTFC omvatten het Self-Repairing Flight Control System (SRFCS) programma, het MD-11 Propulsion Controlled Aircraft (PCA) project, de Self-Designing Controller voor de F-16 VISTA, Reconfigurable Systems for Tailless Fighter Aircraft, het X-36 RESTORE programma, het NASA Intelligent Flight Control System (IFCS) F-15 programma en Damage Tolerant Flight Control Systems for Unmanned Aircraft door Athena/Honeywell. Er zijn vele alternatieve methoden om FTFC te bereiken. Al deze varianten stoten nog steeds op een aantal beperkingen, variërend van een beperkte toepassingsmogelijkheid op een beperkt aantal foutscenario's tot de beperking van het type en de omvang van de schade die wegens een vaste modelstructuur in de identificatieprocedure kan worden gecompenseerd. Een ander vaak weerkerend verschijnsel is het convergentieprobleem. Bovendien verminderen de onbekende "black box"structuren de transparantie van de aanpak, zoals bij neurale netwerken. Voorts is het bij vele methoden niet duidelijk wat er zal gebeuren wanneer het opgelegde referentiegedrag niet haalbaar is nadat de beschadiging is opgetreden.

De benadering zoals uitgewerkt in deze thesis is een fysische modulaire aanpak, waar de nadruk ligt op het gebruik van wiskundige modellen gebaseerd op vluchtdynamica. Alle variabelen die in het model verschijnen, hebben een fysieke betekenis en zijn dus interpreteerbaar, waardoor men onbekende zogenaamde "black of gray box"modellen vermijdt. Naast het feit dat dit een transparantere benadering is, die de ontwerpers en de ingenieurs toelaat om de gegevens in elke stap te interpreteren, wordt verondersteld dat deze fysieke modellen het gemakkelijker zullen maken om ze te certificeren voor toekomstige luchtvaarttoepassingen, aangezien het observeren van variabelen hier meer betekenis heeft.

Globaal gezien bestaat de algemene architectuur van deze modulaire aanpak uit drie belangrijke subgroepen, namelijk het gecontroleerde systeem, de combinatie verantwoordelijk voor de foutdetectie en identificatie (FDI) en de structuur voor fouttolerante vliegtuigbesturing (FTFC). Het gecontroleerde systeem bestaat uit het vliegtuigmodel en de actuator hardware. De mogelijke fouten in dit gecontroleerde systeem zijn respectievelijk structurele beschadigingen in het vliegtuig en defecten in de actuator hardware. Foutieve metingen in de sensoren zijn niet meegenomen in dit onderzoek, aangezien verondersteld kan worden dat de gevolgen van deze defecten minder belangrijk zijn dankzij redundante sensoren en detectie van het verlies van sensoren. Niettegenstaande deze aanname maakt laatstgenoemde categorie van foutscenario's deel uit van aanbevolen toekomstig onderzoek.

De architectuur van de foutdetectie en identificatie (FDI) bestaat uit verscheidene componenten. Het hart van deze structuur is de tweestapsmethode (TSM) module. Deze module bestaat uit een afzonderlijke stap voor de schatting van de vliegtuigtoestand, gevolgd door een stap voor de aërodynamische modelidentificatie, waar de laatstgenoemde een gecombineerde procedure is voor structuurselectie en parameterschatting (SSPE). De stap van de toestandschatting is een niet-lineair probleem dat door een geïtereerde extended Kalman

Filter wordt opgelost. Het aangewezen algoritme voor SSPE is adaptieve recursieve orthogonale kleinste kwadraten (AROLS). Voor het geval dat een structurele beschadiging (in de vliegtuigstructuur of in één van de stuurvlakken) optreedt, wordt de heridentificatie geïnitieerd van zodra de gemiddelde kwadratische innovatie een vooraf bepaalde drempelwaarde overschrijdt. Voor succesvolle identificatie van de besturingsafgeleiden van elk individueel stuurvlak, is evaluatie van de stuureffectiviteit noodzakelijk na het optreden van de fout. Dit kan gerealiseerd worden door multivariabele orthogonale inputsignalen op te leggen aan de actuatoren. Hoewel dit op zorgvuldige wijze moet worden gedaan zodat het beschadigde vliegtuig niet gedestabiliseerd kan worden, is het absoluut noodzakelijk om voldoende informatie te verzamelen over de efficiëntie van de stuurvlakken voor de control allocation module, die deel uitmaakt van de FTFC structuur. Men zou deze evaluatiesignalen kunnen introduceren enkel wanneer ze strikt nodig zijn, d.w.z. wanneer een succesvolle aanpassing van de regelwetten niet mogelijk is, omwille van een gebrek aan informatie over deze stuurvlak efficiëntie. De tweestapsmethode is ideaal om structurele beschadigingen te identificeren, maar voor de opsporing van actuator defecten is een afzonderlijk observatie algoritme voor de servo's nodig, zoals een Actuator Health Monitoring System (AHMS).

Vier andere functies kunnen worden gegroepeerd in de fouttolerante vliegtuigbesturingsstructuur (FTFC). Het centrale deel van deze groep is indirecte adaptieve besturing en control allocation. De indirecte adaptive besturing kan door adaptieve niet-lineaire dynamische inversie (ANDI) worden bereikt. Het voordeel van ANDI is dat het de behoefte aan gain scheduling over verschillende vluchtcondities elimineert en dat het onderlinge input-output relaties effectief loskoppelt. Voorts impliceert het NDI controle-algoritme automatisch één of andere vorm van control allocation, omwille van de structuur van de regelwet. Op basis van deze structuur is een duidelijk onderscheid zichtbaar hoe met verschillende foutscenario's wordt omgegaan. Structurele beschadigingen onafhankelijk van de stuurvlakken worden ontdekt door TSM en deze informatie over de schade wordt doorgegeven aan het ANDI algoritme door middel van de aërodynamische afgeleiden. Anderzijds worden de defecten gerelateerd aan de stuurvlakken, hetzij aërodynamisch hetzij servo gerelateerd, geïdentificeerd door respectievelijk de TSM of het actuator observatie algoritme. Deze informatie wordt doorgestuurd naar het control allocation blok. De voorkeursmethode voor control allocation is het control distributor concept (CDC), dat met de gewogen pseudo-inverse (WPI) wordt gecombineerd. Deze methode veronderstelt de aanwezigheid van een aantal gelijkaardige stuurvlakken voor redundantie. Deze veronderstelling is toegestaan voor het vliegtuigtype dat in dit onderzoeksproject wordt beschouwd, namelijk de Boeing 747. Deze benadering past in het modulaire karakter van de globale aanpak, waar het CDC principe rekening houdt met aërodynamische veranderingen en de WPI zorgt voor de adaptiviteit met betrekking tot actuator defecten. Voorts bepaalt een referentiemodel het referentiegedrag dat de gesloten lus configuratie moet volgen. Nochtans moet dit referentiemodel adaptief zijn, zodanig dat zijn signalen begrensd worden, gebaseerd op de haalbare prestaties van de gesloten lus configuratie inclusief beschadigingen. Deze aanpassing van het referentiesignaal kan door Pseudo Control Hedging (PCH) worden bereikt. Deze modulatie wordt gebaseerd op het verschil tussen het gevraagde stuursignaal en het werkelijke stuursignaal bereikt door de servo's. Deze aanpassing van het referentiesignaal wordt hoofdzakelijk aangestuurd door verzadigingseffecten in de actuatoren. Bovendien houdt deze beschermingsactie rekening met de bijgewerkte modelinformatie via actuator status, aërodynamische en besturingsafgeleiden. Op deze wijze wordt ervoor gezorgd dat geen onhaalbare referentiesignalen worden gegeven aan de gesloten lus configuratie. Deze PCH actie kan beschouwd worden als eerste beschermingsgraad van de veilige vlucht envelope, gebaseerd op de gevolgen van invoerverzadiging en bijgewerkte modelinformatie. Experimenten hebben aangetoond dat vooral het snelheidskanaal gevoelig is voor verzadigingseffecten.

Tijdens dit onderzoek is geconstateerd dat de bescherming van de veilige vlucht envelope een essentieel aspect is in deze stuuropstelling. Het maakt dan ook deel uit van aanbevolen toekomstig onderzoek. Dit beschermingsalgoritme, dat gebaseerd wordt op de haalbare prestaties die kunnen worden geschat op basis van actuator status en modelinformatie, werkt op twee niveaus. Enerzijds moet het algoritme PCH bijstaan door de output van het referentiemodel te beperken. Voorts zou de output van het control allocation blok, en dus de invoer voor de actuators, moeten worden beperkt gebaseerd op deze informatie van de bereikbare vlucht envelope.

De belangrijkste beperking van de indirecte adaptieve besturing zoals hier gekozen is dat het zich baseert op het certainty equivalence principe. Dit betekent dat de parameters van het besturingsmechanisme berekend worden op basis van de geschatte waarden van de systeemparameters alsof zij de werkelijke waarden zijn. Nochtans is er in dit onderzoek aangetoond dat deze veronderstelling niet absoluut noodzakelijk is voor toepassingen op ANDI. Meer bepaald is er geconstateerd dat de combinatie van ANDI en een lineair controlemechanisme in de buitenste lus asymptotisch ongevoelig is voor afwijkingen in de schattingen van de aërodynamische afgeleiden, vooral dankzij de aanwezigheid van integrerende actie in het lineaire controlemechanisme. Anderzijds gaat deze robuustheid niet op voor identificatiefouten in de besturingsafgeleiden. Nochtans zijn deze schattingen relatief eenvoudig identificeerbaar, omwille van de rechtstreeks aangestuurde excitatie van de stuurvlakken.

Deze voornoemde modulaire controlemethode is met succes toegepast op een accuraat simulatiemodel van de Boeing 747-100/200, inclusief verscheidene foutscenario's. Eén van de foutscenario's is gevalideerd met echte data van een specifiek ongeluk, die uit een digitaal registratietoestel van vluchtgegevens werden verkregen. In dit onderzoek is zowel een automatisch als een manueel fouttolerant vliegtuigbesturingsmechanisme ontwikkeld en geïmplementeerd op dit simulatiemodel. Het automatische controlemechanisme voldeed aan de meeste prestatievereisten en slaagde erin om het vliegtuig onder controle te houden. Het manuele controlemechanisme is uitgebreid geëvalueerd in de SIMONA onderzoekssimulator, en er is geconstateerd dat het fouttolerante controlemechanisme succesvol is in het herstellen van de stuurcapaciteit van het beschadigde vliegtuig in de scenario's die in dit onderzoeksproject werden onderzocht. De simulatieresultaten hebben aangetoond dat de hanteringseigenschappen van het fouttolerante controlemechanisme vanuit het perspectief van de piloot opvallend minder verslechteren in de meeste foutscenario's, hetgeen wijst op betere prestaties om de taak uit te voeren. Voorts is er geconstateerd dat de gemiddelde verhoging van werkbelasting na het optreden van de fout aanzienlijk wordt verminderd door het fouttolerante controlemechanisme, in vergelijking met het klassieke besturingssysteem. De gegevens wijzen in de meeste gevallen op meer consistentie onder de piloten voor de FTFC configuratie. Deze observaties zijn van toepassing voor zowel fysieke als mentale werkbelasting. Deze uitgebreide evaluaties hebben ertoe geleid dat de technologie is gestegen op de Technology Readiness Level schaal (TRL) van niveau 3/4 tot 5/6.

Tijdens dit onderzoeksproject zijn enkele vergelijkende studies uitgevoerd voor het SSPE algoritme en voor de ANDI opstelling, in combinatie met een optimalisatieprocedure voor de versterkingen in de buitenlus van het lineaire besturingsmechanisme in de ANDI opstelling. Met betrekking tot de SSPE procedure zijn twee algoritmen vergeleken, namelijk gemodificeerde stapsgewijze regressie (MSWR) en adaptieve recursieve orthogonale kleinste kwadraten (AROLS). Het vergelijken van zowel de structuurselectie als de parameterschattingsprocedures geeft een duidelijk voordeel aan het algoritme AROLS. Eerst en vooral maken het recursieve karakter en de efficiënte berekeningen het geschikt voor real time online toepassingen. Vergeleken met de gemodificeerde stapsgewijze regressieprocedure vergt het slechts een voorwaartse stap, in plaats van de gecombineerde toevoeging- en verwijderingscriteria die voor de laatstgenoemde van toepassing zijn. Voorts zijn geen belangrijke wijzigingen vereist aan AROLS voor toepassingen op beschadigde vliegtuigen, in tegenstelling tot MSWR dat een ordening op prioriteit vergt onder de kandidaat regressoren.

In het ANDI deel is een basisstructuur opgesteld, bestaande uit een dubbele NDI lus, en er is ook een verbeterde controlestructuur ontwikkeld, bestaande uit een drievoudige NDI lus. Vergelijking van simulatieresultaten van beide versies toont duidelijke verbeteringen aan voor de laatstgenoemde structuur. Het feit dat de verbeterde versie een extra inversielus bevat en op minder veronderstellingen gebaseerd is, maakt dat het over meer stuurautoriteit beschikt en resulteert in een ruimere vlucht envelope waarin het vliegtuig onder controle kan worden gehouden, vergeleken met de basisstructuur.

Een op meerdere doelstellingen gebaseerde optimalisatieprocedure is uitgevoerd voor parametersynthese van de versterkingsfactoren in het lineaire controlemechanisme. Dit laat toe om de waarden van deze versterkingsfactoren te verbeteren, gebaseerd op vooraf bepaalde optimaliseringscriteria terwijl rekening wordt gehouden met beperkingen gedefinieerd als ongelijkheden. Het vergelijken van dit geoptimaliseerde resultaat met de initiële prestaties toont subtiele verbeteringen, vooral op het vlak van het wegwerken van snelheidsverstoringen. Dankzij de goede initiële keuze van de waarden van deze versterkingsfactoren volgens het principe van het tijdschaalonderscheid, kan op het gebied van de optimalisatie van deze waarden geen belangrijke verbetering meer worden bereikt. Nochtans kan op meerdere doelstellingen gebaseerde parameteroptimalisering nog kleine verbeteringen afdwingen in het maximaliseren van de optimale prestaties met betrekking tot de expliciet gedefinieerde criteria.

Een belangrijke en grote volgende stap in het ontwikkelingsproces van fouttolerante vliegtuigbesturing is de toepassing van deze fysische modulaire benadering in een testvliegtuig, bij voorkeur een specifiek voor dit doel ontworpen onbemand vliegtuig. Dit is een belangrijke aanbeveling voor toekomstig onderzoek.

Acknowledgements

This thesis is the result of four years of research at the division of Control and Simulation at Delft University of Technology. During these years, many people have played a role in the realisation of this thesis. Although it is almost impossible to list everyone here, I would like to mention some in particular.

First of all, I would like to thank my promoter prof. dr. ir. J.A. (Bob) Mulder and my co-promoter dr. Q.P. (Ping) Chu. Four years ago, they came up with the idea for me to pursue a PhD degree and to do research in the discipline of Fault Tolerant Flight Control. They also launched the idea to focus on a physical approach for this challenging control problem. After four years of research, it has turned out that this physical approach was an excellent idea. During these four years, we had a lot of interesting technical discussions and they often provided me good advice and support to bring this endeavor to a good end. Their decision to involve me in the activities of GARTEUR (Group for Aeronautical Research and Technology in Europe) Action Group FM-AG(16) on Fault Tolerant Flight Control also greatly boosted my enthusiasm in this research project.

I also want to thank my PhD fellow ir. Diederick Joosten, together with his promoter prof. dr. ir. M. (Michel) Verhaegen and his co-promoter dr. ir. T.J.J. (Ton) van den Boom. His research activities at Delft Center of Systems and Control (DCSC) were financially supported under the same STW contract and are related to the results presented in this thesis. Our good cooperation and exchange of information over the past four years greatly improved the quality and pace of work at both sides.

The availability of a trustworthy simulation model, including realistic failure scenarios, was a very important contribution to this study. This model, which was developed by ir. M.H. (Hafid) Smaili and ir. J. (Jan) Breeman from the Dutch Aerospace Laboratory (NLR), provided an essential instrument in order to test the ability of the developed FTFC technologies to deal with a damaged aircraft model in some realistic failure scenarios.

In a research project, it is crucial to change the point of view to the problem at some point. Therefore, from February till May 2009, a research visit has been made at the department of Robotics and Mechatronics in the Deutsches Zentrum für Luft- und Raumfahrt (DLR) in Oberpfaffenhofen. During this period, dr. ir. G.H.N. (Gertjan) Looye acted as advisor. His fresh perspective on the problem resulted in many new ideas and insights. This re-invigorated and extended the research activities significantly. Moreover, the pleasant contact with all colleagues at the department made that four very enjoyable months in Germany passed by very quickly. The lovely area of Munich and the Fünf Seeënland certainly contributed in this...

This research was financially supported by the Dutch Technology Foundation STW (Stichting Toegepaste Wetenschappen) under project number 06515. Moreover, they organized bi-yearly user committee meetings with scientists from Dutch Space, NLR, TNO and Estec, which resulted often in interesting technical discussions, stimulating the research activities. In addition, STW supported financially the aforementioned research visit at DLR.

Another important group to be acknowledged is GARTEUR Action Group FM-AG(16). Cooperating in this group on the same research subject based upon a high fidelity benchmark simulation model, mentioned earlier, and having the opportunity to demonstrate the developed algorithms on the moving base SIMONA Research Simulator provided a spectacular stimulus to and acceleration of the research activities during the first three years of the research project. The intensive progress meetings offered frequent opportunities to share information and to have interesting technical discussions with the colleagues. Some of these group members are the group chairman dr. ir. J. (Jon) King from Qinetiq; the NLR colleagues mentioned before; the DCSC colleagues mentioned before together with dr. ir. R. (Redouane) Hallouzi; dr. ir. P. (Philippe) Goupil from Airbus; prof. dr. ir. C. (Chris) Edwards and dr. ir. H. (Halim) Alwi from Leicester University; prof. dr. ir. J.M. (Jan) Maciejowski from Cambridge University; dr. ir. A. (Andreas) Varga from DLR; prof. dr. ir. A. (Ali) Zolghradi, dr. ir. D. (David) Henri and dr. ir. J. (Jérôme) Cieslak from Bordeaux University; ir. S. (Shadhanan) Manickavasagar and ir. N. (Nick) Swain from Qinetiq; ir. A. (Adolfo) Solazzo from CIRA; and many others...

Several conferences have been attended to present research results of this project. At Safeprocess'09, the 7th IFAC Symposium on Fault Detection, Supervision and Safety of Technical Processes, in Barcelona, Spain, from 30th June to 3rd July 2009, the author has won the ABB award - Best application/case study paper. I would like to express my gratitude for receiving this award, for which I feel very honoured, to the ABB award committee members Prof. R. (Rolf) Isermann from Universität Duisburg-Essen, Prof. J. (Jacob) Stoustrup from Aalborg University, dr. A. (Alf) Isaksson from ABB, and Prof. Izadi-Zamanabadi.

Combining a PhD research with a significant teaching load is not straightforward. In order to be able to combine both successfully, I have had the pleasure to cooperate with some excellent teaching assistants in the past years, namely Rita Valente Pais, Cristina Duque Geraldes, Nuno Ricardo Salgueiro Filipe, Laurens Van Eykeren, Niek Beckers and Tom Verspecht. Without their valuable support, I would have been restricted to spend significantly less time to my research activities. The cooperation with MSc students Hervé Huisman, Ramon Grotens and Michiel van Schravendijk provided also very valuable contributions to my research. Moreover, I would like to express my gratitude to Olaf Stroosma, Herman Damveld and Mark Mulder who helped me to implement and demonstrate the control algorithm on the moving base SIMONA Research Simulator. Together with Hafid and a few professional pilots including Hessel Benedictus, we even managed to organize a complete experiment campaign to investigate the handling qualities and pilot work of this algorithm. Lots of thanks to my other colleagues Coen, Daan, Eddy, Elwin, Erik-Jan, Jan, Joost, Lars, Paul, Peter and Xander for all the nice moments in Delft and abroad during the past years.

I am most grateful to my parents and my brother Bart for their continuous strong support in all possible ways. Also a special word of thanks to my family and friends, who always showed their interest in my research. Finally, I would like to mention my study mate, parabolic flight partner and good friend Patricia Koppenaal (1980-2005), who played an important role in the start up phase of my PhD research.

This thesis is dedicated to my parents, my brother Bart and Patricia.

Thomas Lombaerts
Delft/Tervuren, April 2010

Curriculum Vitae

Thomas Lombaerts was born in Brussels (Etterbeek) on April 19, 1980. From 1992 to 1998 he attended the Sint Jozefscollege in Brussels (Sint Pieters Woluwe).

In 1998, he enrolled as a student at Delft University of Technology. In 2002, he completed a four month internship at the Royal Military Academy of Belgium in Brussels, working on the preliminary design of a mini unmanned aerial vehicle which has been built subsequently. After that, he started his masters program in Flight Guidance and Control and obtained his M.Sc. degree (cum laude) in Aerospace Engineering in April 2004. His final thesis was on the design of an automatic flight control system for the UAV which was designed during the internship.

In 2004 he started as additional lecturer at the division of Control and Simulation of Delft University of Technology, teaching the refurbished fourth year course "Automatic Flight Control System Design". This teaching activity still continues. In 2005 he started as a Ph.D. researcher at the same division. During this research project, he was involved in the GARTEUR (Group for Aeronautical Research and Technology in Europe) Action Group FM-AG(16) on Fault Tolerant Flight Control. He is also co-editor of the book "Fault Tolerant Flight Control - A Benchmark Challenge", published by Springer-Verlag, reporting on the results of this action group. During the Ph.D. project, a four month research visit was done at the Deutsches Zentrum für Luft- und Raumfahrt (DLR), department of Robotics and Mechatronics, in Oberpfaffenhofen, near Munich, Germany. He has won the ABB award - Best application/case study paper at Safeprocess'09, the 7th IFAC Symposium on Fault Detection, Supervision and Safety of Technical Processes, which was organized in Barcelona, Spain, from 30th June to 3rd July 2009, for the paper titled "Flight Control Reconfiguration based on a Modular Approach".

Currently, he is participating in the European funded FP7 research project "ADDSAFE", on Advanced Fault Diagnosis for Safer Flight Guidance and Control. The goal of this project is to develop and apply model-based fault detection and diagnosis methods for civil aircraft in order to increase aircraft safety and reduce development/maintenance costs.

Publications list

Only journal publications and book chapters are included here. There is also an extensive list of conference papers, but these are not included here.

Journal papers

- Lombaerts, T.J.J., H.O. Huisman, Q.P. Chu, J.A. Mulder, and D.A. Joosten; Nonlinear Reconfiguring Flight Control based on Online Physical Model Identification. Journal of Guidance, Control and Dynamics, 32(3):727–748, 2009.

- Lombaerts, T.J.J., M.H. Smaili, O. Stroosma, Q.P. Chu, J.A. Mulder, and D.A. Joosten; Piloted Simulator Evaluation Results of New Fault-Tolerant Flight Control Algorithm. Journal of Guidance, Control and Dynamics, 32(6):1747–1765, 2009.

- Lombaerts, T.J.J., E.R. Van Oort, Q.P. Chu, J.A. Mulder and D.A. Joosten; On-Line Aerodynamic Model Structure Selection and Parameter Estimation for Fault Tolerant Control. Scheduled for publication in the May-June issue of the AIAA Journal of Guidance, Control and Dynamics.

- Thomas Lombaerts, Ping Chu, Jan Albert Mulder, Diederick Joosten; Modular Flight Control Reconfiguration Design and Simulation. Invited for a special Safeprocess'09 section in Control Engineering Practice. Under review.

- Thomas Lombaerts, Gertjan Looye, Ping Chu, Jan Albert Mulder; Fault Tolerant Flight Control, a Physical Model Approach. Submitted to Aerospace Sciences and Technology. Under Review.

Book chapters

- Lombaerts, Thomas, Hafid Smaili and Jan Breeman; Introduction. In: Fault Tolerant Flight Control, A Benchmark Challenge. Lecture Notes in Control and Information Sciences, SpringerVerlag, Berlin, 2010.
- Smaili, Hafid, Jan Breeman, Thomas Lombaerts and Diederick Joosten; RECOVER: A Benchmark for Integrated Fault Tolerant Flight Control Evaluation. In: Fault Tolerant Flight Control, A Benchmark Challenge. Lecture Notes in Control and Information Sciences, SpringerVerlag, Berlin, 2010.
- Lombaerts, Thomas, Diederick Joosten, Hafid Smaili and Jan Breeman. Assessment criteria as specifications for reconfiguring flight control. In: Fault Tolerant Flight Control, A Benchmark Challenge. Lecture Notes in Control and Information Sciences, SpringerVerlag, Berlin, 2010.
- Lombaerts, Thomas, Ping Chu and Jan Albert Mulder. Flight Control Reconfiguration based on online physical model identification and nonlinear dynamic inversion. In: Fault Tolerant Flight Control, A Benchmark Challenge. Lecture Notes in Control and Information Sciences, SpringerVerlag, Berlin, 2010.
- Stroosma, Olaf, Thomas Lombaerts, Hafid Smaili and Mark Mulder. Real-time assessment and piloted evaluation of FTFC methods in the SIMONA research flight simulator. In: Fault Tolerant Flight Control, A Benchmark Challenge. Lecture Notes in Control and Information Sciences, SpringerVerlag, Berlin, 2010.
- Lombaerts, Thomas, Hafid Smaili, Olaf Stroosma, Ping Chu and Jan Albert Mulder. SIMONA evaluation results for online physical model identification and nonlinear dynamic inversion based controller. In: Fault Tolerant Flight Control, A Benchmark Challenge. Lecture Notes in Control and Information Sciences, SpringerVerlag, Berlin, 2010.